Computational Modeling and Impact Analysis of Textile Composite Structures

Hur, Hae-Kyu

Dissertation submitted to the faculty of the
Virginia Polytechnic Institute and State University
in partial fulfillment of the requirements for the degree of

Doctor of Philosophy
in
Aerospace Engineering

Rakesh K. Kapania (Chair)
Liviu Librescu (Co-chair)
Michael W. Hyer
Scott W. Case
Mayuresh Patil

August 15th, 2006
Blacksburg, Virginia

Keywords: Homogenization, Repeating Unit Cell, Textile Composites, Cohesive Element, Ballistic Impact

Copyright ©2006, Hae-Kyu Hur

Computational Modeling and Impact Analysis of Textile Composite Structures

Hur, Hae-Kyu

ABSTRACT

This study is devoted to the development of an integrated numerical modeling enabling one to investigate the static and the dynamic behaviors and failures of 2-D textile composite as well as 3-D orthogonal woven composite structures weakened by cracks and subjected to static-, impact- and ballistic-type loads. As more complicated modeling about textile composite structures is introduced, some of homogenization schemes, geometrical modeling and crack propagations become more difficult problems to solve. To overcome these problems, this study presents effective mesh-generation schemes, homogenization modeling based on a repeating unit cell and sinusoidal functions, and also a cohesive element to study micro-crack shapes.

This proposed research has two: 1) studying behavior of textile composites under static loads, 2) studying dynamic responses of these textile composite structures subjected to the transient/ballistic loading. In the first part, efficient homogenization schemes are suggested to show the influence of textile architectures on mechanical characteristics considering the micro modeling of repeating unit cell. Furthermore, the structures of multi-layered or multi-phase composites combined with different laminar such as a sub-laminate, are considered to find the mechanical characteristics. A simple progressive failure mechanism for the textile composites is also presented.

In the second part, this study focuses on three main phenomena to solve the dynamic problems: micro-crack shapes, textile architectures and textile effective moduli. To obtain a good solutions of the dynamic problems, this research attempts to use four approaches: **I)** determination of governing equations via a three-level hierarchy: micro-mechanical unit cell analysis, layer-wise analysis accounting for transverse strains and stresses, and structural analysis based on anisotropic plate layers, **II)** development of an efficient computational approach enabling one to perform transient response analyses of 2-D plain woven, 2-D braided and 3-D orthogonal woven composite structures featuring matrix cracking and exposed to time-dependent ballistic loads, **III)** determination of the structural characteristics of the textile-layered composites and their degraded features under smeared and discrete cracks, and assessment of the implications of stiffness degradation on dynamic response to impact loads, and finally, **IV)** the study of the micro-crack propagation in the textile/ceramic layered plates.

A number of numerical models have been carried out to investigate the mechanical behavior of 2-D plain woven, 2-D braided and 3-D orthogonal woven textile composites with several geometrical representations, and study also the dynamic responses of multi-layered or textile layered composite structures subjected to ballistic impact penetrations with a developed in-house code.

Acknowledgements

First and foremost the author would like to express a profound gratitude to my father, departed mother, brothers and wife for their eternal support and constant encouragement during my studies.

The author would like to acknowledge Prof. Kapania, Prof. Hyer, Prof. Librescu, Prof. Case and Prof. Patil, for their precious time and helpful suggestions during the past years of this research. The author would also like to thank Dr. A.E. Bogdanovich of 3-TEX Co. for sharing his knowledge and literature of textile composite structures.

The financial support provided by the Chassis Advanced Technology Department at Visteon Corporation, USA and the Korea Electronic Power Research Institute, Korea is appreciated, while completing this research.

Table of Contents

Title i
Abstract ii
Acknowledgements iii
Table of Contents iv
List of Figures ix
List of Tables xviii
Chapter 1 Introduction and Review. 1
1.1 Introduction 1
1.2 Overview of Textile Composite Structures 2
1.2.1 2-D Weaves 3
1.2.2 2-D Braids 3
1.2.3 3-D Braids 3
1.2.4 Orthogonal Non-woven Composites 3
1.2.5 Knitted 3-D Fabrics 3
1.3 Background and Literature Review 4
1.3.1 Analytical/Numerical Modeling for Textile Composites. 4
1.3.2 Impact Modeling for Standard/Textile Composites 5
1.3.3 Impact Modeling for Multi-layered Structures 6
1.3.4 Problem Statement of Textile Composite Structures 7
1.4 Objectives of Dissertation 7
References 8
Chapter 2 Homogenization I of 2-D Plane Woven Textile Composite 16
2.1 Introduction 16
2.2 Geometrical Modeling for Plain Woven Textile Composite 16
2.3 Sine Function Model I (SFM I) for Plain Woven Textile Composite 16
2.4 Sub-domain Zone for Repeating Unit Cell 18
2.5 Equivalent Modulus for Plain Woven Textile Composite 21
2.6 Overall Coefficients of Thermal Expansion (CTE) for 2-D Plain Textile Composite 24
2.7 Validation of Sine Function Model in 2-D Plain Textile Composite 26
2.7.1 Open-Weave Case of Plain Woven Composite 26
2.7.2 Closed Weave Case I of Plain Woven Composite 26
2.7.3 Closed Weave Case II of Plain Woven Composite 27

References . . . 37
Chapter 3 Homogenization II of 2-D Plane Woven Textile Composite . . . 38
3.1 Introduction . . . 38
3.2 Sine Function Model II for Strengthened Plain Woven Textile Composites . . . 38
3.3 Equivalent Modulus for Resin-Strengthened Plain Woven Textile Composite . . . 45
3.4 Validation of Sine Function Model II . . . 46
3.4.1 Open-Weave Case of Plain Woven Composite . . . 46
3.4.2 Closed Weave Case of Plain Woven Composite . . . 48
References . . . 54
Chapter 4 Sub-cell Block Model of 2-D Plain Woven Textile Composite . . . 55
4.1 Introduction . . . 55
4.2 Theoretical Equations of Multi-layered Laminates . . . 55
4.3 Basic Assumptions for Sub-cell Block Model . . . 57
4.4 Average Stresses and Strains of Sub-cell Block Model . . . 57
4.5 The Constitutive Behaviors of the Sub-cell Block Model . . . 62
4.6 The Volume Fraction of Sub-cell Block Model . . . 64
4.7 Effective Elastic Moduli of Sub-cell Block Model . . . 65
4.8 Computational Procedures . . . 65
4.9 Numerical Examples for 2-D Plain Woven Textile Composites . . . 66
4.10 Numerical Examples for Multi-layered Laminates . . . 66
4.11 Discussion . . . 67
References . . . 78
Chapter 5 Homogenization of 2-D Braided / 3-D Woven Textile Composites . . . 79
5.1 Introduction . . . 79
5.2 Geometrical Modeling of 2-D Braided Textile Composites . . . 79
5.3 Equivalent Moduli for 2-D Braided Textile Composites . . . 82
5.4 Model Validation for 2-D Braided Textile Composites . . . 84
5.5 Modeling of 2x2 2-D Tri-axial Braid RUC . . . 95
5.6 Cross Section of Axial and Braider Yarns . . . 97
5.7 Three-Dimensional Effective Moduli for 2x2 2-D Tri-axial Braids . . . 102
5.8 Numerical Results and Comparisons . . . 105
5.9 Models for 3-D Orthogonal Woven Composites . . . 107
5.9.1 Unit-cell Model of 3-D Orthogonal Woven Composites . . . 107
5.9.2 Laminate Block Model of 3-D Orthogonal Woven Composites . . . 107

5.9.3 3-D Mosaic Model of 3-D Orthogonal Woven Composites 107
5.10 Discussion 118
References 118
Chapter 6 Failure Analysis of Micro-Cracked Textile Composites 119
6.1 Introduction 119
6.2 Micro-crack Modeling for Cracked Textile Composites 119
6.3 Numerical Example for Crack Density Scheme 120
6.4 Degraded Equivalent Modulus of Closed Plain Weaves 121
6.5 Degraded Equivalent Modulus of 2-D Closed Weave Braided Textile 121
6.6 Degraded Equivalent Modulus of 3-D Orthogonal Woven Textile Composite 121
6.7 Micro-Crack Modeling for Plain Woven Textile Composite 136
6.8 Material Non-linearity of Yarns 136
6.9 Stress and Strain in ABAQUS UMAT Subroutine 137
6.10 Failure Criteria 137
6.11 Progressive Failure Analysis 138
6.12 Results of Progressive Failure Analysis 139
6.13 Discussion 140
References 153
Chapter 7 Cohesive Element Formulations for Fracture Modeling 154
7.1 Introduction 154
7.2 Cohesive Zone Model 154
7.3 Fundamental Equations of Cohesive Zone Model 156
7.4 Force Vectors of Cohesive Element 158
7.5 Stiffness and Force Matrix of Cohesive Element 163
7.6 Constant Strain Triangle Element 166
7.7 Cohesive Element Modeling for Dynamic Analysis 167
7.8 Algorithm of the Central Difference Method 168
7.9 Cohesive Element Modeling of Simple Bar Cases 169
7.10 Cohesive Element Modeling of Central Split Block Case 174
References 178
Chapter 8 Contact Mechanics of Cohesive Element Modeling 179
8.1 Introduction 179
8.2 Empirical Contact Modeling 179
8.3 Un-cracked Elements' Contact Modeling 180

8.4 Cracked Elements' Contact Modeling 182
8.5 Erosion Contact Modeling 186
8.6 Numerical Examples of Un-cracked Elements' Contact Modeling 186
8.7 Numerical Examples of Cracked Elements' Contact Modeling 189
References 197
Chapter 9 Impact Mechanics Using Cohesive Element Modeling 198
9.1 Introduction 198
9.2 Analytical Impact Modeling 198
9.3 Numerical Examples for Analytical Impact Modeling 200
9.4 Penetration at High Velocity 202
9.5 Numerical Examples for High Velocity Penetration 207
9.6 Penetration of Multi-layered Structures 214
References 227
Chapter 10 Impact Analysis of Micro-Cracked Textile Composites 229
10.1 Introduction 229
10.2 Technical Approach of Micro-Cracked Textile Composites' Impact Modeling 229
10.2.1 Micro-mechanical Analysis 230
10.2.2 Layer-wise Analysis 230
10.2.3 Structural Analysis 231
10.3 Review of General Shell Structures' Dynamic Behaviors 232
10.4 Dynamic Behaviors of Textile Shell Structures 240
10.5 Main Categories of Ballistic Impact Behaviors in Textile Layered Structures 243
10.6 Ballistic Impact Examples of 2-D Plain Woven,
2-D Braided and 3-D Woven Textile Structures 244
10.7 Damage Behavior of 2-D Plain Woven,
2-D Braided and 3-D Woven Textile Structures 254
10.8 Dependency of Mesh Unit Cell Sizes 255
10.9 Meso-scale Modeling of Textile Composite Structures 255
10.9.1 Geometry Modeling of Repeating Unit Cell 256
10.9.2 Layer Modeling 261
10.9.3 Structural Modeling 261
10.10 Concluding Remarks 261
References 268
Chapter 11 Summary and Conclusion 269

11.1 Summary 269
11.2 The Sine Function Model I & II (SFM I&II) and Sub-cell Block Model 270
11.3 The Failure Analysis of Micro-Cracked Textile Composite 270
11.4 The Contact and Impact Mechanics of Cohesive Element Modeling 270
11.5 The Impact Analysis of Micro-Cracked Textile Composites 271
Appendix A: Transformation Matrix of Yarns 272
Appendix B: Transformation Stiffness Matrix of Yarns. 273
Appendix C: Assumptions of Micro-cracking in Composites 275
Appendix D: Micro-mechanical Model of Fiber Composites 277
Appendix E: Elastic-Plastic Implementation 278
Appendix F: Numerical Verifications of Degenerated Shell Program 282
References 288
About the Author 289

List of Figures

1.1 Hierarchical nature of textile reinforced composite materials. 11
1.2 RUC of 3-D orthogonal woven and 2-D plain woven composite without resin and with resin . . 12
1.3 Commonly used 2-D weave patterns 13
1.4 Tri-axial weave 13
1.5 Some common 2-D braid patterns 14
1.6 Structural geometry of 3-D orthogonal composites 15
1.7 Types of stitching used for through the thickness reinforcement 15
2.1 Repeating Unit Cell (RUC) for Plain Weave 19
2.2 Shapes for the fill and warp yarns and resin layers 19
2.3 5-different interval points in RUC 20
2.4 2-sectional points in RUC 20
2.5 Cross sectional shapes at 5-different points. 21
2.6 Sectional shape at B_1-B_1 point: warp direction 22
2.7 Sectional shape at B_2-B_2 point: fill direction 22
2.8 Sectional shape for the open weaves 22
2.9 Sectional shape for the closed weaves 22
2.10 Components of the sub-domain zone and one sectional shape in the RUC 23
2.11 RUC and sectional shapes of 2-D flat-balanced plain weaves 32
2.12 Plain weave moduli, Poisson's ratio and crimp angle with various flat-balanced yarns 33
2.13 Plain weave moduli, Poisson's ratio and
crimp angle with various elliptical yarns of SFM I. 34
2.14 Variation of plain weave crimp angle and CTE's with a various yarn sizes 35
2.15 Variation of plain weave crimp angle and CTE's with yarn sizes and crack densities 36
3.1 Repeating Unit Cell (RUC) for strengthened plain weave 39
3.2 The Repeating Unit Cell (RUC) components of the SFM II. 40
3.3 Interfaced yarn cross-sections: warp and fill directions 41
3.4 Two sectional points in the RUC 42
3.5 Components of the sub-domain zone and a cross-section in the RUC 47
3.6 Variation of E_x as a function of h/a 50
3.7 Variation of G_{xy} as a function of h/a 50

3.8 Variation of ν_{xy} as a function of h/a 50
3.9 Variation of α_x as a function of h/a 50
3.10 E_x as a function of h/a and β values 51
3.11 G_{xy} as a function of h/a and β values. 51
3.12 ν_{xy} as a function of h/a and β values. 51
3.13 α_x as a function of h/a and β values 51
3.14 RUC shapes of three composite systems 52
4.1 Sub-laminate with N-laminae 56
4.2 Homogeneous equivalent medium 56
4.3 RUC and Unit Cell of 2-D plain weaves and 4 sectional points in a unit cell 59
4.4 Sectional views of sub-cell block model 59
4.5 Components of the sub-cell and a sectional shape 60
4.6 Components of the sub-cell block and a sectional shape 61
4.7 Plain weave moduli, Poisson's ratio and crimp angle with various flat-balanced yarns 69
4.8 Plain weave moduli, Poisson's ratio and crimp angle with a number of sub-cell blocks 70
4.9 Dependency of effective moduli on θ for $[0^o/\theta/-\theta/90^o]$ Graphite-Epoxy composite 76
4.10 Dependency of effective Poisson's ratios on θ for $[0^o/\theta/-\theta/90^o]$ Graphite-Epoxy composite 76
4.11 Thickness-wise Poisson's ratios on θ for $[\pm\theta]$ laminate 77
5.1 2-D braided RUC geometry and cross-sectional shapes along the section A-A 80
5.2 Sectional shapes of $+\theta_{br}/-\theta_{br}$ braider yarns along the 1- and 2-axes 82
5.3 Undulating geometry shapes of $+\theta_{br}/-\theta_{br}$ braider yarns along the 1- and 2-axes 86
5.4 Variation of 2-D braid stiffness and Poisson's ratio with braid angles based on SFM I 87
5.5 Variation of 2-D braid stiffness and Poisson's ratio with braid angles using sub-cell block model 88
5.6 Three different yarn shapes (2K, 10K and 18K). 89
5.7 Effect of yarn sizes on E_{xx}, E_{yy} and ν_{xy} with braid angles. 90
5.8 Effect of yarn sizes on E_{zz} and ν_{yz} with braid angles 91
5.9 Effect of yarn sizes on G_{xy} and ν_{xz} with braid angles 92

5.10 Variation of 2-D braided composite crimp angle and CTE's with braid angles 93
5.11 Variation of 2-D braided composite CTE's and crimp angle with braid angles and crack densities 94
5.12 Repeating Unit Cell of a 2x2 2-D tri-axial braided composite; cross-sectional view along the section A-A 96
5.13 Geometry of Repeating Unit Cell plan-form 98
5.14 Geometry of the first axial yarn centerline 98
5.15 Geometry of cross-section along the section B-B 99
5.16 Geometry of braider yarn cross-section. 101
5.17 Undulating geometry of the $+\theta_{br}$ braider yarn 105
5.18 Cross-sectional micrographs of 2x2 2-D tri-axial braided composites from Ref. [5.1] 108
5.19 Variation of stiffness and Poisson's ratio with V_f for 2x2 2-D tri-axial braided composite. . . . 110
5.20 Variation of crimp angle and CTE's with V_f for 2x2 2-D tri-axial braided composite. 110
5.21 Variation of stiffness and Poisson's ratio with V_f considering Rule of mixtures 111
5.22 Variation of crimp angle and CTE's with V_f considering crack density and Rule of mixtures 111
5.23 Variation of stiffness and Poisson's ratio with V_f considering Self-Consistent method 112
5.24 Variation of crimp angle and CTE's with V_f considering crack density and Self-Consistent method 112
5.25 A simplified 3-D orthogonal woven composite 113
5.26 A 3-D orthogonal woven fabric unit cell 113
5.27 A 3-D orthogonal woven unit cell 113
5.28 A simplified 3-D orthogonal woven composite 115
5.29 The laminate block model of 3-D orthogonal woven fabric 115
5.30 The 3-D Mosaic model of 3-D orthogonal woven fabric 117
6.1 Aligned fibers and slit cracks in a continuous matrix 122
6.2 Warp yarn with small diameter fibers and slit cracks 122
6.3 Stiffness changes of VS0054 Graphite/Epoxy composite with longitudinal slit cracks (Unit:GPa) 123
6.4 Fill yarn stiffness reduction of E-Glass / Vinylester with longitudinal slit cracks 125
6.5 Warp yarn stiffness reduction of E-Glass / Vinylester with longitudinal slit cracks 126
6.6 Degraded modulus of closed weaves with a variety of crack densities and

volume fractions 127
6.7 Yarn stiffness reduction of 2-D braided textile composites with longitudinal slit cracks 128
6.8 Degraded modulus of 2-D braids with a variety of crack densities and volume fractions 129
6.9 The laminate block model of 3-D orthogonal woven fabric with resin and no resin 131
6.10 The unit cell model of 3-D orthogonal woven fabric with small diameter fibers and slit cracks 131
6.11 Fill yarn stiffness reduction of 3-D orthogonal woven textile with longitudinal slit cracks . . . 132
6.12 Warp yarn stiffness reduction of 3-D orthogonal woven textile with longitudinal slit cracks . . 133
6.13 Degraded modulus of 3-D orthogonal woven textile with a variety of crack densities and volume fractions 134
6.14 The degraded elastic modulus with various crack densities and packing factors 135
6.15 Flowchart for UMAT implementation in ABAQUS 142
6.16 Geometry of Repeating Unit Cell in the plain weaves 143
6.17 Tensile stress and strain curves for AS4-Carbon / Epoxy plain weave 145
6.18 Shear stress and strain curves for AS4-Carbon / Epoxy plain weave 145
6.19 Compression stress and strain curves for AS4-Carbon / Epoxy plain weave 146
6.20 Tension stress of the warp yarns (Rule of mixture $\beta = 0.0$ case) 146
6.21 Shear stress of the fill and warp yarns (Self-Consistent method $\beta = 0.0$ case) 146
6.22 Tensile stress and strain curves for E-Glass / Epoxy plain weave 147
6.23 Shear stress and strain curves for E-Glass / Epoxy plain weave 147
6.24 Compression stress and strain curves for E-Glass / Epoxy plain weave 148
6.25 Tension stress of the fill and warp yarns (Rule of mixture $\beta = 0.0$ case) 148
6.26 Shear stress of the fill and warp yarns (Self-Consistent method $\beta = 0.0$ case) 148
6.27 Distribution of fiber-damage due to tension in E-Glass / Epoxy plain weaves 149
6.28 Distribution of fiber-damage due to shear in E-Glass / Epoxy plain weaves 150
6.29 Distribution of fiber-damage due to compression in E-Glass / Epoxy plain weaves 151
7.1 Unloading condition of elastic-damaged to the origin 155
7.2 Unloading condition of elastic-undamaged with initial stiffness 155
7.3 Plots between the normal and the shear separations 157
7.4 Multi-phase solid with an interface region from Ref. [7.4] 159
7.5 Plot of the normal traction to the normal separation ($\Delta_t = 0$) 160
7.6 Plot of the shear traction to the shear separation ($\Delta_n = 0$, $q = 1.0$ and $q = 0.4289$) 160
7.7 Unloading cases of the normal traction and separation 161

7.8 Unloading cases of the shear traction and separation 161
7.9 4-cohesive elements' arrangement and node connection 162
7.10 Un-deformed and deformed 4-cohesive elements with integration points 162
7.11 A deformed cohesive element formed by tractions, separations, nodes and angles 163
7.12 Schematics of micro-cracks using the irreversible loading and unloading normal traction value 165
7.13 Reference configuration and current configuration 167
7.14 The bar model subjected to the impulse tension-loading 170
7.15 Applied forces history in the bar 171
7.16 Longitudinal velocities' curve at the monitored node in the bar 171
7.17 Applied loading history and boundary conditions of the compression bar 172
7.18 Deformed shapes of the compression bar at the different time steps 172
7.19 Transient normalized stress waves in the bar under compression 173
7.20 The center split block model and stresses at t =0.4995 μ sec 175
7.21 The deformed shapes and stress (σ_{11}) of the split block 176
7.22 The deformed shapes and stress (σ_{22}) of the split block 177
8.1 Contact forces and indentation for the plastic contact cases 181
8.2 Contact forces and indentation for the elastic contact cases 181
8.3 Contact surfaces between the striker and the target elements 183
8.4 Contact penetration between the contact segments 183
8.5 The penetration point and the target contact segments 184
8.6 A circular pseudo-element and a CST element 185
8.7 Contact conditions between two elements 185
8.8 Stress and strain curve for a ductile material 187
8.9 Updating contact lines for the ductile material 188
8.10 Deformed shapes of two impacted blocks 191
8.11 Resultant force history 191
8.12 Hertzian contact model and contact force history in elastic and plastic models 192
8.13 Transferred impulse of the plate and momentum changes of the cylinder 192
8.14 Configurations and normalized energies of a copper rod contacting the rigid wall 193
8.15 Three contact cases in the linear and angular momentums 194
8.16 The linear and angular momentum history for two element contact cases 195
8.17 Multiple interacted contacts in the cohesive elements 196

9.1 Normalized force curves for plastic impact and perforation impact 199
9.2 The projectile-time history of position, velocity and force for impact by a steel sphere 203
9.3 Impact deformations of the plastic impact case, V_i =199 ft/sec 203
9.4 The projectile-time history of position, velocity and force for impact by a steel sphere 204
9.5 Impact deformations of the perforation impact case, V_i =497 ft/sec 204
9.6 The projectile-time history of position, velocity and force for impact by a cylindro-con 205
9.7 Impact deformations of the perforation impact case, V_i =301 ft/sec 205
9.8 Penetration process of the high velocity projectile 208
9.9 Erosion region between the high velocity projectile and the target 208
9.10 Penetration as function of projectile velocity for high velocity impacts 209
9.11 Penetration velocity as function of projectile velocity for high velocity impacts 209
9.12 Penetration of a gold projectile into an aluminum plate 210
9.13 Schematic geometry for an impacting rod and an infinite block 210
9.14 Comparison of penetrations for different projectile impacts 211
9.15 Comparison of penetrations for different projectile velocities 211
9.16 Penetration shapes for two different material projectiles with a velocity V_P =5000m/sec 212
9.17 Penetration shapes for an aluminum rod with
two different velocities V_P = 2000 & 4000m/sec 213
9.18 Contact forces' history and model of a ceramic plate target and
a circular-nosed projectile 215
9.19 Deformed shapes of a ceramic plate target and a circular-nosed projectile (V =100m/sec) . . . 216
9.20 Deformed shapes of a ceramic plate target and a circular-nosed projectile (V =300m/sec) . . . 217
9.21 A 7.62 mm projectile and
an armor plate consisting of AD-85 alumina bonded to 6061-T6 aluminum 218
9.22 Oblique impact of a 7.62 mm projectile and an armor plate. 218
9.23 Normalized kinetic and internal energies of normal and oblique projectiles 219
9.24 Impact velocities of normal and oblique projectiles 219
9.25 Calculated configurations of an armor plate and
a 7.62 mm ball projectile (V =850 m/sec) 220
9.26 Fracture patterns of an armor plate and
a 7.62 mm ball projectile (V =850 m/sec) 221

9.27 Calculated configurations of an armor plate and
a 7.62 mm ball projectile (V =850 m/sec) 222
9.28 Fracture patterns of an armor plate and
a 7.62 mm ball projectile (V =850 m/sec) 223
9.29 Oblique high-velocity impact of a 7.62 mm projectile and an alumina plate 224
9.30 Normalized kinetic and internal energies and
impact velocities of high speed-oblique projectiles 224
9.31 Calculated configurations of an alumina plate and
a 7.62 mm ball projectile (V =1800 m/sec) 225
9.32 Fracture patterns of an alumina plate and
a 7.62 mm ball projectile (V =1800 m/sec) 226
10.1 The 2-D plain weave and 3-D orthogonal woven fabric without resin 233
10.2 The unit cell model of 3-D woven and 2-D plain woven yarn with small slit cracks 233
10.3 A textile panel with 4 by 4 RUC and 2-D & 3-D textile shapes of 2 by 2 RUC 234
10.4 Four lamina layers of 3-D orthogonal woven fabric (top, fill, warp and bottom lamina) 234
10.5 Three-level hierarchy modeling (micro, layer-wise and structural analyses) 235
10.6 Finite element mesh for simply supported rectangular plate problem 236
10.7 Central deflection and bending moment history for $\alpha = 0.2$ 236
10.8 Central deflection and bending moment history for $\alpha = 0.1$ 237
10.9 Problem plate geometry and loading 237
10.10 Central deflection and bending moment history for an initially stressed plate 238
10.11 Symmetric quadrant of clamped circular plate 238
10.12 Central deflection and bending moment versus time 239
10.13 Symmetric quadrant of the spherical cap with uniform pressure 239
10.14 Central deflection and residual force versus time 240
10.15 Three yarn sizes and symmetric quadrant of clamped circular textile-layered plate 241
10.16 Plate deformations at three different points and central deflection time history 241
10.17 Symmetric quadrant of the spherical textile layered cap with uniform pressure 242
10.18 Central deflection time histories with various crack densities and gap-lengths 242
10.19 Main steps for textile composite structures' dynamic behaviors with the cohesive element . . . 244
10.20 Normal/oblique impact modeling of a 7.62 mm projectile and an alumina and
textile layered plate. 246
10.21 Normal impact velocities of the projectile in two different 2-D plain weave and

ceramic layered plates 247
10.22 Normalized internal and kinetic energies of the projectile during normal impact 247
10.23 Oblique impact velocities of the projectile in two different 2-D plain weave and ceramic layered plates 248
10.24 Normalized internal and kinetic energies of the projectile in the oblique impact 248
10.25 Contact forces of the normal/oblique impact projectile into a 2-D plain weave and ceramic layered plate 249
10.26 Contact forces of the normal/oblique impact projectile into a 2-D plain weave and ceramic layered plate 249
10.27 Normal and oblique impact velocities of the projectile in a different 2-D braid and ceramic layered plate 250
10.28 Normalized internal and kinetic energies of the projectile in the normal and the oblique impact. 250
10.29 Normal and oblique impact velocities of the projectile in a different 2-D braid and ceramic layered plate 251
10.30 Normalized internal and kinetic energies of the projectile in the normal and the oblique impact 251
10.31 Contact forces of the normal/oblique impact projectile into a 2-D braid and ceramic layered plate 252
10.32 Contact forces of the normal/oblique impact projectile into a 2-D braid and ceramic layered plate 252
10.33 Normal impact velocities of the projectile in a different 3-D orthogonal weave and ceramic layered plate 253
10.34 Normalized internal and kinetic energies of the projectile in the normal impact 253
10.35 The normal/oblique impact projectile contact forces of 3-D orthogonal weave and ceramic layered plate 254
10.36 The damage tolerances of normal/oblique impact cases in R.A. Naik model and P. Tan model 256
10.37 The damage tolerances of normal/oblique impact cases in Sine Function Model I and P. Tan model 256
10.38 Normal impact configurations of a 2-D plain woven textile layered armor plate and a bullet 257
10.39 Fracture patterns of a 2-D plain woven textile layered armor plate and a bullet (V =850 m/sec) 258

10.40 Oblique impact configurations of a 2-D plain woven textile layered armor plate and a bullet 259
10.41 Fracture patterns of a 2-D plain woven textile layered armor plate and a bullet (V =850 m/sec) 260
10.42 Three different mesh unit cells for the textile and ceramic layered plates 262
10.43 Normal impact velocities of the projectile in different mesh unit cells 263
10.44 The damage tolerances of normal impact cases in Sine Function Model I and P. Tan model 263
10.45 Oblique impact velocities of the projectile in different mesh unit cells 264
10.46 The damage tolerances of oblique impact cases in Sine Function Model I and P. Tan model 264
10.47 Components and one layer for the 2-D plain woven textile composites 265
10.48 Components and one multi-layer with a ceramic and 2-D plain woven textile composite 266
10.49 Macro- and meso-impact modeling for a 2-D plain woven textile and ceramic layered plate 267

List of Tables

2.1 The geometrical parameters for plain weave fabric yarns from Ref. [2.1] 29
2.2 Elastic properties of fiber and resin from Ref. [2.1] 29
2.3 The fiber volume fractions of V_f^o and V_{fyarn} from Ref. [2.1] 29
2.4 Comparison predicted elastic properties and experimental results of plain weave fabric lamina from Ref. [2.1] 30
2.5 Elastic properties of fiber and resin from Ref. [2.4] 31
2.6 The geometrical parameters for plain weave fabric yarns from Ref.[2.4] 31
2.7 Comparison mechanical properties for the yarns from Ref. [2.4] 31
2.8 Comparison of model and experimental results for the plain weaves from Ref. [2.4] 31
2.9 Yarn and resin properties used in this analysis from Ref. [2.3] 36
3.1 The geometrical parameters for plain weave fabric yarns from Ref. [3.1] 46
3.2 Elastic properties of fiber and resin from Ref. [3.1] 46
3.3 The fiber volume fractions of V_f^o and V_{fyarn} from Ref. [3.1] 48
3.4 Comparison predicted elastic properties and experimental results of plain weave fabric lamina from Ref. [3.1] 49
3.5 Elastic properties of fiber and resin from Ref. [3.3] 53
3.6 The geometrical parameters for plain weave fabric yarns from Ref. [3.3] 53
3.7 Comparison mechanical properties for the yarns from Ref. [3.3] 53
3.8 Comparison of model and experimental results for the plain weaves from Ref.[3.3] 53
4.1 Material properties for laminas in the sub-laminate from Ref. [4.4] 71
4.2 Comparison of effective engineering modulus predictions for Boron-Epoxy sub-laminate . . . 71
4.3 Material properties for $[0/\pm 60]$ Graphite-Epoxy sub-laminate from Ref. [4.1] 73
4.4 Effective engineering modulus for $[0/\pm 60]$ Graphite-Epoxy sub-laminate 73
4.5 Effective thermal expansion constants for $[0/\pm 60]$ Graphite-Epoxy sub-laminate 73
4.6 Effective engineering modulus for $[0_{Al}/90_{Gr}/45_{Gl}/\text{-}45_{Br}]$ sub-laminate 74
4.7 Effective engineering modulus for $[30_{Al}/\text{-}30_{Gr}/30_{Gl}/\text{-}30_{Br}]$ sub-laminate 75
4.8 Moduli for four composite materials from Ref. [4.3] 77
5.1 Comparisons of effective properties for 45-degree braid angle from Refs. [5.1-5.2] 94
5.2 Configurations of 2x2 2-D tri-axial braided composites from Ref. [5.1] 106
5.3 Yarn and resin properties for the 2x2 2-D tri-axial braids from Ref. [5.1] 106

5.4 Comparisons of moduli results for 2x2 2-D tri-axial braids from Ref. [5.1] 109
5.5 Comparisons of Poisson's ratios, yarn thickness ratio and crimp angles from Ref. [5.1] 109
5.6 The geometrical parameters for warp, weft and z-yarns from Ref. [5.6] 114
5.7 The volume fractions of yarns for A~C cases 114
5.8 The equivalent elastic properties for A case from Ref. [5.6] 114
5.9 The geometrical parameters for warp, fill and z-yarns from Ref. [5.6] 116
5.10 The equivalent elastic properties for cases from Ref. [5.6] 116
5.11 The equivalent elastic properties for cases calculated by present analysis 116
5.12 The total volume fractions for warp, fill and z lamina blocks 116
5.13 Comparisons of the effective elastic characteristics from Ref. [5.7] 117
5.14 Comparisons of the effective elastic properties from Ref. [5.7] 117
6.1 Elastic properties for VS 0054 Graphite/Epoxy from Ref. [6.1] 124
6.2 Elastic properties of fiber and resin from Ref. [6.2] 124
6.3 The geometrical parameters for plain weave fabric yarns from Ref. [6.2] 124
6.4 Elastic properties for the 2-D braided textile composites from Ref. [6.3] 124
6.5 The engineering elastic properties for Carbon/Epoxy from Ref. [6.4] 130
6.6 The geometrical parameters for warp, weft and z-yarns from Ref. [6.4] 130
6.7 The yarn volume fractions of A~C cases 130
6.8 Degradation factors for elastic modulus 141
6.9 Degradation factors for Poisson's ratios 141
6.10 The geometrical parameters of AS4 Carbon /Epoxy plain weave from Ref. [6.6] 143
6.11 The mechanical properties of AS4 Carbon fiber and 3501-6 Epoxy from Ref. [6.6] 143
6.12 The geometrical parameters of a plain weave from Ref. [6.11] 144
6.13 The mechanical properties of E-Glass fiber and Epoxy from Ref. [6.11] 144
6.14 The ultimate strengths of AS4 Carbon fiber and 3501-6 Epoxy from Ref. [6.6] 144
6.15 The ultimate strengths of E-Glass fiber and Epoxy from Ref. [6.11] 144
6.16 Comparisons of predicted ultimate tensile and shear strengths for AS4 Carbon / Epoxy composites 152
6.17 Comparisons of predicted ultimate tensile and shear strengths for E-Glass / Epoxy composites 152
7.1 The material properties of Aluminum 7075-T6 170
7.2 The material properties and cohesive element parameters of PMMA from Ref. [7.1] 174
8.1 Mechanical properties for the target plate and the projectile 189
9.1 Mechanical properties for the target plate and the projectile from Ref. [9.2-9.3] 200

9.2 Comparison of plastic impact and perforation impact 202
9.3 Physical and experimental properties of impact rod from Ref. [9.9] 209
9.4 Mechanical properties for the plate target and the circular-nosed projectile 215
9.5 Mechanical properties for AD-85 alumina and 6061-T6 aluminum 218

Chapter 1 Introduction and Review

1.1 Introduction

Textile composites (2-D plain woven, 2-D braided, knitted, stitched and 3-D woven, etc.) have innovative characteristics because of complex reinforcement geometries. The characteristics of these composites provide a variety of possible spatial functions through different curved yarn shapes and reinforce structural or load bearing applications. Moreover these materials are overwhelmingly superior to general composite materials from the points of view of the strengths and stiffness. So the textile structural composites are considered as an advanced material with a performance that is superior to other materials and hence they have applications in many industrial fields.

In general, the textile composites are used for the heavily loaded parts where a stress concentration may often occur and for structural parts where strongest structural elements are needed. To make these reinforced components, the textile composites have to be fiber reinforced by plastic materials. These textile composites are found in aircraft, ship and automobile parts, because their high stiffness is considered to be a good replacement for metal materials. Their high stiffness and strengths are obtained from the assemblage of fibrous materials, so-called yarns or strands. Various textile composite architecture shapes are formed by embedding a resin and fiber material. The textile composite strands/yarns are interlaced with each other in two mutually orthogonal (fill and warp)/bias directions and that leads to a better out-of-plane stiffness, strength and toughness properties as compared to simple planar type composites of a traditional one.

There is thus a high interest in aerospace, naval and mechanical industries towards the use of textile composites, and there have been several attempts to use suitable textile composites instead of steel and other metals since 1960's. For example, the textile composites offer an excellent opportunity to enhance the use of composite primary structures for commercial airplane due to their excellent structural properties and lower fabrication costs. In case of the airplanes, a number of parts, such as fuselage frame, stiffened skins and wing boxes, are already being fabricated using the textile composites. Several investigations on textile composites have conducted on determining structural characteristics and to perform comparison of their behavior with that of the traditional composites and the metallic materials.

Through some of experiments and numerical analyses, it was found that the textile composites exhibit a good structural behavior in terms of impact resistance, damage tolerance and high fracture toughness. The composite impact resistance can be further improved by implementing the fiber reinforced textile composite impregnated with appropriate resin components. It seems important to investigate the impact response of advanced textile composites. However, the impact problems in textile composites are not easily analyzed because several complex phenomena may occur during their operation, such as damage and cracking, while other phenomenon are observed during the impact event.

The last three decades have witnessed a great deal of research activity related to the impact modeling of traditional laminated composite structures. It is a well-known fact that these structures feature a number of shortcomings, such as delamination and transverse cracking induced, among others by the impact loads. In addition, the standard/traditional composite structures are highly vulnerable to the low- and high-velocity impacts and ballistic loadings. Moreover, since the micro-damages of composite structures can occur even at low impact energies, before composites can be used as many primary load carrying structures, studying impact-induced damage in the composite is one of very difficult problems to be addressed.

Among several damage modes in composites, the transverse matrix cracking is an important failure mode that can yield significant strength reductions, and in some conditions, even may lead to a structure's catastrophic failure. It is known that standard composite structures may not possess high damage tolerance and high delamination resistance, two properties that are desirable to ensure their structural survivability when exposed to severe impact loads. The studies related to various damage modes in composites have been aimed at finding appropriate solutions so as to prevent structural damage.

As a result of this increasing interest in studying the impact response of composites, various researchers have developed numerical and analytical models to describe the impact damage and damage tolerance of composites. However, most of the models, even though, they are based on rather complex schemes and effective modeling techniques, provide only approximate solutions to impact problems; they also do not address micro-crack induced in composites by low/high velocity impact loadings. Regarding the issue of describing the crack shapes in textile composites, we mention that it is a very intricate phenomenon due to complicated geometric shapes of the cracks and the micro-mechanical modeling (repeating unit cell) required to analyze damage in textile composite structures. The fundamental difficulty is a suitable crack modeling that should be constituted with the fracture mechanics.

This work is devoted to a study of the micro-mechanical modeling of the mechanical properties of textile, and the model's application to the dynamic/ballistic impact performance of complex textile structures, such as 2-D plain woven/3-D orthogonal textile layered or multi-layered/multi-phase composites. In order to develop an accurate methodology for these layered composites, an improved understanding and significant computational modeling of these complex composite systems are needed. For example, the finite element analysis combined with dynamic fracture mechanics modeling is used to simulate the transient/ballistic behaviors of these layered composites, and to analyze the geometrical effect of the strand/yarn architectures.

In the following chapters, descriptions of micro-mechanical modeling and mechanical behaviors of textile composites will be presented. Some mathematical equations based on geometrical architectures of textile composites are introduced and extended to other different textile composites. From these geometrical models, structural analyses for woven fabrics, such as progressive failures will be described. Secondly, a crack element for the dynamic impact modeling will be discussed and a number of impact modeling of textile-layered composites or multi-layered/multi-phase composites will be briefly outlined. To simulate and design these textile-layered composites, this work develops an in-house code written in Fortran 77/90, Visual C^{++} and Assembler languages. These programs provide a new understanding on how fragmentations and erosion between a target and a projectile take place, how micro-cracks between cohesive element surfaces or interface layer surfaces occur and how projectile penetration into targets occur and generate new different dynamic characteristics during the impact loading. These results for these fracture modes as obtained by experimental analyses and computational simulations still are difficult to compare. However the computational modeling developed here can provide a better understanding of the impact induced damage in textile-layered medium. From this point of view, this study develops an integrated numerical modeling to investigate static and dynamic responses and the fracture of 2-D plain woven/2-D braided textile composites and 3-D orthogonal woven composite structures.

1.2 Overview of Textile Composite Structures

The division into 2-D and 3-D textile composites can be established by considering whether the fiber arrangement can support loads continuously in three or two linearly independent directions. Another classification is based on the structural integrity and fiber architectures: 2-D planar interlaced and 3-D integrated structures. All textile composites have hierarchical structures treaded as three-dimensional complex structures rather than as traditional homogeneous assemblages. Figure 1.1 depicts a hierarchical structure of the textile composite. The main components of the hierarchical structures consist of fiber/matrix, yarn, fabric and composite structures. As illustrated in Chapter 1 of Ref. [1.1], there are different yarn structural forms. A filament fiber is grouped or assembled with several more than one thousand, fibers and then a yarn/strand or a yarn is formed. The fabric or plied yarns are formed by some of interlaced or interloped or intertwined formations with the yarns. Finally, the textile structures are obtained (and modeled) by several plied or fabric yarns.

Another classification of the textile composite is based on the geometrical concept of a periodic textile: unit cells or Repeating Unit Cells. The Repeating Unit Cells of 2-D plain woven and 3-D orthogonal

woven textile composites are illustrated in Figure 1. 2. These unit cells or Repeating Unit Cells usually suggest that the entire textile structures can be constructed from spatially translated copies of these cells, and effective elastic moduli can also be estimated from these basic cells. Using this geometrical classification, several textile composite types can be characterized.

1.2.1 2-D Weaves

Weaves are classified by the interlacing yarn patterns. There are a number of weave structures that originate from different fabric combinations along the in-plane orientation. In general, the basic weaves are of four types: plain, satin, twill and basket weaves, see Fig. 1.3. Most 2-D weaves have at least two orthogonal yarns in the in-plane axes, and these patterns imply weak in-plane shear resistance caused by external loads. Some satin formations prevent thermal warping problems. Another type of weaves, tri-axial weaves, see Figure 1.4, is fabricated by three 60° angled yarns intertwined or interlaced with each other and has nearly iso-tropic in-plane elasticity.

1.2.2 2-D Braids

Braided performs are interlaced by $\pm\theta$ oriented yarns/bias yarns and usually consist of 1×1 or 2×2 pattern shown in Figure 1.5. Here θ means the braid angle and the number of bias yarns between cross over points can be designed as $n\times n$. However braids have poor safety for damage resistance under axial compression in the yarn directions. Braids can be designed for multi-directional preforms by inserting axial yarns between the braid yarns in the longitudinal/vertical direction. By adopting the axial/longitudinal yarns to the bias yarns, the tri-axial braids are formed and controlling the relative size of the axial yarns and braid angles, effective elastic properties are obtained. Also, the tri-axial braids have high torsion resistances.

1.2.3 3-D Braids

The 3-D braid described in Chapter 5 of Ref. [1.1] is one of the textile extensions in that the braiding yarns interlock through a volume of the material. This textile composite is produced by a multi-warp weaving method used in manufacturing of double fabric yarns or more plied yarns. By the weaving method, various fiber architectures can be produced, for example, panels, boxes, I/T shaped beams and trusses. The 3-D braids have generally non-laminar properties, although nominally straight axial yarns are introduced to improve the stiffness and strength in each direction. One shortcoming of the 3-D braids is the difficulty of introducing yarns in the bias direction as in the tri-axial weaving or circular weaving process.

1.2.4 Orthogonal Non-woven Composites

Orthogonal 3-D braids illustrated in Figure 1.6 are fabricated by fixing a series of yarns in a given direction, and the planar yarns are inserted in two orthogonal directions around the fixed yarns. Unlike other textile forms, the reinforcement remains relatively straight throughout all XYZ directions. To get the reinforcement, we need some volume of pure matrix material to fill the substantial interstitial areas made by the fiber bundles. In addition, some different bundle orientations can result in a concept of multiple direction yarns. These are termed n-D materials; for example, a 4-D material can be created with fiber directions connected with the diagonal corners of a cube and this material has a significant strength when shear and multi-directional loading are applied.

1.2.5 Knitted 3-D Fabrics

Knits fabrics consist of one interloped yarns or more, such as warp knit or weft knit along yarn directions. The characteristic of the knitted fabrics is the conformability to other textile composites: plain woven and 2-D braid fabric structures and has specific directional extensibility and better structural stability, shown in Chapter 5 of Ref. [1.1]. The other merits of knitted fabrics are higher tensile strengths

along the translation direction, greater in-plane shear resistance and better manufacturing than general woven composites. Another knitted fabric is a stitching fabric that is reinforced through the thickness directions. This stitching frame has a significant damage tolerance. The two stitching forms are described in Figure 1.7.

1.3 Background and Literature Review

1.3.1 Analytical/Numerical Modeling for Textile Composites

To accurately describe shapes of fabric composites, some of micro-mechanical models have been suggested as early as the 1950's. Physically, the modeling of textile composites is more difficult when compared to the traditional/unidirectional composites due to the geometrical complexity of the fiber bundles/yarns' architecture; for example two or more yarns interlaced with each other. We need refined and accurate models to be able to analyze complicated architectures. Thus, some textile composite engineers have tried to find an effective analytical/numerical modeling for saving time and cost included in the analysis of these structures. From trial and error, several models were developed.

In the analytical/numerical textile modeling, they almost have interest in the prediction of effective material properties using a repeating unit cell (RUC), the so-called unit cell. Each modeling analyzes the micro-mechanical modeling because the over-all mechanical properties are specified by microscopic variables (geometrical lengths, areas and volumes) and properties. Some developed modelings can be divided into three main categories: classical laminate theory, stiffness averaging method and finite element method.

Ishikawa and Chou [1.1-1.3] have developed micro-mechanical models for the strength and stiffness of the two-dimensional woven fabric composites. Their analytical models have been based on the classical laminate theory (CLT), and were extended to mosaic model, fiber crimp model and bridging model. The mosaic model neglects the yarn crimp and so the yarns are considered as cross-ply units. The fiber crimp model includes the undulation regions of the yarns, but fiber continuity and non-uniform stresses and strains in the interlaced regions are not considered. The bridging model is derived from both the mosaic and the fiber crimp models to calculate the load transfer between the interlaced regions. As their all the three models are based on CLT, the moduli do not allow prediction of the effects of the undulations within the interlaced regions, the elastic properties due to out-of-plane effects are underestimated relatively.

The other numerical models are based on the stiffness average method, such as Refs. [1.4-1.7]. Naik and Ganesh [1.4] suggested an analytical model for the 2-D plain weaves and they too modeled the yarn undulations using the CLT. Through the iso-strain and iso-stress assumptions and integration of the sinusoidal RUC volume, the overall stiffness is calculated. Although their models are described by the 3-D geometrical shapes, over-predicted effective moduli are obtained because the cross-sectional shapes of the yarns are uniquely described along the yarn centerline. Therefore, the subsequent homogenization of stiffness and compliance values induces inaccurate elastic coefficients.

Scida *et al.* [1.5] developed a sinusoidal model to accurately describe yarn shapes and compare their results with other results to check the accuracy of their model. But this sinusoidal model does not consider the gap-length between the fill and warp yarns that was suggested in Ref. [1.4]. Naik [1.6-1.7] presented a balanced plain weave model designed by RUC's yarn architecture and iso-strain assumption. After integrating yarn volumes along the center-line and using the stress average technique, three-dimensional mechanical characteristics and thermal coefficients about the 2-D plain woven, 2-D braided and 2-D tri-axial braided composites were obtained. The influence of yarn undulations and orientations were considered but the middle region of yarns was of a flat shape which does not represent physical reality. Several textile composite models were implemented in a computer program (Textile Composite Analysis for Design: TEXCAD). Vandeurzen *et al.* [1.8-1.9] considered an analytical model based on mesh-generation of micro-unit cell and calculated fiber-volume fractions and yarn orientations. This

model is available in a software program (TEXCOMP). But this model did not correct the wrong orientations of yarns induced using various mesh-generation procedures.

A few researchers have used more advanced numerical techniques, like the finite element analysis, to obtain better results of stress and strain distributions in a RUC. The previous models [1.10-1.15] were based on the finite element method. Dasgupta *et al.* [1.10] presented a model considering the yarn undulations and the inter-gap between the yarns where there were no contact points between the yarns, and the separated fill/warp strands. They used hexahedral and tetrahedral elements to model the yarn architecture and the iso-strain boundary conditions were prescribed to find the elastic moduli. However, this model considered only a small unit cell that was limited to get the over-all elastic moduli for an RUC. Cox *et al.* [1.11-1.12] developed three-dimensional finite element model, called the binary model, consisting of two element types. The fiber bundle was modeled by a two-node line element having an axial rigidity, and the composite based on the isotropic and homogeneous medium was represented by an eight-node solid element possessing transverse stiffness, shear stiffness and Poisson's effects. But this model did not consider yarn heterogeneities that were induced from interlocked orthogonal angles.

Master *et al.* [1.13] showed a digitally mapped model of braided composites. The geometry data of braded composites were obtained using a CAD package, and node and the element coordinates were created. The result of axial stiffness and Poisson's ratio were in good agreement, but the transverse values were not in good agreement with the experimental data. Also the results of this model were not better than those of available general analytical models.

Whitcomb *et al.* [1.14-1.15] studied a unit cell of plain woven composite using three-dimensional finite elements to calculate the effects of yarn geometry and yarn volume fractions for thermo-elastic coefficients. This model applied the finite element method between the global and the local models. For example, the stress and strain of the global model were induced from the displacements and forces specified as appropriate boundary conditions on the local model. However, there were some numerical errors in the yarn stiffness as obtained by the global and local models.

Some of numerical models in the 3-D orthogonal woven textile composites were suggested in recent years. Tan *et al.* [1.16] suggested a simple analytical model, referred to as the laminate block model, to predict the mechanical properties of the 3-D orthogonal woven textile composites. This model used lamina blocks for the warp, fill and Z-yarns and shown to be a reasonable model when comparing the predicted and measured results. Bogdanovich [1.17] presented an analytical 3-D mosaic model to find the effective elastic characteristics of 3-D weave composite unit cell. This analytical model still provides higher predicted moduli compared to the experimental data.

1.3.2 Impact Modeling for Standard/Textile Composites

A number of researchers have tried to examine the impact mechanism that occurs during the dynamic penetration and perforation of laminates. The different approaches of dynamic impact problems can be divided into two categories: the analytical/empirical modeling and numerical simulation.

Zhu *et al.* [1.18-1.19] have investigated the penetration of laminated plates by conical-nosed projectiles and estimated various energy-absorbing mechanisms related to the target resistance and the projectile motion. They also have studied dissipative mechanisms including indentation of the projectile tip, fiber failures, delaminations and frictions with simplifying assumptions.

Lee and Sun [1.20] developed a quasi-static model to depict the penetration process of composite laminates struck by blunt projectiles. During penetrations, the load-displacement relations were characterized by a series of static punch tests, and the damage modes were reported to be delamination and plugging. An axi-symmetric finite element analysis was used to simulate the quasi-static penetration process adopting an effective modulus scheme. They showed good agreement between the results of their modeling and testing.

Sun and Potti [1.21] have utilized the energy required for penetration of thick composite laminates in the impact tests. They performed several impact tests for the thick laminates and found that the overall damage patterns in the dynamic case were similar to the static cases. Their results showed some over-

estimated values compared to the experimental data. However this model was considered as an easy and a simple approximation to find the quasi-static punch curve.

Ko and Hartman [1.22] have experimentally revealed that the braided composites possess a higher capacity for damage resistance than the three-dimensional and two-dimensional orthogonal woven fabric composites. Gong and Sankar [1.23] showed that the three-dimensionally braided composites show better damage tolerance than quasi-isotropic laminates in static and impact tests. They have examined the impact damage modes and the factors related to the impact damage patterns.

While a large amount of analytical/empirical impact modeling on the general laminated structures has been presented, only a limited numbers of numerical simulations have been published on the behavior of textile layered and multi-layered/multi-phase composites. The numerical impact models of the 3-D orthogonal woven composite have been suggested recently. Bogdanovich [1.24-1.25] analyzed the transverse impact of 3-D orthogonal weave composite employing the finite element model that is based on geometrical unit cell models. The relations between the damage and the energy absorption have been studied. Also the energy conversion between the projector kinetic energy and the target internal energy were estimated as a function of projectile diameters.

1.3.3 Impact Modeling for Multi-layered Structures

In the last years, the ballistic impact modeling for the multi-layered medium was conducted by a number of researchers. The multi-layered structures mostly consist of several isotropic laminae that are variously brittle and ductile materials to be used as effective armor materials. To design armor structures successfully, we need a detailed understanding of the complex failure mechanisms: plastic deformation, penetration, fragmentations, cracks and erosion. From the early 1990's, a number of analytical methods have been studied to simulate the ballistic impact at high/low velocity and even when impacted by a particle moving at hypervelocity.

A numerical method, the so-called Smooth Particle Hydrodynamics (SPH), was introduced for the hypervelocity impact, during the past several years. This method was introduced by Monaghan [1.26-1.28] and Johnson [1.29-1.30] and used Lagrangian scheme to overcome the highly deformed grid shapes occurring during the ballistic loading. The SPH successfully describes continuum masses moving arbitrarily in an infinite domain, but does not fully perform as accurately as the finite element methods when the SPH is applied into the finite domain systems. Thus, a mixed numerical method, considering SPH and finite element method, was suggested by Johnson [1.31-1.34]. This modeling was focused on the erosion problems based on the effective plastic stress or strain and a critical value. Also Johnson [1.35-37] described more detailed erosion algorithms during the high velocity impact along the interfaced surfaces. However, these modeling are not enough to describe crack propagations between projector and target elements. But these modeling do not fully solve dynamic crack propagations for the brittle materials, and then more specific numerical modeling for the dynamic cracking were needed.

Consequently, alternative approaches for the crack propagations have been developed by some researchers, such as the cohesive zone modeling or interface cohesive modeling. The basic idea for the cohesive model stems from the fact that the concept of infinite stresses at the crack tip is not realistic. Barenblatt [1.38] and Dugdale [1.39] introduced different crack models considering cohesive stresses. These models have at the same time some problems because the solution of associated boundary values involving crack propagations is not possible when the crack growth is curved. Tvergaard [1.40-1.41] has modified the cohesive zone model to describe computational crack propagation, using what are called cohesive interface elements. Cohesive interface elements are defined between the continuum elements instead, that open when the damage occurs and reduces the values of their stiffness coefficients at failure so that the continuum elements become disconnected.

In 1990's, other cohesive zone modeling were proposed by several researchers. Needleman [1.42] has described crack propagation from initial de-bonding to extended complete separations, and this work has used an interfacial strength and surface energy functions per unit area consisting of normal and shear components. Needleman [1.43-1.46] continuously studied crack growth problems, quasi-static cracking and stability of separation procedures with a cohesive zone model and cohesive element modeling.

Siegmund [1.47-1.48] applied the cohesive zone modeling into a commercial finite element program (ABAQUS) and studied appropriate crack shapes.

Some researchers utilized the cohesive element to address the issue of crack propagation in the brittle material impact. Ortiz [1.49] investigated impact damage in the brittle materials with the cohesive zone modeling and used normal and shear displacement functions for obtaining stress components between the elements. Espinosa [1.50-53] presented a discrete damage modeling involving dynamic fragmentations and used the interface cohesive laws that were described as consisting of interface traction functions in the interface element. These two approaches successfully depicted crack fragmentations compared to other previous numerical modeling, but there still were needed more refined cohesive zone modeling to find more accurate dynamic responses. Therefore a better understanding on the cohesive zone model is needed.

1.3.4 Problem Statement of Textile Composite Structures

In contrast to the tremendous research work that has been devoted to the dynamic behavior of standard laminated constructions, little work was done in the context of 2-D or 3-D textile composite structures. However, some authors have developed constitutive models to predict the dynamic responses focused on only global damage problems, not the micro-damages, and even not on the ballistic impact loading problems or physical cracks.

To solve the problem of dynamic response of 2-D textile and 3-D textile composites, as a preliminary requirement, a thorough study of their global mechanical properties and structural behavior is needed. A review of publications on mechanical property predictions and static response analysis of 3-D woven composites can be found in the literature. In the same work of Ref. [1.17], an example of multi-scale predictive analysis of 3-D woven composites exposed to static loads was presented. Some aspects of the aforementioned publications will be implemented in this proposed work for developing a dynamic analysis approach.

It clearly appears that the response to dynamic loads is the most important structural issue in the application of 2-D and 3-D textile composites that must be investigated. Studying damage and failure of 2-D textile and 3-D textile composite structures under severe dynamic loads involves a number of issues of high complexity that should be investigated. They are: complex damage modes in the textile composite materials; the material behavior under different strain rates, and determination of the constitutive behavior of composites in the presence of matrix cracking, and matrix and/or fiber yielding.

It is essential to develop a computational methodology that may lead to an improved understanding of the impact mechanism of textile-layered structures. The main difficulty in this study was the computational complexity in terms of geometry and material modeling. Having an understanding of the dynamic impact/ballistic response of the textile composites, the structural requirement should be fulfilled for both textile-layered composites and the material architecture.

1.4 Objectives of Dissertation

The overall objective of this proposed research is to advance the knowledge and state-of-the-art of the dynamic modeling of the multi-layered textile composite structures as related to the stiffness degradation of the textile composites. And this research is to study the dynamic behavior of 2-D plain weave and 3-D orthogonal woven composite structures, weakened by the existence of damage, and exposed to impact loads. To accomplish this objective, three issues are addressed:

a) Dynamic modeling of 2-D and 3-D textile composite structures, multi-layered composite structures that consist of anisotropic layers featuring transverse matrix micro-cracks, and subjected to impact.

b) The stiffness degradation modeling in the presence of transverse matrix micro-cracks using an efficient homogenization scheme.

c) The dynamic crack propagation at the lamina interfaces, induced by the fast transient impact/ballistic loading.

REFERENCES

1.1 Chou, T.W. and Ishikawa, T., "Analysis and Modeling of Two-dimensional Fabric Composites," *Textile Structural Composites, Composite Material Series, Vol.3*, Chou, Tsu-Wei and Frank, K. Ko (Editors), Elsevier Science Publishers, 1989, pp. 209-264.

1.2 Ishikawa, T. and Chou, T.W., "Elastic Behavior of Woven Hybrid Composites," *Journal of Composite Materials*, Vol. 16, 1982, pp. 2-19.

1.3 Ishikawa, T. and Chou, T.W., "In-plane Thermal Expansion and Thermal Bending Coefficients of Fabric Composites," *Journal of Composite Materials*, Vol. 17, March, 1983, pp. 92-104.

1.4 Naik, N.K. and Ganesh, V.K., "An Analytical Method for Plain Weave Fabric Composites," *Composites*, Vol. 26, No. 4, 1995, pp. 281-289.

1.5 Scida, D., Aboura Z., Benzenggagh M.L. and Bocherens E., "A Micro-mechanics Model for 3-D Elasticity and Failure of Woven-fiber Composite Materials," *Composites Science and Technology*, Vol. 59, No. 4, 1999, pp. 505-517.

1.6 Naik, R.A., "Analysis of Woven and Braided Fabric Reinforced Composites," NASA Contract Report CR-194930, 1994.

1.7 Naik, R.A., "Failure Analysis of Woven and Braided Fabric Reinforced Composites," NASA Contract Report CR-194981, 1994.

1.8 Vandeurzen, P., Ivens, J. and Verpoest, I., "A Three-dimensional Micro-mechanical Analysis of Woven-fabric Composites: I. Geometric Analysis," *Composites Science and Technology*, Vol. 56, No. 11, 1996, pp. 1303-1315.

1.9 Vandeurzen, P., Ivens, J. and Verpoest, I., "A Three-dimensional Micro-mechanical Analysis of Woven-fabric Composites: II. Elastic Analysis," *Composites Science and Technology*, Vol. 56, No. 11, 1996, pp. 1317-1327.

1.10 Dasgupta, A., Agarwal, R.K. and Bhandarkar, S.M., "Three-dimensional Modeling of Woven fabric Composites for Effective Thermo-Mechanical and Thermal Properties," *Composites Science and Technology*, Vol. 56, No. 3, 1996, pp. 209-223.

1.11 Cox, B.N., Carter, W.C. and Fleck, N.A., "A Binary Model of Textile Composites-I. Formulation," *Acta Metallurgica et Materialia*, Vol. 42, No. 10, 1994, pp. 3463-3479.

1.12 Xu, J., Cox, B.N., McGlockton, M.A., and Carter, W.C., "A Binary Model of Textile Composites-II, The Elastic Regime," *Acta Metallurgica et Materialia*, Vol. 43, No. 9, 1995, pp. 3511-3524.

1.13 Master, J.E., Foye, R.L., Pastore, C.M. and Gowayed, Y.A., "Mechanical Properties of Tri-axially Braided Composites: Experimental and Analytical Results," *Composite Technology & Research*, Vol. 15, No. 2, 1993, pp. 112-122.

1.14 Whitcomb, J., Woo, K. and Gundapaneni, S., "Macro Finite Element for Analysis of Textile Composites," *Journal of Composite Materials*, Vol. 28, No. 7, 1994, pp. 607-617.

1.15 Whitcomb, J., Champman, C. and Tang, X., "Simulation of Progressive Failure of Woven Composites," *International Conference on Composite Engineering*, Las Vegas, Nevada, July 5-11, 1998.

1.16 Tan, P., Tong, L. and Steven, G. P., "Modeling Approaches for 3-D Orthogonal Woven Composites," *Journal of Reinforced Plastic and Composites*, Vol. 17, No. 6, 1998, pp. 545-577.

1.17 Bogdanovich, A. E., "Multi-scale Predictive Analysis of 3-D Woven Composites," *Proceedings of 35th International SAMPE Technical Conference*, Vol. 35, Dayton, OH, Sept. 28-Oct. 2, 2003.
1.18 Zhu, G., Goldsmith, W. and Dharan, C.K.H., "Penetration of Laminated Kevlar by Projectiles-I. Experimental Investigations," *International Journal of Solids and Structures*, Vol. 29, No. 4, 1992, pp. 399-420.
1.19 Zhu, G., Goldsmith, W. and Dharan, C.K.H., "Penetration of Laminated Kevlar by Projectiles-II. Analytical Model," *International Journal of Solids and Structures*, Vol. 29, No. 4, 1992, pp. 421-436.
1.20 Lee, S-W.R. and Sun, C.T., "Dynamic Penetration of Graphite/Epoxy Laminates Impacted by a Blunt-Ended Projectile," *Composite Science and Technology*, Vol. 49, No. 4, pp. 369-380, 1993.
1.21 Sun, C.T., and Potti, S.V., "High Velocity Impact and Penetration of Composite Laminates," *Proceedings of the 9th International Conference on Composite Materials* (ICCM/IX), Vol. 5, pp. 261-268, Madrid, Spain, 1993.
1.22 Ko, F.K., and Hartman, D., "Impact Behavior of 2-D and 3-D Glass/Epoxy Composiites," *SAMPE Journal*, Vol. 22, July/Aug., pp. 259-266, 1986.
1.23 Gong, J.C. and Sankar, B.V., "Impact Properties of Three-Dimensional Braided Graphite/Epoxy Composite," *Journal of Composite Materials*, Vol. 25, No. 6, 1991, pp. 715-731.
1.24 Gama, B.A., Haque, M. J., Gillespie, J.W., and Bogdanovich, A. E., "Impact, Damage, and Energy Absorption of 3-D Orthogonal Weave Composite Unit Cell Model," *CD Proceedings SAMPE 2004*, Long Beach, CA, May 16-20, 2004.
1.25 Gama, B.A., Bogdanovich, A.E., Coffelt, R.A., Haque, Md. J., Rahman M., and Gillespie, J.W., "Ballistic Impact Damage Modeling and Experimental Validation a 3-D Orthogonal Weave Fabric Composite," *SAMPE 2005 Technical Conference Proceedings*, Long Beach, CA, May 1-5, 2005.
1.26 Monaghan, J.J., "Why Particle Methods Work," SIAM *Journal of Science in Statistics and Computing*, Vol. 3, No. 4, 1982, pp. 422-433.
1.27 Monaghan, J.J. and Gingold, R.A., "Shock Simulation by the Particle Method SPH," *Journal of Computational Physics*, Vol. 52, No. 2, 1983, pp. 374-389.
1.28 Monaghan, J.J., "Particle Methods for Hydrodynamics," *Computer Physics Report*, Vol. 3, 1985, pp. 71-124.
1.29 Johnson, G.R., Stryk, R.A. and Beissel, S.R., "SPH for High Velocity Impact Computations," *Computer Methods in Applied Mechanics and Engineering*, Vol. 139, No. 1-4, 1996, pp. 347-373.
1.30 Johnson, G.R., "Artificial Viscosity Effects for SPH Impact Computations," *International Journal of Impact Engineering*, Vol. 18, No. 5, 1996, pp. 447-488.
1.31 Johnson, G.R. and Stryk, R.A., "Dynamic Lagrangian Computations for Solids, with Variable Nodal Connectivity for Severe Distortions," *International Journal of Numerical Methods in Engineering*, Vol. 23, No. 3, 1986, pp. 509-522.
1.32 Johnson, G.R. and Stryk, R.A., "Dynamic Three-Dimensional Computations for Solids, with Variable Nodal Connectivity for Severe Distortions," *International Journal for Numerical Methods in Engineering*, Vol. 28, No. 4, 1989, pp. 817-832.
1.33 Johnson, G.R. Petersen, E.H. and Stryk, R.A., "Incorporation of an SPH Option into the EPIC Code for a Wide Range of High Velocity Impact Computations," *International Journal of Impact Engineering*, Vol. 14, No. 1-4, 1993, pp. 385-394.
1.34 Johnson, G.R., "Linking of Lagrangian Particle Methods to Standard Finite Element Methods for High Velocity Impact Computations," *Nuclear Engineering and Design*, Vol. 150, No. 2, 1994, pp. 265-274.
1.35 Johnson, G.R. and Stryk, R.A., "Eroding Interface and Improved Tetrahedral Element Algorithms for High Velocity Impact Computations in Three Dimensions," *International Journal of Impact Engineering*, Vol. 5, No. 1-4, 1987, pp. 411-421.
1.36 Johnson, G.R. and Cook, W.H., "Lagrangian EPIC Code Computations for Oblique, Yawed-Rod Impacts onto Thin-Plate and Spaced-Plate Targets at Various Velocities," *International Journal of Impact Engineering*, Vol. 14, No. 1-4, 1993, pp. 373-383.

1.37 Johnson, G.R. and Stryk, R.A., "Symmetric Contact and Sliding Interface Algorithms for Intense Impulsive Loading Computations," *Computer Methods in Applied Mechanics and Engineering*, Vol. 190, No. 35, 2001, pp. 4531-4549.
1.38 Barenblatt, G., "The Mathematical Theory of Equilibrium Cracks in Brittle Fracture," *Advances in Applied Mechanics*, Vol. 7, No. 1, 1962, pp. 55-129.
1.39 Dugdale, D.S., "Yielding of Steel Sheets Containing Slits," *Journal of the Mechanics and Physics of Solids*, Vol. 8, No. 2, 1960, pp. 100-104.
1.40 Tvergaard, V., "Material Failure by Void Growth to Coalescence," Academic Press, 1990, pp. 85-151.
1.41 Tvergaard, V. and Hutchison, J.W., "The Relation between Crack Growth Resistance and Fracture Process Parameters in Elastic-Plastic Solids," *Journal of the Mechanics and Physics of Solids*, Vol. 40, No. 6, 1992, pp. 1377-1397.
1.42 Needleman, A., "A Continuum Model for Void Nucleation by Inclusion De-bonding," *Journal of Applied Mechanics*, Vol. 54, September, 1987, pp. 525-531.
1.43 Needleman, A., "Micro-mechanical Modeling of Interfacial De-cohesion," *Ultra-microscopy*, Vol. 40, 1992, pp. 203-214.
1.44 Xu, X.P. and Needleman, A., "Numerical Simulations of Fast Crack Growth in Brittle Solids," *Journal of the Mechanics and Physics of Solids*, Vol. 42, No. 9, 1994, pp. 1397-1434.
1.45 Xu, X.P. and Needleman, A., "Numerical Simulations of Dynamic Interfacial Crack Growth allowing for Crack Growth away from the Bond Line," *International Journal of Fracture*, Vol. 74, No. 3, 1995, pp. 253-275.
1.46 Xu, X.P. and Needleman, A., "Numerical Simulations of Crack Growth along an Interface," *International Journal of Fracture*, Vol. 74, No. 4, 1996, pp. 289-324.
1.47 Siegmund, T. and Needleman, A., "A Numerical Study of Dynamic Crack Growth in Elastic-Viscoplastic Solids," *International Journal of Solis and Structures*, Vol. 34, No. 7, 1997, pp. 769-787.
1.48 Siegmund, T., Fleck, N.A. and Needleman, A., "Dynamic Crack Growth across an Interface," *International Journal of Fracture*, Vol. 85, No. 4, 1997, pp. 381-402.
1.49 Camacho, G.T. and Ortiz, M., "Computational Modeling of Impact Damage in Brittle Materials," *International Journal of Solids and Structures*, Vol. 33, No. 21, 1996, pp. 2899-2938.
1.50 Espinosa, H.D., Emore, G.L. and Zavattieri, P.D., "Computational Modeling of Geometric and Material Non-linearities with an Application to Impact Damage in Brittle Materials," *Advances in Failure Mechanism in Brittle Materials*, ed. Clifton R.J. and Espinosa, H.D., MD-75, AMD-219, 1996, pp. 119-161.
1.51 Espinosa, H.D., Zavattieri, P.D. and Dwivedi, S.K., "A Finite Deformation Continuum/Discrete Model for the Description of Fragmentation and Damage in Brittle Materials," *Journal of the Mechanics and Physics of Solids*, Vol. 46, No. 10, 1998, pp. 1909-1942.
1.52 Espinosa, H.D., Dwivedi, S.K. and Zavattieri, P.D., "A Numerical Investigation of Penetration in Multi-layered Material/Structure Systems," *International Journal of Solids and Structures*, Vol. 35, No. 22, 1998, pp. 2975-3001.
1.53 Espinosa, H.D., Zavattieri, P.D. and Emore, G.L., "Adaptive FEM Computation of Geometric and Material Non-linearities with Application to Brittle Failure," *Mechanics of Materials*, Vol. 29, No. 3, 1998, pp. 275-305.
1.54 Cox, B.N., "Handbook of Analytical Methods for Textile Composites," NASA Contract Report CR-194930, 1994.

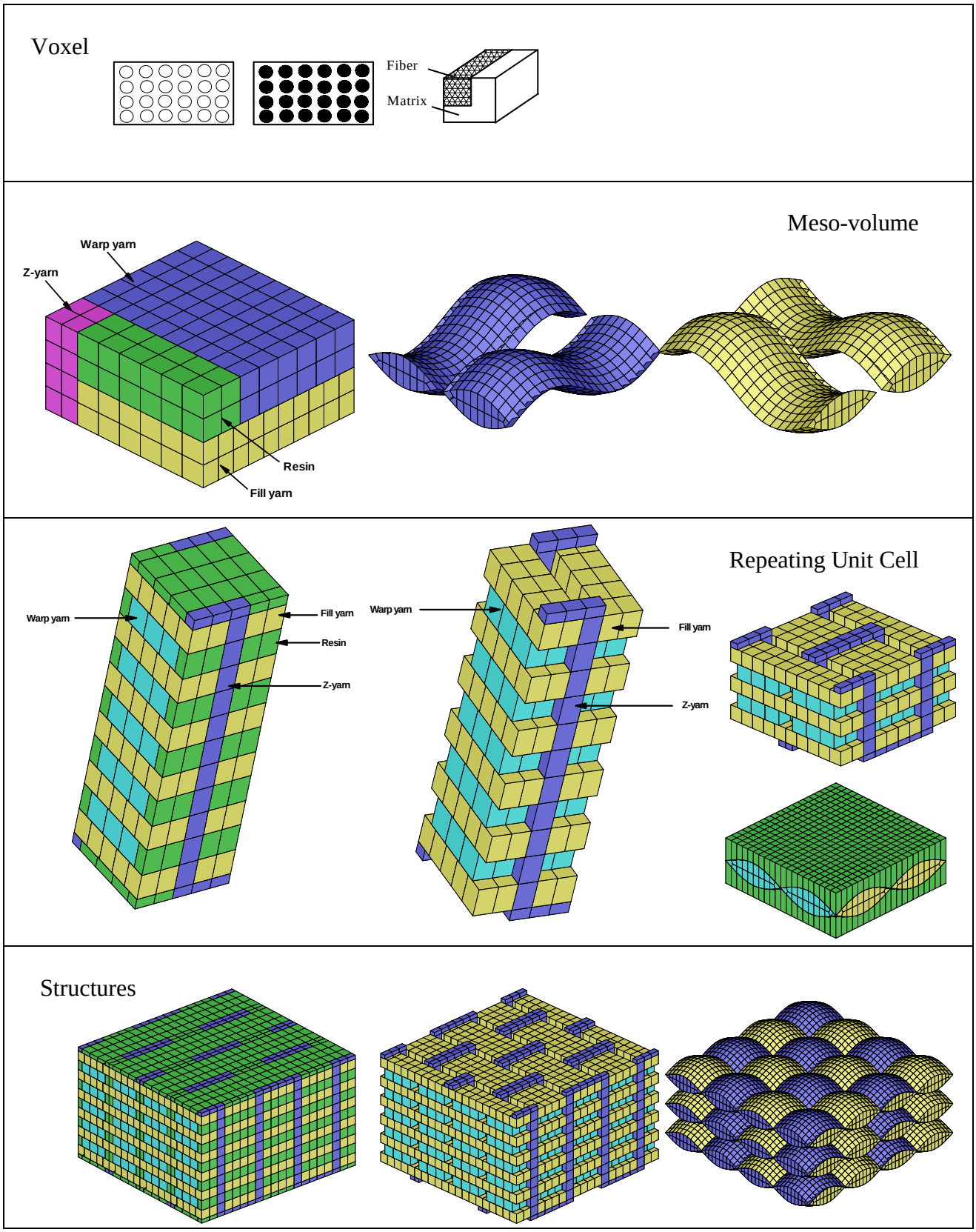

Figure 1.1: Hierarchical nature of textile reinforced composite materials.

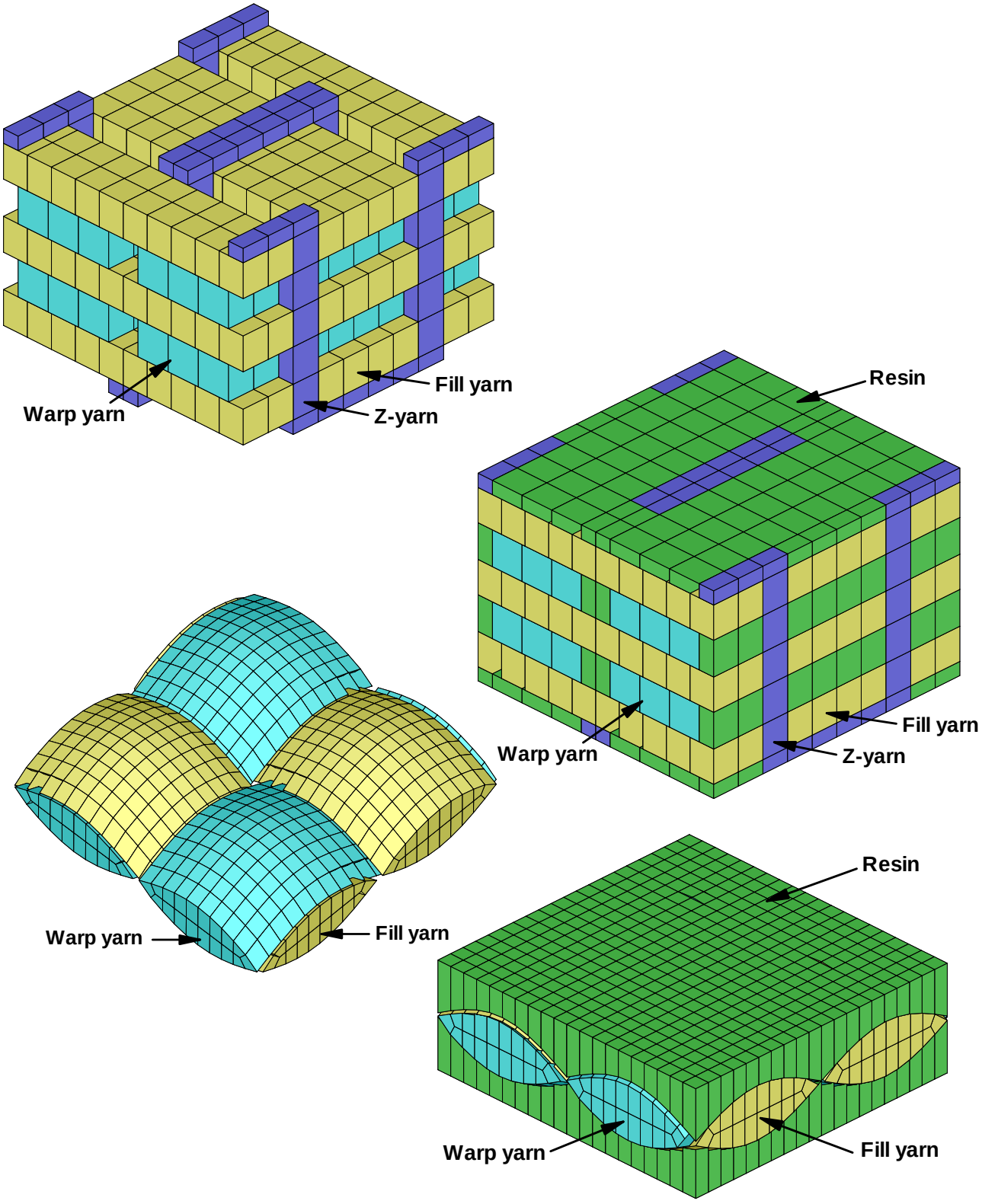

Figure 1.2: RUC of 3-D orthogonal woven and 2-D plain woven composite without resin and with resin.

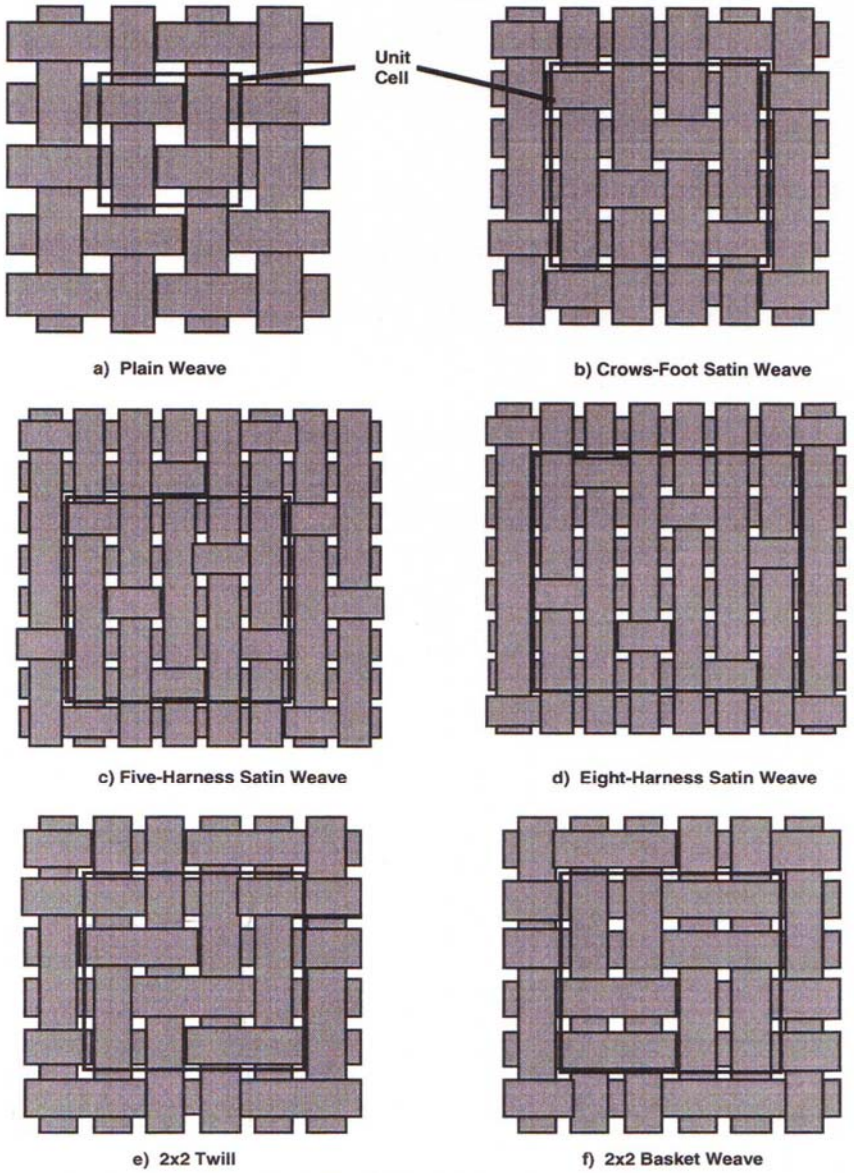

Figure 1.3: Commonly used 2-D weave patterns[1.54].

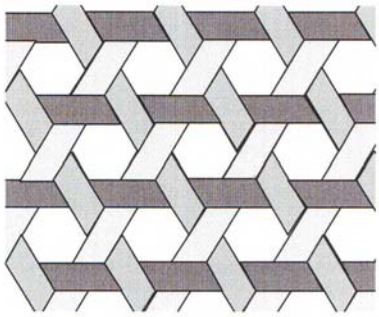

Figure 1.4: Tri-axial weave[1.54].

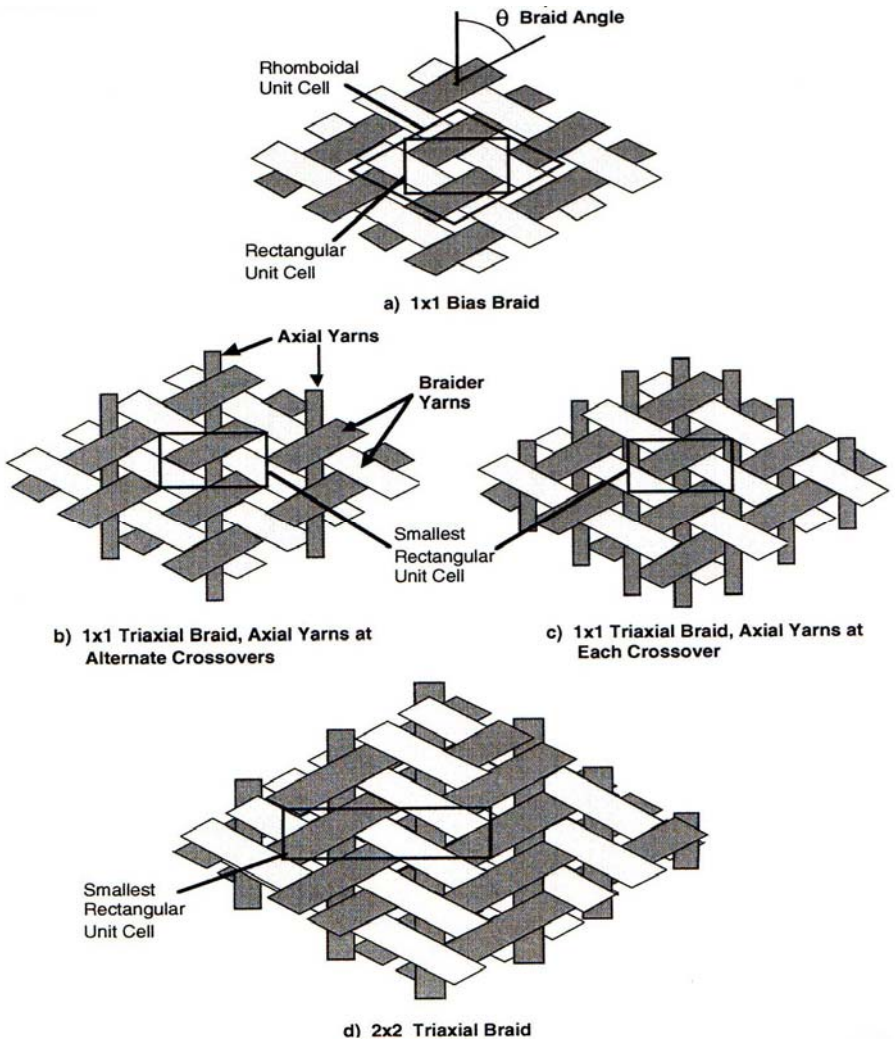

Figure 1.5: Some common 2-D braid patterns[1.54].

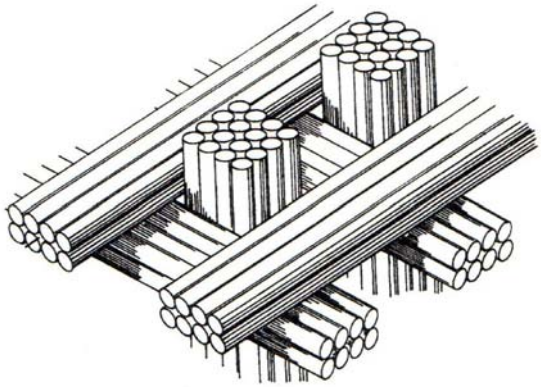

Figure 1.6: Structural geometry of 3-D orthogonal composites[1.54].

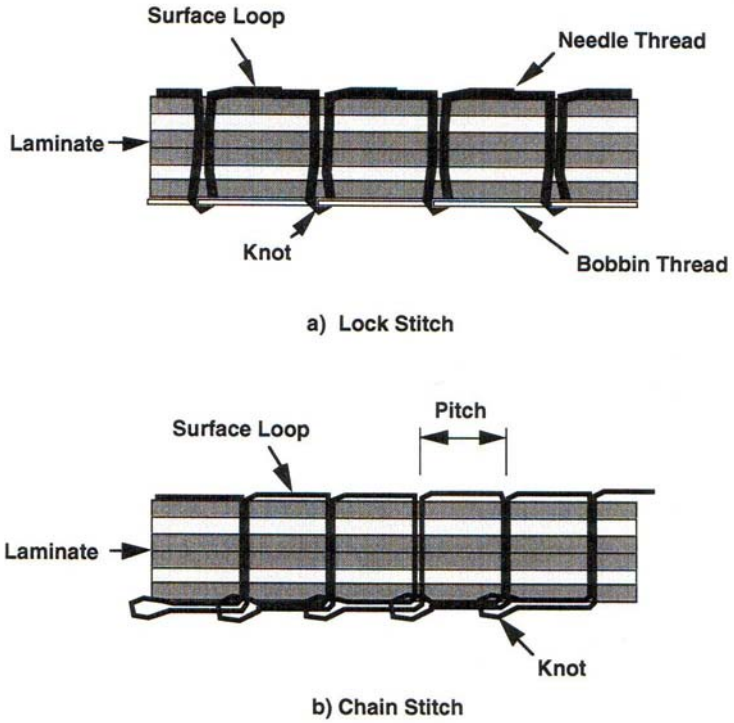

Figure 1.7: Types of stitching used for through the thickness reinforcement[1.54].

Chapter 2 Homogenization I of 2-D Plain Woven Textile Composite

2.1 Introduction

Plain woven textile composite is one of basic textile composites produced by simple orthogonal interlaced yarns: warp and fill. Some applied forms of plain woven composites are continuously developed with different yarns' formations, for example, twill weaves, satin weaves and others. Due to these various forms of plain woven textiles, the plain woven textile composites have been used in a large number of engineering applications. In addition, the dependence of their mechanical behavior on yarns' geometrical shapes is of considerable interest. The overall objective in this chapter is to present a simple analytical model, called Sine Function Model I (SFM I). It is possible to determine the equivalent elastic properties of plain woven textile composites using a Repeating Unit Cell (RUC) concept. Using this concept, one is able to describe the mechanical behavior of both un-symmetric and symmetric elliptical plain woven yarns using the Sine Function Model I.

2.2 Geometrical Modeling for Plain Woven Textile Composite

Geometrically, the plain woven composite can be viewed as to be constituted of small repeating unit cells see Figure 2.1. One of the several Repeating Unit Cells in the plain weaves usually consists of 6 components: 2-warp yarns, 2-fill yarns and 2-resin layers as shown in Figure 2.2. The fill yarns run vertically or along the y -axis in the woven fabrics, while the warp yarns run horizontally or in the x -axis as shown in Figure 2.1. To check the cross-sections, 5-different interval points are considered, see Figure 2.3. Also two points are considered to show geometrical parameters in the sectional shapes, see Figure 2.4. From the sectional shapes in Figure 2.5, it is seen that the un-symmetric shapes of the fills and warps are found and the yarn sectional shapes are of different types when compared to other models, namely, Naik and Ganesh[2.1-2.2], Naik[2.3] and Scida[2.4] *et al.*'s models.

2.3 Sine Function Model I (SFM I) for Plain Woven Textile Composite

Figures 2.6-2.7 describe the geometrical variables of Repeating Unit Cell. The Sine Function Model uses two assumptions suggested by Naik[2.3]: (a) the centerline of the yarn path consists of undulated portions with their centerline described by the sine functions (b) the cross-sectional area and thickness of the yarn normal to its centerline are uniform along the arc-length of the centerline. From Figures 2.3-2.5, it is clear that the geometrical shapes of the plain weave composite can be described by two sine functions in terms of upper and lower surfaces of the yarns. Each geometrical surface of yarns can be expressed by two sinusoidal functions whose variables are defined in terms of the yarn cross-sections and undulation parameters. The cross-sectional shapes suggested in Figure 2.5 are expressed by the upper and lower sine-functions, such as equations of geometrical surfaces; z_1^{up} , z_1^{lower} , z_2^{up} and z_2^{lower} .

$$z_1^{up} = +\frac{t_2}{2}\sin\left[\frac{x\pi}{a_2+g_2}\right]+\frac{t_1}{2}\sin\left[\frac{y\pi}{a_1+g_1}\right],\ z_1^{lower} = +\frac{t_2}{2}\sin\left[\frac{x\pi}{a_2+g_2}\right]-\frac{t_1}{2}\sin\left[\frac{y\pi}{a_1+g_1}\right] \quad (2.1)$$

$$z_2^{up} = +\frac{t_1}{2}\sin\left[\frac{x\pi}{a_1+g_1}\right]-\frac{t_2}{2}\sin\left[\frac{y\pi}{a_2+g_2}\right],\ z_2^{lower} = -\frac{t_1}{2}\sin\left[\frac{x\pi}{a_1+g_1}\right]-\frac{t_2}{2}\sin\left[\frac{y\pi}{a_2+g_2}\right] \quad (2.2)$$

Here, the undulation lengths are $u_1 = a_1 + g_1$ and $u_2 = a_2 + g_2$ along the warp and fill directions respectively.

The centerline coordinates of the fill and warp yarns in the undulations are derived by simple sine-functions as in Eq. (2.3).

$$z_{c1} = \frac{t_2}{2}\sin\left[\frac{x\pi}{a_2 + g_2}\right], \qquad z_{c2} = -\frac{t_1}{2}\sin\left[\frac{y\pi}{a_1 + g_1}\right] \tag{2.3}$$

The crimp angles (θ_{c1} and θ_{c2}) are obtained from the derivatives of Eq. (2.3) that are expressed as the undulation lengths and thickness. The crimp angles have different values along the undulation regions and are written as:

$$\theta_{c1} = \tan^{-1}\left[\frac{t_2\pi}{2(a_2 + g_2)}\cos\left[\frac{\pi x}{(a_2 + g_2)}\right]\right], \ (0 \le x \le u_2)$$

$$\theta_{c1} = \tan^{-1}\left[\frac{-t_2\pi}{2(a_2 + g_2)}\cos\left[\frac{\pi(x - u_2)}{(a_2 + g_2)}\right]\right], \ (u_2 \le x \le 2u_2) \tag{2.4}$$

$$\theta_{c2} = \tan^{-1}\left[\frac{-t_1\pi}{2(a_1 + g_1)}\cos\left[\frac{\pi y}{(a_1 + g_1)}\right]\right], \ (0 \le y \le u_1)$$

$$\theta_{c2} = \tan^{-1}\left[\frac{t_1\pi}{2(a_1 + g_1)}\cos\left[\frac{\pi(y - u_1)}{(a_1 + g_1)}\right]\right], \ (u_1 \le y \le 2u_1) \tag{2.5}$$

The other problem is related to the determination of the equations for the volume fractions that consist of the yarn volume fraction and over-all volume fraction that depends on fiber volume. In the Sine Function Model I, these values are obtained from the integrations of the fill and warp yarns along the undulation paths. To calculate the volume, the sectional areas (A_1 and A_2) of the yarns are given by

$$A_1 = \int_0^{a_1} (z_1^{up} - z_1^{lower})dy = \frac{t_1(a_1 + g_1)}{\pi}\left[1 - \cos\left[\frac{a_1\pi}{(a_1 + g_1)}\right]\right] \tag{2.6}$$

$$A_2 = \int_0^{a_2} (z_2^{up} - z_2^{lower})dx = \frac{t_2(a_2 + g_2)}{\pi}\left[1 - \cos\left[\frac{a_2\pi}{(a_2 + g_2)}\right]\right] \tag{2.7}$$

The fill and warp yarn volumes (V_1 and V_2) are expressed by using the second elliptic integrals. The expressions for the yarn volumes are:

$$V_1 = A_1\int_0^{u_2}\sqrt{1 + (\frac{dz_{c1}}{dx})^2}\,dx = A_1\int_0^{u_2}\sqrt{1 + (\frac{t_2\pi}{2u_2})^2\cos^2(\frac{\pi x}{u_2})}dx \tag{2.8}$$

$$V_2 = A_2\int_0^{u_1}\sqrt{1 + (\frac{dz_{c2}}{dy})^2}\,dy = A_2\int_0^{u_1}\sqrt{1 + (\frac{t_1\pi}{2u_1})^2\cos^2(\frac{\pi y}{u_1})}dy \tag{2.9}$$

In Eqs.(2.8) and (2.9), A_1 and A_2 are obtained from Eqs. (2.6) and (2.7). Like the yarn volumes, the total volume for the Repeating Unit Cell is expressed as the thickness and undulation terms. The total resin thickness is h_m in the Repeating Unit Cell that includes half thickness for upper and lower resin layers, respectively. These yarn volumes are also compared to numerical solutions calculated by trapezoidal rule in the Sine Function Model I.

$$V_{total} = H(a_1 + g_1)(a_2 + g_2) = (h_m + t_1 + t_2)(a_1 + g_1)(a_2 + g_2) \tag{2.10}$$

The resin volume and resin volume fraction (V_{resin} and V_f^r) in the Repeating Unit Cell are expressed as

$$V_{resin} = V_{total} - (V_1 + V_2),\ V_f^r = \frac{V_{resin}}{V_{total}} = \frac{V_{total} - (V_1 + V_2)}{V_{total}} \tag{2.11}$$

The volume fractions for the yarns are specified under different fiber volume fractions about the fill and warp yarns. So, the over-all fiber volume fraction (V_f^o) is given by

$$V_f = V_{f1}\frac{V_1}{V_{total}} + V_{f2}\frac{V_2}{V_{total}} = V_f^o \tag{2.12}$$

2.4 Sub-domain Zone for Repeating Unit Cell

Sine Function Model I introduce a sub-domain zone concept, see Figure 2.10 that enables one to calculate the three-dimensional elastic properties of the plain woven textile composites with the application of the iso- strain assumption, and the micro-mechanical equations are applied to model the fiber and matrix regions in the sub-domain zone. To calculate the equivalent modulus for the strengthened textile composite RUC, the iso-strain assumption is used, and the warp yarns, fill yarns and resin layers are assumed to be perfectly bonded along the interface surfaces. From this assumption, the displacements at the interface between two layers are equal, for example, resin layer and warp yarn, warp layer and fill layer, fill yarn and resin layer. Displacement continuity over these interfacial layers means the displacement gradients in the in-plane $x-y$ directions. By assuming this, one of sub-domains represented by rectangular regions in Figure 2.10 is considered, and this sub-domain is referred to a Cartesian coordinate system, x, y and z. These layers are to be oriented normal to the z-axis so that the interfaces between layers are located by constant values of the z coordinate. From all these facts, the continuity conditions at the interfaces can be obtained. To get the equations of continuity conditions, let's introduce in-plane strain components, $\varepsilon_{11}, \varepsilon_{22}$ and ε_{12} that are continuous between two layers. Also the out-of-plane stresses are spatially uniform through the thickness of the sub-domain, such as σ_{33}, σ_{23} and σ_{13}. Actually the former terms are based on Voigt approximation, i.e. iso-strain condition, and the latter is Reuss approximation, referred to as the iso-stress condition.

$$\begin{aligned}
&\varepsilon_{11}^{resin} = \varepsilon_{11}^{warp}, \varepsilon_{11}^{warp} = \varepsilon_{11}^{fill}, \varepsilon_{11}^{fill} = \varepsilon_{11}^{resin} \\
&\varepsilon_{22}^{resin} = \varepsilon_{22}^{warp}, \varepsilon_{22}^{warp} = \varepsilon_{22}^{fill}, \varepsilon_{22}^{fill} = \varepsilon_{22}^{resin} \\
&\varepsilon_{12}^{resin} = \varepsilon_{12}^{warp}, \varepsilon_{12}^{warp} = \varepsilon_{12}^{fill}, \varepsilon_{12}^{fill} = \varepsilon_{12}^{resin} \\
&\varepsilon_{33}^{resin} = \varepsilon_{33}^{warp}, \varepsilon_{33}^{warp} = \varepsilon_{33}^{fill}, \varepsilon_{33}^{fill} = \varepsilon_{33}^{resin} \\
&\varepsilon_{23}^{resin} = \varepsilon_{23}^{warp}, \varepsilon_{23}^{warp} = \varepsilon_{23}^{fill}, \varepsilon_{23}^{fill} = \varepsilon_{23}^{resin}
\end{aligned} \tag{2.13}$$

$$\varepsilon_{13}^{resin} = \varepsilon_{13}^{warp}, \varepsilon_{13}^{warp} = \varepsilon_{13}^{fill}, \varepsilon_{13}^{fill} = \varepsilon_{13}^{resin} \tag{2.14}$$

For the sub-domain subjected to an imposed macroscopically homogeneous stress or displacement field and in the absence of body forces, the average stress and strain components are defined as

$$\overline{\sigma}_{ij} = \frac{1}{V}\int_V \sigma_{ij} dV = \{\overline{\sigma}\},\ \overline{\varepsilon}_{ij} = \frac{1}{V}\int_V \varepsilon_{ij} dV = \{\overline{\varepsilon}\} \tag{2.15}$$

Here, σ_{ij} and ε_{ij} are the true stresses and strains or micro-stresses and micro-strains in the sub-domain volume (V).

From the application of iso-strain assumption into the sub-domain zone, the strain energy value for each layer is calculated and assembled the strain energy of the sub-domain region. The total strain energy of RUC is finally obtained, and the stiffness and compliance values of RUC also are estimated. After finding the total strain energy, stiffness and compliance, the equivalent modulus of 2-D plain woven textile composites can be calculated.

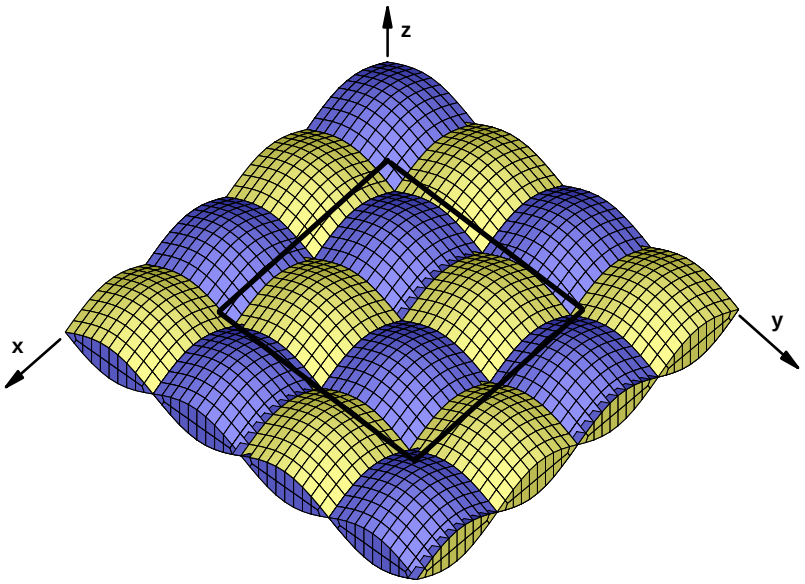

Figure 2.1: Repeating Unit Cell (RUC) for plain weave.

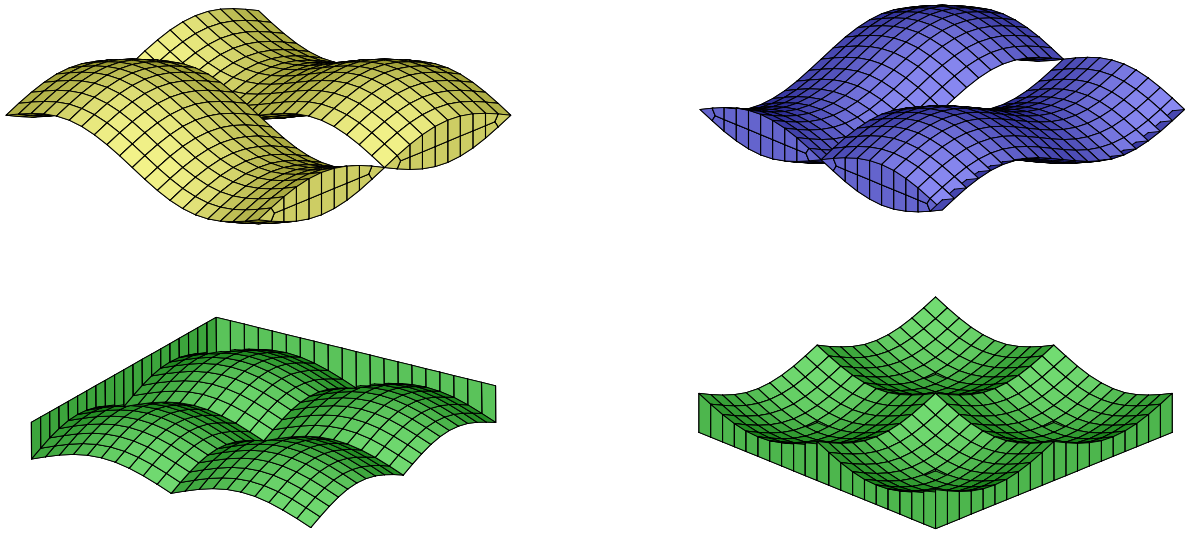

Figure 2.2: Shapes for the fill and warp yarns and resin layers.

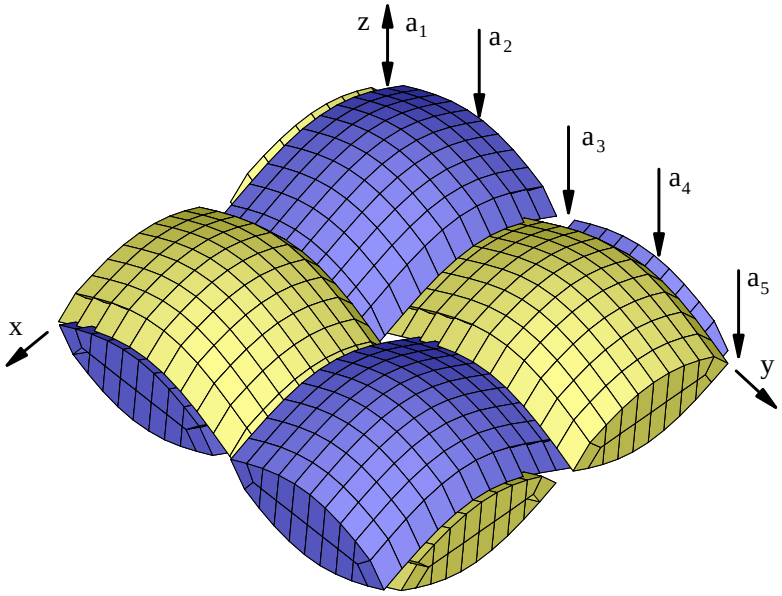

Figure 2.3: 5-different interval points in RUC.

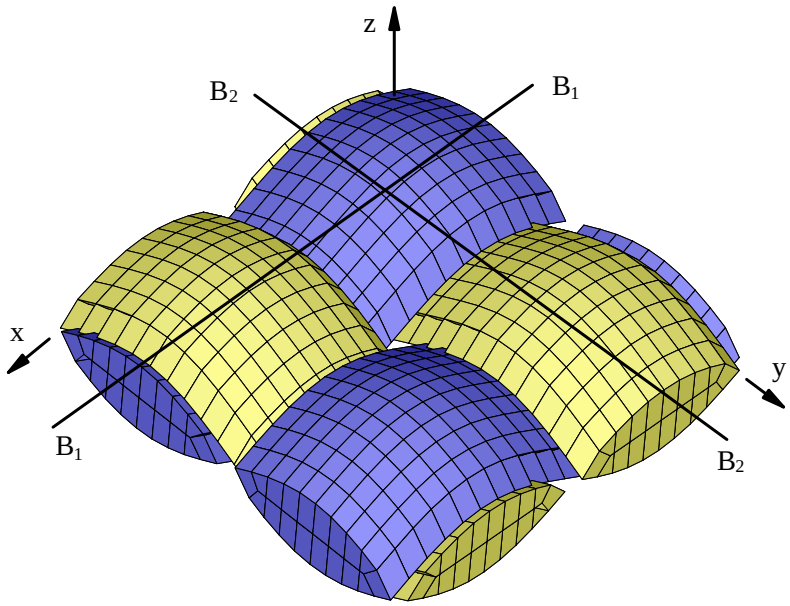

Figure 2.4: 2-sectional points in RUC.

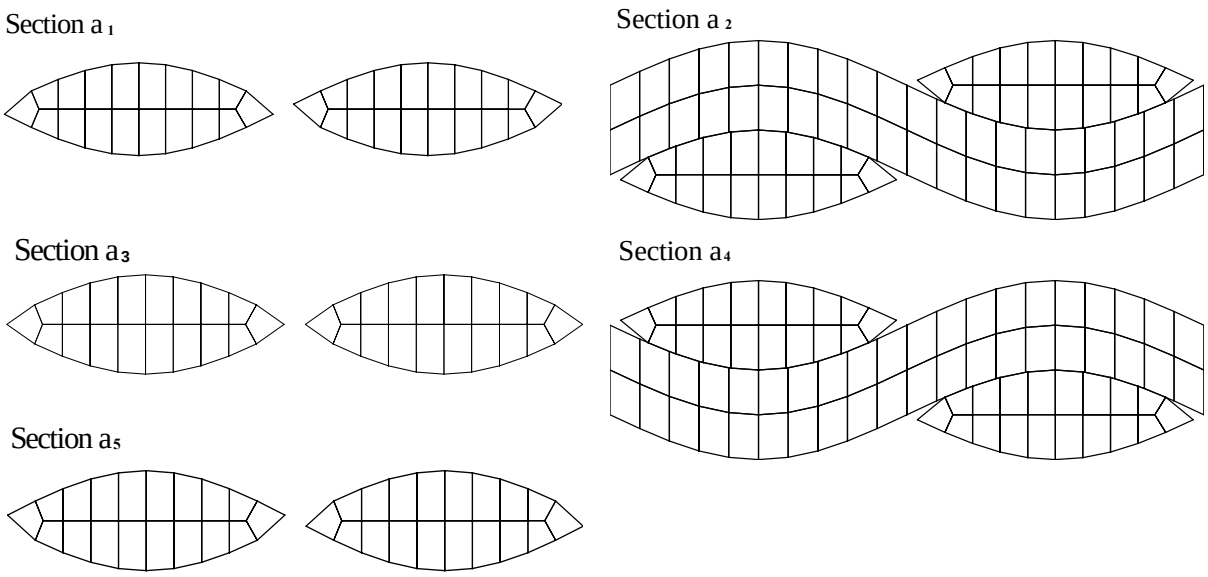

Figure 2.5: Cross sectional shapes at 5-different points.

2.5 Equivalent Modulus for Plain Woven Textile Composite

To calculate the equivalent modulus for the textile composite Repeating Unit Cell, the iso-strain assumption and the micro-mechanical equations for the composite material modeling are considered. The Repeating Unit Cell consists of three components: the fill and warp yarns and resin layers. The strains have constant values for these 3-components and linear elasticity is assumed. The concept of the sub-domain zone in Section 2.3 suggests the iso-strain assumption and introduces the strain energy for the Repeating Unit Cell. In our study, the strain energy and the engineering strains are used to determine the equivalent elastic matrix for the Repeating Unit Cell of textile composites. The strain energy and strain terms are given by

$$U = \frac{1}{2}\int_V \varepsilon^T C \varepsilon dV\,,\ \varepsilon^T = \begin{bmatrix}\varepsilon_x & \varepsilon_y & \varepsilon_z & \gamma_{yz} & \gamma_{zx} & \gamma_{xy}\end{bmatrix} \tag{2.16}$$

$$U = \frac{V}{2}\varepsilon^T C_{eq}\varepsilon\,,\ C_{eq} = \frac{1}{V}\int_V C dV \tag{2.17}$$

In Eqs. (2.16) - (2.17), the volume term (V) is of the same value as the total Repeating Unit Cell volume (V_{total}), and the elastic stiffness matrix (C) is a three-dimensional 6 by 6 matrix. The equivalent elasticity matrix (C_{eq}) is expressed by Eq. (2.17). By using the equivalent elastic matrix, equivalent elastic values for the 3-D components (the fills, warps and resins) are obtained from the volume fractions for each material. The Repeating Unit Cell volume and the volume fractions are already considered in Eqs. (2.10) - (2.12). The equivalent elasticity matrix (C_{eq}) is rewritten as transformation stiffness matrices of fill, warp yarns and resin ($\overline{C}_{eqf}$, $\overline{C}_{eqw}$ and $\overline{C}_{eqr}$).

$$C_{eq} = \frac{1}{V}\left[\int_{V_{fill}} C_{fill} dV + \int_{V_{warp}} C_{warp} dV + \int_{V_{resin}} C_{resin} dV\right] \tag{2.18}$$

$$C_{eq} = V_{f1}\overline{C}_{eqf} + V_{f2}\overline{C}_{eqw} + V_f^r \overline{C}_{eqr} = C_{eqf} + C_{eqw} + C_{eqr} \tag{2.19}$$

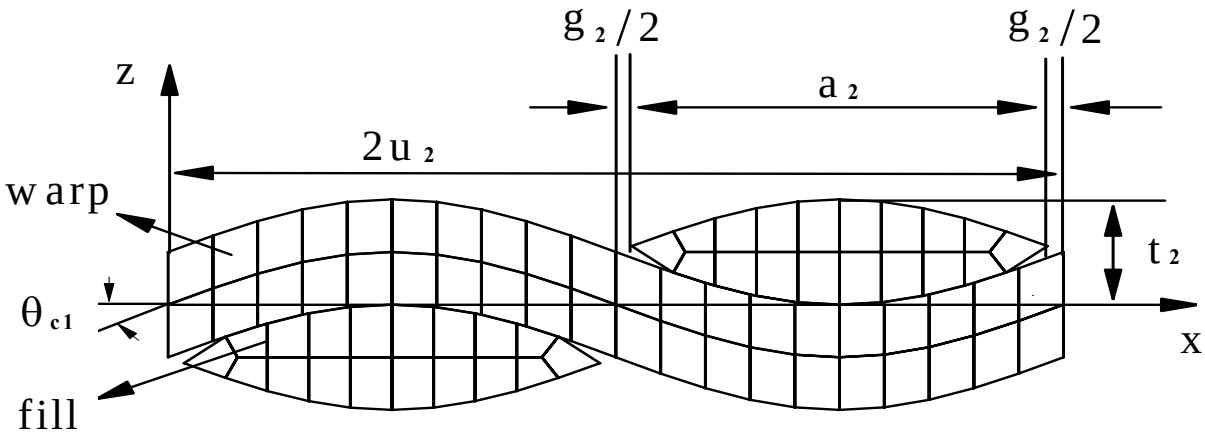

Figure 2.6: Sectional shape at B_1-B_1 point: warp direction.

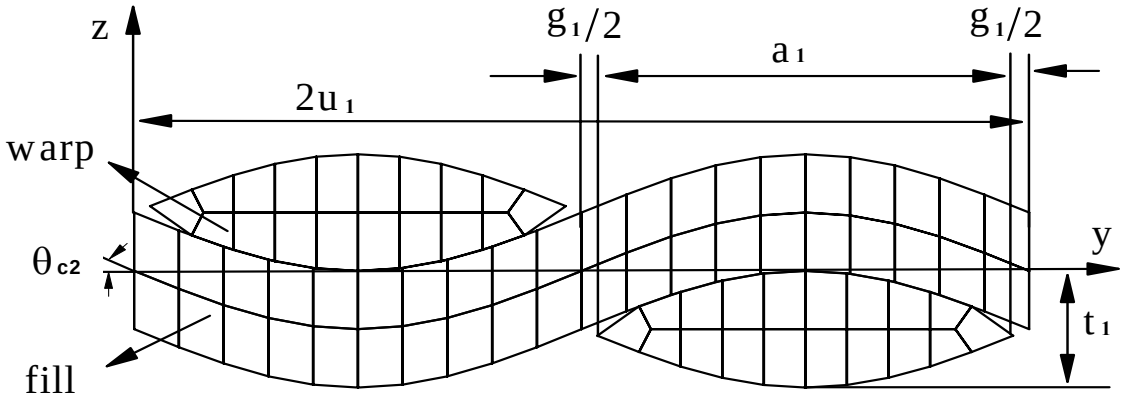

Figure 2.7: Sectional shape at B_2-B_2 point: fill direction.

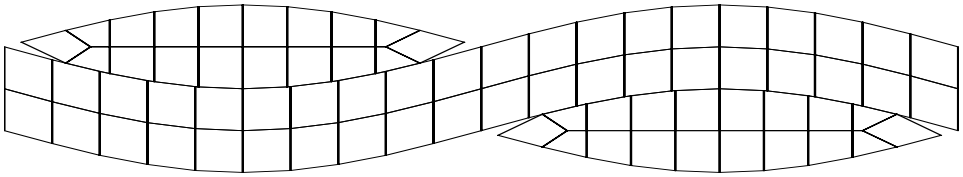

Figure 2.8: Sectional shape for the open weaves.

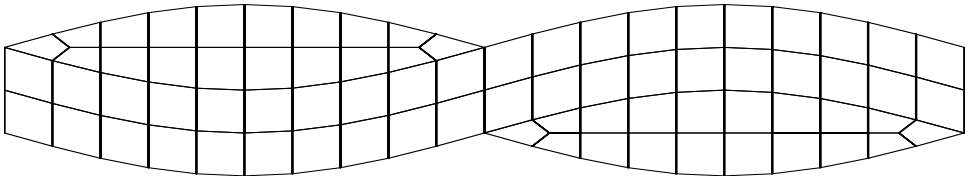

Figure 2.9: Sectional shape for the closed weaves.

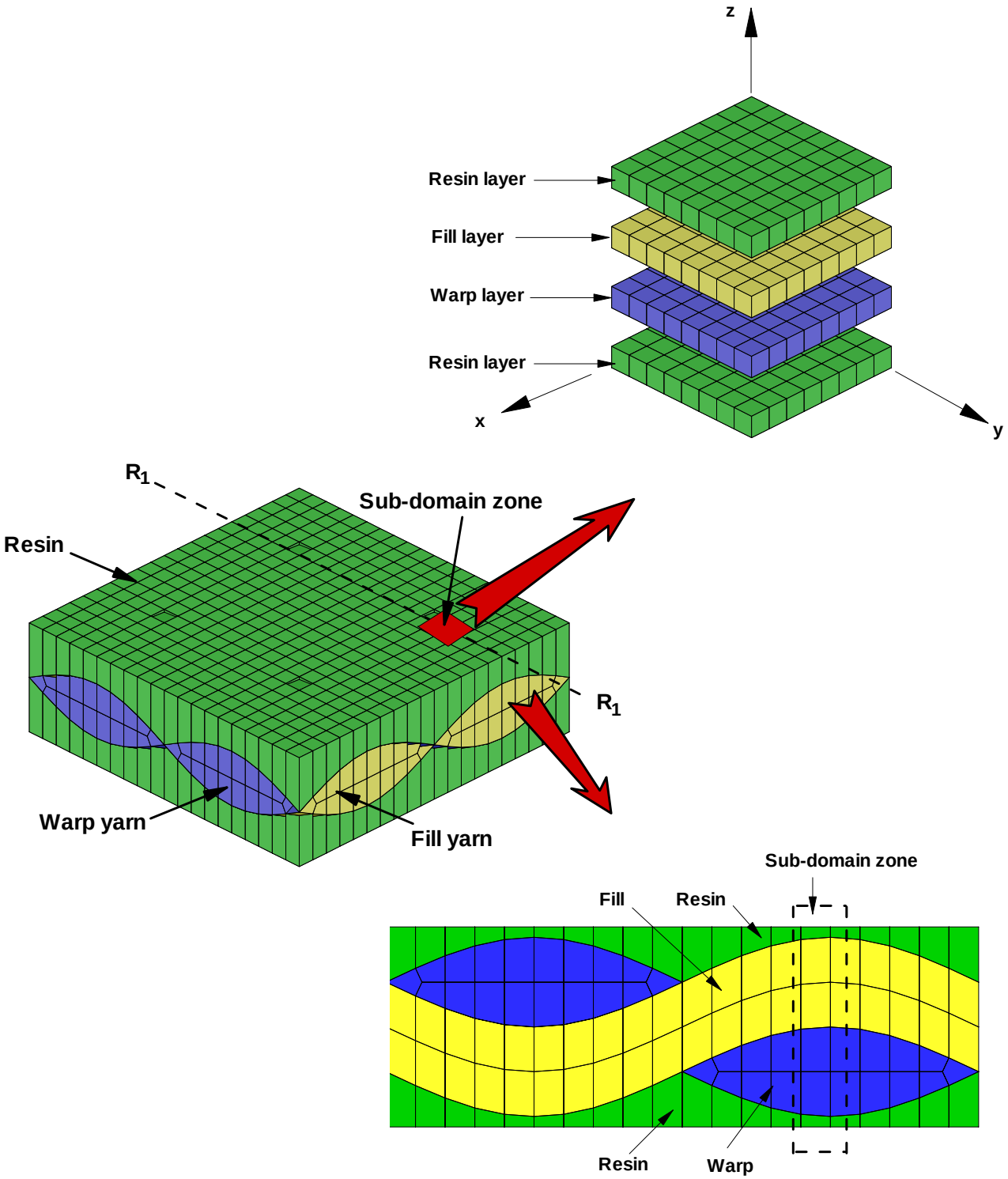

Figure 2.10: Components of the sub-domain zone and one sectional shape in the RUC.

These 3-equivalent elasticity matrices are dependent on the crimp angles and rotation angles (θ_r) included in the transformation matrix (T) between $x-y-z$ and 1-2-3 coordinates. Components for the transformation matrix are shown in Appendix A. To describe the equivalent elasticity matrices, each equivalent matrix is defined as a function of the crimp and rotation angles. In the plain woven case of the fill, the rotation angle assumes a constant value ($\theta_r = \frac{\pi}{2}$) between x and y axes, and the rotation angle for the warp of the plain woven is a zero ($\theta_r = 0$) on the x axis. However, the rotation angles of the fill and warp are not constants in the 2-D braids. Depending on the undulated region of yarns, the crimp angles for the yarns are assumed different values, see Eqs. (2.4) and (2.5). The transformation matrices, $\overline{C}^{ij}_{eqf}$ and $\overline{C}^{ij}_{eqw}$, in Eq. (2.19) are presented in Appendix B. In the Sine Function Model, the equivalent elasticity matrices are defined as in Eqs. (2.20) - (2.21),

$$C_{eqw} = \frac{1}{2A_1 u_2^u} \int_{V_{warp}} C_{warp} dV = \frac{1}{u_2^u} \int_0^{2u_2} C_1(0, \theta_{c1}) \sqrt{1 + (\frac{dz_{c1}}{dx})^2}\, dx \tag{2.20}$$

$$C_{eqf} = \frac{1}{2A_2 u_1^u} \int_{V_{fill}} C_{fill} dV = \frac{1}{u_1^u} \int_0^{2u_1} C_1(\frac{\pi}{2}, \theta_{c2}) \sqrt{1 + (\frac{dz_{c2}}{dy})^2}\, dy \tag{2.21}$$

In the above equations, an arbitrary segment of yarn regions within $2u_1$ or $2u_2$ is considered, $C_1(\theta_r, \theta_{c1})$ or $C_1(\theta_r, \theta_{c2})$ to denote the direction of x and y axes, u_1^u or u_2^u denotes the arc-length along the undulation region of yarns. If the integration region of the yarns is specified as a half undulation (u_1 or u_2), these equations are modified as,

$$C_{eqw} = \frac{2}{u_2^u} \int_0^{u_2} C_1(0, \theta_{c1}) \sqrt{1 + (\frac{dz_{c1}}{dx})^2}\, dx = \frac{2}{u_2^u} \int_0^{u_2} C_1(0, \theta_{c1}) \sqrt{1 + (\frac{t_2 \pi}{2u_2})^2 \cos^2(\frac{\pi x}{u_2})}\, dx \tag{2.22}$$

$$C_{eqf} = \frac{2}{u_1^u} \int_0^{u_1} C_1(\frac{\pi}{2}, \theta_{c2}) \sqrt{1 + (\frac{dz_{c2}}{dy})^2}\, dy = \frac{2}{u_1^u} \int_0^{u_1} C_1(\frac{\pi}{2}, \theta_{c2}) \sqrt{1 + (\frac{t_1 \pi}{2u_1})^2 \cos^2(\frac{\pi y}{u_1})}\, dy \tag{2.23}$$

To determine the elastic properties of the yarns and resin, the micro-mechanical equations for the composite are used. In this study, two composite material modeling (Rule of mixture and Self-Consistent method) based on the micro-mechanical equations are used to determine the elastic properties of fibers and resin.

2.6 Overall Coefficients of Thermal Expansion (CTE) for 2-D Plain Textile Composite

Another problem is related to the overall coefficients of thermal expansion (CTE) in the plain woven textile composites. Unlike unidirectional composite, the textile composite have to consider the crimp angles depending on the yarns' undulation regions and these angles affect the equivalent modulus of the RUC. For the purpose of calculating overall properties, the RUC of the textile composite is treated as a specially oriented fiber composite constituted of yarn slices with transversely isotropic material properties and longitudinal material axes oriented at known rotation angle (θ_r) and crimp angle (θ_{c1}, θ_{c2} or θ_c). An average stress scheme based on an iso-strain assumption within the RUC is used to determine the overall stiffness matrix. Average value equation for the stress is considered as:

$$\overline{\sigma} = \sum v_r \overline{\sigma}_r \tag{2.24}$$

Using the standard contracted notation, the stress-strain relation in matrix form is

$$\{\overline{\sigma}\} = [C_{eff}]\ (\{\overline{\varepsilon}\} - \{\overline{\alpha}\}\Delta T) \tag{2.25}$$

Here, $\{\overline{\sigma}\} = \{\overline{\sigma}_{xx}, \overline{\sigma}_{yy}, \overline{\sigma}_{zz}, \overline{\sigma}_{xy}, \overline{\sigma}_{yz}, \overline{\sigma}_{zx}\}$, where the over-bar denotes average values over the RUC, and the average strain is $\{\overline{\varepsilon}\} = \{\overline{\varepsilon}_{xx}, \overline{\varepsilon}_{yy}, \overline{\varepsilon}_{zz}, \overline{\varepsilon}_{xy}, \overline{\varepsilon}_{yz}, \overline{\varepsilon}_{zx}\}$,and the CTE matrix is $\{\overline{\alpha}\} = \{\overline{\alpha}_{xx}, \overline{\alpha}_{yy}, \overline{\alpha}_{zz}, 0, 0, 0\}$, and the temperature change is ΔT. For a set of displacement boundary conditions applied to the RUC, the average strains in the composite are given by $\{\overline{\varepsilon}\}$. The following procedure was used to determine $\{\overline{\sigma}\}$. An iso-strain state is assumed to exist within the RUC. This provides for compatibility among yarn slices and also leads to displacements that satisfy the boundary conditions. In the global RUC x - y - z coordinate, the strains in each yarn slice (the m^{th} yarn slice) are, therefore, given by

$$\{\overline{\varepsilon}\} = \{\varepsilon\}_m \tag{2.26}$$

Knowing the strains and assuming an iso-thermal state in the RUC, the yarn slice stresses in the local yarn slice material coordinate system (1-2-3) are determined as

$$\{\sigma\}_m = [C]_m (\{\varepsilon\}_m - \{\alpha\}_m \Delta T), \ \{\varepsilon\}_m = [T]_m \{\overline{\varepsilon}\} \tag{2.27}$$

The 6x6 stiffness matrix $[C]_m$ for the m^{th} yarn slice consists of three components: the fill, warp and resin materials. To determine the average stiffness in the RUC, the average stresses are considered. First, transforming yarn slice stresses to the global RUC coordinates are needed, and then computing the volume averages of stresses in the yarn slices, such as the volume fractions, is obtained.

$$\{\overline{\sigma}\} = \sum_{m=1}^{N} V_m \ [T]_m^T \ \{ \ [C]_m (\{\varepsilon\}_m - \{\alpha\}_m \Delta T)_m \ \} \tag{2.28}$$

Here, V_m is the volume fraction of the m^{th} yarn slice in the RUC and this volume fraction consists of three parts: fill, warp and resin components.

From the above equations and the relationships between stress and strain, the effective stiffness matrix of the woven or braided RUC is written as a summation over all the N yarn slices in the RUC, including the interstitial matrix material slice in terms of the yarn slice stiffness matrix.

$$[C_{eff}] = \frac{1}{V} \left[\ \sum_{m=1}^{N} v_m^f \ [\overline{C}_{eqf}] + \sum_{m=1}^{N} v_m^w \ [\overline{C}_{eqw}] + \sum_{m=1}^{N} v_m^r \ [\overline{C}_{eqr}] \ \right] \tag{2.29}$$

Here, v_m^f, v_m^w and v_m^r denote the volumes of fill, warp and resin for the m^{th} yarn slice, respectively. The effective stiffness matrices of the fill, warp and resin are described by transformation matrix $[T]$.

$$[\overline{C}_{eqf}] = [T_m]_{fill}^T \ [C^f]_m \ [T_m]_{fill}, \ [\overline{C}_{eqw}] = [T_m]_{warp}^T \ [C^w]_m \ [T_m]_{warp} \tag{2.30}$$

In Eq. (2.28), the 6x6 stiffness matrix $[C^i]_m$ ($i = f, w$) is defined by the three dimensional stress-strain relationship for the m^{th} yarn slice which is assumed to be a transversely isotropic material. The five independent material constants ($E_{11}, E_{22}, G_{12}, \nu_{12}$ and ν_{23}) that are required to define the $[C^i]_m$ matrix are quantities determined from impregnated yarn tests or could also be estimated using the Rule of mixtures or performing a micro-mechanical analysis using constituent properties, i.e. the Self-Consistent method used in this study. To calculate these effective stiffness matrices, some knowledge of fiber properties, matrix properties and yarn fiber volume fraction are needed. The transformation matrix $[T]$ is defined in Appendix B and is used to transform the strains from the global RUC coordinates in the x - y - z to the slice material coordinates 1-2-3.

The thermal residual stresses in the yarn slices were calculated based on the iso-strain assumption. The thermal stresses for the m^{th} yarn slice were given by

$$\{\sigma^T\}_m = \Delta T \ \left\{ \ [C^f]_m + [C^w]_m + [C^r]_m \ \right\} \left\{ \ [T]_m \{\overline{\alpha}\} - \{\alpha\}_m \ \right\} \tag{2.31}$$

Here, ΔT is the change in temperature from the stress free state, $\{\alpha\}$ are the coefficients of thermal expansion (CTE) of the m^{th} yarn slice and $\{\overline{\alpha}\}$ are the overall CTE for the RUC given by

$$\{\overline{\alpha}\} = [C_{eff}]^{-1} \frac{1}{V} \left[\sum_{m=1}^{N} v_m^f \left[C^f\right]_m \{\alpha\}_m + \sum_{m=1}^{N} v_m^w \left[C^w\right]_m \{\alpha\}_m + \sum_{m=1}^{N} v_m^r \left[C^r\right]_m \{\alpha\}_m \right] \quad (2.32)$$

The appropriate number of yarn slices, N, in the undulating portions of yarns, is used to determine the unchanged overall stiffness values, $[C_{eff}]$. This study finds that the computed stiffness for the plain woven composites is unchanged for $N \geq 12$. The same value of $N = 20$ suggested in Ref. [2.3] is used in the analysis carried out in this study.

2.7 Validation of Sine Function Model in 2-D Plain Textile Composite

To validate the Sine Function Model I, two cases already studied by other researchers are considered. Naik and Ganesh[2.1.-2.2] and D.Scida[2.4] *et al.* suggested their analytical models for the plain woven composites. The elastic properties determined by the Sine Function Model I are compared to other results that were obtained within some experiments for the plain weave composite together. Two different types of the yarns (open-weave yarns and closed weave yarns.) are considered. The open weave type in Figure 2.8 has the gap-length between the yarns, while the close weave type (no gap yarns) in Figure 2.9 does not consider the gap terms.

2.7.1 Open-Weave Case of Plain Woven Composite

Naik and Ganesh[2.1-2.2] have analyzed a plain woven composite using a slice element scheme and predicted some good results about the elastic properties of plain woven composites. Actually the Sine Function Model I is very similar to that in Ref. [2.1-2.2] whose analytical model was obtained using sinusoidal functions to represent geometrical shapes of the yarns and considered the gap geometry. The mechanical properties of the fiber and resin and the yarn geometrical parameters are provided in Tables 2.1-2.2. Also the experimental over-all fiber volume fractions are suggested in Table 2.3. To predict the yarn fiber volume fractions, the Sine Function Model I considers two cases (the Rule of mixture and Self-Consistent method) and calculate the predicted Young's modulus, shear modulus and Poisson's ratios for different geometrical parameters, for example, thickness for the yarns and widths for the resin and yarn.
The yarn fiber volume fractions (V_{fyarn}) based on different geometries, such as yarn shapes, are obtained.

From Tables 2.1 and 2.4, we see that the E-Glass/Epoxy and Graphite/Epoxy are a balanced plain weave while the Carbon/Epoxy is an unbalanced plain weave. The balanced yarns have the same elastic modulus for the fill and warp directions, but the unbalanced yarns have larger modulus (E_{22}) than that (E_{11}) of the warp direction. Similar same trends are found in the Sine Function Model I results.

In this case of the Sine Function Model I, results of the open-weave yarns are in good agreement with the experimental data. In Naik and Ganesh[2.1-2.2] model, slice array model (SAM) and element array model (EAM) commonly used constant centerlines along the fill and warp directions are applied to calculate stiffness and compliance matrices. However, some schemes in Refs. [2.1-2.2] led to some over-predicted values when carrying out integrations for arbitrary elements or regions. Consequently, these will yield some higher value of the equivalent elastic moduli. In general, the plain weaves are very much dependent on the undulation geometry which results in different crimp-angles along the yarn centerline. The Sine Function Model I consider this problem and perform integrations over the yarn centerline. The numerical integrations in this model are done by the trapezoidal rule. For the case of the E-Glass/Epoxy, the predicted elastic properties are in excellent agreement with the experimental data. The results of Carbon/Epoxy case have the same trends as those of other models.

2.7.2 Closed Weave Case I of Plain Woven Composite

D.Scida[2.4] *et al.* have investigated the plain woven composite using a micro-mechanics model and predicted 3-dimensional elastic properties. The model of D.Scida[2.4] *et al.* does not consider the gap geometry, such closed-weave yarns. In Ref. [2.4], experimental data for the over-all fiber volume fraction and the yarn fiber volume fraction have been provided. Also, the experimental values for Young's

modulus, Poisson's ratios and shear modulus were used to compare to properties obtained from the model by D.Scida[2.4] *et al*. To make the closed weave yarns, the Sine Function Model I substitutes zero values into gap-length variables (g_1 and g_2). The properties of the fiber and resin and the geometry parameters are given in Tables 2.5 and 2.6, respectively. By considering the Rule of mixture and the Self-Consistent method, the equivalent elastic properties are predicted. And then the mechanical elastic properties for the yarns are compared in Table 2.7 to those of the model of Ref. [2.4]. From comparison between our predicted values and the experimental data shown in Table 2.8, it becomes apparent that the Rule of mixture case has more favorable results than the Self-Consistent method.

The Sine Function Model I results of the closed-weave yarns give good results compared to experimental data. Geometrically, the closed-weave yarns are of the same shapes as in D.Scida[2.4] *et al.* From Tables 2.7-2.8, the results for the Sine Function Model show good agreement with the experimental data and other available results. In general, the predicted properties are smaller than those of Ref. [2.4] and a little higher than the values of the experimental data. However, transverse shear terms still have some problems in predicting correct elastic properties for the plain woven composites. In the Sine Function Model I, the iso-strain assumption is used and this assumption is a good scheme to find longitudinal Young's modulus but not the transverse Young's modulus and the Shear modulus. The balanced plain weaves does not introduce any problem when it comes to predicting the equivalent properties while for the unbalanced plain weaves there are still some problems in accurately determining the transverse shear modulus. In the Sine Function Model I, the Rule of mixture and Self-Consistent method are considered to calculate the mechanical properties for the yarns and the equivalent modulus of the closed plain weaves shown in Tables 2.7-2.8. We can see that the Self-Consistent method provides a little higher modulus than those of the Rule of mixtures and even experimental data.

Although the geometric undulations and micro-mechanical equations for composite materials are considered, the Sine Function Model I still does not fully predict exact equivalent modulus, three-dimensional equivalent values for the plain weaves. These problems are basically induced from the composite material modeling. If appropriate micro-mechanical assumptions are not used to find the elastic modulus of the fiber and the resin, a good equivalent modulus will not be obtained. To find an accurate equivalent modulus, a more accurate micro-mechanical assumption on the plain-woven composite modeling is needed.

2.7.3 Closed Weave Case II of Plain Woven Composite

Naik[2.3] calculated the 3-dimensional elastic properties of the flat-balanced plain woven textile using some of geometrical equations. Here our SFM I and Naik model analyze the closed weave yarns suggested in Ref. [2.3], and having the same geometry and material properties of fibers and resin are considered for calculating the equivalent moduli for the plain weaves. The SFM I use the curved yarns instead of the flat-curved yarns presented in Ref. [2.3]. The RUC geometry and sectional shapes for 2-D flat-curved plain weaves[2.3] are shown in Figure 2.11. Parametric studies also are performed to study the effects of various fabric parameters on overall properties. All the analyses in this section are made for yarns made of Hercules AS4 graphite fibers impregnated with Hercules 3501-6 epoxy matrix. A yarn packing density, p_d , of 0.75 and a fiber diameter, d_f , of 0.007mm is used in all calculations. The thermo mechanical properties used for the impregnated yarns (V_f =75%) and the resin are given in Table 2.9.

Figures 2.12 show the results of our Fortran code based on Naik modeling, and the effects of yarn sizes on the crimp angles and the stiffness properties for the closed plain woven composite. From the comparisons of results of Figures 2.12a and 2.12b, an excellent agreements between two analyses are found, and the micro-mechanical results of Figures 2.12c and 2.12d have the same trends of Naik results whose modeling are not considered the micro-mechanic equations of composites, such Rule of mixtures and the Self-Consistent method. As the yarn size is increased, the crimp angle is increased. The in-plane moduli, E_{xx} and E_{yy} , decreased while the transverse moduli, E_{zz} increased with increasing the yarn size.

The shear moduli, the in-plane Poisson's ratio, ν_{xy} are kept constant values with respect to the varied yarn sizes. However, transverse Poisson's ratios, ν_{xz} and ν_{yz} are very sensitive to the different yarn sizes.

Figures 2.13b, 2.13c and 2.13d present the results of the SFM I based on the curved yarns and the micro-mechanical schemes about the composites. As the yarn size in the Naik's case is increased, the crimp angle is increased with a little slope. The in-plane moduli, E_{xx} and E_{yy} decrease while the transverse moduli, E_{zz} and the in-plane shear moduli, G_{xy} have almost constant values with the increasing yarn size. The in-plane Poisson's ratio, ν_{xy} decreases a little with respect to the varied yarn sizes. However, the transverse Poisson's ratios, ν_{xz} and ν_{yz} are very sensitive to the different yarn sizes that are shown in Figure 2.13a of the Nailk case.

From Figures 2.12 and 2.13, we note that the mechanical properties of the textile composites are very sensitive to the yarns' geometrical shape. The plain woven textile constituted of curved yarns, elliptical yarns, have more varied stiffness values than the flat-curved yarns.

Another problem, the overall coefficients of thermal expansion (CTE) in the plain woven textile composites, also is studied. All equations of overall thermo-mechanical properties in section 2.5 are implemented by a Fortran code developed in this research, and some results are compared with other previous available results. The CTE's for the impregnated yarns with 75% fiber content are calculated using micro-mechanical equations based on Airy's stress function approach for a square fiber shape. The CTE's for the 3501-6 Epoxy resin (40 μ /^{o}C) was available in the literature. The CTE's for the fiber (α_{11} =-0.61 μ /^{o}C and α_{22} =3.8 μ /^{o}C) were back calculated using the square array micro-mechanical model together with the available CTE's for the resin and for a unidirectional 60% fiber volume fraction AS4/3501-6 laminate. The laminate CTE's were taken from Ref. [2.3].

A yarn spacing of 1.411mm and an overall fiber volume fraction, V_f, of 64% were used for all cases and the yarns had a 75% fiber content and resin layers. Different yarn sizes were considered, such as 2K-18K (K: one thousand filaments). To investigate the effects of yarn size on the overall thermal and mechanical properties, a parametric study is performed by our developed Fortran codes. The micro-mechanical analyses, Rule of mixtures and Self-Consistent method, are considered to check the effects of different crack densities (β). The issue of crack density will be explained in Chapter 5.

Figures 2.14a, 2.14b & 2.14c show the effects of yarn sizes on the crimp angle and the in-plane CTE's with same overall composite volume fraction. From Figure 2.14, it is seen that the in-plane CTE's, α_{xx} and α_{yy}, are not very sensitive to the yarn size. However, thickness CTE's, α_{zz}, is very sensitive to yarn sizes.

Figure 2.14a is calculated directly by the fiber and resin materials, but the results in Figures 2.14b and 2.14c are estimated by the micro-mechanical equations of the composite materials. From these three plots, one can conclude that the micro-mechanical analyses yield higher values of the CTE than that of the direct analysis in Figure 2.14a. Figures 2.15a & 2.15b show the effects of different crack densities in the in-plane CTE's of plain weaves. Two micro-mechanical analyses, the Rule of mixture and the Self-Consistent method, are used respectively. By using these micro-mechanical analyses, the in-plane CTE's (α_{xx} and α_{yy}) reveal the same trends, that are not sensitive to yarns sizes, but the thickness CTE's, α_{xx}, is very sensitive to yarn sizes. In addition, the increased crack densities in Figures 2.15a and 2.15b induces the reduced in-plane CTE's and the same sensitivity of the thickness CTE's already shown in Figures 2.14.

Although the overall composite volume fraction and interstitial matrix volume fraction is kept constant while the yarn size is varied, the CTE's are dependent on geometrical values, such as yarn sizes. In order to investigate the effects of fabric parameters on overall thermal and mechanical properties of textile composites, it is necessary to explicitly model the yarn architecture, the crimp angle and the crack density.

Table 2.1 The geometrical parameters for plain weave fabric yarns from Ref. [2.1]. (Unit: mm)

Material	Fill yarn			Warp yarn			H	V_f^o
	a_2	h_2	g_2	a_1	h_1	g_1		
Carbon / Epoxy	0.96	0.08	0.18	1.10	0.04	0.04	0.16	0.44[a]
E-Glass / Epoxy	0.62	0.10	0.05	0.62	0.10	0.05	0.20	0.42[a]
Graphite / Epoxy	2.00	0.50	0.50	2.00	0.50	0.50	1.00	0.41[b]

[a] Determined experimentally, [b] Calculated from yarn V_{fyarn} of 0.80.

Table 2.2 Elastic properties of fiber and resin from Ref. [2.1]. (Unit: GPa)

Materials	E_{22}	E_{11}	G_{12}	G_{23}	ν_{12}
Carbon	230.0	40.0	24.0	14.3	0.26
E-Glass	72.0	72.0	27.7	27.7	0.30
Graphite	388.0	7.2	6.8	2.4	0.23
Epoxy	3.5	3.5	1.3	1.3	0.35

Table2.3 The fiber volume fractions of V_f^o and V_{fyarn} from Ref. [2.1].

Material	Over-all (V_f^o)	Yarn (V_{fyarn})	Present model (V_{fyarn})
Carbon / Epoxy	0.44	0.78	0.7137
E-Glass / Epoxy	0.42	0.70	0.6684
Graphite / Epoxy	0.41	0.80	0.7103

Table 2.4 Comparison predicted elastic properties and experimental results of plain weave fabric lamina from Ref. [2.1].

Materials	Model	E_{22} (GPa)	E_{11} (GPa)	G_{12} (GPa)	ν_{12}	V_f^o
Carbon /Epoxy	SAM	58.9	52.4	5.1	0.07	-
	EAM – PS	57.1	51.2	4.7	0.10	-
	EAM – SP	35.6	35.4	4.7	0.10	-
	MMPM	57.6	57.6	3.0	0.07	-
	MKM	64.8	58.5	5.3	0.04	0.44
	Kabelka[2.5]	89.3	89.3	7.0	0.04	-
	Experiment	60.3	49.3	-	-	-
	Present Model*	55.4149	52.7236	2.9559	0.0380	-
E-Glass /Epoxy	SAM	20.3	20.3	3.7	0.23	-
	EAM – PS	19.6	19.6	3.7	0.20	-
	EAM – SP	17.9	17.9	3.7	0.20	-
	MMPM	20.7	20.7	2.9	0.17	-
	MKM	21.7	21.5	3.9	0.13	0.42
	Kabelka[2.5]	29.2	29.2	4.9	0.12	-
	Experiment	19.3	19.3	-	-	-
	Present Model*	18.9705	18.9705	3.0708	0.1035	-
Graphite /Epoxy	SAM	28.8	28.8	2.8	0.08	-
	EAM – PS	23.7	23.7	2.8	0.12	-
	EAM – SP	16.2	16.2	2.8	0.12	-
	MMPM	80.1	80.1	2.3	0.02	-
	MKM	32.2	32.2	3.0	0.04	0.41
	Kabelka[2.5]	44.3	44.3	3.7	0.03	-
	Experiment	-	-	-	-	-
	Present Model*	64.3001	64.3001	2.2784	-0.0249	-

SAM: slice array model, EAM-PS / SP: element array model-parallel series / series parallel, MMPM: modified mosaic parallel model, MKM: modified Kabelka's model,*: Rule of mixture.

Table 2.5 Elastic properties of fiber and resin from Ref. [2.4]. (Unit: GPa)

Materials	E_{11}	E_{22}	G_{12}	G_{23}	ν_{12}
E-Glass	73.0	73.0	30.4	30.4	0.20
Vinylester derakane	3.4	3.4	1.49	1.49	0.35

Table 2.6 The geometrical parameters for plain weave fabric yarns from Ref.[2.4]. (Unit: mm)

Material	Fill yarn			Warp yarn			H	V_f^o
	a_2	h_2	g_2	a_1	h_1	g_1		
E-Glass/Vinylester	0.60	0.05	0.0	0.60	0.05	0.0	0.10	0.55

Table 2.7 Comparison mechanical properties for the yarns from Ref. [2.4].

Materials	Model	E_{11} (GPa)	E_{22} (GPa)	G_{12} (GPa)	G_{23} (GPa)	ν_{12}	ν_{23}
	D.Scida[2.4]	57.50	18.80	7.44	7.26	0.25	0.29
E-Glass/ Vinylester (V_{fyarn} = 0.8)	Present Model*	59.0800	14.3303	6.2288	6.2294	0.2300	0.2300
	Present Model**	59.0966	22.2536	9.3559	8.5534	0.2241	0.3009

*: Rule of mixture, **: Self-Consistent method.

Table 2.8 Comparison of model and experimental results for the plain weaves from Ref. [2.4].

Materials	Model	E_{11} (GPa)	E_{33} (GPa)	G_{12} (GPa)	G_{23} (GPa)	ν_{12}	ν_{23}
	Experimental	24.8 ± 1.1	8.5 ± 2.6	6.5 ± 0.8	4.2 ± 0.7	0.1 ± 0.01	0.28 ± 0.07
	D.Scida[2.4]	25.33	13.46	5.19	5.24	0.12	0.29
E-Glass/ Vinylester (V_{fyarn} = 0.8)	Present Model*	24.5405	10.8728	4.5046	4.4801	0.1072	0.2865
	Present Model**	27.0674	16.0375	6.4932	6.3381	0.1323	0.2854

*: Rule of mixture, **: Self-Consistent method.

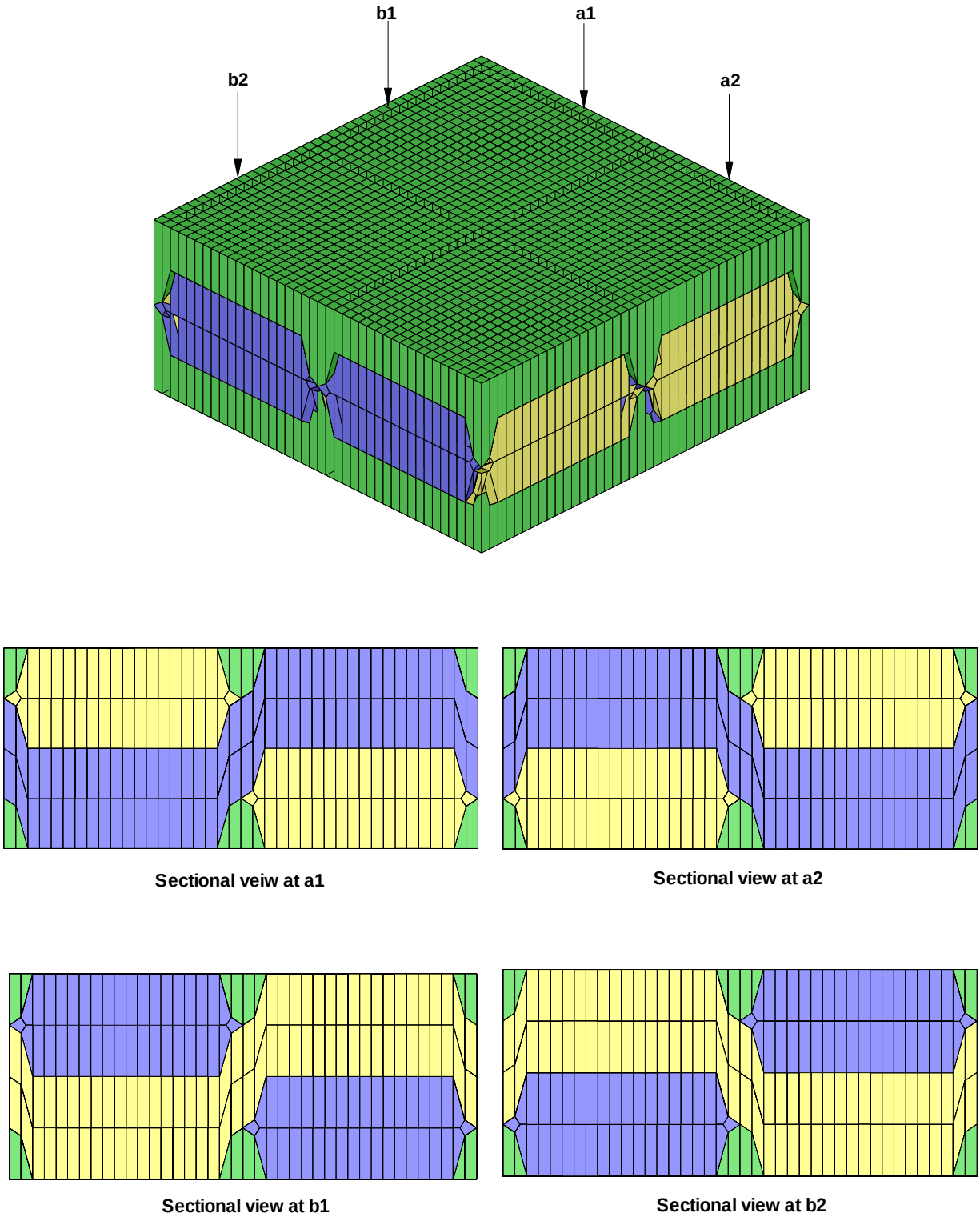

Figure 2.11: RUC and sectional shapes of 2-D flat-balanced plain weaves[2.3].

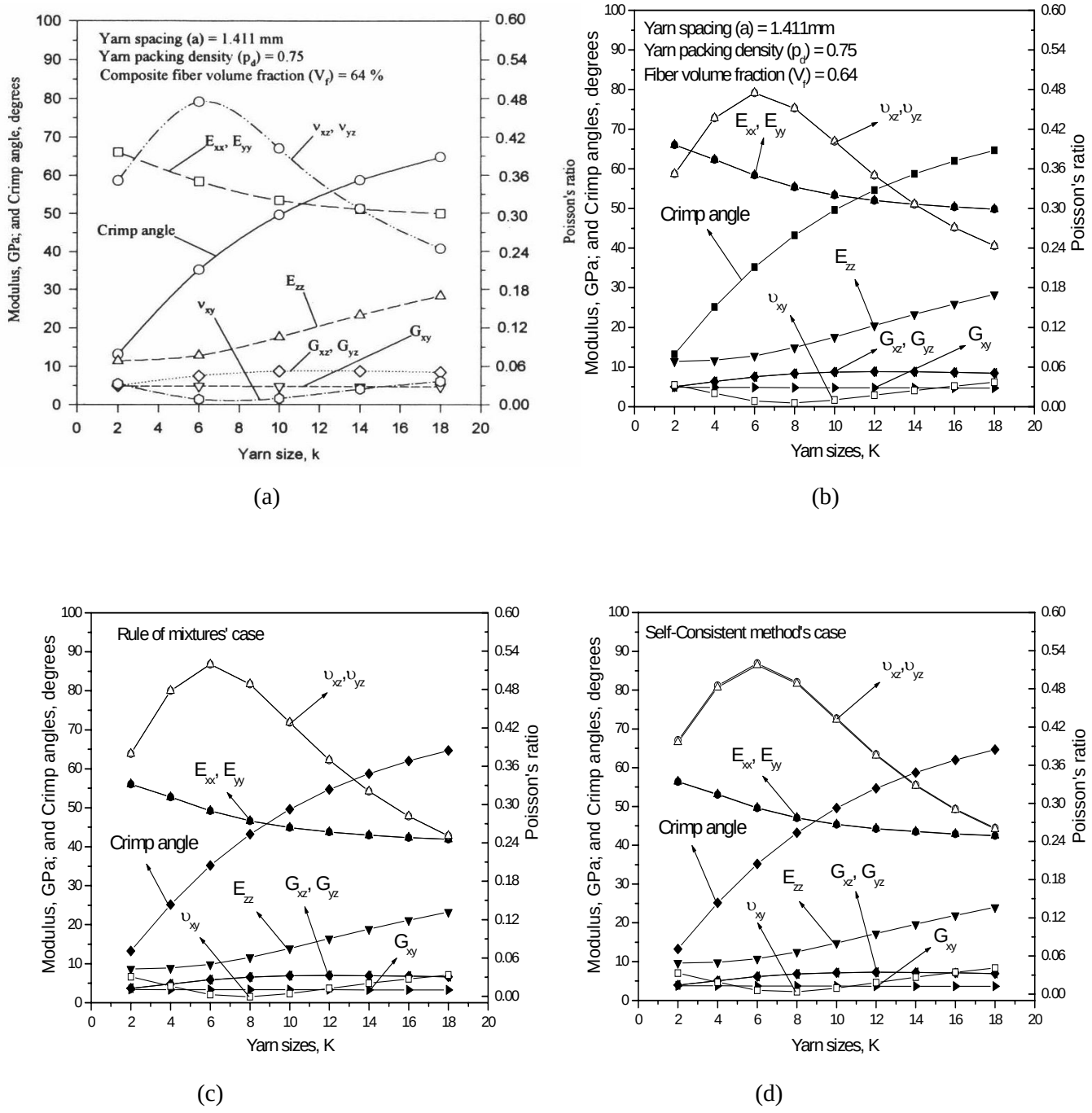

Figure 2.12: Plain weave moduli, Poisson's ratio and crimp angle with various flat-balanced yarns[2.3].

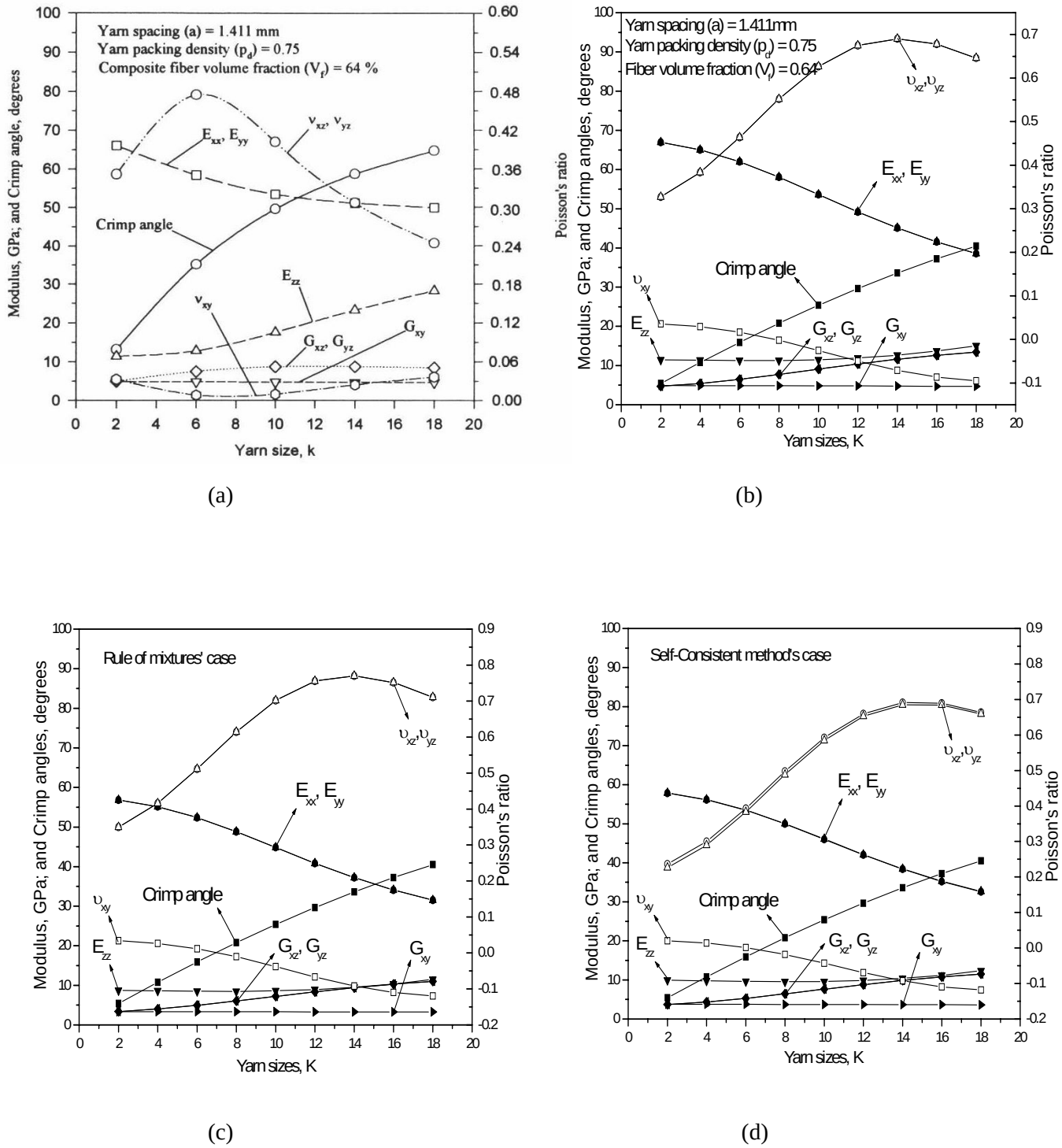

Figure 2.13: Plain weave moduli, Poisson's ratio and crimp angle with various elliptical yarns of SFM I.

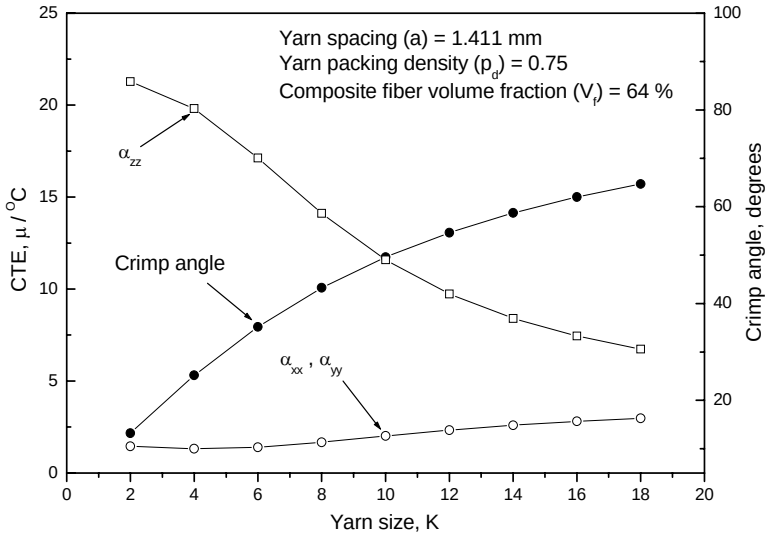

(a)

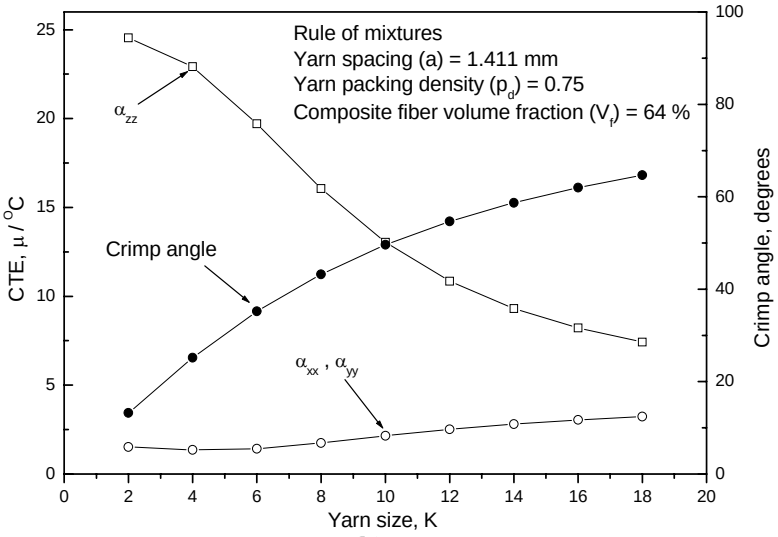

(b)

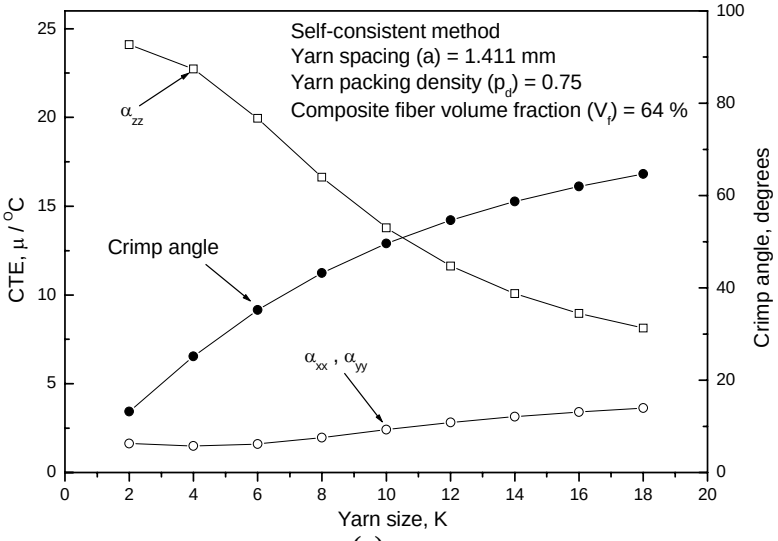

(c)

Figure 2.14: Variation of plain weave crimp angle and CTE's with a various yarn sizes.

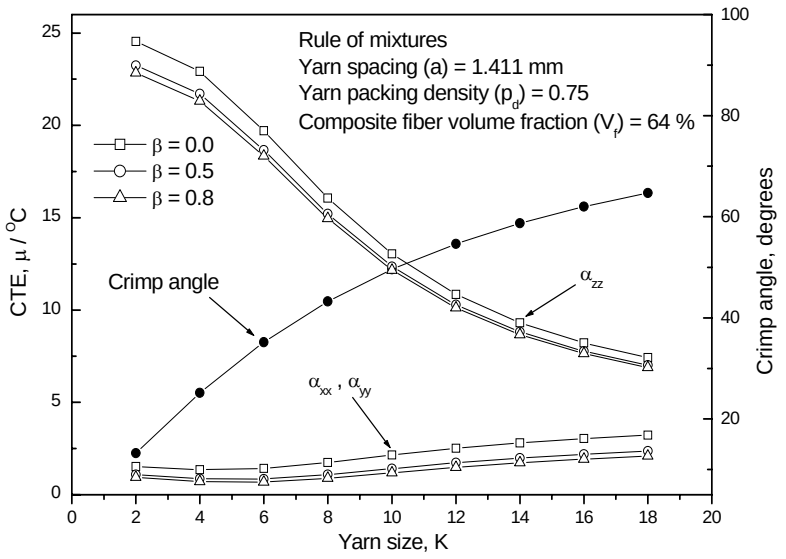

(a)

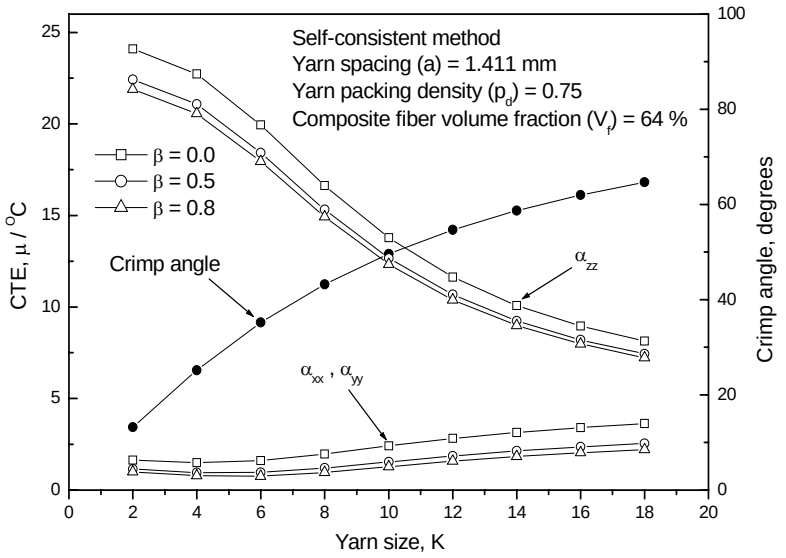

(b)

Figure 2.15: Variation of plain weave crimp angle and CTE's with yarn sizes and crack densities.

Table 2.9 Yarn and resin properties used in this analysis from Ref. [2.3]. (Unit: GPa, μ /°C)

Materials	E_{11}	$E_{22} = E_{33}$	$\nu_{12} = \nu_{13}$	ν_{23}	$G_{12} = G_{13}$	CTE α_{11}	CTE α_{22}
Yarn	144.80	11.73	0.23	0.30	5.52	-0.324	14.000
Resin	3.45	3.45	0.35	0.35	1.28	40.000	40.000

REFERENCES

2.1 Naik, N.K., and Ganesh, V.K., "Prediction of On-axes Elastic Properties of Plain Weave Fabric Composite," *Composites Science and Technology*, Vol. 45, No. 2, 1992, pp. 135–152.

2.2 Naik, N.K., and Ganesh, V.K., "An Analytical Method for Plain Weave Fabric Composite," *Composites*, Vol. 26, No. 4, 1995, pp. 281–289.

2.3 Naik, R.A., "Analysis of Woven and Braided Fabric Reinforced Composites," NASA Contract Report CR–194930, 1994.

2.4 Scida, D., Aboura, Z., Benzeggagh, M. L. and Bocherens, E., "A Micro-mechanics Model for 3D Elasticity and Failure of Woven-Fiber Composite Materials," *Composites Science and Technology*, Vol. 59, No. 4, 1999, pp. 505–517.

2.5 Kabelka J., "Prediction of the Thermal Properties of Fiber-resin Composites," In Developments in Reinforced Plastics-3, G. Pritchard (Ed.), Elsevier Applied Science Publishers, London, 1984, pp. 167–202.

Chapter 3 Homogenization II of 2-D Plain Woven Textile Composite

3.1 Introduction

In Chapter 2, a simple analytical modeling, Sine Function Model I, for the 2-D plain woven textile composite was suggested and its numerical accuracy as compared to other previous modeling is evaluated. The Sine Function Model I (SFM I), and other previous modeling of 2-D plain weaves, do not consider interfaced/strengthened layers, between the yarns; warps, fills and resin layers. The interfaced/strengthened layers in the plain woven textile composites have an important role to combine the fill or warp yarns. Although, there are some studies on this problem, still its modeling and mechanical behaviors have not been adequately examined. This study suggests one interfaced plain-woven textile model, referred to as Sine Function Model II (SFM II) and its mechanical behavior is studied.

3.2 Sine Function Model II for Strengthened Plain Woven Textile Composites

As shown in Fig 3.1-3.2, the Repeating Unit Cell of strengthened plain woven composites consists of 10 components; 2-resin layers, 2-fill yarns, 2-warp yarns and 4-interface layers. Similar to Sine Function Model I (SFM I), that used two sine functions for upper and lower surfaces of the yarns, the geometrical shape of the RUC will be sufficiently described using the same representation. The SFM II uses the same two assumptions as were used in SFM I: (a) the centerline of the yarn path consists of undulation portions with the centerline of the undulating portions described by the sine functions, (b) the cross-sectional area and thickness of the yarn normal to its centerline are uniform along the arc-length of the centerline. The sectional yarn shapes in Figure 3.3 based on 2-points (B_1 and B_2) in Figure 3.4 are expressed by the upper and lower sine-functions, such as equations of geometrical surfaces; z_1^{up}, z_1^{lower}, z_2^{up} and z_2^{lower}. Here, the subscripts 1 and 2 mean warp-yarn and fill-yarn, respectively.

$$z_1^{up} = \frac{t_2}{2}\sin\left[\frac{x\pi}{a_2+g_2}\right] + \frac{g_2}{2}\tan\left[\frac{t_2\pi}{2(a_2+g_2)}\cos\left[\frac{\pi g_2}{2(a_2+g_2)}\right]\right] + \frac{t_1}{2}\sin\left[\frac{y\pi}{a_1+g_1}\right] - \frac{g_1}{2}\tan\left[\frac{t_1\pi}{2(a_1+g_1)}\cos\left[\frac{\pi g_1}{2(a_1+g_1)}\right]\right] \quad (3.1)$$

$$z_1^{lower} = \frac{t_2}{2}\sin\left[\frac{x\pi}{a_2+g_2}\right] + \frac{g_2}{2}\tan\left[\frac{t_2\pi}{2(a_2+g_2)}\cos\left[\frac{\pi g_2}{2(a_2+g_2)}\right]\right] - \frac{t_1}{2}\sin\left[\frac{y\pi}{a_1+g_1}\right] + \frac{g_1}{2}\tan\left[\frac{t_1\pi}{2(a_1+g_1)}\cos\left[\frac{\pi g_1}{2(a_1+g_1)}\right]\right] \quad (3.2)$$

$$z_2^{up} = \frac{t_2}{2}\sin\left[\frac{x\pi}{a_2+g_2}\right] - \frac{g_2}{2}\tan\left[\frac{t_2\pi}{2(a_2+g_2)}\cos\left[\frac{\pi g_2}{2(a_2+g_2)}\right]\right] - \frac{t_1}{2}\sin\left[\frac{y\pi}{a_1+g_1}\right] - \frac{g_1}{2}\tan\left[\frac{t_1\pi}{2(a_1+g_1)}\cos\left[\frac{\pi g_1}{2(a_1+g_1)}\right]\right] \quad (3.3)$$

$$z_2^{lower} = -\frac{t_2}{2}\sin\left[\frac{x\pi}{a_2+g_2}\right] + \frac{g_2}{2}\tan\left[\frac{t_2\pi}{2(a_2+g_2)}\cos\left[\frac{\pi g_2}{2(a_2+g_2)}\right]\right] -$$

$$\frac{t_1}{2}\sin\left[\frac{y\pi}{a_1+g_1}\right]-\frac{g_1}{2}\tan\left[\frac{t_1\pi}{2(a_1+g_1)}\cos\left[\frac{\pi g_1}{2(a_1+g_1)}\right]\right] \tag{3.4}$$

Here the undulation lengths are $u_1=a_1+g_1$ and $u_2=a_2+g_2$ along the warp and fill directions. The centerline coordinates; z_{c1} and z_{c2}, of the resin strengthened yarns in the undulations are

$$\begin{aligned} z_{c1} &= \frac{t_2}{2}\sin\left[\frac{x\pi}{a_2+g_2}\right]+\frac{g_2}{2}\tan\theta_{c1} \\ &= \frac{t_2}{2}\sin\left[\frac{x\pi}{a_2+g_2}\right]+\frac{g_2}{2}\tan\left[\frac{t_2\pi}{2(a_2+g_2)}\cos\left[\frac{\pi g_2}{2(a_2+g_2)}\right]\right] \end{aligned} \tag{3.5}$$

$$\begin{aligned} z_{c2} &= -\frac{t_1}{2}\sin\left[\frac{y\pi}{a_1+g_1}\right]-\frac{g_1}{2}\tan\theta_{c2} \\ &= -\frac{t_1}{2}\sin\left[\frac{y\pi}{a_1+g_1}\right]-\frac{g_1}{2}\tan\left[\frac{t_1\pi}{2(a_1+g_1)}\cos\left[\frac{\pi g_1}{2(a_1+g_1)}\right]\right] \end{aligned} \tag{3.6}$$

From Eqs. (3.5) and (3.6), the crimp angles are varied by different undulation regions. As suggested in SFM I, the crimp angles can be written by different x and y values along the x and y axes.

$$\begin{aligned} \theta_{c1} &= \tan^{-1}\left[\frac{t_2\pi}{2(a_2+g_2)}\cos\left[\frac{\pi x}{(a_2+g_2)}\right]\right],\ (0\le x\le u_2) \\ \theta_{c1} &= \tan^{-1}\left[\frac{-t_2\pi}{2(a_2+g_2)}\cos\left[\frac{\pi(x-u_2)}{(a_2+g_2)}\right]\right],\ (u_2\le x\le 2u_2) \end{aligned} \tag{3.7}$$

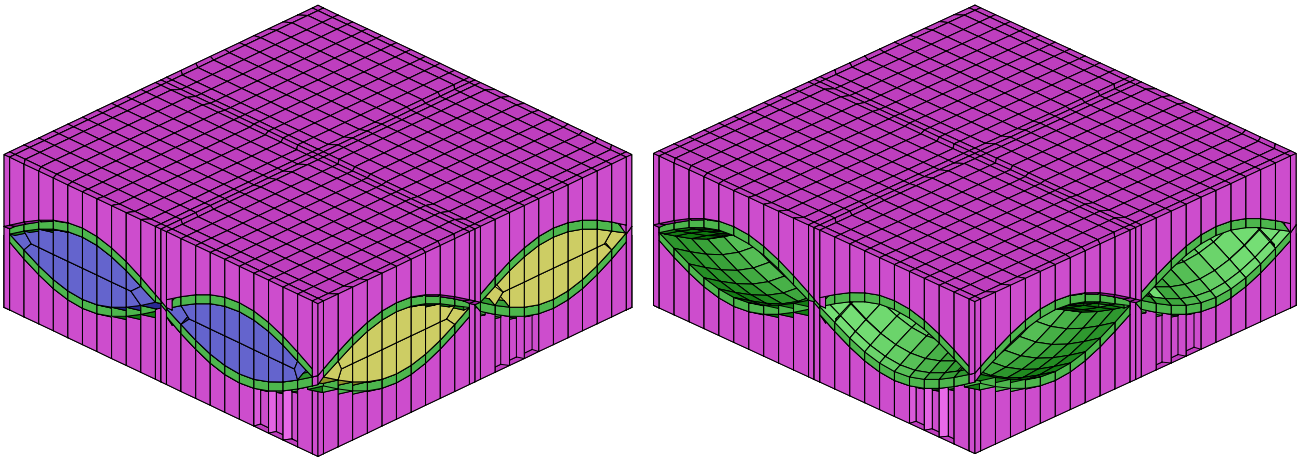

Figure 3.1: Repeating Unit Cell (RUC) for strengthened plain weave.

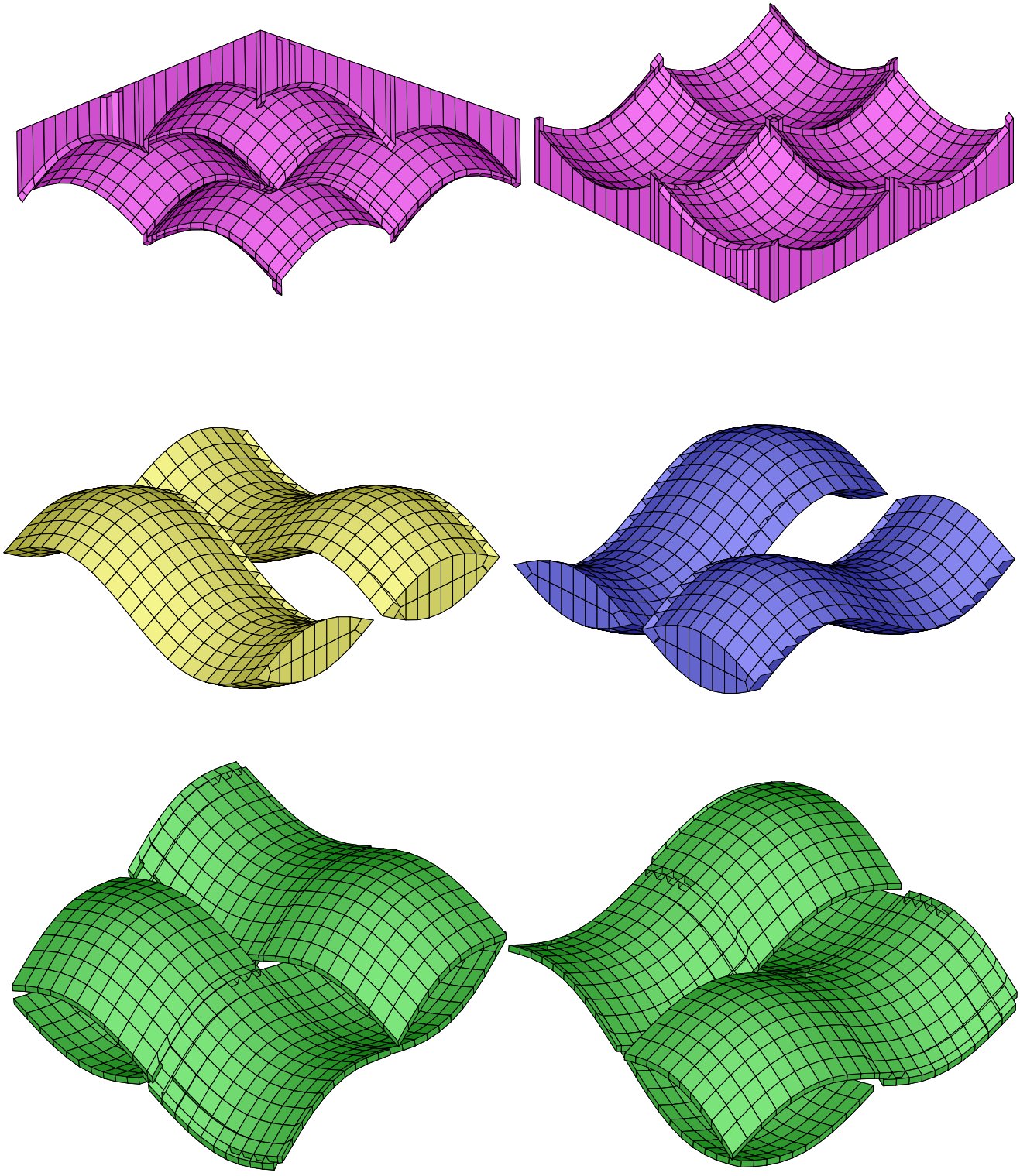

Figure 3.2: The Repeating Unit Cell (RUC) components of the SFM II.

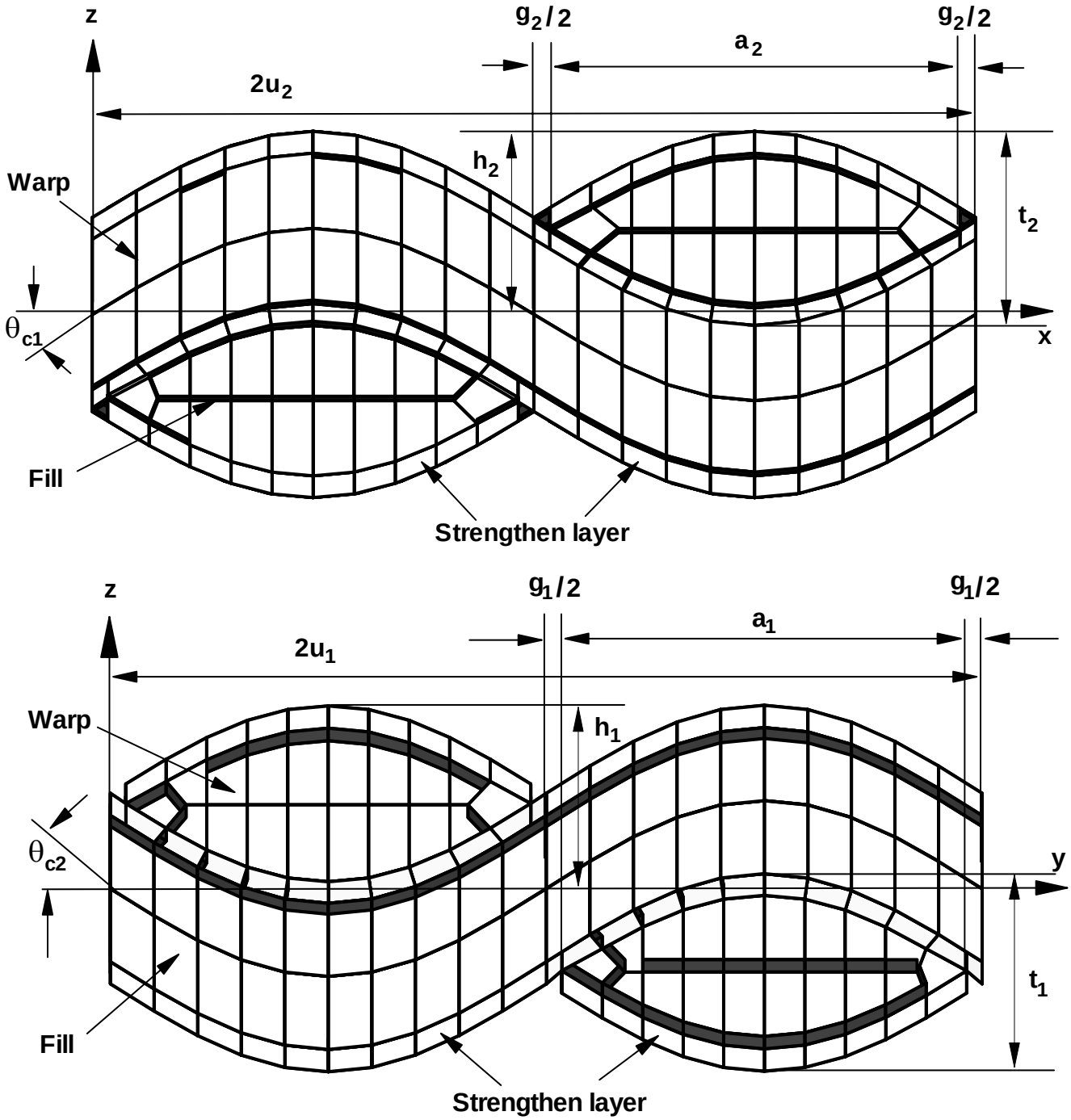

Figure 3.3: Interfaced yarn cross-sections: warp and fill directions.

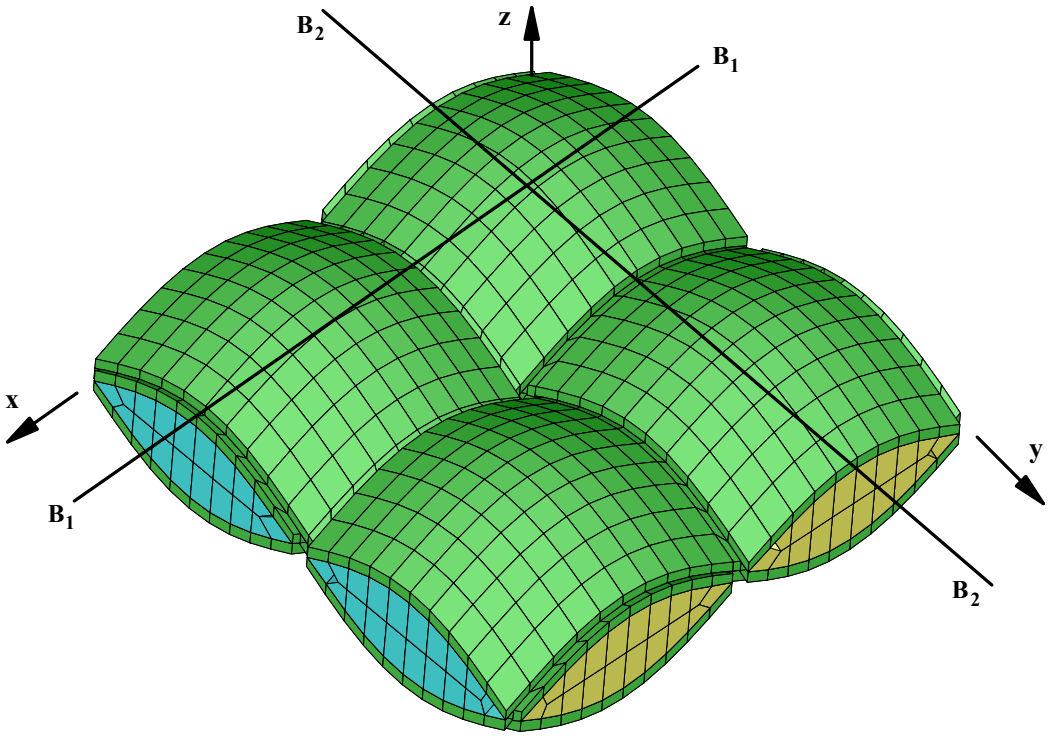

Figure 3.4: Two sectional points in the RUC.

$$\theta_{c2} = \tan^{-1}\left[\frac{-t_1\pi}{2(a_1+g_1)}\cos\left[\frac{\pi y}{(a_1+g_1)}\right]\right],\ (0 \le y \le u_1)$$

$$\theta_{c2} = \tan^{-1}\left[\frac{t_1\pi}{2(a_1+g_1)}\cos\left[\frac{\pi(y-u_1)}{(a_1+g_1)}\right]\right],\ (u_1 \le y \le 2u_1) \qquad (3.8)$$

To find the equations of volume fractions of the yarns, yarn sectional areas (A_1 and A_2) are induced by integrating the yarns along the undulation paths. The interfaced fill and warp strands' area equations are as follows.

$$A_1 = \int_0^{a_1}(z_1^{up} - z_1^{lower})dy$$

$$= 2\int_0^{a_1}\left\{\frac{t_1}{2}\sin\left[\frac{y\pi}{a_1+g_1}\right] - \frac{g_1}{2}\tan\left[\frac{t_1\pi}{2(a_1+g_1)}\cos\left[\frac{\pi g_1}{2(a_1+g_1)}\right]\right]\right\}dy$$

$$= \frac{t_1(a_1+g_1)}{\pi}\left[1-\cos\left[\frac{a_1\pi}{(a_1+g_1)}\right]\right] - (g_1a_1)\tan\left[\frac{t_1\pi}{2(a_1+g_1)}\cos\left[\frac{g_1\pi}{2(a_1+g_1)}\right]\right] \qquad (3.9)$$

$$A_2 = \int_0^{a_2} (z_2^{up} - z_2^{lower})dx$$

$$= 2\int_0^{a_2} \left\{ \frac{t_2}{2} \sin\left[\frac{x\pi}{a_2 + g_2} \right] - \frac{g_2}{2} \tan\left[\frac{t_2\pi}{2(a_2 + g_2)} \cos\left[\frac{\pi g_2}{2(a_2 + g_2)} \right] \right] \right\} dx$$

$$= \frac{t_2(a_2 + g_2)}{\pi} \left[1 - \cos\left[\frac{a_2\pi}{(a_2 + g_2)} \right] \right] - (g_2 a_2) \tan\left[\frac{t_2\pi}{2(a_2 + g_2)} \cos\left[\frac{g_2\pi}{2(a_2 + g_2)} \right] \right] \quad (3.10)$$

The expressions for volumes (V_1 and V_2) of interfaced yarns are in the form of the Second Elliptic integrals (**E**). By using hyper-geometric series, the elliptical integrals can be evaluated. In the SFM I, this problem is already approached by using the relationship between the hyper-geometric function and the Second Elliptical integrals, considering linear order terms. So, higher-order terms for the hyper-geometric function are not used to determine approximate yarn volumes in the Second Elliptic integrals. The expressions for the yarn volumes of the SFM II are

$$V_1 = A_1 \int_0^{u_2} \sqrt{1 + (\frac{dz_{c1}}{dx})^2} dx = A_1 \int_0^{u_2} \sqrt{1 + (\frac{t_2\pi}{2u_2})^2 \cos^2(\frac{\pi x}{u_2})} dx \quad (3.11)$$

$$V_2 = A_2 \int_0^{u_1} \sqrt{1 + (\frac{dz_{c2}}{dy})^2} dy = A_2 \int_0^{u_1} \sqrt{1 + (\frac{t_1\pi}{2u_1})^2 \cos^2(\frac{\pi y}{u_1})} dy \quad (3.12)$$

The thickness (h_1 and h_2) of interfaced fill and warp yarns feature the common resin strengthened layers in the z direction. From Eqs. (3.1)-(3.4) and yarn geometry, the interfaced yarn thickness is

$$h_1 = t_1 - \frac{1}{2} g_2 \tan\left[\frac{t_2\pi}{2(a_2 + g_2)} \cos\left[\frac{g_2\pi}{2(a_2 + g_2)} \right] \right]$$

$$h_2 = t_2 - \frac{1}{2} g_1 \tan\left[\frac{t_1\pi}{2(a_1 + g_1)} \cos\left[\frac{g_1\pi}{2(a_1 + g_1)} \right] \right] \quad (3.13)$$

The thickness of the resin layer h_m is

$$h_m = \frac{g_1}{2} \tan\left[\frac{t_1\pi}{2(a_1 + g_1)} \cos\left[\frac{g_1\pi}{2(a_1 + g_1)} \right] \right] + \frac{g_2}{2} \tan\left[\frac{t_2\pi}{2(a_2 + g_2)} \cos\left[\frac{g_1\pi}{2(a_2 + g_2)} \right] \right] \quad (3.14)$$

The volumes of interfaced layers are very small as compared to the fill and warp yarns' volumes. To find the volumes of strengthen layers, we have to know the thicknesses (t_f^i and t_w^i) of fill and warp yarns in the strengthen layers in the unit cell, because one RUC has four unit cells that include three resin strengthened layers in each of them. The equations of resin strengthened layer's thickness in the warp and fill yarns (t_f^i and t_w^i) are described by crimp angles.

$$t_f^i = g_2 \tan\left[\frac{t_2\pi}{2(a_2 + g_2)} \cos\left[\frac{g_2\pi}{2(a_2 + g_2)} \right] \right], \; t_w^i = g_1 \tan\left[\frac{t_1\pi}{2(a_1 + g_1)} \cos\left[\frac{g_1\pi}{2(a_1 + g_1)} \right] \right] \quad (3.15)$$

The centerline coordinates (z_{c1}^i and z_{c2}^i) of the resin strengthened layers along the undulations are

$$z_{c1}^{i} = (\frac{h_1}{2} - \frac{t_w^i}{2})\sin\left[\frac{\pi y}{a_1}\right] + \frac{h_1}{2},\ z_{c2}^{i} = (\frac{h_2}{2} - \frac{t_f^i}{2})\sin\left[\frac{\pi x}{a_2}\right] + \frac{h_2}{2} \tag{3.16}$$

The undulation lengths of the strengthened layers are obtained from derivatives of Eq. (3.16) expressed as the undulation lengths and thickness.

$$\frac{dz_{c1}^{i}}{dy} = \frac{\pi}{a_1}(\frac{h_1}{2} - \frac{t_w^i}{2})\cos\left[\frac{\pi y}{a_1}\right],\ \frac{dz_{c2}^{i}}{dx} = \frac{\pi}{a_2}(\frac{h_2}{2} - \frac{t_f^i}{2})\cos\left[\frac{\pi x}{a_2}\right] \tag{3.17}$$

To find the strengthened yarns' volumes, the yarn sectional areas (A_f^i and A_w^i) integrations are performed along the undulation paths in the interfaced layers. The yarn sectional areas of the strengthened layers are

$$A_w^i = t_w^i \int_0^{a_1} \sqrt{1 + (\frac{dz_{c1}^{i}}{dy})^2}\, dy,\ A_f^i = t_f^i \int_0^{a_2} \sqrt{1 + (\frac{dz_{c2}^{i}}{dx})^2}\, dx \tag{3.18}$$

The strengthened yarns' volumes (V_f^i and V_w^i) with the yarn sectional areas are determined through the integrations along the undulation regions.

$$V_w^i = t_w^i \int_0^{a_1} \sqrt{1 + (\frac{dz_{c1}^{i}}{dy})^2}\, dy \int_0^{u_2} \sqrt{1 + (\frac{dz_{c1}}{dx})^2}\, dx,\ V_f^i = t_f^i \int_0^{a_2} \sqrt{1 + (\frac{dz_{c2}^{i}}{dx})^2}\, dx \int_0^{u_1} \sqrt{1 + (\frac{dz_{c2}}{dy})^2}\, dy \tag{3.19}$$

If these three strengthened layers are considered by two-warp yarn's interfaces and one-fill yarn's interfaces, the strengthened layer volume can be expressed as:

$$V_{str} = V_w^i + V_w^i / 2 + V_f^i + V_f^i / 2 = V_{str}^w + V_{str}^f \tag{3.20}$$

The total volume of RUC is expressed in the thickness and undulation terms. The total resin thickness (h_m) in the RUC includes a half thickness for upper and lower resin layers, respectively. All these volumes are calculated using the same integration scheme as used in the SFM I and by considering the appropriate number of uniform yarn slices along the slices' centerlines that are uniform along the centerline arc-length.

$$V_{total} = H(a_1 + g_1)(a_2 + g_2) = (h_m + h_1 + h_2)(a_1 + g_1)(a_2 + g_2) \tag{3.21}$$

The resin volume V_{resin}, the resin volume fraction V_f^r and the strengthened volume fractions for the fill and the warp (V_f^{strf} V_f^{strw}) in the RUC are

$$V_{resin} = V_{total} - (V_1 + V_2 + V_{str}),\ V_f^r = \frac{V_{resin}}{V_{total}} = \frac{V_{total} - (V_1 + V_2 + V_{str}^f + V_{str}^w)}{V_{total}},\ V_f^{strf} = \frac{V_{str}^f}{V_{total}},\ V_f^{strw} = \frac{V_{str}^w}{V_{total}} \tag{3.22}$$

The volume fractions for the yarns are specified under different fiber volume fractions about the fill and warp yarns. So, over-all fiber volume fraction (V_f^o) is given by

$$V_f = V_{f1}\frac{V_1}{V_{total}} + V_{f2}\frac{V_2}{V_{total}} = V_f^o \tag{3.23}$$

If the fiber volume fractions for the yarns are the same, $V_{f1} = V_{f2} = V_{fyarn}$, the equation of V_{fyarn} is

$$V_{fyarn} = V_f^o \frac{V_{total}}{(V_1 + V_2)} = \frac{V_f^o V_{total}}{(V_{total} - V_{resin})} \tag{3.24}$$

3.3 Equivalent Modulus for Resin-Strengthened Plain Woven Textile Composite

To calculate the equivalent modulus for the resin-strengthened textile composite RUC, the iso-strain assumption is used, and the warp yarns, fill yarns, strengthen layers and resin layers in a small sub-domain zone are assumed to be perfectly bonded. From this assumption, the displacements at the interface between two layers; for example, warp yarn and resin layer, warp yarn and strengthen layer, fill yarn and strengthen layer, fill yarn and resin layer are equal. The displacement continuity over these interfacial layers means the displacement gradients in the in-plane $x - y$ directions. This assumption is invoked in one of the sub-domains represented by the three-dimensional rectangular shapes, see Figure 3.5, and the small sub-domain is depicted in the x - y - z Cartesian coordinate system. In agreement with the Voigt approximation (iso-strain condition), and the Reuss approximation (iso-stress condition), we can derive Eqs. (3.25)-(3.26).

$$\begin{aligned}
&\varepsilon_{11}^{resin} = \varepsilon_{11}^{warp}, \varepsilon_{11}^{warp} = \varepsilon_{11}^{str}, \varepsilon_{11}^{str} = \varepsilon_{11}^{fill}, \varepsilon_{11}^{fill} = \varepsilon_{11}^{resin} \\
&\varepsilon_{22}^{resin} = \varepsilon_{22}^{warp}, \varepsilon_{22}^{warp} = \varepsilon_{22}^{str}, \varepsilon_{22}^{str} = \varepsilon_{22}^{fill}, \varepsilon_{22}^{fill} = \varepsilon_{22}^{resin} \\
&\varepsilon_{12}^{resin} = \varepsilon_{12}^{warp}, \varepsilon_{12}^{warp} = \varepsilon_{12}^{str}, \varepsilon_{12}^{str} = \varepsilon_{12}^{fill}, \varepsilon_{12}^{fill} = \varepsilon_{12}^{resin} \qquad (3.25) \\
&\sigma_{33}^{resin} = \sigma_{33}^{warp}, \sigma_{33}^{warp} = \sigma_{33}^{str}, \sigma_{33}^{str} = \sigma_{33}^{fill}, \sigma_{33}^{fill} = \sigma_{33}^{resin} \\
&\sigma_{23}^{resin} = \sigma_{23}^{warp}, \sigma_{23}^{warp} = \sigma_{23}^{str}, \sigma_{23}^{str} = \sigma_{23}^{fill}, \sigma_{23}^{fill} = \sigma_{23}^{resin} \\
&\sigma_{13}^{resin} = \sigma_{13}^{warp}, \sigma_{13}^{warp} = \sigma_{13}^{str}, \sigma_{13}^{str} = \sigma_{13}^{fill}, \sigma_{13}^{fill} = \sigma_{13}^{resin} \qquad (3.26)
\end{aligned}$$

In agreement with the average stress of Eq. (2.15) and the strain energy concept of Eqs. (2.16)-(2.17) as presented in Chapter 2, we can derive the equivalent stress components in the layers.

$$\begin{aligned}
&\overline{\sigma}_{ij} = \frac{1}{V}\int_V \sigma_{ij} dV = \frac{1}{V}\left\{ V_{warp}\overline{\sigma}_{ij}\Big|_{warp} + V_{fill}\overline{\sigma}_{ij}\Big|_{fill} + V_{str}^{f}\overline{\sigma}_{ij}\Big|_{strf} + V_{str}^{w}\overline{\sigma}_{ij}\Big|_{strw} + V_{resin}\overline{\sigma}_{ij}\Big|_{resin} \right\} \\
&\{\overline{\sigma}\} = V_{f1}\{\overline{\sigma}\}_{fill} + V_{f2}\{\overline{\sigma}\}_{warp} + V_f^{strf}\{\overline{\sigma}\}_{strf} + V_f^{strw}\{\overline{\sigma}\}_{strw} + V_f^{r}\{\overline{\sigma}\}_{resin} \\
&\{\overline{\sigma}\} = V_{f1}\left[\overline{C}_{eqf}\right]\{\overline{\varepsilon}\}_{fill} + V_{f2}\left[\overline{C}_{eqw}\right]\{\overline{\varepsilon}\}_{warp} + V_f^{strf}\left[\overline{C}_{eqstrf}\right]\{\overline{\varepsilon}\}_{strf} + V_f^{strw}\left[\overline{C}_{eqstrw}\right]\{\overline{\varepsilon}\}_{strw} \\
&\quad + V_f^{r}\left[\overline{C}_{eqr}\right]\{\overline{\varepsilon}\}_{resin} = \left[C_{eq}\right]\{\overline{\varepsilon}\}
\end{aligned} \qquad (3.27)$$

From the iso-strain assumption in Eq.(3.27), we obtain another equation for equivalent material properties of the RUC.

$$C_{eq} = \frac{1}{V}\left[\int_{V_{fill}} C_{fill}dV + \int_{V_{warp}} C_{warp}dV + \int_{V_{str}^{f}} C_{strf}dV + \int_{V_{str}^{w}} C_{strw}dV + \int_{V_{resin}} C_{resin}dV\right] \qquad (3.28)$$

$$\begin{aligned}
C_{eq} &= V_{f1}\overline{C}_{eqf} + V_{f2}\overline{C}_{eqw} + V_f^{strf}\overline{C}_{eqstrf} + V_f^{strw}\overline{C}_{eqstrw} + V_f^{r}\overline{C}_{eqr} \\
&= C_{eqf} + C_{eqw} + C_{eqstrf} + C_{eqstrw} + C_{eqr}
\end{aligned} \qquad (3.29)$$

Applying the transformation matrix shown in Appendix B to the matrices $\overline{C}_{eqf}^{ij}$ and $\overline{C}_{eqw}^{ij}$ in Eq.(3.29), the equivalent matrices are

$$C_{eqw} = \frac{2}{u_2^u}\int_0^{u_2} C_1(0,\theta_{c1})\sqrt{1+(\frac{dz_{c1}}{dx})^2}\,dx = \frac{2}{u_2^u}\int_0^{u_2} C_1(0,\theta_{c1})\sqrt{1+(\frac{t_2\pi}{2u_2})^2\cos^2(\frac{\pi x}{u_2})}dx \qquad (3.30)$$

$$C_{eqf} = \frac{2}{u_1^u}\int_0^{u_1} C_1(\frac{\pi}{2},\theta_{c2})\sqrt{1+(\frac{dz_{c2}}{dy})^2}\,dy = \frac{2}{u_1^u}\int_0^{u_1} C_1(\frac{\pi}{2},\theta_{c2})\sqrt{1+(\frac{t_1\pi}{2u_1})^2\cos^2(\frac{\pi y}{u_1})}dy \qquad (3.31)$$

3.4 Validation of Sine Function Model II

This study uses one Sine Function Model, called Sine Function Model II (SFM II), to predict the equivalent modulus for the resin strengthened textile composites. To evaluate the accuracy of SFM II, two analytical models are considered and our numerical results are compared to results given by others, for example, Naik and Ganesh[3.1-3.2] and D.Scida[3.3] *et al.*'s. From several numerical examples, the characteristics of the interfaced yarns are compared. Naik and Ganesh[3.1-3.2] studied the open weave type on the plain weave textile composite having gap-lengths between the fill and warp yarns, while D.Scida[3.3] *et al.* analyzed the closed weave type textile composites but without considering the gap-lengths. In these studies, they did not consider the interfaced/strengthen layers that are filled with resin materials between the resin and yarn regions. Although they are different model types, this study and the previous models are compared in terms of effective elastic characteristics as a function of different geometrical parameters of SFM II.

3.4.1 Open-Weave Case of Plain Woven Composite

In order to examine the micro-mechanical modeling for the plain woven composite, this study uses three material systems with different geometries as suggested in Tables 3.1-3.3. The fabric geometrical parameters of Carbon/Epoxy, Graphite/Epoxy and E-glass/Epoxy woven fabric lamina are taken from Ref. [3.1].

It is noted that the E-glass/Epoxy and Graphite/Epoxy plain weave fabrics consist of balanced strands while the Carbon/Epoxy consists of unbalanced strands. The Carbon/Epoxy woven fabrics feature larger transverse Young's modulus (E_{22}) than that of longitudinal Young's modulus (E_{11}) in the effective elastic moduli. The undulation effects also are found in the coupling terms, respectively. For example, the Carbon/Epoxy woven fabric has been affected more by the high coupling terms than the E-glass/Epoxy or Graphite/Epoxy plain weaves. This is because less undulation regions induce larger local bending terms in each yarn slice that affect the compliance of RUC. In the two cases, the Graphite/Epoxy and the E-glass/Epoxy, the Graphite/Epoxy woven composite has smaller coupling terms in the effective elastic properties as compared to the E-glass/Epoxy and with the Carbon/Epoxy. This result is caused by the large ratios of Young's moduli (E_{11}/E_{22}) and the greater undulations of the strands.

Table 3.1 The geometrical parameters for plain weave fabric yarns from Ref. [3.1]. (Unit: mm)

Material	Fill yarn			Warp yarn			H	V_f^o
	a_2	h_2	g_2	a_1	h_1	g_1		
Carbon / Epoxy	0.96	0.08	0.18	1.10	0.04	0.04	0.16	0.44[a]
E-Glass / Epoxy	0.62	0.10	0.05	0.62	0.10	0.05	0.20	0.42[a]
Graphite / Epoxy	2.00	0.50	0.50	2.00	0.50	0.50	1.00	0.41[b]

[a] Determined experimentally, [b] Calculated from yarn V_{fyarn} of 0.80.

Table 3.2 Elastic properties of fiber and resin from Ref. [3.1]. (Unit: GPa)

Materials	E_{22}	E_{11}	G_{12}	G_{23}	ν_{12}
Carbon	230.0	40.0	24.0	14.3	0.26
E-Glass	72.0	72.0	27.7	27.7	0.30
Graphite	388.0	7.2	6.8	2.4	0.23
Epoxy	3.5	3.5	1.3	1.3	0.35

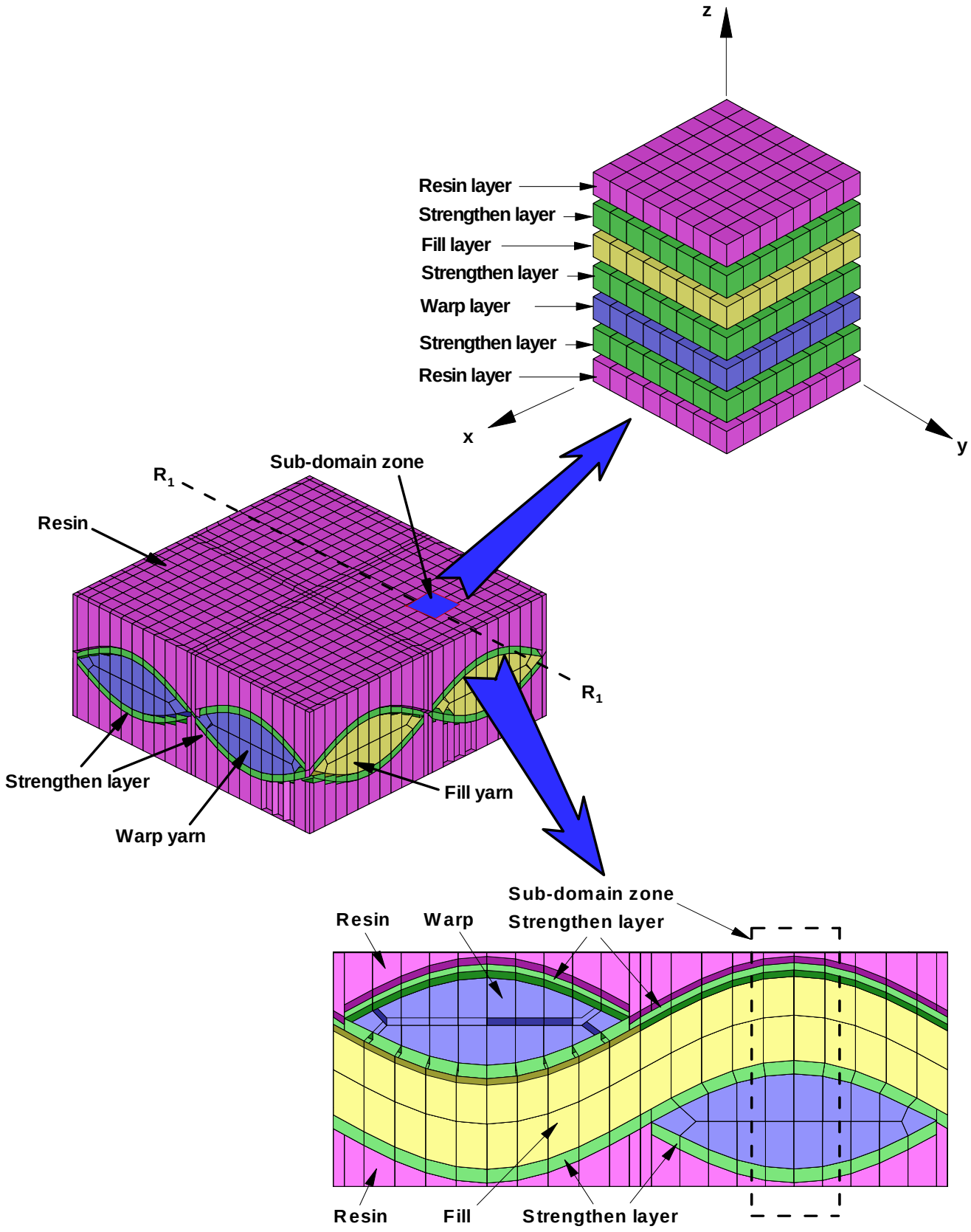

Figure 3.5: Components of the sub-domain zone and a cross-section in the RUC.

Table 3.3 The fiber volume fractions of V_f^o and V_{fyarn} from Ref. [3.1].

Material	Over-all (V_f^o)	Yarn (V_{fyarn})	Present model[a] Over-all (V_f^o)	Present model[b] (V_{fyarn})
Carbon / Epoxy	0.44	0.78	0.3813	0.8
E-Glass / Epoxy	0.42	0.70	0.3929	0.8
Graphite / Epoxy	0.41	0.80	0.2148	0.8

[a] Calculated by Rule of mixtures, [b] Maximum fiber volume fractions of yarns.

The effect of h/a ratio on the effective elastic properties and the coefficients of thermal expansion (CTE) are presented in Figs. 3.6-3.13 for the balanced plain weave fabrics. The same material whose elastic properties are provided in Table 3.2 is considered. To obtain a balanced plain weave fabric, the same dimensional parameters of the yarn length and thickness that are: $a_1 = a_2$, $t_1 = t_2 = h$ and gap lengths $g_1 = g_2 = 0$ are used.

In Figure 3.6, it is shown that the effective Young's modulus (E_x) decreases as the ratio (h/a) increases. This trend is induced from the effect of increased undulations with increased h/a , yielding a decay of E_x . The rate of decrease is greater for higher Young's moduli ratio (E_{11}/E_{22}), corresponding to the yarns. The variation G_{xy} as a function of h/a is presented in Figure 3.7. For T-50 Graphite/Epoxy, G_{xy} decay as h/a increases, while for T-300 Carbon/Epoxy, G_{xy} is constant and E-glass/Epoxy lightly decreases. These results are induced from the different values of G_{12} and G_{23} in material properties. For example, T-300 Carbon/Epoxy has the small different values between these, and T-50 Graphite/Epoxy has a higher value of G_{12} than G_{23} . Figure 3.8 shows the variation of Poisson's ratio (ν_{xy}) as a function of h/a . As h/a increases, the Poisson's ratio in all these three cases decreases. This is attributed to the fact that the effect of undulation increases with increasing h/a leading to the reduction of Poisson's ratio. Figure 3.9 presents the variation of CTE as a function of the thickness ratio h/a . With the increases of h/a , due to the increased undulation, smaller values of CTE α_x are obtained. The undulation effects are found in the CTE. For example, the Carbon/Epoxy woven fabric has been more strongly affected by the high coupling terms than those of the E-glass/Epoxy or Graphite/Epoxy plain weaves. This is due to the less undulation regions that have induced larger local bending terms in each yarn slice, and these affect the compliance of RUC found in the effective elastic moduli. In addition, a crack density scheme is applied into the effects of h/a ratio on the effective elastic properties and the CTE shown in Figures 3.6-3.9 for the balanced plain weaves. Figures 3.10-3.13 show some results of the variation of the effective E_x , G_{xy} , ν_{xy} and α_x with the variation of the ratio (h/a). These results show similar trends given in Figures 3.6-3.9 with various crack densities. Figure 3.14 shows three-dimensional Repeating Unit Cell shapes of E-glass/Epoxy, Graphite/Epoxy and Carbon/Epoxy cases.

3.4.2 Closed-Weave Case of Plain Woven Composite

D.Scida[3.3] *et al*. have investigated the plain woven composite using a micro-mechanics model and have predicted 3-D elastic properties. The closed weave model without the gap geometry is analyzed by using Sine Function Model I. To make the closed weave yarns, the SFM II substitutes zero values into gap-length variables (g_1 and g_2). The properties of the fiber and resin and the geometric parameters are provided in Tables 3.5 and 3.6, respectively. Through the Rule of mixture and Self-Consistent method, the equivalent elastic properties are predicted. The mechanical elastic properties for the strand are also compared to those given by D.Scida[3.3] model in Table 3.7. From Table 3.8, it is noted that the results for the closed weaves have the same value as given by SFM I. Because when there are no gap-lengths, SFM

II turns into SFM I. From comparisons between our results and the experimental data given in Table 3.8, we see that the Rule of mixture shows a better agreement with the experimental data than the Self-Consistent method.

Table 3.4 Comparison of predicted elastic properties and experimental results of plain weave fabric lamina from Ref. [3.1].

Materials	Model	E_{22} (GPa)	E_{11} (GPa)	G_{12} (GPa)	ν_{12}	V_f^o
Carbon /Epoxy	SAM	58.9	52.4	5.1	0.07	-
	EAM – PS	57.1	51.2	4.7	0.10	-
	EAM – SP	35.6	35.4	4.7	0.10	-
	MKM	64.8	58.5	5.3	0.04	0.44
	Kabelka[3.4]	89.3	89.3	7.0	0.04	-
	Experiment	60.3	49.3	-	-	-
	Rule of mixture Self-Consistent mtd.	56.8567 58.1189	41.5146 43.0396	3.2866 4.5398	0.0410 0.0512	-
E-Glass /Epoxy	SAM	20.3	20.3	3.7	0.23	-
	EAM – PS	19.6	19.6	3.7	0.20	-
	EAM – SP	17.9	17.9	3.7	0.20	-
	MKM	21.7	21.5	3.9	0.13	0.42
	Kabelka[3.4]	29.2	29.2	4.9	0.12	-
	Experiment	19.3	19.3	-	-	-
	Rule of mixture Self-Consistent mtd.	20.0489 21.8044	20.0489 21.8044	3.4990 4.9394	0.1418 0.1766	-
Graphite /Epoxy	SAM	28.8	28.8	2.8	0.08	-
	EAM – PS	23.7	23.7	2.8	0.12	-
	EAM – SP	16.2	16.2	2.8	0.12	-
	MKM	32.2	32.2	3.0	0.04	0.41
	Kabelka[3.4]	44.3	44.3	3.7	0.03	-
	Experiment	-	-	-	-	-
	Rule of mixture Self-Consistent mtd.	43.9791 44.7065	43.9791 44.7065	2.1383 2.3723	-0.0112 -0.0361	-

SAM: slice array model, EAM-PS / SP: element array model-parallel series / series parallel,
MKM: modified Kabelka's model

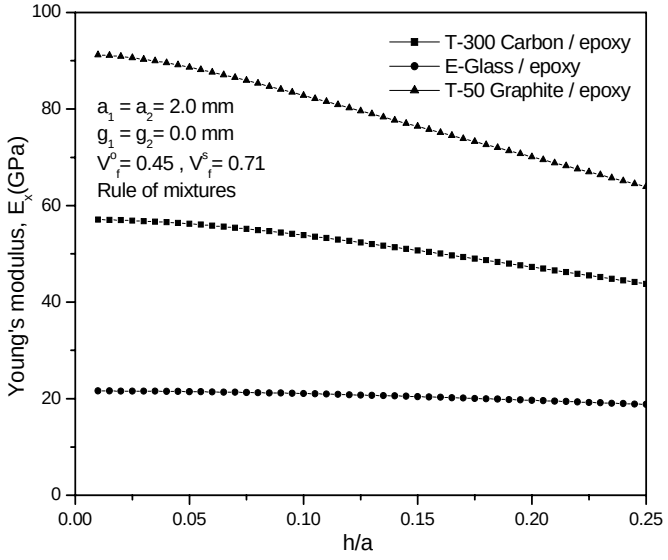

Figure 3.6: Variation of E_x as a function of h/a.

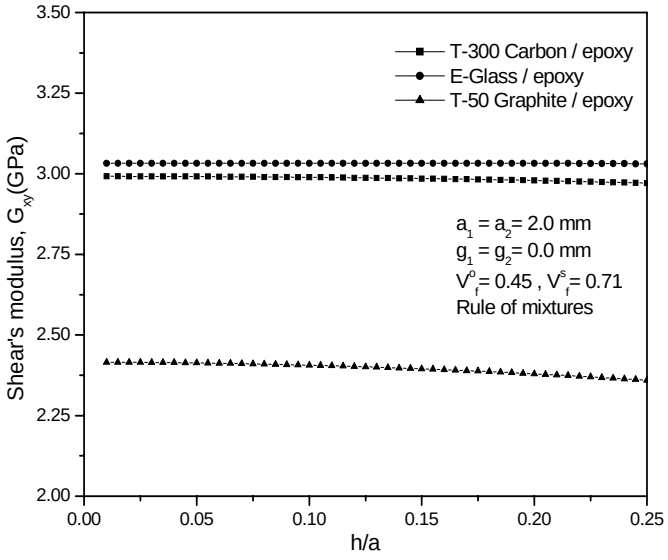

Figure 3.7: Variation of G_{xy} as a function of h/a.

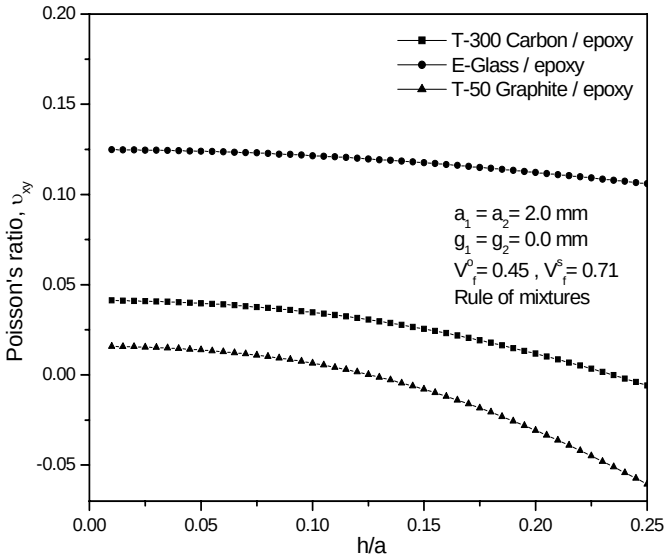

Figure 3.8: Variation of ν_{xy} as a function of h/a.

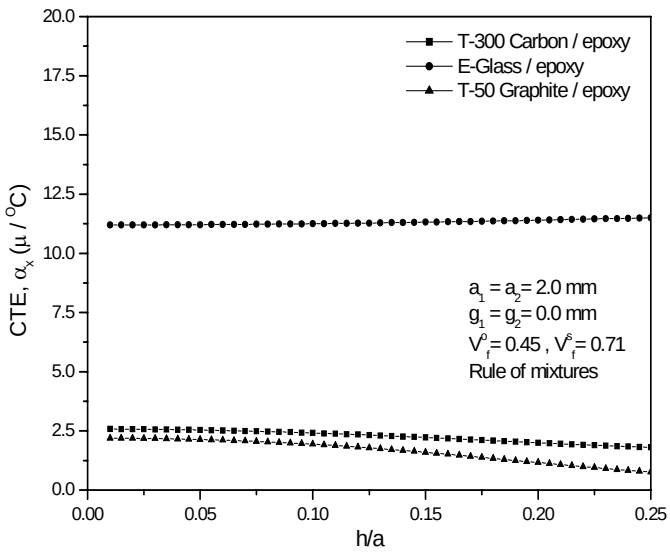

Figure 3.9: Variation of α_x as a function of h/a.

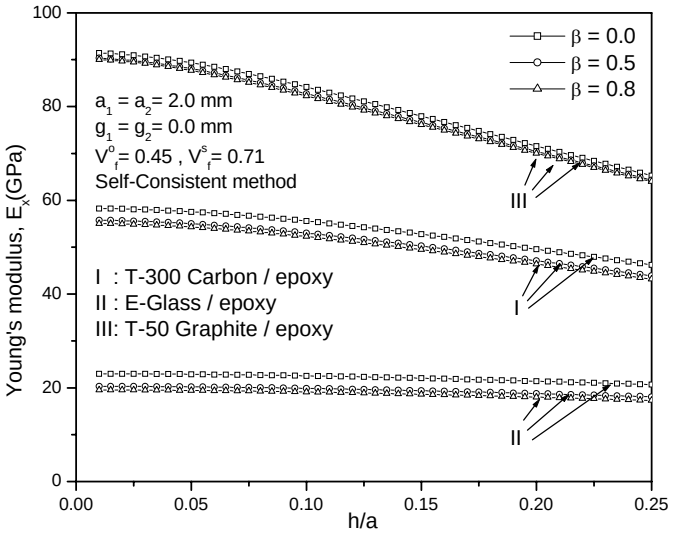

Figure3.10: E_x as a function of h/a and β values.

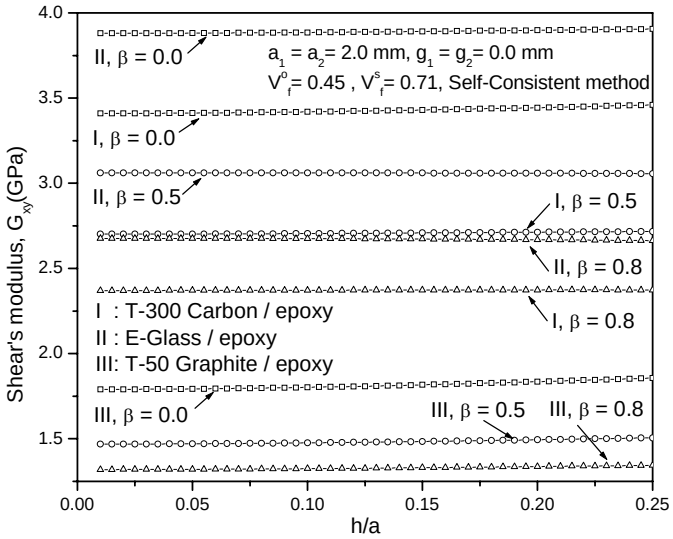

Figure 3.11: G_{xy} as a function of h/a and β values.

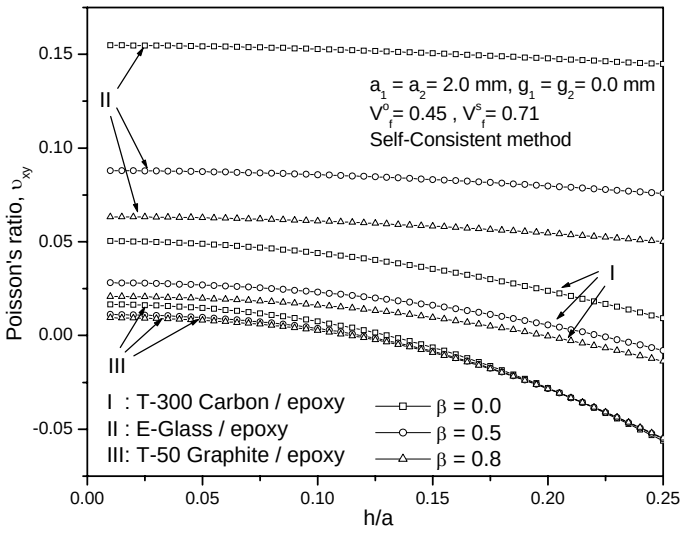

Figure 3.12: ν_{xy} as a function of h/a and β values.

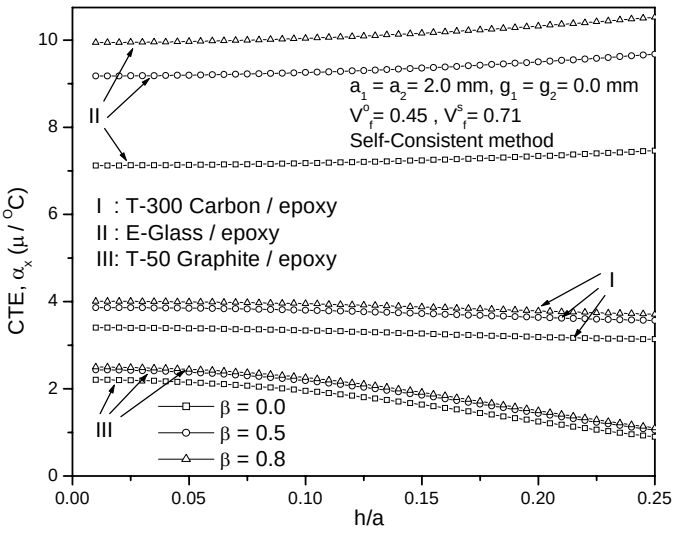

Figure 3.13: α_x as a function of h/a and β values.

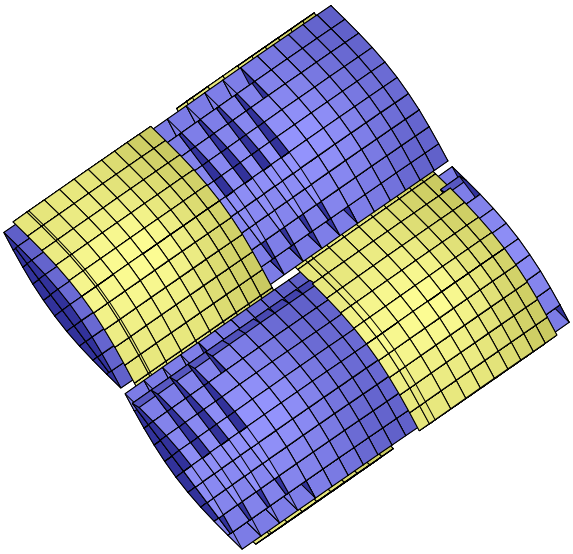

Carbon / epoxy plain weave without resin

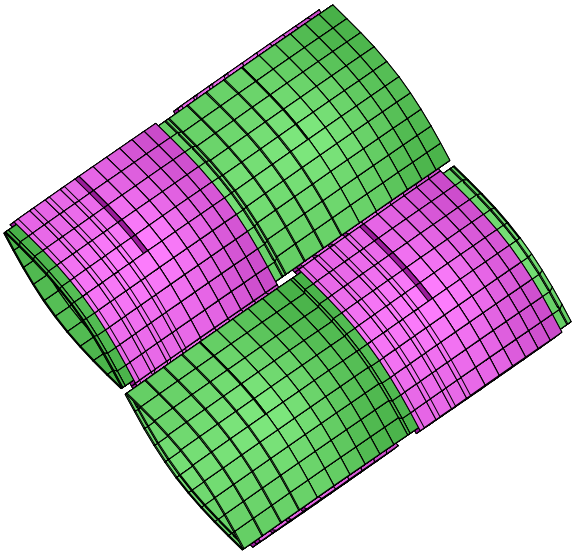

Strengthen layers of Carbon / epoxy

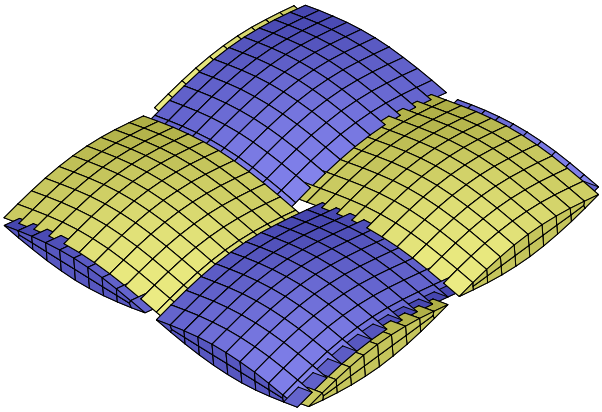

E-glass / epoxy plain weave without resin

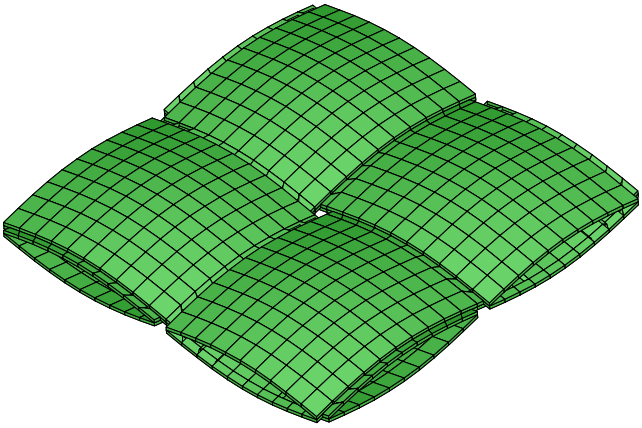

Strengthen layers of E-glass / epoxy

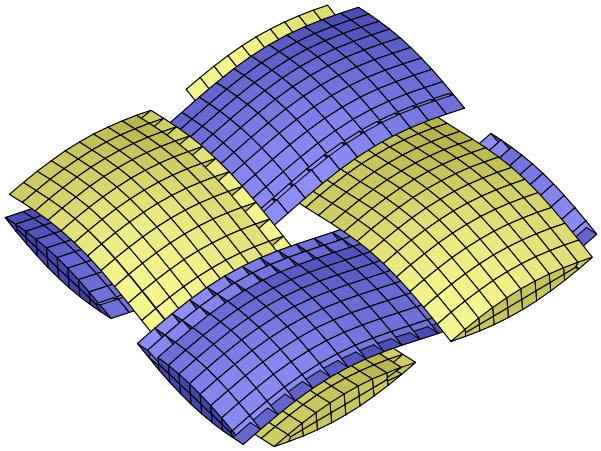

Graphite / epoxy plain weave without resin

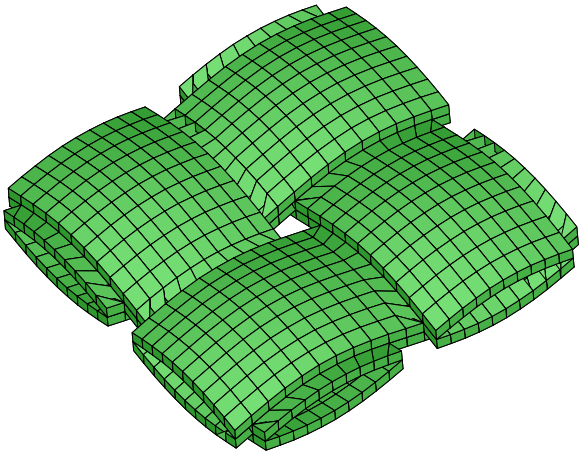

Strengthen layers of Graphite / epoxy

Figure 3.14: RUC shapes of three composite systems.

Table 3.5 Elastic properties of fiber and resin from Ref. [3.3]. (Unit: GPa)

Materials	E_{11}	E_{22}	G_{12}	G_{23}	ν_{12}
E-Glass	73.0	73.0	30.4	30.4	0.20
Vinylester derakane	3.4	3.4	1.49	1.49	0.35

Table 3.6 The geometrical parameters for plain weave fabric yarns from Ref. [3.3]. (Unit: mm)

Material	Fill yarn			Warp yarn			H	V_f^o
	a_2	h_2	g_2	a_1	h_1	g_1		
E-Glass / Vinylester	0.60	0.05	0.0	0.60	0.05	0.0	0.10	0.55

Table 3.7 Comparison of mechanical properties for the yarns from Ref. [3.3].

Materials	Model	E_{11} (GPa)	E_{22} (GPa)	G_{12} (GPa)	G_{23} (GPa)	ν_{12}	ν_{23}
E-Glass / Vinylester (V_{fyarn} = 0.8)	D.Scida[3.3]	57.50	18.80	7.44	7.26	0.25	0.29
	Present Model*	59.0800	14.3303	6.2288	6.2294	0.2300	0.2300
	Present Model**	59.0966	22.2536	9.3559	8.5534	0.2241	0.3009

*: Rule of mixture, **: Self-Consistent method with SFM II.

Table 3.8 Comparison of model and experimental results for the plain weaves from Ref.[3.3].

Materials	Model	E_{11} (GPa)	E_{33} (GPa)	G_{12} (GPa)	G_{23} (GPa)	ν_{12}	ν_{23}
E-Glass / Vinylester (V_{fyarn} = 0.8)	Experimental	24.8 $\pm$ 1.1	8.5 $\pm$ 2.6	6.5 $\pm$ 0.8	4.2 $\pm$ 0.7	0.1 $\pm$ 0.01	0.28 $\pm$ 0.07
	D.Scida[3.3]	25.33	13.46	5.19	5.24	0.12	0.29
	Present Model*	24.5405	10.8728	4.5046	4.4801	0.1072	0.2865
	Present Model**	27.0674	16.0375	6.4932	6.3381	0.1323	0.2854

*: Rule of mixture, **: Self-Consistent method with SFM II.

REFERENCES

3.1 Naik, N.K., and Ganesh, V.K., "Prediction of On-axes Elastic Properties of Plain Weave Fabric Composite," *Composites Science and Technology*, Vol. 45, No. 2, 1992, pp. 135–152.

3.2 Naik, N.K., and Ganesh, V.K., "An Analytical Method for Plain Weave Fabric Composite," *Composites*, Vol. 26, No. 4, 1995, pp. 281–289.

3.3 Scida, D., Aboura, Z., Benzeggagh, M. L. and Bocherens, E., "A Micro-mechanics Model for 3D Elasticity and Failure of Woven-Fiber Composite Materials," *Composites Science and Technology*, Vol. 59, No. 4, 1999, pp. 505–517.

3.4 Kabelka J., "Prediction of the Thermal Properties of Fiber-resin Composites," In Developments in Reinforced Plastics-3, G. Pritchard (Ed.), Elsevier Applied Science Publishers, London, 1984, pp. 167–202.

Chapter 4 Sub-cell Block Model of 2-D Plain Woven Textile Composite

4.1 Introduction

In the previous chapters, the study proposed two analytical models (SFM I/II) to represent the 3-D shapes of the plain weave textiles and predicted the effective elastic properties. These two models are based on selected geometrical parameters and some numerical schemes. In this section, another analytical model, called Sub-cell Block Model, is presented to find the effective elastic properties for the plain weave textiles. The sub-cell block model consists of finite sub-cells made of anisotropic layers, such as multi-laminar composites. A number of finite sub-cells can describe the three dimensional shapes of yarns and resin layers in a Repeating Unit Cell (RUC). From this sub-cell block model, this study obtains characteristics of the plain weave fabrics.

4.2 Theoretical Equations of Multi-layered Laminates

To find the effective elastic moduli of the plain woven composites, the equations of multi-layered laminates have to be derived. By considering a representative sub-laminate containing several composite laminas, the sub-laminate can be described in the Cartesian coordinate system (x, y and z) as shown in Fig.4.1. Each lamina is normal to the z-axis, and the interfaces between the laminae lie in a fixed x-y plane. Each lamina is characterized by a uniform thickness that can be different for the various laminae. The sub-laminate consists of N orthotropic laminae, and the thickness t_k of k-th lamina and the total thickness t are used to describe the sub-laminate. In the sub-cell block model of N orthotropic laminas, each sub-cell has N-laminae. The displacements along the x, y and z directions are denoted by u_1, u_2 and u_3, respectively. Using the concept of engineering strains, we have:

$$\varepsilon_1 = \varepsilon_{11} = \frac{\partial u_1}{\partial x},\ \varepsilon_2 = \varepsilon_{22} = \frac{\partial u_2}{\partial y},\ \varepsilon_3 = \varepsilon_{33} = \frac{\partial u_3}{\partial z}$$

$$\varepsilon_4 = \varepsilon_{23} = \frac{\partial u_2}{\partial z} + \frac{\partial u_3}{\partial y},\ \varepsilon_5 = \varepsilon_{13} = \frac{\partial u_3}{\partial x} + \frac{\partial u_1}{\partial z},\ \varepsilon_6 = \varepsilon_{12} = \frac{\partial u_1}{\partial y} + \frac{\partial u_2}{\partial x} \tag{4.1}$$

Also, we can denote the stress components: $\sigma_1 = \sigma_{11}$, $\sigma_2 = \sigma_{22}$, $\sigma_3 = \sigma_{33}$, $\sigma_4 = \sigma_{23}$, $\sigma_5 = \sigma_{31}$ and $\sigma_6 = \sigma_{12}$. Each lamina is assumed to behave as a linear elastic medium associated with these. The strain energy density function is denoted as the strain terms: $U_0(\varepsilon_i)$. This provides the stresses as

$$\sigma_i = \frac{\partial U_0}{\partial \varepsilon_i},\ i = 1\sim6 \tag{4.2}$$

The stress components have to satisfy Eq. (4.2). To describe the linear lamina strains, the complementary strain energy density $U_0^*(\sigma_i)$ is also considered. The complementary strain energy density is given as:

$$U_0^* = -U_0 + \sigma_i \varepsilon_i,\ i = 1\sim6 \tag{4.3}$$

From Eq. (4.3), the strains are

$$\varepsilon_i = \frac{\partial U_0^*}{\partial \sigma_i},\ i = 1\sim6 \tag{4.4}$$

Considering the integration of the strain energy terms in Eqs. (4.3) and (4.4), the variations of the total strain energy and complementary energy densities of the sub-laminate are:

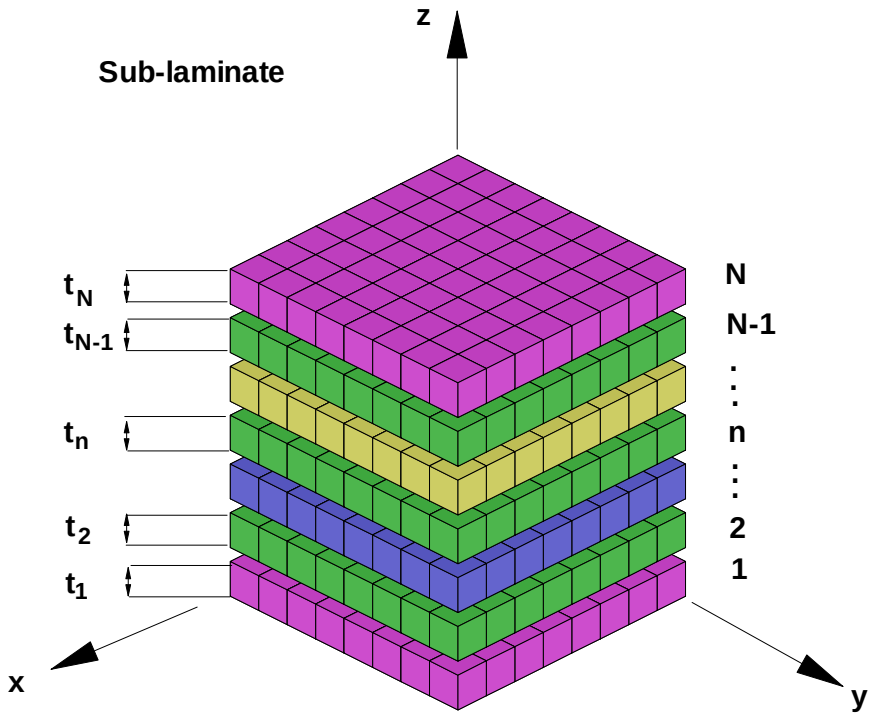

Figure 4.1: Sub-laminate with N-laminae.

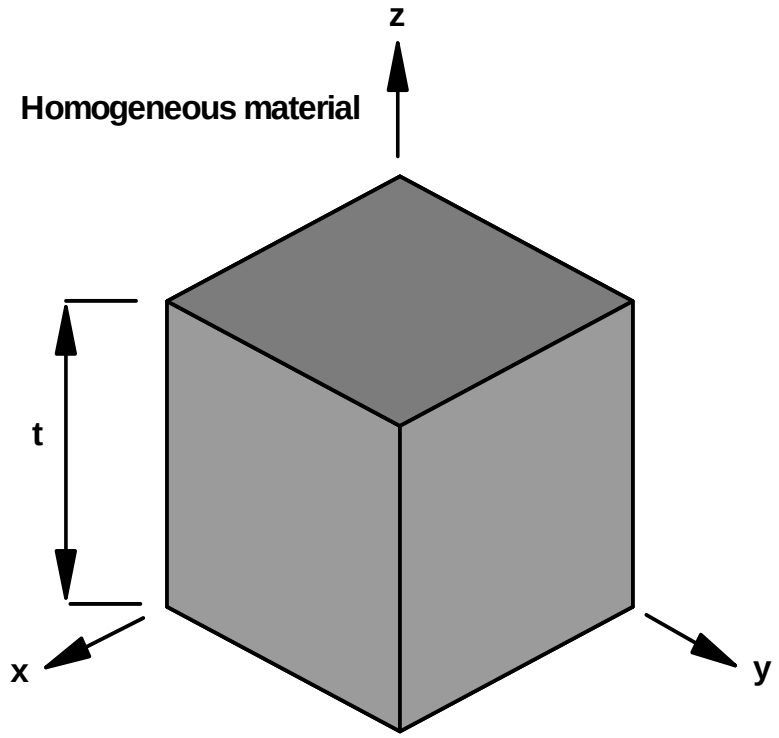

Figure 4.2: Homogeneous equivalent medium.

$$\delta\overline{U}_0 = \int_0^h \sigma_i \delta\varepsilon_i dz \,,\ \delta\overline{U}_0^* = \int_0^h \varepsilon_i \delta\sigma_i dz \tag{4.5}$$

In Eqs. (4.5), the energy densities are measured per unit area of the sub-laminate. For example, the two energy densities of the sub-laminate consisting of N -laminae are given as:

$$\delta\overline{U}_0 = \sum_{k=1}^{N} \int_{t_k^-}^{t_k^+} \sigma_i^k \delta\varepsilon_i^k dz \,,\ \delta\overline{U}_0^* = \sum_{k=1}^{N} \int_{t_k^-}^{t_k^+} \varepsilon_i^k \delta\sigma_i^k dz \tag{4.6}$$

In Eq. (4.6), t_k^- and t_k^+ are respectively the lower and upper coordinates of the k -th lamina's interfaces. Equation (4.5) means the energy densities of the equivalent homogeneous laminae shown in Fig. 4.2, whereas Eq. (4.6) represents the actual energy densities of the sub-laminate. Thus, we can calculate the 3-D constitutive characteristics of the multi-layered composites from Eqs. (4.5) and (4.6). If the 2-D plain woven textile composite structures are assumed as an assemblage of multi-layered sub-cells, the two energy densities, Eqs. (4.5) and (4.6), can be applied into the sub-cell block model to predict the RUC characteristics.

4.3 Basic Assumptions for Sub-cell Block Model

One RUC of the 2-D plain weave has 2 fill-yarns, 2 warp-yarns and 2 resin layers described in Figure 4.3. In this study one of 4 unit cells consisting of the RUC is considered, see the sectional views of Fig. 4.4. Geometrical shapes of yarns in the unit cell can be modeled by a number of small sub-cells shaped block types as shown in Figures 4.5 and 4.6. This study applies the concept of anisotropic layers to the small cells. Each cell in the plain weaves has four layers: lower resin, fill/warp yarns and upper resin as shown in Figure 4.6. The resin layers are isotropic layers while the fill and warp yarns are considered as anisotropic laminas. One assumes that each lamina of the cell is perfectly bonded along interfaces, such as the lower and upper surfaces and the displacements of the interfaces have constant values. The similar assumption is used in the SFM I/II and extended into Repeating Unit Cell. From this assumption, the displacement continuity over the interfaces has the same gradients along the in-plane surface (x - y plane), such as in-plane strain components, $\varepsilon_1, \varepsilon_2$ and ε_6 having continuous displacements at the contiguous interfaces. The iso-strain condition (Voigt assumption) and the iso-stress (Ruess assumption) are applied into the interface continuity at common interfaces of the cell. The interface continuities at $z = t_k^+$, k =1, 2, 3 and 4 are expressed by Voigt and Ruess assumptions.

$$\varepsilon_1^k = \varepsilon_1^{k+1},\ \varepsilon_2^k = \varepsilon_2^{k+1},\ \varepsilon_6^k = \varepsilon_6^{k+1} \tag{4.7}$$

$$\sigma_1^k = \sigma_1^{k+1},\ \sigma_2^k = \sigma_2^{k+1},\ \sigma_6^k = \sigma_6^{k+1} \tag{4.8}$$

Eqs. (4.7)-(4.8) can be extended into the lowest surface and the top surface of the cell ($t_1^- \le z \le t_N^+$).

$$\varepsilon_1(x,y) = \varepsilon_1^k(x,y),\ \varepsilon_2(x,y) = \varepsilon_2^k(x,y),\ \varepsilon_6(x,y) = \varepsilon_6^k(x,y)\ \ k=1, 2, 3 \,\&\, 4 \tag{4.9}$$

$$\sigma_1(x,y) = \sigma_1^k(x,y),\ \sigma_2(x,y) = \sigma_2^k(x,y),\ \sigma_6(x,y) = \sigma_6^k(x,y)\ \ k=1, 2, 3 \,\&\, 4 \tag{4.10}$$

4.4 Average Stresses and Strains of Sub-cell Block Model

From Eqs. (4.5), (4.9) and (4.10), the variations in the two energy densities of homogeneous equivalent material are induced

$$\delta\overline{U}_0 = t\left(\overline{\sigma}_1\delta\varepsilon_1 + \overline{\sigma}_2\delta\varepsilon_2 + \overline{\sigma}_3\delta\varepsilon_3 + \overline{\sigma}_4\delta\varepsilon_4 + \overline{\sigma}_5\delta\varepsilon_5 + \overline{\sigma}_6\delta\varepsilon_6\right) \tag{4.11}$$

$$\delta\overline{U}_0^* = t\left(\varepsilon_1\delta\sigma_1 + \varepsilon_2\delta\sigma_2 + \varepsilon_3\delta\sigma_3 + \varepsilon_4\delta\sigma_4 + \varepsilon_5\delta\sigma_5 + \varepsilon_6\delta\sigma_6\right) \tag{4.12}$$

The average strain and stress components are defined as:

$$\bar{\varepsilon}_i = \frac{1}{t}\int_0^t \varepsilon_i dz = \frac{1}{V}\int_V \varepsilon_i dV \ , \ \bar{\sigma}_i = \frac{1}{t}\int_0^t \sigma_i dz = \frac{1}{V}\int_V \sigma_i dV \tag{4.13}$$

To get the average lamina strain and stress of the sub-cell, the variations of the two energy densities of the homogeneous equivalent material are used:

$$\delta\overline{U}_0 = \sum_{k=1}^{4} t_k \left[\bar{\sigma}_1^k \delta\varepsilon_1 + \bar{\sigma}_2^k \delta\varepsilon_2 + \bar{\sigma}_3^k \delta\varepsilon_3 + \bar{\sigma}_4^k \delta\varepsilon_4 + \bar{\sigma}_4^k \delta\varepsilon_5 + \bar{\sigma}_6^k \delta\varepsilon_6\right] \tag{4.14}$$

$$\delta\overline{U}_0^* = \sum_{k=1}^{4} t_k \left[\varepsilon_1 \delta\bar{\sigma}_1^k + \varepsilon_2 \delta\bar{\sigma}_2^k + \varepsilon_3 \delta\bar{\sigma}_3^k + \varepsilon_4 \delta\bar{\sigma}_4^k + \varepsilon_5 \delta\bar{\sigma}_5^k + \varepsilon_6 \delta\bar{\sigma}_6^k\right] \tag{4.15}$$

Here, we have defined the average lamina strain and stress components as:

$$\bar{\varepsilon}_i^k = \frac{1}{t_k}\int_{t_k^-}^{t_k^+} \varepsilon_i^k dz \,, \qquad \bar{\sigma}_i^k = \frac{1}{t_k}\int_{t_k^-}^{t_k^+} \sigma_i^k dz \tag{4.16}$$

In Eqs. (4.13) and (4.16), the average in-plane strain and stress are defined as:

$$\bar{\varepsilon}_i^k = \bar{\varepsilon}_i = \varepsilon_i \,, \ i = 1, 2, 6: \ k = 1, 2, 3 \ \& \ 4 \tag{4.17}$$

$$\bar{\sigma}_i^k = \bar{\sigma}_i = \sigma_i \quad i = 3, 4, 5: \ k = 1, 2, 3 \ \& \ 4 \tag{4.18}$$

Eqs. (4.11) and (4.14) are used to obtain the out-of plane stresses and strains in the sub-cell. Let the variations of the displacements to be $\delta u_1^k = \delta u_1(x, y) \neq 0$, $\delta u_2^k = \delta u_2(x, y) \neq 0$ and $\delta u_3^k = 0$ for all laminae. The variations in the strain components are:

$$\delta\varepsilon_1^k = \delta\varepsilon_1 \neq 0 \,, \ \delta\varepsilon_2^k = \delta\varepsilon_2 \neq 0 \,, \ \delta\varepsilon_6^k = \delta\varepsilon_6 \neq 0 \,, \ \delta\varepsilon_3 = \delta\varepsilon_4 = \delta\varepsilon_5 = 0 \tag{4.19}$$

By substituting Eq. (4.11) into Eq. (4.14), the variations of the homogeneous equivalent material and the sub-cell are:

$$t\left(\bar{\sigma}_1 \delta\varepsilon_1 + \bar{\sigma}_2 \delta\varepsilon_2 + \bar{\sigma}_6 \delta\varepsilon_6\right) = \sum_{k=1}^{4} t_k \left[\bar{\sigma}_1^k \delta\varepsilon_1 + \bar{\sigma}_2^k \delta\varepsilon_2 + \bar{\sigma}_6^k \delta\varepsilon_6\right] \tag{4.20}$$

By using the volume fraction of the lamina, $v_k = t_k / t$, the average in-plane stress components are defined as:

$$(\bar{\sigma}_1, \bar{\sigma}_2, \bar{\sigma}_6) = \sum_{k=1}^{4} v_k (\bar{\sigma}_1^k, \bar{\sigma}_2^k, \bar{\sigma}_6^k) \tag{4.21}$$

Equation (4.21) implies that the in-plane stress conditions between the homogeneous medium and the sub-cell are given by the Voigt approximation. The complementary strain energy density described by Eqs. (4.12) and (4.15) is used to get out-of plane average strain components. Consider the variations of the in-plane stress components to be zero, yielding:

$$\delta\bar{\sigma}_1^k = 0 \,, \ \delta\bar{\sigma}_2^k = 0 \,, \ \delta\bar{\sigma}_3^k = 0 \,, \ \delta\bar{\sigma}_4 \neq 0 \,, \ \delta\bar{\sigma}_5 \neq 0 \,, \ \delta\bar{\sigma}_6^k = 0 \tag{4.22}$$

The variation terms are based on the Reuss approximation for the sub-cell and the homogeneous material. We can obtain the average strains using the out-of plane components from Eqs. (4.12) and (4.15).

$$t\left(\bar{\varepsilon}_3 \delta\bar{\sigma}_3 + \bar{\varepsilon}_4 \delta\bar{\sigma}_4 + \bar{\varepsilon}_5 \delta\bar{\sigma}_5\right) = \sum_{k=1}^{4} t_k \left[\bar{\varepsilon}_3^k \delta\bar{\sigma}_3 + \bar{\varepsilon}_4^k \delta\bar{\sigma}_4 + \bar{\varepsilon}_5^k \delta\bar{\sigma}_5\right] \tag{4.23}$$

From Eq. (4.23), the average out-of plane strain components are also defined by the volume fraction of the lamina, $v_k = t_k / t$.

$$(\bar{\varepsilon}_3, \bar{\varepsilon}_4, \bar{\varepsilon}_5) = \sum_{k=1}^{4} v_k (\bar{\varepsilon}_3^k, \bar{\varepsilon}_4^k, \bar{\varepsilon}_5^k) \tag{4.24}$$

Eq. (4.24) implies that using the Voigt approximation between the homogeneous medium and the sub-cell, one can get the equivalent conditions for the out-of plane strain components.

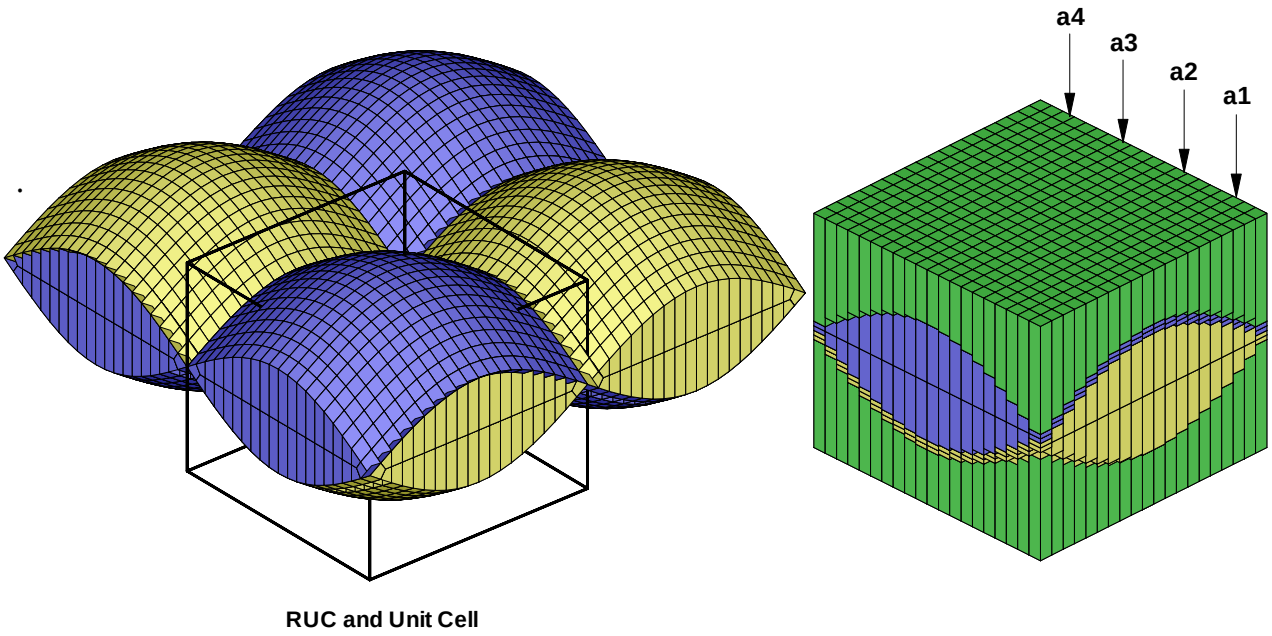

Figure 4.3: RUC and Unit Cell of 2-D plain weaves and 4 sectional points in a unit cell.

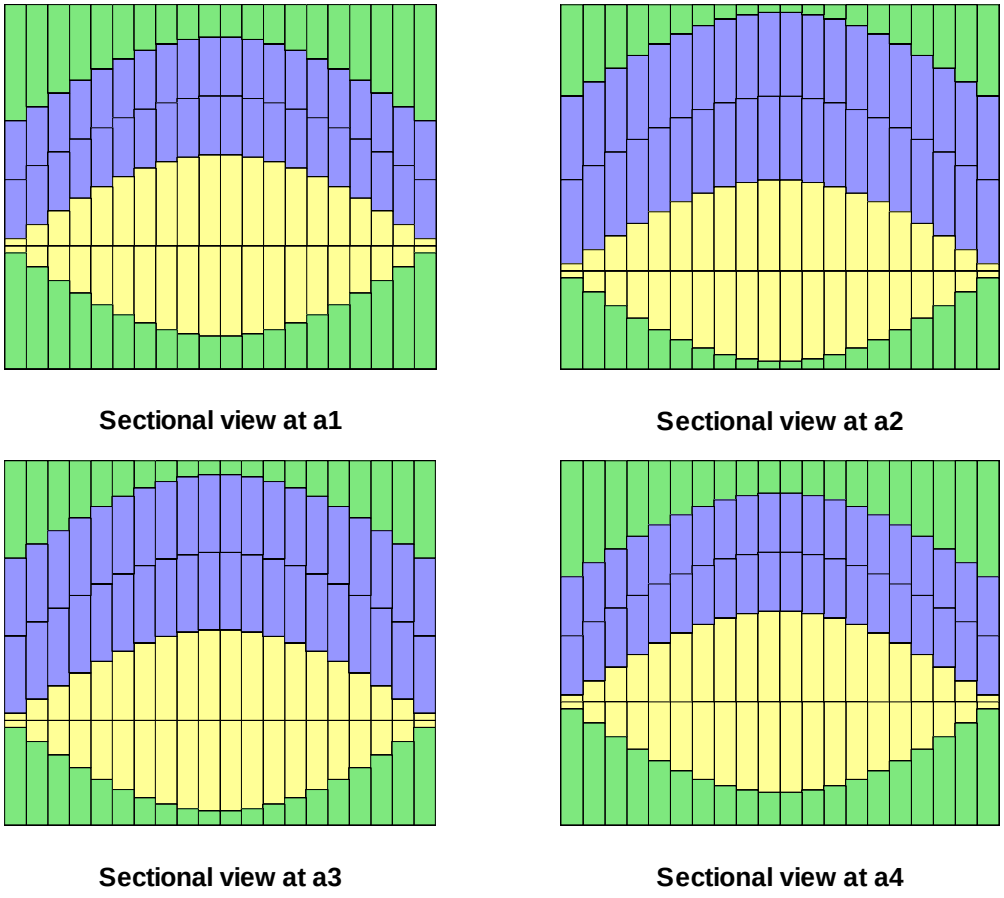

Figure 4.4: Sectional views of sub-cell block model.

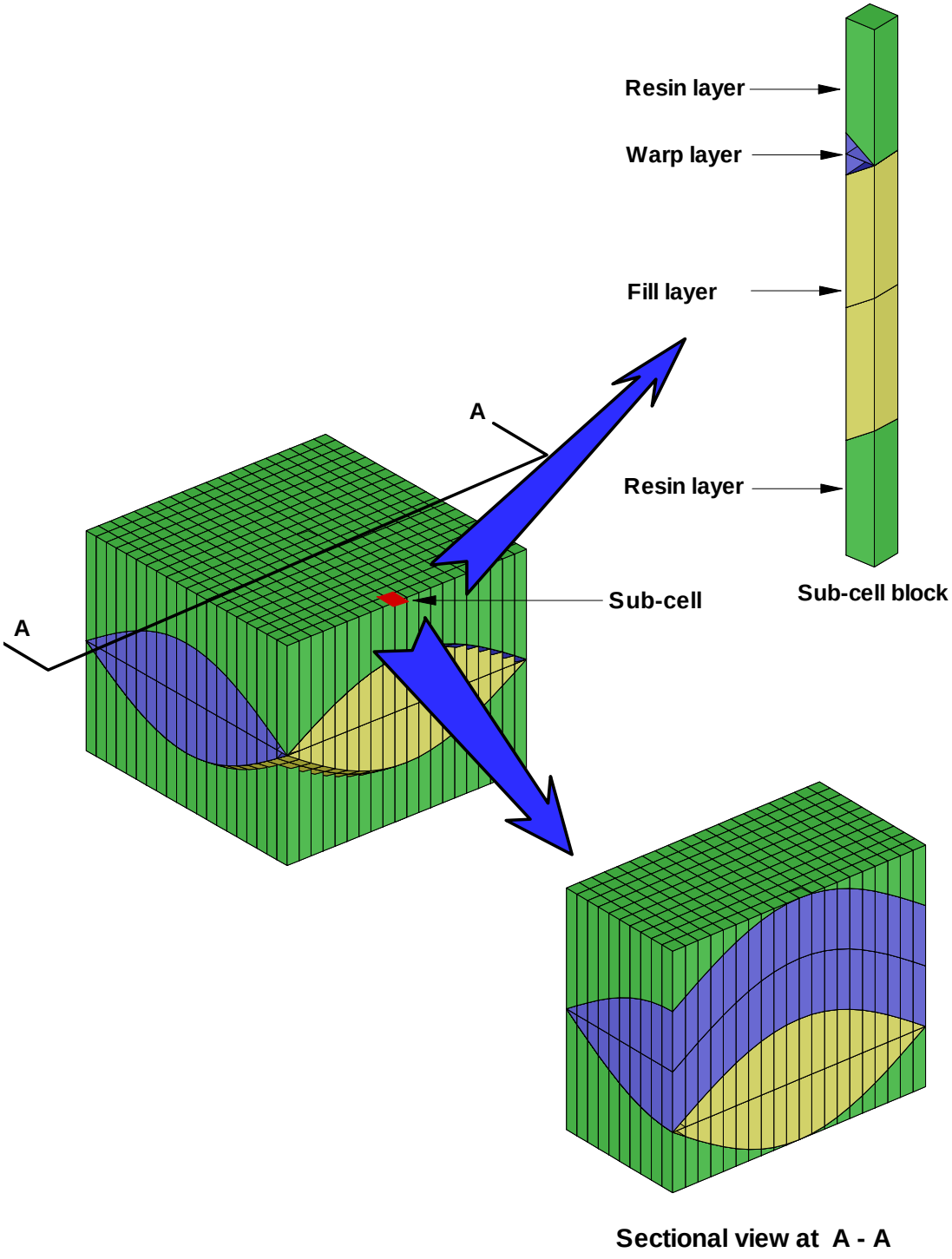

Figure 4.5: Components of the sub-cell and a sectional shape.

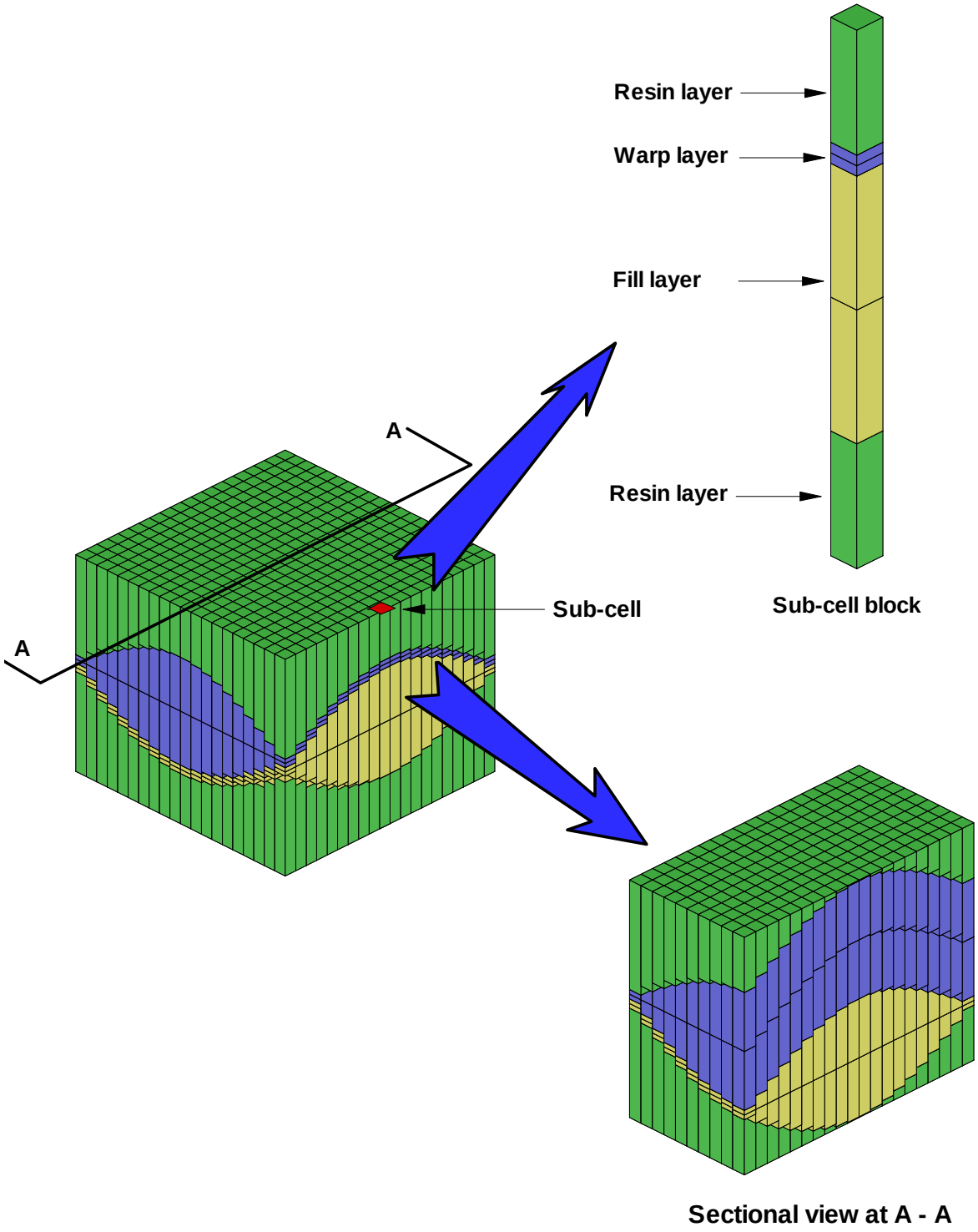

Figure 4.6: Components of the sub-cell block and a sectional shape.

4.5 The Constitutive Behaviors of the Sub-cell Block Model

Recall that we assumed that the linear elasticity theory of the anisotropic material is applied above in the present case, as a result, the stress and strain components for the k -th lamina are:

$$\varepsilon_i^k = S_{ij}^k \sigma_j^k + \alpha_i^k \Delta T \ \ (i, j = 1,\ldots,6 : \ k = 1, \ldots, 4) \tag{4.25}$$

$$\sigma_i^k = C_{ij}^k \varepsilon_j^k - \alpha_i^k \Delta T \ \ (i, j = 1,\ldots,6 : \ k = 1, \ldots, 4) \tag{4.26}$$

Here, C_{ij}^k and S_{ij}^k denote the symmetric stiffness and the compliance matrices, respectively, ΔT is the change of temperature field measured from a reference stress free temperature T_O and α_i^k are the coefficients of thermal expansion in the orthogonal directions. By considering Eqs.(4.25) and (4.26), the strain and the complementary energy densities of the k -th lamina are rewritten as:

$$U_0^k = \frac{1}{2} C_{ij}^k \varepsilon_i^k \varepsilon_j^k - \alpha_i^k \Delta T \varepsilon_i^k \tag{4.27}$$

$$U_0^{k*} = \frac{1}{2} S_{ij}^k \sigma_i^k \sigma_j^k + \alpha_i^k \Delta T \sigma_i^k \tag{4.28}$$

The strain energy of the sub-cell per unit area can be written in terms of the average strain and strain terms.

$$\overline{U}_0 = \sum_{k=1}^{4} t_k \left[\frac{1}{2} C_{ij}^k \overline{\varepsilon}_i^k \overline{\varepsilon}_j^k - \alpha_i^k \Delta T \overline{\varepsilon}_i^k \right] \tag{4.29}$$

$$\overline{U}_0^* = \sum_{k=1}^{4} t_k \left[\frac{1}{2} S_{ij}^k \overline{\sigma}_i^k \overline{\sigma}_j^k + \alpha_i^k \Delta T \overline{\sigma}_i^k \right] \tag{4.30}$$

To find the energy density of the homogeneous material per unit area, Eqs. (4.25) and (4.26) are substituted into Eqs. (4.11) and (4.12).

$$\overline{U}_0 = t \left[\frac{1}{2} C_{ij} \overline{\varepsilon}_i \ \overline{\varepsilon}_j - \alpha_i \Delta T \overline{\varepsilon}_i \right] \tag{4.31}$$

$$\overline{U}_0^* = t \left[\frac{1}{2} S_{ij} \overline{\sigma}_i \ \overline{\sigma}_j + \alpha_i \Delta T \overline{\sigma}_i \right] \tag{4.32}$$

To obtain the homogeneous material elastic constants, Eqs. (4.29)~(4.32) are compared each other. We can obtain the following equations in terms of the volume fractions (v_k^{sub}).

$$\sum_{k=1}^{4} v_k^{sub} \left[\frac{1}{2} C_{ij}^k \overline{\varepsilon}_i^k \overline{\varepsilon}_j^k - \alpha_i^k \Delta T \overline{\varepsilon}_i^k \right] = \left[\frac{1}{2} C_{ij} \overline{\varepsilon}_i \ \overline{\varepsilon}_j - \alpha_i \Delta T \overline{\varepsilon}_i \right] \tag{4.33}$$

$$\sum_{k=1}^{4} v_k^{sub} \left[\frac{1}{2} S_{ij}^k \overline{\sigma}_i^k \overline{\sigma}_j^k + \alpha_i^k \Delta T \overline{\sigma}_i^k \right] = \left[\frac{1}{2} S_{ij} \overline{\sigma}_i \ \overline{\sigma}_j + \alpha_i \Delta T \overline{\sigma}_i \right] \tag{4.34}$$

Considering Eqs.(4.17), (4.18), (4.21), (4.24) (4.26) and (4.33), we can find the homogeneous material constants (C_{ij}^{sub}) of each sub-cell block. Similar equations are suggested in Ref. [4.1].

$$C_{ij}^{sub} = \sum_{k=1}^{4} v_k^{sub} \left[C_{ij}^k - \frac{C_{i3}^k C_{3j}^k}{C_{33}^k} + \frac{C_{i3}^k}{C_{33}^k} \frac{\sum_{l=1}^{4} v_l^{sub} \dfrac{C_{3j}^l}{C_{33}^l}}{\sum_{l=1}^{4} \dfrac{v_l^{sub}}{C_{33}^l}} \right] \ \ i, j = 1,2,3 \text{ and } 6 \tag{4.35}$$

The constitutive relations for i and j =4 and 5 are:

$$C_{ij}^{sub}=\frac{\sum_{k=1}^{4} v_k^{sub}\frac{C_{ij}^k}{\Delta_k}}{\sum_{k=1}^{4}\sum_{l=1}^{4}\frac{v_k^{sub}}{\Delta_k}\frac{v_l^{sub}}{\Delta_l}(C_{44}^k C_{55}^k - C_{45}^k C_{45}^l)},\ \Delta_k = C_{44}^k C_{55}^k - C_{45}^k C_{45}^k \tag{4.36}$$

Other components are

$$C_{ij}^k = C_{ij}^k = 0,\ i = 1,2,3 \text{ and } 6 : j = 4 \text{ and } 5 \tag{4.37}$$

$$\left[C_{ij}^k\right] = \begin{bmatrix} C_{11}^k & C_{12}^k & C_{13}^k & 0 & 0 & C_{16}^k \\ C_{21}^k & C_{22}^k & C_{23}^k & 0 & 0 & C_{26}^k \\ C_{31}^k & C_{32}^k & C_{33}^k & 0 & 0 & C_{36}^k \\ 0 & 0 & 0 & C_{44}^k & C_{45}^k & 0 \\ 0 & 0 & 0 & C_{45}^k & C_{55}^k & 0 \\ C_{61}^k & C_{62}^k & C_{63}^k & 0 & 0 & C_{66}^k \end{bmatrix} = [T]^T \left[C_{ij}^*\right][T] \tag{4.38}$$

Here, $[C_{ij}^*]$ is the stiffness matrix in the material coordinate system (1-2-3 axis) and $[T]$ is a transformation matrix between 1-2-3 and x - y - z axes. The sub-cell block model has to consider the crimp angle, θ_c and the rotation angle, θ_r between the local and the global coordinates. This sub-cell block model uses the same transformation matrix described in the plain weave modeling (SFM I/II). Each sub-cell has a different crimp angle along the yarn centerlines. The warp yarn has zero values, while the fill yarn has 90 degree about the rotation angles. The transformation matrix $[T]$ also is depicted in Appendix A. The crimp angles (θ_c or θ_{c1}/θ_{c2}) of each fill/warp sub-cell layer are obtained from the derivatives of the yarn centerline equations along the different undulated regions ($x-y$ axes), as SFM I/II are used.

$$\theta_{c1} = \tan^{-1}\left[\frac{t_2\pi}{2(a_2+g_2)}\cos\left[\frac{\pi x}{(a_2+g_2)}\right]\right],\ (0 \le x \le u_2)$$

$$\theta_{c2} = \tan^{-1}\left[\frac{-t_1\pi}{2(a_1+g_1)}\cos\left[\frac{\pi y}{(a_1+g_1)}\right]\right],\ (0 \le y \le u_1) \tag{4.39}$$

If a N number of multi-layered composite is considered, Eq.(4.35) can be written as:

$$C_{ij} = \sum_{k=1}^{N} v_k \left[C_{ij}^k - \frac{C_{i3}^k C_{3j}^k}{C_{33}^k} + \frac{C_{i3}^k}{C_{33}^k}\frac{\sum_{l=1}^{N} v_l \frac{C_{3j}^l}{C_{33}^l}}{\sum_{l=1}^{N}\frac{v_l}{C_{33}^l}} \right],\ i, j = 1,2,3 \text{ and } 6 \tag{4.40}$$

Eqs.(4.36)-(4.38) can be written as:

$$C_{ij} = \frac{\sum_{k=1}^{N} v_k \frac{C_{ij}^k}{\Delta_k}}{\sum_{k=1}^{N}\sum_{l=1}^{N}\frac{v_k}{\Delta_k}\frac{v_l}{\Delta_l}(C_{44}^k C_{55}^k - C_{45}^k C_{45}^l)},\ \Delta_k = C_{44}^k C_{55}^k - C_{45}^k C_{45}^k \tag{4.41}$$

$$C_{ij} = C_{ji} = 0,\ i = 1,2,3,\ 6 : j = 4 \text{ and } 5 \tag{4.42}$$

$$\left[C_{ij}\right]=\begin{bmatrix} C_{11} & C_{12} & C_{13} & 0 & 0 & C_{16} \\ C_{21} & C_{22} & C_{23} & 0 & 0 & C_{26} \\ C_{31} & C_{32} & C_{33} & 0 & 0 & C_{36} \\ 0 & 0 & 0 & C_{44} & C_{45} & 0 \\ 0 & 0 & 0 & C_{45} & C_{55} & 0 \\ C_{61} & C_{62} & C_{63} & 0 & 0 & C_{66} \end{bmatrix}=\left[T\right]^{T}\left[C_{ij}^{*}\right]\left[T\right] \tag{4.43}$$

In Eq.(4.43) the transformation matrix $\left[T\right]$ between x' - y' and x - y axes is

$$\left[T\right]=\begin{bmatrix} m^2 & n^2 & 0 & 0 & 0 & mn \\ n^2 & m^2 & 0 & 0 & 0 & -mn \\ 0 & 0 & 1 & 0 & 0 & 0 \\ 0 & 0 & 0 & m & -n & 0 \\ 0 & 0 & 0 & n & m & 0 \\ -2mn & 2mn & 0 & 0 & 0 & m^2-n^2 \end{bmatrix},\ m=\cos\theta=\cos\theta_r \text{ and } n=\sin\theta=\sin\theta_r \tag{4.44}$$

The coefficients of thermal expansions (α) in the sub-cell block model is

$$[\alpha]=[T]^{-1}[\alpha'] \tag{4.45}$$

Here, $[\alpha']$ are coefficients of the thermal expansion (CTE) in the material coordinates. The thermal constants of the cell (a_i^{sub} for $i=1,2,3$ and 6) are derived from Eqs. (4.17), (4.18), (4.21), (4.24) (4.26) and (4.33).

$$a_i^{sub}=\sum_{k=1}^{4} v_k^{sub}\left[a_i^k-\frac{C_{i3}^k}{C_{33}^k}a_3^k+\frac{C_{i3}^k}{C_{33}^k}\frac{\sum_{l=1}^{4} v_l^{sub}\dfrac{a_3^l}{C_{33}^l}}{\sum_{l=1}^{4}\dfrac{v_l^{sub}}{C_{33}^l}}\right] \tag{4.46}$$

4.6 The Volume Fraction of Sub-cell Block Model

Eqs.(4.33)-(4.36) and (4.41) are related to the volume fractions in the sub-cell. This study derives some volume fraction equations from the sub-cell block based on the unit cell size. To get the volume fraction of each sub-cell layer, the sub-cell volumes are respectively determined and their summation along each sub-cell layer is carried out. Each sub-cell volume for the lower/upper resin, fill and warp layers is

$$V_1^{sub}=V_2^{sub}=V_3^{sub}=V_4^{sub}=\left|\ (x_1-x_2)(y_1-y_2)(z_4-z_1)\ \right|_{sub}=\left|\ \Delta x\Delta y\Delta z\ \right|_{sub} \tag{4.47}$$

Here, the values of x_1, x_2, y_1, y_2, z_1 and z_4 are the coordinates of the node 1,2 and 4 in each sub-cell layer. The volumes of fill/warp yarn parts in the sub-cell, V_1 and V_2, are:

$$V_1=\sum_{f=1}^{ns}\left[V_2^{sub}\right]_f,\ V_2=\sum_{w=1}^{ns}\left[V_3^{sub}\right]_w \tag{4.48}$$

The ns in Eq. (4.48) refers to the total sub-cell number in the unit cell size. The total unit cell volume V_{total} is

$$V_{total}=H(a_1+g_1)(a_2+g_2)=(h_m+t_1+t_2)(a_1+g_1)(a_2+g_2) \tag{4.49}$$

The resin layers' volume is

$$V_{resin}=V_{total}-(V_1+V_2) \tag{4.50}$$

The volume fractions of the fill/warp layers and resin parts within a unit cell are described by the overall volume fraction term, V_f^o.

$$V_f^1 = V_f^o(\frac{V_{total}}{V_1}),\ V_f^2 = V_f^o(\frac{V_{total}}{V_2}),\ V_f^r = (\frac{V_{resin}}{V_{total}}) \tag{4.51}$$

The volume fractions of the layers within a sub-cell in Eqs.(4.33)-(4.36) and (4.41) are

$$v_1^{sub} = 0.5\left[\frac{V_1^{sub}}{V_{total}}\right] V_f^r,\ v_2^{sub} = \left[\frac{V_2^{sub}}{V_{total}}\right] V_f^1,\ v_3^{sub} = \left[\frac{V_3^{sub}}{V_{total}}\right] V_f^2,\ v_4^{sub} = 0.5\left[\frac{V_4^{sub}}{V_{total}}\right] V_f^r \tag{4.52}$$

4.7 Effective Elastic Moduli of Sub-cell Block Model

After calculating the homogeneous material constants (C_{ij}^{sub}) and the thermal constants (a_i^{sub}) of each sub-cell, all sub-cells are assembled into a unit cell and determine the stiffness matrix as to calculate the effective elastic properties. The unit cell stiffness matrix (C_{ij}^{unit}) and thermal constants (a_i^{unit}) become:

$$C_{ij}^{unit} = \sum_{p=1}^{ns} C_{ij}^{sub}\Big|_p,\ a_i^{unit} = \sum_{p=1}^{ns} a_i^{sub}\Big|_p \tag{4.53}$$

It is obvious that the compliance matrix for the unit cell is needed to find the effective elastic moduli. The compliance matrix is defined as:

$$\overline{S}_{ij} = [C_{ij}^{unit}]^{-1} \tag{4.54}$$

The effective moduli for the three-dimensional homogeneous anisotropic solid and the coefficients of thermal expansions are obtained as:

$$\overline{E}_{11} = \frac{1}{\overline{S}_{11}},\ \overline{E}_{22} = \frac{1}{\overline{S}_{22}},\ \overline{E}_{33} = \frac{1}{\overline{S}_{33}},\ \overline{\nu}_{23} = -\frac{\overline{S}_{23}}{\overline{S}_{22}},\qquad \overline{\nu}_{13} = -\frac{\overline{S}_{31}}{\overline{S}_{11}},\ \overline{\nu}_{12} = -\frac{\overline{S}_{21}}{\overline{S}_{11}}$$

$$\overline{G}_{23} = \frac{1}{\overline{S}_{44}}, \overline{G}_{13} = \frac{1}{\overline{S}_{55}}, \overline{G}_{12} = \frac{1}{\overline{S}_{66}},\ \alpha_i = [C_{ij}^{unit}]^{-1} a_j^{unit} = \overline{S}_{ij} a_j^{unit} \tag{4.55}$$

4.8 Computational Procedures

To find the three-dimensional effective moduli of the sub-cell block model made of orthotropic layers, Eqs. (4.35) and (4.36) are considered. The computational procedure consists of the following steps:

a. Calculate the engineering constants of each sub-cell layer: E_{11}, E_{22}, E_{33}, ν_{23}, $\nu_{13}, \nu_{12}, G_{12}, G_{23}, G_{13}$ and node coordinates.
b. Determine the stiffness matrix $[C_{ij}^*]$ of the fill/warp and resin layers within the sub-cell is obtained from the material coordinate system.
c. The transformed stiffness matrix $[C_{ij}^k]$ is calculated using the transformation Eq. (4.38).
d. The volume fraction of the fill/warp and resin layers within the sub-cell v_k^{sub} is calculated.
e. The components of effective stiffness matrix in Eqs. (4.35) and (4.36) are calculated considering the volume fraction of fill/warp and resin layers.
f. Assemble each stiffness matrix
g. Effective compliance matrix $[\overline{S}_{ij}]$ is obtained from the inverse of the stiffness matrix, $[C_{ij}^{unit}]$.
h. Effective three-dimensional moduli are found form Eq. (4.55).

4.9 Numerical Examples for 2-D Plain Woven Textile Composites

This study applies the sub-cell block model to 2-D plain weave textile composite and obtains its characteristics for various yarn sizes. In the Ref. [4.2], the 2-D plain weave textile composite was analyzed and obtained the elastic characteristics for the 2-D flatten and balanced plain weaves. This study considers two plain weave types, i.e. flat-balanced yarns[4.2] and elliptical yarns studied earlier in Chapter 2. The first case utilizes the same dimensions, fiber and resin materials and geometrical modeling equations as suggested in Ref. [4.2], while the second case uses different geometrical yarn-shapes, oval-shapes, considering the presented modeling equations of the sub-cell block modeled here, see the unit cell of Figure 4.3. For these two yarn types, three examples of the 2-D plain-woven textiles are respectively analyzed in this study. First, the elastic properties for the fiber and resin in the yarns are directly calculated without micro-mechanical equations. For the other two cases, the micro-mechanical equations are used to calculate the elastic moduli for the fill/warp yarns. The second case is based on the Rule of mixtures, and the third case uses the Self-Consistent method.

Figures 4.7-4.8 show results for these three cases. They show the same mechanical characteristics with various yarn sizes. In these results, one can see that the effects of the yarns size on the crimp angles and stiffness properties for the plain weave composites. The in-plane moduli, E_{xx} and E_{yy}, show large decrements, while E_{zz} is increased with the increasing yarn size. The shear moduli G_{xy}, Poisson's ratio ν_{xy} are not sensitive to the yarn sizes, but the Poisson's ratios ν_{xz} and ν_{yz} of the thickness components are very sensitive to the yarn sizes.

By comparing the results with different plain weaves, we can identify some interesting features. For the flat-balanced plain weave composites, the in-plane moduli feature less sensitivity to the increased yarn size, but the in-plane moduli of the elliptical plain weave show high sensitivities to the increased yarn size. These results are obtained from the geometrical shapes of the elliptical yarns; for example, the large yarns have more curved yarn sections normal to the tangential surface, but the flat-balanced yarns have less curved yarn sections with varying yarn sizes. This fact also induces the large sensitivity of through-the thickness Poisson's ratios in the oval-shaped yarns. From this point of view, we can conclude that the flat-balanced yarns are efficient towards avoiding the sensitivity of the yarn sizes, and that the elliptical strands are efficient towards obtaining the effects of different yarns.

4.10 Numerical Examples for Multi-layered Laminates

In this study, two types of multi-layered laminates are analyzed: angle-plied laminates and hybrid laminates. The effective material properties for Boron-Epoxy laminate are presented and compared in Refs. [4.1, 4.3 & 4.4]. The material properties of the Boron-Epoxy angle-plied laminate are presented in Table 4.1 with those of Glass-Epoxy, Graphite-Epoxy and AlO_3 laminates. Four cases of the Boron-Epoxy angle-plied laminate are studied: $[\pm 30]$, $[0/90/\pm 45]$, [30/45] and $[90_3/\pm 45/90_2/\pm 45/90_2]_s$. Also, Graphite-Epoxy sub-laminate, $[0/\pm 60]$, is analyzed. In the case of the hybrid laminates, $[0_{Al}/90_{Gr}/45_{Gl}/-45_{Br}]$ and $[30_{Al}/-30_{Gr}/30_{Gl}/-30_{Br}]$ equivalent material properties of the sub-laminates are obtained.

(1) Boron-Epoxy layered medium

The first sub-laminate is based on several angle-ply Boron-Epoxy laminae. In the $[\pm 30]$ sub-laminate, the results of Enie and Rizzo[4.4] have different values for the effective material properties with Poisson's ratio $\overline{\nu}_{31}$. The predictions of Enie and Rizzo[4.4] result in positive $\overline{\nu}_{31}$=0.118, while in the other and present models, negative Poisson's ratio $\overline{\nu}_{31}$ are resulting. For the unbalanced [30/45] case, only small differences are observed between Sun and Li[4.3] and present results. In the balanced $[0/90/\pm 45]$ sub-laminate case, all models yield the same values.

Reference [4.3] however has two typographical flaws. In Table 2 of Ref. [4.3], the material name should be Boron-Epoxy, not Graphite- Epoxy. And the result for $\overline{G}_{12}$ provides to high values, not low values. Another case, that of $[90_3/\pm 45/90_2/\pm 45/90_2]_s$ laminae, is also analyzed, but different shear moduli based

on the experimental data of Ref. [4.4] are given as: $G_{13}=G_{12}$ =1.2 Msi and G_{23} =0.2Msi are used here. In this case, the results for sub-laminate have small discrepancies between the finite element results of Enie and Rizzo[4.4] model and those from the present model for the Poisson' ratios $\overline{\nu}_{12}$ and $\overline{\nu}_{23}$. From Table 2, one can see that the present results are very close to those of other research works, see Refs. [4.1, 4.3 and 4.4].

(2) Graphite-Epoxy layered medium
The effective engineering constants of $[0/\pm 60]$ sub-laminate are calculated and compared to results of Refs. [4.1&4.5] as shown in Tables 4.4-4.5. As one can see from the results presented in Table 4.4, the properties obtained here agree very well in general. Only small differences, in the predictions of Poisson's ratios and Young's modulus, between the present model and Ref. [4.5] has been found.

(3) Hybrid sub-laminate
The next sub-laminate, the so-called hybrid sub-laminate, is composed of several different materials, such as Aluminum, Boron-Epoxy, Graphite-Epoxy and Glass-Epoxy laminar. In this study, two cases are considered: $[0_{Al}/90_{Gr}/45_{Gl}/\text{-}45_{Br}]$, $[30_{Al}/\text{-}30_{Gr}/30_{Gl}/\text{-}30_{Br}]$ sub-laminate. The results in Tables 4.6 and 4.7 are compared to those in Refs. [4.1 and 4.3] and the comparisons show a good agreement with Sun and Li[4.3]'s results, except those for Poisson's ratios $\overline{\nu}_{23}$, $\overline{\nu}_{13}$, Young's modulus $\overline{E}_{11}$ and shear modulus $\overline{G}_{12}$.

(4) Angle-ply sub-laminate
The next example considers a four-layered sub-laminate made from Graphite-Epoxy with a ply sequence of $[0/+\theta/-\theta/90]$. The engineering constants, $\overline{E}_{11}$, $\overline{E}_{22}$ and $\overline{G}_{12}$, as a function of angle θ are presented in Fig.4.9. Effective Young's moduli $\overline{E}_{11}$ and $\overline{E}_{22}$ are symmetric with respect to θ=45°. The effective shear modulus $\overline{G}_{12}$ has a symmetric plot with the maximum value at θ=45°.
In Fig.4.10, effective Poisson's ratios; $\overline{\nu}_{23}$, $\overline{\nu}_{13}$ and $\overline{\nu}_{12}$ are shown as a function of angle θ. All effective Poisson'ratios are non-symmetric with respect to the ply-angle. The effective Poisson ratio $\overline{\nu}_{12}$ has a maximum value at $\theta \approx 37°$ that is several times higher than the values of this Poisson's ratio at θ=0° and θ=90°. The other effective Poisson's ratios ($\overline{\nu}_{23}$ & $\overline{\nu}_{13}$) have minimum values at θ=35 degree and θ=55 degree, respectively. The differences between maximum and minimum of these Poisson's ratios are smaller than that of $\overline{\nu}_{12}$.

(5) Thickness-wise Poisson's ratios
Herakovich[4.7] studied 2-D laminate theory combined with 3-D anisotropic constitutive equations to get thickness-wise Poisson's ratios $\overline{\nu}_{13}$ and $\overline{\nu}_{23}$. This study considers a $[\pm\theta]$ laminate of different composite systems, whose characteristics are given in Table 4.8. The values of $\overline{\nu}_{13}$ for different angles and materials are presented in Fig. 4.11. For the material 1-3, the maximum negative value of $\overline{\nu}_{13}$ are reached at θ=20°. It is also noted that the thickness-wise Poisson's ratio $\overline{\nu}_{13}$ is very much dependent on the angle of anisotropic composites.

4. 11 Discussion
In this chapter, a numerical analysis modeling, the sub-cell block model, has been presented for calculating the equivalent properties of the 2-D plain woven textile composites. The geometrical parameters of the sub-cell model are based on Sine Function Model I (SFM I) and its formulations are extended from the multi-layered sub-laminate. Consistent equations of the three-dimensional effective elastic material constants for a sub-laminate, i.e. sub-cell block, have been presented using a variational

method. The Voigt (in-plane strains) and the Ruess (out-of stresses) approximations are assumed to be in the thickness direction. Each lamina is considered to be constituted of a linear elastic and anisotropic material. Based on these assumptions, numerical simulations and comparisons with results obtained elsewhere are studied and the results are compared with those given in these references. The results of sub-cell block model have been compared with those of existing analytical modeling and checked for the modeling accuracy. Good agreement between the present and the previous results was revealed.

Furthermore, the sub-cell block model was applied to investigate several multi-layered laminates as suggested in the literature. In the cited References, Chou, *et al.*[4.1] derived equations for both compliance and stiffness, and Sun and Li[4.3] suggested stiffness equations for the 3-D effective moduli, respectively. The comparisons of the available results in the literature with our results reveal that the present results on the effective moduli, are in good agreement. In particular, the numerical results of Sun and Li[4.3] and those by Chou, *et al*.[4.1] have been seen to have the same trends as those of the present study. Exceptions are the minor differences in results for Poisson's ratios that can be explained as computational round-off errors.

The success of the present analytical modeling, sub-cell block model, gives us confidence to predict the effective moduli for both the 2-D plain woven textile composite and multi-layered sub-laminate, and provides an efficient computational tool enabling one to model the textile composite structures without requiring a highly complex modeling, such as a highly detailed 3-D finite element model.

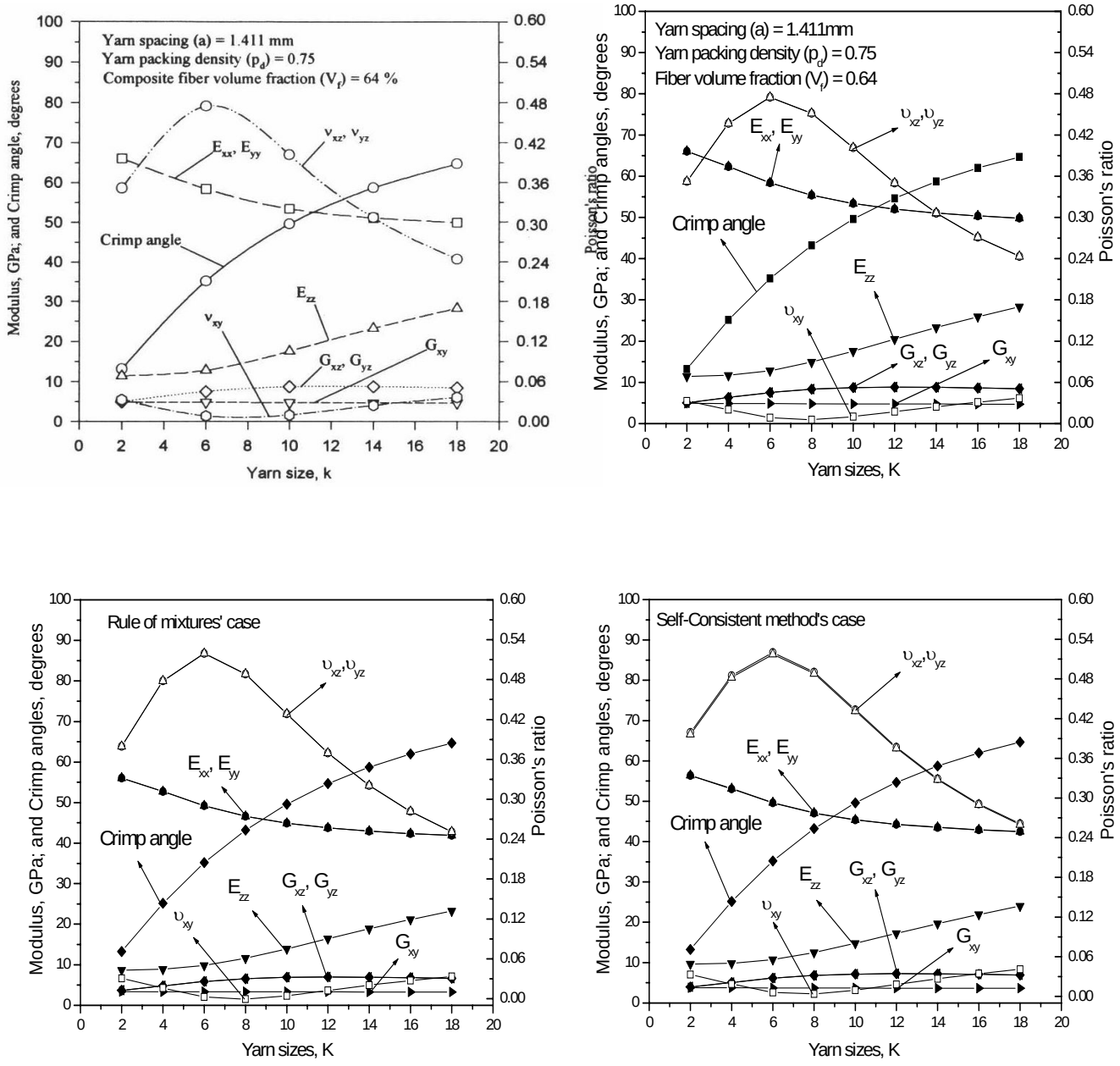

Figure 4.7: Plain weave moduli, Poisson's ratio and crimp angle with various flat-balanced yarns[4.2].

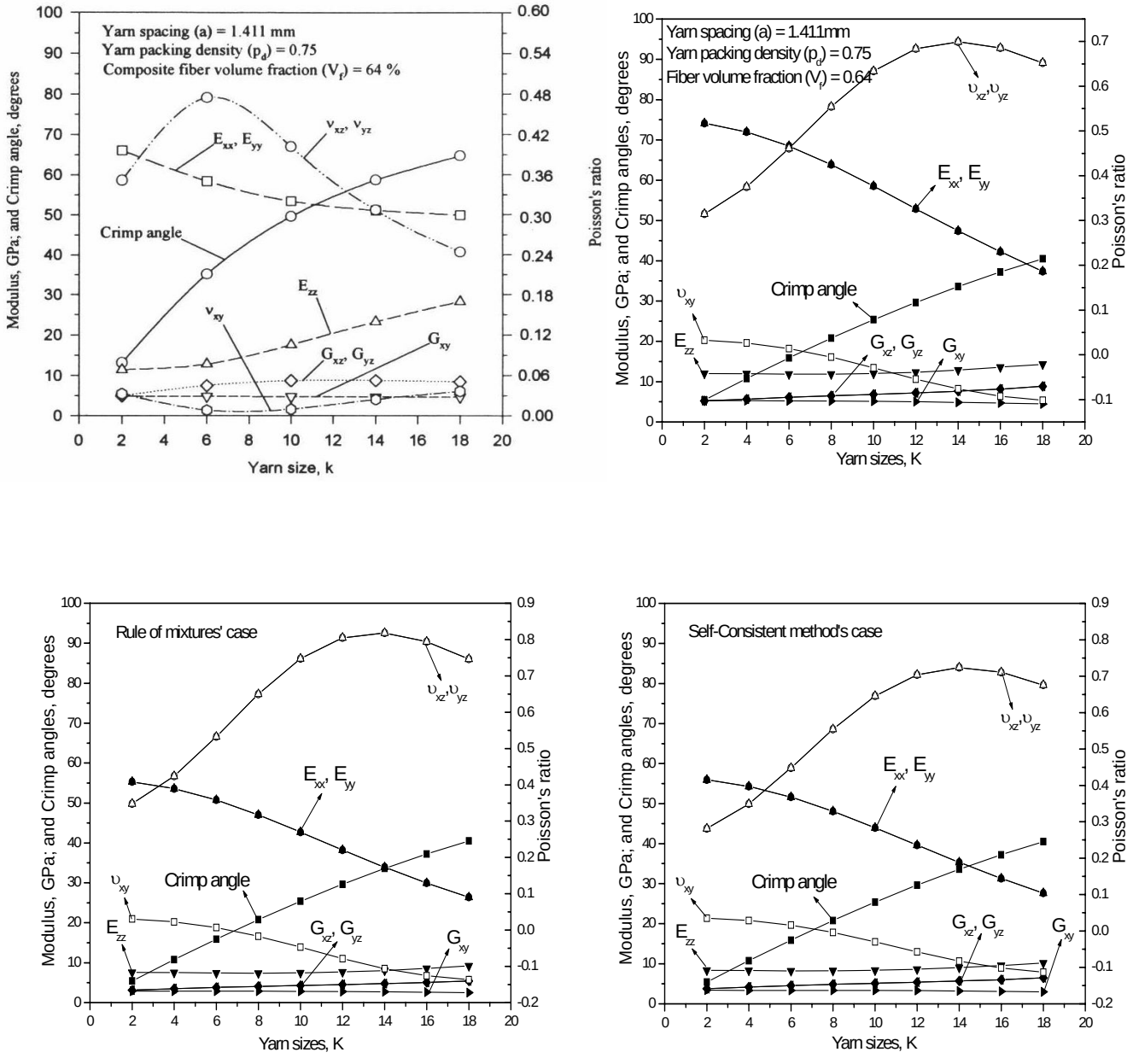

Figure 4.8: Plain weave moduli, Poisson's ratio and crimp angle with a number of sub-cell blocks.

Table 4.1: Material properties for laminas in the sub-laminate from Ref. [4.4]. (Unit: *Msi*)

Material	E_{11}	E_{22}	E_{33}	ν_{23}	ν_{13}	ν_{12}	G_{23}	G_{13}	G_{12}
Boron-Epoxy	33.30	3.3	3.3	0.32	0.26	0.26	0.50	0.80	0.80
Glass-Epoxy	7.80	2.60	2.60	0.25	0.25	0.35	1.10	1.30	1.30
Graphite-Epoxy	26.00	1.45	1.45	0.49	0.23	0.26	1.04	1.04	1.04
Al O_3	10.30	10.20	10.20	0.33	0.33	0.33	3.84	3.84	3.84

Table 4.2: Comparison of effective engineering modulus predictions for Boron-Epoxy sub-laminate.

Modulus	Model	$[\pm 30]$	$[90_3/\pm 45/90_2/\pm 45/90_2]_s$	[30/45]	[0/90/$\pm$45]
$\overline{E}_{11}$,Msi	Enie &Rizzo[4.4]	10.33	5.86	-	-
	Sun & Li[4.3]	10.40	-	4.60	12.80
	Chou, *et al.*[4.1]	10.40	5.71	4.48	12.80
	Present	10.3933	5.7101	4.4768	12.8013
$\overline{E}_{22}$, Msi	Enie &Rizzo[4.4]	2.54	22.20	-	-
	Sun & Li[4.3]	2.54	-	3.37	12.80
	Chou, *et al.*[4.1]	2.54	22.06	3.39	12.80
	Present	2.5415	22.0549	3.3888	12.8013
$\overline{E}_{33}$, Msi	Enie &Rizzo[4.4]	3.33	3.30	-	-
	Sun & Li[4.3]	3.42	-	3.31	3.57
	Chou, *et al.*[4.1]	3.42	3.49	3.30	3.57
	Present	3.4171	3.4876	3.3049	3.5685
$\overline{\nu}_{23}$	Enie &Rizzo[4.4]	0.217	0.195	-	-
	Sun & Li[4.3]	0.216	-	0.215	0.224
	Chou, *et al.*[4.1]	0.216	0.138	0.215	0.224
	Present	0.2161	0.1378	0.2149	0.2238
$\overline{\nu}_{13}$	Enie &Rizzo[4.4]	0.118	0.261	-	-
	Sun & Li[4.3]	-0.125	-	0.175	0.224
	Chou, *et al.*[4.1]	-0.125	0.278	0.179	0.224
	Present	-0.1253	0.2777	0.1790	0.2238

Table 4.2: Comparison of effective engineering modulus predictions for Boron-Epoxy sub-laminate.

Modulus	Model	$[\pm 30]$	$[90_3/\pm 45/90_2/\pm 45/90_2]_s$	[30/45]	[0/90/$\pm$45]
$\overline{\nu}_{12}$	Enie &Rizzo[4.4]	1.395	0.624	-	-
	Sun & Li[4.3]	1.40	-	0.472	0.336
	Chou, *et al.*[4.1]	1.40	0.159	0.459	0.336
	Present	1.4011	0.1593	0.4593	0.3363
$\overline{G}_{23}$, Msi	Enie &Rizzo[4.4]	0.555	0.592	-	-
	Sun & Li[4.3]	0.552	-	0.582	0.615
	Chou, *et al.*[4.1]	0.552	0.6	0.582	0.615
	Present	0.5517	0.6000	0.5818	0.6154
$\overline{G}_{13}$, Msi	Enie &Rizzo[4.4]	0.704	0.225	-	-
	Sun & Li[4.3]	0.696	-	0.653	0.615
	Chou, *et al.*[4.1]	0.696	0.24	0.653	0.615
	Present	0.6957	0.2400	0.6531	0.6154
$\overline{G}_{12}$, Msi	Enie &Rizzo[4.4]	6.71	4.25	-	-
	Sun & Li[4.3]	6.79	-	2.62	0.479*
	Chou, *et al.*[4.1]	6.79	4.23	2.55	4.79
	Present	6.7849	4.2319	2.5509	4.7899
$\overline{\eta}_{16}$	Chou, *et al.*[4.1]	0.0	0.0	-0.813	0.0
	Present	0.0	0.0	-0.8134	0.0
$\overline{\eta}_{26}$	Chou, *et al.*[4.1]	0.0	0.0	-0.291	0.0
	Present	0.0	0.0	-0.2913	0.0
$\overline{\eta}_{36}$	Chou, *et al.*[4.1]	0.0	0.0	0.289	0.0
	Present	0.0	0.0	0.2889	0.0
$\overline{\mu}_{45}$	Chou, *et al.*[4.1]	0.0	0.0	-0.204	0.0
	Present	0.0	0.0	-0.2036	0.0
$\alpha_1 (10^{-6}/^{o}\text{F})$	Chou, *et al.*[4.1]	0.2055	7.216	6.22	3.62
	Present	0.2055	7.2163	6.2180	3.6177
$\alpha_2 (10^{-6}/^{o}\text{F})$	Chou, *et al.*[4.1]	11.42	2.32	8.92	3.62
	Present	11.4205	2.3196	8.9237	3.6177
$\alpha_3 (10^{-6}/^{o}\text{F})$	Chou, *et al.*[4.1]	14.0	14.68	12.85	15.43
	Present	13.9999	14.6826	12.8517	15.4339
$\alpha_6 (10^{-6}/^{o}\text{F})$	Chou, *et al.*[4.1]	0.0	0.0	-10.1	0.0
	Present	0.0000	0.0000	-10.0978	0.0000

*:Typographical error

Table 4.3: Material properties for [0/±60] Graphite-Epoxy sub-laminate from Ref. [4.1]. (Unit: MPa)

E_{11}	E_{22}	E_{33}	ν_{23}	ν_{13}	ν_{12}	G_{23}	G_{13}	G_{12}
144.0	9.65	9.65	0.52	0.31	0.31	3.17	5.24	5.24

Table 4.4: Effective engineering modulus for [0/±60] Graphite-Epoxy sub-laminate. (Unit:MPa)

Model	$\overline{E}_{11}$	$\overline{E}_{22}$	$\overline{E}_{33}$	$\overline{\nu}_{12}$	$\overline{\nu}_{13}$	$\overline{\nu}_{32}$	$\overline{G}_{23}$	$\overline{G}_{13}$	$\overline{G}_{12}$
Ref. [4.1]	55.5	55.5	12.45	0.309	0.347	0.347	3.95	3.95	21.2
Ref. [4.5]	55.0	55.0	13.4	0.329	0.302	0.302	3.95	3.95	20.7
Present	55.5013	55.5013	12.4487	0.3091	0.3469	0.3469	3.9502	3.9502	21.1980

Table 4.5: Effective thermal expansion constants for [0/±60] Graphite-Epoxy sub-laminate.

Model	α_1 (10^{-6}/°C)	α_2 (10^{-6}/°C)	α_3 (10^{-6}/°C)
Ref. [4.1]	1.0	1.0	18.12
Ref. [4.5]	-	-	-
Present	0.9909	0.9909	18.1247

Table 4.6: Effective engineering modulus for [$0_{Al}/90_{Gr}/45_{Gl}/-45_{Br}$] sub-laminate. (Unit: *Msi*)

Modulus	Model		
	Sun & Li[4.3]	Chou, *et al.*[4.1]	Present
$\overline{E}_{11}$	5.61	5.54	5.5483
$\overline{E}_{22}$ i	11.0	11.0	10.9718
$\overline{E}_{33}$	3.06	3.04	3.0353
$\overline{\nu}_{23}$	0.15	0.171	0.1749
$\overline{\nu}_{13}$	0.29	0.306	0.3152
$\overline{\nu}_{12}$	0.25	0.239	0.2460
$\overline{\eta}_{16}$	-	0.296	0.2936
$\overline{\eta}_{26}$	-	0.205	0.1999
$\overline{\eta}_{36}$	-	-0.086	-0.0884
$\overline{\mu}_{45}$	-	0.083	0.0828
$\overline{G}_{23}$	1.09	1.09	1.0852
$\overline{G}_{13}$	1.09	1.09	1.0852
$\overline{G}_{12}$	3.63	3.59	3.5977
$\alpha_1\,(10^{-6}/^{o}\mathrm{F})$	-	11.47	11.8099
$\alpha_2\,(10^{-6}/^{o}\mathrm{F})$	-	3.36	4.0802
$\alpha_3\,(10^{-6}/^{o}\mathrm{F})$	-	17.44	17.3075
$\alpha_6\,(10^{-6}/^{o}\mathrm{F})$	-	4.53	4.8677

Table 4.7: Effective engineering modulus for [30_{Al}/-30_{Gr}/30_{Gl}/-30_{Br}] sub-laminate. (Unit: *Msi*)

Modulus	Model		
	Sun & Li[4.3]	Chou, *et al.*[4.1]	Present
$\overline{E}_{11}$	8.47	7.97	7.9390
$\overline{E}_{22}$	4.42	4.39	4.4192
$\overline{E}_{33}$	3.04	3.0	2.9929
$\overline{\nu}_{23}$	0.27	0.266	0.2744
$\overline{\nu}_{13}$	0.11	0.173	0.1771
$\overline{\nu}_{12}$	0.59	0.55	0.5582
$\overline{\eta}_{16}$	-	0.734	0.7374
$\overline{\eta}_{26}$	-	0.012	0.0127
$\overline{\eta}_{36}$	-	-0.123	-0.1263
$\overline{\mu}_{45}$	-	0.068	0.0676
$\overline{G}_{23}$	1.02	1.02	1.0234
$\overline{G}_{13}$	1.15	1.155	1.1549
$\overline{G}_{12}$	3.49	3.27	3.2566
α_1 (10^{-6}/^{o}F)	-	4.84	5.2182
α_1 (10^{-6}/^{o}F)	-	12.09	12.8314
α_1 (10^{-6}/^{o}F)	-	16.64	16.8780
α_1 (10^{-6}/^{o}F)	-	7.5	7.4281

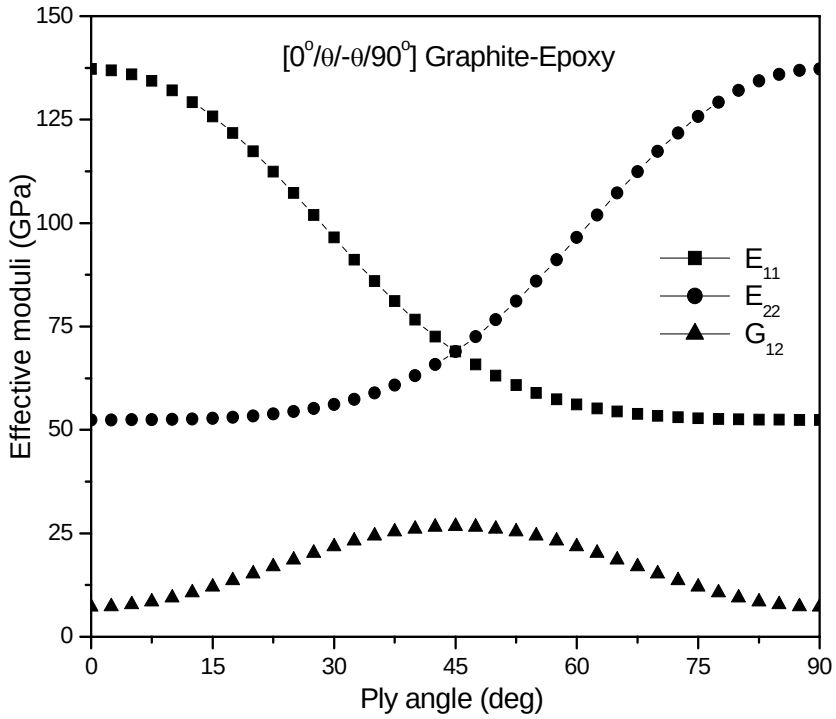

Figure 4.9: Dependency of effective moduli on θ for $[0^o/\theta/-\theta/90^o]$ Graphite-Epoxy composite.

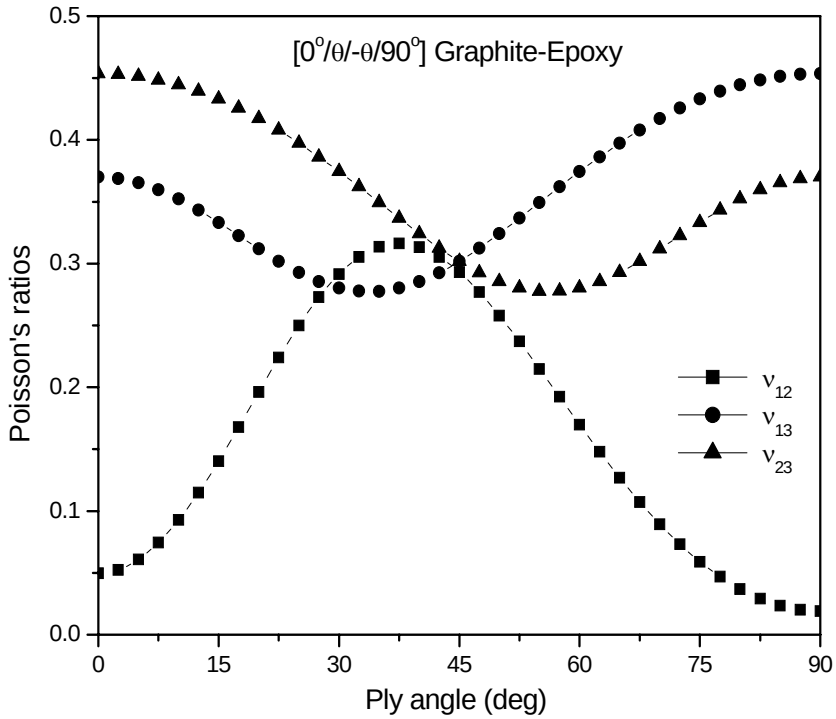

Figure 4.10: Dependency of effective Poisson's ratios on θ for $[0^o/\theta/-\theta/90^o]$ Graphite-Epoxy composite.

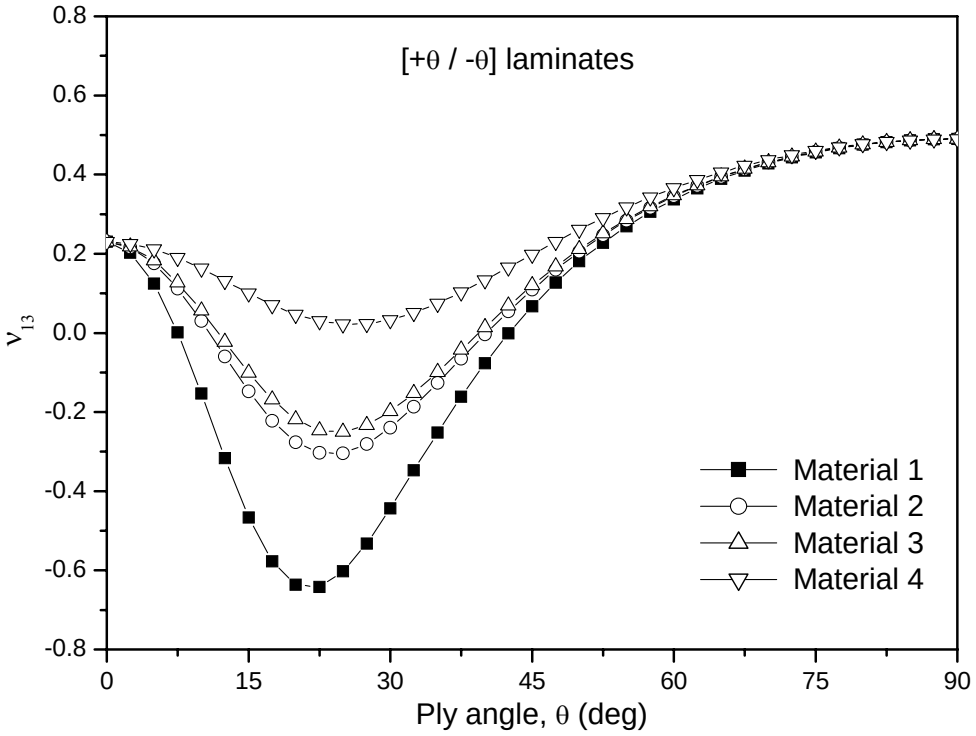

Figure 4.11: Thickness-wise Poisson's ratios on θ for $[\pm\theta]$ laminate.

Table 4.8: Moduli for four composite materials from Ref. [4.3]. (Unit: *Msi*)

Material	E_{11}	E_{22}	E_{33}	ν_{23}	ν_{13}	ν_{12}	G_{23}	G_{13}	G_{12}
1	46.40	1.45	1.45	0.49	0.23	0.23	1.04	1.04	1.04
2	26.00	1.45	1.45	0.49	0.23	0.23	1.04	1.04	1.04
3	23.20	1.45	1.45	0.49	0.23	0.23	1.04	1.04	1.04
4	11.60	1.45	1.45	0.49	0.23	0.23	1.04	1.04	1.04

REFERENCES

4.1 Chou, P.C., Carleone,J. and Hsu, C.M., "Elastic Constants of Layered Media", *Journal of Composite Materials*, Vol. 6, January, 1972, pp. 80-93.

4.2 Naik, R.A., "Analysis of Woven and Braided Fabric Reinforced Composites," NASA Contract Report CR-194930, 1994.

4.3 Sun, C.T., and Li, S., "Three-Dimensional Effective Elastic Constants for Thick Laminates," *Journal of Composite Materials*, Vol. 22, July, 1988, pp. 629-639.

4.4 Enie, R.B., and Rizzo, R.R., "Three-Dimensional Laminate Moduli," *Journal of Composite Materials*, Vol. 14, January, 1970, pp. 150-154.

4.5 Christensen, R.M. and Zywicz, E., "A Three-Dimensional Constitutive Theory for Fiber Composite Laminated Media," *Trans. of ASME*: *Journal of Applied Mechanics*, Vol. 57, December, 1990, pp. 948-955.

4.6 Postma, G.W., "Wave Propagation in a Stratified Medium," *Geophysics*, Vol. 20, No. 4, 1955, pp. 780-806.

4.7 Herakovich, C.T., "Composite Laminates with Negative through the Thickness Poisson's Ratios," *Journal of Composite Materials*, Vol. 18, No. 5, 1984, pp. 447-455.

Chapter 5 Homogenization of 2-D Braided / 3-D Woven Textile Composites

5.1 Introduction

In this chapter, we focus on geometrical modeling and a parametric study of 2-D braids, 2-D tri-axial braids and 3-D orthogonal woven composites. The geometrical modeling of 2-D braided Repeating Unit Cell (RUC) uses sinusoidal functions suggested in Sine Function Model I as to determine three-dimensional yarn shapes and to find homogenized properties by employing the iso-strain assumption and strain energy for the RUC. A simple modeling of 2-D tri-axial braids based on the RUC geometrical equations is presented. Another modeling of the 3-D orthogonal woven fabrics is introduced. For the parametric study, various yarn sizes and braid angles are used into the 2-D braids and 2-D tri-axial braids' modeling and various characteristics of effective elastic moduli are considered.

5.2 Geometric Modeling of 2-D Braided Textile Composites

The 2-D braided composites have two interlaced yarns mutually oriented in non-orthogonal directions with respect to the local coordinate system, 1-2-3, see Figure 5.1. One of the yarns is called $+\theta_{br}$ braider yarn and the other is named $-\theta_{br}$ braider yarn. These $+\theta_{br}$ and $-\theta_{br}$ braider yarns make braid angles of $+\theta_{br}$ and $-\theta_{br}$, clockwise, with the y-axis of a global coordinate system, respectively, and the resin component is constituted of the upper and lower layers. This architecture is similar to the plain-weave composites but the 2-D braid have different rotation angles, $\pi/2-\theta_{br}$ and $\pi/2+\theta_{br}$ with respect to the x-axis. The braider yarns have the number of filaments, n, with the same diameter, d_f, and packing density, p_d.

Geometrically, the shape of 2-D braided composites is depicted using sinusoidal curve equations, for example, sine-functions, described in the chapters on plain weave textile composites. Figure 5.2 describes the geometrical variables of RUC along the x- and y-axes. This study introduces upper and lower surface curve equations for the $+\theta_{br}/-\theta_{br}$ braider yarns defined by the sine-functions. The equations for the upper and lower sine-functions are

$$z^{up}_{+\theta_{br}} = +\frac{t_2}{2}\sin\left[\frac{x\pi}{a_2+g_2}\sin(2\theta_{br})\right]+\frac{t_1}{2}\sin\left[\frac{y\pi}{a_1+g_1}\right]$$

$$z^{lower}_{+\theta_{br}} = +\frac{t_2}{2}\sin\left[\frac{x\pi}{a_2+g_2}\sin(2\theta_{br})\right]-\frac{t_1}{2}\sin\left[\frac{y\pi}{a_1+g_1}\right] \tag{5.1}$$

$$z^{up}_{-\theta_{br}} = +\frac{t_2}{2}\sin\left[\frac{x\pi}{a_2+g_2}\right]-\frac{t_1}{2}\sin\left[\frac{y\pi}{a_1+g_1}\sin(2\theta_{br})\right]$$

$$z^{lower}_{-\theta_{br}} = -\frac{t_2}{2}\sin\left[\frac{x\pi}{a_2+g_2}\right]-\frac{t_1}{2}\sin\left[\frac{y\pi}{a_1+g_1}\sin(2\theta_{br})\right] \tag{5.2}$$

Here, the gap-lengths are g_1 and g_2 along the $+\theta_{br}/-\theta_{br}$ braider yarns, respectively. The centerline equations of the braider yarns are expressed as:

$$z^{c}_{+\theta_{br}} = +\frac{t_2}{2}\sin\left[\frac{x\pi}{a_2+g_2}\sin(2\theta_{br})\right],\ z^{c}_{-\theta_{br}} = \frac{t_1}{2}\sin\left[\frac{y\pi}{a_1+g_1}\sin(2\theta_{br})\right] \tag{5.3}$$

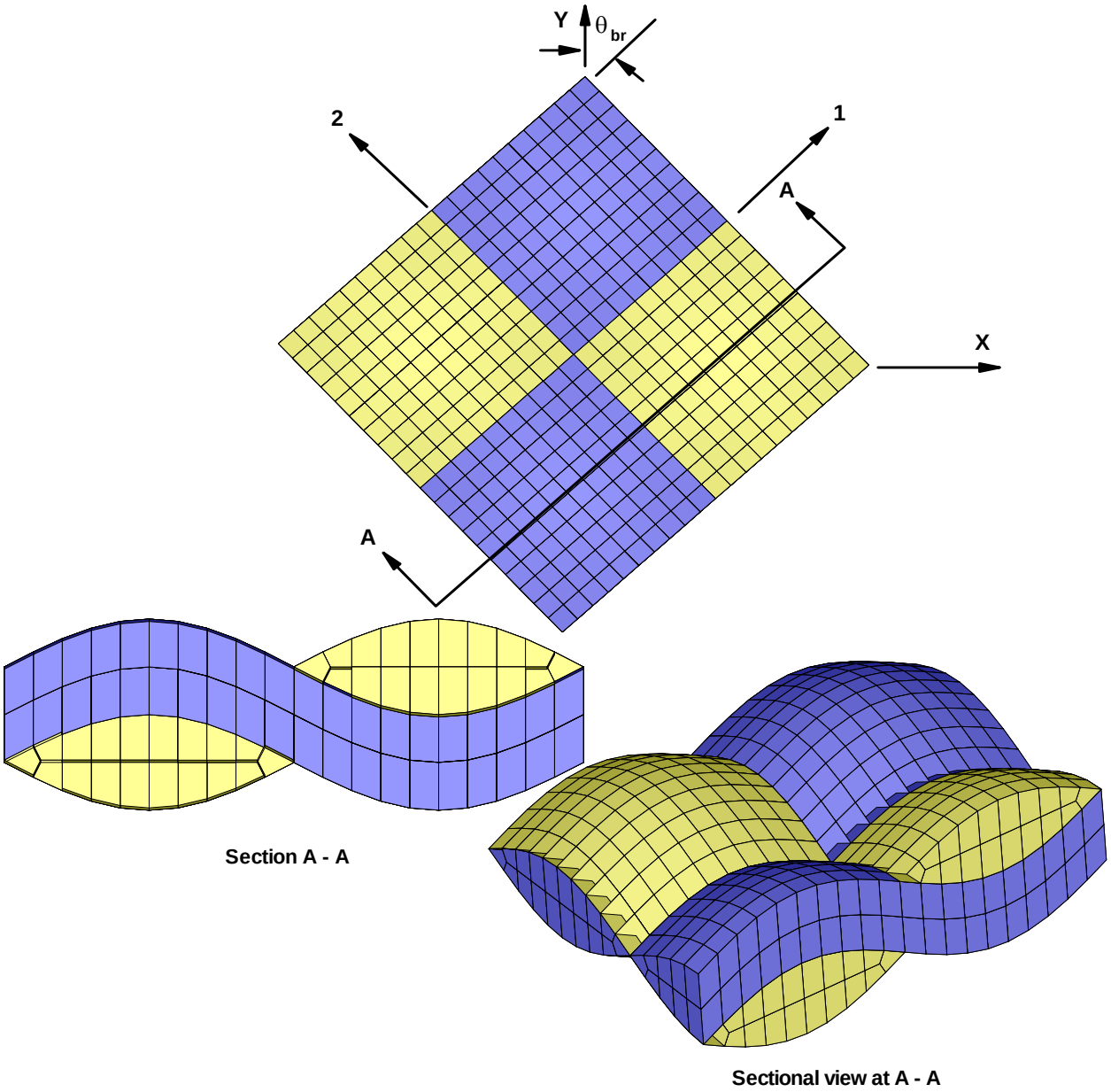

Figure 5.1: 2-D braided RUC geometry and cross-sectional shapes along the section A-A.

The crimp angles ($\theta_c^{+br}, \theta_c^{-br}$) of the $+\theta_{br}/-\theta_{br}$ braider yarns are found by obtaining the derivatives of $z^c_{+\theta_{br}}$ and $z^c_{-\theta_{br}}$ with respect to the x and y, respectively.

$$\frac{dz^c_{+\theta_{br}}}{dx} = \tan\theta_c^{+br} = \frac{t_2\pi}{2(a_2+g_2)}\cos\left[\frac{\pi x}{(a_2+g_2)}\sin(2\theta_{br})\right]$$

$$\frac{dz^c_{-\theta_{br}}}{dy} = \tan\theta_c^{-br} = -\frac{t_1\pi}{2(a_1+g_1)}\cos\left[\frac{\pi y}{(a_1+g_1)}\sin(2\theta_{br})\right] \quad (5.4)$$

From Eq. (5.4), the different crimp angles of half regions along the x- and y-axes are obtained.

$$\theta_c^{+br} = \tan^{-1}\left[\frac{t_2\pi}{2(a_2+g_2)}\cos\left[\frac{\pi x}{(a_2+g_2)}\sin(2\theta_{br})\right]\right],\quad x\in(0,\ u_2/2\sin(2\theta_{br}))$$

$$\theta_c^{+br} = \tan^{-1}\left[-\frac{t_2\pi}{2(a_2+g_2)}\cos\left[\frac{\pi(x-u_2^*)}{(a_2+g_2)}\sin(2\theta_{br})\right]\right],\ x\in(u_2/2\sin(2\theta_{br}),\ u_2/\sin(2\theta_{br}))$$

$$\theta_c^{-br} = \tan^{-1}\left[-\frac{t_1\pi}{2(a_1+g_1)}\cos\left[\frac{\pi y}{(a_1+g_1)}\sin(2\theta_{br})\right]\right],\ \ y\in(0,\ u_1/2\sin(2\theta_{br}))$$

$$\theta_c^{-br} = \tan^{-1}\left[\frac{t_1\pi}{2(a_1+g_1)}\cos\left[\frac{\pi(y-u_1^*)}{(a_1+g_1)}\sin(2\theta_{br})\right]\right],\quad y\in(u_1/2\sin(2\theta_{br}),\ u_1/\sin(2\theta_{br}))\qquad(5.5)$$

Here, the undulation lengths are $u_1 = a_1 + g_1$, $u_2 = a_2 + g_2$, $u_1^* = u_1/\sin(2\theta_{br})$, $u_2^* = u_2/\sin(2\theta_{br})$, $g_1^* = g_1/\sin(2\theta_{br})$ and $g_2^* = g_2/\sin(2\theta_{br})$ in the x-y-z and 1-2-3 systems. To find the braider yarns' volume, the sectional areas, $A_{+\theta_{br}}$ and $A_{-\theta_{br}}$, are obtained, first.

$$A_{+\theta_{br}} = \int_0^{a_1}(z_{+\theta_{br}}^{up} - z_{+\theta_{br}}^{lower})dy = \frac{t_1(a_1+g_1)}{\pi}\left[1-\cos\left[\frac{a_1\pi}{(a_1+g_1)}\right]\right]$$

$$A_{-\theta_{br}} = \int_0^{a_2}(z_{-\theta_{br}}^{up} - z_{-\theta_{br}}^{lower})dx = \frac{t_2(a_2+g_2)}{\pi}\left[1-\cos\left[\frac{a_2\pi}{(a_2+g_2)}\right]\right]\qquad(5.6)$$

The volumes of the $+\theta_{br}/-\theta_{br}$ braider yarns are derived by the area and the undulation lengths. These are also functions of the braid angles. We can get the braider yarns' volumes:

$$V_{+\theta_{br}} = A_{+\theta_{br}}\int_0^{u_2^*}\sqrt{1+(\frac{dz_{+\theta_{br}}^c}{dx})^2}\,dx = A_{+\theta_{br}}\int_0^{u_2^*}\sqrt{1+(\frac{t_2\pi}{2u_2^*})^2\cos^2(\frac{\pi x}{u_2^*})}dx\qquad(5.7)$$

$$V_{-\theta_{br}} = A_{-\theta_{br}}\int_0^{u_1^*}\sqrt{1+(\frac{dz_{-\theta_{br}}^c}{dy})^2}\,dy = A_{-\theta_{br}}\int_0^{u_1^*}\sqrt{1+(\frac{t_1\pi}{2u_1^*})^2\cos^2(\frac{\pi y}{u_1^*})}dy\qquad(5.8)$$

The total volume of the RUC is expressed in terms of the thickness and the undulation variables, namely. The total resin thickness is denoted as h_m in the RUC, that includes half the thickness for the upper and the lower resin layers, respectively.

$$V_{total} = H(a_1+g_1)(a_2+g_2)/\sin(2\theta_{br}) = (h_m+t_1+t_2)(a_1+g_1)(a_2+g_2)/\sin(2\theta_{br})\qquad(5.9)$$

The resin volume and resin volume fraction in the RUC, V_{resin} and V_f^r, are

$$V_{resin} = V_{total} - (V_{+\theta_{br}} + V_{-\theta_{br}}),\ V_f^r = \frac{V_{resin}}{V_{total}} = \frac{V_{total} - (V_{+\theta_{br}} + V_{-\theta_{br}})}{V_{total}}\qquad(5.10)$$

If different volume fractions for the braider yarns are specified, the over-all fiber volume fraction (V_f^o) is

$$V_f = V_{f+\theta_{br}}\frac{V_{+\theta_{br}}}{V_{total}} + V_{f-\theta_{br}}\frac{V_{-\theta_{br}}}{V_{total}} = V_f^o\qquad(5.11)$$

If the fiber volume fractions for the braider yarns are the same $V_{f+\theta_{br}} = V_{f-\theta_{br}} = V_{fyarn}$, the equation of V_{fyarn} is

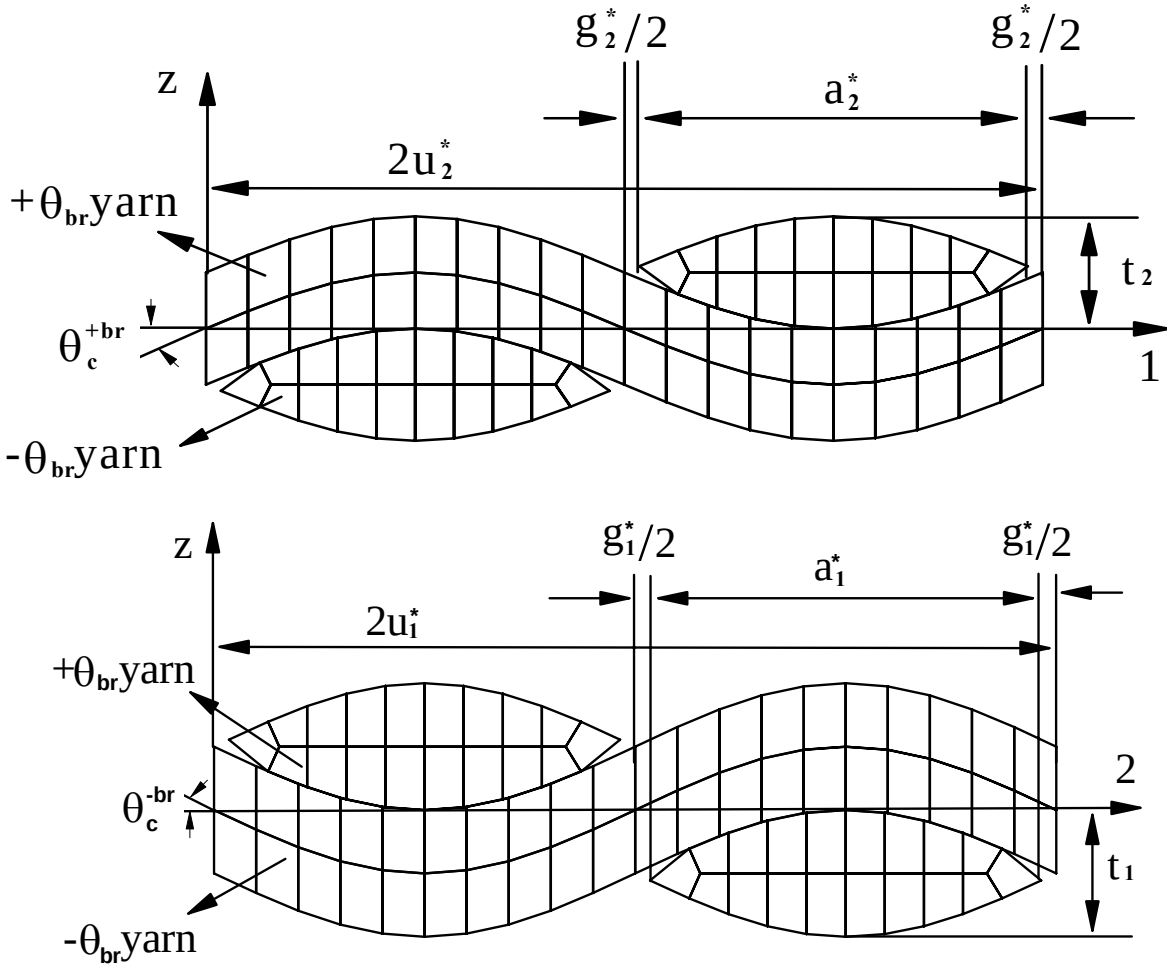

Figure 5.2: Sectional shapes of $+\theta_{br}/-\theta_{br}$ braider yarns along the 1- and 2-axes.

$$V_{fyarn} = V_f^o \frac{V_{total}}{(V_{+\theta_{br}} + V_{-\theta_{br}})} = \frac{V_f^o V_{total}}{(V_{total} - V_{re\sin})} \tag{5.12}$$

The braider yarns' fiber volume fraction, $V_{f+\theta_{br}}$ and $V_{f-\theta_{br}}$, are generally obtained from experimental tests.

5.3 Equivalent Moduli for 2-D Braided Textile Composites

We have already introduced the concepts of strain energy and the iso-strain assumption into the RUC of plain-woven textile composites. The 2-D braided textile composites also use both these concepts to calculate three-dimensional effective moduli. The RUC of 2-D braided textile has three media: two $+\theta_{br}$ braider yarns, two $-\theta_{br}$ braider yarns, and two resin layers. These three components feature constant strains within the RUC volume and linear elasticity. Using the concept of the strain energy in the RUC, equivalent elastic values for the 3-components ($+\theta_{br}$ braider yarns, $-\theta_{br}$ braider yarns and resins) can be described in terms of the volume fractions for each phase. The RUC volume and the volume fractions are already included in Eqs. (5.7)-(5.12).

$$C_{eq} = \frac{1}{V}\left[\int_{V_{+\theta_{br}}} C_{+\theta_{br}} dV + \int_{V_{-\theta_{br}}} C_{-\theta_{br}} dV + \int_{V_{re\sin}} C_{re\sin} dV \right] \tag{5.13}$$

Eq.(5.13) is rewritten as transformation stiffness matrices of $+\theta_{br}/-\theta_{br}$ braider yarns and resin: $\overline{C}_{eq+\theta_{br}}$, $\overline{C}_{eq-\theta_{br}}$ and $\overline{C}_{eqr}$.

$$C_{eq} = V_{f+\theta_{br}}\overline{C}_{eq+\theta_{br}} + V_{f-\theta_{br}}\overline{C}_{eq-\theta_{br}} + V_f^r\overline{C}_{eqr} = C_{eq+\theta_{br}} + C_{eq-\theta_{br}} + C_{eqr} \tag{5.14}$$

The equivalent elasticity matrices are dependent on the crimp angles ($\theta_c^{+br}, \theta_c^{-br}$) and rotation angles ($+\theta_{br}, -\theta_{br}$) denoted by a transformation matrix (T) between $x-y-z$ and $1-2-3$ coordinates. To obtain the equivalent elasticity matrices, each equivalent matrix has to be defined as a function of the crimp and rotation angles. As for the plain woven case of the fill and warp yarns, the values $\theta_r = \pi/2 - \theta_{br}$ or $\theta_r = \pi/2 + \theta_{br}$ between the x and y axes are specified into the $+\theta_{br}/-\theta_{br}$ yarns, respectively. These rotation angles of the braider yarns do not always have constant values in the 2-D braids that will be of different values if the braiders have different braid angles. The crimp angles for the braider yarns have different values depending on the regions specified in Eq. (5.5). The matrices, $\overline{C}^{ij}_{eq+\theta_{br}}$ and $\overline{C}^{ij}_{eq-\theta_{br}}$, in the Eq. (5.14) have different components compared to those of the plain weave textiles. As the Sine Function Model I suggested, the equivalent elasticity matrices are defined using the two angles between the local and global systems, for example, the rotation angle and the crimp angle.

$$C_{eq+\theta_{br}} = \frac{1}{2A_{+\theta_{br}}u_2^{u^*}} \int_{V_{+\theta_{br}}} C_{+\theta_{br}} dV = \frac{1}{u_2^{u^*}} \int_0^{2u_2^*} C_1\left(\frac{\pi}{2} - \theta_{br}, \theta_c^{+br}\right)\sqrt{1+\left(\frac{dz^c_{+\theta_{br}}}{dx}\right)^2}\,dx$$

$$C_{eq-\theta_{br}} = \frac{1}{2A_{-\theta_{br}}u_1^{u^*}} \int_{V_{-\theta_{br}}} C_{-\theta_{br}} dV = \frac{1}{u_1^{u^*}} \int_0^{2u_1^*} C_1\left(\frac{\pi}{2} + \theta_{br}, \theta_c^{-br}\right)\sqrt{1+\left(\frac{dz^c_{-\theta_{br}}}{dy}\right)^2}\,dy \tag{5.15}$$

In Eq. (5.15), the integration region of $2u_1^*$ or $2u_2^*$ is considered. If the integration region of the yarns is specified as the half undulation (u_1^* or u_2^*) and the undulation arc-length ($u_1^{u^*}$ or $u_2^{u^*}$), Eq. (5.15) can be re-written as:

$$C_{eq+\theta_{br}} = \frac{2}{u_2^{u^*}} \int_0^{u_2^*} C_1\left(\frac{\pi}{2} - \theta_{br}, \theta_c^{+br}\right)\sqrt{1+\left(\frac{dz^c_{+\theta_{br}}}{dx}\right)^2}\,dx$$

$$= \frac{2}{u_2^{u^*}} \int_0^{u_2^*} C_1\left(\frac{\pi}{2} - \theta_{br}, \theta_c^{+br}\right)\sqrt{1+\left(\frac{t_2\pi}{2u_2^*}\right)^2 \cos^2\left(\frac{\pi x}{u_2^*}\right)}\,dx$$

$$C_{eq-\theta_{br}} = \frac{2}{u_1^{u^*}} \int_0^{u_1^*} C_1\left(\frac{\pi}{2} + \theta_{br}, \theta_c^{-br}\right)\sqrt{1+\left(\frac{dz^c_{-\theta_{br}}}{dy}\right)^2}\,dy$$

$$= \frac{2}{u_1^{u^*}} \int_0^{u_1^*} C_1\left(\frac{\pi}{2} + \theta_{br}, \theta_c^{-br}\right)\sqrt{1+\left(\frac{t_1\pi}{2u_1^*}\right)^2 \cos^2\left(\frac{\pi y}{u_1^*}\right)}\,dy \tag{5.16}$$

The volume fractions of $+\theta_{br}/-\theta_{br}$ braider yarns and resin matrix in Eq. (5.14) are

$$V_{f+\theta_{br}} = 2A_{+\theta_{br}}u_2^{u^*}/V_{total},\ V_{f-\theta_{br}} = 2A_{-\theta_{br}}u_1^{u^*}/V_{total},\ V_f^r = V_r/V_{total} \tag{5.17}$$

The equivalent elastic matrices of the resin consist of isotropic material components.

$$C_{eqr} = \frac{1}{V_{resin}} \int_{V_{resin}} C_{resin} dV = C_{resin} \tag{5.18}$$

By applying the iso-strain assumption into the RUC, the average stress and strain components are obtained. From the average stress concept, $\overline{\sigma} = \sum v_r \overline{\sigma}_r$, the stress-strain relationships between the 1-2-3 local and x-y-z global coordinates are described as:

$$\begin{aligned} \{\overline{\sigma}\} &= V_{f+\theta_{br}} \{\overline{\sigma}\}_{+\theta_{br}} + V_{f-\theta_{br}} \{\overline{\sigma}\}_{-\theta_{br}} + V_f^r \{\overline{\sigma}\}_{resin} \\ &= V_{f+\theta_{br}} \left[\overline{C}_{eq+\theta_{br}}\right] \{\overline{\varepsilon}\}_{+\theta_{br}} + V_{f-\theta_{br}} \left[\overline{C}_{eq-\theta_{br}}\right] \{\overline{\varepsilon}\}_{-\theta_{br}} + V_f^r \left[\overline{C}_{eqr}\right] \{\overline{\varepsilon}\}_{resin} \end{aligned} \tag{5.19}$$

Let's adopt iso-strain assumption, $\{\overline{\varepsilon}\} = \{\overline{\varepsilon}\}_{+\theta_{br}} = \{\overline{\varepsilon}\}_{-\theta_{br}} = \{\overline{\varepsilon}\}_{resin}$, and use it in Eq. (5.19). The average stress then is:

$$\{\overline{\sigma}\} = \frac{1}{V} \left[\sum_{m=1}^{n} v_m^{+\theta_{br}} \left[\overline{C}_{eq+\theta_{br}}\right] + \sum_{m=1}^{n} v_m^{-\theta_{br}} \left[\overline{C}_{eq-\theta_{br}}\right] + \sum_{m=1}^{n} v_m^{r} \left[\overline{C}_{eqr}\right] \right] \{\overline{\varepsilon}\} \tag{5.20}$$

Here, $v_m^{+\theta_{br}}$, $v_m^{-\theta_{br}}$ and v_m^r mean the volumes of the $+\theta_{br} / -\theta_{br}$ braider yarns and resin for the m^{th} yarn slice, respectively. Using Eqs. (5.19) and (5.20), the transformation stiffness matrices for the braider yarns can be derived:

$$\left[\overline{C}_{eq+\theta_{br}}\right] = \left[T_m\right]_{+\theta_{br}}^T \left[C_{+\theta_{br}}\right]_m \left[T_m\right]_{+\theta_{br}}, \left[\overline{C}_{eq-\theta_{br}}\right] = \left[T_m\right]_{-\theta_{br}}^T \left[C_{-\theta_{br}}\right]_m \left[T_m\right]_{-\theta_{br}} \tag{5.21}$$

Here, $\left[T\right]^T$ means the transpose of the matrix $\left[T\right]$, a function of the braid and crimp angles. The $C_{+\theta_{br}}^{ij}$ and $C_{-\theta_{br}}^{ij}$ (6×6) are stiffness matrices of the $+\theta_{br} / -\theta_{br}$ braider yarns for each m^{th} yarn slice. Eq. (5.19) is re-expressed as the equivalent elasticity matrix, C_{eq} in Eq. (5.13): $\{\overline{\sigma}\} = [C_{eq}] \{\overline{\varepsilon}\}$. Finally taking the inverse matrix $\left[C_{eq}\right]^{-1} = \left[S_{eq}\right]$, the three-dimensional effective moduli can be found.

The $+\theta_{br} / -\theta_{br}$ braider yarns are divided into n , piecewise straight slices perpendicular to the in-plane direction and normal to the x-y plane, see Figure 5.3. The centerline path is represented by the sine function interconnected by n small approximate lines. For the braider yarn, a projected in-plane length of each slice yarn is used, such $2u_1^* / n$ or $2u_2^* / n$. When considering the integrations of the braider yarns, the number of yarn slices, n in the undulating region of the braiders can be determined.

5.4 Model Validation for 2-D Braided Textile Composites

Naik[5.1] predicted effective moduli for the 2-D flat-balanced braided textiles by using TEXCAD program and has presented the parametric characteristics of the 2D braids with various braid angles, while Foye[5.2] used Finite Element method to find the effective moduli and mechanical properties of the 2-D braids described as a 45-degree braid angle with the same parameters of Naik[5.1]. To find the accuracy of our 2-D braided textile modeling, this study considers the same material and dimensions of the 2-D flat-balanced braids as those suggested in Ref. [5.1], but uses a different model, Sine Function Model I, to analyze a different geometrical shape; i. e., an elliptical strand section and sinusoidal varying shapes. A yarn spacing of 1.411mm, a 2K-yarn size, a 0.75 yarn packing density p_d , a 0.007mm fiber diameter and a 64 % overall fiber volume fraction for the 2-D braids are used for determining the effective moduli.

SFM I, Sub-cell block model and Naik[5.1]'s results for the 2-D braids are given in Figs. 5.4-5.5 as a function of the braid angles (θ_{br}) and also this study considers micro-mechanical equations to find appropriate fiber and matrix moduli in the yarns, namely the Rule of mixtures and the Self-Consistent method. From Figures 5.4-5.5, the in-plane properties, E_{xx} , E_{yy} , G_{xy} and ν_{xy} have values varying with

the braid angle, but through the thickness moduli, E_{zz}, ν_{xz} and ν_{yz}, are less sensitive to the braid angles. Our 2-D braid textile modeling considers the effects of three yarn sizes shown in Figure 5.6 and results suggested in Figs. 5.7-5.9 are obtained. In Figures 5.7-5.9, the effects of the yarn sizes on the E_{xx}, E_{yy} and G_{xy} are less powerful as compared to Poisson's ratios. Poisson's ratios, ν_{xy}, ν_{yz} and ν_{xz} are more sensitive to the yarn size variations. Only through the thickness modulus, E_{zz} in Fig. 5.8 shows unchangeable values with various yarn sizes.

Foye[5.2] predicted the effective moduli of 2-D flat-balanced braided textiles angled by 45 degree braid angle by using finite element method. SFM also obtains results for the same braid parameters and compared the results with those of Ref. [5.2]. Table 5.1 shows the comparisons with the FEM results by Foye[5.2] and Naik[5.1]'s TEXCAD results. Ref. [5.1 and 5.2] obtained the same results because their models are based on the same geometrical shapes, i.e., flat-balanced strand types while SFM depicts elliptical balanced yarn shapes. From these results, it can be seen that the 2-D braided textile composite is very dependent regarding the effective elastic moduli on the geometrical architecture.

As another problem, the overall coefficients of thermal expansion (CTE) in the 2-D braided textile composites, is studied. The same overall thermo-mechanical properties suggested in Section 2.5 of Chapter 2 are used for the 2-D braids. A parametric study was performed to study the effects of the braid angle variations on CTE's. Figures 5.10a, 5.10b and 5.10c show the effects of the braid angle on the crimp angle and thermal properties of the 2-D flat-balanced braided composites. Crimp angles varied between 15 and 75 degrees for the braid angles. The in-plane CTE's (α_{xx} and α_{yy}) vary significantly with the braid angle. Through thickness CTE's, α_{zz} was less sensitive to the braid angle. Figure 5.10a is calculated directly by the fiber and resin materials, but Figure 5.10b and 5.10c are analyzed by the Rule of mixtures and Self-Consistent method as applied to the the composite materials. As in the plain woven composites, in general, the micro-mechanical analyses resulted in higher CTE's values than that of the direct analysis case without micro-mechanic equations for composites. Also this study tried to check the effects of different crack densities (β) on the CTE's.

Figures 5.11a and 5.11b are obtained by using the geometrical equations of 2-D braids and the CTE equations of Section 2.6. The micro-mechanical results of Figs. 5.11a & 5.11b have the same trends as that of Naik[5.1] whose modeling is not based on the micro-mechanical equations for composites, such as Rule of mixtures and the Self-Consistent method. Crimp angles in our results varied between 5 and 85 degrees for braid angles, in Naik[5.1]'s model the angle varies between 15 and 75 degrees. The increased crack densities in Figures 5.11a and 5.11b induce the increased in-plane CTE's that are sensitive to the braid angles. The less sensitivity of the thickness CTE's were shown in Figs. 5.11a and 5.11b. These trends of CTE's are all different between the plain woven and 2-D braid textile composites. An interesting result, at 45 degree of braid angle, is noticed. The in-plane CTE's at this point is not dependent on the various crack densities. However, the braid angles are closer to the 0 or 90 degrees, and the in-plane CTE's values are more dependent on the various crack densities. The crack density will be explained in Chapter 6.

By comparing the results of the two models, i.e. the flat-balanced braided yarns and the sinusoidal curved yarns, for the 2-D braided textile composites with various crack densities, the 2-D braided composite shows a greater sensitivity to the geometrical parameters, such as yarn sizes and braid angles. Furthermore, increased values of CTE's in the 2-D braided composite are shown by the increase of the crack density and the braid angles. So it is needed an appropriate modeling of CTE of degraded textile composite having micro-cracks in the yarns. Also, a more detailed investigation on the effects of fabric parameters on overall thermal properties of textile composites is needed.

In Chapter 2, we had shown that the CTE's of 2-D plain woven textile composite are considerably dependent on the geometrical values, such as the yarn sizes. From the analyses of the CTE's for the 2-D plain woven and 2-D braided textile composites, the geometrical parameter of yarn sizes induce various CTE's values while the overall composite volume fraction and the interstitial matrix volume fraction is

kept constant. The similar CTE's values for the 2x2 2-D tri-axial braided textile composite are also suggested in a later section of this chapter.

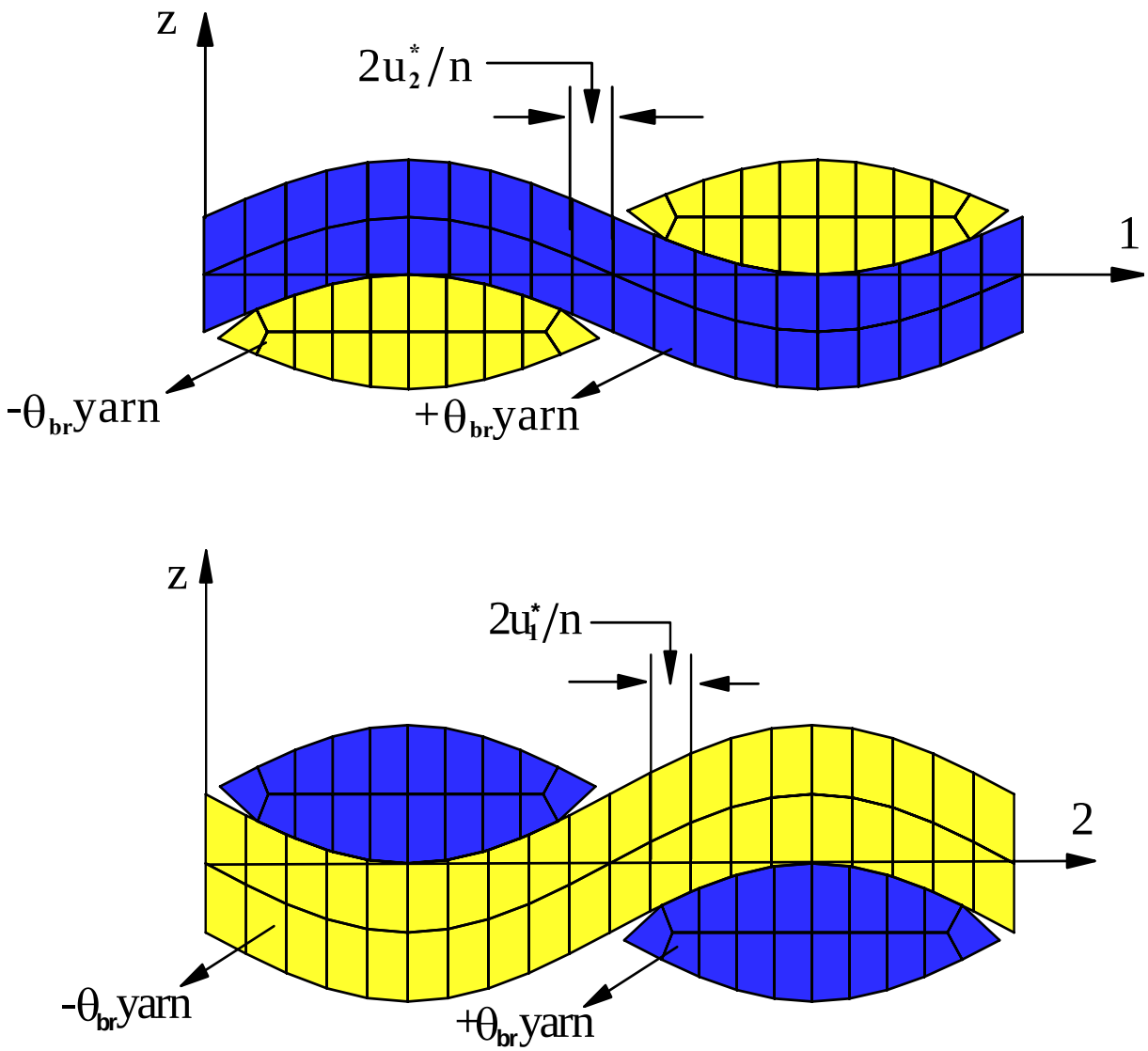

Figure 5.3: Undulating geometry shapes of $+\theta_{br}/-\theta_{br}$ braider yarns along the 1- and 2-axes.

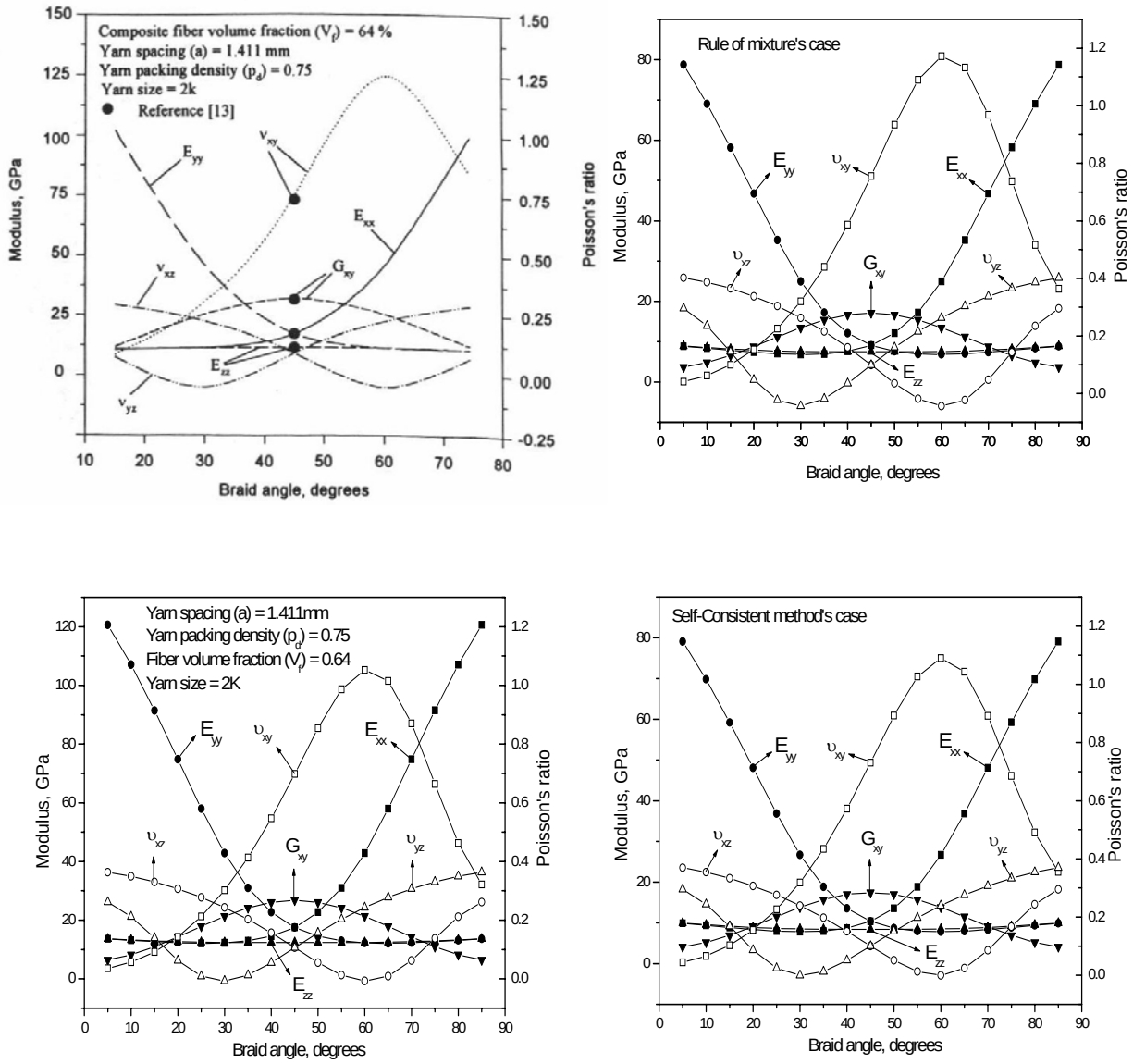

Figure 5.4: Variation of 2-D braid stiffness and Poisson's ratio with braid angles based on SFM I.

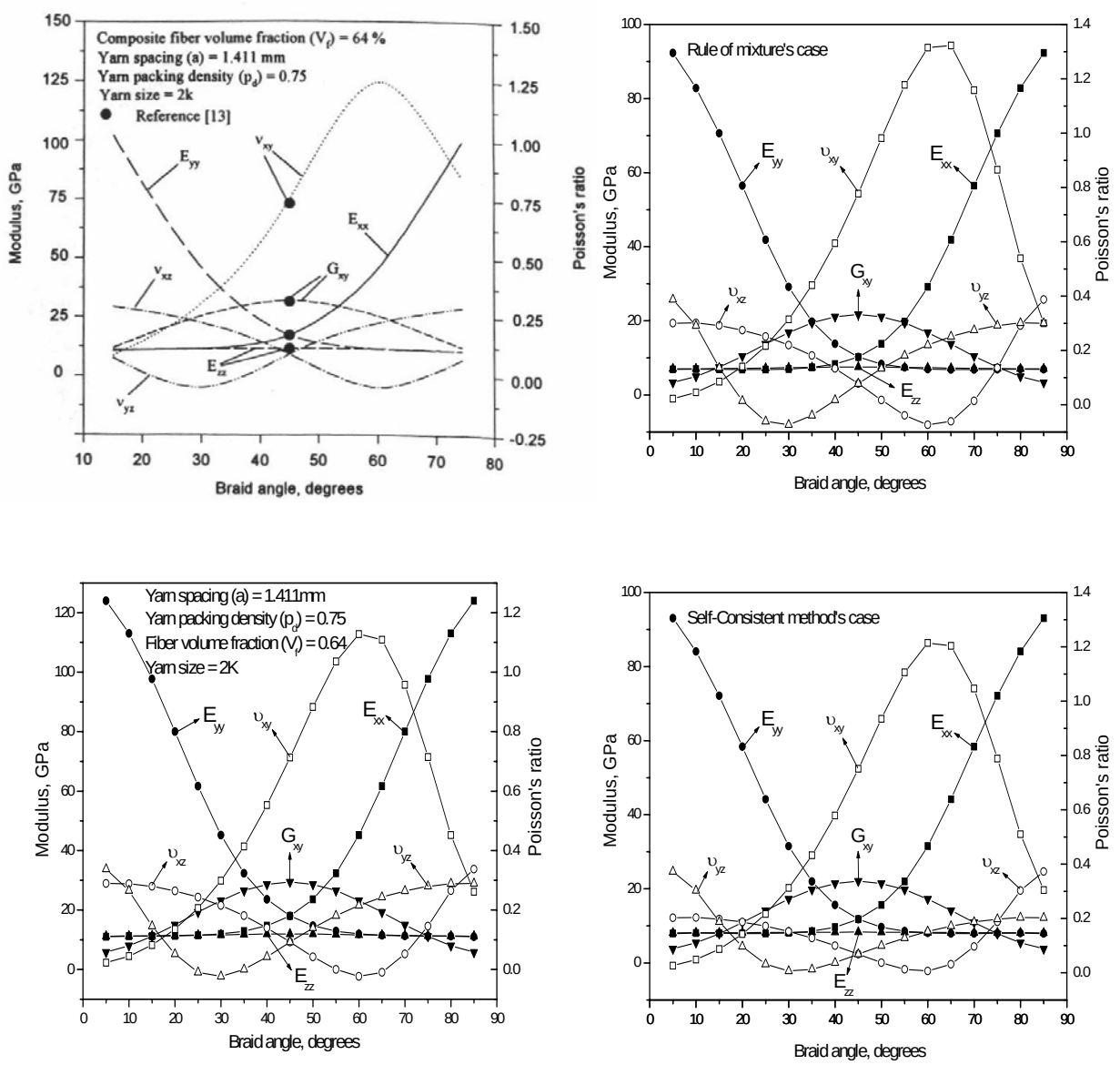

Figure 5.5: Variation of 2-D braid stiffness and Poisson's ratio with braid angles using sub-cell block model.

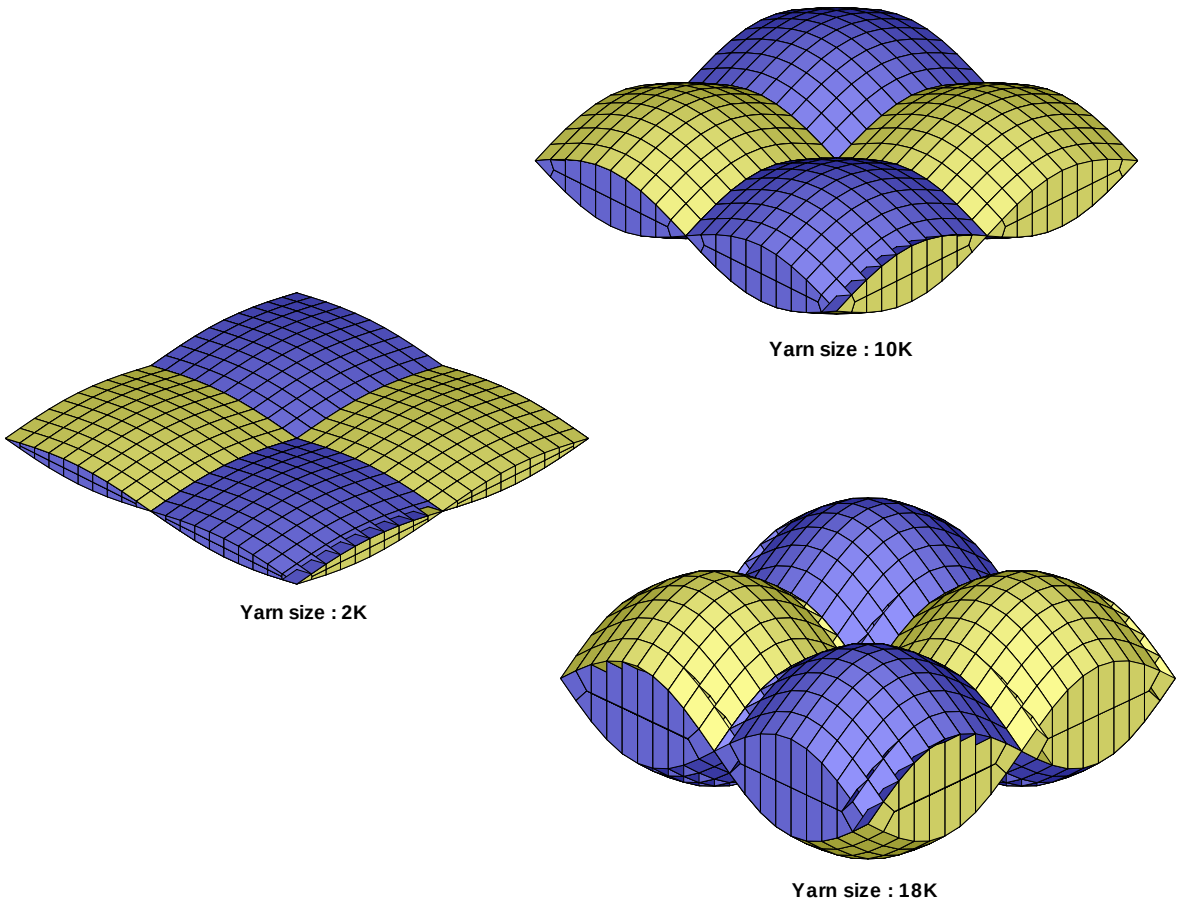

Figure 5.6: Three different yarn shapes (2K, 10K and 18K).

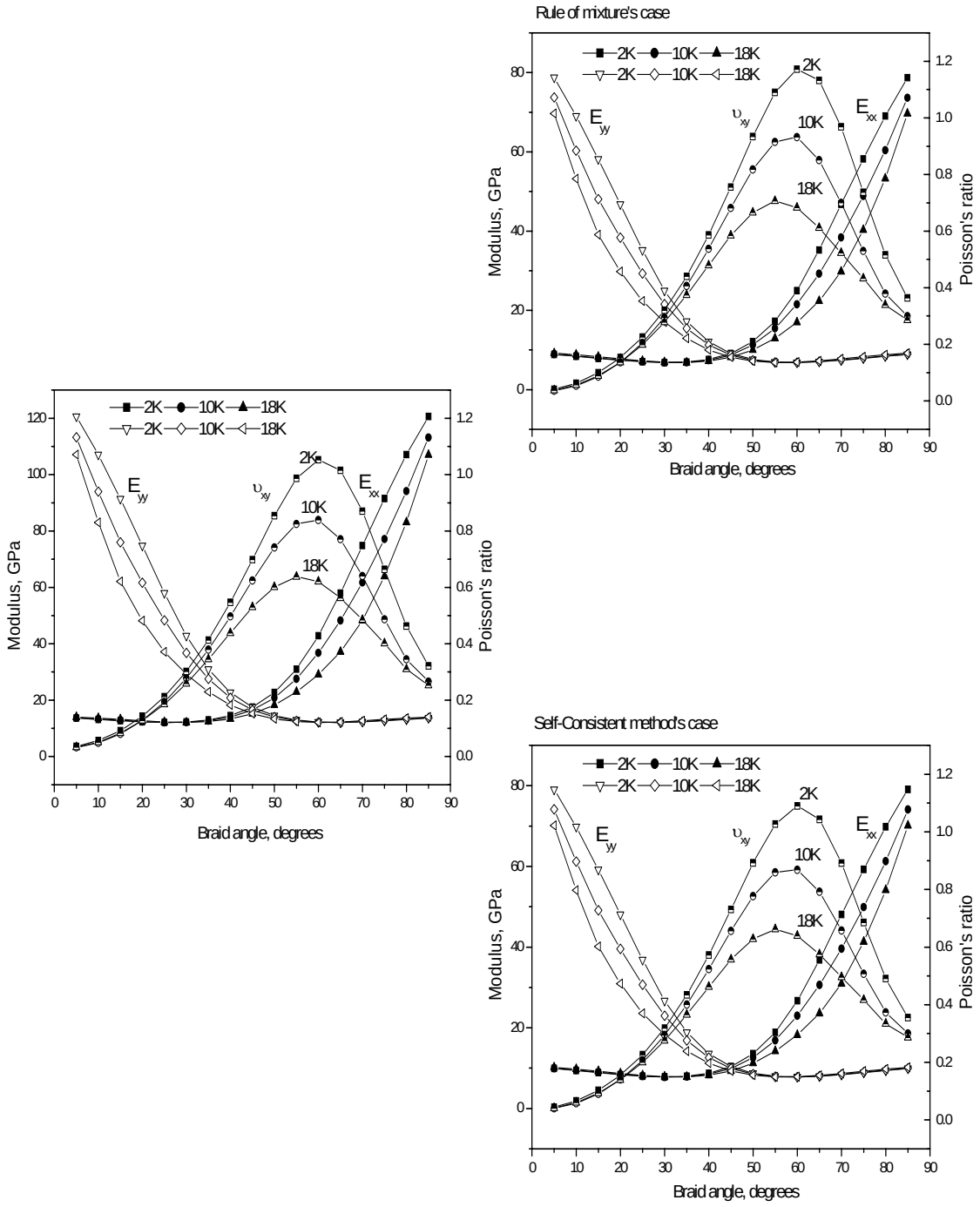

Figure 5.7: Effect of yarn sizes on E_{xx}, E_{yy} and ν_{xy} with braid angles.

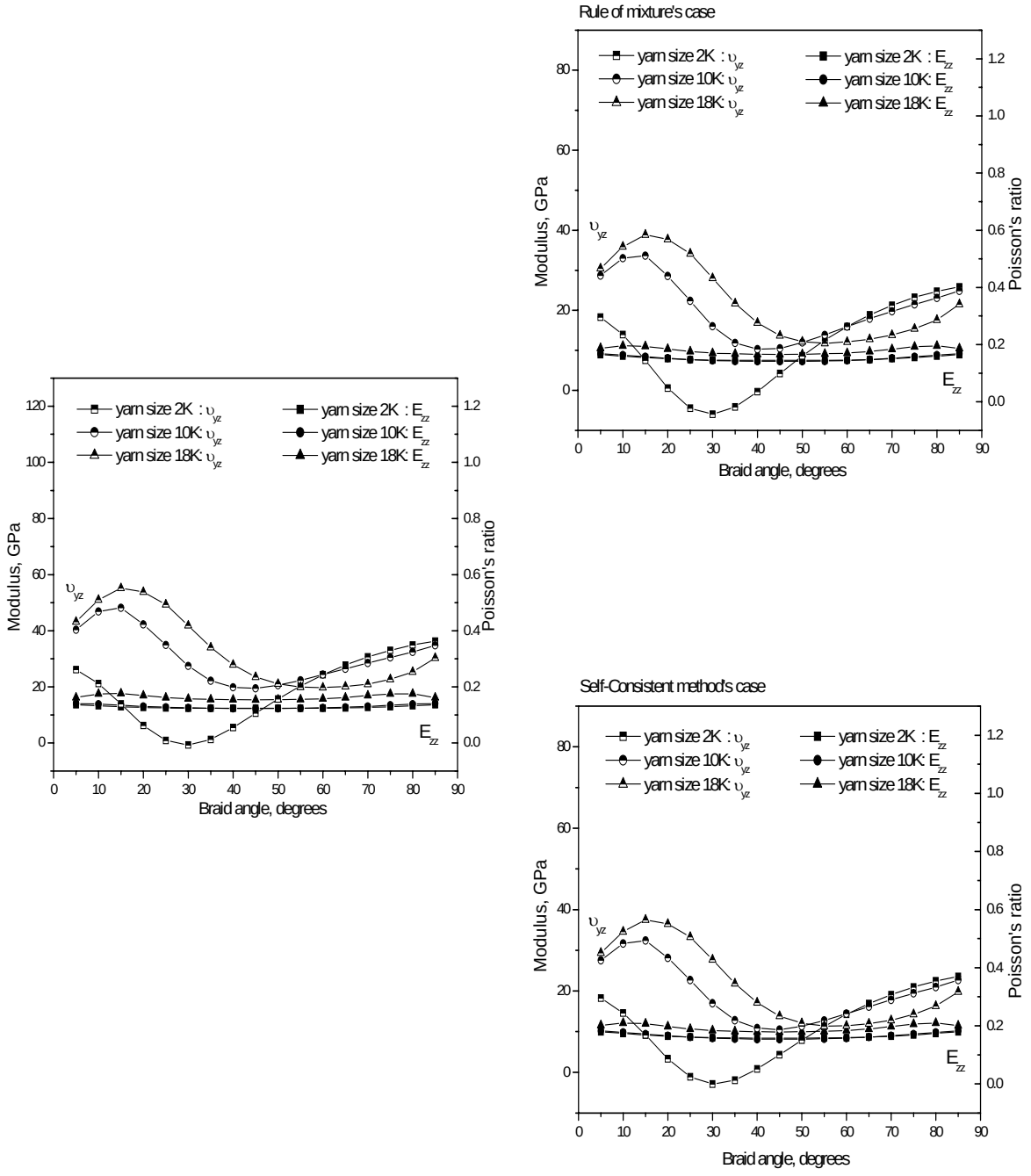

Figure 5.8: Effect of yarn sizes on E_{zz} and ν_{yz} with braid angles.

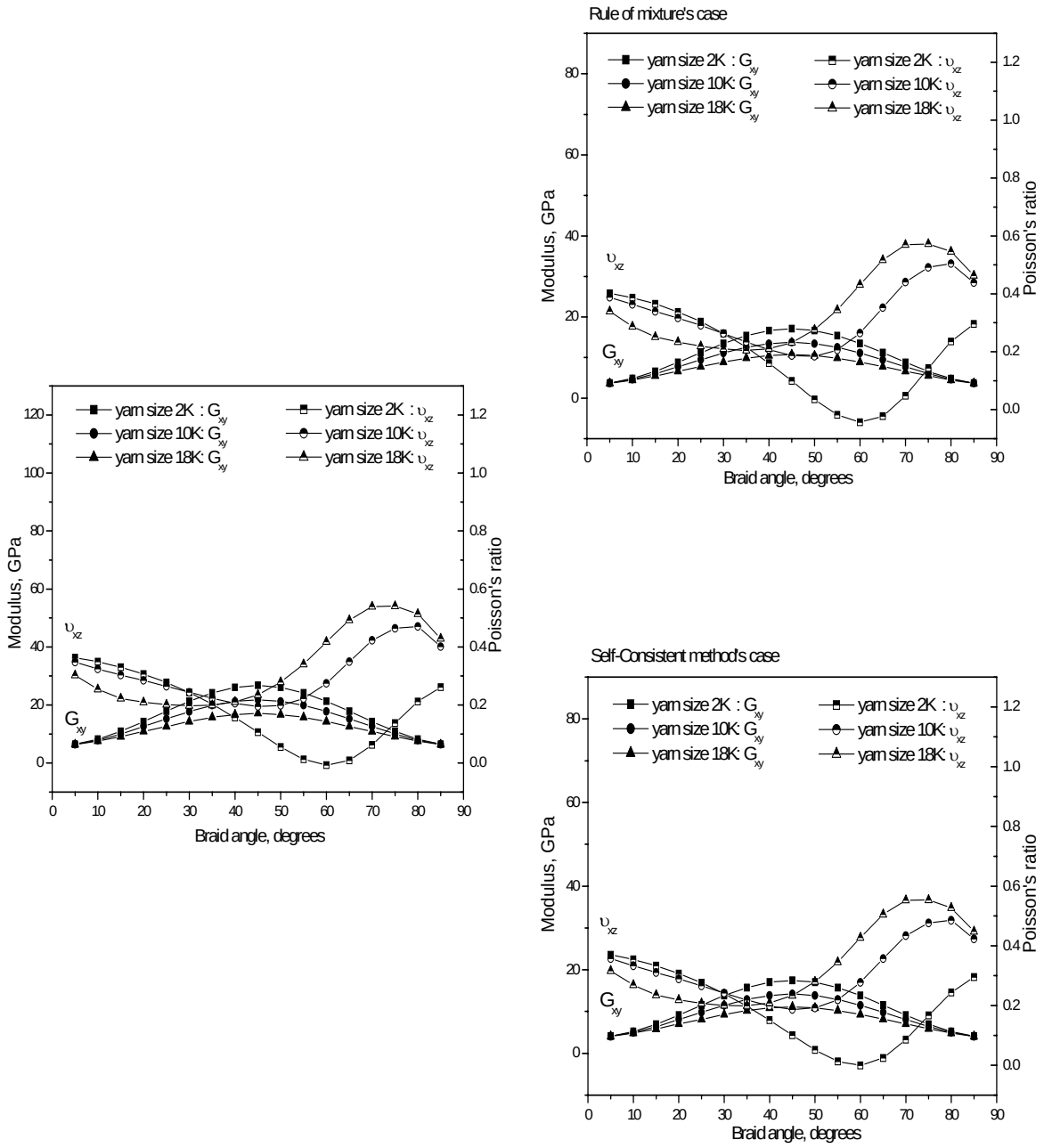

Figure 5.9: Effect of yarn sizes on G_{xy} and ν_{xz} with braid angles.

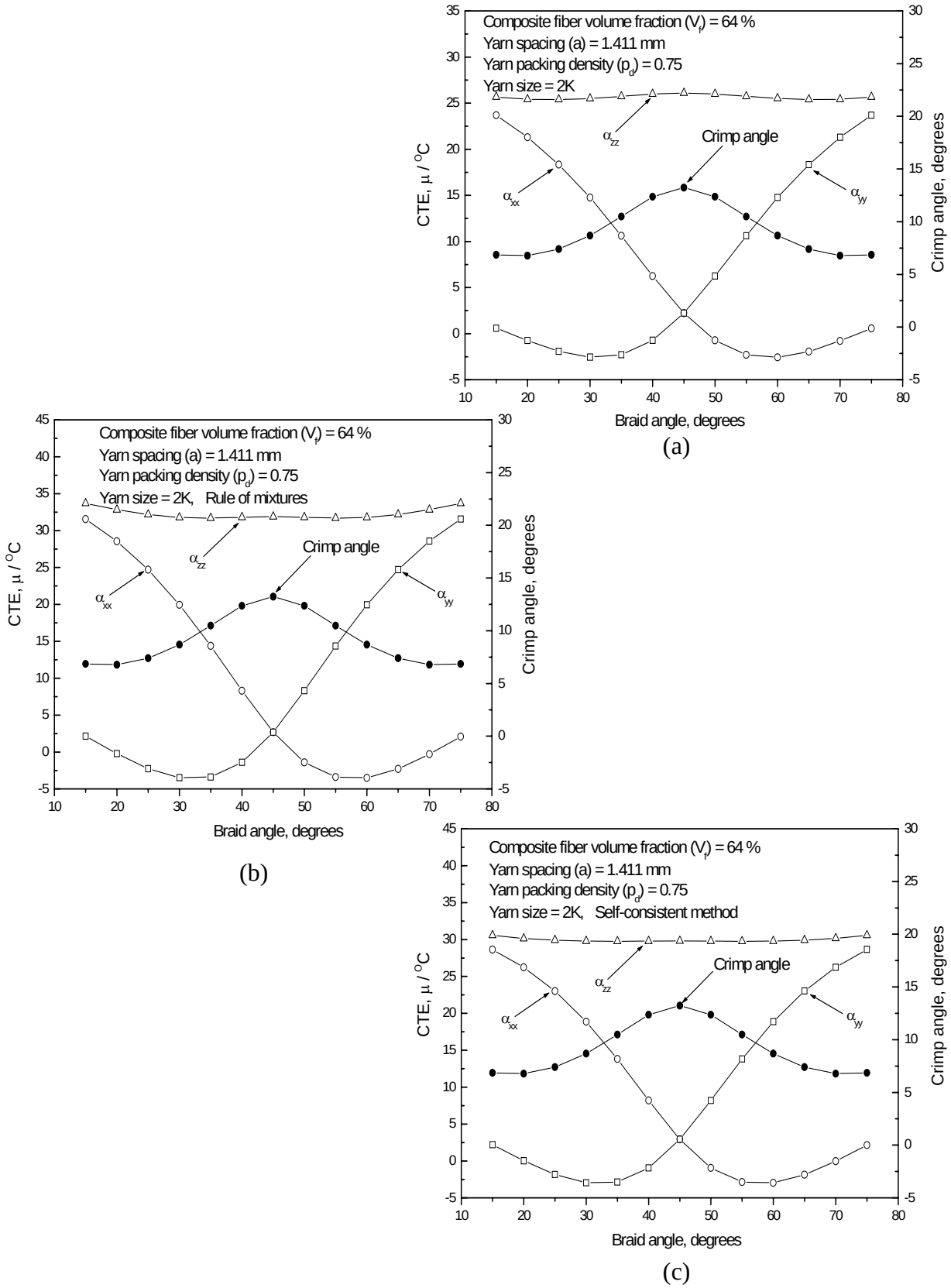

Figure 5.10: Variation of 2-D braided composite crimp angle and CTE's with braid angles.

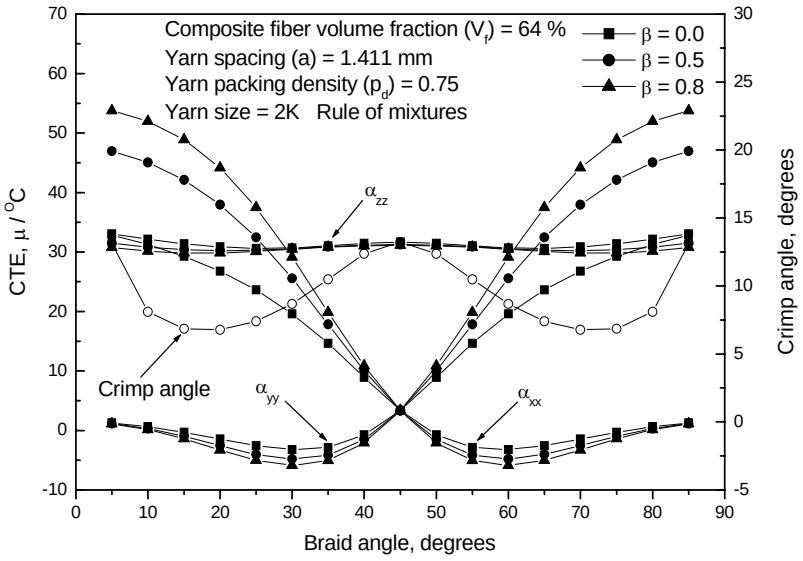

(a)

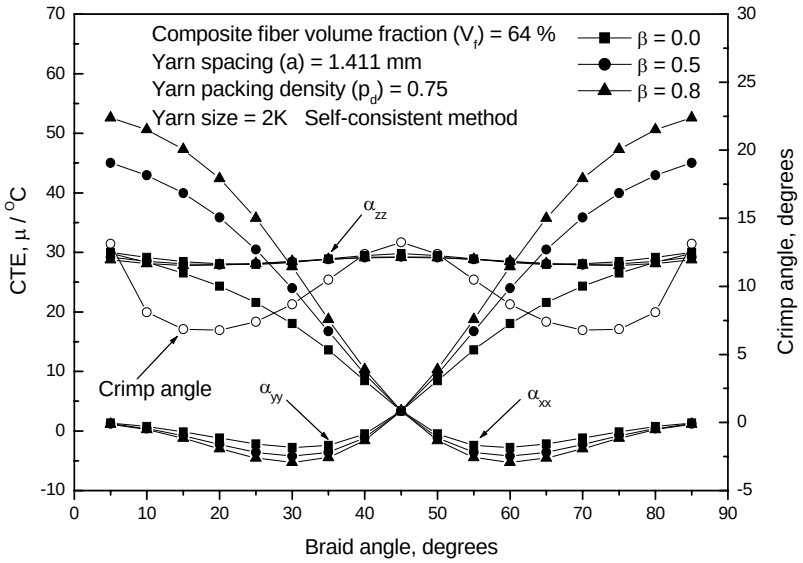

(b)

Figure 5.11: Variation of 2-D braided composite CTE's and crimp angle with braid angles and crack densities.

Table 5.1: Comparisons of effective properties for 45-degree braid angle from Refs. [5.1-5.2]. (Unit: GPa)

Model	E_{xx}	E_{yy}	E_{zz}	ν_{xy}	ν_{yz}	ν_{xz}	G_{xy}	G_{zx}	G_{yz}
SFM I	17.8945	17.8945	12.4749	0.7336	0.0996	0.0996	31.1007	5.2334	5.2334
Naik[5.1]	17.9	17.9	12.5	0.74	0.098	0.098	32.2	-	-
Foye[5.2]	17.9	17.9	12.5	0.74	0.098	0.098	32.2	-	-

5.5 Modeling of 2x2 2-D Tri-axial Braid RUC

A complicated Repeating Unit Cell (RUC) is shown in Fig. 5.12, where four axial yarns pass straight through the center-undulated sections formed along the transverse direction and encapsulated by four undulating braider yarns. In addition, the braider yarns are oriented by two braid angles, positive and negative clockwise with respect to the vertical axis, or y-axis. This study uses Naik[5.1,5.5]'s RUC concept of the 2x2 2-D tri-axial braded laminate and modified equations of Naik[5.1,5.5]'s RUC to calculate a better set of homogenized elastic values. The axial yarn width is denoted w_0 and spacing between each yarn is d_0. The two braid angles are denoted by $+\theta_{br}$ and $-\theta_{br}$, with respect to the vertical axis. The projected length, L_b of the braider yarns in the mid-plane of the RUC is defined in terms of the axial yarn spacing and the braid angles.

$$L_b = (2d_0)/\sin\theta_{br} \tag{5.22}$$

The width of braider yarns w_b is obtained from the relations between $+\theta_{br}$ and $-\theta_{br}$ yarn paths and their projection widths $w_b'\sin(2\theta_{br}) = w_b$. From Fig. 5.13, the projection width also is defined by the axial yarn spacing.

$$w_b'\cos(\pi/2-\theta_{br}) = d_0/2,\ w_b' = d_0/(2\sin\theta_{br}) \tag{5.23}$$

Using Eq. (5.23) and eliminating w_b', the width of braider yarns w_b can be obtained in terms of the axial yarn spacing and braid angle.

$$w_b = d_0\cos\theta_{br} \tag{5.24}$$

From Figure 5.14 of RUC, note that the projected length of the braider yarns is $L_b = 4w_b'$, and the centerline length of the axial yarn on the left of the RUC is defined as $2(w_b'/2)\cos\theta_{br}$. In addition, the other axial yarns' centerline lengths can be estimated, and then the total length of the four axial yarns in RUC is obtained: as $L_0 = 16w_b'\cos\theta_{br}$. Using Eq. (5.23), one can get the total length of the axial yarns.

$$L_0 = 8d_0\cot\theta_{br} \tag{5.25}$$

Unlike the Naik[5.1,5.5] model, we consider that the thickness of the axial yarn is much thicker than the braider yarn's thickness, and these all yarns consist of the same packing density p_d and fiber diameter d_f. Let n_0 and n_b denote the number of filaments in the axial yarns and the braider yarns, respectively, with usually $n_0 > n_b$. Also let A_0 denotes the cross-sectional area of the axial yarns and A_b denotes the cross-sectional area of the braider yarns. These cross-sectional shapes of yarns are remained constant for any through the thickness section perpendicular to the yarn in-plane direction. By the yarn packing density and the volume fraction of the filaments in the yarns, the cross-sectional areas of the yarns are given:

$$A_0 = \frac{\pi d_f^2 n_0}{4p_d},\ A_b = \frac{\pi d_f^2 n_b}{4p_d} \tag{5.27}$$

The plan-from area of the RUC is $L_b^2\sin(2\theta_b)$, and the overall thickness of the RUC is defined by the thickness of the axial and braider yarns, t_0 and t_b.

$$H = 2t_b + t_0 \tag{5.28}$$

As a result, the total volume of the RUC is

$$V = L_b^2\sin(2\theta_b)H \tag{5.29}$$

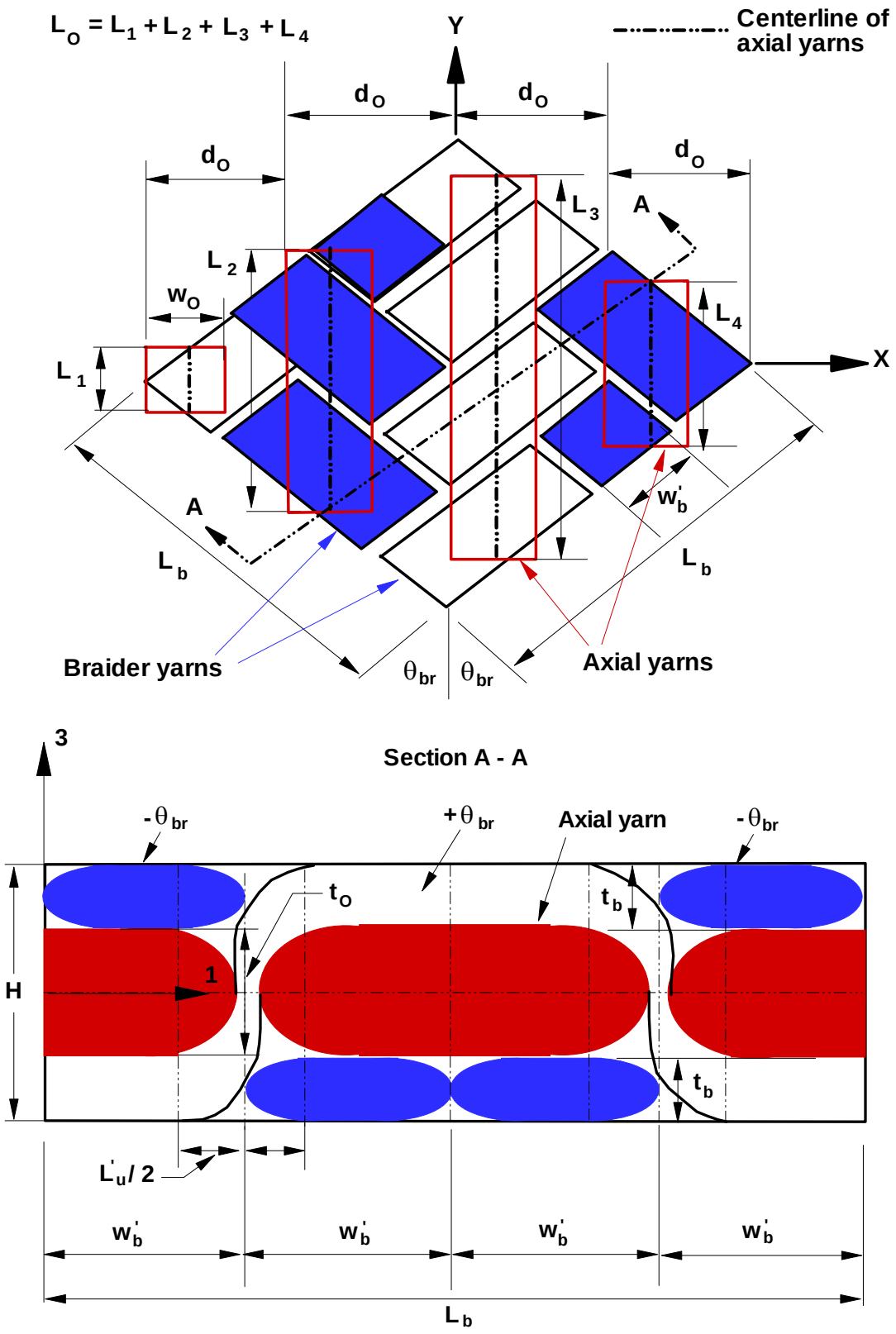

Figure 5.12: Repeating Unit Cell of a 2x2 2-D tri-axial braided composite; cross-sectional view along the section A-A.

To find approximate braider yarn volume V_b and axial yarn volume V_0, the small crimp angle θ_c is assumed along the yarn centerline. The braider yarn volume consisting of 8 braider yarns is defined as the product of cross-sectional areas and projected lengths.

$$V_b = 8L_b A_b \tag{5.30}$$

The volume of straight axial yarn is

$$V_0 = L_0 A_0 \tag{5.31}$$

The total fiber volume occupied by the yarns is $V_0 + V_b = 8L_b A_b + L_0 A_0$. So the total fiber volume fraction of the RUC, V_f, is given as

$$V_f = (V_0 + V_b)/V = \frac{p_d (L_0 A_0 + 8L_b A_b)}{HL_b^2 \sin(2\theta_b)} \tag{5.32}$$

By using the values of L_b and L_0 into Eq. (5.32), we can get the fiber volume fraction of RUC.

$$V_f = \frac{p_d (A_0 \sin(2\theta_b) + 4\sin\theta_b A_b)}{Hd_0 \sin(2\theta_b)} \tag{5.33}$$

5.6 Cross Sections of Axial and Braider Yarns

The cross-section of B-B is described in Fig. 5.15 with a global coordinate (x-y-z). From this figure, the centerline curve equation $z^c_{+\theta_{br}}(x)$ of the top $+\theta_{br}$ braider yarn is derived by sinusoidal functions for $x \in [0, d_0]$:

$$z^c_{+\theta_{br}}(x) = \begin{cases} \dfrac{t_0 + t_b}{2} \sin\dfrac{\pi x}{L_u} & 0 \le x \le L_u/2 \\ \dfrac{t_0 + t_b}{2} & L_u/2 \le x \le d_0 - L_u/2 \\ -\dfrac{t_0 + t_b}{2} \sin\dfrac{\pi(x - d_0)}{L_u} & d_0 - L_u/2 \le x \le d_0 \end{cases} \tag{5.34}$$

The curve equation corresponding to the lower surface of the top $+\theta_{br}$ braider yarn is obtained by a vertical shift of $-t_b/2$ into Eq. (5.34).

$$z^{lower}_{+\theta_{br}}(x) = \begin{cases} \dfrac{t_0 + t_b}{2} \sin\dfrac{\pi x}{L_u} - \dfrac{t_b}{2} & 0 \le x \le L_u/2 \\ \dfrac{t_0}{2} & L_u/2 \le x \le d_0 - L_u/2 \\ -\dfrac{t_0 + t_b}{2} \sin\dfrac{\pi(x - d_0)}{L_u} - \dfrac{t_b}{2} & d_0 - L_u/2 \le x \le d_0 \end{cases} \tag{5.35}$$

Also the equation for the upper surface of the top $+\theta_{br}$ braider yarn will be obtained by an addition of vertical distance $t_b/2$ to Eq. (5.34).

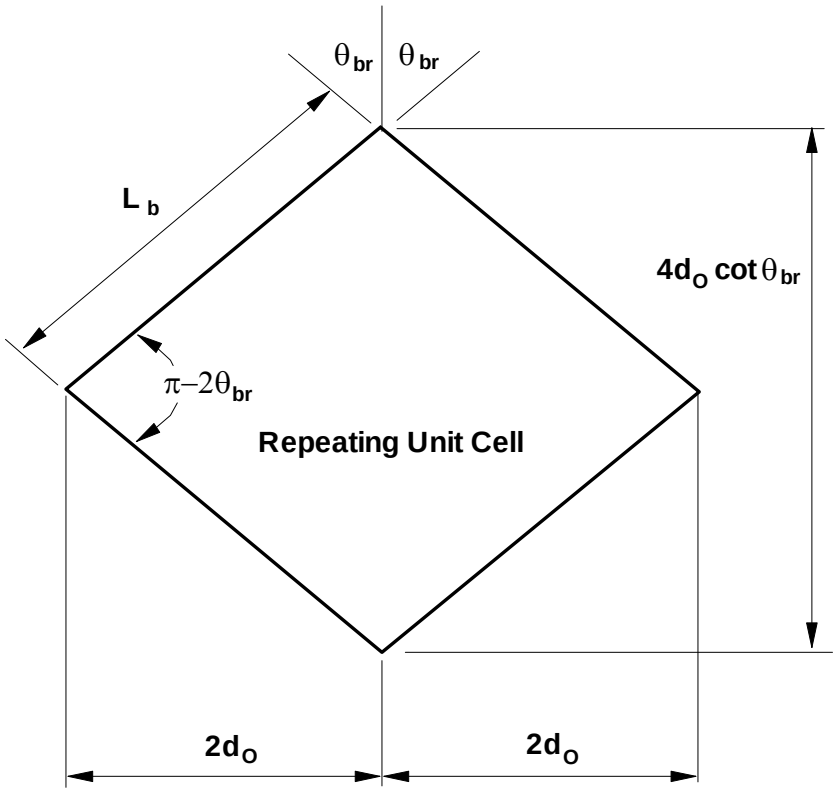

Figure 5.13: Geometry of Repeating Unit Cell plan-form.

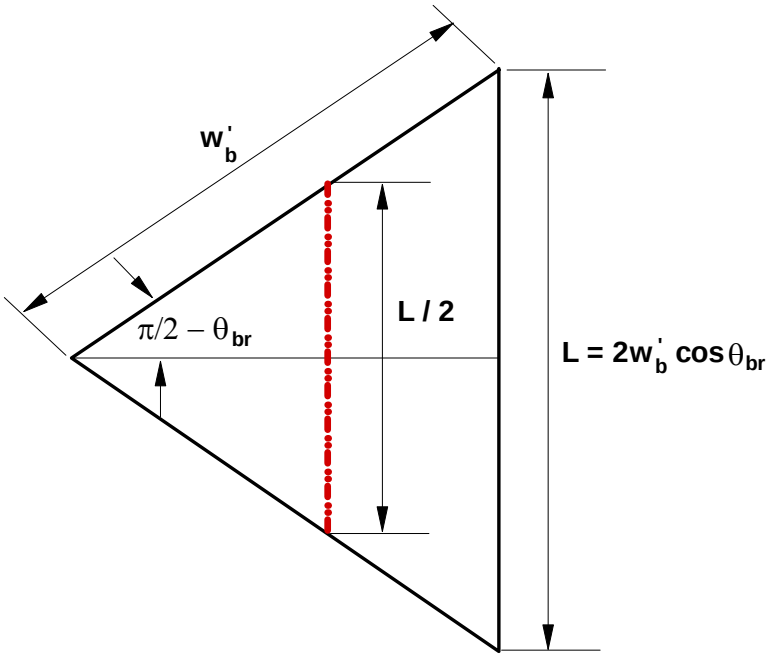

Figure 5.14: Geometry of the first axial yarn centerline.

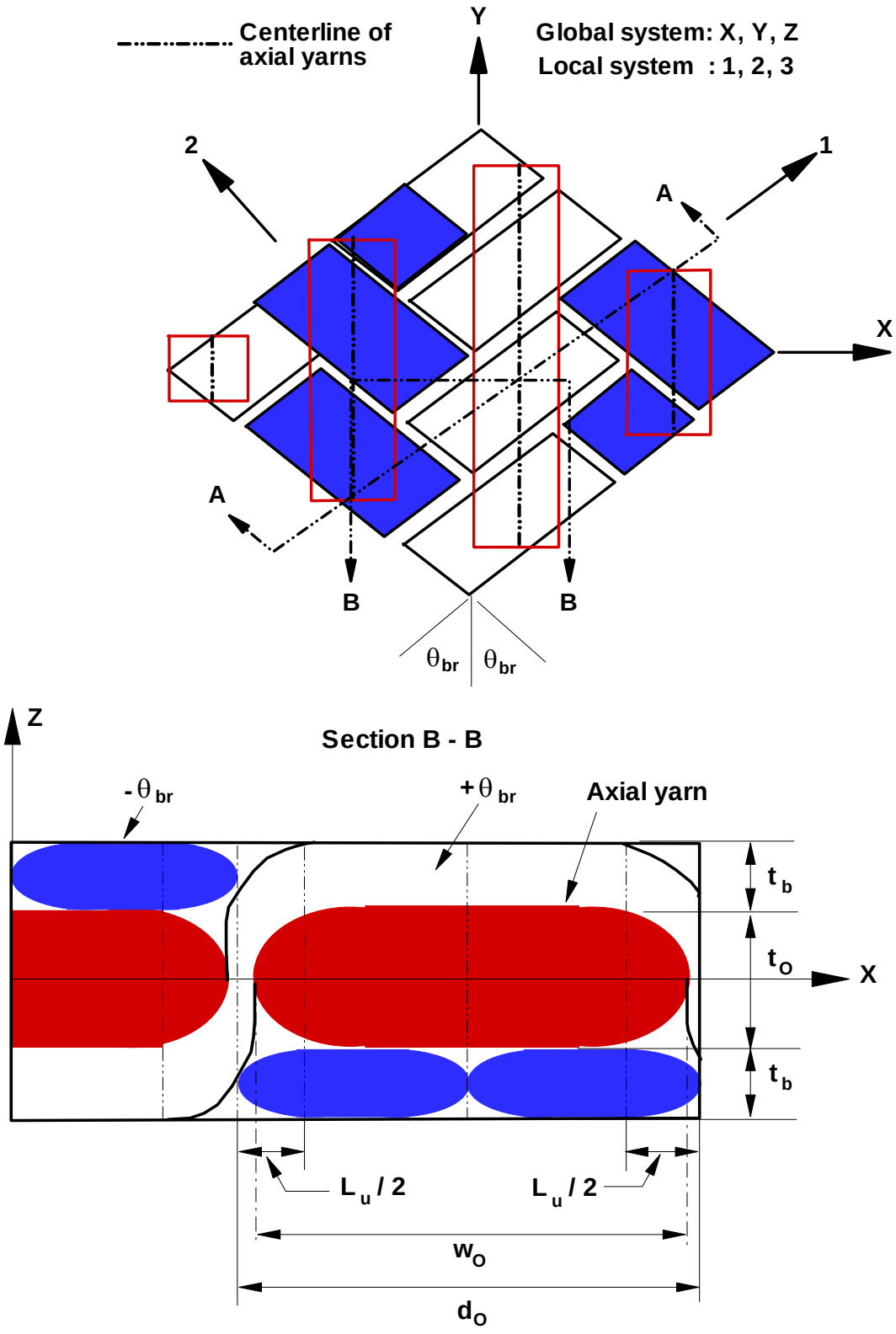

Figure 5.15: Geometry of cross-section along the section B-B.

$$z_{+\theta_{br}}^{up}(x)=\begin{cases}\dfrac{t_0+t_b}{2}\sin\dfrac{\pi x}{L_u}+\dfrac{t_b}{2} & 0\le x\le L_u/2\\ \dfrac{t_0}{2}+t_b & L_u/2\le x\le d_0-L_u/2\\ -\dfrac{t_0+t_b}{2}\sin\dfrac{\pi(x-d_0)}{L_u}+\dfrac{t_b}{2} & d_0-L_u/2\le x\le d_0\end{cases} \tag{5.36}$$

To find the relation between the axial yarn spacing and the width, the packaging constraint is introduced into the axial cross-section area aligned with the cross-over points of the braider yarns. The constraint is

$$z_{+\theta_{br}}^{lower}\left(\frac{d_0-w_0}{2}\right)=0,\ \frac{t_0+t_b}{2}\sin\left(\frac{\pi(d_0-w_0)}{2L_u}\right)-\frac{t_b}{2}=0 \tag{5.37}$$

Eq. (5.37) is written again:

$$\sin\left(\frac{\pi(d_0-w_0)}{2L_u}\right)=\frac{t_b}{t_b+t_0} \tag{5.38}$$

In Ref. [5.1] is defined a parameter s, that is used in Eq. (5.38). As a result, Eq. (5.38) becomes

$$d_0-w_0=(2L_u s)/\pi,\ s=\sin^{-1}\left(\frac{t_b}{t_b+t_0}\right) \tag{5.39}$$

The cross-sectional area of the axial yarn is calculated from symmetric shapes with respect to the X-axis.

$$A_0=2\int_{\frac{d_0-w_0}{2}}^{\frac{d_0+w_0}{2}} z_{+\theta_{br}}^{lower}(x)\ dx \tag{5.40}$$

After integration of Eq. (5.40), the cross-sectional area of the axial yarn is expressed as

$$A_0=t_0w_0-L_uV_s\left(1-\frac{2}{\pi}\ [s+\cos s]\right) \tag{5.41}$$

Here, the vertical shift between the yarns is $V_s=t_0+t_b$. There are two unknown parameters: the crimp angles θ_c and the yarn thickness ratio m. The crimp-angle is calculated from the derivatives of the sine function with respect to the X-axis. The crimp angle is expressed in terms of the undulating length.

$$L_u=\frac{\pi(t_0+t_b)}{2\tan(\theta_c)} \tag{5.42}$$

The relations between the yarn thickness ratio and the thickness of the axial and braider yarns are

$$m=\frac{t_0}{t_b},\ t_b=\frac{H}{2+m},\ t_0=\frac{Hm}{2+m} \tag{5.43}$$

To solve these two un-known parameters, one more equation is needed. This is obtained from the braider yarn cross-sectional area. The equation of braider yarn cross-sectional area, A_b, can be depicted by the sinusoidal function. The upper curve of the braider yarn sections is obtained from Fig. 5.15. Figure 5.16 shows upper and lower curves of one braider yarn section. The upper curve equation of the braider yarn section is

$$z_{-\theta_{br}}^{up}(x)=\begin{cases}\dfrac{t_0+t_b}{2}\sin\dfrac{\pi x}{L_u}-\dfrac{t_0}{2} & 0\le x\le x_0\\ \dfrac{t_b}{2}-\dfrac{t_0}{2} & x_0\le x\le w_b-x_0\\ -\dfrac{t_0+t_b}{2}\sin\dfrac{\pi(x-w_b)}{L_u}-\dfrac{t_0}{2} & w_b-x_0\le x\le w_b\end{cases} \tag{5.44}$$

The length of the undulating region in the braider yarns is x_0. To calculate the undulating length, the curve continuity for this curve equation at $x = x_0$ is applied.

$$\frac{t_b+t_0}{2}\sin(\frac{\pi x_0}{L_u})=\frac{t_b}{2} \tag{5.45}$$

And then we can get the equation for x_0.

$$x_0=\frac{L_u s}{\pi} \tag{5.46}$$

The cross-sectional area of the braider yarn, A_b, is derived from the symmetric shape with respect to the X-axis.

$$A_b=2\int_0^{w_b} z_{-\theta_{br}}^{up}(x)\ dx \tag{5.47}$$

After integrating Eq. (5.47), this equation is

$$A_b=w_b t_b-\frac{2}{\pi}L_u[t_b s-V_s(1-\cos s)] \tag{5.48}$$

Considering the equations of L_u, w_b, V_s, t_0 and t_b into Eqs. (5.41) and (5.48), one can get two different equations expressed as functions of known values (H, θ_{br}, s and d_0) and unknown parameters (m and θ_c).

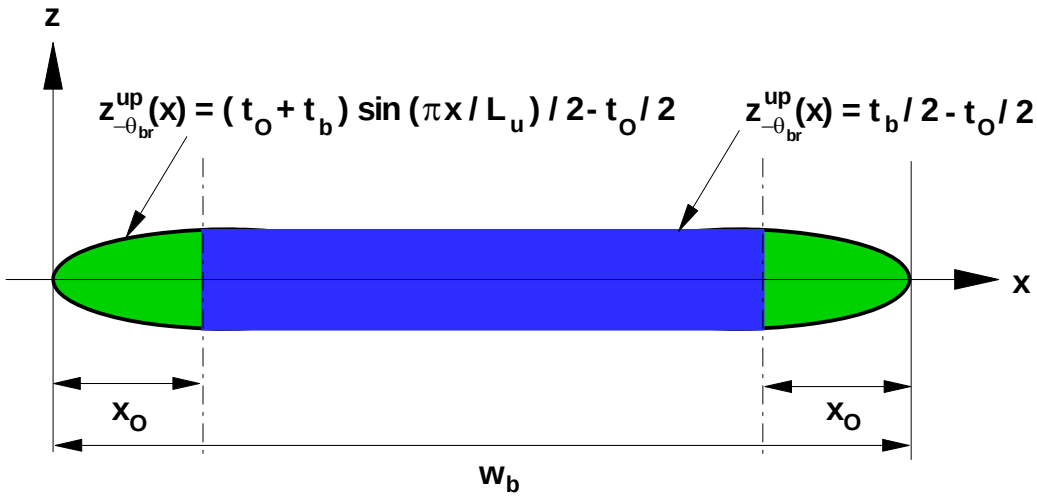

Figure 5.16: Geometry of braider yarn cross-section.

$$A_0 = \frac{H^2(1+m)}{(2+m)^2 \tan\theta_c}\left[(1+m)(\cos s - \frac{\pi}{2}) + s\right] + \frac{d_0 H m}{(2+m)} = f_1(m,\theta_c) \tag{5.49}$$

$$A_b = \frac{H^2(1+m)}{(2+m)^2 \tan\theta_c}\left[(1+m)(1-\cos s) - s\right] + \frac{d_0 H \cos\theta_{br}}{(2+m)} = f_2(m,\theta_c) \tag{5.50}$$

Newton-Raphson method based on an iteration scheme is applied to the two Eqs. (5.49), (5.50) to solve for the two unknown variables: m , θ_c .

$$\begin{matrix} f_1(m,\theta_c) = 0 \\ f_2(m,\theta_c) = 0 \end{matrix}, \quad \begin{bmatrix} \frac{\partial f_1}{\partial m} & \frac{\partial f_1}{\partial \theta_c} \\ \frac{\partial f_2}{\partial m} & \frac{\partial f_2}{\partial \theta_c} \end{bmatrix} \begin{Bmatrix} \Delta m \\ \Delta\theta_c \end{Bmatrix} = \begin{Bmatrix} -f_1 \\ -f_2 \end{Bmatrix} \tag{5.51}$$

After determining appropriate values for m and θ_c, some geometry parameters are updated, for example, the axial and braider yarns' thickness (t_0, t_b), the undulating length (L_u) and the axial/braider yarns' cross-sectional areas (A_0, A_b). These parameters are obtained from the crimp angle (θ_c). The other parameters are specified by the known input variables with no changes.

5.7 Three-Dimensional Effective Moduli for 2x2 2-D Tri-axial Braids

To find the three-dimensional effective moduli, the iso-strain assumption is applied to the RUC of 2x2 2-D tri-axial braids. The RUC consists of three components: the braider yarns, axial yarns and the resin part. These components are four $+\theta_{br}/-\theta_{br}$ braider yarns, four axial yarns and rein matrix. The equivalent elastic matrix, constitutive relations, is expressed as the sum of volume fractions for each material over the RUC volume. The equivalent elasticity matrix, C_{eq} is

$$C_{eq} = \frac{1}{V}\left[4A_b\int_0^{L_b} C_{+\theta_{br}}dx + 4A_b\int_0^{L_b} C_{-\theta_{br}}dx + A_o\int_0^{L_o} C_{ax}dx + \int_{V_{re\sin}} C_{re\sin}dV\right] \tag{5.52}$$

Eq. (5.52) is rewritten as transformation stiffness matrices ($\overline{C}_{eq+\theta_{br}}$, $\overline{C}_{eq-\theta_{br}}$, $\overline{C}_{eqax}$ and $\overline{C}_{eqr}$) and volume fractions about the $+\theta_{br}/-\theta_{br}$ braider yarns, the axial yarns and the resin matrix.

$$C_{eq} = V_{f+\theta_{br}}\overline{C}_{eq+\theta_{br}} + V_{f-\theta_{br}}\overline{C}_{eq-\theta_{br}} + V_{fax}\overline{C}_{eqax} + V_f^r\overline{C}_{eqr} = C_{eq+\theta_{br}} + C_{eq-\theta_{br}} + C_{eqax} + C_{eqr} \tag{5.53}$$

The volume fractions of $+\theta_{br}/-\theta_{br}$ braider yarns, axial yarns and resin matrix are

$$V_{f+\theta_{br}} = V_{f-\theta_{br}} = 4A_bL_b/V\ ,\ V_{fax} = A_0L_0/V\ ,\ V_f^r = V_r/V \tag{5.54}$$

Each equivalent elastic matrix in Eq. (5.53) can be defined in terms of two angle notations: rotation and crimp angles. The equivalent elastic matrices of the braider yarns are

$$C_{eq+\theta_{br}} = \frac{1}{L_b}\int_0^{L_b} C_{+\theta_{br}}dx = \frac{1}{L_b}\int_0^{L_b} C_1(\frac{\pi}{2} - \theta_{br}, \theta_c^{+br})dx$$

$$C_{eq-\theta_{br}} = \frac{1}{L_b}\int_0^{L_b} C_{-\theta_{br}}dx = \frac{1}{L_b}\int_0^{L_b} C_1(\frac{\pi}{2} + \theta_{br}, \theta_c^{-br})dx \tag{5.55}$$

The axial yarns' equivalent elastic matrix is the same yarns' elastic material components.

$$C_{eqax} = \frac{1}{L_0}\int_0^{L_0} C_{ax}dx = \frac{1}{L_0}\int_0^{L_0} C_1(\frac{\pi}{2},\ 0)dx \tag{5.56}$$

Since the resin is considered to be as an isotropic material, the equivalent elastic matrices of the resin is

$$C_{eqr} = \frac{1}{V_{re\sin}} \int_{V_{re\sin}} C_{re\sin} dV = C_{re\sin} \tag{5.57}$$

The crimp angles θ_c^{+br}, θ_c^{-br} of the $+\theta_{br}$ / $-\theta_{br}$ braider yarns are obtained from derivatives of the centerline curve equations with respect to the local 1 and 2 axes (here, these axes are conveniently denoted by x and y axes, not the global coordinate). The centerline curve equation of the $+\theta_{br}$ braider yarn's centerline along the section A-A described in Fig. 5.12 can be expressed as:

$$z^c_{+\theta_{br}} = \begin{cases} 0 & x \in (0,\ w_b'-L_u'/2) \\ \frac{t_0+t_b}{2}\sin[\frac{\pi(x-w_b')}{L_u'}] & x \in (w_b'-L_u'/2,\ w_b'+L_u'/2) \\ \frac{t_0+t_b}{2} & x \in (w_b'+L_u'/2,\ 3w_b'-L_u'/2) \\ -(\frac{t_0+t_b}{2})\sin[\frac{\pi(x-2w_b')}{L_u'}] & x \in (3w_b'-L_u'/2,\ 3w_b'+L_u'/2) \\ 0 & x \in (3w_b'+L_u'/2,\ 4w_b') \end{cases} \tag{5.58}$$

The derivative of the centerline curve equation about the $+\theta_{br}$ braider yarn is:

$$\frac{d}{dx}(z^c_{+\theta_{br}}) = (z^c_{+\theta_{br}})' = \begin{cases} 0 & x \in (0,\ w_b'-L_u'/2) \\ \frac{\pi(t_0+t_b)}{2L_u'}\cos[\frac{\pi(x-w_b')}{L_u'}] & x \in (w_b'-L_u'/2,\ w_b'+L_u'/2) \\ 0 & x \in (w_b'+L_u'/2,\ 3w_b'-L_u'/2) \\ -\frac{\pi(t_0+t_b)}{2L_u'}\cos[\frac{\pi(x-2w_b')}{L_u'}] & x \in (3w_b'-L_u'/2,\ 3w_b'+L_u'/2) \\ 0 & x \in (3w_b'+L_u'/2,\ 4w_b') \end{cases} \tag{5.59}$$

The equation of centerline curve of the $-\theta_{br}$ braider yarn along 2-axis or y-axis is:

$$z^c_{-\theta_{br}} = \begin{cases} \frac{t_0+t_b}{2}\sin\frac{\pi y}{L_u'} & y \in (0,\ L_u'/2) \\ \frac{t_0+t_b}{2} & y \in (L_u'/2,\ 2w_b'-L_u'/2) \\ -(\frac{t_0+t_b}{2})\sin[\frac{\pi(y-2w_b')}{L_u'}] & y \in (2w_b'-L_u'/2,\ 2w_b'+L_u'/2) \\ 0 & y \in (2w_b'+L_u'/2,\ 4w_b'-L_u'/2) \\ \frac{t_0+t_b}{2}\sin[\frac{\pi(y-4w_b')}{L_u'}] & y \in (4w_b'-L_u'/2,\ 4w_b') \end{cases} \tag{5.60}$$

The derivative of the centerline curve equation about the $-\theta_{br}$ braider yarn is:

$$\frac{d}{dy}(z^c_{-\theta_{br}}) = (z^c_{-\theta_{br}})' = \begin{cases} \dfrac{\pi(t_0+t_b)}{2L_u'}\cos\dfrac{\pi y}{L_u'} & y \in (0,\ L_u'/2) \\ 0 & y \in (L_u'/2,\ 2w_b'-L_u'/2) \\ -\dfrac{\pi(t_0+t_b)}{2L_u'}\cos[\dfrac{\pi(y-2w_b')}{L_u'}] & y \in (2w_b'-L_u'/2,\ 2w_b'+L_u'/2) \\ 0 & y \in (2w_b'+L_u'/2,\ 4w_b'-L_u'/2) \\ \dfrac{\pi(t_0+t_b)}{2L_u'}\cos[\dfrac{\pi(y-4w_b')}{L_u'}] & y \in (4w_b'-L_u'/2,\ 4w_b') \end{cases} \tag{5.61}$$

Here, the undulating terms of the undulating length and the width of the cross-section of the braider yarn $L_u' = L_u / \cos\theta_{br}$ and $w_b' = w_b / \sin 2\theta_{br}$. Using Eqs. (5.59) and (5.61), the crimp angles of the braider yarns are determined:

$$\theta_c^{+br} = \tan^{-1}[(z^c_{+\theta_{br}})'],\ \theta_c^{-br} = \tan^{-1}[(z^c_{-\theta_{br}})'] \tag{5.62}$$

And then we have to find the overall properties of the RUC. The RUC of the braider yarns was treated as spatially oriented fibers that consist of yarn slices with transversely isotropic material axes oriented at the rotation ($\theta_r = \pi/2 - \theta_{br}$ or $\theta_r = \pi/2 + \theta_{-br}$) and crimp angles ($\theta_{c1} = \theta_c^{+br}$ and $\theta_{c2} = \theta_c^{-br}$), see Fig. 5.17. To apply the iso-strain assumption within RUC, components of the the average stress and strain have to be specified. By using the average stress concept, $\overline{\sigma} = \sum v_r \overline{\sigma}_r$, one can derive the stress-strain relationships in the 1-2-3 local and x-y-z global coordinates described as the transformation matrix.

$$\begin{aligned} \{\overline{\sigma}\} &= V_{f+\theta_{br}}\ \{\overline{\sigma}\}_{+\theta_{br}} + V_{f-\theta_{br}}\ \{\overline{\sigma}\}_{-\theta_{br}} + V_{fax}\ \{\overline{\sigma}\}_{ax} + V_f^r\ \{\overline{\sigma}\}_{re\sin} \\ &= V_{f+\theta_{br}}\ [\overline{C}_{eq+\theta_{br}}]\ \{\overline{\varepsilon}\}_{+\theta_{br}} + V_{f-\theta_{br}}\ [\overline{C}_{eq-\theta_{br}}]\ \{\overline{\varepsilon}\}_{-\theta_{br}} + V_{fax}\ [\overline{C}_{eqax}]\ \{\overline{\varepsilon}\}_{ax} + V_f^r\ [\overline{C}_{eqr}]\ \{\overline{\varepsilon}\}_{re\sin} \end{aligned} \tag{5.63}$$

Apply the iso-strain assumption, $\{\overline{\varepsilon}\} = \{\overline{\varepsilon}\}_{+\theta_{br}} = \{\overline{\varepsilon}\}_{-\theta_{br}} = \{\overline{\varepsilon}\}_{ax} = \{\overline{\varepsilon}\}_{re\sin}$, into Eq. (5.63). The average stress is rewritten as:

$$\{\overline{\sigma}\} = \frac{1}{V}\left[\ \sum_{m=1}^{n} v_m^{+\theta_{br}}\ [\overline{C}_{eq+\theta_{br}}] + \sum_{m=1}^{n} v_m^{-\theta_{br}}\ [\overline{C}_{eq-\theta_{br}}] + \sum_{m=1}^{n} v_m^{ax}\ [\overline{C}_{eqax}] + \sum_{m=1}^{n} v_m^{r}\ [\overline{C}_{eqr}]\ \right]\{\overline{\varepsilon}\} \tag{5.64}$$

Here, $v_m^{+\theta_{br}}$, $v_m^{-\theta_{br}}$, v_m^{ax} and v_m^r denote the volumes of the $+\theta_{br}/-\theta_{br}$ braider yarns, axial yarns and resin for the m^{th} yarn slice, respectively. Using Eqs. (5.63) and (5.64), the transformation stiffness matrices for the braider yarns can be derived:

$$[\overline{C}_{eq+\theta_{br}}] = [T_m]^T_{+\theta_{br}}\ [C_{+\theta_{br}}]_m\ [T_m]_{+\theta_{br}},\ [\overline{C}_{eq-\theta_{br}}] = [T_m]^T_{-\theta_{br}}\ [C_{-\theta_{br}}]_m\ [T_m]_{-\theta_{br}} \tag{5.65}$$

Here, $[T]^T$ means the transpose of the matrix $[T]$, as a function of the rotation and crimp angles. The $C^{ij}_{+\theta_{br}}$ and $C^{ij}_{-\theta_{br}}$ (6×6) are stiffness matrices of the $+\theta_{br}/-\theta_{br}$ braider yarns for the m^{th} yarn slice. The transformation stiffness matrix for the axial yarns is:

$$[\overline{C}_{eqax}] = [T_m]^T_{ax}\ [C_{ax}]_m\ [T_m]_{ax} \tag{5.66}$$

The matrix $[T_m]_{ax}$ in Eq. (5.66) is dependent on only the rotation angle ($\theta_r = \pi/2$). Eq. (5.64) can be re-written in terms of the equivalent elasticity matrix, C_{eq} in Eq. (5.52): $\{\overline{\sigma}\} = [C_{eq}]\ \{\overline{\varepsilon}\}$. After taking the inverse matrix $[C_{eq}]^{-1} = [S_{eq}]$, the three-dimensional effective moduli are obtained.

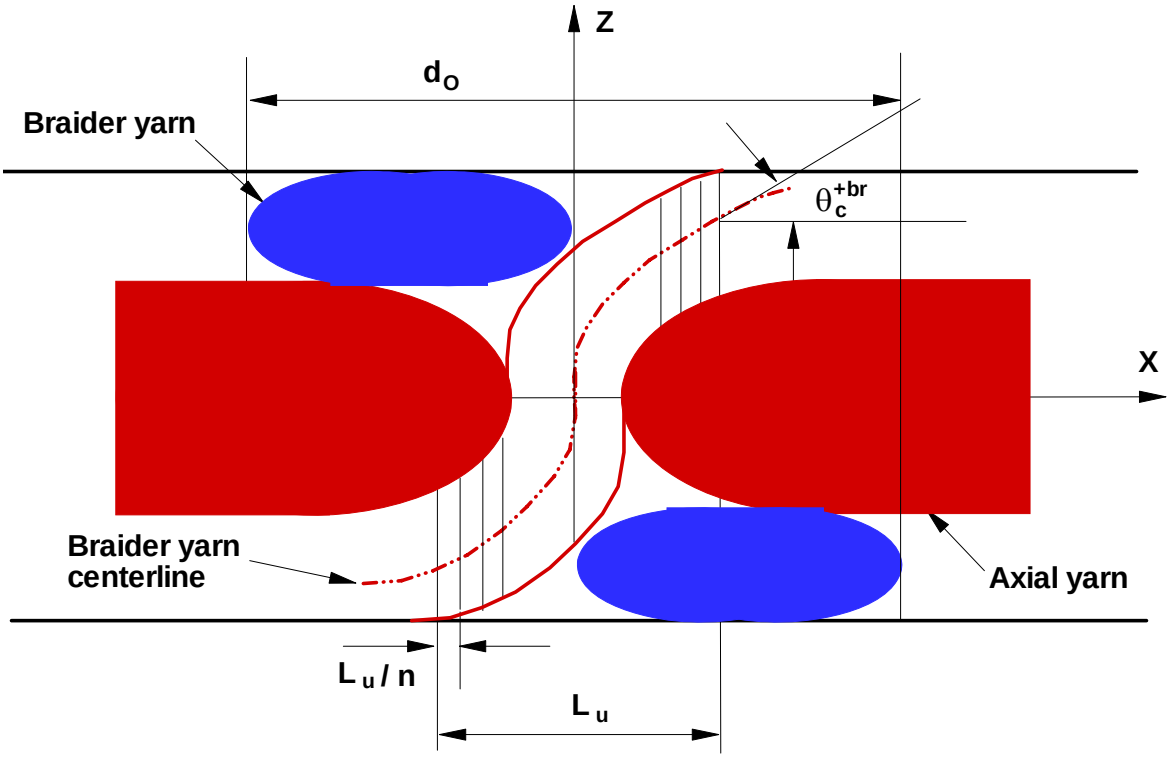

Figure 5.17: Undulating geometry of the $+\theta_{br}$ braider yarn.

In this study, the $+\theta_{br}$ / $-\theta_{br}$ braider yarns is divided into n, piecewise straight slices made perpendicular to its in-plane direction and normal to the x-y plane, see Figure 5.17. The undulating path can be depicted by the sinusoidal function (e.g. sine function) approximated by n straight lines. For the braider yarn, a projected in-plane length and the volume of each slice yarn are used, such as L_u'/n and $A_b L_u'/n$. A convergence is considered as to determine the appropriate number of yarn slices, n, in the undulating region of the braider yarns. In this study, a value of n =20 is used for all the analyses, because the equivalent elasticity matrix C_{eq} converges for number of yarn slice, $n \geq 15$ as suggested in Ref. [5.3].

5.8 Numerical Results and Comparisons

Masters[5.3] *et al.* performed experimental tests and suggested finite element modeling to predict mechanical properties for the 2x2 2-D tri-axial braids, and Naik [5.1] compared TEXCAD analysis' results with the experimental predictions[5.3] and finite element results[5.3]. This study uses the same geometrical parameters such as the braid angles θ_{br}, yarn sizes n_b / n_0, yarn spacing d_0, yarn packing density p_d and overall volume fraction V_f^0. The three types of 2x2 2-D tri-axial given in Table 5.2 are used and use a yarn packing density of 0.75 and a fiber diameter of 0.007mm as in Ref. [5.1]. These yarns are made up of AS4 Graphite fiber and 1895 Epoxy resin listed in Table 5.3. The cross-sectional micrographs of these 2x2 2-D tri-axial braided composites are described in Fig. 5.18.

Table 5.2 Configurations of 2x2 2-D tri-axial braided composites from Ref. [5.1].

2-D tri-axial braids	Braid angle (degree)	Braider yarn size (K)	Axial yarn size (K)	Axial yarn spacing (mm)	Overall fiber volume fraction (%)
A1	62.3	12	24	6.096	54.0
B1	67.4	6	18	5.320	51.2
B2	67.9	6	18	5.820	52.0

Table 5.3 Yarn and resin properties for the 2x2 2-D tri-axial braids from Ref. [5.1]. (Unit: GPa)

Material	E_{11}	E_{22}	G_{12}	ν_{12}	ν_{23}
Yarn	144.80	11.73	5.52	0.23	0.3
Resin	3.45	3.45	1.28	0.35	0.35

Our results for each configuration are compared with the results of other previous models in Tables 5.4 and 5.5. Naik[5.1] showed good analytical results compared to experimental data, however a few discrepancies still remained. The small differences may be induced by the numerical schemes to find appropriate geometrical parameters. Our predictions and those by R.A. Naik[5.1] show that the effective in-plane moduli and Poisson's ratios are in a good agreement with the test data for different configurations. We can see that the crimp angle θ_c is increased but the yarn thickness ratio (m) is decreased with more large yarn sizes. Ref. [5.1] using the TEXCAD conducted parametric studies to investigate the effects of fiber volume fractions on the overall stiffness and the in-plane coefficients of thermal expansion (CTE) for the 2x2 2-D tri-axial braided composites.

Figure 5.19 based on the B1 configuration shows the effects of various fiber volume fractions on stiffness and Poisson's ratios. Young's moduli E_{xx}, E_{yy} are increased proportionally with the increase of fiber volume fractions V_f, while Poisson's ratios, shear modului and Young's modulus E_{zz} are less sensitive to the variations of V_f. These same trends also were found in the test data of Ref. [5.3].

Figure 5.20 uses the B1 configuration and shows the effects of various fiber volume fractions on the in-plane coefficients of thermal expansion (CTE) for the 2x2 2-D tri-axial braided composites. The in-plane CTE α_{xx} and α_{yy} are very little changed but through the thickness CTE α_{zz} is significantly decreasing with the increase of fiber volume fractions, V_f. The crimp angle also is increasing as the fiber volume fraction is increased. The similar trends were also found in TEXCAD results of Ref. [5.1].

The second set of analyses are carried out by considering various fiber volume fractions, crack densities and Rule of mixtures and Self-Consistent method that are based on micro-mechanical equations. These are used to determine the stiffness values of the yarns and resin materials suggested in Ref. [5.1]. After calculating the effective moduli and CTE's, one can see some notable trends with different increased fiber volume fractions. For example, Figures 5.21-5.22 whose results are based on the Rule of mixtures case show a considerably similar trend as compared to the results of Ref. [5.1]. But the Poisson's ratios, except the in-plane Poisson's ratio ν_{xy}, shear and through-thickness Young's moduli (E_{zz}) are more sensitive to the variation of fiber volume fraction. In the CTE results, obtained using the Rule of mixtures, the through-thickness CTE α_{zz} experiences a significant decay with increased fiber volume fractions. In Figure 5.23, for the Self-Consistent method case, Poisson's ratios experience large decay while the fiber volume fraction is increased, except the in-plane Poisson's ratio. The CTE of Self-Consistent method in Figure 5.24 shows the same trends as those provided by the Rule of mixtures case.

5.9 Models for 3-D Orthogonal Woven Composites

Our sub-cell block model presented in Chapter 4 is applied to the 3-D orthogonal woven composites and their mechanical characteristics are predicted. Three type models are considered: Unit-cell model[5.6], laminate block model[5.6] and 3-D Mosaic model[5.7]. The first two analytical models are suggested by Tan[5.6] *et al.* and the other was suggested by Bogdanovich[5.7]. We compare our predictions with their results.

5.9.1 Unit-cell Model of 3-D Orthogonal Woven Composites

Tan[5.6] *et al.* have suggested a unit cell for the 3-D orthogonal woven composites that consists of a number of rectangular blocks with the rectangular sections and then proposed four models, namely XYZ, YXZ, ZXY and ZYX. The schematic representation of the simplified 3-D orthogonal woven shape is shown in Fig. 5.25 and the rectangular unit cell, like Fig. 5.26 is suggested. Our sub-cell block model in Figure 5.27 considers the same material properties as suggested in Ref. [5.6] and the geometrical dimensions proposed in Table 5.6, and uses the iso-stress method to calculate the volume fractions for the yarns shown in Table 5.7. Our analytical cases are identical to the three cases considered by Tan[5.6] *et al.* One of three cases suggested in Table 5.6 is compared to other results, see Table 5.8. The results in Table 5.8 reveal that our analytical solutions are similar to the results of XYZ model and are closer to those of the FEA model.

5.9.2 Laminate Block Model of 3-D Orthogonal Woven Composites

Reference [5.6] suggests a laminate block model in a 3-D orthogonal woven composite represented by some of lamina blocks along the z-axis. The architecture of the laminate block model is represented in Fig. 5.28 and assembled by a number of warp lamina blocks, weft lamina blocks and z lamina blocks. To find the equivalent elastic characteristics, Tan[5.6] *et al.* considered two models (the XY model and the Z-model) of the warp lamina blocks, weft lamina blocks, top lamina blocks, bottom lamina blocks and overall stiffness constants. Like the Z-model, our sub-cell block model in Figure 5.29 uses the iso-strain methods to find the volume fractions of each lamina layer along the z-axis. To analyze the laminate block model, the same material properties suggested in Ref. [5.6] and the dimensions used Tan[5.6] *et al.* are considered. The geometrical variables for the warp, weft and z-yarns in the laminate block are listed in Table 5.9. Both analytical solutions for the equivalent elastic properties of all four cases are shown in Tables 5.10 and 5.11, respectively. The total volume fractions for the laminate blocks are compared to each other in Table 5.12.

5.9.3 3-D Mosaic Model of 3-D Orthogonal Woven Composites

To evaluate the sub-cell block model, a 3-D Mosaic model of the 3-D orthogonal woven composite is considered. Here we use the same model dimension and elastic properties suggested in Ref. [5.7]. The 3-D Mosaic Model is shown in Fig. 5.30. The geometrical values and elastic properties are:

$F_x = 4.326$ mm, $f_x = 3.028$ mm, $Z_x = 0.292$ mm, $2a = W_x = F_x + Z_x = 4.618$ mm,

$W_y = 4.171$ mm, $Z_y = 0.909$ mm, $2b = F_y = W_y + Z_y = 5.08$ mm,

$W_z = 0.637$ mm, $F_z = 0.614$ mm, $f_z = 0.292$ mm, $2c = Z_z = 2W_z + F_z + 2f_z = 2.472$ mm

Herein, the elastic V_f S-2 Glass/Dow Derakane 8084 Vinyl Ester-Epoxy composite are used:

$E_f = 86.90$ GPa, $\nu_f = 0.22$, $E_m = 3.17$ GPa, $\nu_m = 0.35$, $V_f = 0.6$

In Table 5.13, the effective elastic characteristics about V_f S-2 Glass/Dow Derakane 8084 Vinyl Ester-Epoxy composite are shown and compared to each other. The effective elastic properties are also displayed in Table 5.14. The results in these tables reveal that the predictions based on our sub-cell block model have the same trends as those of the 3-D Mosaic model as obtained by Bogdanovich[5.7].

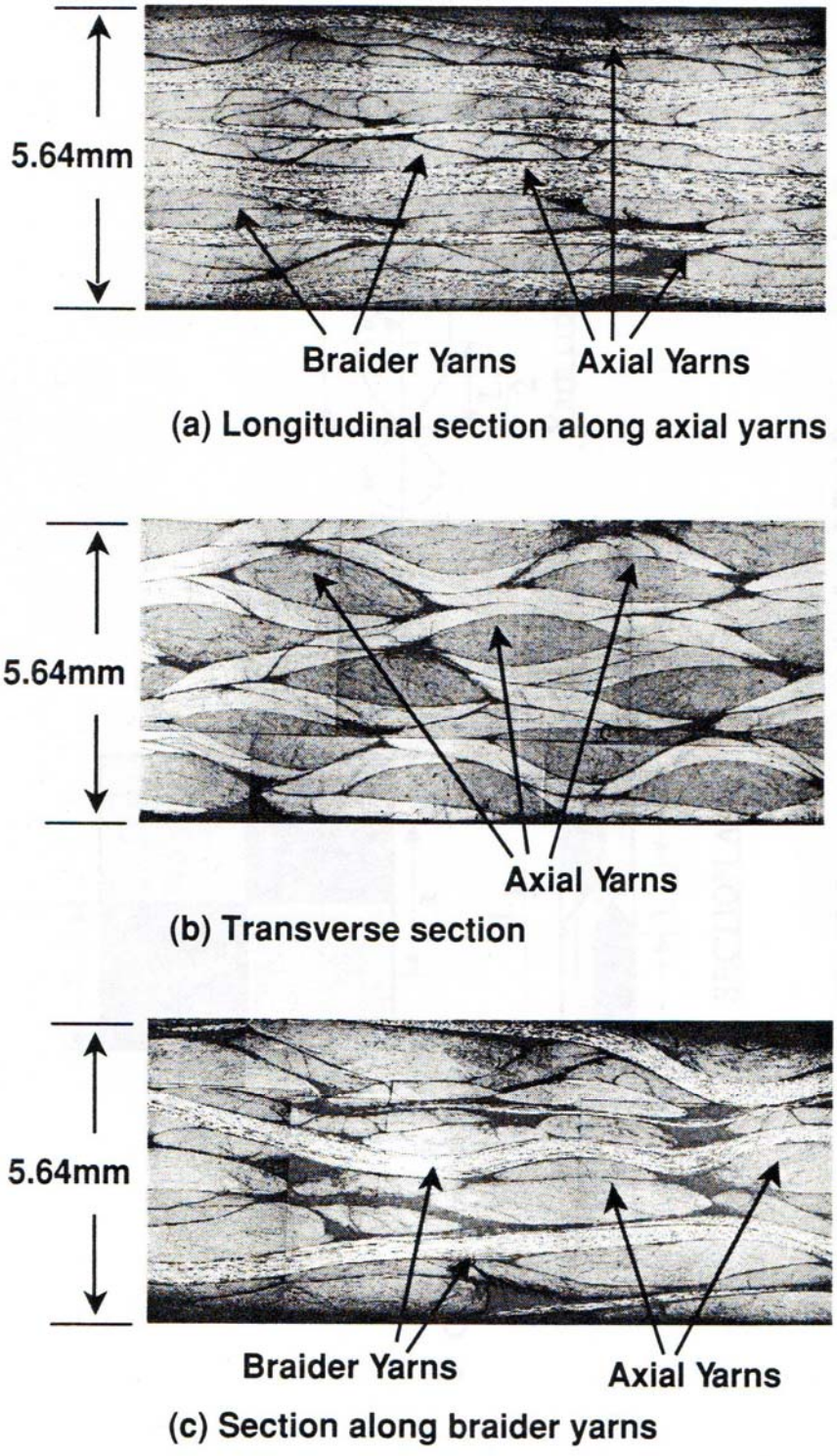

Figure 5.18: Cross-sectional micrographs of 2x2 2-D tri-axial braided composites from Ref. [5.1].

Table 5.4 Comparisons of moduli results for 2x2 2-D tri-axial braids from Ref. [5.1]. (Unit: GPa)

Braid type	Approach	E_{xx}	E_{yy}	E_{zz}	G_{xy}	G_{zx}	G_{yz}
A1	TEXCAD [5.1]	45.14	40.10	10.42	14.84	4.64	4.13
	FEM [5.2]	53.16	46.95	-	-	-	-
	Test [5.3]	45.44	45.64	-	-	-	-
	Present model	44.8420	41.5443	12.0737	14.5533	4.7569	4.5268
B1	TEXCAD [5.1]	48.42	42.48	10.13	11.07	4.40	3.90
	FEM [5.2]	62.12	47.51	-	-	-	-
	Test [5.3]	44.47	45.16	-	-	-	-
	Present model	46.3132	43.5468	11.3866	10.5749	4.5590	4.2381
B2	TEXCAD [5.1]	50.42	42.63	10.23	11.08	4.31	3.90
	FEM [5.2]	51.09	43.58	12.07	12.41	-	-
	Test [5.3]	48.47	43.51	-	-	-	-
	Present model	48.1447	43.6995	11.4823	10.5561	4.5230	4.2549

Table 5.5 Comparisons of Poisson's ratios, yarn thickness ratio and crimp angles from Ref. [5.1].

Braid type	Approach	ν_{xy}	ν_{xz}	ν_{yz}	θ_c (degree)	m
A1	TEXCAD [5.1]	0.291	-	-	-	-
	FEM [5.2]	0.305	-	-	-	-
	Test [5.3]	0.307	-	-	-	-
	Present model	0.2790	0.2648	0.2598	12.7089	1.1610
B1	TEXCAD [5.1]	0.205	-	-	-	-
	FEM [5.2]	0.211	-	-	-	-
	Test [5.3]	0.199	-	-	-	-
	Present model	0.1946	0.3084	0.2902	10.9332	1.4059
B2	TEXCAD [5.1]	0.205	-	-	-	-
	FEM [5.2]	0.214	-	-	-	-
	Test [5.3]	0.190	-	-	-	-
	Present model	0.1944	0.3011	0.2917	9.6233	1.3384

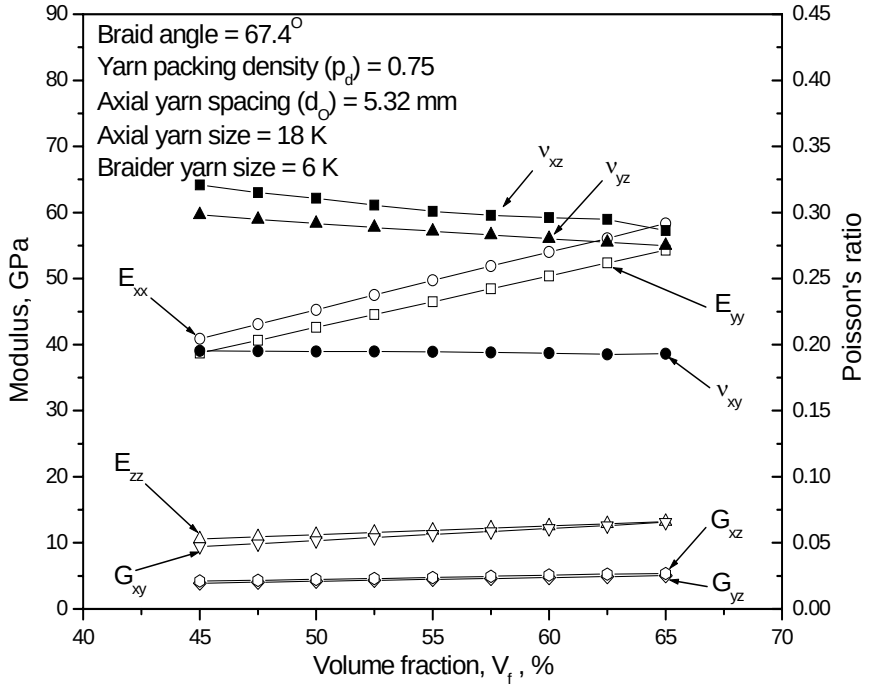

Figure 5.19: Variation of stiffness and Poisson's ratio with V_f for 2x2 2-D tri-axial braided composite.

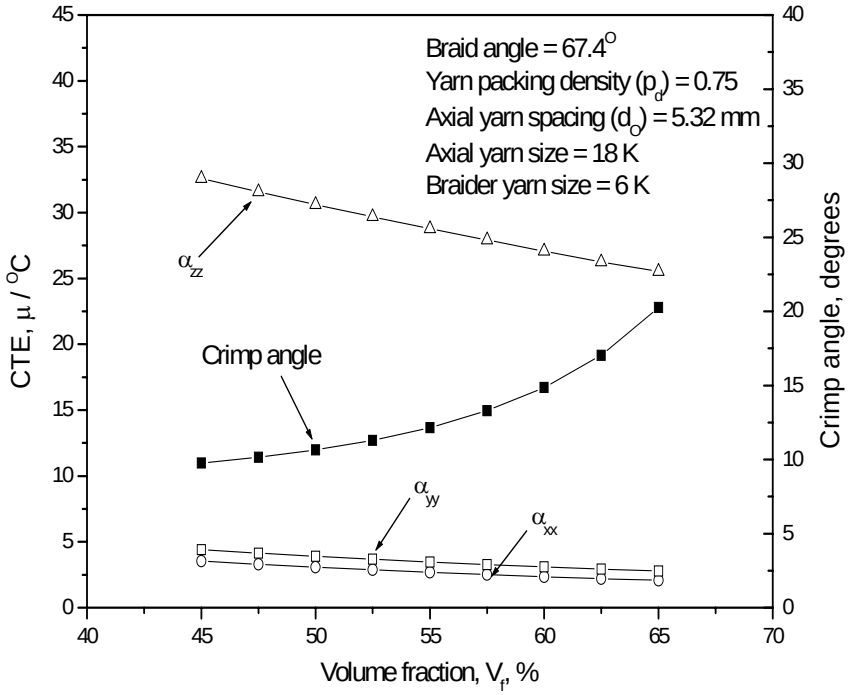

Figure 5.20: Variation of crimp angle and CTE's with V_f for 2x2 2-D tri-axial braided composite.

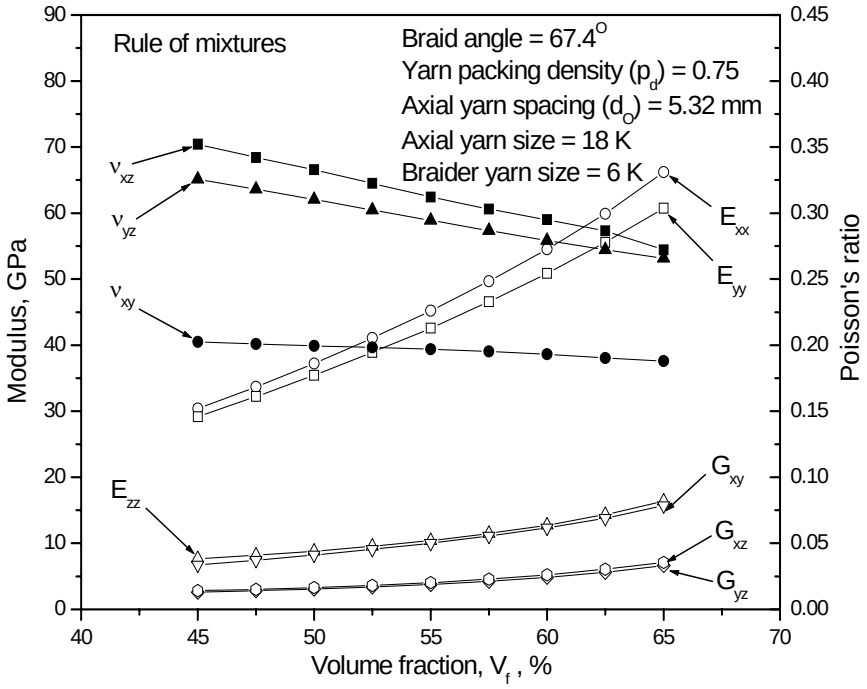

Figure 5.21: Variation of stiffness and Poisson's ratio with V_f considering Rule of mixtures.

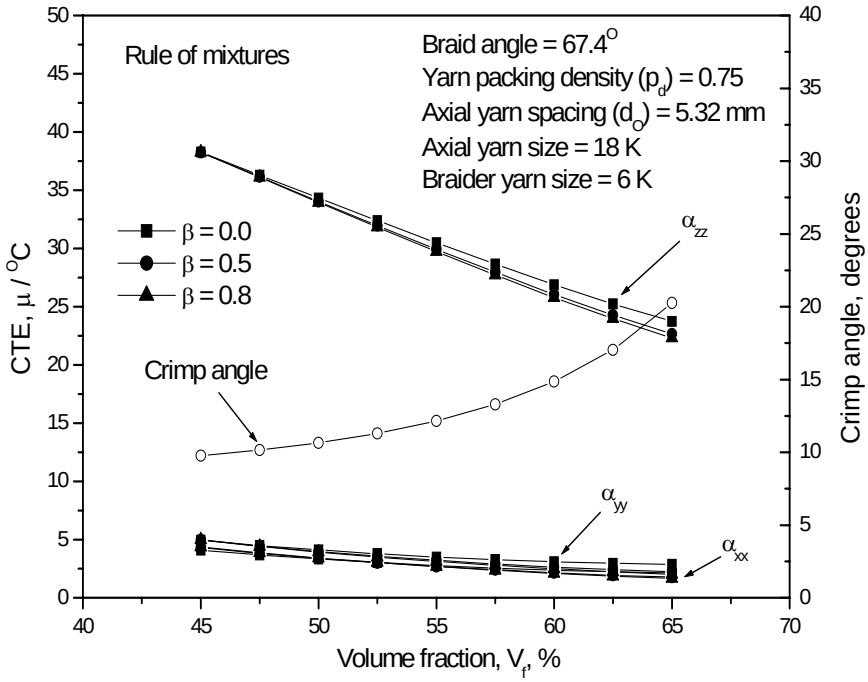

Figure 5.22: Variation of crimp angle and CTE's with V_f considering crack density and Rule of mixtures.

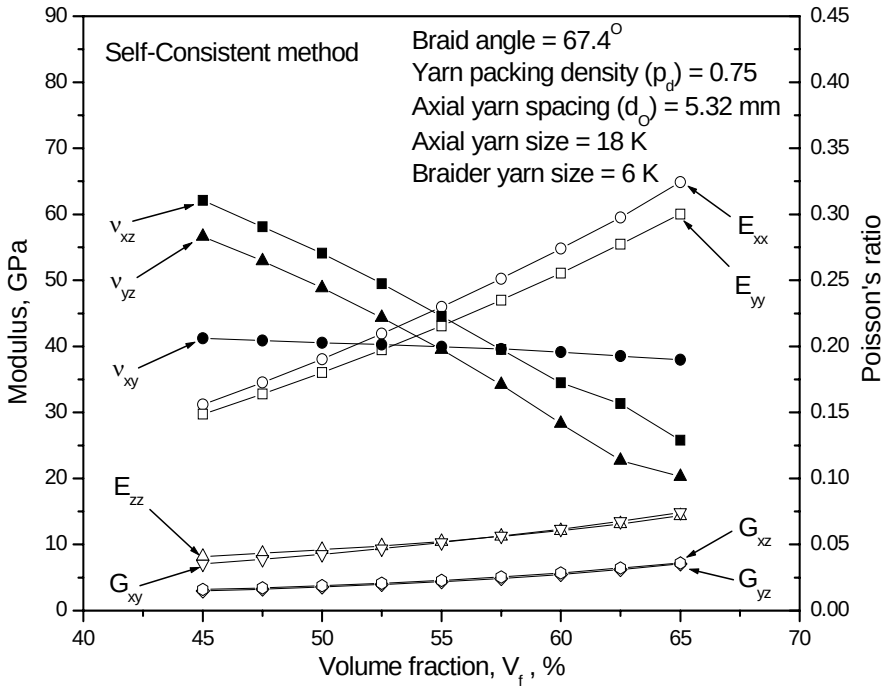

Figure 5.23: Variation of stiffness and Poisson's ratio with V_f considering Self-Consistent method.

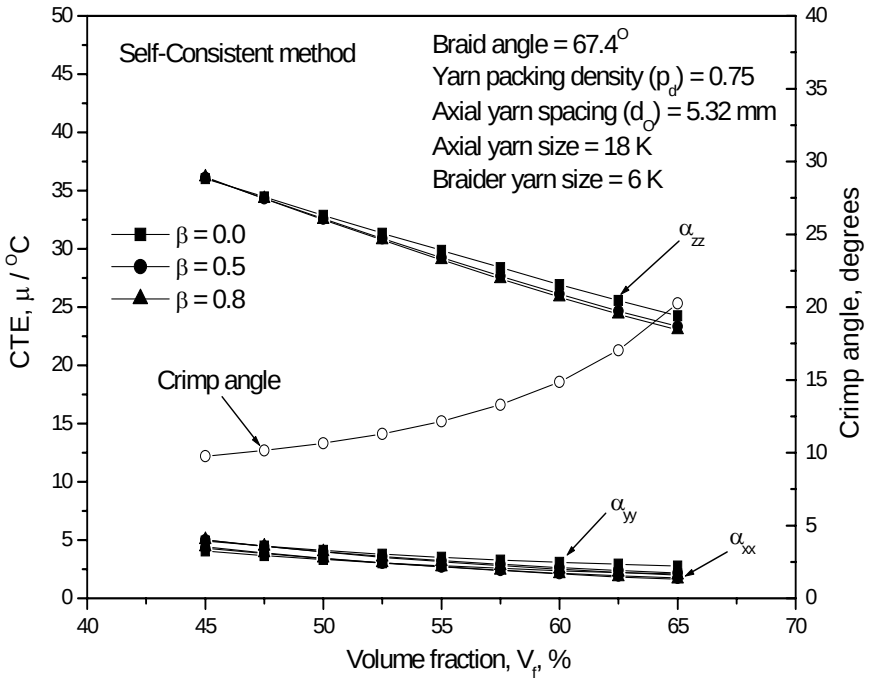

Figure 5.24: Variation of crimp angle and CTE's with V_f considering crack density and Self-Consistent method.

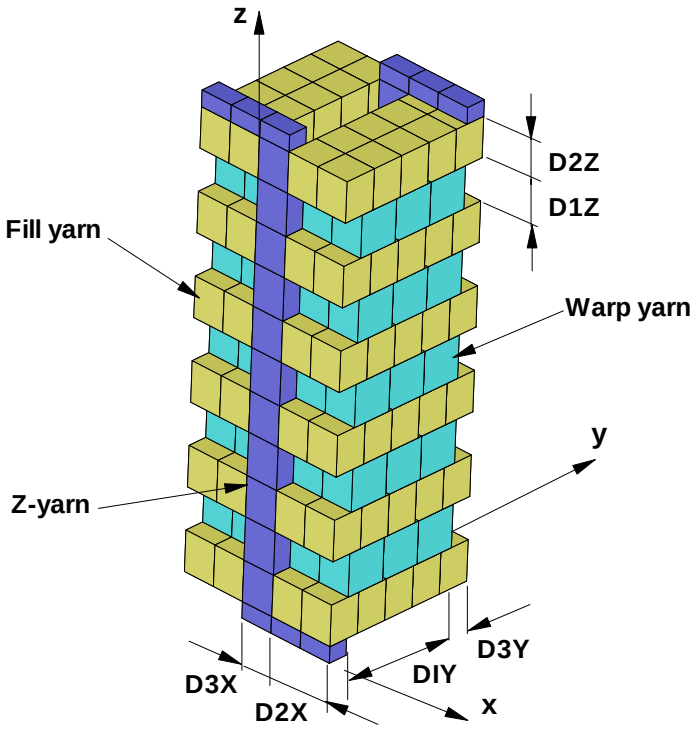

Figure 5.25: A simplified 3-D orthogonal woven composite[5.6].

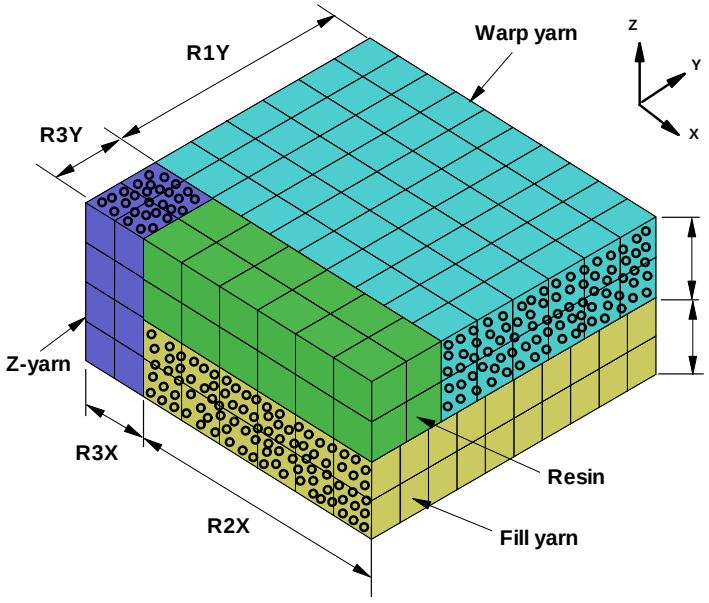

Figure 5.26: A 3-D orthogonal woven fabric unit cell[5.6].

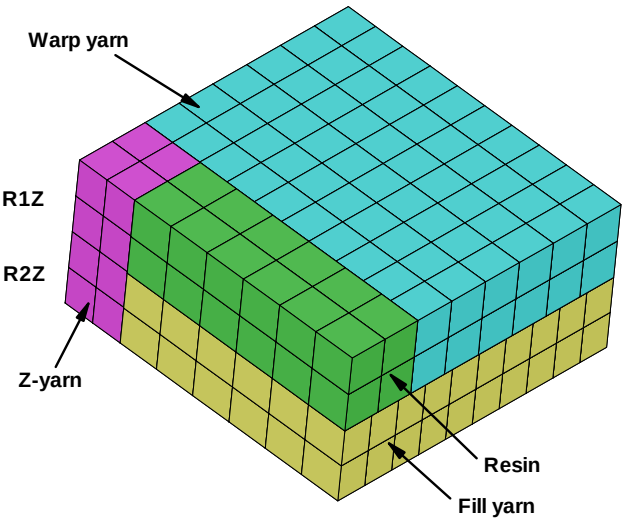

Figure 5.27: A 3-D orthogonal woven unit cell.

Table 5.6 The geometrical parameters for warp, weft and z-yarns from Ref. [5.6]. (Unit: mm)

Cases	Warp Yarn		Weft Yarn		Z-Yarn	
	R1Y	R1Z	R2X	R2Z	R3X	R3Y
A	0.691	0.2335	0.762	0.2235	0.193	0.2235
B	0.591	0.2535	0.782	0.2035	0.173	0.3235
C	0.491	0.2735	0.802	0.1835	0.153	0.4235

Table 5.7 The volume fractions of yarns for A~C cases.

Cases	V_f^O(%)	V_f^w(%)	V_f^f(%)	V_f^z(%)
A	82.57	38.60	39.02	4.939
B	78.72	35.85	36.46	6.408
C	73.27	32.13	33.72	7.419

Table 5.8 The equivalent elastic properties for A case from Ref. [5.6]. (Unit: GPa)

Models	E_{11}	E_{22}	E_{33}	ν_{12}	ν_{13}	ν_{23}	G_{12}	G_{23}	G_{13}
FEA	57.77	58.24	16.96	0.0623	0.2913	0.2906	4.211	3.54	3.57
XYZ[5.6]	57.57	58.23	17.44	0.0627	0.2836	0.2878	4.120	3.68	3.15
YXZ[5.6]	57.79	57.98	17.44	0.0654	0.2904	0.2796	4.250	3.42	3.76
ZXY[5.6]	58.07	58.63	16.85	0.0654	0.2925	0.2943	4.540	3.44	3.19
ZYX[5.6]	58.11	58.58	16.85	0.0661	0.2944	0.2921	4.570	3.12	3.49
Present	57.57	58.09	16.4296	0.0600	0.2861	0.2858	4.0131	3.5118	3.5057

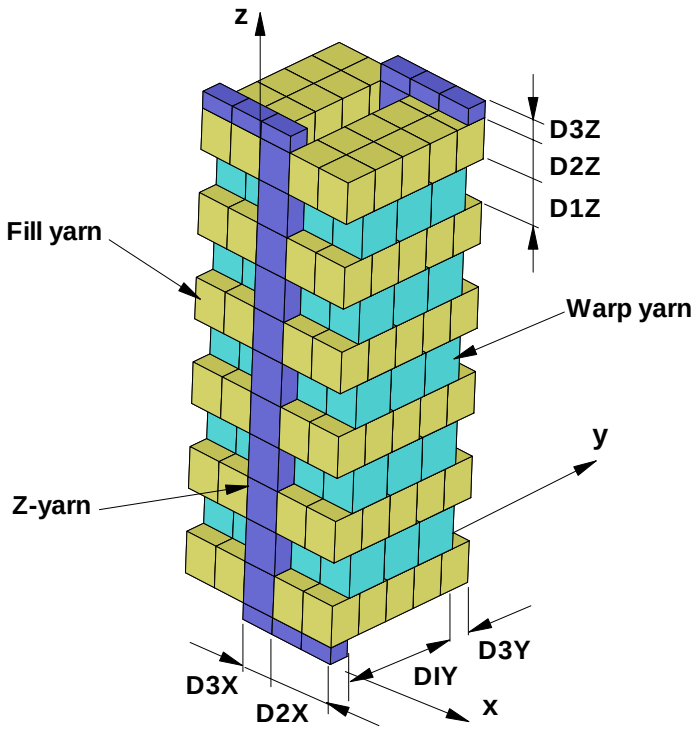

Figure 5.28: A simplified 3-D orthogonal woven composite[5.6].

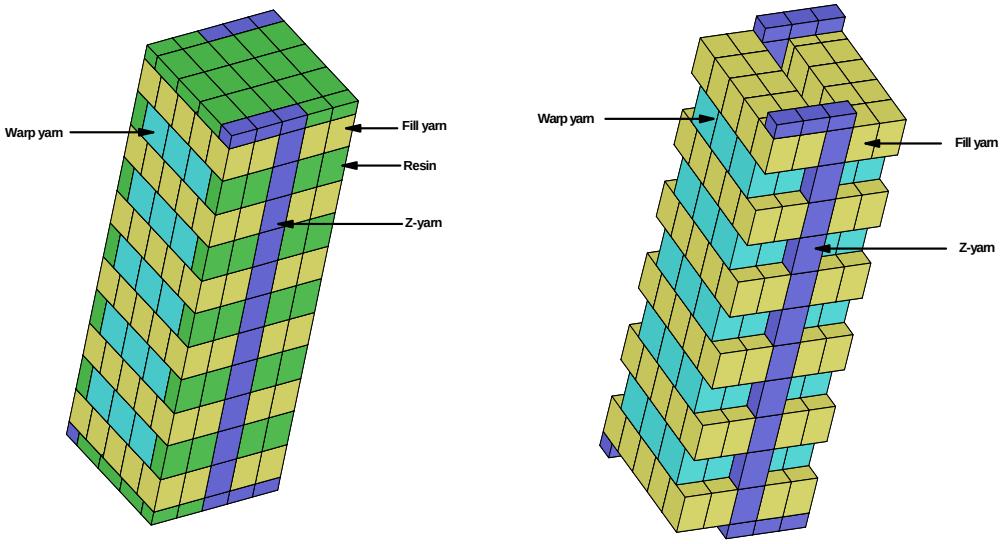

Figure 5.29: The laminate block model of 3-D orthogonal woven fabric.

Table 5.9 The geometrical parameters for warp, fill and z-yarns from Ref. [5.6]. (Unit: mm)

Cases	Layer No.	Warp Yarn		Weft Yarn			Z-Yarn	
		D1Y	D1Z	D2X	D2Y	D3X	D3Y	D3Z
A	5	1.3820	0.4670	1.5240	0.4470	0.3860	0.4470	0.1800
B	7	1.3820	0.4670	1.5240	0.4470	0.3860	0.4470	0.1800
C	9	1.3820	0.4670	1.5240	0.4470	0.3860	0.4470	0.1800
D	11	1.3820	0.4670	1.5240	0.4470	0.3860	0.4470	0.1800
E	2	1.3820	1.1675	1.5240	0.8940	0.3860	0.4470	0.1800
F	7	1.3820	0.3336	1.5240	0.3353	0.3860	0.4470	0.1800

Table 5.10 The equivalent elastic properties for cases from Ref. [5.6]. (Unit: GPa)

Cases	E_{11}	E_{22}	E_{33}	ν_{12}	ν_{13}	ν_{23}	G_{12}	G_{23}	G_{13}
A (No=5)	50.30	58.98	17.68	0.0623	0.2796	0.2724	4.02	3.39	3.35
B (No=7)	52.16	58.78	17.61	0.0627	0.2820	0.2758	4.07	3.45	3.44
C (No=9)	53.30	58.72	17.55	0.0629	0.2837	0.2781	4.10	3.49	3.49
D (No=11)	54.05	58.69	17.51	0.0631	0.2848	0.2791	4.12	3.51	3.53

Table 5.11 The equivalent elastic properties for cases calculated by present analysis.(Unit: GPa)

Cases	E_{11}	E_{22}	E_{33}	ν_{12}	ν_{13}	ν_{23}	G_{12}	G_{23}	G_{13}
A (No=5)	50.6331	59.1005	16.5045	0.0611	0.3056	0.2991	4.4594	3.8696	3.7239
B (No=7)	52.5098	58.9598	16.7215	0.0618	0.3039	0.2990	4.5148	3.8961	3.7852
C (No=9)	53.6268	58.8759	16.8502	0.0623	0.3029	0.2990	4.5477	3.9119	3.8216
D (No=11)	54.3679	58.8202	16.9354	0.0626	0.3022	0.2989	4.5696	3.9223	3.8458

Table 5.12 The total volume fractions for warp, fill and z lamina blocks. (Unit: $\times 100\,\%$)

Tan's Cases	Total V_f^w	Total V_f^f	Total V_f^z	Present Cases	Total V_f^w	Total V_f^f	Total V_f^z
A (No=5)	0.4345	0.4986	0.0670	A (No=5)	0.43426	0.49879	0.06695
B (No=7)	0.4536	0.4960	0.0500	B (No=7)	0.45371	0.49632	0.04997
C (No=9)	0.4653	0.4950	0.0398	C (No=9)	0.46529	0.49485	0.03985
D (No=11)	0.4730	0.4944	0.0332	D (No=11)	0.47298	0.49387	0.03315

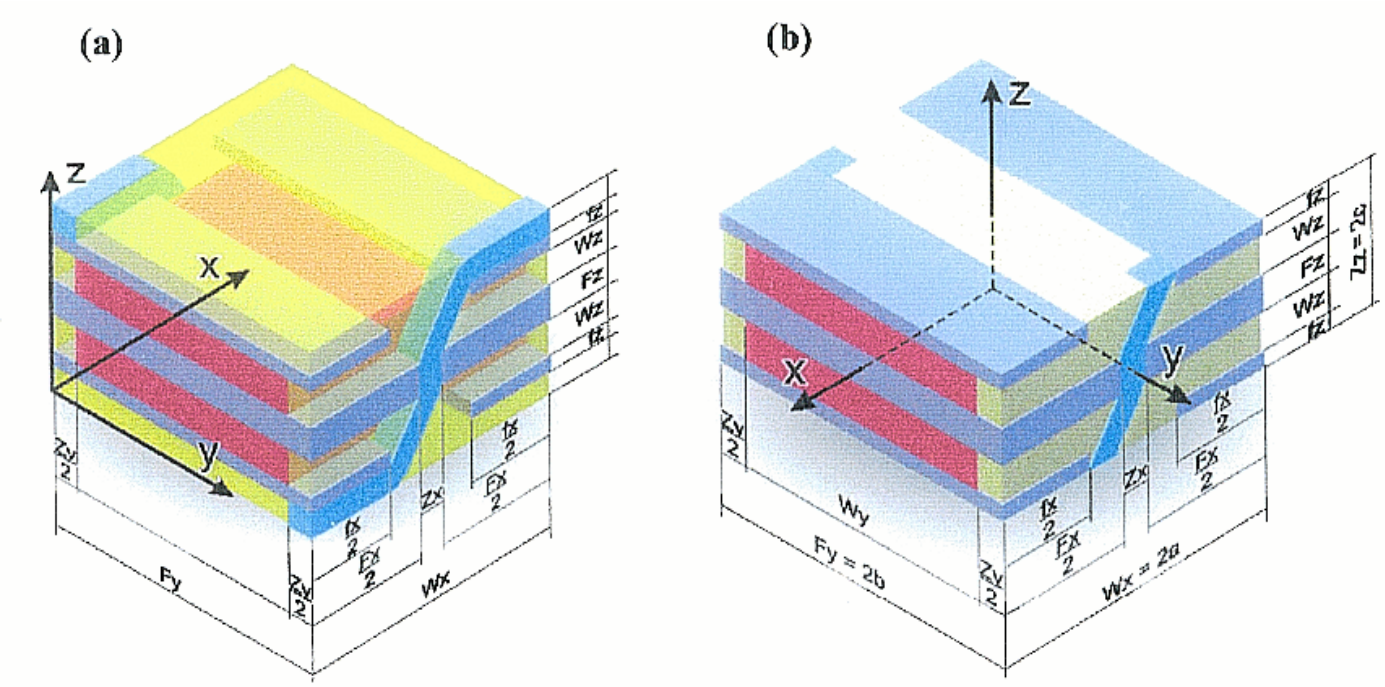

Figure 5.30: The 3-D Mosaic model of 3-D orthogonal woven fabric[5.7].

Table 5.13 Comparisons of the effective elastic characteristics from Ref. [5.7]. (Unit: GPa)

Cases	E_{11}	E_{33}	ν_{13}	ν_{23}	G_{12}	G_{23}
Bogdanovich	53.12	14.68	0.265	0.267	4.28	3.92
OAM	53.42	10.68	0.265	0.449	4.18	3.69
Experimental	56.00	18.00	0.270	-	7.50	-
Present	55.5870	19.0627	0.2632	0.2676	6.9530	6.9720

Table 5.14 Comparisons of the effective elastic properties from Ref. [5.7]. (Unit: GPa)

Cases	E_{11}	E_{22}	E_{33}	ν_{12}	ν_{13}	ν_{23}	G_{12}	G_{13}	G_{23}
Bogdanovich	27.31	25.70	9.98	0.125	0.432	0.448	3.58	3.52	3.34
SAM	27.54	24.89	9.72	0.093	0.402	0.402	3.16	3.02	2.97
Experimental (tension)	24.68	20.75	-	0.11	-	-	-	-	-
Present	28.7219	21.0942	9.6842	0.1256	0.3177	0.3243	3.3683	3.3683	3.3759

5.10 Discussion

Although the 2x2 2-D tri-axial braded textile composites feature more complicated architectures and have more difficulties in modeling their geometrical shapes than those of the 2-D braids, our geometrical model is a simple and accurate numerical solution. Comparing our results with other results and test data, our results are comparable to other textile composite models.

The present model provides a useful scheme to predict effective moduli and thermo-elastic constants for the 2-D braided and 2x2 2-D tri-axial braids. They provide a mean to perform sensitivity studies for the geometrical parameters that can affect the stiffness properties of the textile composites. In addition, 3-D orthogonal woven fabric model is implemented to obtain its mechanical characteristics. From these results, we can state that the present geometrical modeling can estimate the equivalent modulus of the 2-D braids, the 2x2 2-D tri-axial braids and 3-D orthogonal woven fabrics without expensive experiments and with only a little computational time.

REFERENCES

5.1 Naik, R.A., "Analysis of Woven and Braided Fabric Reinforced Composites," NASA Contractor Report CR-194930, 1994.

5.2 Foye, R.L., "Finite Element Analysis of the Stiffness of Fabric Reinforced Composites," NASA CR-18597, Feb. 1992, National Aeronautics and Space Administration, Hampton, Virginia.

5.3 Masters, J.E., Foye, R.L., Pastore, C.M. and Gowayed, Y.A., "Mechanical Properties of Tri-axial Braided Composites: Experimental and Analytical Results," *Journal of Composites Technology and Research*, Vol. 15, No. 2, 1993, pp. 112-122.

5.4 Masters, J.E., Fedro, M.J. and Ifju, P.G., "An Experimental and Analytical Characterization of Three Tri-axially Braided Composites," Proc. Third NASA Advanced Composites Technology Conference, NASA CP 3178, Part 1, Vol. 1, 1992, pp. 263-286.

5.5 Naik, R.A., Ifju, P.G. and Masters, J.E., "Effect of Fiber Archtecture Parameters on Deformations Fields and Elastic Moduli of 2-D Braided Composites," *Journal of Composites Materials*, Vol. 28, No. 7, 1994, pp. 656-681.

5.6 Tan, P., Tong, L. and Steven, G.P., "Modeling Approaches for 3D Orthogonal Woven Composites," *Journal of Reinforced Plastic and Composites*, Vol. 17, No. 6, 1998, pp. 545-577.

5.7 Bogdanovich, A.E., "Multi-scale Predictive Analysis of 3D Woven Composites," *35th Int'l. SAMPE Technical Conference*, 2003.

Chapter 6 Failure Analysis of Micro-Cracked Textile Composites

6.1 Introduction

In Chapters 2-4, the micro-mechanical model of 2-D plain woven and 3-D orthogonal woven textile composites are suggested to predict effective moduli of a Repeating Unit Cell, and good predictions based on Sine Function Model I and II were reported. Various mechanical characteristics using yarn's geometry and orientations as parameters and using the Repeating Unit Cell also were presented. Although the mechanical behavior and modeling of textile composites using Repeating Unit Cells were investigated, due to the inherent complexities in modeling the geometrical and material non-linearity along with micro-cracking, the micro-mechanical analysis of the cracked textile composites were not sufficiently well investigated. The aim of this Chapter is to study the failure behaviors when a micro-cracked textile composite is subjected to external loadings and stiffness degradations in the textile composites occur.

6.2 Micro-crack Modeling for Cracked Textile Composites

This study considers a crack-density scheme related to micro-slit cracks in a continuous matrix and anisotropic elastic medium, and is aimed at establishing the relationship between stiffness and compliance tensors in a linear-solid of textile yarns. An analytical damage model considering the transverse matrix cracking based on the yarns' geometrical shape of Repeating Unit Cells, such as 2-D plain weaves, 2-D braids and 3-D orthogonal woven textile composites is presented. Similar to the assumptions of Ref. [6.1] used toward determining the behavior of transverse matrix cracking, the four assumptions are made to represent a degraded textile composite:

i) Transverse matrix cracks exist in the fills and warps along with the yarn directions, such as longitudinal slit cracks along the fibers.
ii) The matrix and fibers are transversely isotropic with respect to the yarn fiber axes.
iii) The overall behavior of the cracked textile composites is orthotropic in material axes.
iv) The matrix cracks are dependent on the fiber diameters, such as the three-phase or two-phase cracks.

To study the small diameter fibers and elliptical shape cracks, the two-phase crack model is toward determination of the overall elastic properties for cracked textile yarns, the Self-consistent method suggested in Laws[6.1] *et al.* is used. The two-phase crack model assumes that fiber diameters are very small compared with the crack length or lamina thickness shown in Figure 6.1. To investigate the stiffness degradation in two-phase cracks, we assume that the elliptic cylindrical inclusions exist in an infinite homogeneous solid as shown in Figure 6.1 and the solid consists of fibrous composite with longitudinal cracks (x_1-direction) as shown in Figure 6.2. By assuming that parallel slit cracks are equally distributed in the composite and have the same direction as that of the fibers, a small inclusion is expressed as

$$\frac{x_2^2}{b^2}+\frac{x_3^2}{a^2}=1,\ |x_1|<\infty \tag{6.1}$$

Here, an elliptic void with semi-axes (a) and (b) is used to represent the crack. By introducing a crack density scheme, the reduced stiffness values for the textile yarns will be determined. The crack density (β) is defined as the average number of cracks of length ($2a$) in a square of side ($2a$) in the yarn sections. Also, the number (η) of voids per unit area (x_2 - x_3 plane) in the yarn sections is used. So the volume fraction of voids is:

$$\pi a^2\eta\delta=\frac{1}{4}\pi\beta\delta,\ \delta=\frac{b}{a} \tag{6.2}$$

Let us assume that the aspect ratio (δ) has the limits of the elliptical cylinder, and describes the cracks in the yarn section. The cracks can be modeled by taking the aspect ratio in the elliptic cylinder to be zero. As a result, we choose phase 2 (matrix) to contain voids and to take the limit $\delta \to 0$ to represent the cracks. To find the elastic properties of the inclusion, we assume that the elliptical inclusion is subjected to a certain uniform strain already used in Ref.[6.1]. Our work uses the same solution tensor (P) for Eq. (6.1) as suggested in Ref. [6.1]. The tensor (P) is strongly related to the stiffness tensor (C). To work with tensors P and C, another tensor (Q) related to compliance tensor (S) is defined for the elliptical inclusion. This theory is based on the solution for the elliptic cylinder in anisotropic elastic medium. The constitutive equations are

$$\sigma = C\varepsilon,\ \varepsilon = S\sigma,\ CS = SC = I \tag{6.3}$$

$$Q = C - CPC \tag{6.4}$$

Here I is the unit diagonal matrix. In Eq. (6.4) the tensors P and Q are dependent on the aspect ratio of the elliptic inclusion and the effective medium (C and S). The two-phase crack for the yarn sections is shown in Figure 6.2. The un-cracked and cracked compliance and stiffness are written as:

$$C = C_u - \frac{1}{4}\pi\beta C_u \Lambda C,\ S = S_u + \frac{1}{4}\pi\beta\Lambda \tag{6.5}$$

Here, C_u and S_u mean the un-cracked stiffness and compliance, respectively and Λ is non-zero parametric tensor suggested explicitly in Ref. [6.1]. By taking the limit ($\delta \to 0$), the product δQ_1^{-1} reduces to Λ, that is defined by

$$\lim_{\delta \to 0} \delta Q_1^{-1} = \Lambda \tag{6.6}$$

The subscript 1 in Eq. (6.6) means the crack direction that is parallel to the fiber direction. This Λ tensor suggested in Ref. [6.1] has three non-zero components in the two-phase crack that are

$$\Lambda_{22} = \frac{C_{33}(\alpha_1^{1/2} + \alpha_2^{1/2})}{(C_{22}C_{33} - C_{23}^2)},\ \Lambda_{44} = \frac{1}{4(C_{44}C_{66})^{1/2}},\ \Lambda_{55} = \frac{(C_{22}C_{33})^{1/2}(\alpha_1^{1/2} + \alpha_2^{1/2})}{4(C_{22}C_{33} - C_{23}^2)} \tag{6.7}$$

$$C_{33}C_{55}\alpha^2 - (C_{22}C_{33} - C_{23}^2 - 2C_{23}C_{55})\alpha + C_{22}C_{55} = 0 \tag{6.8}$$

Here, α_1 and α_2 are the roots of the quadratic Eq. (6.8). From Eq. (6.5), the stiffness is rewritten as

$$C = \left[I + \frac{1}{4}\pi\beta C_u \Lambda(C) \right]^{-1} C_u \tag{6.9}$$

Noting that the tensor (Λ) is dependent on the stiffness tensor (C), in order to find components of Λ, a numerical iterative scheme is used. The iterative scheme starts with $C = C_u$ and continues with iterations on Eq. (6.5) until the convergence condition.

$$\frac{\left\| C^{k+1} - C^k \right\|}{\left\| C^k \right\|} \le \Delta \tag{6.10}$$

Here, k and $k+1$ are the number of steps and Δ is the error bound, in this study taken to be 0.001. The stiffness tensor (C) for the cracked case, in Eq. (6.9), has nine independent components that are determined from the un-cracked state. Also this iteration scheme is applied for each cracked-fill and warp yarns in the sub-domain zone of the RUC.

6.3 Numerical Example for Crack Density Scheme

To validate the crack density scheme, some of the examples investigated in Ref.[6.1] are considered. For the numerical study of composite laminated structures, the material properties for Graphite/Epoxy are used as shown in Table 6.1. The elastic modulus and Poisson's ratio are based on the composite laminate including matrix cracking, stiffness matrix being obtained from the material properties. The un-cracked

stiffness matrix is calculated using the crack density and the fiber volume fraction (v_f). The cracked stiffness is obtained from Eq. (6.9) to satisfy the convergence criteria given in Eq. (6.10). As shown in Figure 6.3, stiffness changes for the Graphite/Epoxy composite with slit cracks are considerably dependent on the crack densities and the fiber volume fractions.
By comparing the results with that of Laws[6.1] *et al.*, the crack density scheme used in this study appears to be consistent with Laws' results. The next step is to apply this crack density scheme to determine the equivalent modulus of the cracked textile yarns. To calculate the correct value of equivalent properties in the plain woven and 2-D braids, a geometrical model to represent these textile composites is needed. In Chapters 2-4 this study suggested analytical models, such as two Sine Function Models to obtain three-dimensional shapes for the plain weaves and 2-D braids and predict their equivalent modulus. Using the Sine Function Model and crack density scheme, the mechanical behavior and stiffness degradation of cracked textile composites are analyzed.

6.4 Degraded Equivalent Modulus of Closed Plain Weaves

To analyze the Repeating Unit Cell with transverse matrix cracks, this study considers the model by D.Scida[6.2] *et al.* and assumes that this closed-weave has the transverse matrix cracks in the fill and warp yarns. For a variety of crack densities and volume fractions, the stiffness changes and the equivalent modulus are calculated using the Repeating Unit Cell approach. From Figures 6.4-6.6, some of different values in the stiffness and equivalent properties for the closed weaves have been found. In Figures 6.4 and 6.5, the warp stiffness is affected by the crack shapes along the y-axis because the crack shapes are varied with respect to the x-axis. However, the fill stiffness is changed along the x-axis. So, the y-stiffness components of the warp are considerably changed and the small changes are shown in the x-stiffness components, with increasing volume fractions. The degraded equivalent properties for the closed weaves are shown in Figure 6.6, with a variety of crack densities and volume fractions. From these graphs, the degraded properties of the closed weaves are similar to orthogonal laminates' properties along the z-axis. The z-components of the reduced properties present constants values, but the other values are changed with the different crack densities and fiber volume fractions.

6.5 Degraded Equivalent Modulus of 2-D Closed Weave Braided Textile

To calculate the 2-D degraded braids, the Sine Function Model assumes that the warp and fill yarns feature transverse matrix cracks and the micro-mechanical equations are considered to predict the equivalent modulus. As the case of the plain woven, the 2-D braided textile is studied by considering a variety of crack densities and volume fractions. The stiffness changes and the equivalent moduli are calculated by using the Rule of mixture's equations, and the same geometrical parameters and material properties presented in Ref. [6.3] are used. The properties of the fiber and resin and the geometry parameters used in Naik[6.3] are given in Table 6.4. The results of Figures 6.7 and 6.8 are calculated for the case of $\theta_{br} = \pm 45^{\circ}$ braid angles. From these graphs, the degraded properties of the 2-D braids are similar to the degraded plain woven along the z-axis. The components in the z-direction are constant values, but the other values are changed by the different crack densities and fiber volume fractions. As the fiber volume is increased, large changes in the degraded stiffness are found. However, Poisson's ratio ν_{12} is the one only that has different trends as compared to the case of the degraded plain weaves. This means that the 2-D braids are more dependent on the geometrical shapes of yarns, as suggested in the Chapter 5.

6.6 Degraded Equivalent Modulus of 3-D Orthogonal Woven Textile Composite

In Chapter 5, the 3-D orthogonal woven textile composite is modeled by using the unit cell model and the equivalent moduli are determined. Here the same material and unit cell suggested by Ref. [6.4] are used to obtain the degraded equivalent moduli. The material and geometrical values of Tong[6.4] model are listed in Table 6.5-6.6. The yarn volume fractions of each case are presented in Table 6.7. Simplified 3-D

orthogonal woven preforms are shown in Figure 6.9. To calculate the degraded stiffness, the matrix cracks are considered in the x, y yarns, and the z-yarn described in Figure 6.10.

The degraded stiffness of the warp and fill are plotted as a function of various crack densities and volume fractions. Here, the vertical yarn (z) does not consider the crack density scheme, because this yarn does not satisfy the laminate theory. The only two yarns (warp and fill) have transverse matrix cracking. From Figures 6.11 and 6.12, it appears that there is a strong dependence between the volume fraction and the z-yarn. Although the larger fiber components in the warp and fill yarns yield an increase of the volume fraction, the stiffness values are dependent on the fiber terms in the z-yarn. This fact encourages from Figures 6.11-6.12 and Figure 6.13. Actually, the z-yarn can not be assumed to be a general vertical yarn through the laminate theory. So, this study does not consider the transverse matrix cracking in the z-yarn, and only the effects of the z-yarn in the degraded stiffness are considered in the 3-D orthogonal woven textiles.

Here, we consider another 3-D orthogonal woven model that was studied earlier by Bogdanovich in Ref. [6.5], and we obtain the stiffness degradation of the 3-D orthogonal woven composite. The same geometrical parameters and material properties for the 3-D Mosaic model as described in Ref. [6.5] are used. These values were also described in Chapter 5. The tow packing-factor is considered as a stiffness degradation parameter. In general, its values are different for each fiber packing type. The tow packing-factor in the hexagonal packed fibers does not exceed 0.9, and the maximum tow packing-factor in the quadrilateral packed fibers was selected to be 0.78. In our analytical model, the fiber packing type is assumed to be the hexagonal packed fibers, and the same 3-D Mosaic model suggested by Bogdanovich [6.5] is used. By using a variety of crack densities (β) and tow packing factors (p_f), the changes in the effective elastic characteristics are calculated, and presented in Figure 6.14. The graphs in Figure 6.14 reveal that the degraded elastic properties are considerably dependent on the crack density values.

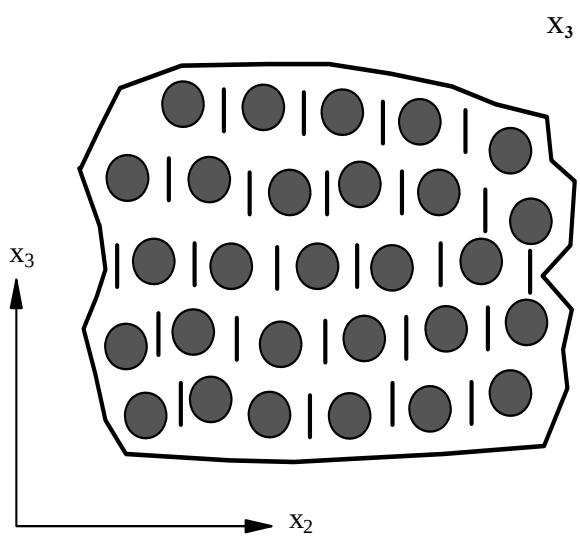

Figure 6.1:Aligned fibers and slit cracks in a continuous matrix.

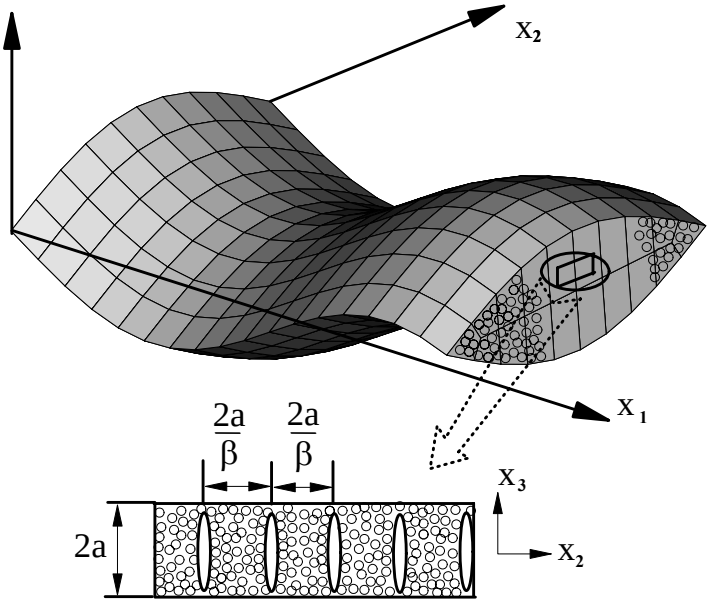

Figure 6.2:Warp yarn with small diameter fibers and slit cracks.

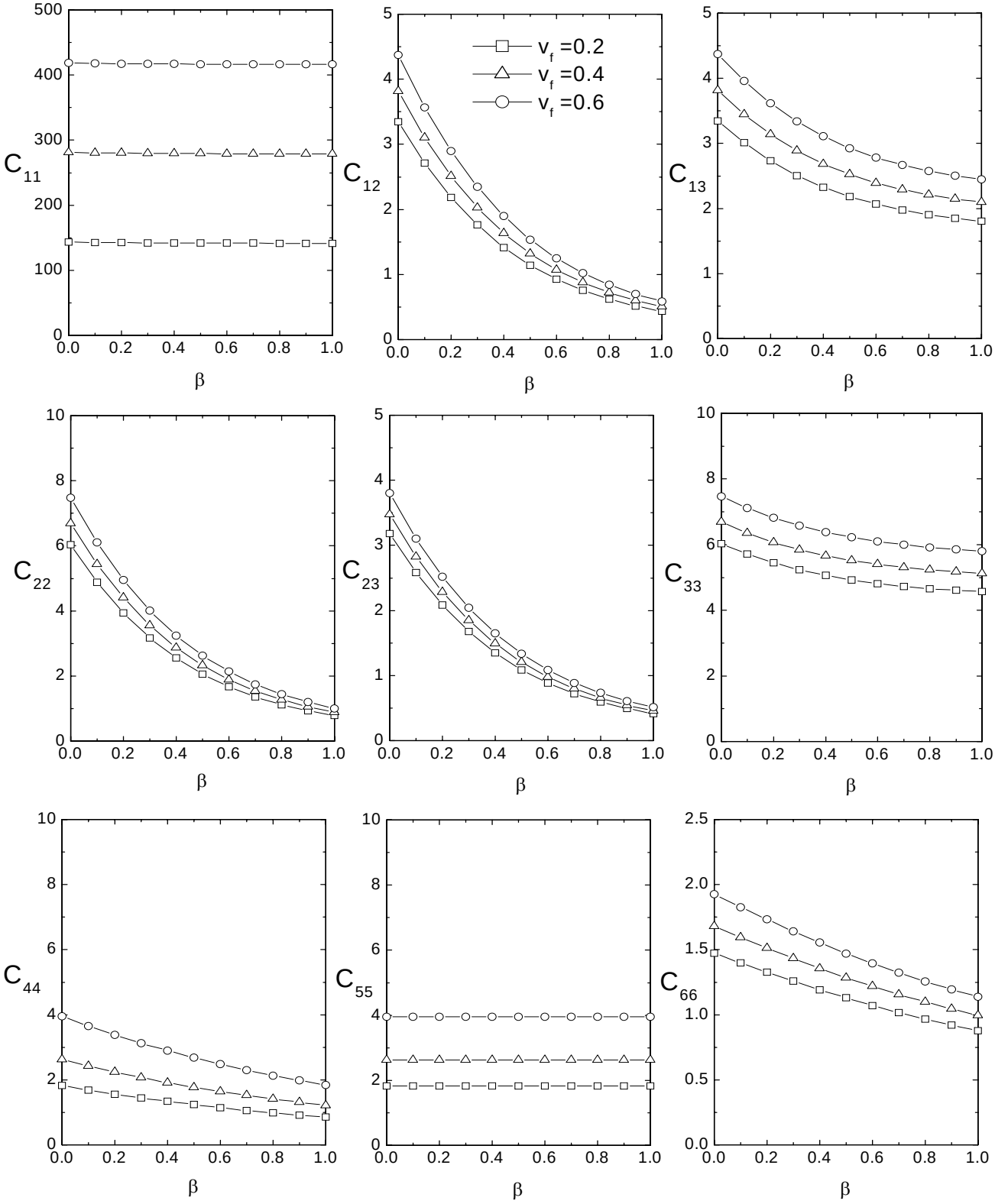

Figure 6.3: Stiffness changes of VS0054 Graphite/Epoxy composite with longitudinal slit cracks (Unit: GPa).

Table 6.1 Elastic properties for VS 0054 Graphite/Epoxy from Ref. [6.1]. (Unit: GPa)

Materials	E_{11}	E_{22}	G_{12}	G_{23}	ν_{12}
Fiber	689.5	7.6	15.2	2.6	0.41
Matrix	3.4	3.4	1.3	1.3	0.35

Table 6.2 Elastic properties of fiber and resin from Ref. [6.2]. (Unit: GPa)

Materials	E_{11}	E_{22}	G_{12}	G_{23}	ν_{12}
E-Glass	73.0	73.0	30.4	30.4	0.20
Vinylester derakane	3.4	3.4	1.49	1.49	0.35

Table 6.3 The geometrical parameters for plain weave fabric yarns from Ref. [6.2]. (Unit: mm)

Material	Fill yarn			Warp yarn			H	V_f^o
	a_2	h_2	g_2	a_1	h_1	g_1		
E-Glass / Vinylester	0.60	0.05	0.0	0.60	0.05	0.0	0.10	0.55

Table 6.4 Elastic properties for the 2-D braided textile composites from Ref. [6.3]. (Unit: GPa)

Materials	E_{11}	E_{22}	G_{12}	ν_{12}	ν_{23}
Yarn	144.80	11.73	5.52	0.23	0.3
Resin	3.45	3.45	1.28	0.35	0.35

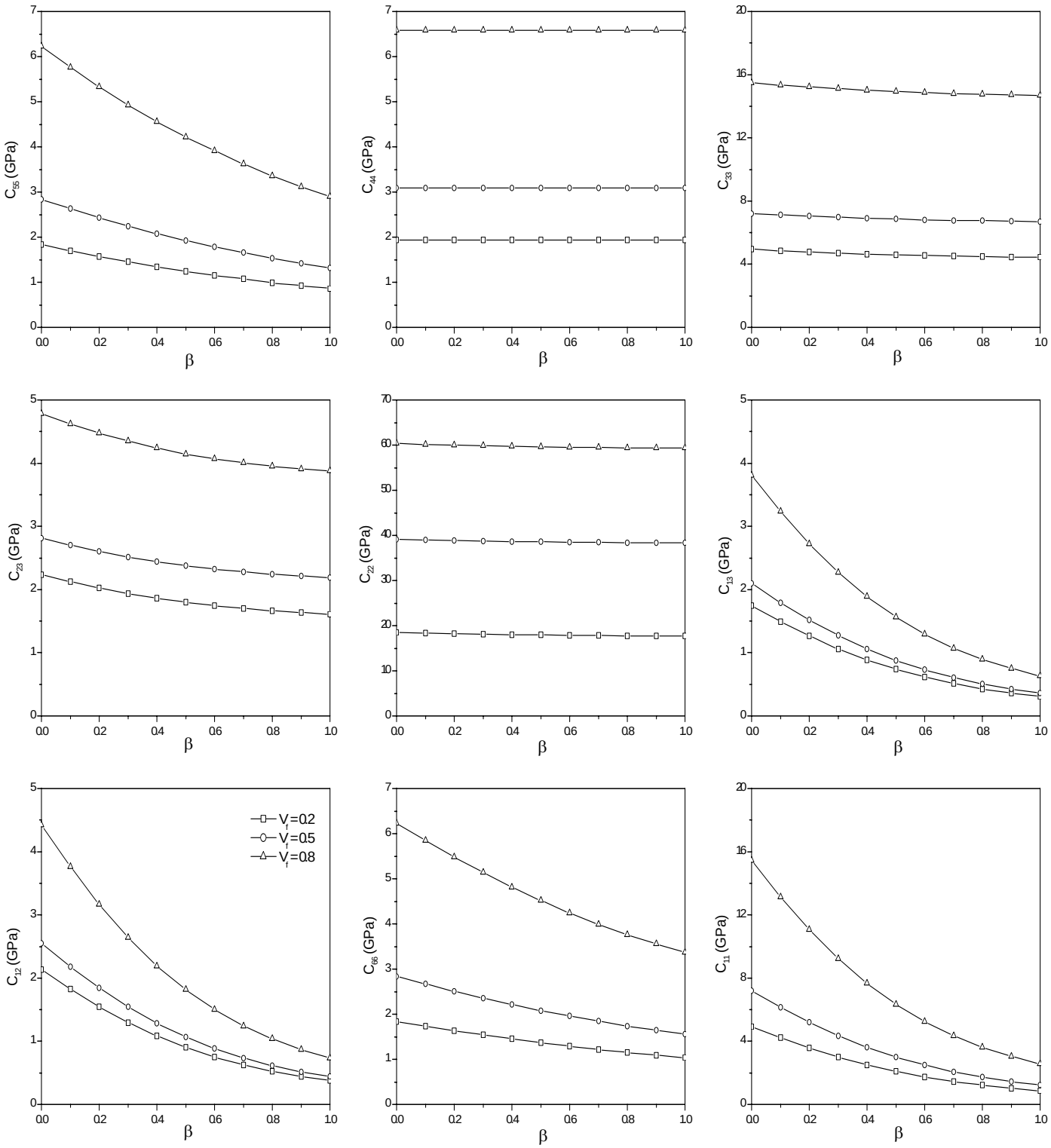

Figure 6.4: Fill yarn stiffness reduction of E-Glass / Vinylester with longitudinal slit cracks.

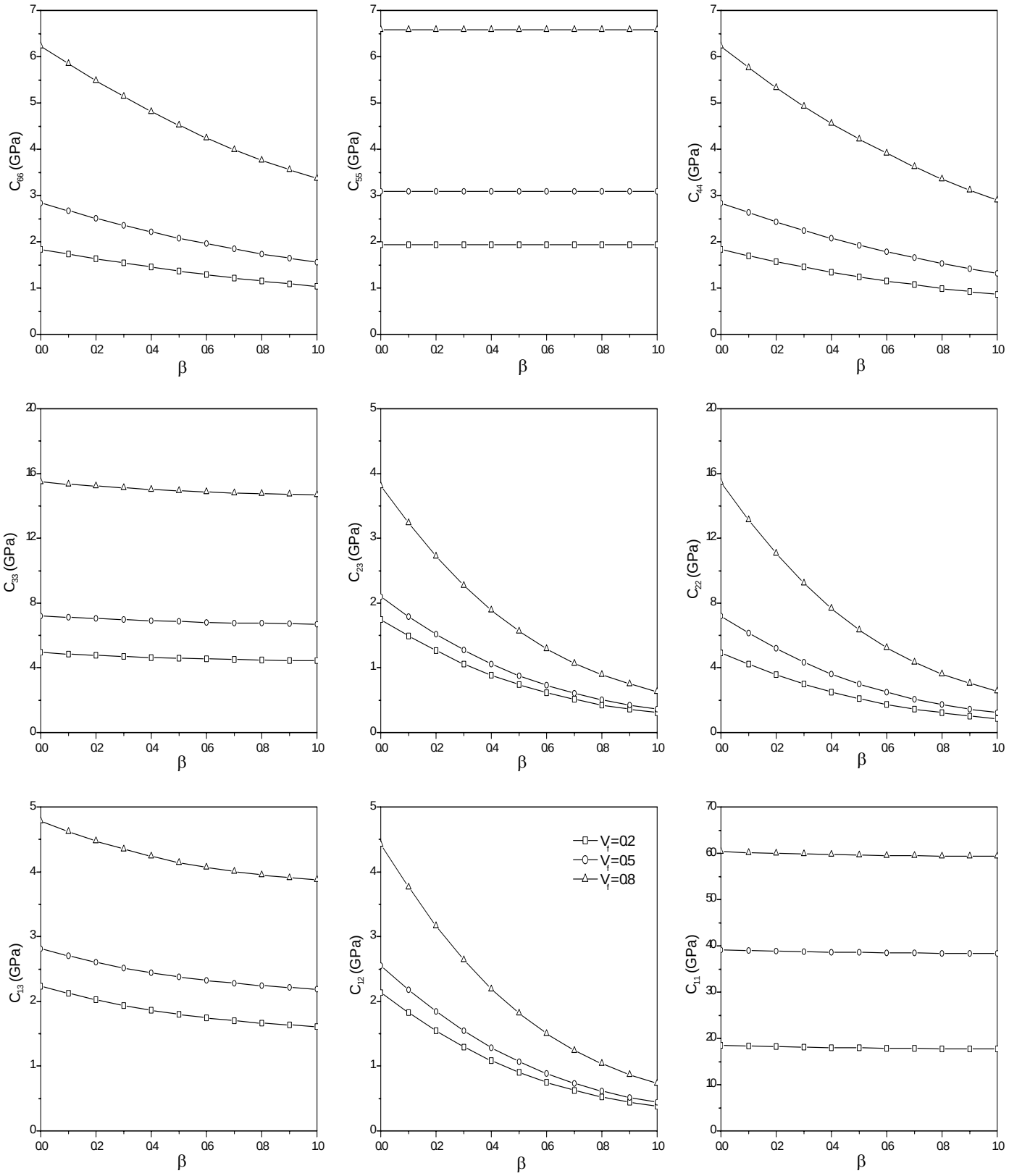

Figure 6.5: Warp yarn stiffness reduction of E-Glass / Vinylester with longitudinal slit cracks.

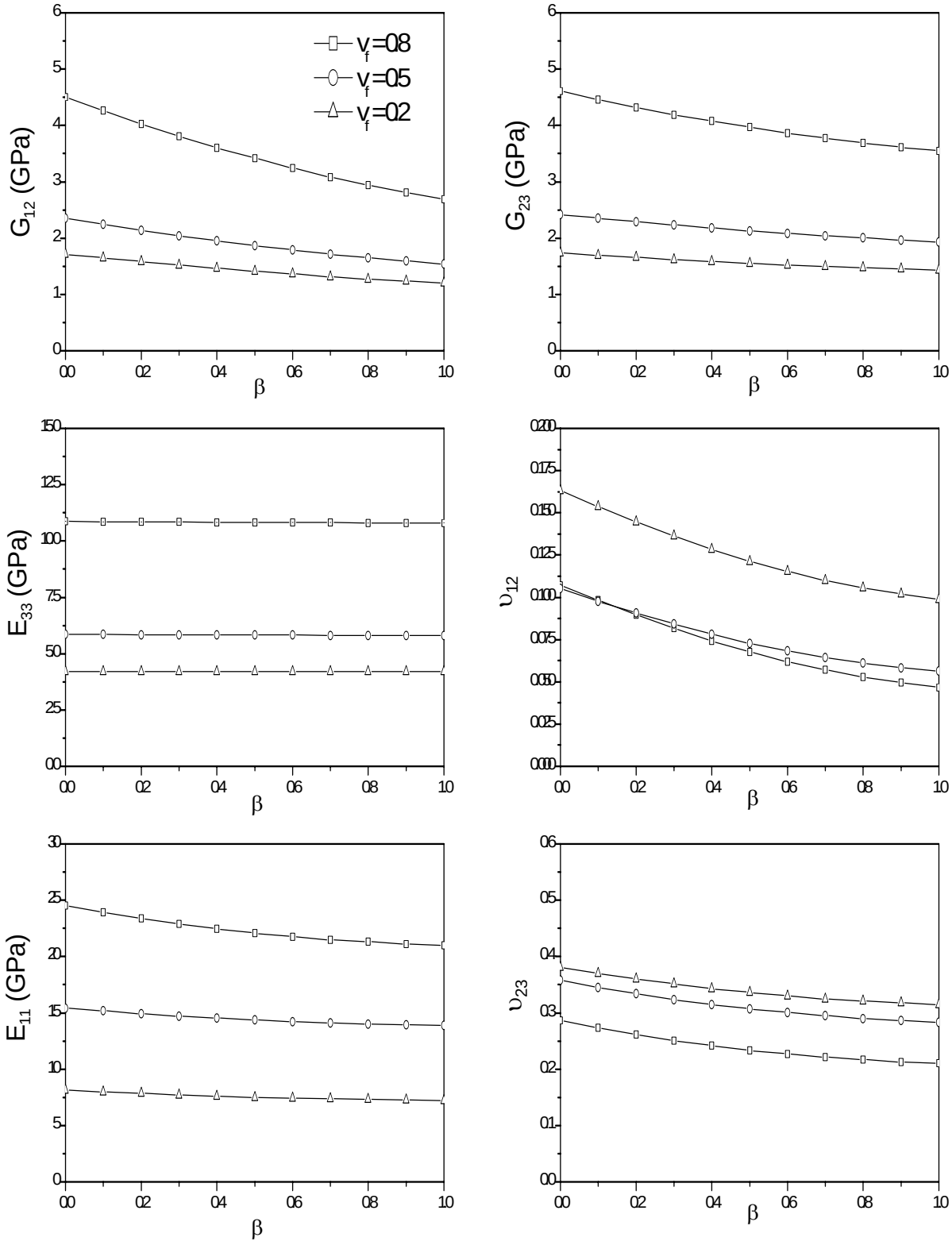

Figure 6.6: Degraded modulus of closed weaves with a variety of crack densities and volume fractions.

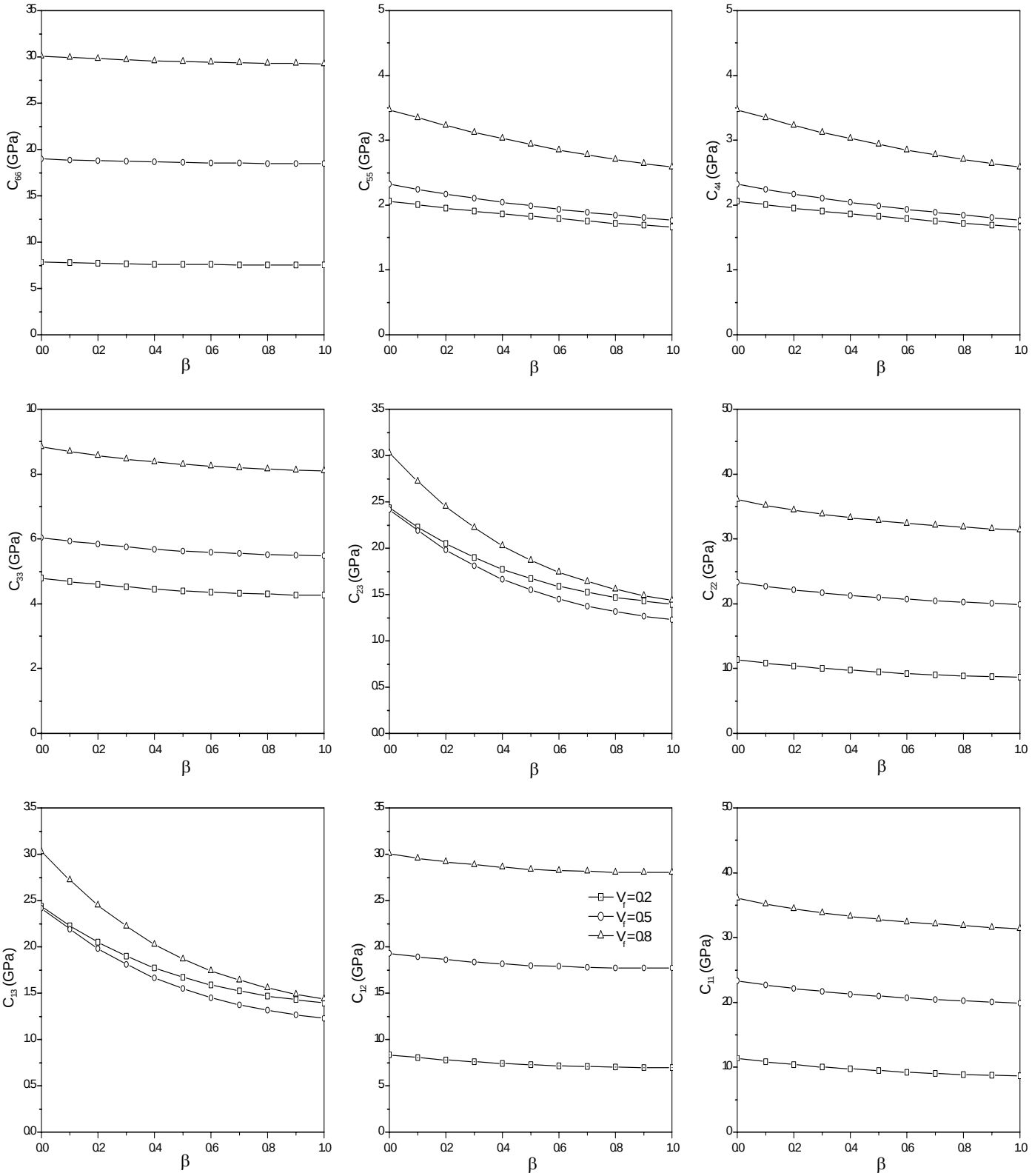

Figure 6.7: Yarn stiffness reduction of 2-D braided textile composites with longitudinal slit cracks.

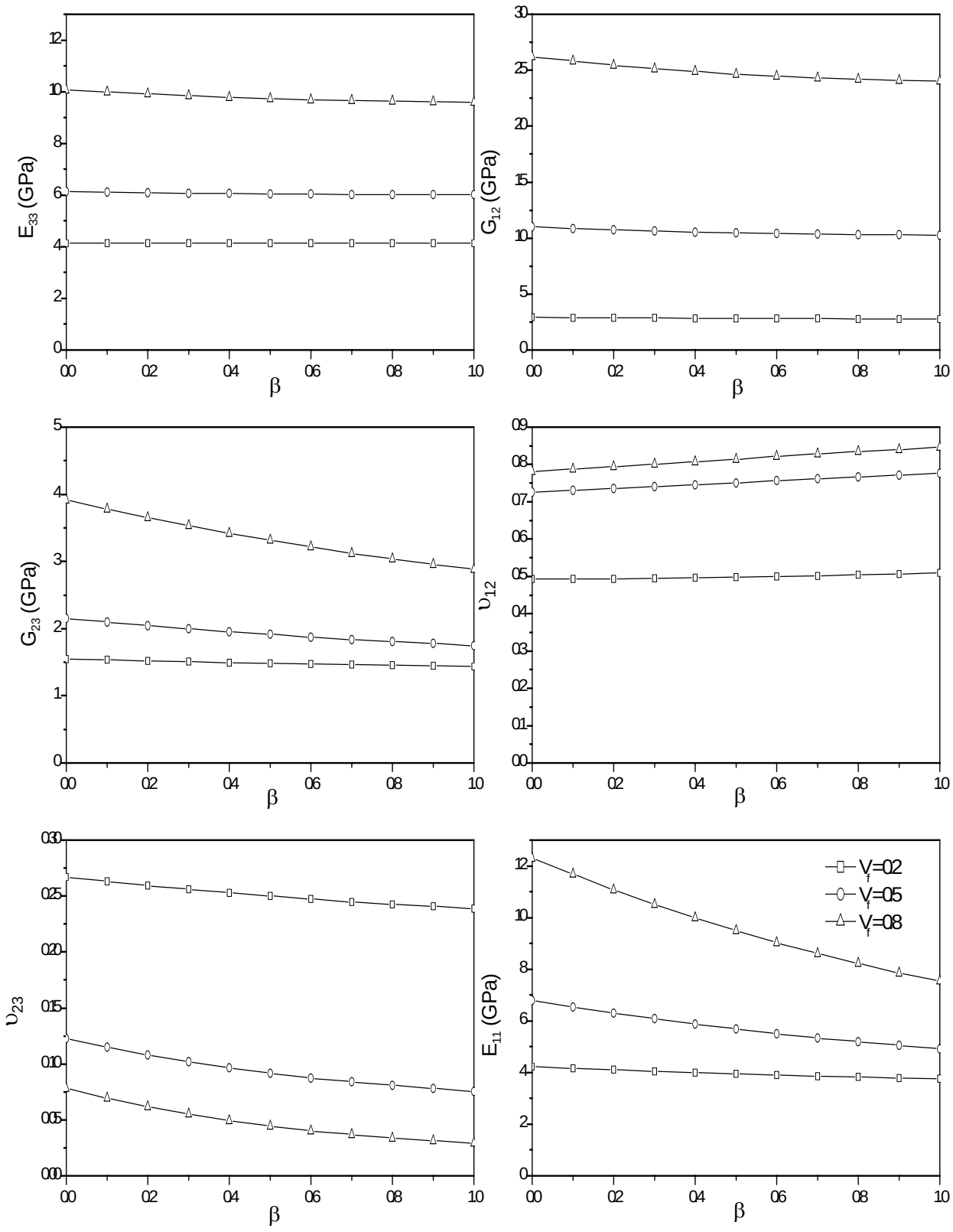

Figure 6.8: Degraded modulus of 2-D braids with a variety of crack densities and volume fractions.

Table 6.5 The engineering elastic properties for Carbon/Epoxy from Ref. [6.4]. (Unit: GPa)

Materials	E_{11}	$E_{22}=E_{33}$	$\nu_{12}=\nu_{13}$	ν_{23}	$G_{12}=G_{13}$	G_{23}
Carbon/Epoxy (yarn)	134.0	10.20	0.30	0.49	5.52	3.43
Epoxy resin	3.45	3.45	0.35	0.35	1.28	1.28

Table 6.6 The geometrical parameters for warp, weft and z-yarns from Ref. [6.4]. (Unit: mm)

Cases	Warp Yarn		Weft Yarn		Z-Yarn	
	R1Y	R1Z	R2X	R2Z	R3X	R3Y
A	0.691	0.2335	0.762	0.2235	0.193	0.2235
B	0.591	0.2535	0.782	0.2035	0.173	0.3235
C	0.491	0.2735	0.802	0.1835	0.153	0.4235

Table 6.7 The yarn volume fractions of A~C cases.

Cases	V_f^O(%)	V_f^w(%)	V_f^f(%)	V_f^z(%)
A	82.57	38.60	39.02	4.939
B	78.72	35.85	36.46	6.408
C	73.27	32.13	33.72	7.419

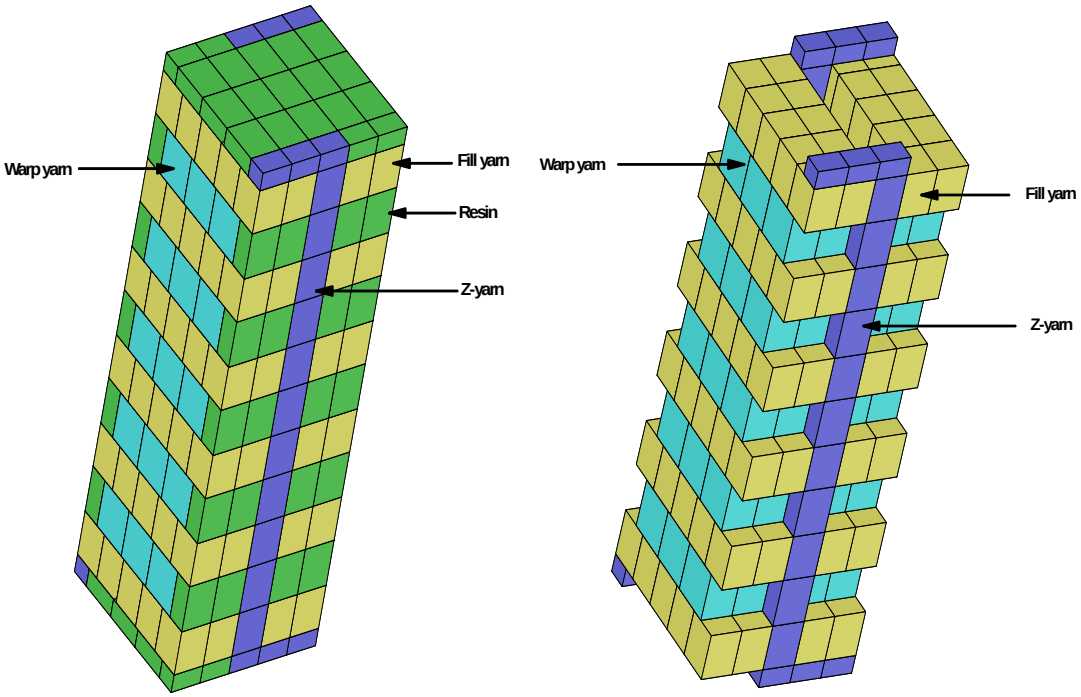

Figure 6.9: The laminate block model of 3-D orthogonal woven fabric with resin and no resin.

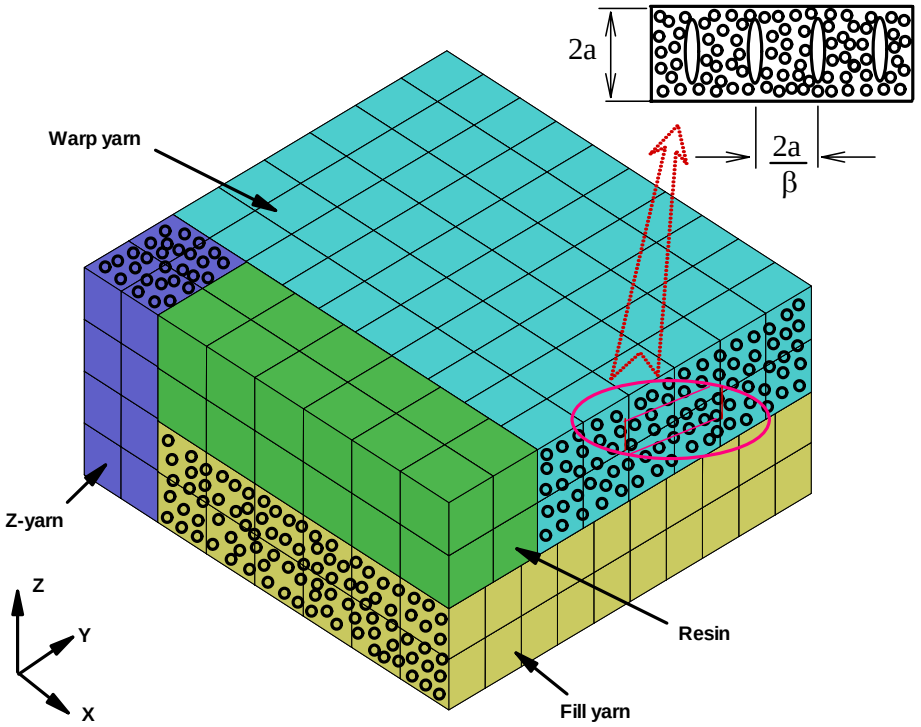

Figure 6.10: The unit cell model of 3-D orthogonal woven fabric with small diameter fibers and slit cracks.

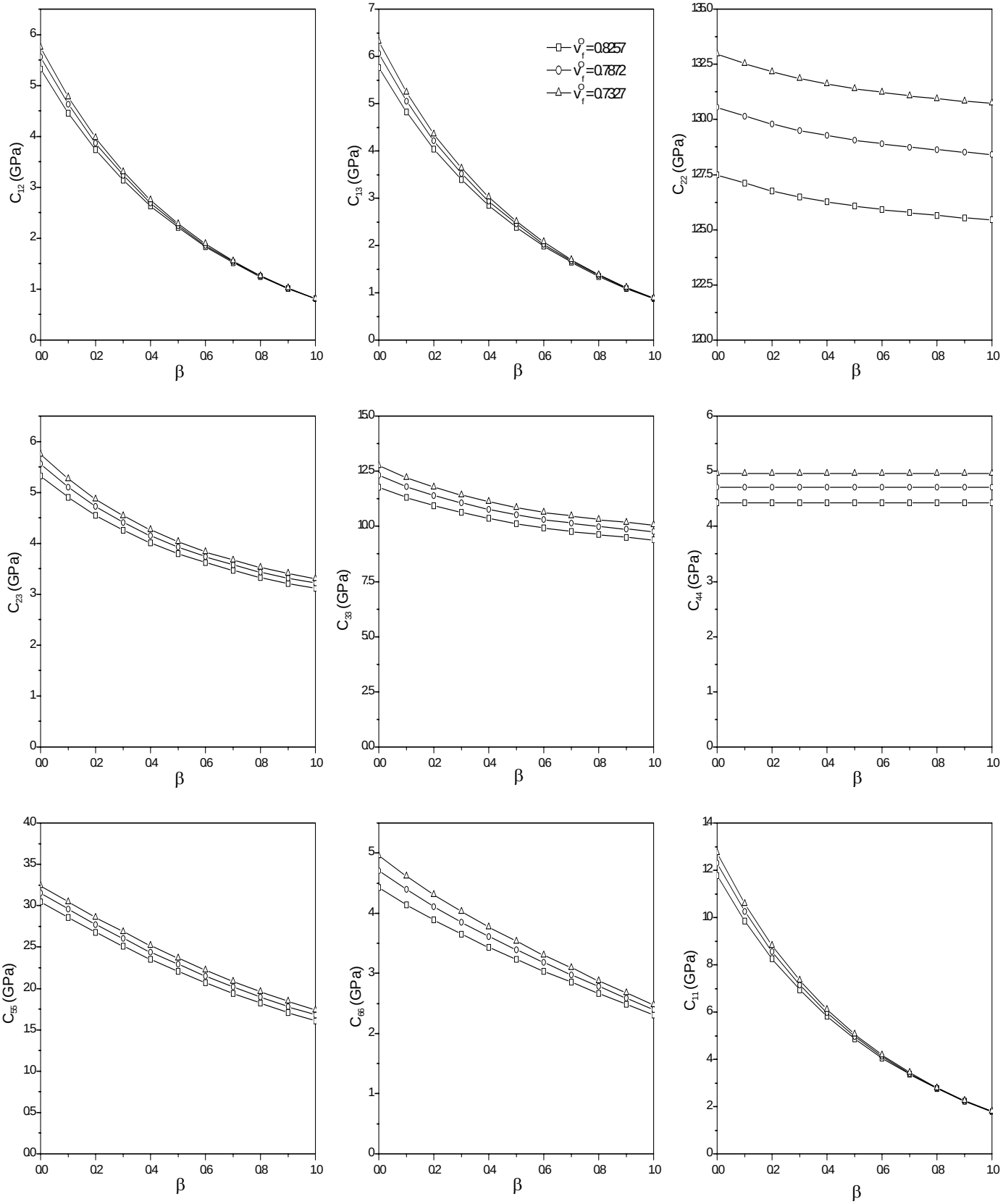

Figure 6.11: Fill yarn stiffness reduction of 3-D orthogonal woven textile with longitudinal slit cracks.

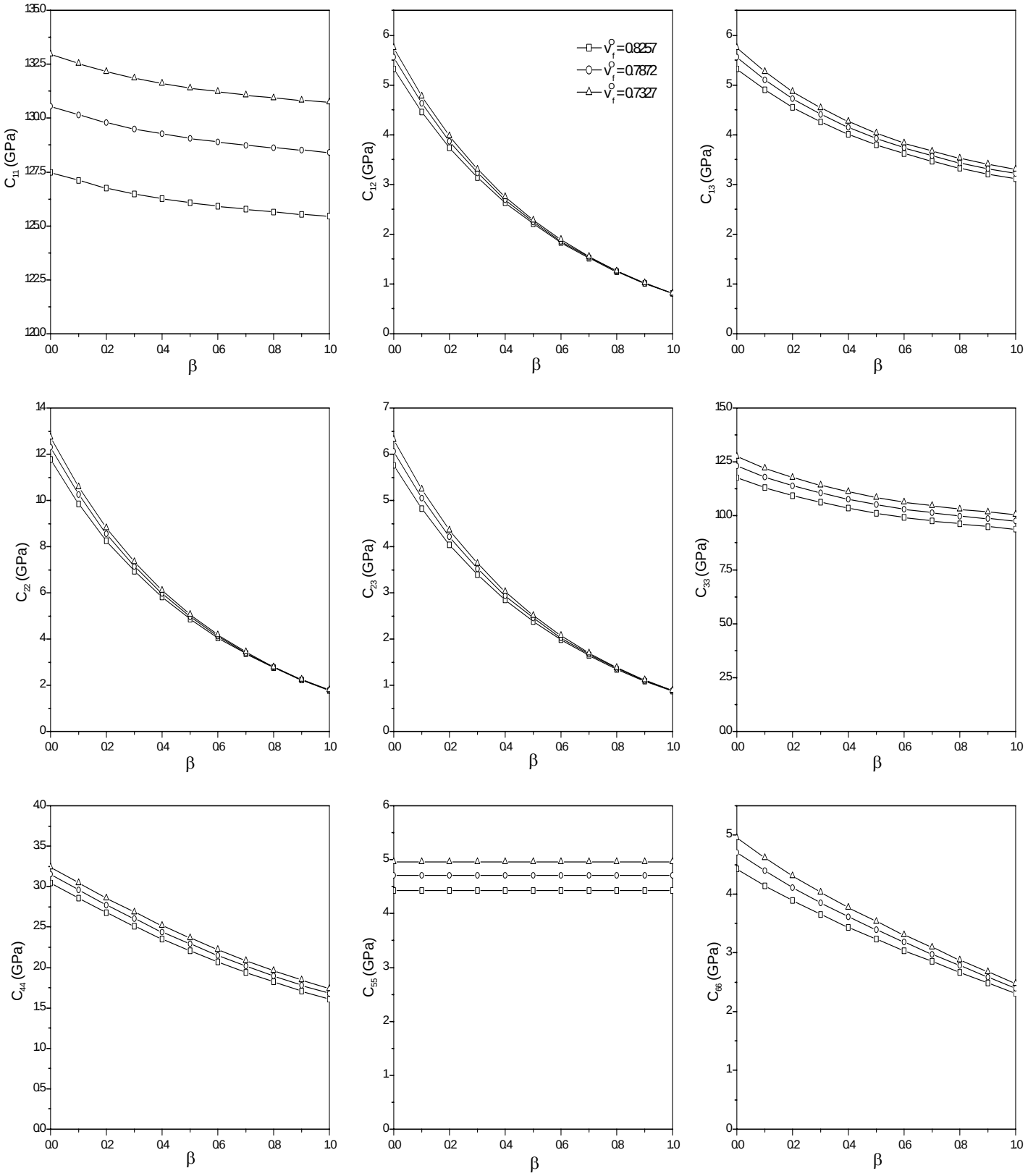

Figure 6.12: Warp yarn stiffness reduction of 3-D orthogonal woven textile with longitudinal slit cracks.

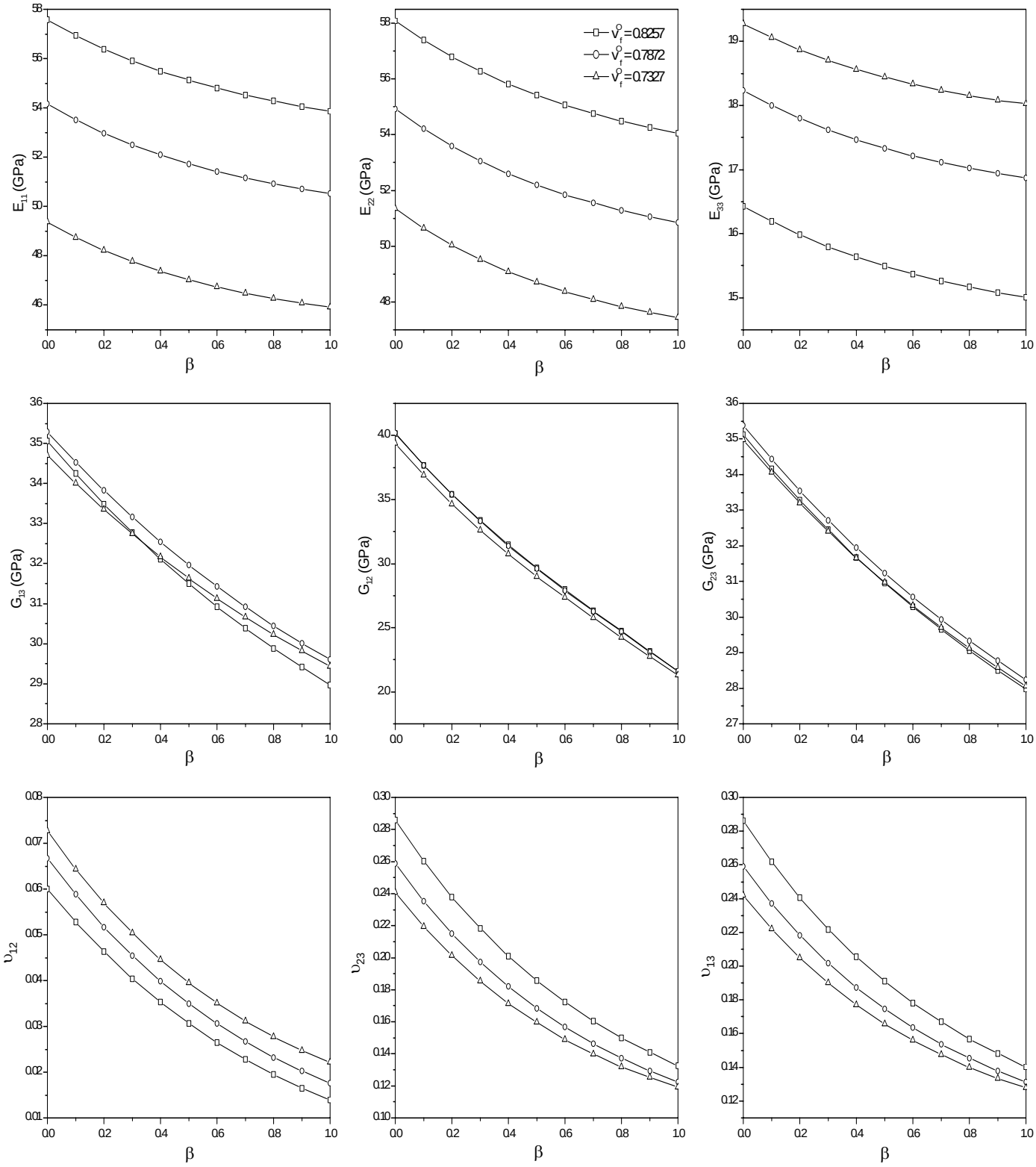

Figure 6.13: Degraded modulus of 3-D orthogonal woven textile with a variety of crack densities and volume fractions.

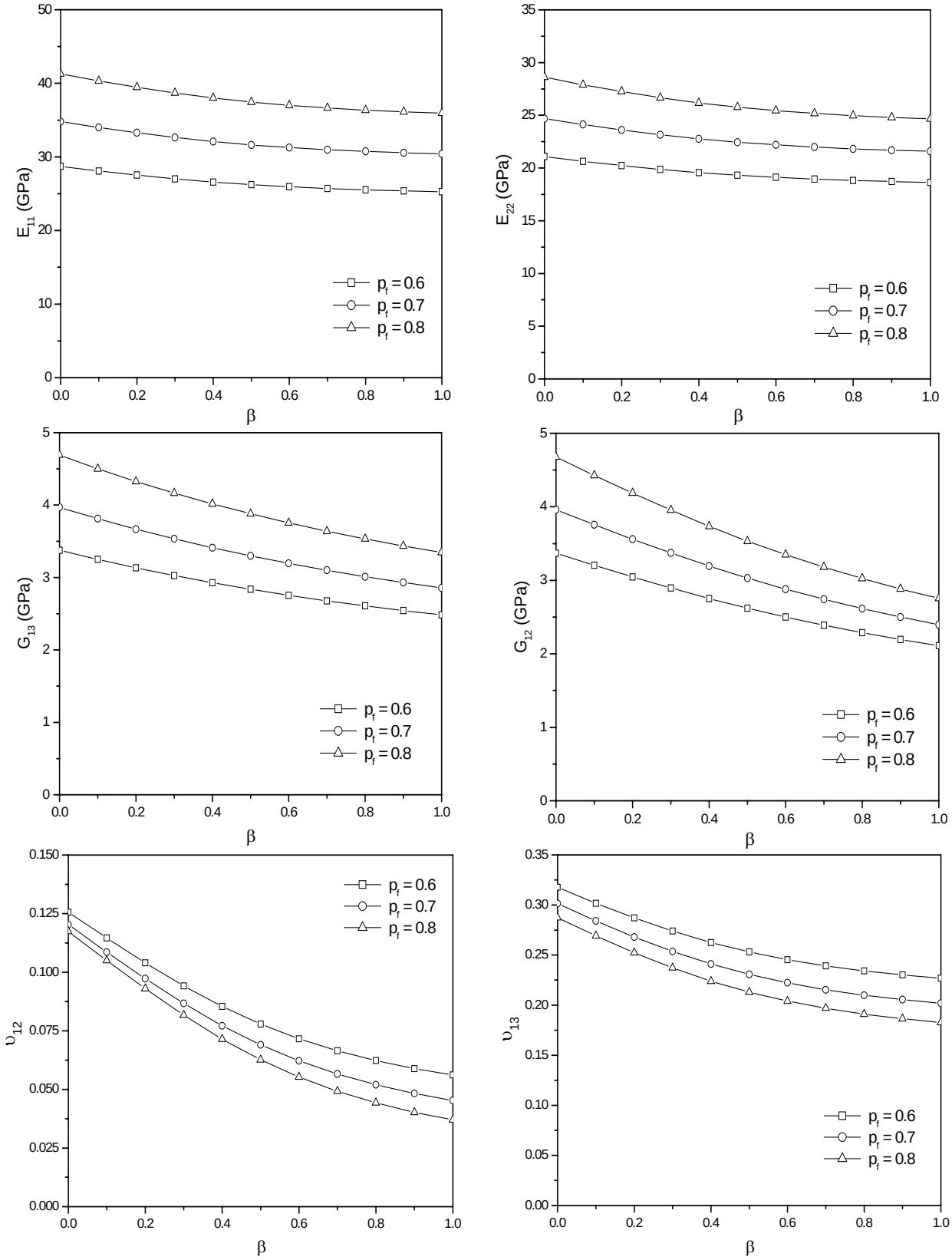

Figure 6.14: The degraded elastic modulus with various crack densities and packing factors.

6.7 Micro-Crack Modeling for Plain Woven Textile Composite

In Chapter 2, the 2-D plain weave is modeled, and a numerical constitutive model to calculate effective moduli is developed. However, the constitutive model does not consider the micro-crack problem in the yarns. In order to apply a damage crack model in the general structural analysis programs, such as ABAQUS, we have to define the material properties and three-dimensional geometry of the yarns, and implement a failure mechanism scheme in the textile composites. To form the yarn shapes, we develop Fortran programs for mesh generations. The developed Fortran code is based on the geometrical parameters, introduced in Chapter 2, as input. Different geometrical shapes for the plain weaves are easily modeled by changing the geometrical parameters. The present study considers two main aspects to analyze the degraded strength of the plain woven textile composite: (i) Sine Function Model I (SFM I) and (ii) the development of a UMAT subroutine for use in ABAQUS. The SFM I is used to generate a mesh of three-dimensional solid-elements consisting of 8-nodes in the ABAQUS, along with a UMAT subroutine, to perform the finite element analysis of the plain-weave composites.

In the first step, the previously presented Sine Function Model I is considered to form the RUC shape that consists of two sets of warp, fill yarns and resin layers, see Chapter 2. The coordinates of the nodes in the RUC are calculated by the mesh generation code developed here and imported to the ABAQUS as an input file and also combined with the user defined material subroutines, called UMAT, to calculate the three-dimensional equivalent moduli. The second step is to calculate the degraded material properties for the plain weave having transverse micro-cracks. Next, the degraded stiffness of the yarns and matrix is calculated from the yarn and resin elements at Gaussian integration points in the UMAT subroutine. For the elastic modeling of the composites, the Rule of Mixture and the Self-Consistent method are respectively used. By comparing the predictions, we can estimate which method is more effective to solve the cracked textile composites. The Self-Consistent method is based on the averaged stress and strain fields in the fibers with inclusions (micro-cracks). The elastic properties are determined by the relationships between the un-cracked stress and strain and the homogeneous cracked stress and strain. In these two methods, we have considered the transverse matrix cracking with a crack density scheme to represent the crack and generate the degraded elastic moduli in the cracked elements. And the damaged elements (fill and warp yarns, matrix) are found by using a failure criterion and ultimate strengths of materials. Here, the stresses of un-cracked properties and the current stresses of degraded properties are used to find the failure elements at the Gaussian integration points within each element. The corresponding damaged properties are calculated by the degradation factors for Poisson's ratios and elastic moduli as shown in Tables 6.8-6.9, and compared with those presented in Ref. [6.6]. All these steps are carried out until no more failed elements were found in the RUC and then, the computations were terminated. These steps are described in a flowchart presented in Figure 6.15.

6.8 Material Non-linearity of Yarns

In the textile composites, the properties of the fiber and matrix are dependent on constitutive equations; because their transformation matrices have different values along the centerline of the yarn paths, for example, rotation angles and crimp angles. As the yarns are subjected to an increasing load, the fiber and resin undergo various deformations. Also, there are changes in the material properties of the yarns. Furthermore, we need to incorporate a micro-modeling to determine stiffness of the yarns that can be obtained by the knowledge of the current deformations of both the fiber and the matrix in the yarns. This means that the micro-modeling of the textile yarns must consider micro-level strengths under the loads transferred to the micro-level. To determine the micro-level stress and strains, we used the Gauss integration points in an element of an RUC as the points where nonlinear material models will be used. The UMAT subroutine in ABAQUS program that can include the non-linear shear stress-strain relationship for the matrix, Romberg-Osgood equation, is used. The Romberg-Osgood equation for a matrix material is given as:

$$\varepsilon_{ij} = \varepsilon_{ij}^{e} + \frac{b}{2G}\left(\frac{\tau_e}{\tau_0}\right)^{n-1} s_{ij} = \varepsilon_{ij}^{e} + \varepsilon_{ij}^{p} \tag{6.11}$$

Here, ε_{ij}^{e} and ε_{ij}^{p} are the elastic and the plastic strains, respectively and s_{ij} are the principal deviatoric stresses given by $s_{ij} = \sigma_{ij} - (\sigma_{kk}/3)\delta_{ij}$. The octahedral stress is $\tau_e = \sqrt{s_{ij}s_{ij}/2}$ and the shear modulus for the matrix is G. The variables b, τ_0 and n are constants dependent on the matrix materials.

One simple micro-model for unidirectional composite was suggested by Sun and Chen[6.7]. Sun and Chen[6.7] assumed that the fiber is linearly elastic, while the matrix to be a nonlinear isotropic material. In Ref. [6.7] it was also assumed that the matrix behaviors in the unidirectional composites follow the power law and the J_2-flow rule[6.7], to represent plastic behavior. In this research, the power law[6.7] is used to describe the relation between the effective matrix stress, $\bar{\sigma}$ and the effective matrix plastic strain, $\bar{\varepsilon}^{p}$,

$$\bar{\varepsilon}^{p} = \beta(\bar{\sigma})^{n} \tag{6.12}$$

In Eq. (6.12), the parameters, (β and n) of the power law are generally obtained from the experimental data for the case of uni-axial stress-strain behavior of the matrix. Values for these material parameters have been suggested in the literature. Blackketter[6.6] *et al*. provided these parameters for Epoxy 3501-6. Kollegal and Sridharan[6.8-6.9] used the experimental parameters (β and n) of E-glass/Epoxy to determine the plain woven fabric's stress-strain behavior. Here we use these same values of parameters (β and n) as suggested in Ref. [6.7], to represent the nonlinear constitutive behavior of the matrix. For the matrix non-linearity, a UMAT subroutine in the ABAQUS program is developed to obtain this micro-level stress and strains in the degraded yarns.

6.9 Stress and Strain in ABAQUS UMAT Subroutine

This current damage analysis consists of two steps; (i) the first step involves a micro-mechanical implementation of cracked composite materials in the yarns, (ii) the second step involves an ABAQUS structural analysis with a UMAT subroutine supplied by us. The first part determines the degraded modulus of the cracked textile yarns by using the crack density scheme and micro-mechanical equations. In the second part, the UMAT subroutine determines the progressive failure element using current stress components and failure criterion.

UMAT is a user-written material subroutine in Fortran language to allow users to define a material's mechanical behavior for use in ABAQUS. In the UMAT, the material Jacobian matrix, $J = \partial\Delta\sigma/\partial\Delta\varepsilon$, is used to define the change of the stress and strain components at the end of load increments. Here, $\Delta\sigma$ and $\Delta\varepsilon$ are the stress increments and the strain increments, respectively. Current stress components at each increment are updated by the previous stress, current strain and Jacbian matrix, such as $\sigma_i = \sigma_{i-1} + J_i\Delta\varepsilon_i$, ($i$ = the number of displacement increments). Another variable, STATEV called solution-dependent state variable, in the UMAT subroutine is defined to store failure states of the material points. In the STATEV, four failure types are stored: (i) no failure, (ii) matrix failure, (iii) single fiber failure, and (iv) ultimate failures. The STATEV information on the warp and fill yarn failure contain these four failure states, such as STATEV (1 or 2) = 1, 2, 3 and 4. The flowchart for UMAT Implementation in the ABAQUS is described in Figure 6.15.

6.10 Failure Criteria

A small size element of the yarn is needed to analyze the failure because each fill or warp yarn in the RUC has various undulation regions. The small size element of the yarn is treated as a unidirectional laminate block with transversely isotropic properties, but the element has various crimp angles. Based on this assumption, a laminated composite failure theory to calculate material failures is applied for the fill and warp yarns. The fill and warp yarns are modeled by several undulation regions and each region has

several small elements, three-dimensional 8-node elements. Each element has material points, Gauss-integration points, to check for damages.

In the present analysis, the stresses calculated from the Gauss-integration points are applied into failure criteria for the fiber and the matrix. If a failure is detected, the reduction of material properties is introduced into linearized elastic stiffness coefficients for the failure element. As the initial elastic properties are multiplied by appropriate degraded factors at each Gauss-integration point, the reduced values of moduli of fiber and matrix are obtained. Selected degradation factors of elastic and Poisson's ratios are listed in Tables 6.8-6.9. Tsai-Wu failure criteria in terms of local stresses and von Mises criterion is used to predict failure in the fill and warp yarn's elements throughout the RUC. The failure criterion is as follows;

$$F_i\sigma_i + F_{ij}\sigma_i\sigma_j = 1 \tag{6.13}$$

Here i , j =1,2,…,6 and F_i and F_{ij} are strength parameters of Tsai-Wu failure criteria. If the value of the left side of Eq. (6.13) exceeds 1, the failure occurs. Due to the difficulty in obtaining the out of plane parameters, F_{ij} , here the Tsai-Wu failure criterion is used. If only the in-plane components are considered:

$$F_1\sigma_1 + F_2\sigma_2 + F_{11}\sigma_1^2 + F_{22}\sigma_2^2 + F_{66}\sigma_{66}^2 + 2F_{12}\sigma_1\sigma_2 = 1 \tag{6.14}$$

The strength parameters are given as function of the material strengths:

$$F_{11} = \frac{1}{X_t X_c} \quad F_{22} = \frac{1}{Y_t Y_c} \quad F_1 = \frac{1}{X_t} - \frac{1}{X_c} \quad F_2 = \frac{1}{Y_t} - \frac{1}{Y_c} \quad F_{66} = \frac{1}{S^2} \tag{6.15}$$

and the F_{12} term is estimated by a combined stress, such as the von Mises criterion $F_{12} = -0.5/\sqrt{X_t X_c Y_t Y_c}$. The material strengths for the yarns: X_t , X_c , Y_t , Y_c and S are the tensile strength in the fiber-direction, the compressive strength in the fiber-direction, the tensile strength in the transverse-direction, the compressive strength in the transverse-direction and the in-plane longitudinal shear strength, respectively. The reduced stiffness for the cracked yarns in the local coordinates is obtained from the initial material properties considered by the crack density values and an iterative scheme[6.10].

6.11 Progressive Failure Analysis

Progressive failure models for the plain weave are analyzed under three modes of in-plane loadings. The displacement control loading in tension, compression and in-plane shear is used in the ABAQUS program. Here two types of plain-woven composites are considered: AS4 Carbon fiber and 3501-6 Epoxy resin[6.6], E-Glass/Epoxy resin[6.11]. Their material properties and geometrical dimensions are listed in Tables 6.10-6.13. The material strengths for the yarns; X_t , X_c , Y_t , Y_c and S are obtained from the ultimate strengths shown in Tables 6.14-6.15. Next the Tsai-Wu failure criterion is applied to Eqs. 6.14-6.15. After finding the strength parameters, F_{ij} , the UMAT subroutine calculates the failure states.

This study uses the boundary conditions of Repeating Unit Cells to develop three in-plane load cases: tension, shear and compression. Displacement controls are applied to x and y -axes and in-plane displacements are applied along these axes. For the in-plane cases, the symmetric and anti-symmetric boundary conditions are considered in the RUC of Figure 6.16. When extensional loads are applied for the x - y axes, the symmetry conditions are needed, and when the repeating unit cell is subjected to the in-plane shear loads, the anti-symmetric conditions are used. For the in-plane loading cases, Kollegal and Sridharan[6.8-6.9] described symmetric and anti-symmetric boundary conditions of quarter unit cell in the plain weaves. To specify these boundary conditions, one RUC of the plain weave, center-nodes along the x - y axes and top-bottom nodes are considered. The boundary conditions of the degraded RUC include two cases: the in-plane tension/compression case and the shear case.

(i) Boundary conditions for the in-plane tension/compression case

- Nodes on the plane $x = 2u_2$: $u(2u_2, y, z) = u_0 / 2$ (prescribed displacements)
- Nodes on the plane $y = 2u_1$: $v(x, 2u_1, z) =$ uniform
- Nodes on the plane $z = 0$ and $z = H$: $w(x, y, H) = w(x, y, 0)$
- Nodes on the plane: $x = 0$

$u(0, y, z) = -u(0, y, -z)$, $v(0, y, z) = v(0, y, -z)$, $w(0, y, z) = -w(0, y, -z)$

- Nodes on the plane: $y = 0$

$u(x, 0, z) = u(x, 0, -z)$, $v(x, 0, z) = -v(x, 0, -z)$, $w(x, 0, z) = -w(x, 0, -z)$

(ii) Boundary conditions for the in-plane shear case

- Nodes on the plane $y = 2u_1$: $u(x, 2u_1, z) = u_0 / 2$ (prescribed displacements), $w(x, 2u_1, z) = 0$
- Nodes on the plane $x = 2u_2$: $v(2u_2, y, z) = v_0 / 2$ (prescribed displacements), $w(2u_2, y, z) = 0$
- Nodes on the plane: $x = 0$

$u(0, y, z) = -u(0, y, -z)$, $v(0, y, z) = v(0, y, -z)$, $w(0, y, z) = -w(0, y, -z)$

- Nodes on the plane: $y = 0$

$u(x, 0, z) = u(x, 0, -z)$, $v(x, 0, z) = -v(x, 0, -z)$, $w(x, 0, z) = -w(x, 0, -z)$

6.12 Results of Progressive Failure Analysis

After simulating UMAT of ABAQUS and crack density scheme, pertinent results are obtained. The results for two plain woven composites are given in Figures 6.17-6.29, and our results are compared with those appearing in the literature, see Tables 6.16-6.17.

(1) Uni-axial tensile loading: The results for tensile stress-strain curves, Figures 6.17 and 6.22, show good agreement with the results given in Refs. [6.6 and 6.11], and the stress-strain curves for the damaged composite show a decreased stiffness as the crack density increases. The same trend using Self-Consistent method case was found. For the plain weave subjected to the uni-axial tensile loading, the initial failure was obtained in the elements of the flat parts of transverse yarns due to σ_{11}. The damage, due to high value of σ_{11}, was initiated in the tip region rather than in the region with the maximum thickness, and propagated towards the crimp region. Also, the region around the maximum thickness of the longitudinal yarns adjacent to the inter-lamina matrix elements were damaged due to high value of σ_{33}, and this damage propagated towards the other elements of the longitudinal yarns, which was the predominant damage mode. Finally, the inter-lamina matrix elements were damaged due to σ_{33}. In these two cases (AS4 Carbon/Epoxy and E-Glass/Epoxy), only the E-Glass/Epoxy plain weave shows "knee" problems in the tension stress vs strain response using the Self-Consistent method, see Figure 6.22. This means that AS4 Carbon/Epoxy has a higher strength than the E-Glass/Epoxy along the warp-direction. We found that the sequence of failures in these two cases when subjected to a tensile loading. The first failure mode is a transverse tensile failure in the fill yarns and the second failure mode of matrix is seen in the fill yarns in which stress-concentration is present in in-plane shear direction. The third failure mode is a matrix failure in tension in the warp yarns and the fourth is a matrix failure in out-of-plane shear in the fill yarns. And finally, the fiber failure in the warp yarns occurs in tension direction.

(2) In-plane shear loading: The in-plane shear stress-strain curves in Figures. 6.18 and 6.23 show good results compared to the values of Refs.[6.6 and 6.11], and the degraded stress-strain curves for the case of the shear show the same trends as the uni-axial tensile case does, with increasing the crack density. The initial failure was observed in the crimp parts' region of the longitudinal yarns due to the high values of σ_{66}. The damage was, once again, initiated at the tip region and is propagated towards the region with the maximum thickness. A transverse yarn had the same type of damage as that in the longitudinal yarn, again, due to high value of σ_{66}. The damage in both the longitudinal yarn and the transverse yarn

occurred almost at the same displacement load. These are the prime damage modes. Later, the matrix elements around the two edges were damaged due to σ_{66}. The sequence of failures is found in these two cases under shear modes. The first failure mode is the failure of the matrix in the fill yarns and the second is the failure of the matrix in the warp yarns. The third failure mode is that of the matrix in the fill yarns due to transverse tension, and finally the matrix failure of the warp yarns is seen in the in-plane shear direction.

(3) In-plane compression loading: The compression stress-strain curves dependence is shown in Figures 6.19 and 6.24. However, due to lack of available results, these results can not be compared to any in the existing literatures. The degraded stress-strain behavior reveals a reduced strength as the crack density increases. The same trends using Self-Consistent method case were found as shown in Figures 6.19 and 6.24. In both these cases, these materials exhibit significant non-linearity, in stark contrast to the tensile cases. Obviously, this is due to the combined influence of geometric non-linearity and material damage. The E-Glass/Epoxy plain weave exhibits greater "ductility" in that it exhibits greater softening and fails at the higher strains than the AS4 Carbon/Epoxy plain weave. Finally, the fiber failure is due to the failure of the composite in the warp yarns due to their micro-buckling. From these two cases of compression loading, we see that the compression failure mode is found in the warp and fill yarns at the same loading point.

To find an appropriate-simple damage model of plain weaves, a user of the UMAT subroutines in ABAQUS should think of mesh alignments and appropriate shapes for the fill and warp yarns, because the mesh shapes will affect results for the small size elements of textile composites. For example, the mesh sizes and shapes for the fill and warp yarns along the cross-sectional area will have different load values corresponding to failure. Also exact parameters (β and n) related to effective matrix plastic strain $\bar{\varepsilon}^{p}$, have to be found to get correct damaged strengths. The results of this study will be needed for comparing to numerical damage results[6.8-6.9] suggesting simple numerical damage models for the plain-woven textile composites. There is also a need of further studies of macro-damage models for plain-woven textile beam, plate and shell structures.

6.13 Discussion

We have developed a micro-mechanical model for cracked 2-D plain, 2-D braided and 3-D orthogonal woven textile composites and have extended these models to investigate the progressive failure of a Repeating Unit Cell (RUC) of these composites. The 3-D finite element model is used in the micro-mechanical damage analysis to find the damage modes in the RUC and the stress-strain curves in the presence of transverse cracks represented using crack density parameter. The homogenized elastic properties of the damaged RUC are calculated during each displacement increment in a micro-mechanical damage analysis. Although there is a general lack of experimental data to support the verification of the models in the micro-mechanical analysis, the results of this study were compared and shown to be in good agreement with whatever experimental results are available. However, a further study is necessary to establish the validity of damage models for plain weave textile composites and to determine a detailed behavior of the cracked textile composites. In this chapter, we have treated only continuous micro-cracking and static loading cases, not discontinuous cracking induced from transient dynamic loading. The discontinuous cracking and crack elements will be discussed in the following chapters.

Table6.8 Degradation factors for elastic modulus. (*: Out-of plane components in the stresses)

Failures	Materials	E_{11}	E_{22}	E_{33}	G_{12}	G_{23}	G_{13}
σ_1	All	0.01	-	-	0.01	-	0.01
σ_2	All	-	0.01	-	0.01	0.01	-
σ_3*	All	-	-	0.01	-	0.01	0.01
σ_{66}	Matrix	0.01	0.01	-	0.01	0.01	0.01
	Fill yarns	0.01	0.5	-	0.01	0.01	0.01
	Warp yarns	0.5	0.01	-	0.01	0.01	0.01
σ_{55}*	Matrix	-	0.01	0.01	0.01	0.01	0.01
	Warp yarns	-	0.5	0.01	0.01	0.01	0.01
	Fill yarns	-	0.01	0.01	0.01	0.01	0.01
σ_{44}*	Matrix	0.01	-	0.01	0.01	0.01	0.01
	Fill yarns	0.01	-	0.01	0.01	0.01	0.01
	Warp yarns	0.5	-	0.01	0.01	0.01	0.01

Table 6.9 Degradation factors for Poisson's ratios. (*: Out-of plane components in the stresses)

Failures	Materials	ν_{11}	ν_{22}	ν_{33}	ν_{12}	ν_{23}	ν_{13}
σ_1	All	0.01	-	0.01	-	-	-
σ_2	All	-	0.01	-	0.01	-	-
σ_3*	All	-	-	-	-	0.01	0.01
σ_{66}	Matrix	0.01	0.01	0.01	0.01	-	-
	Fill yarns	0.01	0.5	0.01	0.5	-	-
	Warp yarns	0.5	0.01	0.5	0.01	-	-
σ_{55}*	Matrix	-	0.01	-	0.01	0.01	0.01
	Warp yarns	-	0.5	-	0.5	0.01	0.01
	Fill yarns	-	0.01	-	0.01	0.01	0.01
σ_{44}*	Matrix	0.01	-	0.01	-	0.01	0.01
	Fill yarns	0.01	-	0.01	-	0.01	0.01
	Warp yarns	0.5	-	0.5	-	0.01	0.01

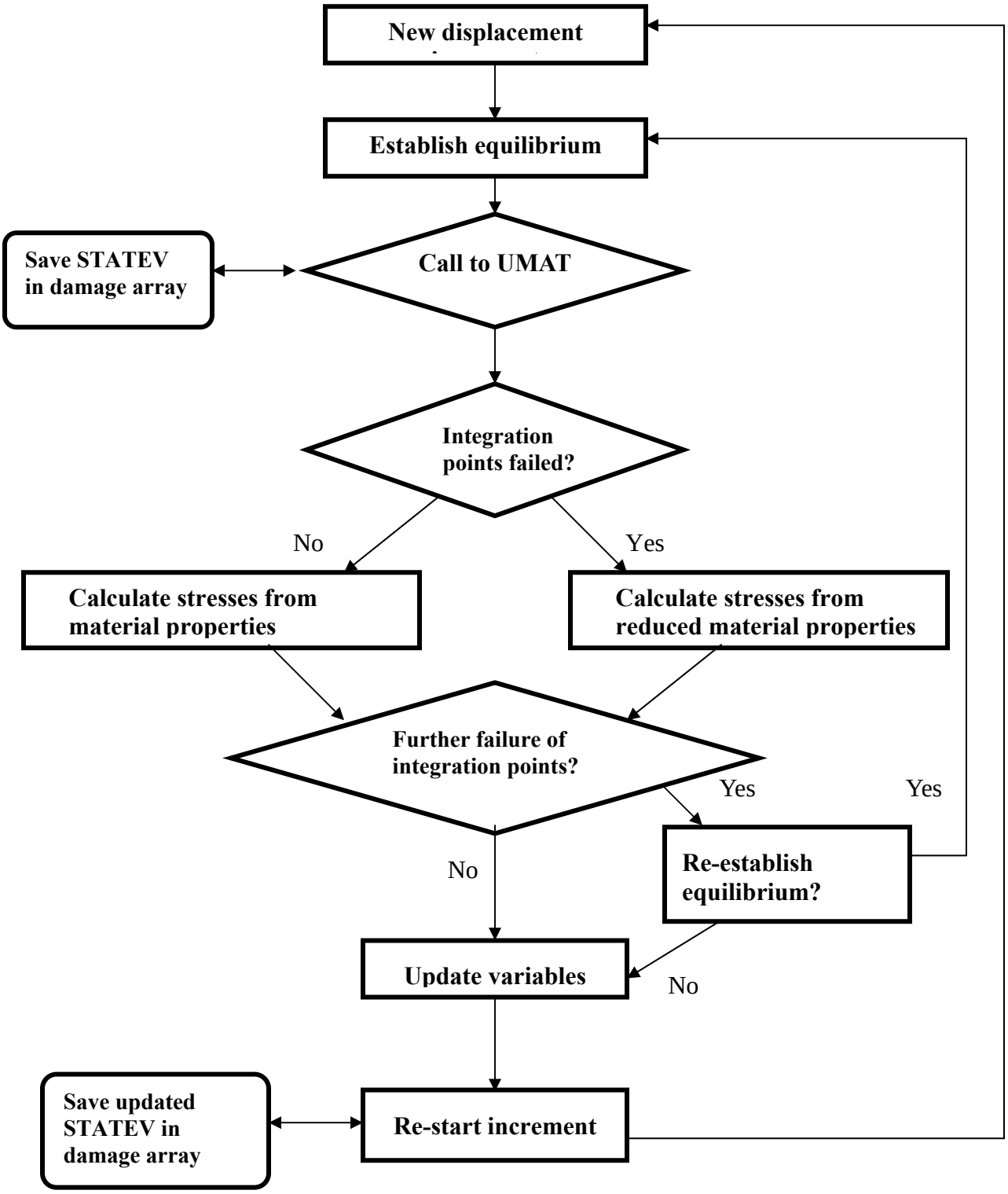

Figure 6.15: Flowchart for UMAT implementation in ABAQUS.

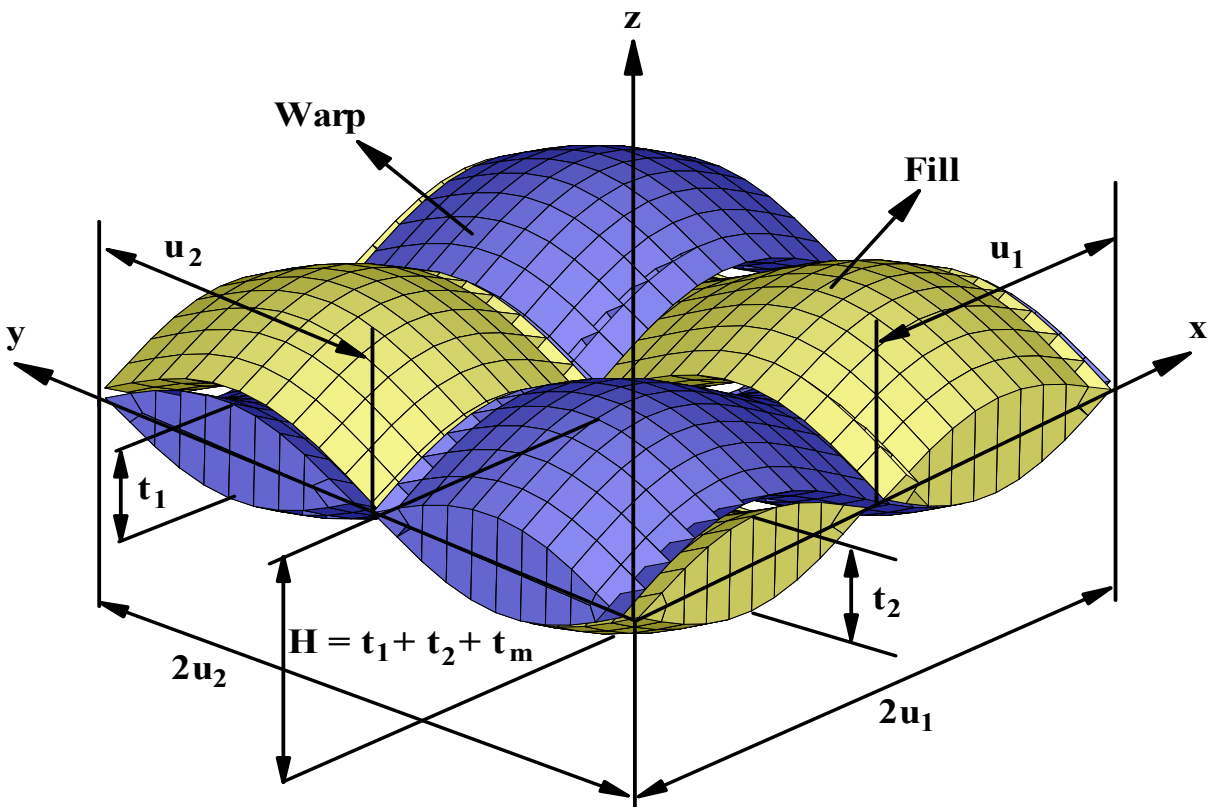

Figure 6.16: Geometry of Repeating Unit Cell in the plain weaves.

Table 6.10 The geometrical parameters of AS4 Carbon /Epoxy plain weave from Ref. [6.6]. (Unit: mm)

Material	$a_{1,2}$	$t_{1,2}$	g	t_m
AS4 Carbon / 3501-6 Yarns	1.0	0.04	0.00	0.001

Table 6.11 The mechanical properties of AS4 Carbon fiber and 3501-6 Epoxy from Ref. [6.6]. (Unit: GPa)

Material	E_{11}	E_{22}, E_{33}	G_{23}	G_{12}, G_{13}	ν_{12}, ν_{13}	ν_{23}
AS4 Carbon Fiber	221	13.8	5.5	13.8	0.20	0.25
3501-6 Epoxy	4.4	4.4	1.7	1.7	0.34	0.34
AS4 Carbon / 3501-6 Yarns	151	10.1	3.4	5.7	0.24	0.5

Table 6.12 The geometrical parameters of a plain weave from Ref. [6.11]. (Unit: mm)

Material	$a_{1,2}$	$t_{1,2}$	g	t_m
E-Glass fiber and Epoxy Yarns	0.752	0.1	0.00	0.001

Table 6.13 The mechanical properties of E-Glass fiber and Epoxy from Ref. [6.11]. (Unit: GPa)

Material	E_{11}	E_{22}, E_{33}	G_{23}	G_{12}, G_{13}	ν_{12}, ν_{13}	ν_{23}
E-Glass fiber	72.4	72.4	29.67	29.67	0.22	0.22
Epoxy	3.45	3.45	1.26	1.26	0.37	0.37

Table 6.14 The ultimate strengths of AS4 Carbon fiber and 3501-6 Epoxy from Ref. [6.6]. (Unit: MPa)

Material	S_{11}	S_{22}, S_{33}	S_{12}, S_{13}	S_{23}
AS4 Carbon Fiber	3585	400	1793	200
3501-6 Epoxy	159	159	110	110
AS4 Carbon / 3501-6 Yarns	2550	152	97	55

Table 6.15 The ultimate strengths of E-Glass fiber and Epoxy from Ref. [6.11]. (Unit: MPa)

Material	S_{11}	S_{22}, S_{33}	S_{12}, S_{13}	S_{23}
E-Glass fiber	2413	2413	1206.5	1206.5
Epoxy	103	103	89.6	89.6
E-Glass fiber and Epoxy Yarns	1108	7.5	22.4	5.45

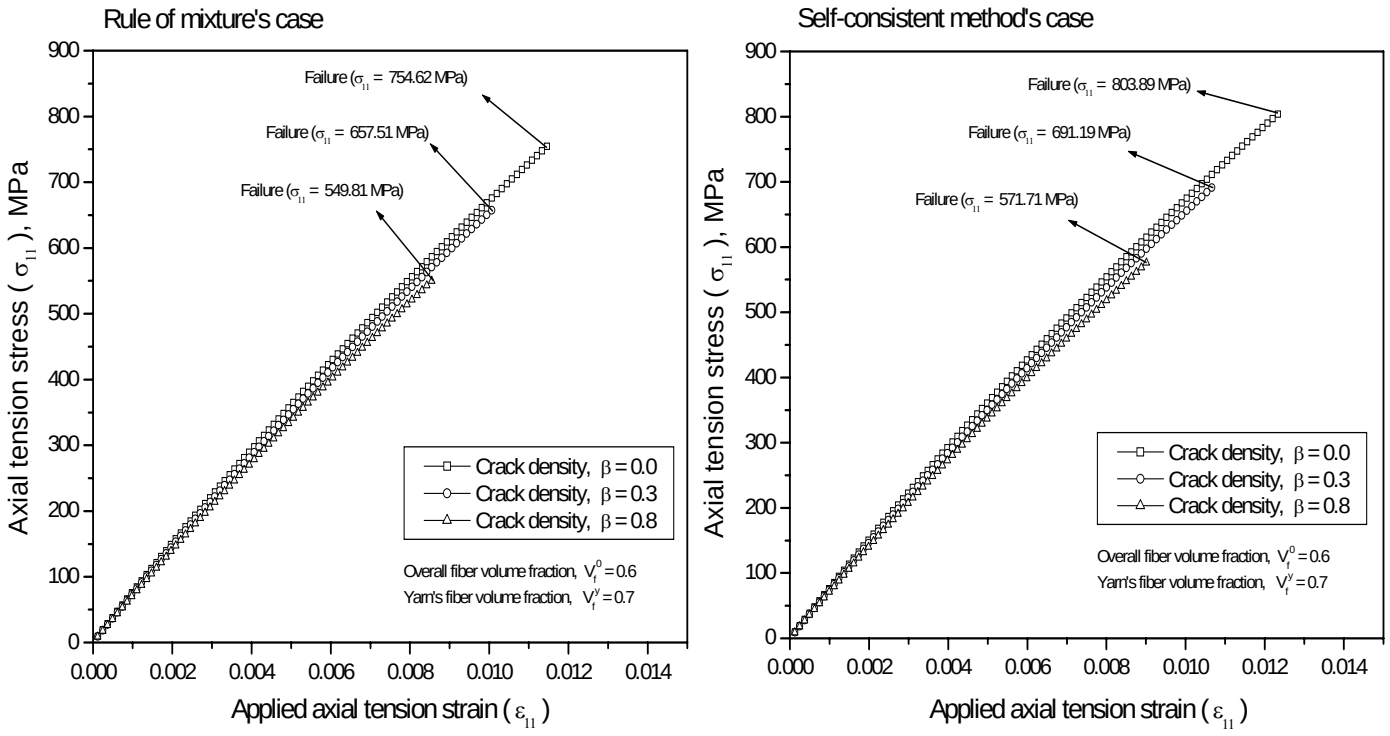

Figure 6.17: Tensile stress and strain curves for AS4-Carbon / Epoxy plain weave.

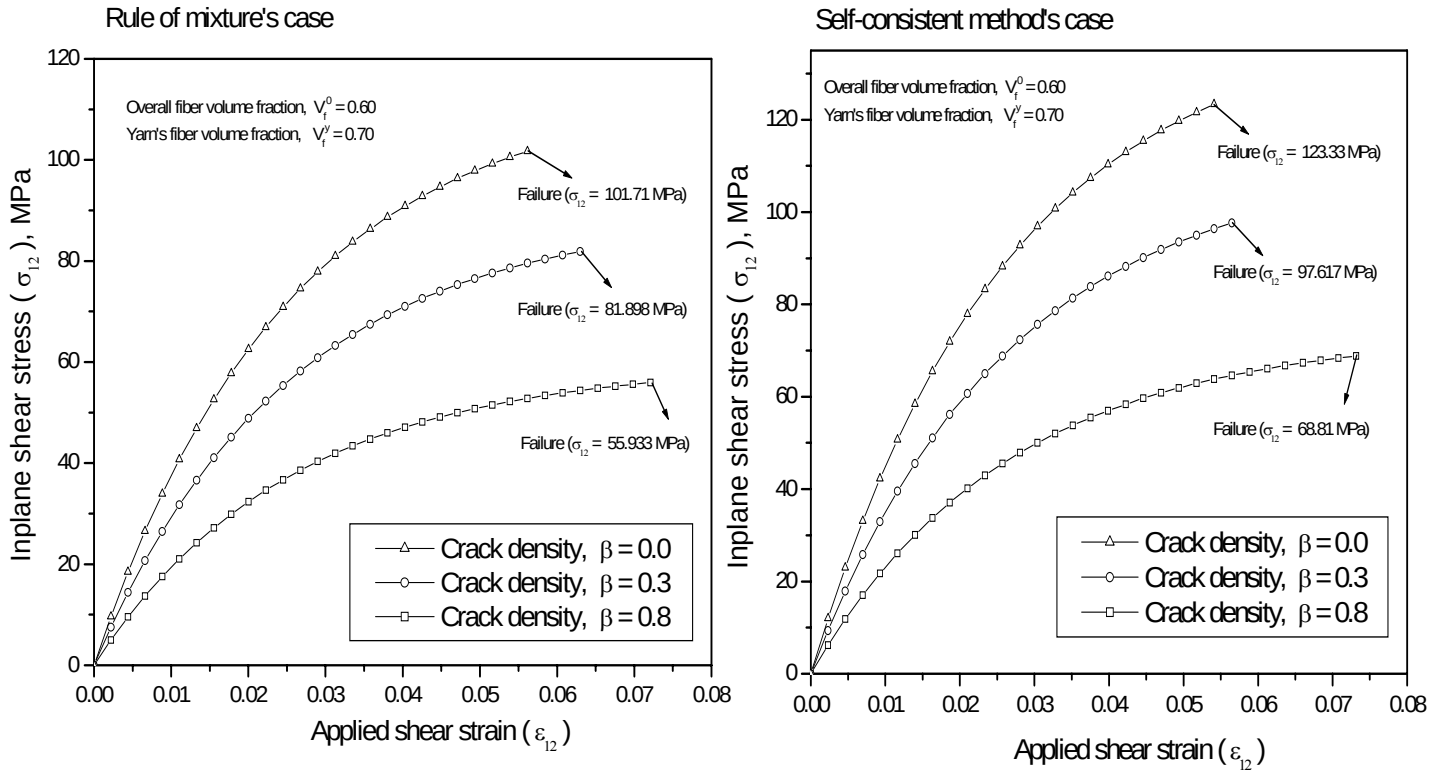

Figure 6.18: Shear stress and strain curves for AS4-Carbon / Epoxy plain weave.

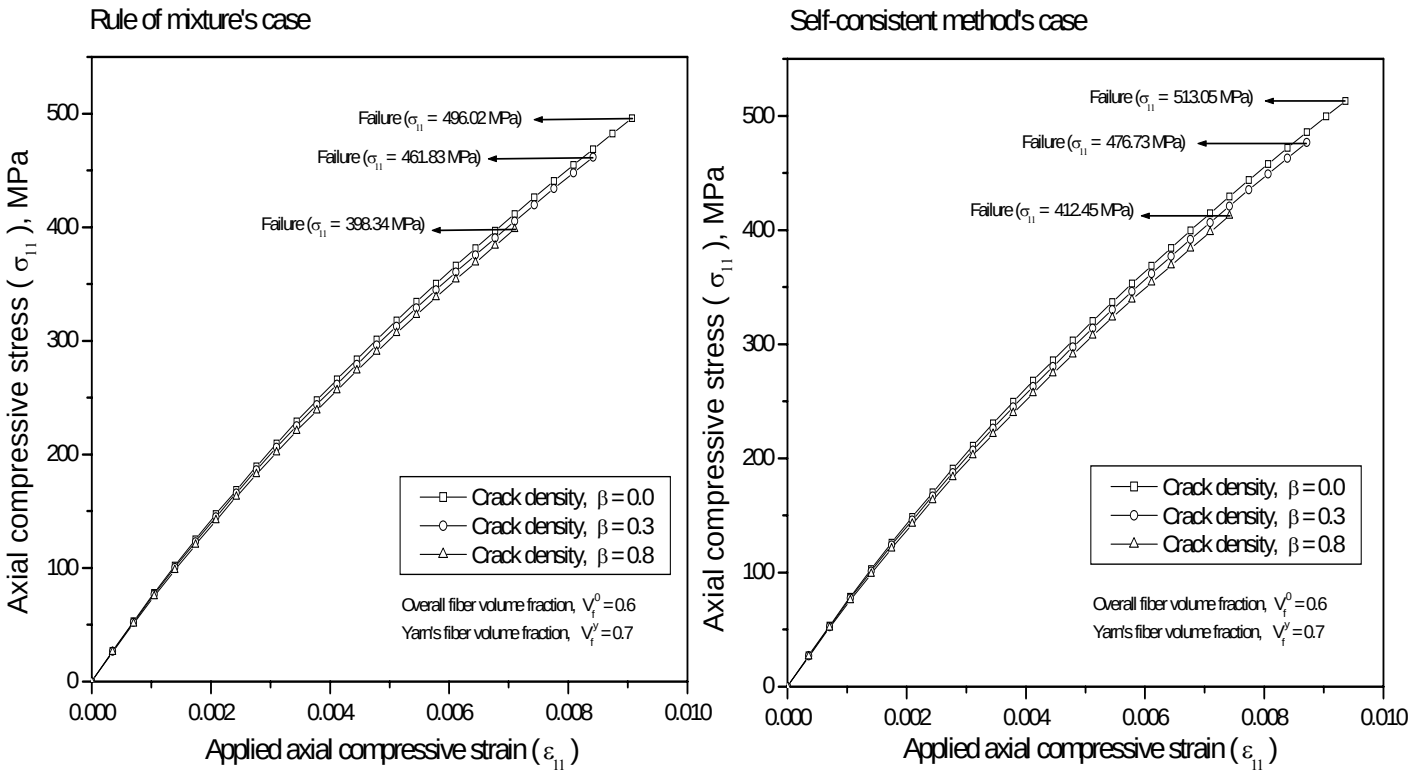

Figure 6.19: Compression stress and strain curves for AS4-Carbon / Epoxy plain weave.

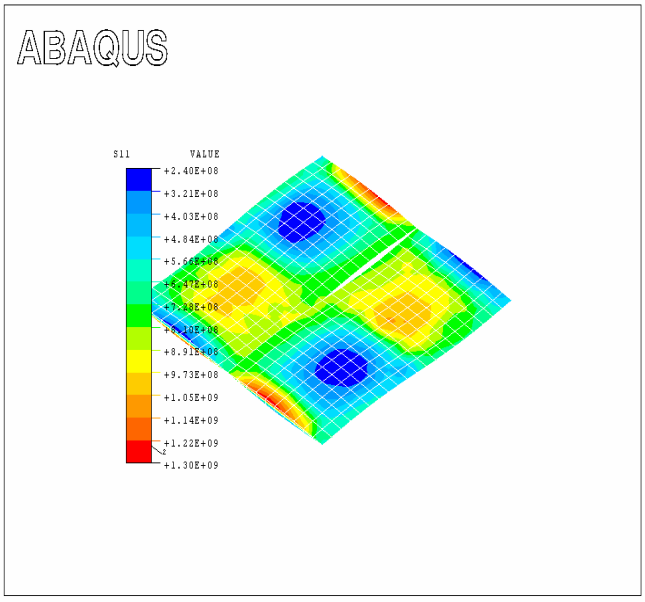

Figure 6.20: Tension stress of the warp yarns. (Rule of mixture $\beta = 0.0$ case)

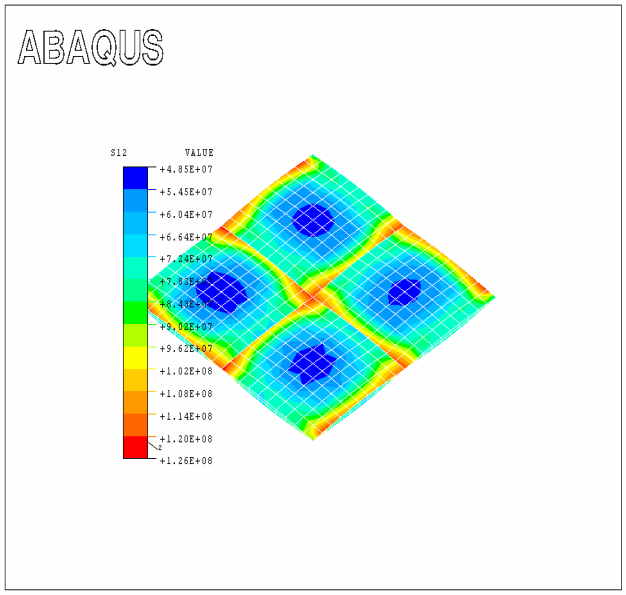

Figure 6.21: Shear stress of the fill and warp yarns. (Self-Consistent method $\beta = 0.0$ case)

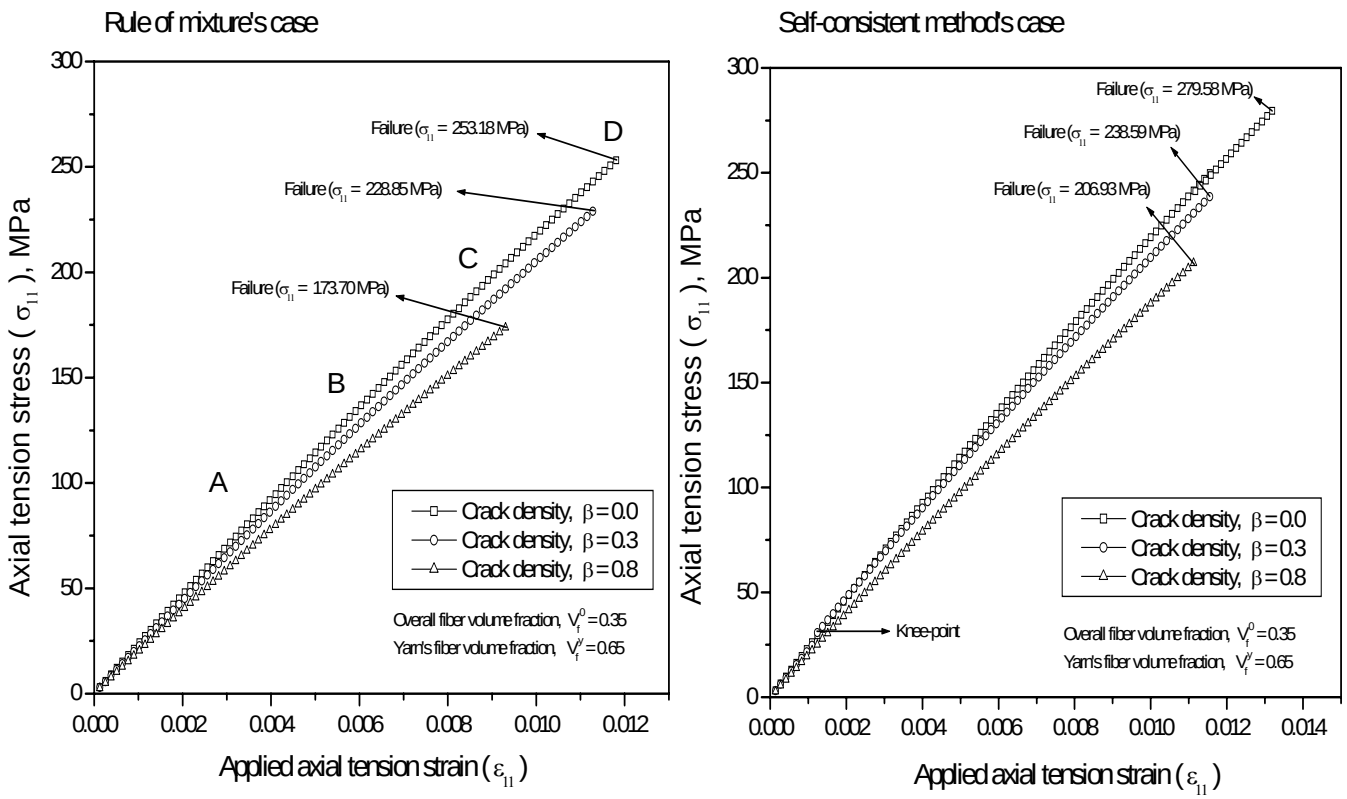

Figure 6.22: Tensile stress and strain curves for E-Glass / Epoxy plain weave.

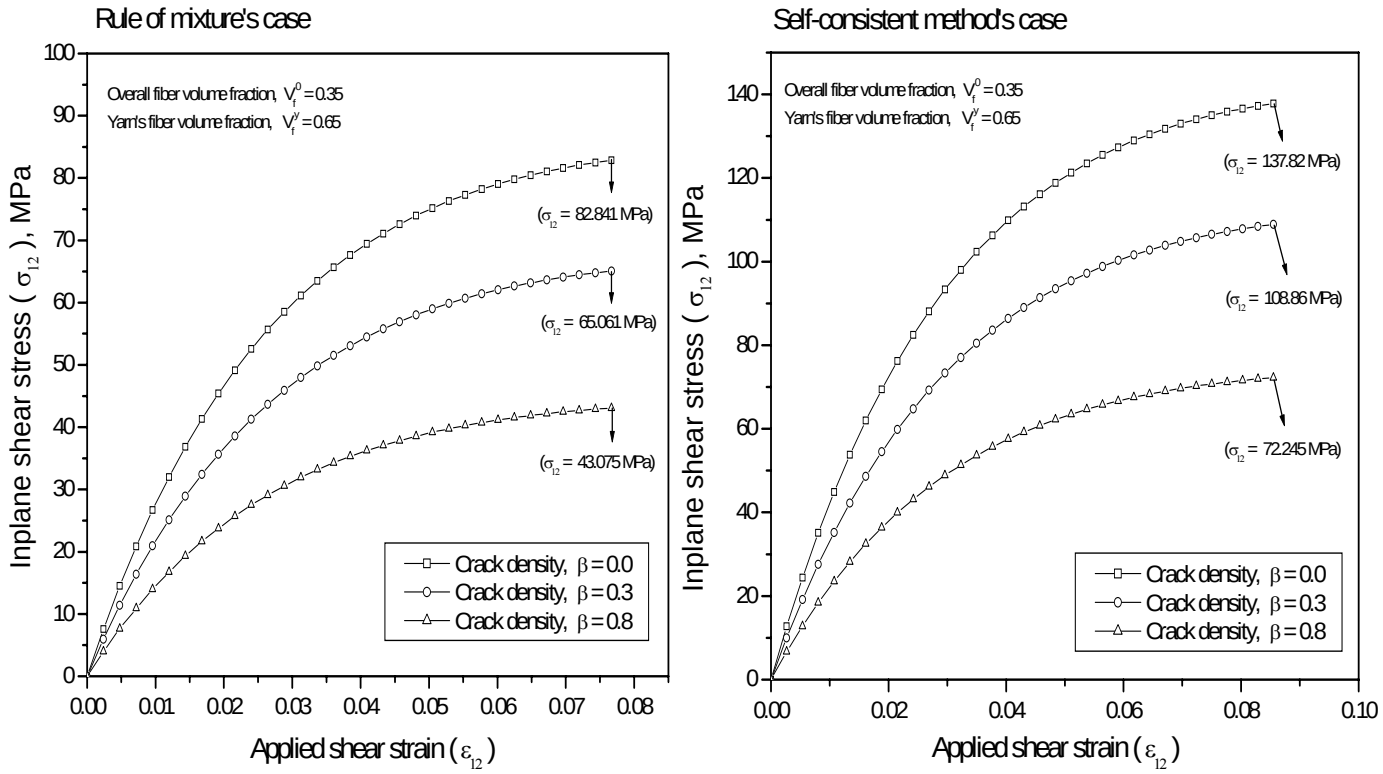

Figure 6.23: Shear stress and strain curves for E-Glass / Epoxy plain weave.

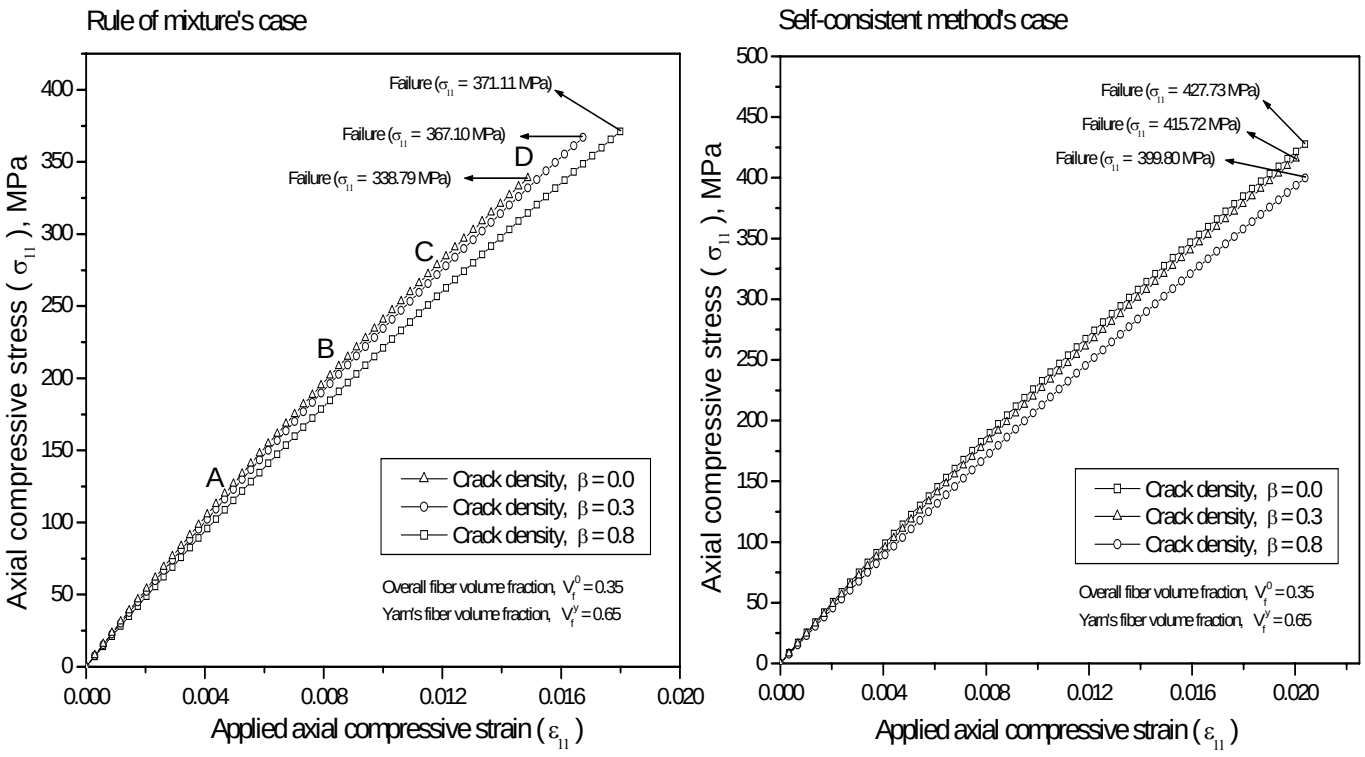

Figure 6.24: Compression stress and strain curves for E-Glass / Epoxy plain weave.

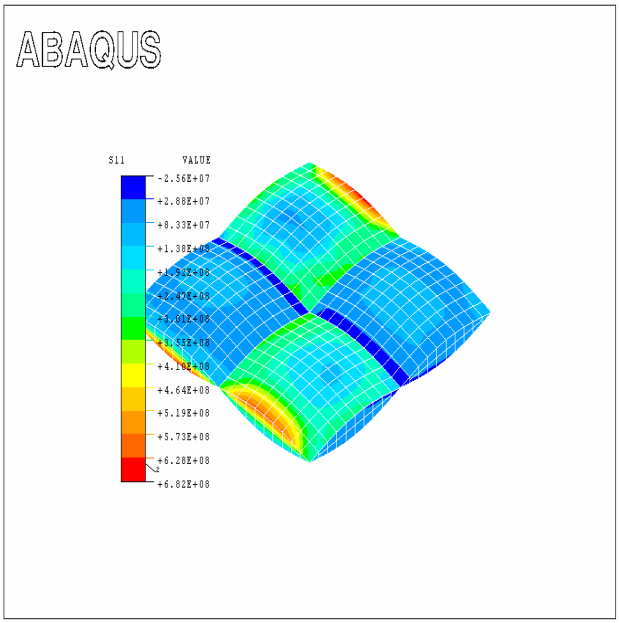

Figure 6.25: Tension stress of the fill and warp yarns. (Rule of mixture $\beta = 0.0$ case)

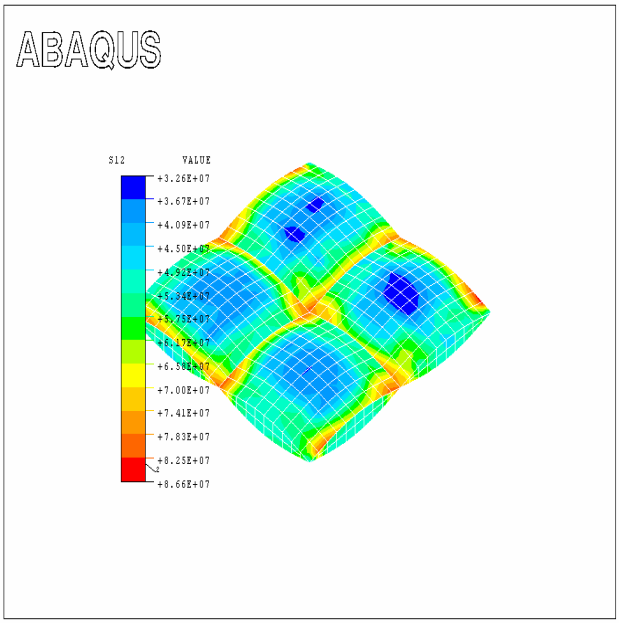

Figure 6.26: Shear stress of the fill and warp yarns. (Self-Consistent method $\beta = 0.0$ case)

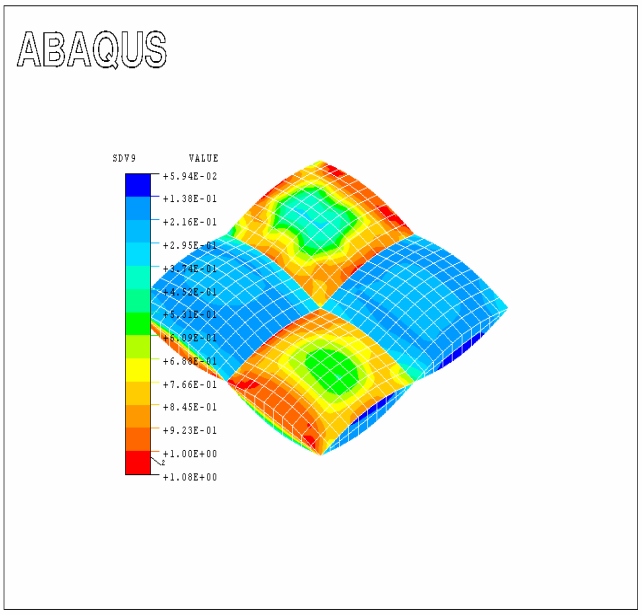

Point A

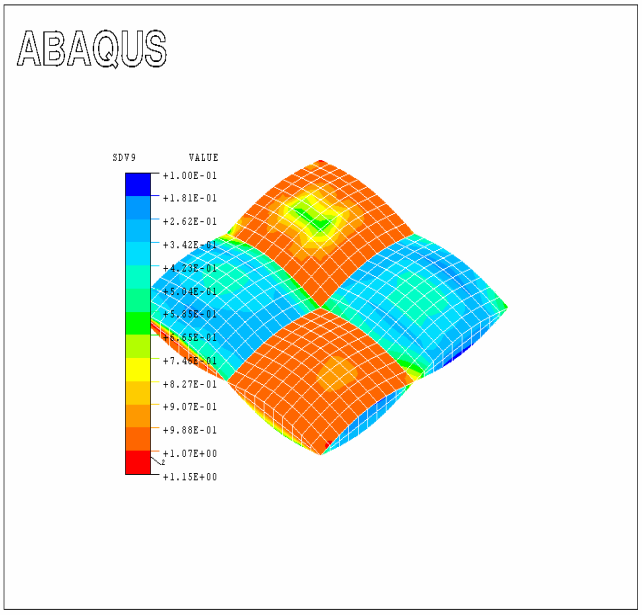

Point B

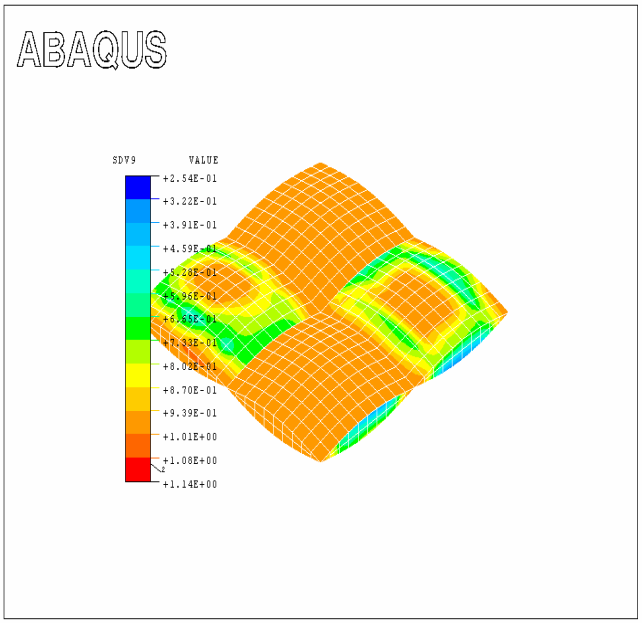

Point C

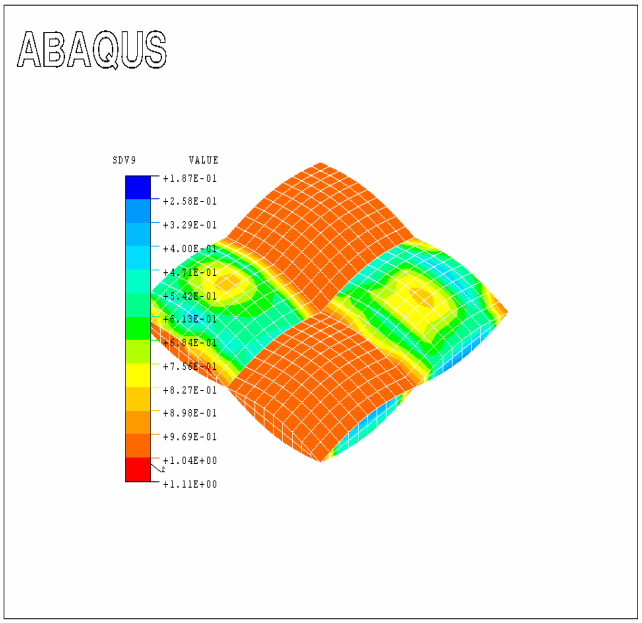

Point D

Figure 6.27: Distribution of fiber-damage due to tension in E-Glass / Epoxy plain weaves.

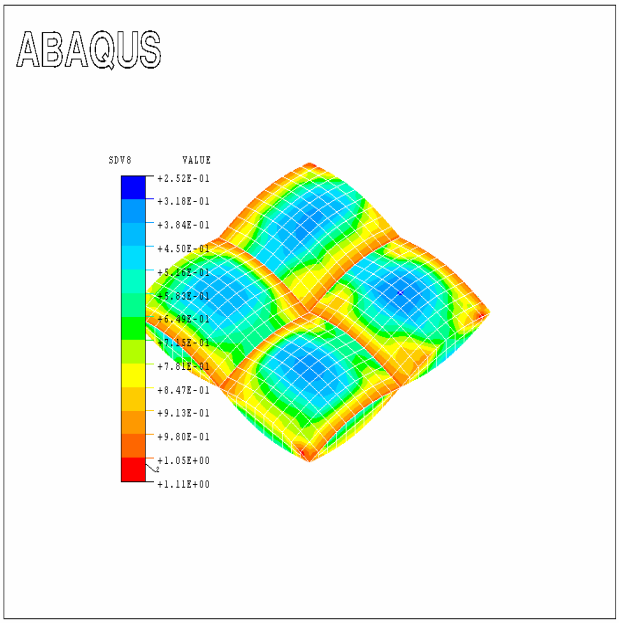

Point A

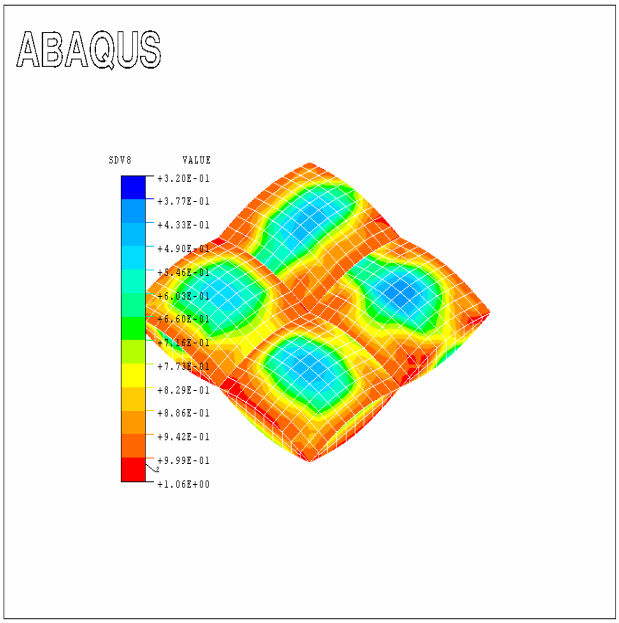

Point B

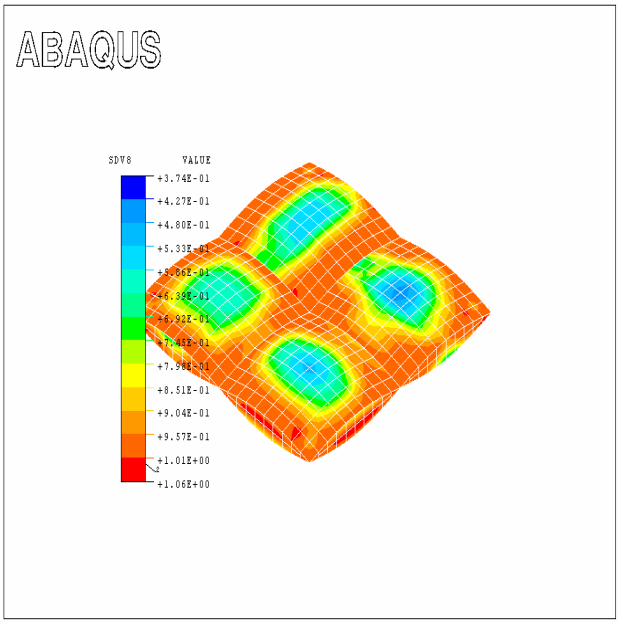

Point C

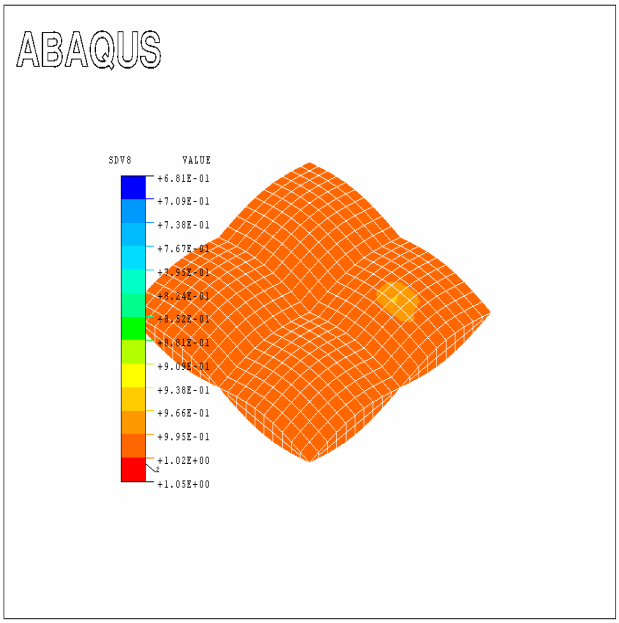

Point D

Figure 6.28: Distribution of fiber-damage due to shear in E-Glass / Epoxy plain weaves.

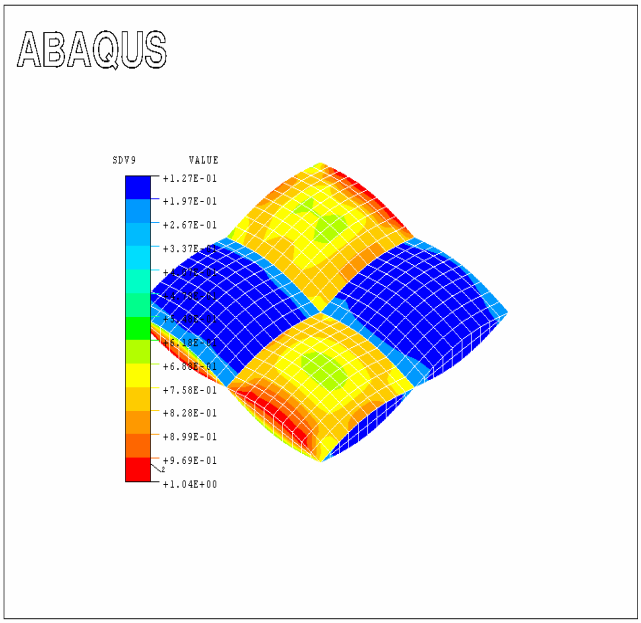

Point A

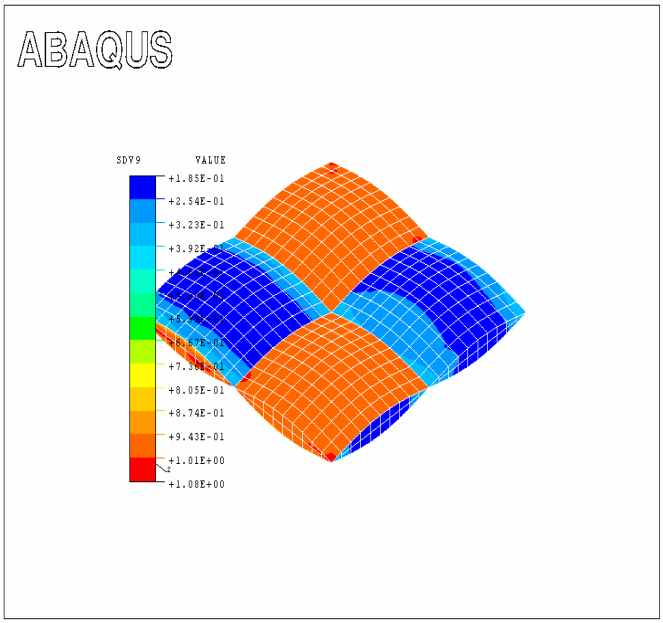

Point B

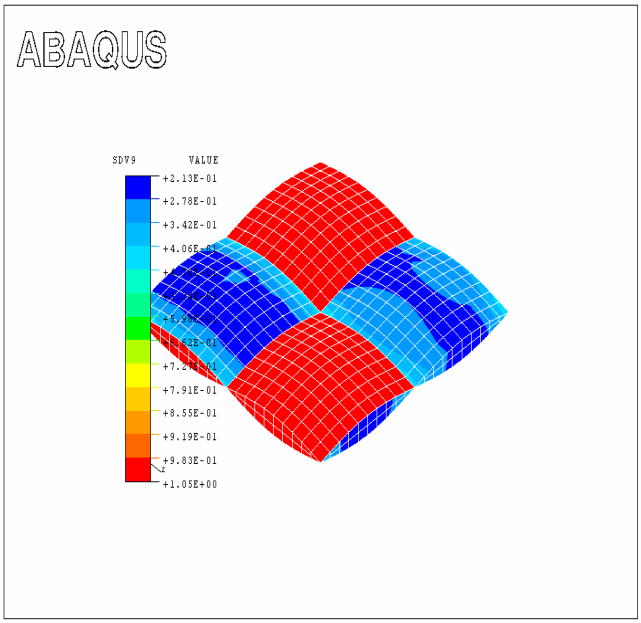

Point C

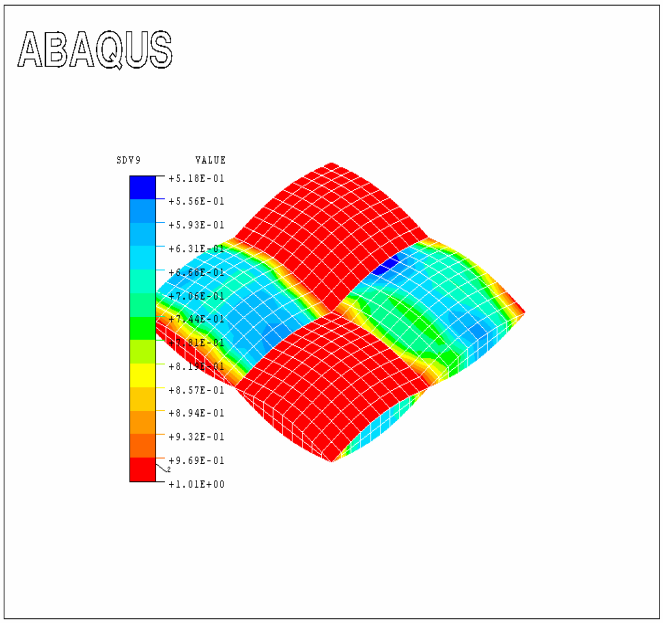

Point D

Figure 6.29: Distribution of fiber-damage due to compression in E-Glass / Epoxy plain weaves.

Table 6.16 Comparisons of predicted ultimate tensile and shear strengths for AS4 Carbon / Epoxy composites.(Unit:MPa)

Experimental values[6.6] (Tension)	Rule of mixture values (Tension)	Self-Consistent Method values (Tension)	Experimental values[6.6] (Shear)	Rule of mixture values (Shear)	Self-Consistent Method values (Shear)
737.5	754.62 ($\beta = 0.0$)	803.89 ($\beta = 0.0$)	102.5	101.71 ($\beta = 0.0$)	123.33 ($\beta = 0.0$)
	657.51 ($\beta = 0.3$)	691.19 ($\beta = 0.3$)		81.898 ($\beta = 0.3$)	97.617 ($\beta = 0.3$)
	549.81 ($\beta = 0.8$)	571.71 ($\beta = 0.8$)		55.933 ($\beta = 0.8$)	68.81 ($\beta = 0.8$)

Table 6.17 Comparisons of predicted ultimate tensile and shear strengths for E-Glass / Epoxy composites. (Unit: MPa)

Experimental values[6.11] (Tension)	Rule of mixture values (Tension)	Self-Consistent method values (Tension)	Experimental values[6.11] (Shear)	Rule of mixture values (Shear)	Self-Consistent method values (Shear)
265.0	253.18 ($\beta = 0.0$)	279.58 ($\beta = 0.0$)	92.0	82.841 ($\beta = 0.0$)	137.82 ($\beta = 0.0$)
	228.85 ($\beta = 0.3$)	238.59 ($\beta = 0.3$)		65.061 ($\beta = 0.3$)	108.86 ($\beta = 0.3$)
	173.70 ($\beta = 0.8$)	206.93 ($\beta = 0.8$)		43.075 ($\beta = 0.8$)	72.245 ($\beta = 0.8$)

REFERENCES

6.1 Laws, N., Dvorak, G..J. and Hejazi, M., "Stiffness Changes in Unidirectional Composites Caused by Crack Systems," *Mechanics of Materials*, Vol. 2, No. 2, 1983, pp. 123–137.

6.2 Scida, D., Aboura, Z., Benzeggagh, M.L. and Bocherens, E., "A Micro-mechanics Model for 3D Elasticity and Failure of Woven-Fiber Composite Materials," *Composites Science and Technology*, Vol. 59, No. 4, 1999, pp. 505–517.

6.3 Naik, R.A., "Analysis of Woven and Braided Fabric Reinforced Composites," NASA Contract Report CR–194930, 1994.

6.4 Tong, P.L., and Steven, G..P., "Modeling Approaches for 3-D Orthogonal Woven Composites," *Journal of Reinforced Plastics and Composites*, Vol. 17, No. 6, 1998, pp. 545-577.

6.5 Bogdanovich, A.E. "Multi-scale Predictive Analysis of 3-D Woven Composites," *Proc. of 35th Int. SAMPE Technical Conference*, Vol. 35, Dayton, OH, September 28-October 2, 2003.

6.6 Blackketter, D., Walrath D., and Hansen A., "Modeling Damage in a Plain Weave Fabric-reinforced Composite Material," *Journal of Composites Technology and Research*, Vol. 15, No. 2, 1993, pp. 136-142.

6.7 Sun, C. T. and Chen, J. L., "A Micromechanical Model for Plastic Behavior of Fibrous Composites," *Composites Science and Technology*, Vol. 40, No. 2, 1991, pp. 115-129.

6.8 Kollegal, M. G. and Sridharan, S., "Strength Prediction of Plain Woven Fabrics," *Journal of Composite Materials*, Vol. 34, No. 3, 2000, pp 240-257.

6.9 Kollegal, M. G. and Sridharan, S., "A Simplified Model for Plain Woven Fabrics," *Journal of Composite Materials*, Vol. 34, No. 20, 2000, pp 1756-1786.

6.10 Dvorak, G. J. and Laws, N., "Analysis of Progressive Matrix Cracking in Composite Laminates Thermo-elastic Properties of a Ply with Cracks,"*Journal of Composite Materials*, Vol. 19, No. 3, 1985, pp. 216-234.

6.11 Dasgupta A., and Bhandarkar S., "Effective Thermo-mechanical Behavior of Plain-weave Fabric Reinforced Composites Using Homogenization Theory," *Journal of Engineering Materials and Technology*, Vol. 116, No. 1, 1994, pp. 99-105.

Chapter 7 Cohesive Element Formulations for Fracture Modeling

7.1 Introduction

In this chapter, we propose a discontinuous crack element to model crack shapes and crack propagation growing dynamically in a solid material. To obtain a more fundamental view of fracture in damaged structures, it is necessary to introduce a new concept for a fracture process zone, so called cohesive zone, found in the weakening solid structures surrounding a crack tip. This chapter introduces cohesive elements to simulate the dynamic crack growth occurring along the cohesive zone. Some fracture models, as applied to textile composites and the cohesive element are studied here.

7.2 Cohesive Zone Model

To describe the discontinuous cracking, a cohesive zone modeling was suggested by Needleman[7.1]. Reference [7.1] suggested a material separation law based on the components of tractions and separations in the cohesive zone and introduced the concept of cohesive surfaces along the cohesive elements to calculate tractions and forces. In this study, an irreversible type of cohesive zone model is considered using traction components of cohesive elements when loading and unloading conditions are used in the cohesive zone. If the evolution of cracking exists in the cohesive zone, the cohesive zone model assumes an analogy to material plasticity and strain softening problems. To model the material plasticity, the two terms, loading and unloading in the cohesive zone model are used in the sense of increasing or decreasing the separation, as the traction decreases also under an increasing separation at a critical stress point ($\sigma_{\max}$), see Figure 7.1. There are two limiting cases of unloading conditions[7.2] one in the normal and the other in shear separation. Figures 7.1 and 7.2 suggest two limiting cases for unloading conditions possible in the cohesive zone model. The cohesive zone materials subjected to the unloading can arrive at failure between two extreme limits: i) elastic-damaged and unloading to the origin, ii) elastic-undamaged and unloading with the initial stiffness. Other unloading points can fall between the two limits. The material separation of the cohesive zone are modeled using the cohesive element, and the traction separation law of constitutive equations[7.1], that consists of tangential and normal separations are used to form crack shapes. The separation of the cohesive interfaces is calculated from the separation processes, such as

$$\delta = \Delta u = u^{+} - u^{-} \tag{7.1}$$

The meaning of u^{+} and u^{-} are the displacements in the direction of the normal to the top and bottom of the cohesive element, respectively. The separation vectors in the irreversible cohesive model are described as tangential separation δ^{T} and normal separation δ^{N} depending on whether the shear stress or the normal stress is acting on the surface of the interface elements. Eq. (7.1) is,

$$\delta = \sqrt[m]{\left(\delta^{N}\right)^{m} + \left(\delta^{T}\right)^{m}} \tag{7.2}$$

Here, m is one of the connection parameters. If the value of m in Eq. (7.2) is 1, this means a linear connection between the normal and the tangential tractions, while the meaning of $m = \infty$ yields the vanishing influence of the two separations. From Eq. (7.2), the ratio of the actual separation to the maximum separations δ_0^{N}, δ_0^{T}, δ_0 is defined as:

$$D = \frac{\delta}{\delta_0} = \sqrt[m]{\left(\frac{\delta^{N}}{\delta_0^{N}}\right)^{m} + \left(\frac{\delta^{T}}{\delta_0^{T}}\right)^{m}} \tag{7.3}$$

The plots for different values of m in Eq. (7.3) are shown in Figure 5.3. When the value of m is 2, the separation vector is equal to the maximum separation values.

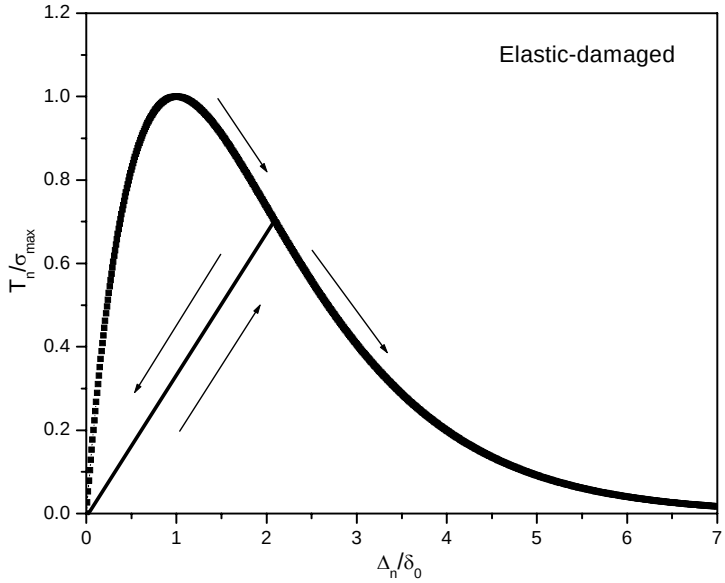

Figure 7.1: Unloading condition of elastic-damaged to the origin.

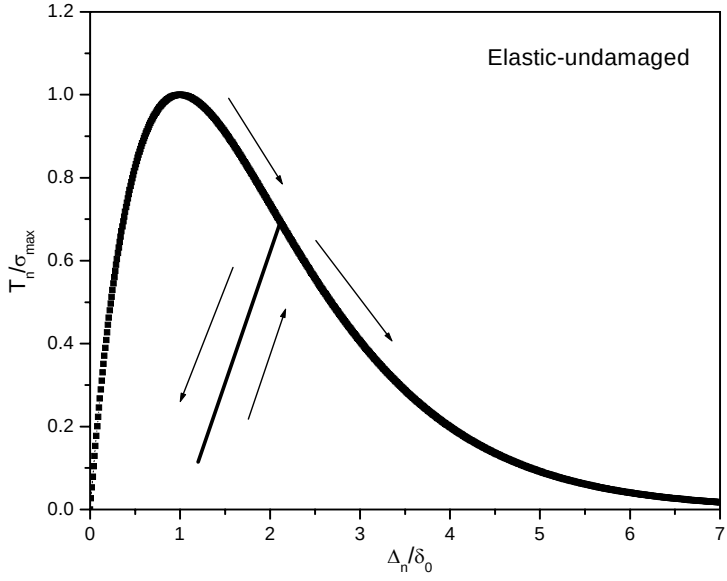

Figure 7.2: Unloading condition of elastic-undamaged with initial stiffness.

7.3 Fundamental Equations of Cohesive Zone Model

Needleman[7.1] suggested pertinent equations related to the cohesive zone model. In this work, the basic continuum equations are based on the Needleman equations. To induce the continuum equation (7.4) of multiphase solids, an interface region is considered as shown in Figure 7.4 and suggested in Ref. [7.3]. The independent variables are the position of material point in the reference configuration $\mathbf{x}$ and time t. A fixed Cartesian frame is used to define deformation gradient $\mathbf{F}$ and displacement vectors $\mathbf{u} = \bar{\mathbf{x}} - \mathbf{x}$. The principle virtual work can be written in the form:

$$\int_V \mathbf{s} : \delta\mathbf{F} dV = \int_{S_{ext}} \mathbf{T}_e \cdot \delta\mathbf{u} dS - \int_V \rho \frac{\partial^2 \mathbf{u}}{\partial t^2} \cdot \delta\mathbf{u} dV \tag{7.4}$$

Here, the nominal stress tensor, $\mathbf{s} = \mathbf{F}^{-1} \cdot \boldsymbol{\tau} = \mathbf{F}^{-1} \det(\mathbf{F})\boldsymbol{\sigma}$, is described by Cauchy stress $\boldsymbol{\sigma}$ and Kirchhoff stress $\boldsymbol{\tau}$, $\mathbf{u}$ is the separation vector, $\mathbf{F}$ the deformation gradient, and $\mathbf{T}_e$ the traction vector on the external surface of the body. The traction vectors are related to $\mathbf{s}$ by the surface normal vector $\mathbf{n}$ as $\mathbf{T} = \mathbf{n} \cdot \mathbf{s}$, having the meaning if the forces over unit-area that is transmitted. In the volume terms, $\mathbf{A} : \mathbf{B}$ denotes $A^{ij} : B_{ji}$, A^{ij} is the inverse of matrix tensor (A_{ij}), and $A_{ij} = \mathbf{A}_i \cdot \mathbf{A}_j$. The solid is assumed to consist of several material phases. In practical, one phase is distributed in regions having one dimension h, described in Figure 7.4, much smaller than any other characteristic dimension of the solid. If some of interface regions are distributed, the boundaries of other phases are sketched as in Figure 7.4. The principle of virtual work, Eq. (7.4), is re-written as

$$\int_{V^*} \mathbf{s} : \delta\mathbf{F} dV + \int_{V_{\text{int}}} \mathbf{s} : \delta\mathbf{F} dV = \int_{S_{ext}} \mathbf{T}_e \cdot \delta\mathbf{u} dS - \int_V \rho \frac{\partial^2 \mathbf{u}}{\partial t^2} \cdot \delta\mathbf{u} dV \tag{7.5}$$

Here, V_{int} is the volume occupied by the interface and $V^* = V - V_{\text{int}}$. Applying the Gauss divergence theorem to the integral over V_{int} gives

$$\int_{V^*} \mathbf{s} : \delta\mathbf{F} dV - \int_{S^+} \mathbf{T} \cdot \delta\mathbf{u}^+ dS + \int_{S^-} \mathbf{T} \cdot \delta\mathbf{u}^- dS = \int_{S_{ext}} \mathbf{T}_e \cdot \delta\mathbf{u} dS - \int_V \rho \frac{\partial^2 \mathbf{u}}{\partial t^2} \cdot \delta\mathbf{u} dV \tag{7.6}$$

The variables S^+ and S^- denote the opposite sides of the interface shown in Figure 7.4. By taking the limit $h \to 0$, $V^* \to V$ and $S^+ \to S^- = S_{\text{int}}$. These imply that the equilibrium of the multiphase solid requires continuity of tractions. The principle of virtual work is finally re-written as

$$\int_V \mathbf{s} : \delta\mathbf{F} dV - \int_{S_{\text{int}}} \mathbf{T}_{CZ} \cdot \delta\boldsymbol{\Delta} dS = \int_{S_{ext}} \mathbf{T}_e \cdot \delta\mathbf{u} dS - \int_V \rho \frac{\partial^2 \mathbf{u}}{\partial t^2} \cdot \delta\mathbf{u} dV \tag{7.7}$$

In Eq. (7.7), $\mathbf{s}$ is the non-symmetric nominal stress tensor, $\boldsymbol{\Delta} = u^+ - u^-$ is the displacement jump across the cohesive or interface surface, V is the system volume, ρ is the material density in the reference configuration, and S_{int} and S_{ext} are the internal and the external cohesive surface areas of the body, respectively. Cracks in the cohesive zone surface are described by the integral over the internal surface, S_{int}.

Needleman[7.1] suggested that the relations between the traction $\mathbf{T}$ and the material separation $\boldsymbol{\Delta}$ to be described by exponential functions for cohesive surface energies on the cohesive zone model. In this thesis, the Needleman's exponential functions are applied into the irreversible cohesive zone model and two type tractions, namely normal and shear components T_n and T_t are considered. The traction across the cohesive zone surface is given by

$$\phi(\Delta_n, \Delta_t) = e\sigma_{\max}\delta_n - e\sigma_{\max}\delta_n e^{(-\Delta_n/\delta_n)} \left[1 + \frac{\Delta_n}{\delta_n}\right] e^{(-\Delta_t^2/\delta_t^2)}, \quad \mathbf{T} = -\frac{\partial\phi}{\partial\boldsymbol{\Delta}} \tag{7.8}$$

By modifying the exponential equations of the potential work ϕ_i ($i = n$ and t), the constitutive relations to show the material separations at the critical loads are shown in Figures 7.5-7.8, and can be expressed as:

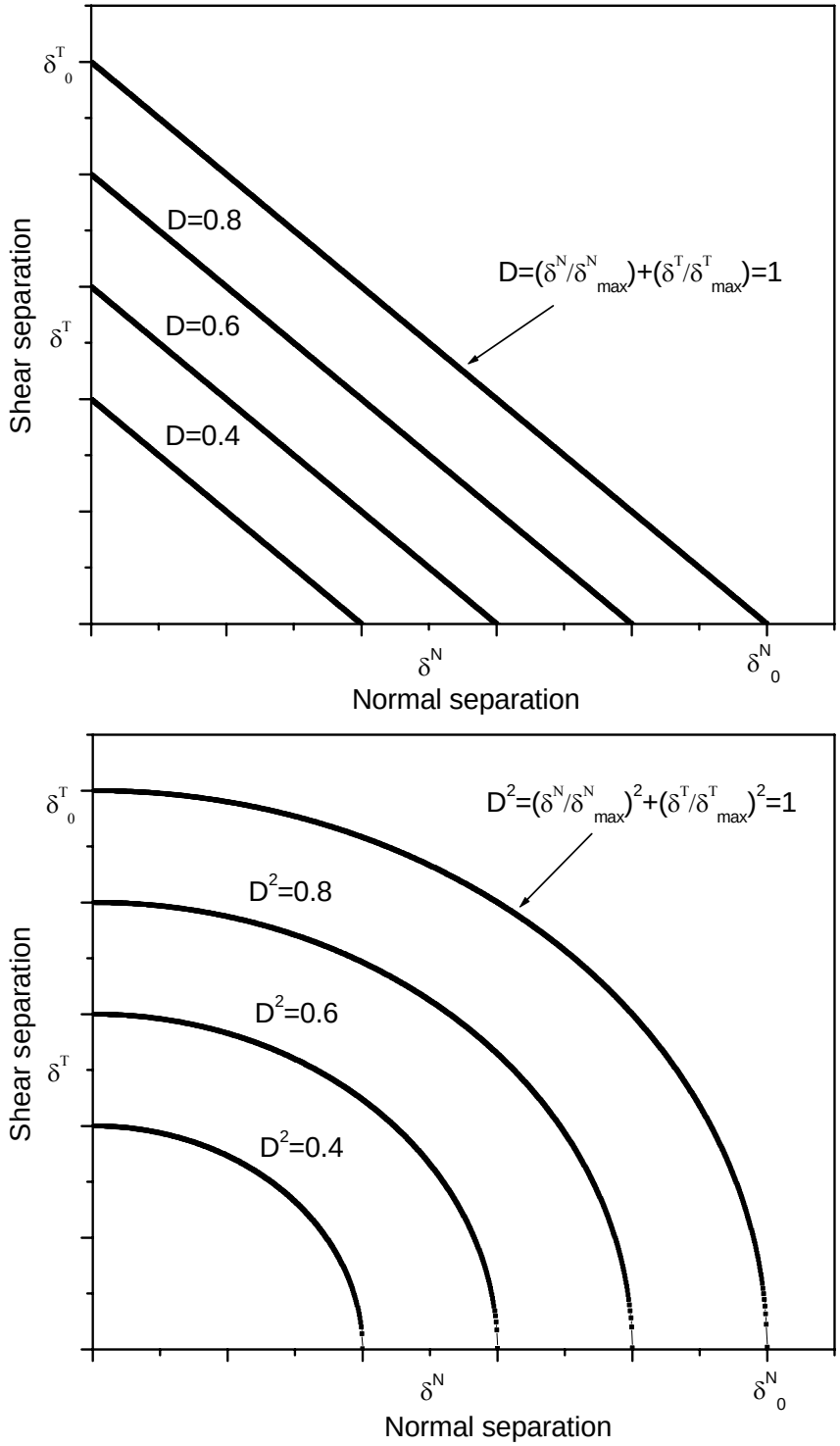

Figure 7.3: Plots between the normal and the shear separations.

$$T_n = \sigma_{\max} e \exp(-\Delta u) \left\{ \Delta u \exp\left(-\Delta v^2\right) + (1-q) \left[1 - \exp\left(-\Delta v^2\right) \right] \Delta u \right\}$$

$$\frac{\partial T_n}{\partial \Delta_n} = \frac{\sigma_{\max} e}{\delta_0} \exp(-\Delta u) \left\{ \exp\left(-\Delta v^2\right) + (1-q) \left[1 - \exp\left(-\Delta v^2\right) \right] \right\} (1-\Delta u) \tag{7.9}$$

$$\frac{\partial T_n}{\partial \Delta_t} = -2 \frac{\sigma_{\max} e}{\delta_0} \Delta u \Delta v \exp(-\Delta u) \exp\left(-\Delta v^2\right) q$$

$$T_t = 2\sigma_{\max} e \Delta v q (1+\Delta u) \exp(-\Delta u) \exp\left(-\Delta v^2\right)$$

$$\frac{\partial T_t}{\partial \Delta_n} = -2 \frac{\sigma_{\max} e}{\delta_0} \Delta u \Delta v \exp(-\Delta u) \exp\left(-\Delta v^2\right) q \tag{7.10}$$

$$\frac{\partial T_t}{\partial \Delta_t} = -2 \frac{\sigma_{\max} e}{\delta_0} \left(1 - 2\Delta v^2\right) (1+\Delta u) \exp(-\Delta u) \exp\left(-\Delta v^2\right) q$$

Here, the characteristic distance of the normal and shear is assumed to be $\delta_0 = \delta_n = \delta_t$. The normalized displacement jump-vectors Δu and Δv are defined by the normal and shear separations and the characteristic distances such as $\Delta u = \frac{\Delta_n}{\delta_0}$ and $\Delta v = \frac{\Delta_t}{\delta_0}$. The variable q is used to scale the normal and shear cohesive stresses. Eqs. (7.9) and (7.10) are the relations between the cohesive tractions in normal and shear T_n and T_t, and the normal and shear separation Δ_n and Δ_t. The normal cohesive and shear cohesive stress are $\sigma_{\max}$ and $\tau_{\max} = \sqrt{2e} q \sigma_{\max}$, respectively. The cohesive energy of the normal and shear ϕ_n and ϕ_t are defined as:

$$\phi_n = \sigma_{\max} \delta_0 e, \ \phi_t = \sigma_{\max} \delta_0 e q \tag{7.11}$$

In Eq. (7.11), the normal and shear initial stiffness k_n and k_t in the cohesive traction laws are obtained from the energy relations, respectively.

$$k_n = \frac{\sigma_{\max} e}{\delta_0}, \ k_t = 2 \frac{\sigma_{\max} e}{\delta_0} q \tag{7.12}$$

Using the equations (5.9) and (5.10), the loading paths have to be found as the Figures 7.5 and 7.6. The unloading conditions are obtained from the normal and shear traction components in Eqs. (7.9)-(7.10), respectively.

$$T_n = T_{n,\max} + k_n (\Delta_n - \Delta_{n,\max}), \ \frac{\partial T_n}{\partial \Delta_n} = k_n, \ \frac{\partial T_n}{\partial \Delta_t} = 0.0 \tag{7.13}$$

$$T_t = T_{t,\max} + k_t (\Delta_t - \Delta_{t,\max}), \ \frac{\partial T_t}{\partial \Delta_t} = k_t, \ \frac{\partial T_t}{\partial \Delta_n} = 0.0 \tag{7.14}$$

The corresponding behaviors for normal unloading and shear unloading are given in Figures 7.7 and 7.8.

7.4 Force Vectors of Cohesive Element

In this study, Needleman's cohesive element model[7.1] is used, and the cohesive element is schematically represented in Figure 7.9. In Figure 7.9, one cohesive element consists of two basic triangular elements based on the constant-strain triangular element (CST). The cohesive element has two integration points on each side, and four nodes between the two basic triangular elements, see Figure 7.10. To specify the local coordinates of the two sides of the CST elements, the parameter of average angles is introduced. The normal and shear tractions are calculated from the separation of the nodes in the interfaced elements. Through these tractions, the cracks between the two CST elements are considered, and Figure 7.11 shows the traction components and the average angle of the elements.

To calculate the average angle θ, of the two CST elements, the nodal coordinates, x_1, y_1, x_2, y_2, x_3, y_3, x_4 and y_4, for 4-nodes are used, and two angles, θ_1 and θ_2, are considered. The angles θ_1 and θ_2 are calculated from the nodal coordinates of the CST element consisting of nodes 1 and 2, and 3 and 4. For the angles θ_1 and θ_2, the equations are given as:

$$\theta_1 = \cos^{-1}\left[\frac{x_1 - x_2}{\sqrt{(x_1 - x_2)^2 + (y_1 - y_2)^2}}\right],\ \theta_2 = \cos^{-1}\left[\frac{x_3 - x_4}{\sqrt{(x_3 - x_4)^2 + (y_3 - y_4)^2}}\right],\ \theta = \frac{\theta_1 + \theta_2}{2} \tag{7.15}$$

The normal and shear separation of the CST elements, Δ_n^{nodal} and Δ_t^{nodal} are calculated by the average angle. Like the average angle term, the separations, Δ_n^{nodal} and Δ_t^{nodal}, are calculated from the nodal coordinates and the average angle. To calculate the nodal separations, two integration-points a and b, are considered between the CST elements. The equations of the nodal separations, $\Delta_{n,a}^{nodal}$, $\Delta_{t,a}^{nodal}$, $\Delta_{n,b}^{nodal}$ and $\Delta_{t,b}^{nodal}$ are shown below:

$$\begin{bmatrix}\Delta_{n,a}^{nodal}\\ \Delta_{t,a}^{nodal}\end{bmatrix} = \begin{bmatrix} S & -C \\ C & -S\end{bmatrix}\begin{bmatrix}\Delta_{13}^{x}\\ \Delta_{13}^{y}\end{bmatrix},\ \begin{bmatrix}\Delta_{n,b}^{nodal}\\ \Delta_{t,b}^{nodal}\end{bmatrix} = \begin{bmatrix} S & -C \\ C & -S\end{bmatrix}\begin{bmatrix}\Delta_{24}^{x}\\ \Delta_{24}^{y}\end{bmatrix} \tag{7.16}$$

Here $\Delta_{13}^{x} = (x_1 - x_3),\ \Delta_{13}^{y} = (y_1 - y_3),\ \Delta_{24}^{x} = (x_2 - x_4),\ \Delta_{24}^{y} = (y_2 - y_4)$ and $C = \cos(\theta),\ S = \sin(\theta)$.

The normal and shear separations at the integration points (a and b): $\Delta_{n,a}, \Delta_{t,a}, \Delta_{n,b}$ and $\Delta_{t,b}$, are written as:

$$\Delta_{n,a} = \Delta_{n,a}^{nodal} + 0.2113\left(\Delta_{n,b}^{nodal} - \Delta_{n,a}^{nodal}\right),\ \Delta_{t,a} = \Delta_{t,a}^{nodal} + 0.2113\left(\Delta_{t,b}^{nodal} - \Delta_{t,a}^{nodal}\right)$$

$$\Delta_{n,b} = \Delta_{n,a}^{nodal} + 0.7887\left(\Delta_{n,b}^{nodal} - \Delta_{n,a}^{nodal}\right),\ \Delta_{t,b} = \Delta_{t,a}^{nodal} + 0.7887\left(\Delta_{t,b}^{nodal} - \Delta_{t,a}^{nodal}\right) \tag{7.17}$$

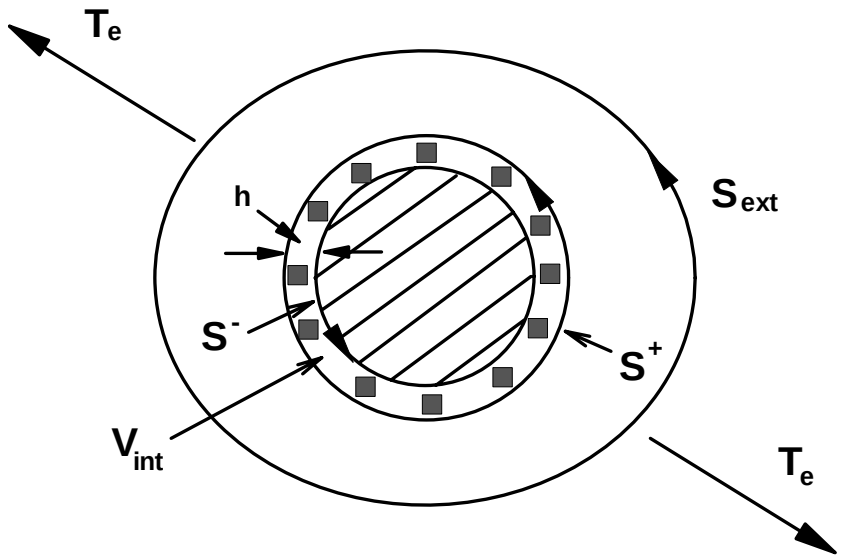

Figure 7.4: Multi-phase solid with an interface region from Ref. [7.4].

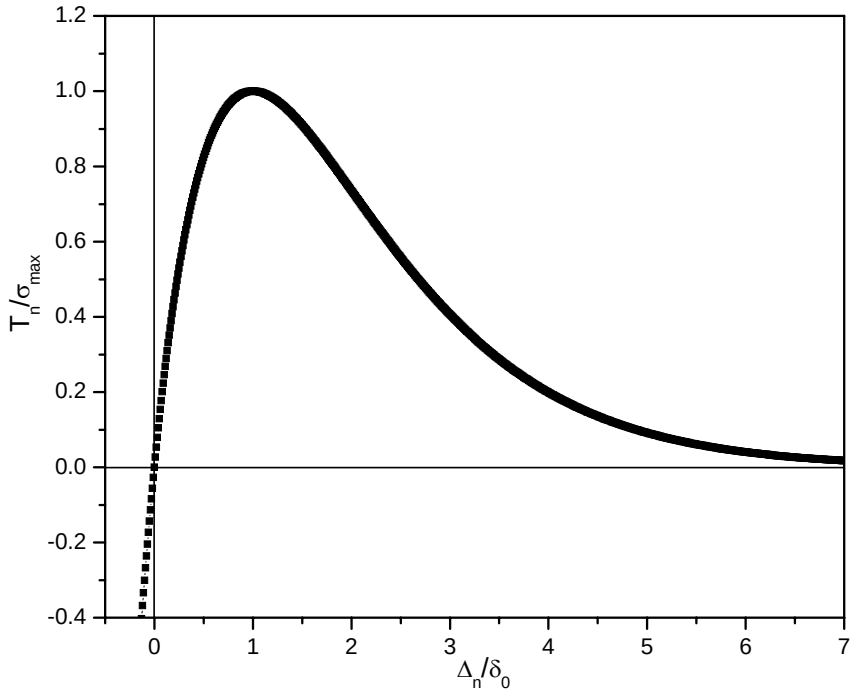

Figure 7.5: Plot of the normal traction to the normal separation ($\Delta_t = 0$).

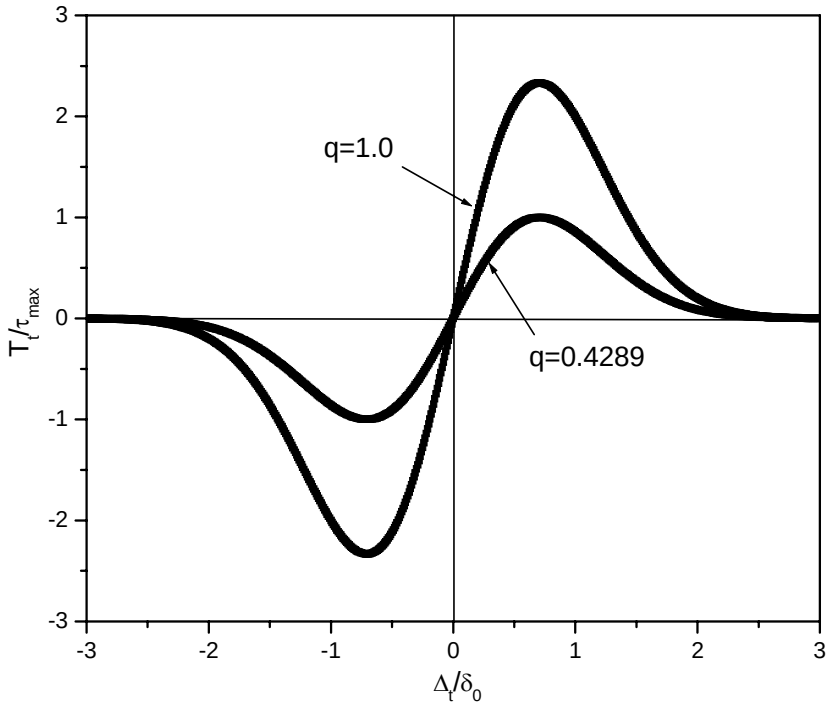

Figure 7.6: Plot of the shear traction to the shear separation ($\Delta_n = 0$, $q = 1.0$ and $q = 0.4289$).

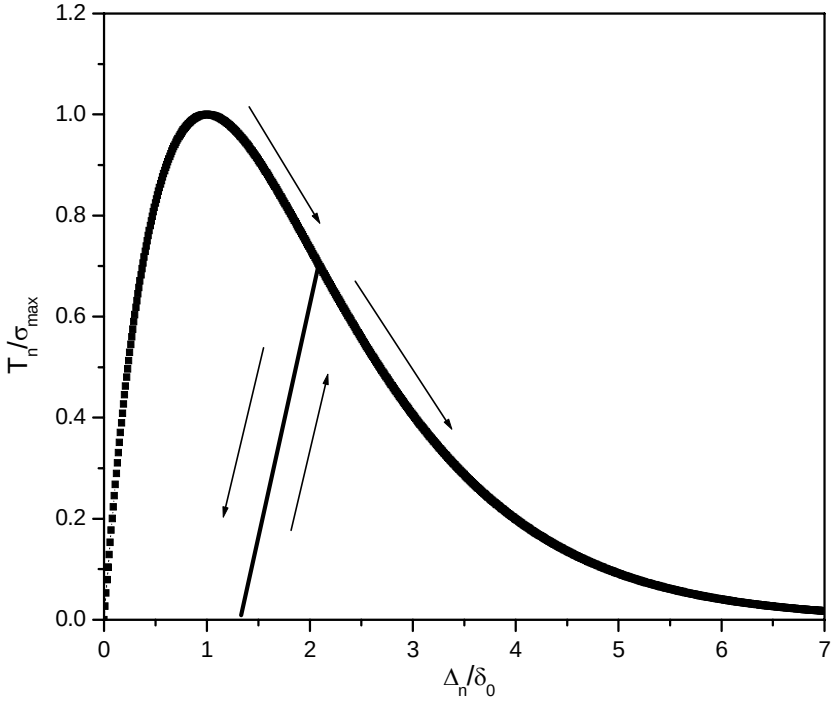

Figure 7.7: Unloading cases of the normal traction and separation.

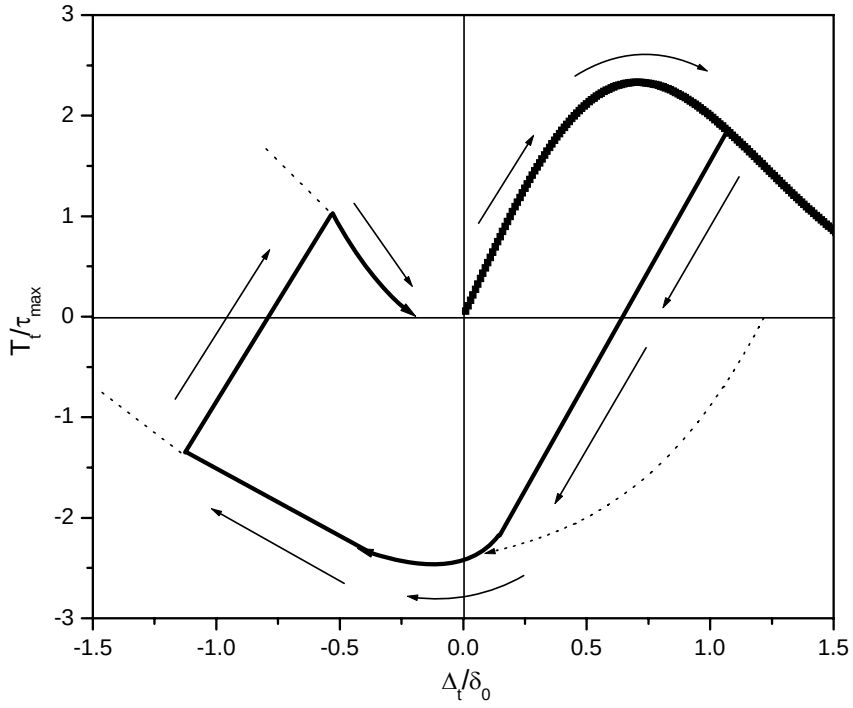

Figure 7.8: Unloading cases of the shear traction and separation.

The constants of 0.2113 and 0.7887 in Eq. (7.17) mean the weighted factors to determine the normal and shear separations of integration points between the nodal separations. The traction and stiffness are calculated by using the normal and shear separations at the integration points and appropriate traction and separation equations (7.9), (7.10) and (7.12). By multiplying the traction and stiffness into weighted areas corresponding to each integration points, the normal and shear loads at the nodes, $F_{n,a}^{nodal}$, $F_{t,a}^{nodal}$, $F_{n,b}^{nodal}$ and $F_{t,b}^{nodal}$ are found. These normal and shear nodal loads are applied into the reference coordinates, r - s, to find the normal and shear loads at the integration nodes, $F_{r,a}$, $F_{s,a}$, $F_{r,b}$ and $F_{s,b}$. The equations of the normal and shear loads at the integration nodes in the reference system, r - s, are given as:

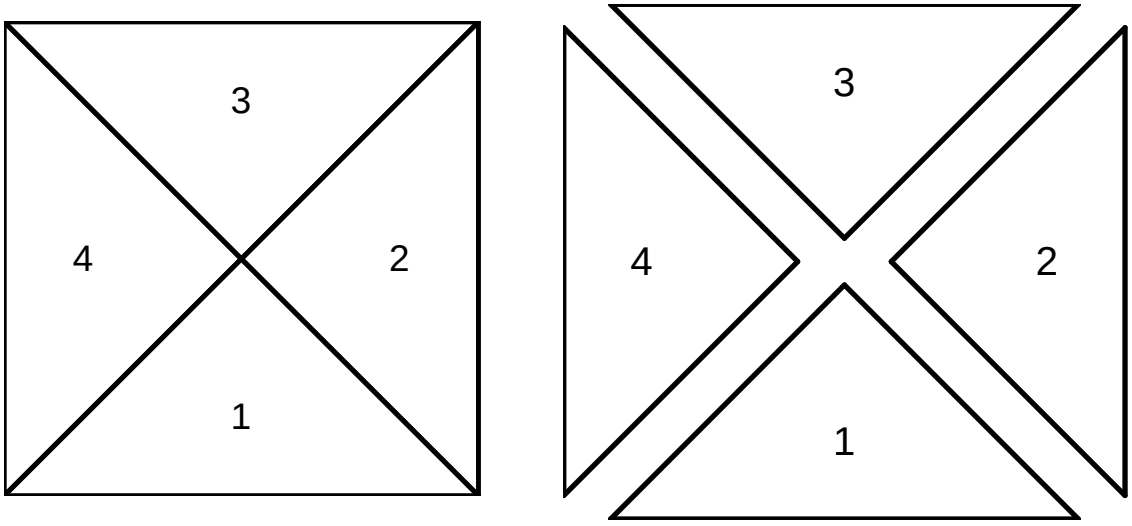

Figure 7.9: 4-cohesive elements' arrangement and node connection.

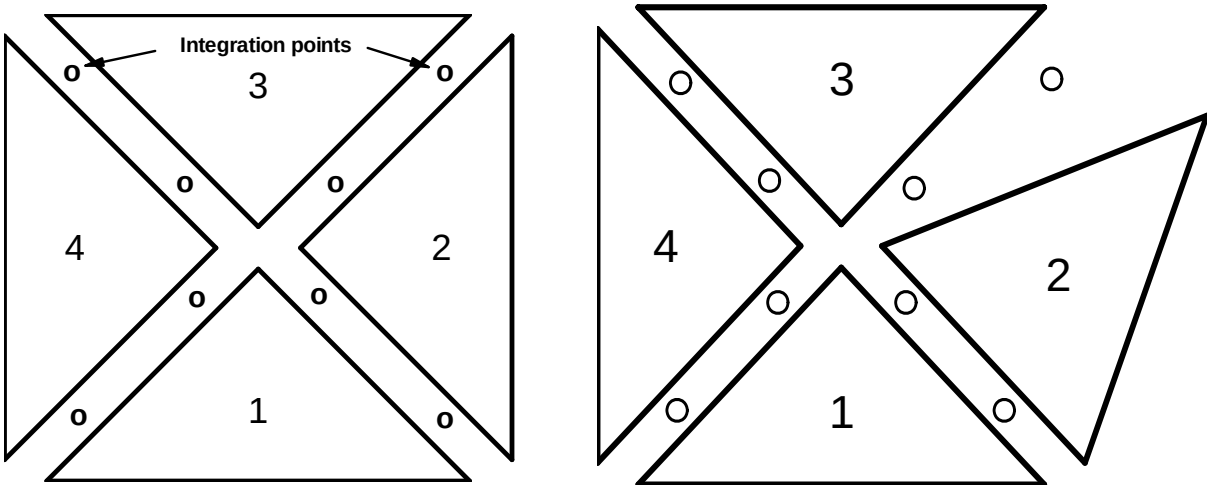

Figure 7.10: Un-deformed and deformed 4-cohesive elements with integration points.

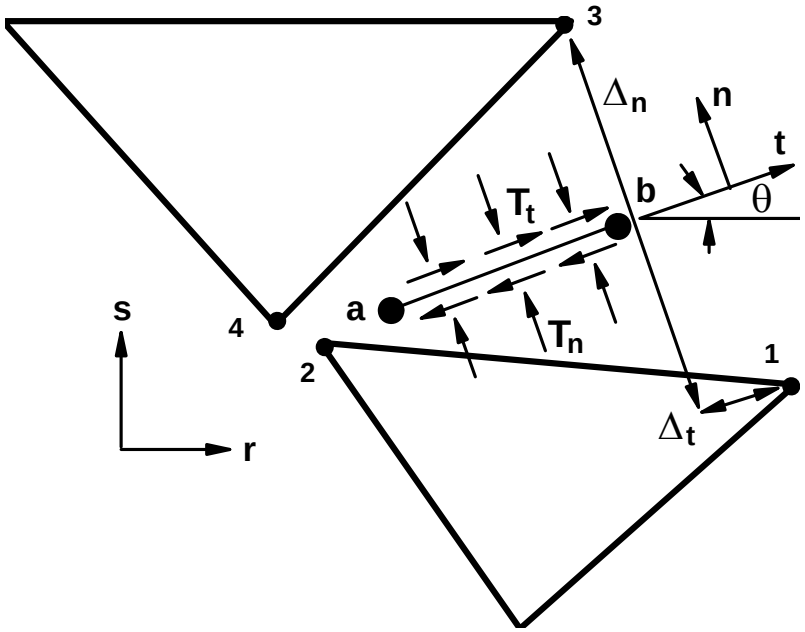

Figure 7.11: A deformed cohesive element formed by tractions, separations, nodes and angles.

$$\begin{bmatrix} F_{r,a} \\ F_{s,a} \end{bmatrix} = \begin{bmatrix} S & C \\ -C & S \end{bmatrix} \begin{bmatrix} F_{n,a}^{nodal} \\ F_{t,a}^{nodal} \end{bmatrix}, \begin{bmatrix} F_{r,b} \\ F_{s,b} \end{bmatrix} = \begin{bmatrix} S & C \\ -C & S \end{bmatrix} \begin{bmatrix} F_{n,b}^{nodal} \\ F_{t,b}^{nodal} \end{bmatrix} \tag{7.18}$$

The four forces in Eq. (7.18) are applied to model the crack shapes between the CST elements, and their signs are opposite but of the same magnitudes at the integration points. With the cohesive elements, micro-crack shapes can be obtained such as in Figure 7.12.

7.5 Stiffness and Force Matrix of Cohesive Element

The stiffness matrix of the cohesive element subjected to external loads is derived via the principle of virtual work from Eq. (7.7). The virtual work of stress for the cohesive element is given as:

$$\delta\Pi_i = \int_{S_{\text{int}}} \mathbf{T}_{CZ} \cdot \delta\boldsymbol{\Delta}\, dS = \int_S \mathbf{T} \cdot \delta\bar{\mathbf{u}} dS \tag{7.19}$$

The traction vectors include nonlinear exponential functions of displacements, and the nodal displacements fulfill nonlinear equations. The displacements $\bar{\mathbf{u}}$ are described as the shape function $\mathbf{N}_{\bar{u}}$ and the node displacement $\bar{\mathbf{u}}_e$.

$$\bar{\mathbf{u}} = \mathbf{N}_{\bar{u}} \cdot \bar{\mathbf{u}}_e \tag{7.20}$$

The shape function matrix, $\mathbf{N}_{\bar{u}}$ is

$$N_{\bar{u}ij} = \begin{pmatrix} N_1 & 0 & 0 & N_2 & 0 & 0 & & N_n & 0 & 0 \\ 0 & N_1 & 0 & 0 & N_2 & 0 & \cdots & 0 & N_n & 0 \\ 0 & 0 & N_1 & 0 & 0 & N_2 & & 0 & 0 & N_n \end{pmatrix} \tag{7.21}$$

From Eq. (7.20), the equation of the virtual work of stress for the cohesive element is rewritten as:

$$\delta\Pi_i = \delta\bar{\mathbf{u}}_e \cdot \int_S \mathbf{N}_{\bar{u}}^T \cdot \mathbf{T}\, dS \tag{7.22}$$

The tangential stiffness matrix $\mathbf{K}$ is calculated from the total differential of the traction vectors $\mathbf{T}$. The tangential stiffness matrix is:

$$d\mathbf{T} = \frac{\partial \mathbf{T}}{\partial \bar{\mathbf{u}}} \cdot d\bar{\mathbf{u}} \tag{7.23}$$

By using the difference of total displacement, $\Delta\bar{\mathbf{u}}_e$, between $t + \Delta t$ and t, the force increment is described as:

$$\mathbf{K} \cdot \Delta\bar{\mathbf{u}}_e = \int_S \mathbf{N}_{\bar{u}}^T \frac{\partial \mathbf{T}}{\partial \bar{\mathbf{u}}} \cdot \mathbf{N}_{\bar{u}} dS \cdot \Delta\bar{\mathbf{u}}_e \tag{7.24}$$

In Eq. (7.24), the stiffness term can be re-written by Gauss integration.

$$\mathbf{K} = \int_S \mathbf{N}_{\bar{u}}^T \frac{\partial \mathbf{T}}{\partial \bar{\mathbf{u}}} \cdot \mathbf{N}_{\bar{u}} dS = \sum_i \left[\mathbf{N}_{\bar{u}}^T \frac{\partial \mathbf{T}}{\partial \bar{\mathbf{u}}} \cdot \mathbf{N}_{\bar{u}} \right]_i w_i J_i \tag{7.25}$$

Here, w_i are the weight functions for the Gauss integration, and J_i is the Jacobian determinant of the cohesive elements in the specified Gauss points. The 2-dimensional Jacobian determinant of the cohesive elements is written as:

$$\mathbf{J} = \begin{bmatrix} \dfrac{\partial r}{\partial \xi} & \dfrac{\partial s}{\partial \xi} \\ \dfrac{\partial r}{\partial \eta} & \dfrac{\partial s}{\partial \eta} \end{bmatrix} \tag{7.26}$$

The integration term in Eq. (7.25) can be written

$$\mathbf{N}_{\bar{u}}^T \frac{\partial \mathbf{T}}{\partial \bar{\mathbf{u}}} \cdot \mathbf{N}_{\bar{u}} = \begin{bmatrix} N_1^2 T_{r,r} & N_1^2 T_{r,s} & N_1^2 T_{r,t} & N_1 N_2 T_{r,r} & & & & & \\ N_1^2 T_{s,r} & N_1^2 T_{s,s} & N_1^2 T_{s,t} & & & \ddots & & & \\ N_1^2 T_{t,r} & N_1^2 T_{t,s} & N_1^2 T_{t,t} & & & & & & \\ N_1 N_2 T_{r,r} & & & N_2^2 T_{r,r} & & & \ddots & & \\ & & & & \ddots & & & & \\ & & \ddots & & & N_n^2 T_{r,r} & N_n^2 T_{r,s} & N_n^2 T_{r,t} & \\ & & & & & N_n^2 T_{s,r} & N_n^2 T_{s,s} & N_n^2 T_{s,t} & \\ & & & & \ddots & N_n^2 T_{t,r} & N_n^2 T_{t,s} & N_n^2 T_{t,t} & \end{bmatrix} \tag{7.27}$$

The external nodal force loadings on the top and bottom faces of the cohesive elements are calculated from the principal of virtual work and Eq. (7.19):

$$\delta\Pi = \delta\Pi_i = \delta\bar{\mathbf{u}}_e \mathbf{F}_C \tag{7.28}$$

The nodal forces $\mathbf{F}_C$ of the cohesive elements are written as:

$$\mathbf{F}_C = \int_S \mathbf{N}_{\bar{u}}^T \cdot \mathbf{T} dS \tag{7.29}$$

And the equation (7.25) of the cohesive forces is re-written as:

$$\mathbf{F}_C = \sum_i \left[\mathbf{N}_{\bar{u}}^T \cdot \mathbf{T} \right]_i w_i J_i \tag{7.30}$$

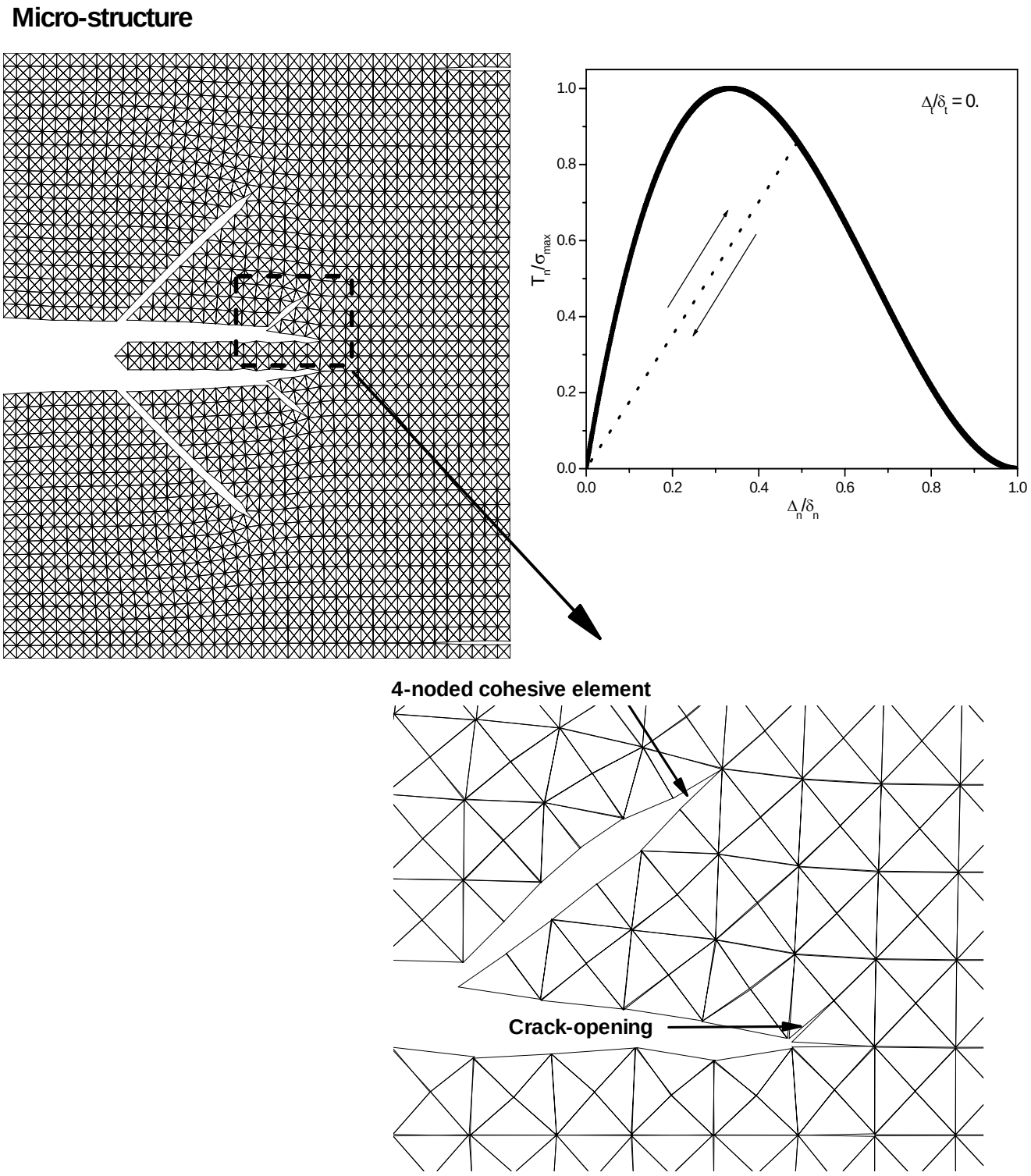

Figure 7.12: Schematics of micro-cracks using the irreversible loading and unloading normal traction value.

7.6 Constant Strain Triangle Element

In this study, the simplest continuum element, implying constant strain triangle (CST) element, is used to formulate the continuous elements between the cohesive elements. Consider a triangle with three nodes as shown Figure 7.9. Let us introduce a new reference coordinate nature (x - y) in the CST. We can write the displacement equations.

$$x(x,y)=\sum_i^3 h_i(x,y)x_i\ ,\ u(x,y)=\sum_i^3 h_i(x,y)u_i$$

$$y(x,y)=\sum_i^3 h_i(x,y)y_i\ ,\ v(x,y)=\sum_i^3 h_i(x,y)v_i \tag{7.31}$$

Here $h_i(x,y)$ are the linear triangle interpolation functions and A is an element area. These interpolation functions will be applied at all times during the deformations. The displacement gradients are given by

$$\frac{\partial u}{\partial x}=\sum\frac{\partial h_i}{\partial x}u_i=\frac{1}{2A}\sum_i b_i u_i\ ,\ \frac{\partial v}{\partial x}=\sum\frac{\partial h_i}{\partial x}v_i=\frac{1}{2A}\sum_i b_i v_i$$

$$\frac{\partial u}{\partial y}=\sum\frac{\partial h_i}{\partial y}u_i=\frac{1}{2A}\sum_i c_i u_i\ ,\ \frac{\partial v}{\partial y}=\sum\frac{\partial h_i}{\partial y}v_i=\frac{1}{2A}\sum_i c_i v_i \tag{7.32}$$

Here, the coefficients b_i and c_i have to be evaluated with respect to the original configuration. The strains are

$$\varepsilon_{xx}=\frac{\partial u}{\partial x}\ ,\ \varepsilon_{yy}=\frac{\partial v}{\partial y}\ ,\ 2\varepsilon_{xy}=\frac{\partial u}{\partial y}+\frac{\partial v}{\partial x} \tag{7.33}$$

These are expressed in matrix form as the strain-displacement matrix $\mathbf{B}_L$.

$$\begin{Bmatrix}\varepsilon_{xx}\\ \varepsilon_{yy}\\ 2\varepsilon_{xy}\end{Bmatrix}=\frac{1}{2A}\begin{bmatrix}b_1 & 0 & b_2 & 0 & b_3 & 0\\ 0 & c_1 & 0 & c_2 & 0 & c_3\\ c_1 & b_1 & c_2 & b_2 & c_3 & b_3\end{bmatrix}\begin{Bmatrix}u_1\\ v_1\\ u_2\\ v_2\\ u_3\\ v_3\end{Bmatrix},\ \boldsymbol{\varepsilon}=\mathbf{B}_L\mathbf{u} \tag{7.34}$$

The stresses based on the plane stress of Hooke's law are

$$\begin{Bmatrix}\sigma_{xx}\\ \sigma_{yy}\\ \sigma_{xy}\end{Bmatrix}=\frac{E}{1-\nu^2}\begin{bmatrix}1 & \nu & 0\\ \nu & 1 & 0\\ 0 & 0 & (1-\nu)/2\end{bmatrix}\begin{Bmatrix}\varepsilon_{xx}\\ \varepsilon_{yy}\\ 2\varepsilon_{xy}\end{Bmatrix},\ \boldsymbol{\sigma}=\mathbf{D}\ \boldsymbol{\varepsilon} \tag{7.35}$$

The virtual work for a panel consisting of CST elements in plane stress is

$$\delta W=\int_V\left[\sigma_{xx}\delta\bar{\varepsilon}_{xx}+\sigma_{yy}\delta\bar{\varepsilon}_{yy}+\sigma_{xy}\delta\bar{\gamma}_{xy}\right]dV\ ,\ \delta W=\int_V\boldsymbol{\sigma}\ \ \delta\boldsymbol{\varepsilon}\ \ dV \tag{7.36}$$

By substituting Eqs. (7.35) and (7.36) into Eq. (7.37), the virtual work in terms of the considered degree of freedom is

$$\delta W=\int_V\mathbf{u}^T{\mathbf{B}_L}^T\mathbf{D}\ \mathbf{B}_L\ \delta\mathbf{u}\ dV \tag{7.37}$$

The virtual work is calculated by integrating over the volume dependent on the position coordinates.

$$\delta W=\mathbf{u}^T{\mathbf{B}_L}^T\mathbf{D}\ \mathbf{B}_L\ \delta\mathbf{u}\ V \tag{7.38}$$

The nodal forces $\mathbf{F}$ is

$$\delta W=\mathbf{F}^T\delta\mathbf{u}=\mathbf{u}^T{\mathbf{B}_L}^T\mathbf{D}\ \mathbf{B}_L\ \delta\mathbf{u}\ V\ ,\ \mathbf{K}\equiv{\mathbf{B}_L}^T\mathbf{D}\ \mathbf{B}_L\ V\ ,\ \mathbf{F}=\mathbf{K}\ \mathbf{u} \tag{7.39}$$

Here the $[6\times 6]$ square matrix $\mathbf{K}$ is called the stiffness matrix of the Constant Strain Triangle (CST) element.

7.7 Cohesive Element Modeling for Dynamic Analysis

To obtain the field equations describing the material response of the structures consisting of cohesive elements, one should use a Lagrangian approach. Consider a solid of volume V_0 in the reference configuration as represented in Figure 7.13, and a deformed solid of volume V characterized by the base displacement vector, $\overline{\mathbf{X}} = \mathbf{u} + \mathbf{x}$. At time, $t = 0$, a material point is located at $\mathbf{x}$, and at an arbitrary time, this material point is deformed by the displacement vectors $\mathbf{u}$. The relation of the fixed Cartesian frame is denoted as $\mathbf{x}$ that is the position of a material point in the initial configuration. In the current configuration, the material point initially at $\mathbf{x}$, is at $\overline{\mathbf{X}}$. The displacement vector $\mathbf{u}$ and the deformation gradient $\mathbf{F}$ are defined by

$$\mathbf{F} = \frac{\partial \overline{\mathbf{X}}}{\partial \mathbf{x}} = \frac{\partial(\mathbf{u}+\mathbf{x})}{\partial \mathbf{x}},\ \mathbf{F} = \mathbf{I} + \frac{\partial \mathbf{u}}{\partial \mathbf{x}} \tag{7.40}$$

Using the deformation gradient, $\mathbf{F}$, as suggested in Ref.[7.5], the stress integration term in Eq. (7.7) is re-written in terms of the second Piola-Kirchhoff stress tensor $\mathbf{S}$ and Lagrangian strain $\mathbf{E}$.

$$\int_V \mathbf{S} : \delta\mathbf{E} dV - \int_{S_{\text{int}}} \mathbf{T}_{CZ} \cdot \delta\boldsymbol{\Delta} dS = \int_{S_{ext}} \mathbf{T}_e \cdot \delta\mathbf{u} dS - \int_V \rho \frac{\partial^2 \mathbf{u}}{\partial\, t^2} \cdot \delta\mathbf{u} dV,\ \mathbf{S} = \mathbf{s} \cdot \mathbf{F}^{-T},\ \mathbf{E} = \frac{1}{2}(\mathbf{F}^{\mathbf{T}} \cdot \mathbf{F} - \mathbf{I}) \tag{7.41}$$

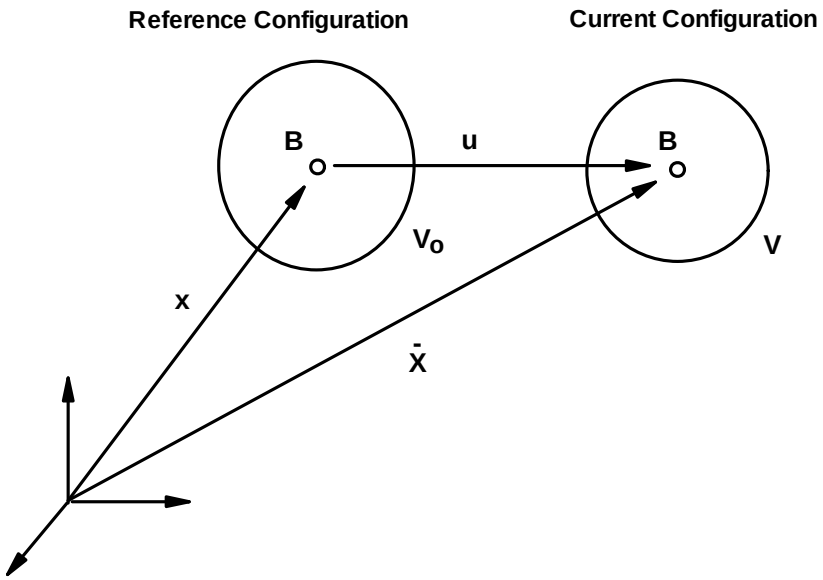

Figure 7.13: Reference configuration and current configuration.

The governing equation of the dynamic response of the cohesive element is obtained from Eqs. (7.7) and (7.41). The applied load vectors $\mathbf{P}$ and the nodal body-force vectors $\mathbf{F}_B$ and cohesive-force vectors $\mathbf{F}_C$ due to the body forces and the cohesive element stresses are used to derive the equilibrium equation by including the mass matrix $\mathbf{M}$, the damping matrix $\mathbf{C}$, and the stiffness matrix $\mathbf{K}$:

$$\mathbf{M}\ \ddot{\mathbf{u}}_t + \mathbf{C}\ \dot{\mathbf{u}}_t + \mathbf{K}\ \mathbf{u}_t = \mathbf{P}_t - \mathbf{F}_{C_t},\ \mathbf{M}\ \ddot{\mathbf{u}}_t + \mathbf{C}\ \dot{\mathbf{u}}_t = \mathbf{P}_t - \mathbf{F}_{B_t} - \mathbf{F}_{C_t} = \mathbf{P}_t - \mathbf{F}_t \tag{7.42}$$

In this work, one of dynamic programs on the cohesive element using the explicit and implicit integration schemes[7.6] is developed, and the explicit scheme is used exclusively in the dynamic analysis program of the cohesive element model. Herein, the explicit integration scheme, a central different method, is considered. The explicit time integration scheme starts by assuming the solution is completely known at the time t and it is desired to find the solution at time $t + \Delta t$.

From the equation (7.42), the difference equations for the nodal velocity vectors $\dot{\mathbf{u}}$ and the acceleration vectors $\ddot{\mathbf{u}}$ at the current time are given:

$$\dot{\mathbf{u}}_t = \frac{1}{2\Delta t}\left[\mathbf{u}_{t+\Delta t} - \mathbf{u}_{t-\Delta t}\right],\ \ddot{\mathbf{u}}_t = \frac{1}{\Delta t^2}\left[\mathbf{u}_{t+\Delta t} - 2\mathbf{u}_t - \mathbf{u}_{t-\Delta t}\right] \tag{7.43}$$

After substituting Eq. (7.43) into the equilibrium equation (7.42) and re-arranging this, the quantities in the left hand side of Eq. (7.42) are evaluated at time $t + \Delta t$.

$$\left[\frac{1}{2\Delta t}\mathbf{C} + \frac{1}{\Delta t^2}\mathbf{M}\right]\ \mathbf{u}_{t+\Delta t} = \mathbf{P}_t - \mathbf{F}_t - \left[-\frac{2}{\Delta t^2}\mathbf{M}\right]\ \mathbf{u}_t - \left[\frac{1}{\Delta t^2}\mathbf{M} - \frac{1}{2\Delta t}\mathbf{C}\right]\ \mathbf{u}_{t-\Delta t} \tag{7.44}$$

The initial conditions are assigned as $\mathbf{u}_0$ and $\dot{\mathbf{u}}_0$ and from Eq. (7.44) and the equation of motion, the initial acceleration $\ddot{\mathbf{u}}_0$, if it is not specified. These equations also yield the displacement vectors $\mathbf{u}_{-\Delta t}$ using the values for the velocity and accelerations.

$$\mathbf{u}_{-\Delta t} = \mathbf{u}_0 - (\Delta t)\ \dot{\mathbf{u}}_0 + \frac{1}{2}(\Delta t)^2 \ddot{\mathbf{u}}_0 \tag{7.45}$$

The mass and damping matrices are arranged to be diagonal, and the solution for the displacements is a trivial computational effort. To calculate the cohesive force vectors $\mathbf{F}_C$ in Eq. (7.30) or (7.42), the traction vectors on the cohesive surfaces are considered and assembled by the cohesive elements. When some of cracks are present between the cohesive elements, one of the contact algorithms is applied, and then post-ruptured elements are separated into the cohesive elements. After finding the post-ruptured elements in each time step, the cohesive element related to the post-ruptured elements are not considered in calculating the cohesive forces or contact forces. Only no post-ruptured elements are assembled with the nodal body-force vectors and the applied load vectors, and then the global load vectors are formed. The new displacement increments obtained from the next time step, and the geometry, stress and strain are updated. The contact algorithm for the post-rupture is discussed later in Chapter 8.

7.8 Algorithm of the Central Difference Method

The algorithm of the central difference method was suggested in Ref. [7.6]. The explicit integration method is very useful for studies in which loading at high rates are expected. The time steps used by the explicit calculations are limited by stability, so some cares must be taken in selecting an appropriate time step for calculations. The main steps of the central difference method in the cohesive element model are as following:

Step 1: Specify initial parameters: time steps, initial velocities, accelerations and displacements.
Step 2: Set up the geometry and material data, boundary conditions.
Step 3: Initialize the stiffness matrix $\mathbf{K}$.
Step 4: Assemble the effective inertia matrix.

$$\mathbf{M}_{eff} = \left[\frac{1}{2\Delta t}\mathbf{C} + \frac{1}{\Delta t^2}\mathbf{M}\right]$$

Step 5: Decompose the effective inertia matrix if necessary.

$$\mathbf{M}_{eff} = \mathbf{U}^T\mathbf{D}\ \mathbf{U}$$

Step 6: Find the accelerations $\ddot{\mathbf{u}}$ from the equation of motion, by using initial conditions $\mathbf{u}_0$ and $\dot{\mathbf{u}}_0$.
Step 7: Read the applied loads and form the applied load vectors $\mathbf{P}$ and the cohesive load vectors $\mathbf{F}_C$.
Step 8: Begin the loop over time increments.
Step 8.1: Assemble the nodal load vectors $\mathbf{F} = \mathbf{F}_B + \mathbf{F}_C$.
Step 8.2: Form the effective load vectors $\mathbf{P}_{eff}$.

$$\mathbf{P}_{eff_t} = \mathbf{P}_t - \mathbf{F}_t - \left[-\frac{2}{\Delta t^2}\mathbf{M}\right]\mathbf{u}_t - \left[\frac{1}{\Delta t^2}\mathbf{M} - \frac{1}{2\Delta t}\mathbf{C}\right]\mathbf{u}_{t-\Delta t}$$

Step 8.3: Solve for the new displacement increments.

$$\mathbf{U}^T\mathbf{D}\ \mathbf{U}\ \mathbf{u}_{t+\Delta t} = \mathbf{P}_{eff_t}$$

Step 8.4: Update the geometry, velocity, stresses and strains.
Step 8.5: Store results from this time step.
Step 9: End loop over the time increments.
Step 10: End.

7.9 Cohesive Element Modeling of Simple Bar Cases

This section considers two examples to describe dynamic behavior, i.e., fracture and crack propagation, when a structure modeled using cohesive elements is subjected to dynamic loading. A simple bar made of Aluminum 7075-T6 is considered and the material properties are provided in Table 7.1. First, the bar model shown in Figure 7.14 is impacted by an impulse load (P) at one of its ends. The boundary conditions are symmetric along the $y = 0$ and all the other three edges are free. The force history is shown in Figure 7.15 in which the rise time is $1\,\mu$sec and two different maximum forces are P_{max}=350 and 800 KN, and the time step used in the calculations is Δt =0.01 μ sec. The cohesive parameters, σ_{max} =7.24 GPa, $\delta = 1.54\times10^{-3}\,mm$, are considered. The velocities are monitored at the specified node point. To prove effective validations of the cohesive element modeling, this bar model are also analyzed by the finite element method using the CST element. In this model, the velocity results of the cohesive element and finite element methods are compared to each other in Figure 7.16. In Figure 7.16 we can see that the results of cohesive element modeling are matched considerably well with the results of finite element method.

For the second bar model, there is a rupturing problem induced by a compressive impulse loading shown in Figure 7.17. In order to see the sudden-rupture cracking, this study considers a small aluminum bar subjected to a compressive transient load, and the modeling as described in Table 7.1 and Figure 7.14.

Figure 7.17 shows the compressive loading history and the boundary conditions for the aluminum bar to induce the rod rupture. The compressive impulse load is applied to the bar between a finite duration (1-6 μ sec), as a rectangular shape, and the deformed shapes of the bar each time step are shown in Figure 7.18. When the bar is subjected to the compressive loads, a compression stress wave of duration 9-

9.5 μ sec travels through the bar during that time. After that, the bar reaches the returning point, and the compression stress wave returns as the tensile stress wave at 9.5 μ sec. The stress wave is reflected as a tension wave as shown in Figure 7.18. When the maximum stress in the bar reaches the ultimate value, such a point of 10.5 μ sec, few cracks in the cohesive element surfaces are formed as shown in Figure 7.18. From Figure 7.18, it appears that the compressive stress does not cause the rupture while the reflected tensile stress induces the rupture when the bar becomes subjected to a higher tensile ultimate stress between the cohesive surfaces. Figure 7.19 describes the normalized stress wave of cohesive elements lying along the symmetric boundary surface at each time step. When the cohesive element reaches the critical point $\sigma_{\max}$, the cohesive surfaces form cracks and the cohesive elements in the mid-point of the bar induce few cracks.

Table 7.1 The material properties of Aluminum 7075-T6

Elastic Modulus	72.0 GPa	Ultimate Strength	570.0 MPa
Poisson's ratio	0.333	Density	2810 Kg/m^3
$\sigma_{\max}$	7.24 GPa	δ	$1.54\times10^{-3}\,mm$

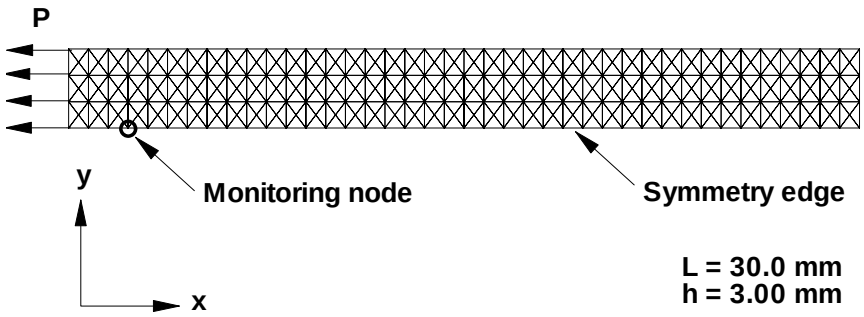

Figure 7.14: The bar model subjected to the impulse tension-loading.

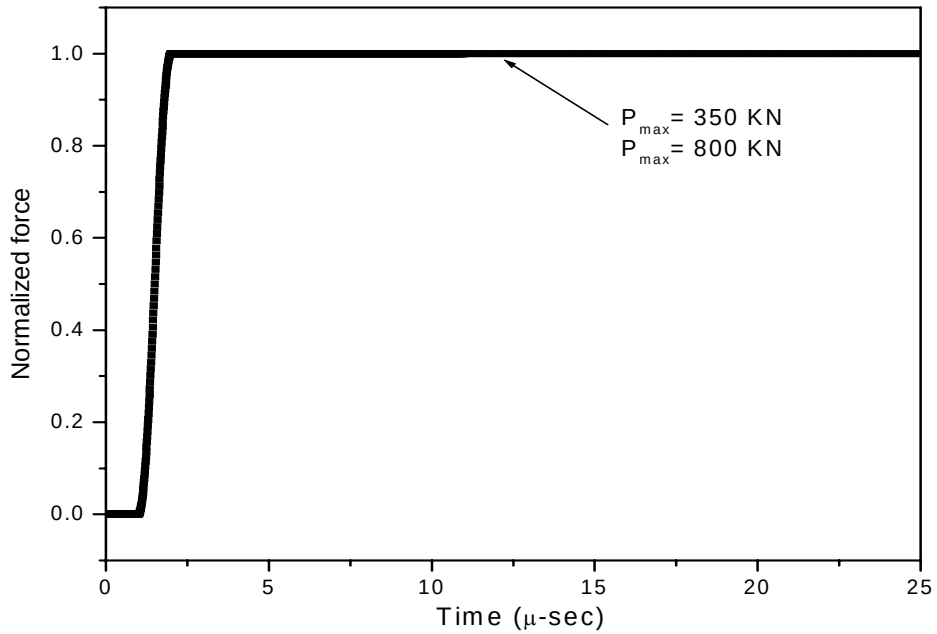

Figure 7.15: Applied forces history in the bar.

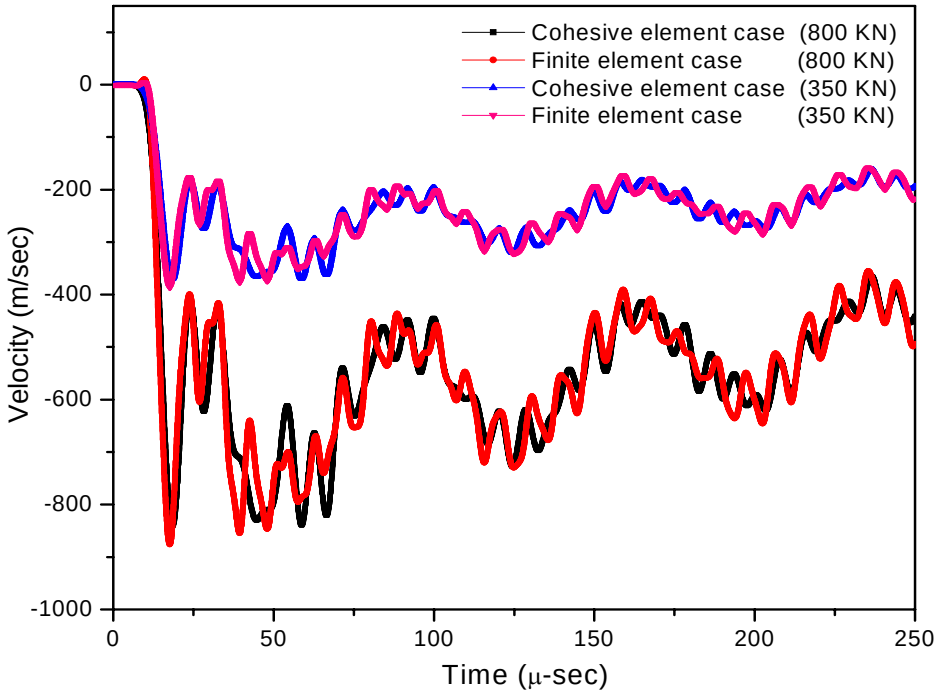

Figure 7.16: Longitudinal velocities' curve at the monitored node in the bar.

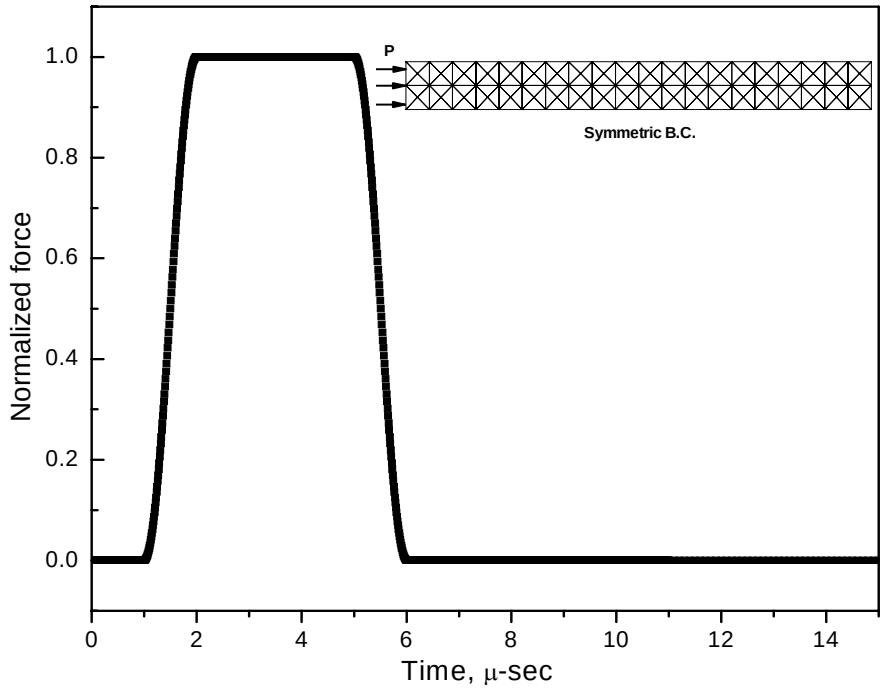

Figure 7.17: Applied loading history and boundary conditions of the compression bar.

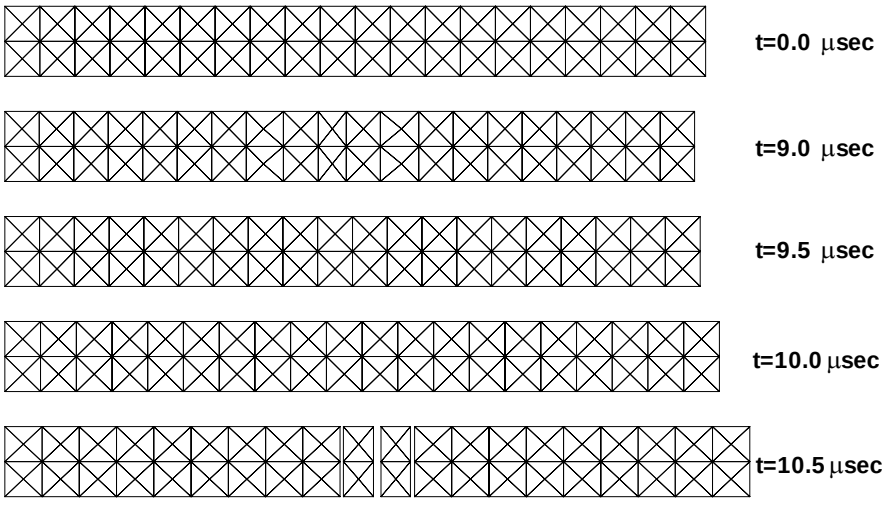

Figure 7.18: Deformed shapes of the compression bar at the different time steps.

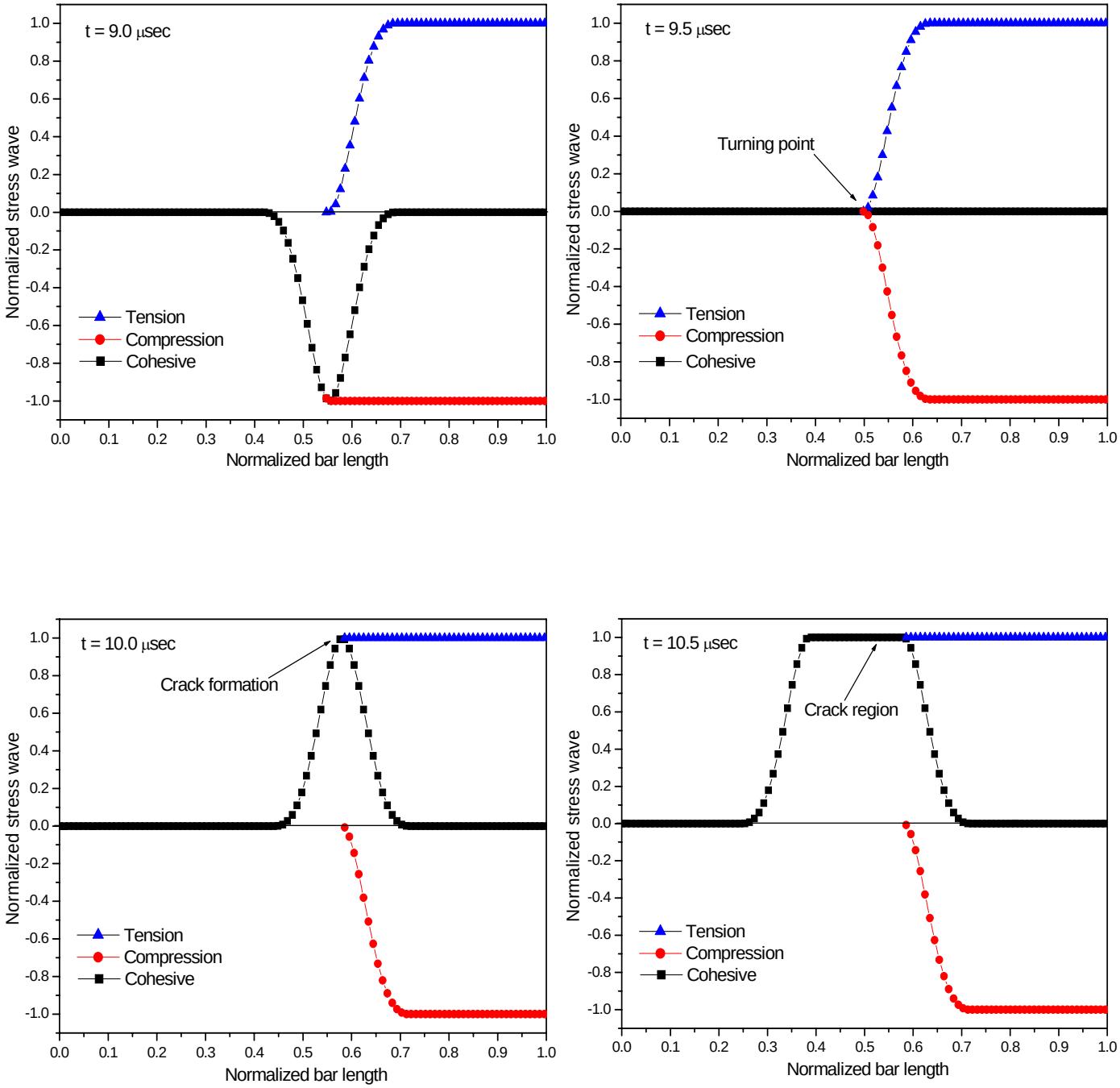

Figure 7.19: Transient normalized stress waves in the bar under compression.

7.10 Cohesive Element Modeling of Central Split Block Case

Another cohesive modeling on a block with an initial central crack shown in Figure 7.20 is analyzed via the computational methodology of the cohesive elements to find crack shapes. The dimensions of the specimen studied by Needleman[7.1] are: the length 2L=3mm and the width 2W=6mm. An initial material separation size is 2a=0.6mm, which lies along the x axis. The material properties are PMMA displayed in Table 7.2. Since the block is symmetric, the simulation is carried out using only half of the model. The initial conditions at t=0 are stipulated to be zero. The model has a uniform stress mixed with constant velocities applied at the boundaries to produce a tensile wave that propagates through the specimen, and then reflects from the traction free boundaries as a compressive stress wave. These reflections introduce some complexities in the system of stresses and so the dimensions are chosen in order to minimize these.

Some results of stresses and deformed shapes are shown in Figures 7.20 through 7.22. The deformed shapes show the crack propagation with several branching. Through the stress distributions, we know that the crack will propagate along the cohesive elements having the stress concentrations. At the crack tip, because of the stress concentration, the stress level eventually exceeds the critical value of cohesive stress and de-cohesion initiates and starts propagating: if the stress generated by the wave exceeds σ_{max}, de-cohesions occur at the surfaces between the cohesive elements. Once the crack begins propagating, the moving tip crack produces stress concentration at the new tip crack that causes continuous crack propagation. Moreover, from this split block model, it can be concluded that the characteristics of dynamic crack propagations are dependent upon a threshold value of load to initiate a limiting crack speed, crack branching, and the possibility of crack arrests.

Table 7.2 The material properties and cohesive element parameters of PMMA from Ref. [7.1].

Elastic Modulus	3.24 GPa	Shear Modulus	1.20 GPa	σ_{max}	324.0 MPa	$\delta_n = \delta_t$	4.0×10^{-7} m
Poisson's ratio	0.35	Density	1199 Kg/m^3	τ_{max}	755.4 MPa	$\phi_n = \phi_t$	352.3 J/m^2

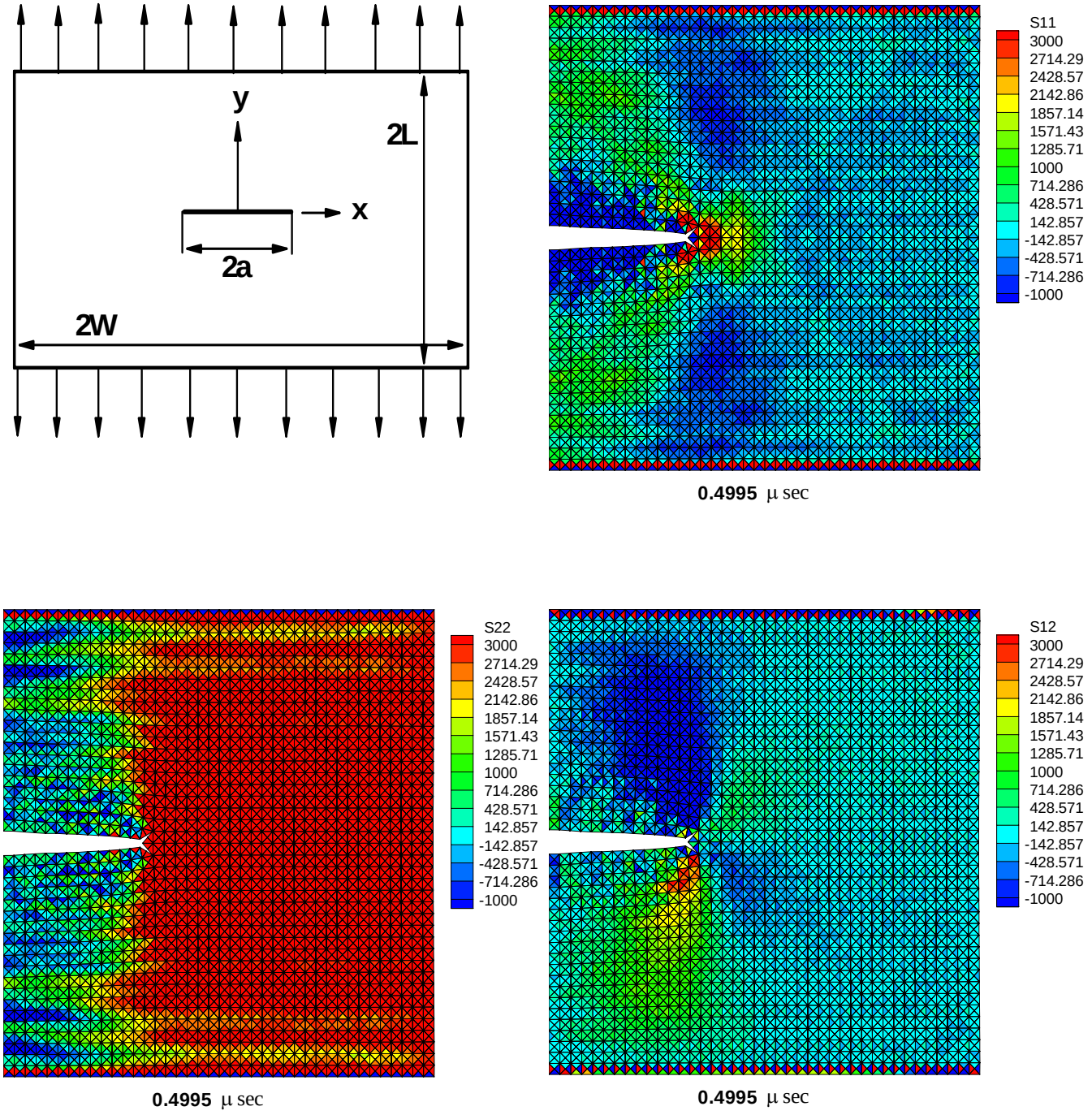

Figure 7.20: The center split block model and stresses at t =0.4995 μ sec.

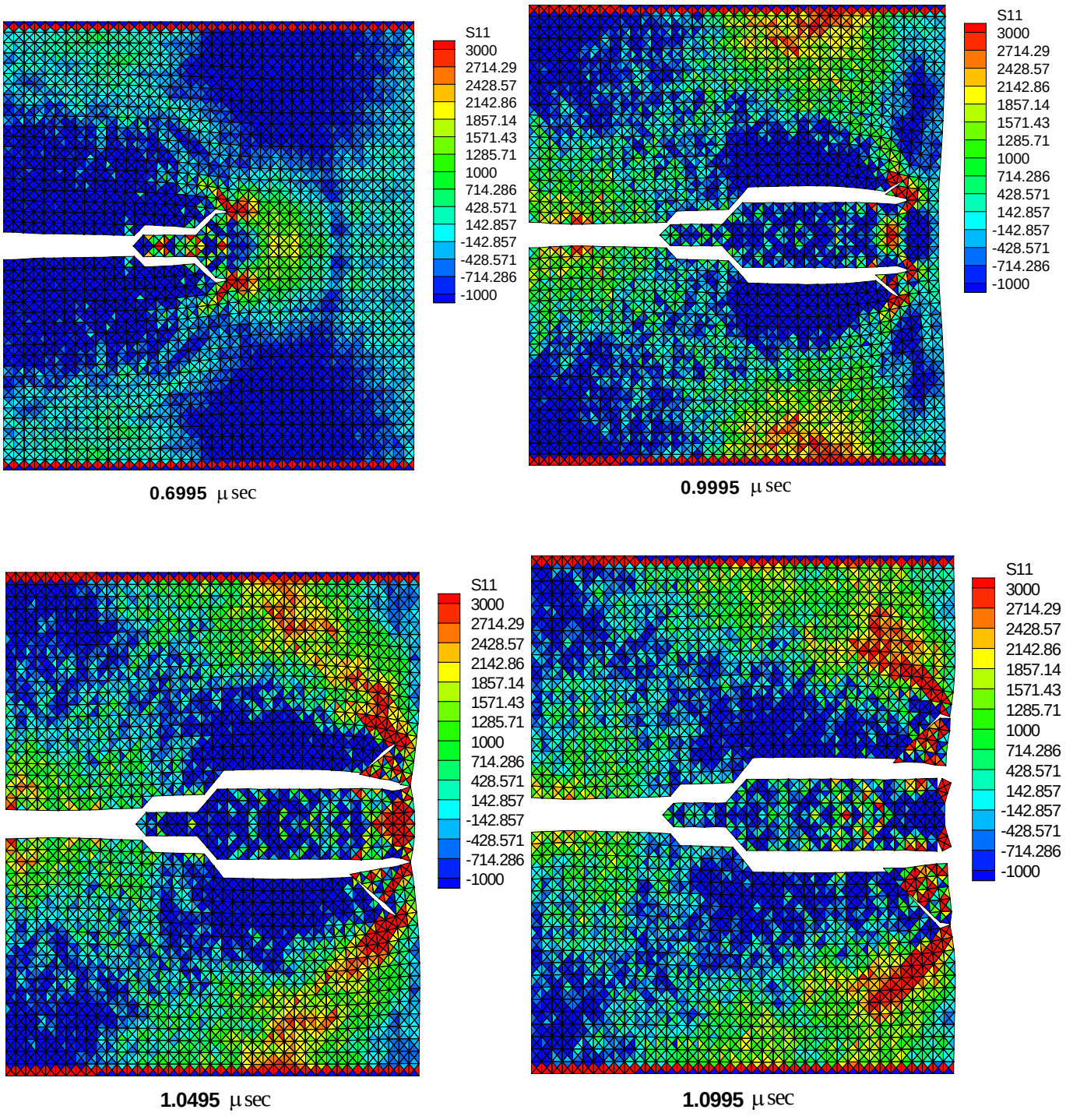

Figure 7.21: The deformed shapes and stress (σ_{11}) of the split block.

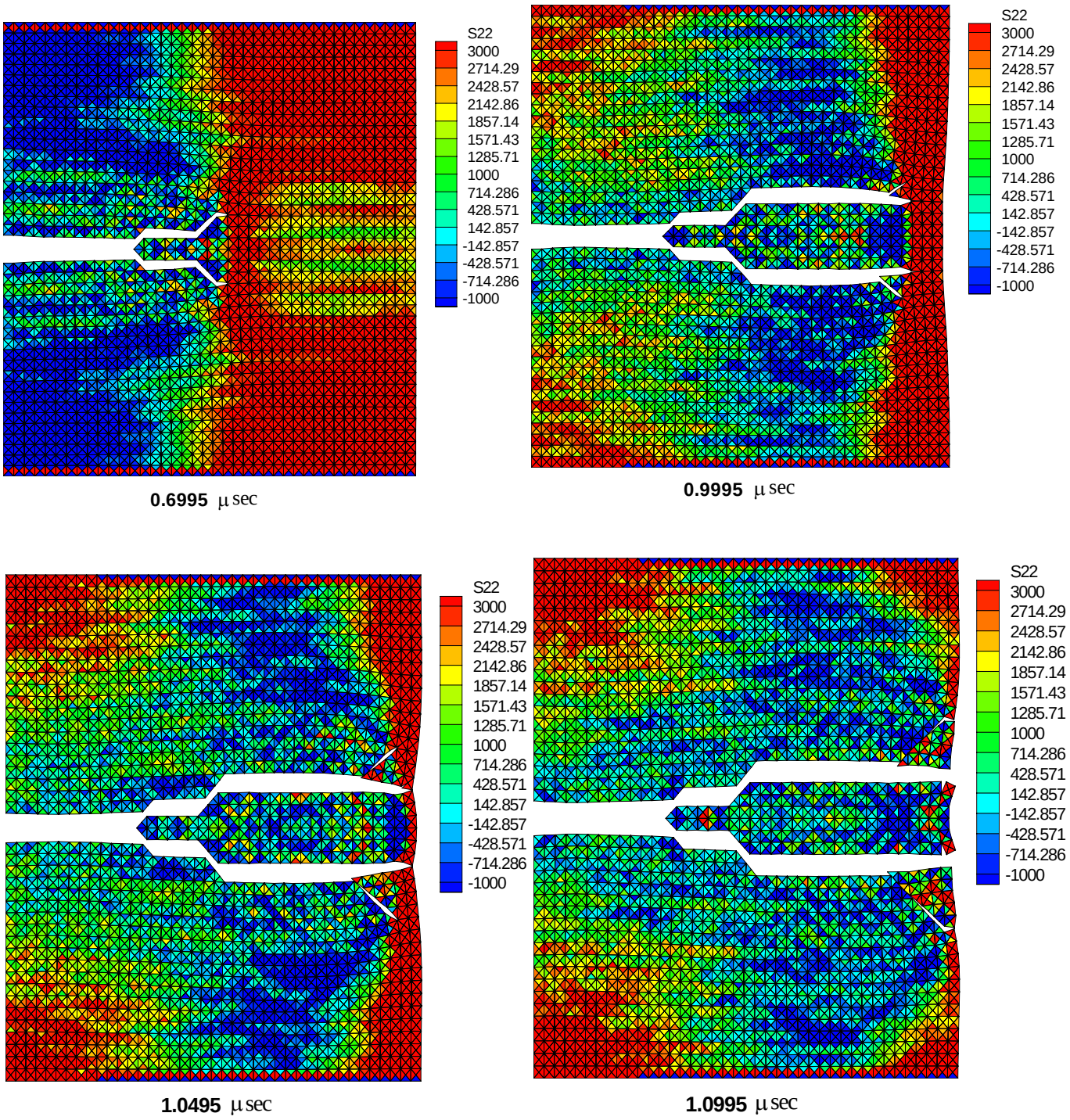

Figure 7.22: The deformed shapes and stress (σ_{22}) of the split block.

REFERENCES

7.1 Xu, X.-P. and A. Needleman, "Numerical Simulations of Fast Crack Growth in Brittle Solids," *Journal of the Mechanics and Physics of Solids,* Vol. 42, No. 9, 1994, pp. 1397-1434.

7.2 Chaboche, J.L., R. Girard and P. Levasseur, "On the Interface De-bonding Models," *International Journal of Damage Mechanics*, Vol. 6, No. 3, 1997, pp. 220-257.

7.3 Needleman, A., "Micro-mechanical Modeling of Interfacial De-cohesion," *Ultra-microscopy*, Vol. 40, No. 3, 1992, pp. 203-214.

7.4 Needleman, A., "A Continuum Model for Void Nucleation by Inclusion De-bonding," *Journal of Applied Mechanics*, Vol. 54, September, 1987, pp. 525-531.

7.5 Coker, D., A.J. Rosakis and A. Needleman, "Dynamic Crack Growth along a Polymer Composite-Homalite," *Journal of the Mechanics and Physics of Solids*, Vol. 51, No. 3, 2003, pp. 425-460.

7.6 Bathe, K. J., "Finite Element Procedures in Engineering Analysis," Prentice-Hall Inc., 1982.

Chapter 8 Contact Mechanics of Cohesive Element Modeling

8.1 Introduction

In Chapter 7, we have briefly discussed the cohesive element modeling and investigated the response of some examples, numerically using this modeling. When the cohesive elements are used to study impact and contact phenomena, an effective separation algorithm for the contact is needed between the striker and target elements consisting of cracked or un-cracked elements. The separation algorithm has to apply effectively into even post-ruptured material and fragmentation problems during the impact. This chapter is focused on effective contact algorithms to be used in conjunction with the cohesive element modeling depending upon the material types, i.e. ductile or brittle-target modeling. Semi-empirical contact modeling and contact procedures as applied to the cohesive modeling also are studied. But complicated friction contact problems between the striker and target modeling are not considered, since the friction modeling in itself is a very difficult task. It is suggested that a future study investigates the role of friction in damage mechanics of impact loaded textile structures.

8.2 Empirical Contact Modeling

If a striker strikes one of the targets, a momentum transfer due to a complex contact force interactions between two materials take places. In order to calculate both the contact force and the momentum during the contact, it is necessary to know some of contact laws that are related to the material properties of the striker and target. There are two kinds of contact laws, i.e. plastic and elastic contact laws. In these cases, the indentation concept is used to calculate approximate forces for the plastic and elastic contacts. In the first case, to derive the empirical plastic contact modeling, we use several variables. The yield stress of the both materials, radius R of the striker, the relative indentation α and the radius a of the area of contacts are considered for modeling a plastic contact.

$$\alpha = v_s - v_t = \frac{a^2}{2R} \tag{8.1}$$

The contact force P is based on the average stresses when the target can be assumed to have reached the yield situation.

$$P = 2\sigma_Y at \tag{8.2}$$

Here, t is the thickness of projectiles. The plastic contact force is

$$P = 2\sigma_Y t\sqrt{2Rv_s} = \gamma\alpha^{1/2} \tag{8.3}$$

Figure 8.1 shows the plastic contact cases where a hard striker hits a soft target and also where a soft striker hits a hard target. For the second case, the elastic contact force can be derived using the indentation theory. This study considers two spheres contacting as shown in Figure 8.2. This can be depicted Hertzian theory[8.1-8.2] of contact stresses and leads to a nonlinear form of contact laws.

$$P = K\alpha^{3/2} = K(v_s - v_t)^{3/2},\ K = \frac{4}{3}\sqrt{\frac{R_s R_t}{R_s + R_t}\left(\frac{k_s k_t}{k_s + k_t}\right)},\ k_s = \frac{E_s}{1-\nu_s^2},\ k_t = \frac{E_t}{1-\nu_t^2} \tag{8.4}$$

Here E_s and E_t is the Young's modulus and ν_s and ν_t is the Poisson's ratio for the striker and the target, respectively. Using this equation the elastic contact forces and indentation are represented in Figure 8.2.

These empirical contact modeling have their limits in modeling contact problems and even cohesive element modeling combined with micro-cracking and fragmentations. This study considers two contact algorithms to solve the complicated contact problems in conjunction with the cohesive modeling: un-cracked elements' contact algorithm and cracked elements' contact algorithm. The un-cracked elements' contact algorithm is a general surface contact algorithm used in classic finite element analysis while the cracked elements' contact algorithm is used in the cohesive element analysis.

8.3 Un-cracked Elements' Contact Modeling

For the contact modeling in un-cracked elements, this study presents a surface contact algorithm[8.1-8.11] for both the striker and target modeling. The description of the surface for each of the two objects, the striker and target, is provided by collecting node lists that consist of structure surfaces in two dimensions. In the dynamic analysis, node displacements and stresses are calculated, and then the contact conditions are applied to the candidate contact surfaces to find relative movement of the two structures. To find exact contact points, appropriate conditions for determining contact are needed. The following contact detection algorithm presents detailed contact conditions[8.1], pushback directions for penetrated slave nodes and contact forces of contacting nodes. The appropriate conditions for determining contact are induced by some contact segments, surface tangents and penetrated slave nodes. Figure 8.3 shows the simplest possible case, two dimensional contacts with bilinear discrete projectiles. By using the dot products for node coordinates, two nearest master elements are examined to find the contact points. The dot products of the two master elements adjoining the corner node X^1_{i+1} are calculated by the surface tangent vectors, $\mathbf{e}^1_{i+2}$ and $\mathbf{e}^1_{i+1}$, see Figures 8.4-8.5. These vectors are based upon the reference frames $(r-s\,, r^*-s^*)$.

$$(\mathbf{X}^2_{k+1}-\mathbf{X}^1_{i+1})\bullet\mathbf{e}^1_{i+2}\,,\ (\mathbf{X}^2_{k+1}-\mathbf{X}^1_{i+1})\bullet\mathbf{e}^1_{i+1} \tag{8.5}$$

The contact point is determined according to the following four cases of pushback directions:

- If $(\mathbf{X}^2_{k+1}-\mathbf{X}^1_{i+1})\bullet\mathbf{e}^1_{i+2}\le 0$ and $(\mathbf{X}^2_{k+1}-\mathbf{X}^1_{i+1})\bullet\mathbf{e}^1_{i+1}<0$, the master segment (X^1_{i+2} - X^1_{i+1}), contains the contact point $\bar{\mathbf{y}}$.
- If $(\mathbf{X}^2_{k+1}-\mathbf{X}^1_{i+1})\bullet\mathbf{e}^1_{i+2}>0$ and $(\mathbf{X}^2_{k+1}-\mathbf{X}^1_{i+1})\bullet\mathbf{e}^1_{i+1}\ge 0$, the master segment (X^1_{i+1} - X^1_i), contains the contact point $\bar{\mathbf{y}}$.
- If $(\mathbf{X}^2_{k+1}-\mathbf{X}^1_{i+1})\bullet\mathbf{e}^1_{i+2}\le 0$ and $(\mathbf{X}^2_{k+1}-\mathbf{X}^1_{i+1})\bullet\mathbf{e}^1_{i+1}\ge 0$, the master segment (X^1_{i+1} - X^1_i), contains the contact point $\bar{\mathbf{y}}$ or the master segment (X^1_{i+2} - X^1_{i+1}), contains the contact point $\bar{\mathbf{y}}$. Here by considering much more large values between $\left|(\mathbf{X}^2_{k+1}-\mathbf{X}^1_{i+1})\right|$ and $\left|(\mathbf{X}^2_{k+1}-\mathbf{X}^1_{i+1})\right|$, the pushback direction is determined.
- If $(\mathbf{X}^2_{k+1}-\mathbf{X}^1_{i+1})\bullet\mathbf{e}^1_{i+2}>0$ and $(\mathbf{X}^2_{k+1}-\mathbf{X}^1_{i+1})\bullet\mathbf{e}^1_{i+1}<0$, the corner node X^1_{i+1} is itself the contact point $\bar{\mathbf{y}}$.

After deciding the pushback directions and finding the contact point assumed as locating in the master segment (X^1_{i+2} - X^1_{i+1}), the distance of penetration, p , is calculated from the slave node X^2_{k+1} to the contact point $\bar{\mathbf{y}}$ on the master surface.

$$p=\left|\ \mathbf{d}_{ms}\bullet\mathbf{e}^1_{i+2}\ \right| \tag{8.6}$$

Here the length of vector $\mathbf{d}_{ms}$ is written as the coordinate of the node X^1_{i+2} and X^2_{k+1} shown in Figure 8.5.

$$d_{ms}=\sqrt{(x^2_s-x^1_{i+2})^2+(y^2_s-y^1_{i+2})^2} \tag{8.7}$$

In the next step, the total contact force vectors, $\mathbf{F}_s$ acting on the contacting nodes are calculated from contact stiffness matrix, $\mathbf{K}_s$ and contact nodal mass of the master elements. To get the contact forces, we have to know the surface tangent vectors of the contact point at each time step, first. The distance of penetration, p , has the same surface tangent vector, $\mathbf{p}_t=\mathbf{e}^1_{i+2}$ that is the same direction of the pushback. The coordinate of the contact point $\bar{\mathbf{y}}$ $(x_c\,, y_c)$ in Figure 8.5 is determined by intersecting the master surface with the pushback direction.

$$(x_c, y_c)\ =\ (x_s, y_s)\ +\ (p(\mathbf{p}_t\bullet\mathbf{r}), p(\mathbf{p}_t\bullet\mathbf{s})) \tag{8.8}$$

To get the relative angle, θ , between nodes X^1_{i+2} and X^1_{i+1}, these nodes' coordinates are used.

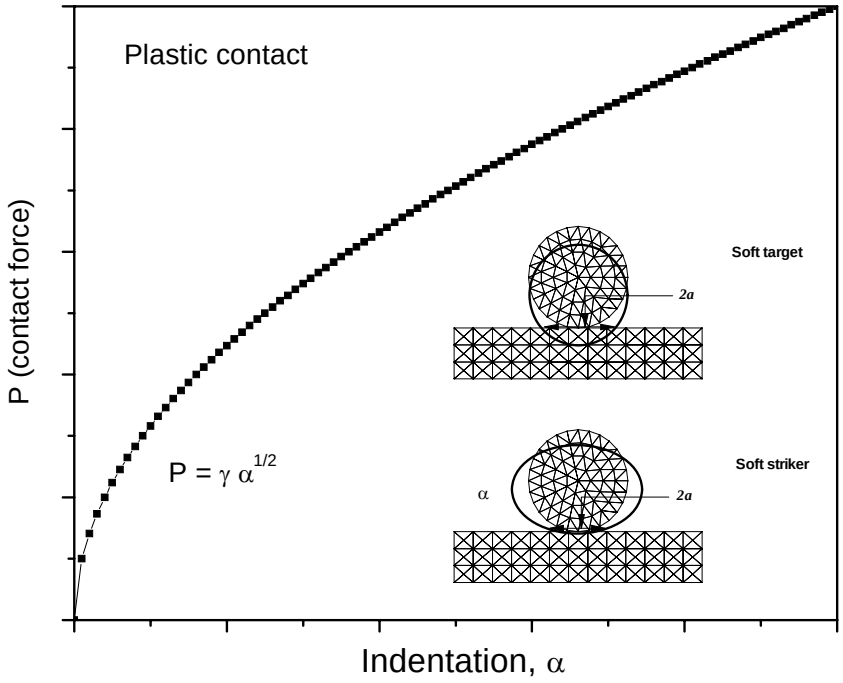

Figure 8.1: Contact forces and indentation for the plastic contact cases.

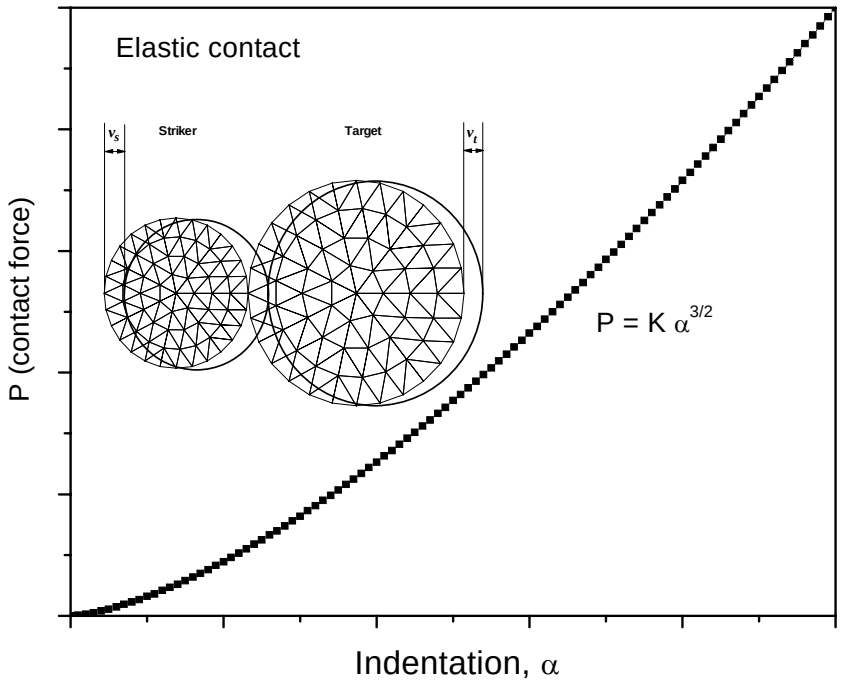

Figure 8.2: Contact forces and indentation for the elastic contact cases.

$$\theta = \tan^{-1}\left(\frac{y^1_{i+2} - y^1_{i+1}}{x^1_{i+2} - x^1_{i+1}}\right) \tag{8.9}$$

Using the notation of Hallquist[8.3-8.6] and letting

$$a = \frac{\left[(x_c - x^1_{i+1})^2 + (y_c - y^1_{i+1})^2\right]^{1/2}}{\left[(x^1_{i+2} - x^1_{i+1})^2 + (y^1_{i+2} - y^1_{i+1})^2\right]^{1/2}} \tag{8.10}$$

And then the contact stiffness matrix $\mathbf{K}_s$ about the contact point $\bar{\mathbf{y}}$ and the contact nodes X^1_{i+2} and X^1_{i+1}, is

$$\mathbf{K}_s = k \begin{bmatrix} s^2 & -sc & -(1-a)s^2 & (1-a)sc & -as^2 & asc \\ & c^2 & (1-a)sc & -(1-a)c^2 & asc & -ac^2 \\ & & (1-a)^2 s^2 & -(1-a)^2 sc & (1-a)as^2 & -(1-a)asc \\ & & & (1-a)^2 c^2 & -(1-a)asc & (1-a)ac^2 \\ & & & & a^2c^2 & -a^2sc \\ & & sym. & & & a^2c^2 \end{bmatrix} = \begin{bmatrix} K^c_{sx} \\ K^c_{sy} \\ K^{i+1}_{sx} \\ K^{i+1}_{sy} \\ K^{i+2}_{sx} \\ K^{i+2}_{sy} \end{bmatrix} \tag{8.11}$$

Here k is defined by $k = m/\Delta t^2$ and s & c mean $s = \sin\theta$ and $c = \cos\theta$, respectively. The term of m is the contacting target node mass, and Δt means the time step size. The contact force matrix $\mathbf{F}_s$ about the contact point $\bar{\mathbf{y}}$ and the contact nodes X^1_{i+2} and X^1_{i+1}, is

$$\mathbf{F}_s = kp \begin{bmatrix} -s \\ c \\ (1-a)s \\ -(1-a)c \\ as \\ -ac \end{bmatrix} = \begin{bmatrix} F^c_{sx} \\ F^c_{sy} \\ F^{i+1}_{sx} \\ F^{i+1}_{sy} \\ F^{i+2}_{sx} \\ F^{i+2}_{sy} \end{bmatrix} \tag{8.12}$$

This general surface contact algorithm is only effective in finite element method and also in the un-cracked cohesive elements but is not effective to study the post ruptured cohesive elements or even cracked elements. The cohesive elements have a lot of post ruptured elements, fragmentations, inter-element collisions and erosion elements during the impact duration.

8.4 Cracked Elements' Contact Modeling

If a brittle target is impacted, a lot of element fragmentations are obtained, and the fragmentations could possibly move into other elements that may not be of the actual phenomenon. Some of inter-element collisions occur through fragmentation element faces. The striker and target contact surfaces could not be easily represented during a very fast dynamic analysis even if very fine time steps are used. This means that general contact segments, the collected node groups, are not more effective methods for contact problems for solving problems related to the brittle material impact, because some of post-rupture cracks and prost-rupture crack surfaces are formed after each time step.

To prevent this, an effective contact algorithm is needed, and in the present analysis one simple application is introduced to reduce computational effort. Each CST element is defined in which an inner circle is included, see Figure 8.6. The diameter of the circle $2r$ is calculated from three node coordinates, the central node of the circular pseudo-element and angle values (θ_1, θ_2 & θ_3). In Figure 8.6 the central node's coordinate of the circular pseudo-element is calculated as the average position of the three corner nodes.

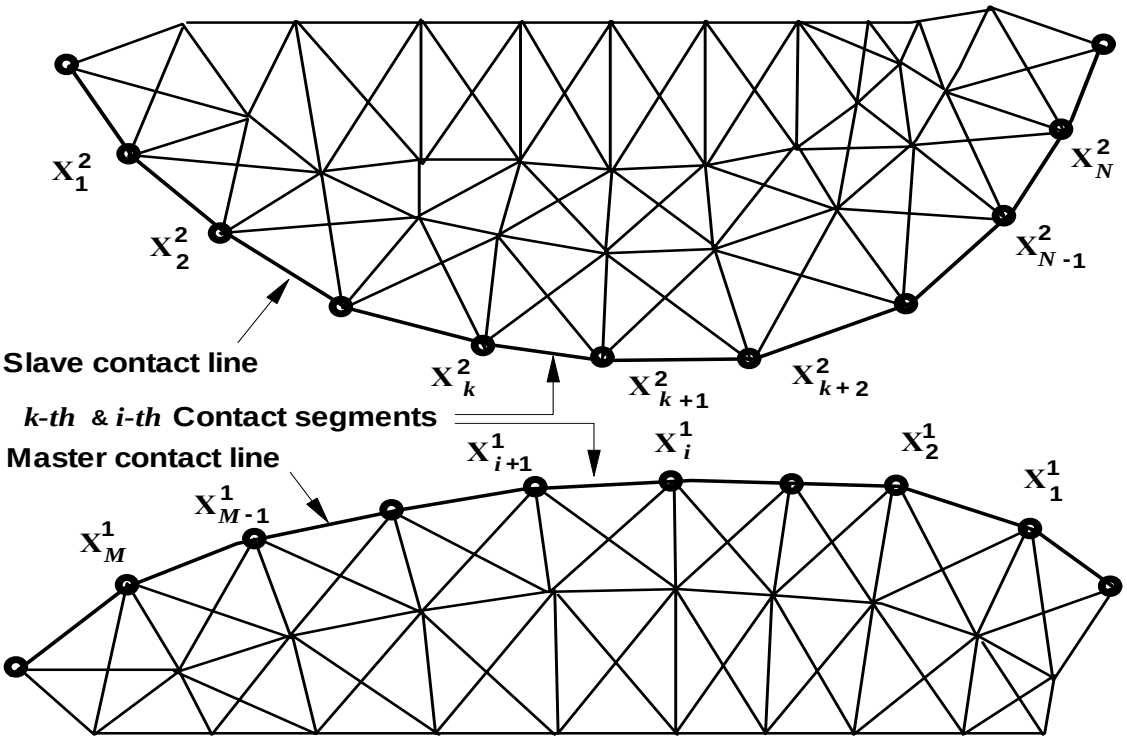

Figure 8.3: Contact surfaces between the striker and the target elements[8.1].

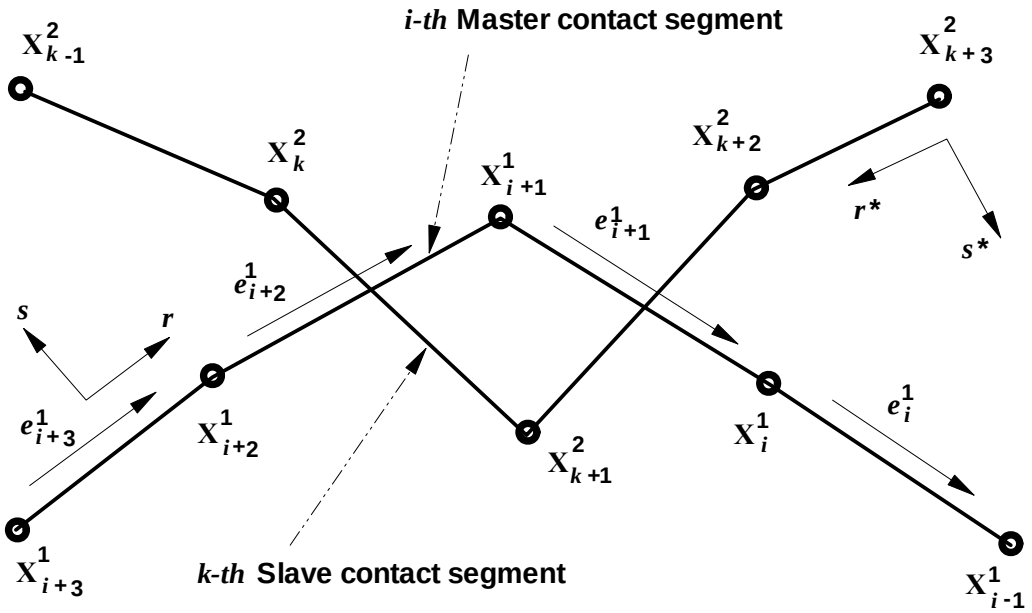

Figure 8.4: Contact penetration between the contact segments[8.1].

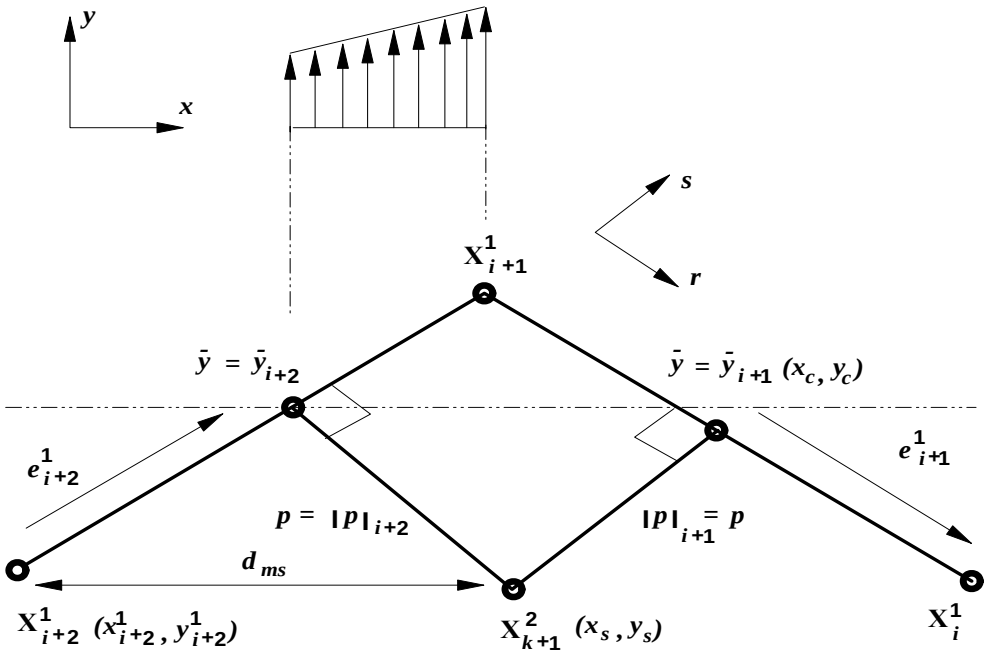

Figure 8.5: The penetration point and the target contact segments[8.1].

$$(x_1, y_1) \;=\; \frac{1}{3}(x_1^p + x_2^p + x_3^p,\;\; y_1^p + y_2^p + y_3^p) \tag{8.13}$$

The circular pseudo-element radius, r, is described by the angle terms θ_i of corner nodes.

$$r = \sin(\frac{\theta_i}{2})\sqrt{(x_1 - x_i^p)^2 + (y_1 - y_i^p)^2}\;,\; i = 1,2,3 \tag{8.14}$$

During the analysis, the position of the target element is compared to the position of all other elements that are not currently connected to the target elements, such as fragmentation elements. If the circular region between collision elements, i and j is found to be within the circular region of the target element, the inter-penetration distance, δ, is calculated as shown in Figure 8.7.

$$\delta = \sqrt{(x_2 - x_1)^2 + (y_2 - y_1)^2}\;,\; 2r = r_i + r_j \tag{8.15}$$

To find the penetration length, d, there is a need for a penetration criteria between the collision elements. The criteria are if $d = 2r - \delta \le 0$, there is no collisions, and if $d = 2r - \delta > 0$, there is collisions. However node pushback problems are not needed, because the penetration length is used. This distance of penetration is used to calculate a collision contact force based on an elastic collision. As the un-cracked elements' contact is used, the contact force of cracked elements is calculated from $F = md/\Delta t^2$. The term m is the node mass of contacting cohesive elements, and Δt means the step size. Using the distribution parameters for nodal contact forces (α_i, β_i and γ_i), the contact force is equally divided into two collision elements and distributed among the contacted element nodes. The magnitude of the distribution is relative to the nodal mass versus the element mass such that the force creates rigid body accelerations. The direction of the force is co-linear with the line connecting the central node of the target and collision elements. The direction and the distribution of the forces are shown in Figure 8.7.

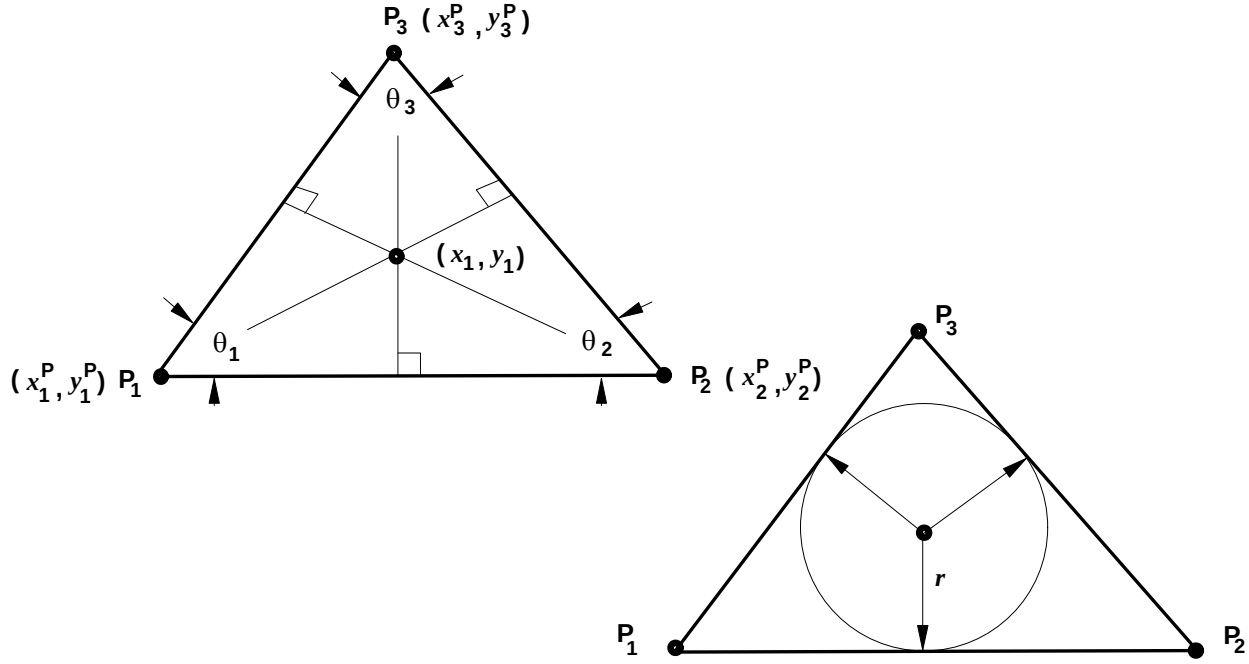

Figure 8.6: A circular pseudo-element and a CST element.

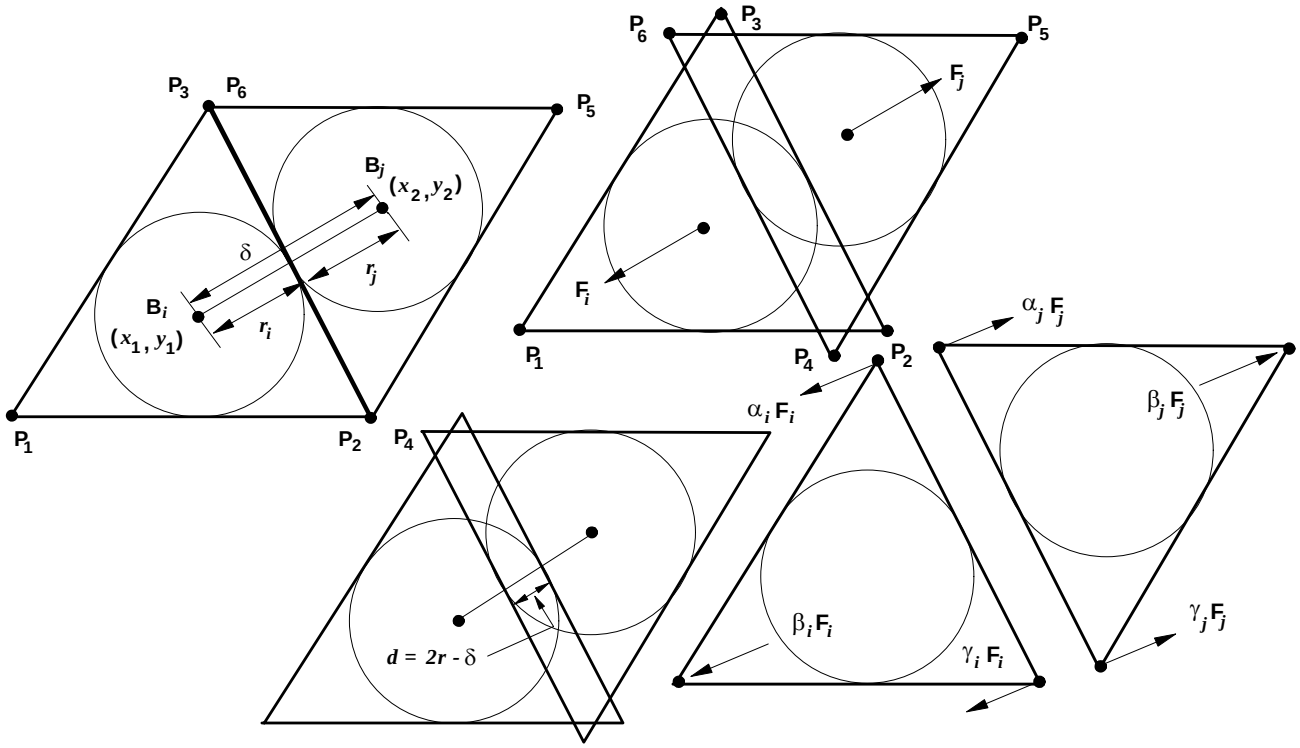

Figure 8.7: Contact conditions between two elements.

8.5 Erosion Contact Modeling

When the contact problem of the ductile material is considered in a high velocity impact, there is needed an appropriate model for plastic deformations because of a large amounts of plastic deformation and severe distortions and erosions in the contact regions. If the ductile material target is subjected to the high velocity projectile, the material between the projectile and target can be eroded off. So a good contact algorithm for the ductile materials will be needed. During last several years, the plastic deformations and the plastic flow theory for the erosion problems have been insufficient to explain the erosion phenomenon. Researchers[8.12-20] have tried to find other solutions to explain this. During the penetration phenomena, a material experiences large deformations and becomes to deteriorate, and finally failure states, such as degraded materials, are made. The degraded materials do not have any ability to support the structural stiffness or even the impact loads. Some experiences show that the ductile materials experience a large drop of stiffness before the material is eroded off. For this problem, a simple linear damage rule is suggested.

$$E_T = (1-d)E_0,\ d = \frac{\alpha}{1-\alpha}\left(1-\frac{\varepsilon_d}{\varepsilon_t}\right),\ \alpha\varepsilon_d < \varepsilon_t < \varepsilon_{er} \tag{8.16}$$

Here, ε_t is total effective strain, ε_{er} and ε_d are related by $\varepsilon_{er} = \alpha\varepsilon_d$ to each other. In this equation, the material deformation is plastic up to strain, ε_d, but when the strains exceed the value of ε_d, the stiffness degrades and the erosion takes place of the material as shown in Figure 8.8.

An erosion contact algorithm was suggested in Ref. [8.16], and used an erosion strain and a failure strain. The strain exceeds the value of ε_{er} in Eq. (8.16), and then failure problems can take place in both the striker and target elements. Once failures occur, the mass is redistributed into a number of neighboring elements by removing the failure elements in the contact algorithm. The other problem is that the contact forces depend considerably on the cohesive forces. When the failed elements are found, the failure elements are removed and re-connected the un-failure elements each other.

The erosion contact algorithm allows the failure element to be removed after each time step and re-form new contact segments that are used in the next time step. For example, Figure 8.9 shows several elements contacting each other along the contact surfaces. In the cohesive element, each element has three nodes and three contact surfaces consist of two nodes that will be matched with similar nodes on the other contact surfaces. In this study the reference frame and contact laws have been described in previous sections and are used to check the contact regions. Once the contact segments are found, the effective plastic strain of contact elements are examined whether or not the effective plastic strain exceeds the erosion strain ε_{er}. In Figure 8.9 several elements have failed and erosion algorithm is applied to remove these elements. One of the slave contact elements has one side ($X_1^2 - X_3^2$) on the contact surface, and the effective plastic strains have exceeded and this element is considered totally failed. The current contact surface ($X_1^2 - X_3^2 - X_4^2 - X_5^2$) in the slave elements have been removed and a new contact surface ($X_1^2 - X_2^2 - X_3^2 - X_4^2$ or $X_1^1 - X_{M+1}^1 - X_3^1 - X_4^1 - X_5^1$) of slave and master elements is re-formed. If another element on the contact surfaces has failed, i.e. two sides ($X_3^1 - X_4^1 - X_5^1$), this element is checked for the erosion strain. The exceed strains in the contacted master elements are found and then these current contact surfaces are eliminated again. Another new contact surface ($X_1^2 - X_2^2 - X_3^2 - X_4^2$ or $X_1^1 - X_{M+1}^1 - X_3^1 - X_5^1$) is formed. Once erosion takes place in an element, the element is removed by following aforementioned steps, and its mass is redistributed into the neighbor nodes.

8.6 Numerical Examples of Un-cracked Elements' Contact Modeling

To evaluate the surface contact algorithm of Finite Element Analysis already described in the section 8.3, a simple example is considered. An aluminum rectangular projectile, 0.1×0.1 m^2, strikes into a

ceramic target with a velocity of 100 m/s. Some deformation shapes of the target are shown in Figure 8.10. This velocity range causes linear deformation in the striker, and therefore this problem can be solved as normal contact problem with degradation of material and the contact between striker and target taken into account. Figure 8.11 shows the resultant contact force and indicates a smooth contact force history over the contact duration. Another case with a low velocity of 50 m/s is next studied. The contact algorithm in our research shows a good ability to detect the contact conditions, contact points and calculate contact forces between the two structures; the target and the striker.

To check one of contact algorithms, we studied Heritzian contact problem. Figure 8.12(a) shows a 6061-T6 aluminum plate subjected to an impact of ETG-100 steel cylinder having different impact velocities. The dimension of plate and cylinder are: the cylinder radius R =7 mm, the plate height H =13 mm and the plate span L =52 mm. The material properties of the steel and aluminum are listed in Table 8.1. To calculate contact forces at different impact velocities, two models, an elastic model and a plastic model, are considered respectively. From Figure 8.12(b), the elastic model shows larger contact forces than those for the case of plastic model. In the elastic model when the low impact velocity is applied, the contact duration is increased, while in the high impact velocity case, the contact duration is decreased. The contact forces also form the symmetric shapes along the contact duration. However, the plastic model shows a much large contact durations and smaller contact forces for different impact velocities. In addition irregular shapes for the contact forces are formed.

Figure 8.13 (a) shows impulses imparted to the target during both the elastic and plastic cases. The elastic model has a linear curve but the plastic model has a little irregular linear curve at higher impact velocities. From Figures 8.12(b) and 8.13(a), we can see that the impulse imparted in the elastic case satisfies the momentum conservation quite accurately. Figure 8.13(b) shows the momentum transfer from the striker in the two cases. In the elastic model, the momentum changes are the same constants but the plastic model has some changes in the momentum values. In the low impact velocity case, the difference in these two models is small, while at the higher impact velocity case, the difference between two models is large and remains almost constant as the impact velocity changes. This nearly constant difference in the momentum transfer is introduced by the plastic deformation of the target. This problem can be explained using the fact that plastic deformation of the plate absorbs the high kinetic energy, by absorbing this energy due to plastic deformation. As a result, the rebound velocity of the cylinder is only approximately 0.2 times the initial impact velocity.

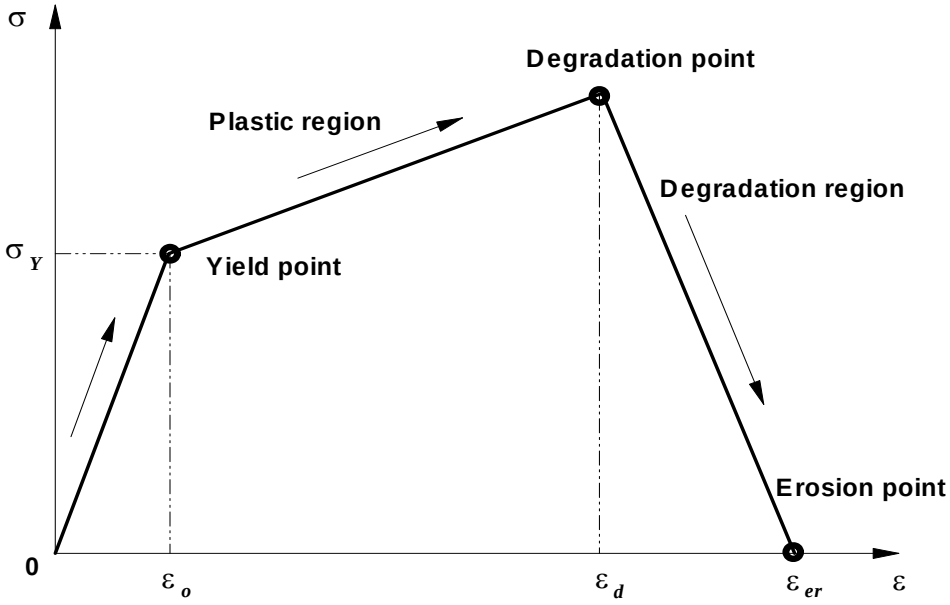

Figure 8.8: Stress and strain curve for a ductile material.

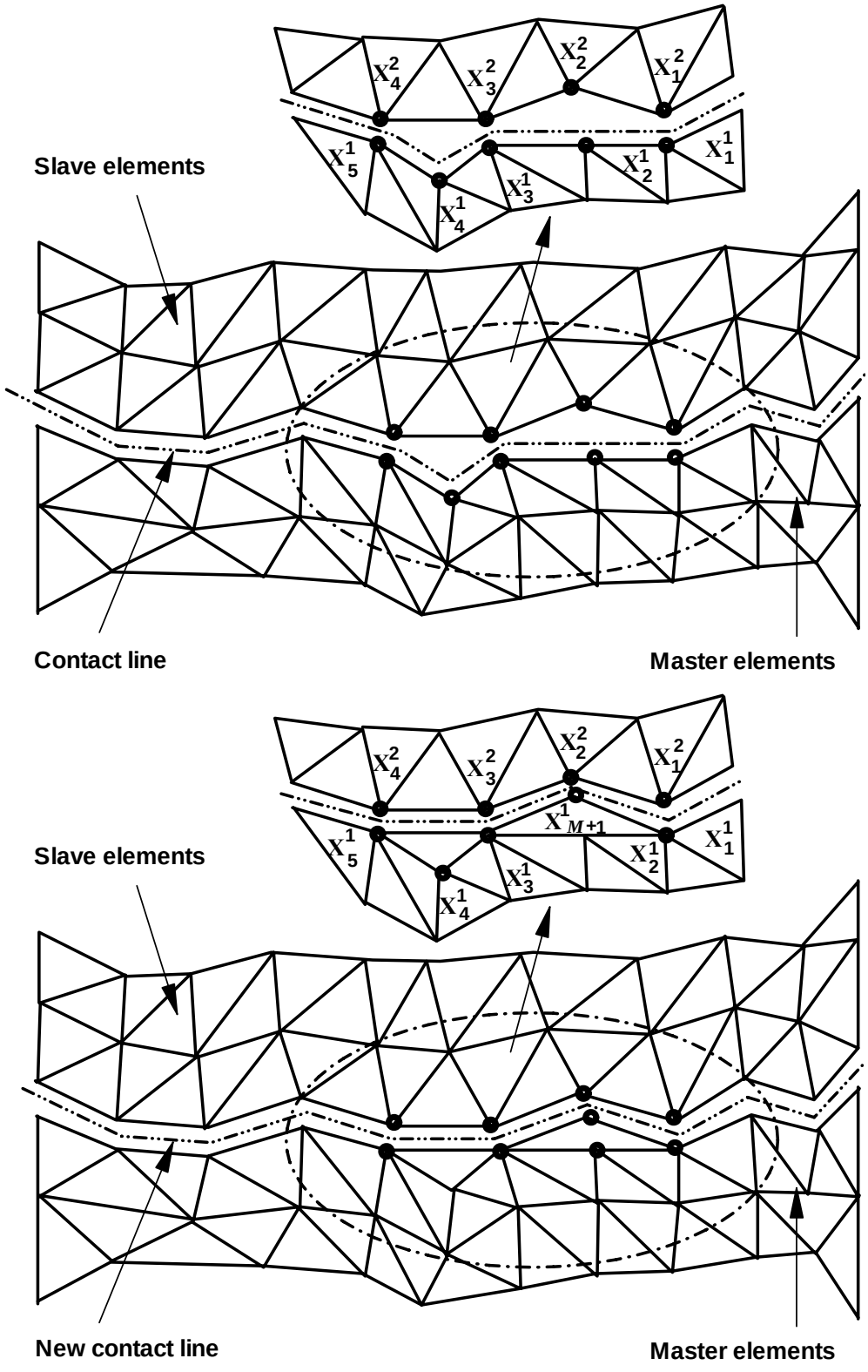

Figure 8.9: Updating contact lines for the ductile material.

Another contact problem is investigated for a rigid wall contact case, impact of a copper rod with a rigid striker, see Figure 8.14. The copper rod strikes a wall with an initial velocity of 227 m/sec. The radius and length of the rod are 3.2 mm and 32.4 mm, respectively. This study assumes the deformation to be axi-symmetric along the left side. For the simple geometrical shape, the contact conditions are applied to the rigid surface nodes that come into contact with the wall. The rod consist of mass density ρ =8930 Kg/m^3, Young's modulus E =117 GPa, Poisson's ratio ν =0.35, and yield stress 400MPa. To compare results with other model, this study uses plastic modulus E_t =100MPa and the elastic-plastic implementation suggested in Appendix E. This rigid wall contact is carried out up to a time of 80 μ sec. This contact duration is approximately of the same value as suggested in previous literature. Deformed rod shapes at different time steps and normalized internal, kinetic, and hourglass energies are shown in Figure 8.14. From various deformed rod shapes, shown in Figure 8.14, the deformation initially starts at t =3.5e-8 sec and then drastically decreases at t =45 μ sec due to extreme element distortions.

Table 8.1 Mechanical properties for the target plate and the projectile.

Materials	E	ν	σ_y	σ_s	ρ
Aluminum plate	70.3 GPa	0.33	310 MPa	200 MPa	2705 Kg/m^3
Steel projectile	201 GPa	0.29	1030 MPa	590 MPa	7800 Kg/m^3

8.7 Numerical Examples of Cracked Elements' Contact Modeling

We mentioned that the cohesive element modeling has a number of cracked elements formed by crack propagations and also suggested one contact algorithm for cracked elements in the section 8.4. To check performance of contact algorithm for cracked elements, this study uses two constant strain triangle (CST) elements as cracked elements and for different contact cases are considered here. The first contact case is the vertex contact problem, where a vertex of the CST element impacts another vertex of a second CST element. The CST elements use the same material properties, dimensions and boundary conditions. Variations of deformations as a function of time are shown in Figure 8.15(a). Figure 8.16(a) shows the linear and angular momentum history for each case. The angular and linear momentum histories show that both these momenta for the two CST elements are conserved quite accurately. To check the momentum conservation in time, this study does not consider friction and other energy dissipation during the contact duration. In this case there is no angular momentum initially, friction, and only linear momentums are transferred between the two CST elements.

The second case is the face-to-face contact shown in Figure 8.15(b). One CST element is subjected to linear momentum and contacts with a surface of another CST element. The top triangle has an initial velocity for initial boundary conditions whereas the bottom triangle is at rest without any boundary conditions. The contact faces coincides exactly with each other. To check the conservation of linear momentum, this study also uses surface contact algorithm suggested in the section 8.3. This contact algorithm effectively detects the over-lapped contact surfaces penetrated other surface of the triangles. Figure 8.16(b) show linear and angular momentum history. These histories also show very good momentum conservation.

The third problem is the edge-to-edge contact shown in Figure 8.16(c). Some structures are sometimes contacted with edge surfaces of another structure. In this case, unconstrained boundary conditions are used and only the initial condition is applied into the top triangle having the angular momentum whereas the bottom triangle having no boundary and momentums except maintaining a stationary value. The main difference compared to the previous two cases is an initial angular momentum that exists for the two CTS elements. Figure 8.15(c) show linear and angular momentum history. Since there is no initial linear

momentum, the linear momentum in this system stays zero while the angular term is non-zero. The time history shows very good energy conservation.

For the cohesive element a case of special interest is the complex post-rupture, i.e. multiple collision sequence, and involving multiple fragments in the dynamic impact problem. In the last part of Fig.8.7, one of the post-rupture contact algorithms is explained, and this is applied into one simple problem, i.e. a multiple contact. With reference to the first figure in Figure 8.17, the packed triangle (CST) elements with four cohesive elements are initially at rest before being impacted by the moving body, striker, that also consist of densely packed four triangle (CST) elements along with four cohesive elements at the element interfaces. The dimension of each square is $2.54\ \text{mm} \times 2.54\text{mm}$. The initial velocity of the moving square is 100 m/s. The triangle (CST) elements are restrained in their subsequent motion by three walls. Snapshots of each step of the dynamic response are shown in Figure 8.17. By checking a shaded element, the contact situations are described. This example, involving target CST elements that undergo multiple contacts during the impact, illustrates the ability of the present post-rupture contact algorithm to solve the complex contact situations.

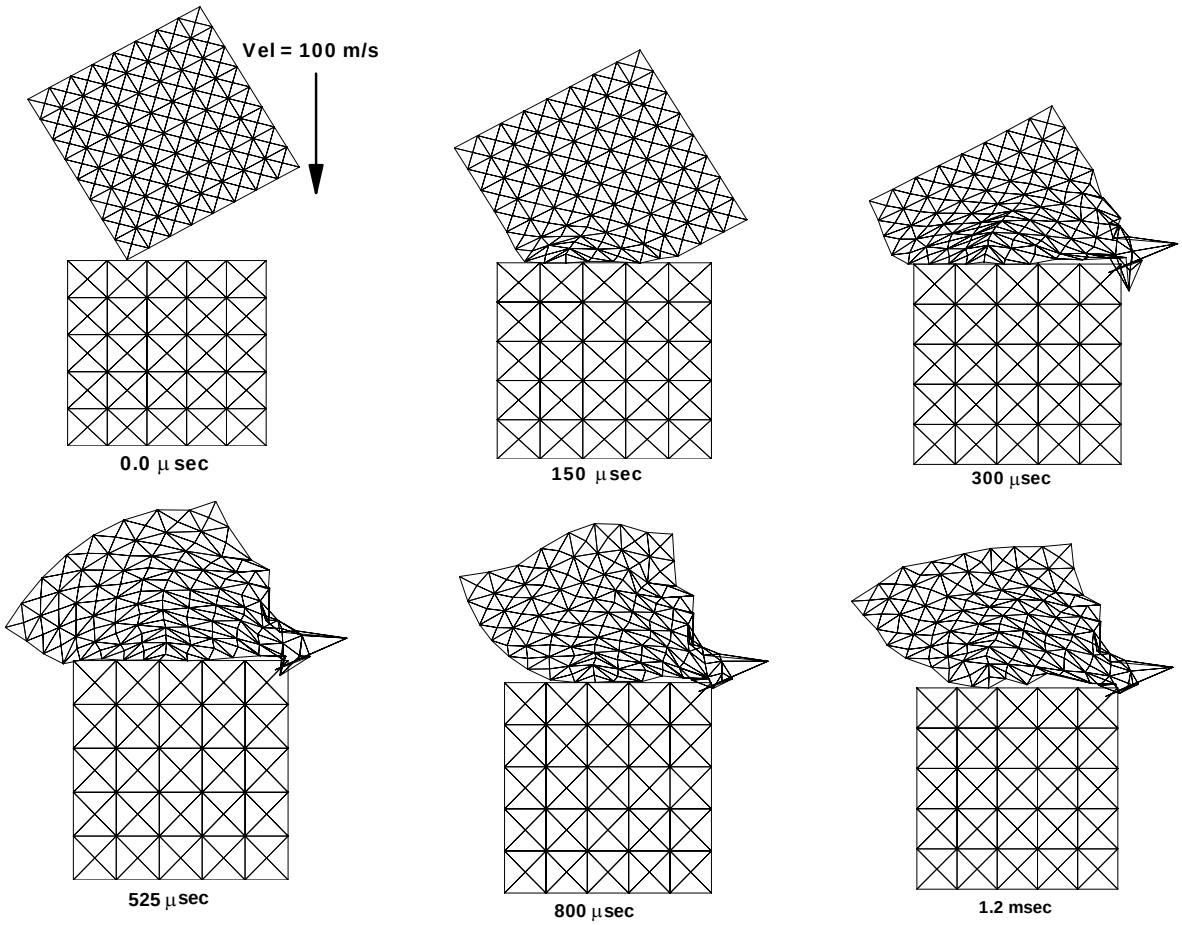

Figure 8.10: Deformed shapes of two impacted blocks.

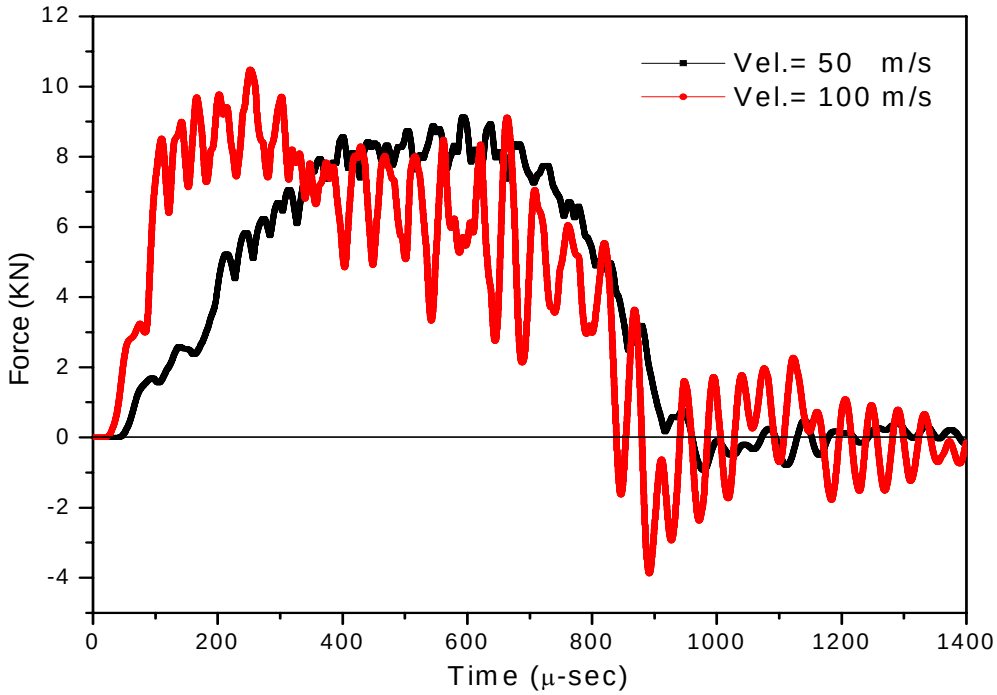

Figure 8.11: Resultant force history.

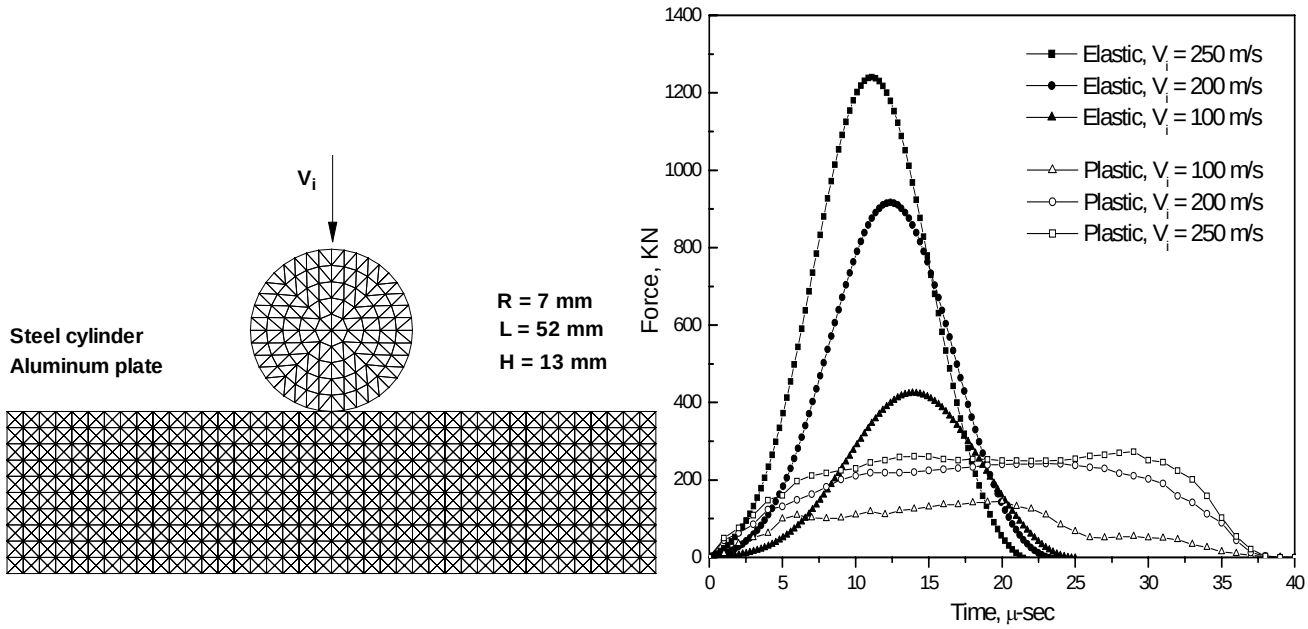

(a) (b)

Figure 8.12: Hertzian contact model and contact force history in elastic and plastic models.

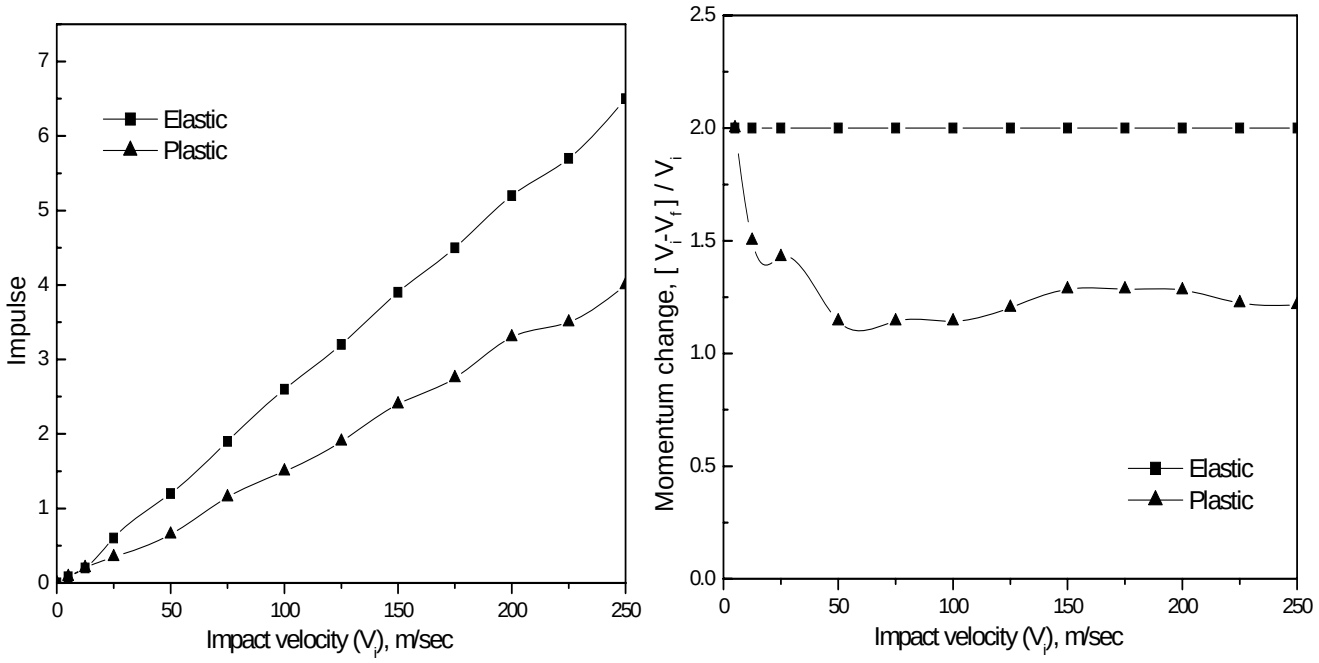

(a) (b)

Figure 8.13: Transferred impulse of the plate and momentum changes of the cylinder.

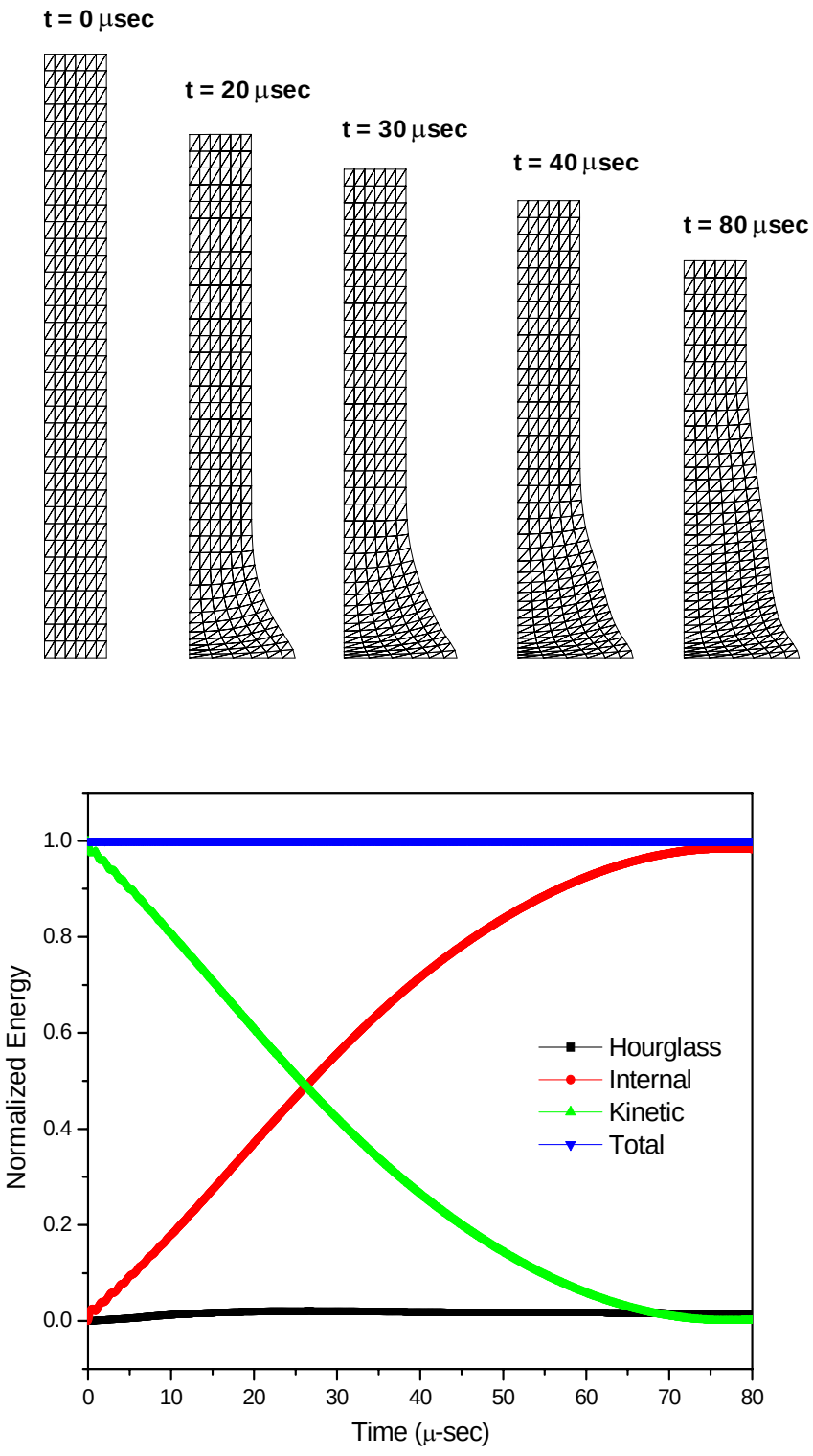

Figure 8.14: Configurations and normalized energies of a copper rod contacting the rigid wall.

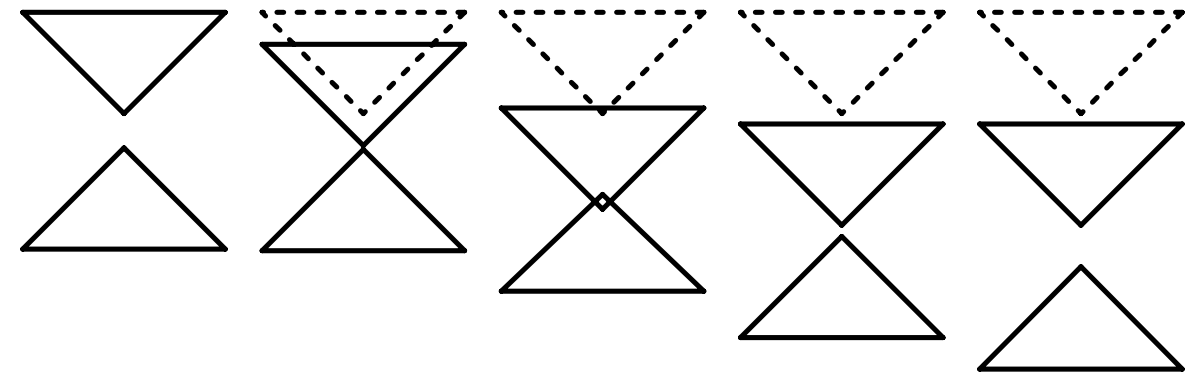

(a)

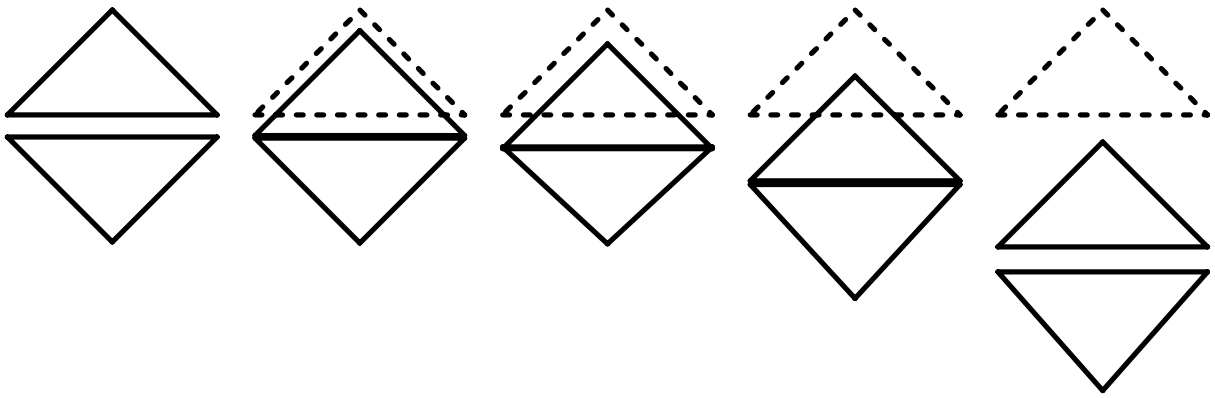

(b)

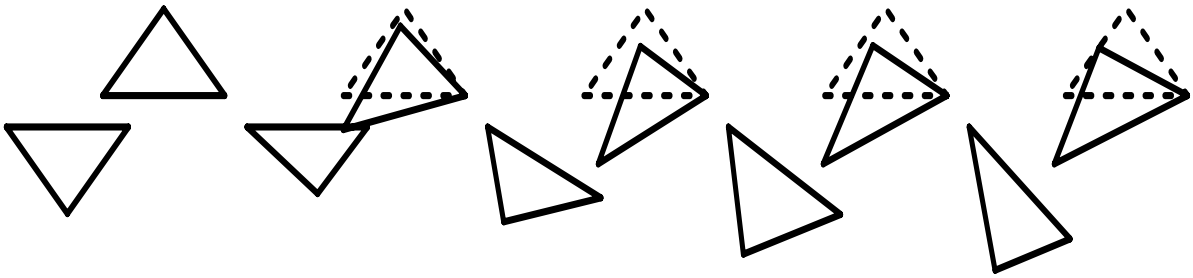

(c)

Figure 8.15: Three contact cases in the linear and angular momentums.

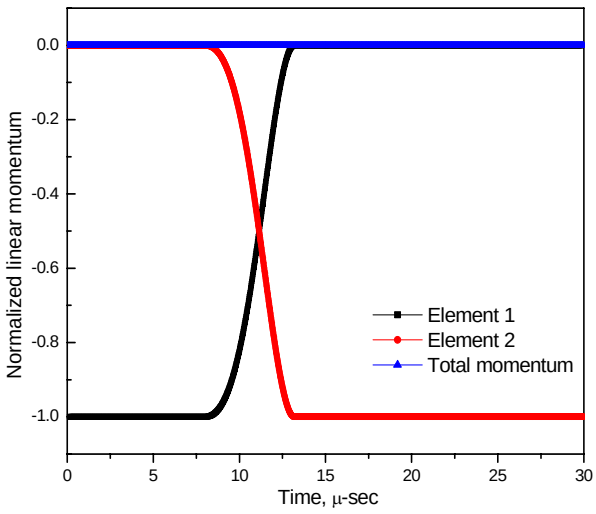

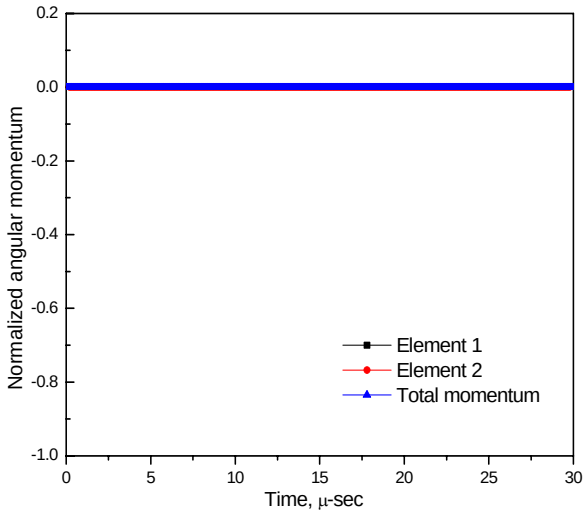

(a)

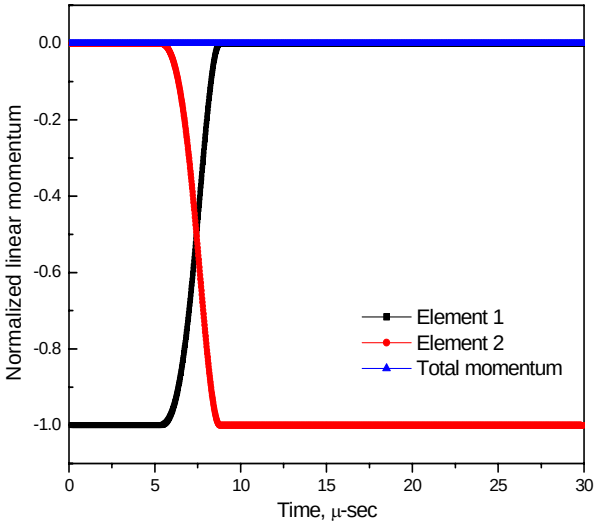

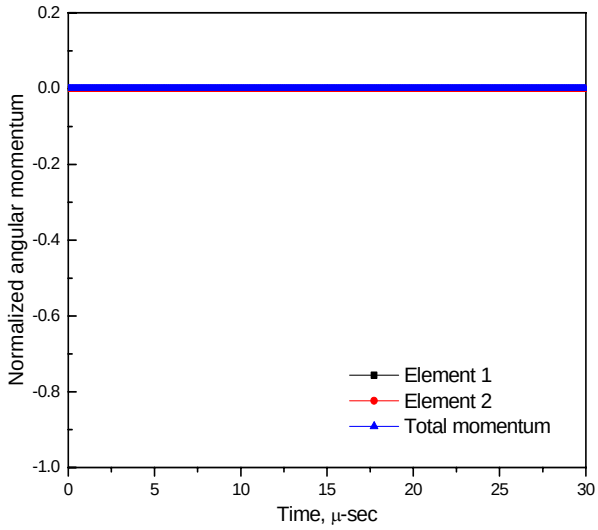

(b)

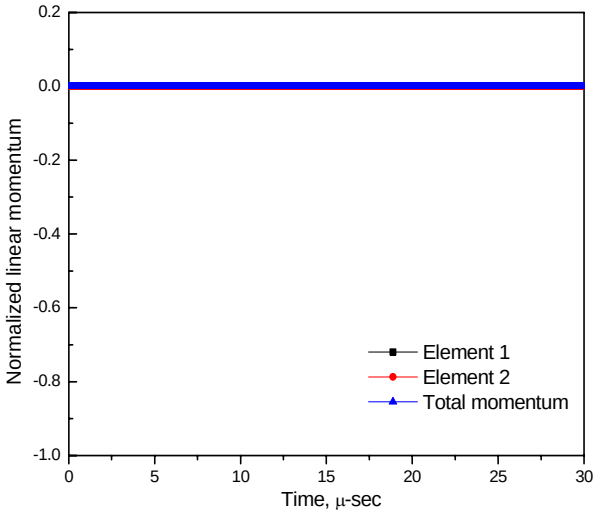

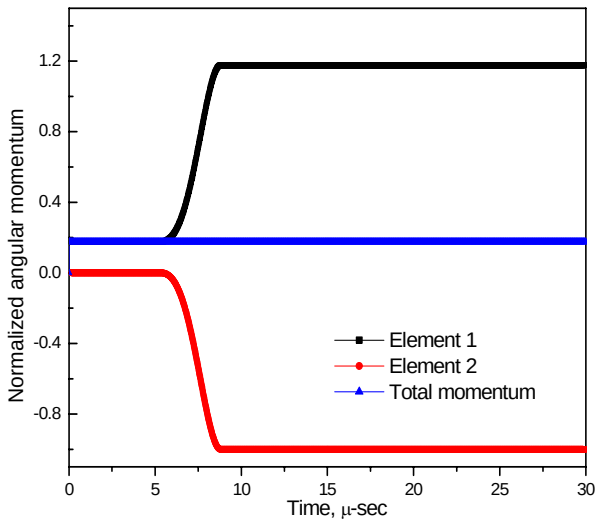

(c)

Figure 8.16: The linear and angular momentum history for two element contact cases.

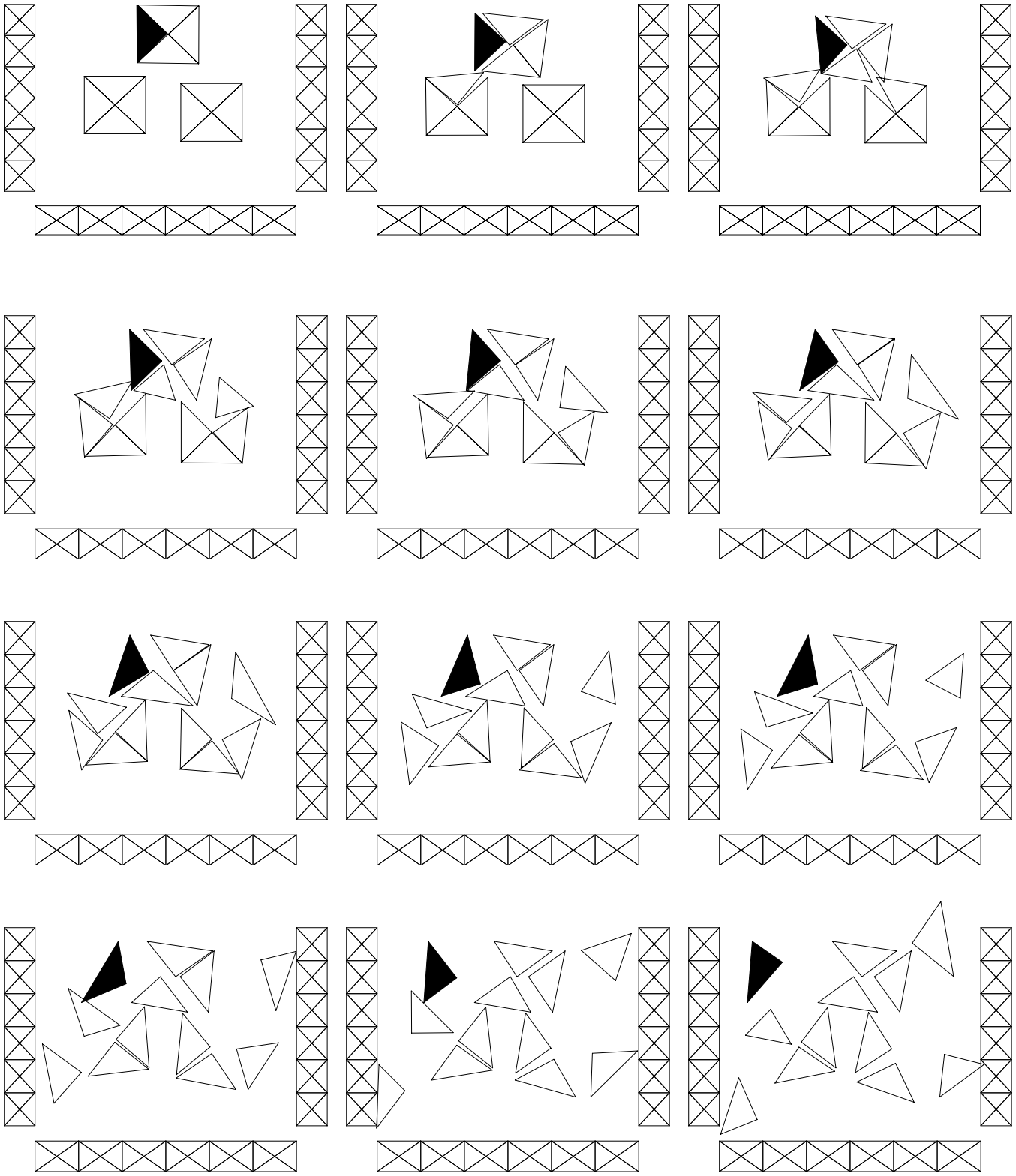

Figure 8.17: Multiple interacted contacts in the cohesive elements.

REFERENCES

8.1 T.A. Laursen, "Computational Contact and Impact Mechanics: *Fundamentals of Modeling Interfacial Phenomena in Non-linear Finite Element Analysis*," Springer-Verlag Berlin Heidelberg New York, 2002, pp. 152-158.

8.2 Zhong, Z.H., "Finite Element Procedures for Contact-Impact Problems," Oxford University Press, Oxford, 1993.

8.3 Hallquist, J.O., "NIKE2D, A Vectorized Implicit, Finite Deformation Finite Element Code for Analyzing the Static and Dynamic Response of 2-D Solids with Interactive Rezoning and Graphics," UCID-19677, Lawrence Livermore National Laboratories, 1986.

8.4 Hallquist, J.O., *User's Manual for DYNA2D*, "An Explicit Two-Dimensional Hydrodynamic Finite Element Code with Interactive Rezoning," UCID-18756, Lawrence Livermore National Laboratories, 1984.

8.5 Hallquist, J.O. and Benson, D.J., *User's Manual for DYNA3D*, "Non-linear Dynamic Analysis of Structures," UCID-19592, Lawrence Livermore National Laboratories, 1987.

8.6 Hallquist, J.O., "NIKE3D, An Implicit, Finite Deformation Finite Element Code for Analyzing the Static and Dynamic Response of Three-Dimensional Solids," UCID-18822, Lawrence Livermore National Laboratories, 1984.

8.7 Taylor, L.M. and Flanagan, D.P., "*PRONTO2D*: A Two-Dimensional Transient Solid Dynamics Program," SAND86-0594, Sandia National Laboratories, Albuquerque, NM87185, 1987.

8.8 Taylor, L.M. and Flanagan, D.P., "*PRONTO3D*: A Three-Dimensional Transient Solid Dynamics Program," SAND86-1912, Sandia National Laboratories, Albuquerque, NM87185, 1989.

8.9 Attaway, S.W., "*Update of PRONTO2D and PRONTO3D* Transient Solid Dynamics Programs," SAND90-0102, Sandia National Laboratories, Albuquerque, NM87185, 1990.

8.10 Benson, B.J. and Hallquist, J.O., "A Single Surface Contact Algorithm for the Post-Buckling Analysis of Structures," *Computer Methods in Applied Mechanics and Engineering*, Vol. 78, No. 2, 1990, pp. 141-163.

8.11 Zhong, Z.H. and Nilsson, L., "A Contact Searching Algorithm for General 3-D Contact Impact Problems," *Computers and Structures*, Vol. 34, No. 2, 1990, pp. 327-335.

8.12 Belytschko, T., *A New Interaction Algorithm with Erosion for EPIC-3*, BRL-CR-540, 1985.

8.13 Kimsey, K.D. and Zukas, J.A., *Contact Surface Erosion for Hypervelocity Problems*, BRL-MR-3495, 1986.

8.14 Belytschko, T. and Lin, J.I., "A Three-Dimensional Impact Penetration Algorithm with Erosion," *Computers and Structures*, Vol. 25, No. 1, 1987, pp. 95-104.

8.15 Belytschko, T. and Neal M.O., "Contact-Impact by the Pinball Algorithm with Penalty and Lagrangian Methods," *International Journal for Numerical Methods in Engineering*, Vol. 31, No. 3, 1991, pp. 547-572.

8.16 Johnson, G.R. and Stryk, R.A., "Eroding Interface and Improved Tetrahedral Element Algorithms for High Velocity Impact Computations in Three Dimensions," *International Journal of Impact Engineering*, Vol. 5, No. 1-4, 1987, pp. 411-421.

8.17 Stephen, R.B. and Johnson, G.R., "An Abrasion Algorithm for Projectile Mass Loss during Penetration," *International Journal of Impact Engineering*, Vol. 24, No. 2, 2000, pp. 103-116.

8.18 Stephen, R.B. and Johnson, G.R., "A Three-Dimensional Abrasion Algorithm for Projectile Mass Loss during Penetration," *International Journal of Impact Engineering*, Vol. 27, No. 7, 2002, pp. 771-789.

8.19 Johnson, G.R., Stryk, R.A., Beissel, S.R., "An Algorithm to Automatically Convert Distorted Finite Elements into Meshless Particles during Dynamic Deformation," *International Journal of Impact Engineering*, Vol. 27, No. 10, 2002, pp. 997-1013.

8.20 Johnson, G.R. and Stryk, R.A., "Conversion of 3-D Distorted Elements into Meshless Particles during Dynamic Deformation," *International Journal of Impact Engineering*, Vol. 28, No. 9, 2003, pp. 947-966.

Chapter 9 Impact Mechanics Using Cohesive Element Modeling

9.1 Introduction

In previous Chapters 7 and 8, we have described the formulations and contact algorithms for cohesive element modeling and showed some numerical validations. This Chapter explains some physical impact phenomena that result when a homogeneous or multi-layer structure is subjected to impact of a mass with varying impact speeds using the cohesive elements and cohesive contact modeling. Using cohesive element modeling, different penetrations or perforations of brittle, ductile and brittle/ductile type targets are studied. In addition, a simple analytical impact modeling based on empirical equations and numerical scheme for projectile position, velocity and forces is presented.

9.2 Analytical Impact Modeling

To understand penetration mechanism, a simple empirical approach was suggested by Goldsmith[9.1-9.5] and Calder[9.2-9.3]. Reference [9.2] depicted dynamic responses of thin plates subjected to projectile impact under a range of normal impact velocity and gave an analytical solution compared with experimental measurements related to projectile's displacement-time. Furthermore, it predicted velocity- and force-time history of projectiles using simple empirical equations. The present research uses this analytical solution presented in Ref. [9.2] and cohesive element method to find the dynamic response of thin plates subjected to various values of impact velocity. First, cohesive elements are used to get the target and projectile displacements, initial and final velocities as input values, and then these are applied into the analytical method[9.2-9.3] to predict the displacement-, force- and velocity-time history of projectiles. By combining the cohesive elements and the empirical approach of Ref. [9.3], this research investigates the physical process of the perforation in impacted thin plates.

When a projectile impacts a target, at a certain velocity the target may be perforated until the projectile either penetrates the target completely and emerges on the other side with some reduced velocity or stops in the target with an almost zero velocity. To calculate the force and velocity of the projectiles, Calder and Goldsmith[9.2-9.3] suggested deceleration-time relation forms for plastic impacts and perforation cases based on both analytical and empirical data, respectively.

$$\ddot{y}(t) = At^2 e^{-Bt},\ \ddot{y}(t) = Ae^{-Bt}\sin^2 t \tag{9.1}$$

In Eq.(9.1), A and B are unknown parameters that are obtained empirically. In the case of a permanent dent, (plastic impact) one of the parameters is eliminated from the initial impact velocity, V_i. In the perforation case, these unknown A and B parameters are decided from the measured initial and final penetration velocities, V_i and V_f. If the value of B is unity, normalized force curves for the permanent dent and perforation cases can be obtained as shown in Figure 9.1.

Calder and Goldsmith[9.2-9.3] integrated Eq. (9.1) to get the velocity and displacement equations of the projectile as a function of time. This research uses the time integration of Eq. (9.1) to obtain the projectile velocity and displacement. First, for the plastic impact case, $\ddot{y}(t) = At^2 e^{-Bt}$, is considered. Integrating Eq. (9.1) gives

$$\dot{y}(t) = -\frac{A}{B^3}e^{-Bt}(B^2t^2 + 2Bt + 2) + \frac{2A}{B^3} + V_i \tag{9.2}$$

The integration of Eq. (9.2) again gives

$$y(t) = \frac{A}{B^4}e^{-Bt}(B^2t^2 + 4Bt + 6) + (V_i + \frac{2A}{B^3})t + D \tag{9.3}$$

Second, for the perforation case, $\ddot{y}(t) = Ae^{-Bt}\sin^2 t$, is integrated as a function of time, just like in the permanent dent case.

$$\dot{y}(t) = -\frac{B(V_i - V_f)}{2(e^{-\pi B} - 1)} e^{-Bt}(B\sin^2 t + \sin 2t + \frac{2}{B}) + \frac{V_i e^{-\pi B} - V_f}{e^{-\pi B} - 1} \tag{9.4}$$

$$y(t) = -\frac{B(V_i - V_f)e^{-Bt}}{2(B^2 + 4)(e^{-\pi B} - 1)}(B^2\sin^2 t + 2B\sin 2t + 2\cos 2t + 4 + \frac{8}{B^2}) + \frac{(V_i e^{-\pi B} - V_f)t}{e^{-\pi B} - 1} + D \tag{9.5}$$

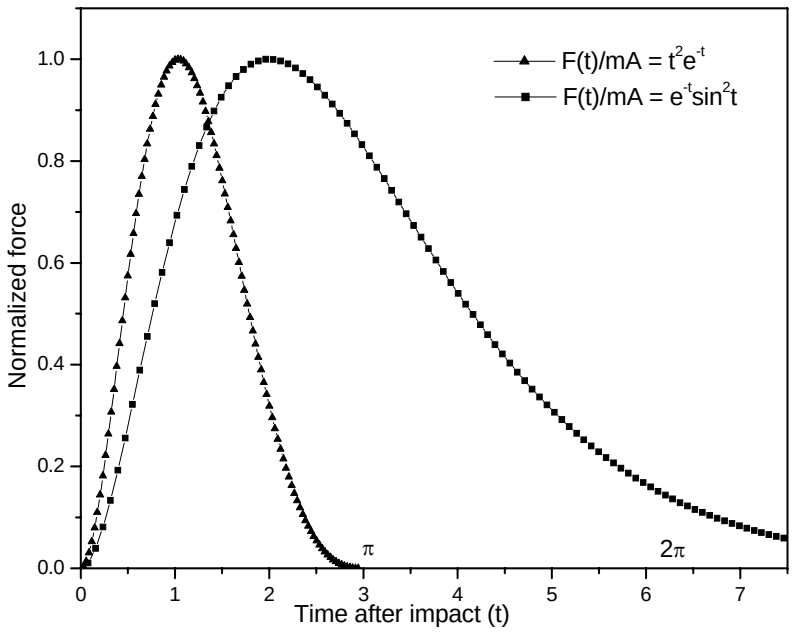

Figure 9.1: Normalized force curves for plastic impact and perforation impact.

To obtain the constants, A, B and D of Eqs.(9.1)-(9.5), a least square method applied to the initial and final velocities and based on experimental data at each time point was presented in Refs. [9.2-9.3]. Our study uses the cohesive element to get projectile displacements at each time step and then the least square method is used to obtain the empirical constants so that Eqs.(9.1)-(9.5) are satisfied in a least square method. As the forms of the equations are nonlinear in the unknown parameters, the unknown constants of Eqs.(9.3) or (9.5) are obtained by the least square method each time point, respectively. As a form of nonlinear equations, the condition function F_j for plastic impacts and perforation cases is introduced here.

$$F_j = y(t_j) + \frac{B(V_i - V_f)e^{-Bt_j}}{2(B^2 + 4)(e^{-\pi B} - 1)}(B^2\sin^2 t_j + 2B\sin 2t_j + 2\cos 2t_j + 4 + \frac{8}{B^2}) - \frac{(V_i e^{-\pi B} - V_f)t_j}{e^{-\pi B} - 1} - D \tag{9.6}$$

$$F_j = y(t_j) - \frac{A}{B^4}e^{-Bt_j}(B^2 t_j^2 + 4Bt_j + 6) + (V_i + \frac{2A}{B^3})t_j - D,\ j = 1,\ldots,n \tag{9.7}$$

Here, the function F_j is defined by $F_j(t_j, y_j, C_j) = y(t_j) - f(t_j, C_j) = 0$ .We next implement differentiation of the condition function, $\frac{\partial F_j}{\partial A}$, $\frac{\partial F_j}{\partial B}$ and $\frac{\partial F_j}{\partial D}$, $j = 1,\ldots,n$. To obtain these differentiate matrices, the parameter residual ($C_j, j = 1,\ldots,n$) and the approximation ($F_0^j, j = 1,\ldots,n$) matrices are

calculated at the initial point. The approximation matrix is obtained from experimental data or from the displacement values calculated by the cohesive element method each time step, $j = 1, \ldots, n$.

$$F_0^j = y_j + \frac{B_0(V_i - V_f)e^{-B_0 t_j}}{2(B_0^2+4)(e^{-\pi B_0}-1)}(B_0^2 \sin^2 t_j + 2B_0 \sin 2t_j + 2\cos 2t_j + 4 + \frac{8}{B_0^2}) - \frac{(V_i e^{-\pi B_0} - V_f)t_j}{e^{-\pi B_0}-1} - D_0 \quad (9.8)$$

$$F_0^j = y_j - \frac{A_0}{B_0^4} e^{-B_0 t_j}(B_0^2 {t_j}^2 + 4B_0 t_j + 6) - (V_i + \frac{2A_0}{B_0^3})t_j - D_0, \ j = 1, \ldots, n \quad (9.9)$$

In Eqs.(9.8)-(9.9), the variable y_j means the displacement value and the values of A_0, B_0 and D_0 are the parameter approximations at the j -th time point. The relation between the empirical constants (A, B and D) and the parameter approximations (A_0, B_0 and D_0) is written by the parameter residual (C).

$$A = A_0 - C_1, \ B = B_0 - C_2, \ D = D_0 - C_3 \quad (9.10)$$

Using Eqs.(9.6)-(9.9), the matrices of the condition function ($\mathbf{F}$), the parameter residual ($\mathbf{C}$) and the approximation ($\mathbf{F}_0$) are all written in matrix form. From these matrices, the approximate values of the empirical constants, A, B and D of Eqs.(9.1)-(9.5) are easily obtained using an iterative algorithm.

$$\mathbf{F}\ \mathbf{C} = \mathbf{F}_0, \ \mathbf{F}^T\mathbf{F}\ \mathbf{C} = \mathbf{F}^T\mathbf{F}_0 \quad (9.11)$$

The definition of matrices ($\mathbf{F}$, $\mathbf{C}$ and $\mathbf{F}_0$) is given as:

$$\mathbf{F} = \begin{bmatrix} \frac{\partial F_1^1}{\partial A} & \frac{\partial F_2^1}{\partial A} & \frac{\partial F_3^1}{\partial A} & \cdots\cdots & \frac{\partial F_n^1}{\partial A} \\ \frac{\partial F_1^2}{\partial B} & \frac{\partial F_2^2}{\partial B} & \frac{\partial F_3^2}{\partial B} & \cdots\cdots & \frac{\partial F_n^2}{\partial B} \\ \frac{\partial F_1^3}{\partial D} & \frac{\partial F_2^3}{\partial D} & \frac{\partial F_3^3}{\partial D} & \cdots\cdots & \frac{\partial F_n^3}{\partial D} \end{bmatrix}, \ \mathbf{C} = \begin{bmatrix} C_1 \\ C_2 \\ C_3 \end{bmatrix}, \ \mathbf{F}_0 = \begin{bmatrix} F_0^1 \\ F_0^2 \\ F_0^3 \end{bmatrix} \quad (9.12)$$

In Eq. (9.12) the parameter residual ($\mathbf{C}$) is dependent on suitable initial approximations (A_0, B_0 and D_0). After calculating the parameter residual and substituting into Eq.(9.10), the approximate displacement, velocity and force curve Eqs.(9.1)-(9.5) are finally determined.

9.3 Numerical Examples for Analytical Impact Modeling

Numerical results for a thin plate under an impact load are presented in this part. A spherical or cylindro-conical projectile impacts the thin plate with an initial velocity. To analyze the thin plate under impact, this study uses the cohesive elements and the empirical constants obtained using the least mean-square procedure to find projectile displacements, velocities and forces. A clamped aluminum thin plate of 14.25 in diameter and 0.05 in thickness is considered. The target material consisted of 2024-0 aluminum sheets. The spherical steel projectile having a 0.5 in diameter and cylindro-conical steel projectile with a 60^o cone angle and 0.75 in length are used. The mass of spherical and cylindro-conical steel projectiles are m =4.78E-5 lb-sec^2/in and m =6.66E-5 lb-sec^2/in, respectively. Mechanical properties of the target plate and projectile are listed in Table 9.1.

Table 9.1 Mechanical properties for the target plate and the projectile from Ref. [9.2-9.3].

Materials	E	ν	σ_p	σ_u	ρ
2024-0 Aluminum target plate	10.6×10^6 lb/in^2	0.33	12.8×10^3 lb/in^2	34.0×10^3 lb/in^2	2.5×10^{-4} lb-sec^2/in^4
Steel projectile	29.6×10^6 lb/in^2	0.29	64.0×10^3 lb/in^2	71.0×10^3 lb/in^2	7.36×10^{-4} lb-sec^2/in^4

In the first problem, the plastic impact is studied, and the spherical projectile with an initial velocity, V_i =199 ft/sec impacts a clamped circular thin plate. The results of cohesive elements, displacements, are calculated before applying these into the least mean-square procedure. By using the displacement out puts, the assumed deceleration-time relation, $\ddot{y}(t) = At^2 e^{-Bt}$ and Eqs.(9.2)-(9.3), (9.11)-(9.12), and the least mean-square method, the projectile position, velocity and force-time curves are obtained. Figure 9.2 shows the projectile-time history of position, velocity and force. Figure 9.3 shows the impact deformations of the plastic impact case in which a clamped 2024-0 aluminum plate is subjected to V_i =199 ft/sec. From the comparison between Ref.[9.2] and our results, some difference are found, and these may be due to different value of initial approximations (A_0 , B_0 and D_0) in the least mean-square procedure and displacement values at each time point solved by cohesive element method or specified by the experimental data. In both these results of projectile time history, considerably similar trends are found.

The second problem is the perforation impact problem. The same spherical projectile as used in the plastic impact case is used with an initial velocity, V_i =497 ft/sec. At this speed, the projectile perforates through the clamped aluminum plate. The assumed force-time relation, $\ddot{y}(t) = Ae^{-Bt} \sin^2 t$, is taken, and the projectile position, velocity and force-time curves are calculated by Eqs.(9.4)-(9.5), (9.11)-(9.12) respectively. For determining the fracture behavior, the cohesive elements are used, and the initial-time and the end-time of perforation are checked along the time step. The final exit velocity, V_f =287.45 ft/sec, calculated by cohesive element method is lower than the experimental value suggested in Refs. [9.2-9.3]. Figure 9.4 shows the position, velocity and force time history of the spherical projectile. Figure 9.5 shows the impact deformation of the perforation impact case for the clamped 2024-0 aluminum plate with a steel sphere, V_i =497 ft/sec. The impact duration of perforation case is shorter than that for the plastic impact. These results support the fact that the energy in the plastic impact case, the material, due to plastic deformations, can absorb energy under a low impact force but not in the case of an impact that causes perforation.

The third problem is a different perforation impact case. The cylindro-conical projectile impacts the thin plate target with an initial velocity, V_i =301 ft/sec and penetrates the clamped aluminum plate. For this case, the same assumed force-time relation, $\ddot{y}(t) = Ae^{-Bt} \sin^2 t$, is used, and for the fracture simulation and the projectile displacements each time step, the cohesive elements are considered. From the cohesive element method, the final penetration velocity, V_f =194.57 ft/sec is obtained. Figure 9.6 suggests the position, velocity and force time history of the cylindro-conical projectile. Figure 9.7 describes the impact deformations of the perforation impact case; a clamped 2024-0 aluminum plate with a cylindro-conical projectile, V_i =301 ft/sec. The cylindro-conical projectile, due to the projectile geometry, shows smaller decrements of velocity and lager impact duration than those for the spherical projectile.

From the comparison between the sphere and the cylindro-conical projectile impacts, a general observation is made a decreasing impulse-momentum loss happens for increasing impact velocity. As expected, it is found that the loss in impulse-momentum and in kinetic energy for the spherical projectile is considerably greater than that for the cylindro-conical projectile for the same target plate. This is due to the much larger plastic deformation induced from the geometrical shape of projectiles. This fact can be estimated from the plate deformations suggested in Figures 9.3, 9.5 and 9.7. Table 9.2 also provides a summary of the plastic impact and perforation impact on these three cases. All impact cases are conducted on the clamped aluminum plate (14.25in diameter $\times$ 0.05in thickness).

Table9.2 Comparison of plastic impact and perforation impact.

Impact types	Projectiles	V_i (ft/sec)	V_f (ft/sec)	V_f (ft/sec) [Ref.9.1]
Plastic impact	Sphere	199	0.1923	-
Perforation impact	Sphere	497	287.4518	315
Perforation impact	Cylindro-conical	301	194.5669	195

9.4 Penetration at High Velocity

One of high velocity penetrations into the semi-infinite targets was suggested by Birkhoff [9.6] *et al.* Reference [9.6] solved the high velocity penetration with a hydrodynamic theory based on Bernoulli's theorem. This study uses the hydrodynamic theory to analyze the high velocity penetration. Let's consider a projectile as shown in Figure 9.8 having a constant length L, velocity V_P, and density ρ_p, penetrating a semi-infinite target of density ρ_t, with a velocity U. Figure 9.8 depicts the situation before, and after impact and the steady state condition during the penetration process where the bottom of an erosion surface of the impact rod travels at velocity U. In a moving coordinate system, the impact rod moves to the right with a velocity $V_P - U$ while the target moves to the left at a velocity U. In such a moving coordinate system, the steady-state will be found, and the stresses between the target and the rod also is treated as a stagnation stress. From the moving coordinate system, Bernoulli's theorem is applied into the stationary surfaces of erosion regions as shown in Figure 9.9.

$$\frac{1}{2}\rho_p (V_P - U)^2 = \frac{1}{2}\rho_t U^2 + \phi \tag{9.13}$$

Here the term ϕ can be considered to be dynamic yield strength of the target with respect to the material properties of the impact rod. The dynamic yield strength is regarded as a strain-rate function, such a material characteristics of the target and rod materials. Eq. (9.13) is valid for incompressible steady state, but a compressible isentropic steady state also can be applied. The target velocity in the steady-state condition is

$$U = \frac{\rho_P V_P - [\rho_P^2 V_P^2 - 2(\rho_P - \rho_t)\cdot(\frac{1}{2}\rho_P V_P^2 - \phi)]^{1/2}}{\rho_P - \rho_t} \tag{9.14}$$

The duration of penetration is

$$t = \frac{L}{V_P - U} \tag{9.15}$$

The total penetration depth, P, is defined:

$$P = \frac{UL}{V_P - U} \tag{9.16}$$

Using Eqs.(9.14) and (9.16), the penetration depth is re-written

$$P = L\cdot\frac{[\rho_P^2 V_P^2 - 2(\rho_P - \rho_t)\cdot(\frac{1}{2}\rho_P V_P^2 - \phi)]^{1/2} - \rho_P V_P}{\rho_t V_P - [\rho_P^2 V_P^2 - 2(\rho_P - \rho_t)\cdot(\frac{1}{2}\rho_P V_P^2 - \phi)]^{1/2}} \tag{9.17}$$

If the dynamic yield strength is negligible in the limit of high velocity, Eqs.(9.16) and (9.17) are

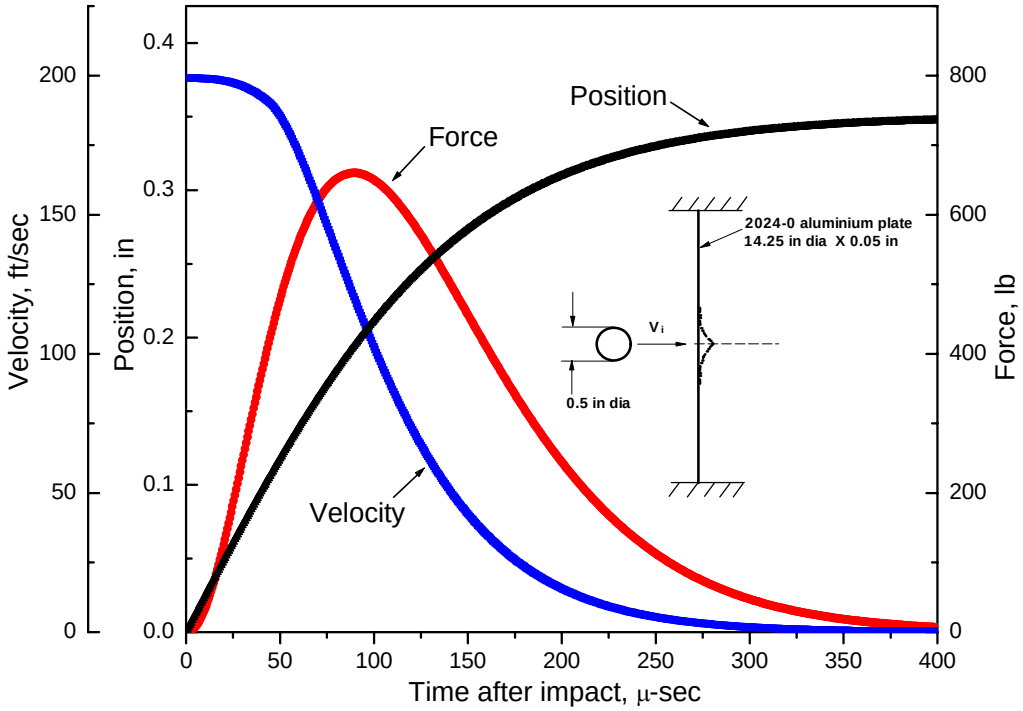

Figure 9.2: The projectile-time history of position, velocity and force for impact by a steel sphere.

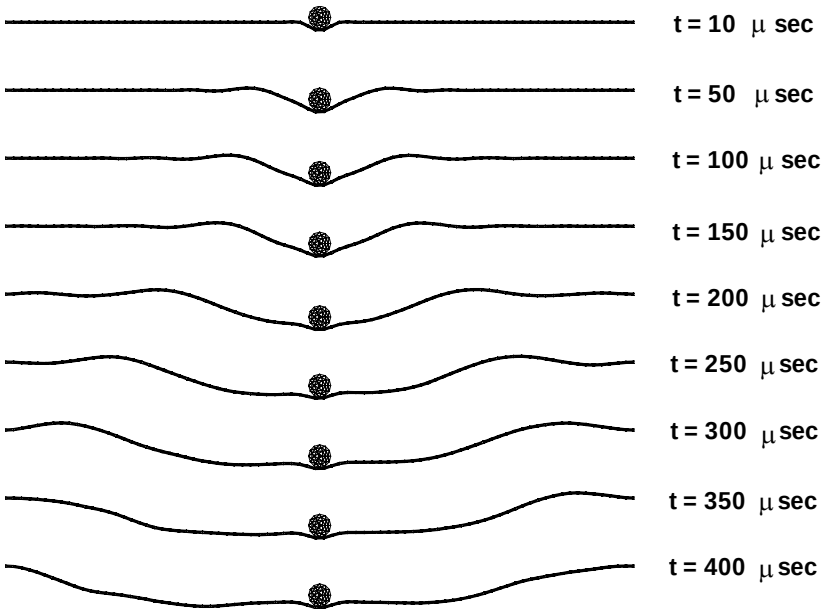

Figure 9.3: Impact deformations of the plastic impact case, V_i =199 ft/sec.

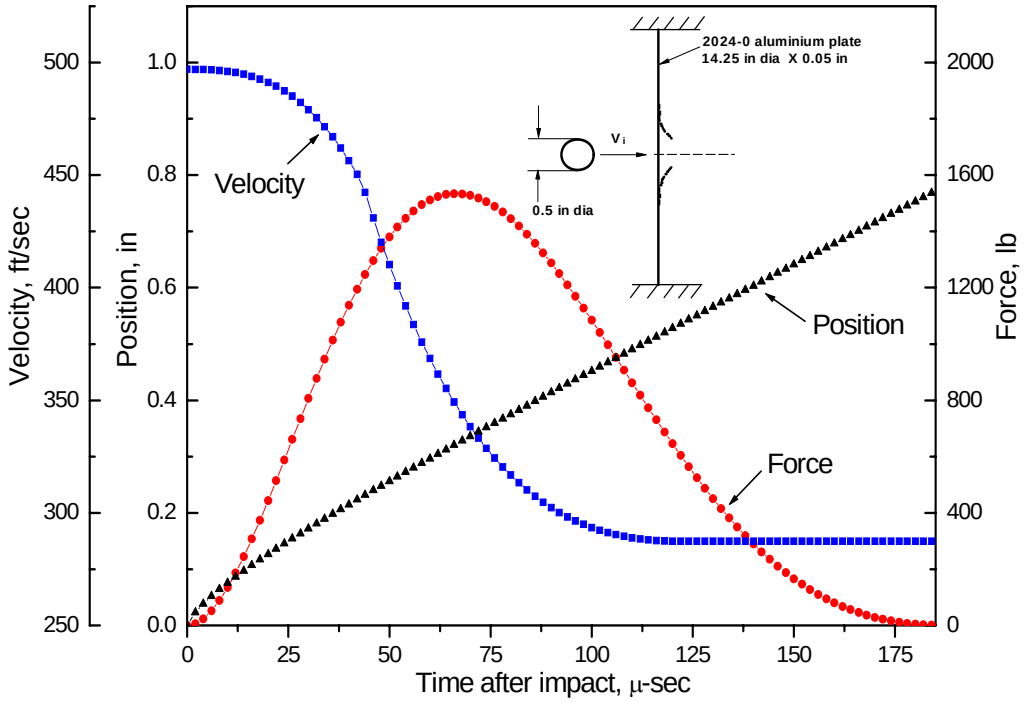

Figure 9.4: The projectile-time history of position, velocity and force for impact by a steel sphere.

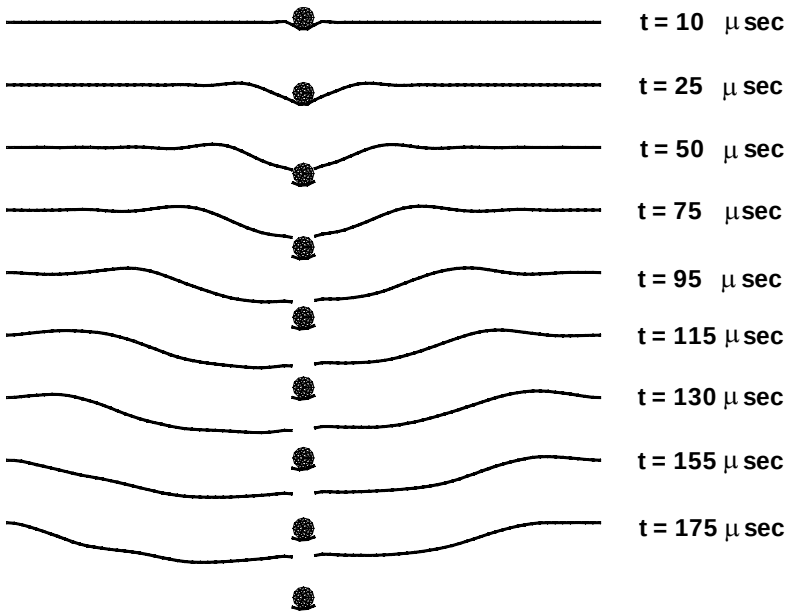

Figure 9.5: Impact deformations of the perforation impact case, V_i =497 ft/sec.

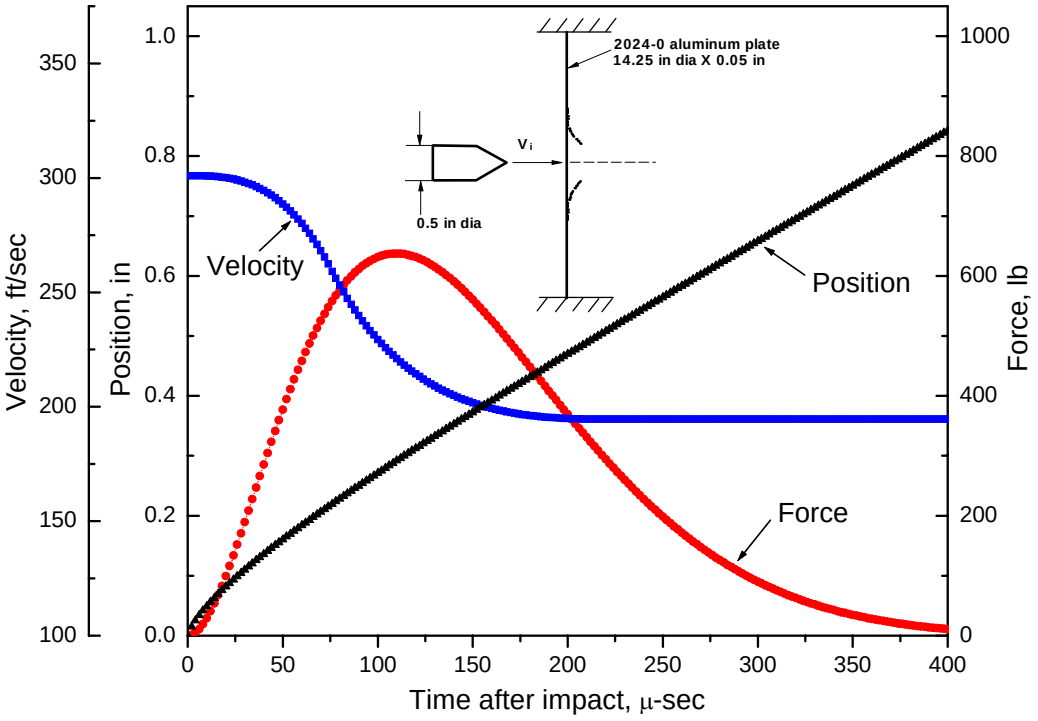

Figure 9.6: The projectile-time history of position, velocity and force for impact by a cylindro-con.

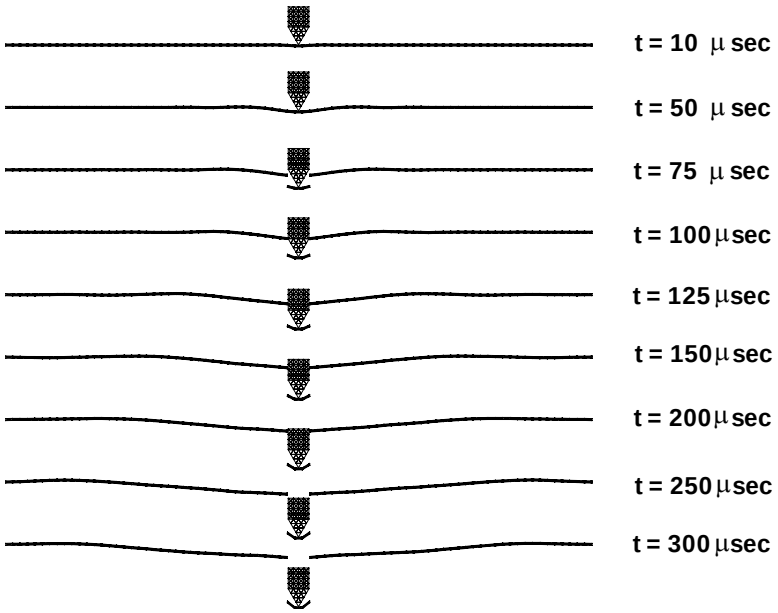

Figure 9.7: Impact deformations of the perforation impact case, V_i =301 ft/sec.

$$U = \frac{V_P}{(1+\sqrt{\rho_t / \rho_p})},\ P = Ut = L(\rho_p / \rho_t)^{1/2} \tag{9.18}$$

The critical dynamic yield strength at $V_P = V_0$ is defined as $\phi_0 = \frac{1}{2}\rho_P V_0^2$, and the critical impact velocity V_0 is the speed before the steady-state penetration happens. Reference [9.6] introduced a relative penetration y to describe empirical curves for several different rods impacting an aluminum target with an adjustable parameter a. The relative penetration is

$$y = \sqrt{\frac{\rho_t}{\rho_P}} \cdot \frac{a(V_P - V_0)}{(1-a)(V_P - V_0) + V_0}, \qquad y = \frac{P}{L} \cdot \sqrt{\frac{\rho_t}{\rho_P}} \tag{9.19}$$

To describe the target velocity, U, in terms of impact and critical velocities, the target velocity in Eq.(9.16) is solved

$$U = \frac{PV_P}{P + L} \tag{9.20}$$

And eliminating y in Eq.(9.19) and substitute into Eq.(9.20), the target velocity, U is

$$U = a(V_P - V_0) \tag{9.21}$$

To find the dynamic yield strength ϕ, substitute Eq.(9.21) into Eq.(9.13) and obtain the 2'nd order equation of the penetration velocity based on the strain-rate function for the target material.

$$\phi = \frac{1}{2}\rho_P V_0^2 - \rho_P V_0 (1 - \frac{1}{a})U + \frac{1}{2}[\rho_P (1 - \frac{1}{a})^2 - \rho_t]U^2 = \phi_0 + bU + cU^2 \tag{9.22}$$

Here the variables ϕ_0, b, c are obtained from experimental data of projectile with respect to the target materials. Another problem in the high velocity penetration is a secondary penetration or residual penetration suggested in Refs. [9.6-9.9]. When the impact rod having a considerably large density is almost used up, the target velocity in the moving coordinate system is usually reflected from the bottom of erosion surface in the rod and the reflected target velocity will be $V_r = 2U - V_P$. After the impact rod is used up, the reflected pressure lines are not affected a change of direction and retains the same magnitude of reflected target velocity. However in the case of an impact rod having a low density, the reflected target velocity is negligible compared with V_P. The reflected target velocity is calculated from Eq.(9.14) and the relation $V_r = 2U - V_P$.

$$V_r = \frac{2 \cdot [\rho_P^2 V_P^2 - 2(\rho_P - \rho_t) \cdot (\frac{1}{2}\rho_P V_P^2 - \phi)]^{1/2} - (\rho_P V_P + \rho_t V_P)}{\rho_t - \rho_P} \tag{9.23}$$

If $V_r >> V_0$, the secondary penetration can occur where a large penetration velocity compared to the 2'nd critical penetration velocity V_c is made. The velocity V_c is obtained from Eq.(9.23) and $\phi_0 = \frac{1}{2}\rho_P V_0^2$.

$$V_c = \frac{V_0(3\rho_P + \rho_t)}{\rho_P - \rho_t} \tag{9.24}$$

And the relative penetration in the secondary penetration is

$$y = y(V_c) + \frac{a(V_P - V_c)}{(1-a)(V_P - V_c) + V_c} \cdot \sqrt{\frac{\rho_t}{\rho_P}} \tag{9.25}$$

9.5 Numerical Examples for High Velocity Penetration

Reference [9.8] suggested a short metal wire segment impacting an aluminum target and showed some experimental results about the high velocity penetration. This study uses the same material and dimension of penetration model as used in Ref. [9.8]. The diameter of metal wire segment is 0.0737 cm, and the length L is 0.465 cm, and is made of lead. The lead density ρ_P is 11.09 g/cc. The value of adjustable parameters a and V_0 appeared in empirical equation, Eq. (9.19), 0.81329 and 583 m/sec, are used respectively. Other several metal wire types are applied into the aluminum target and made relative penetration curves as function of projectile velocity, as Figure 9.10. Some other metals used in the relative penetration curves are listed in Table 9.3. Using Eq.(9.21) and physical properties shown in Table 9.3, the penetration velocity as a function of projectile velocity for the projectile impacting the target is plotted in Figure 9.11. Ref. [9.6] reported the secondary penetration induced from the high-density rod and illustrated the theoretical and experimental results.

The secondary penetration of gold rod case is represented in Figure 9.12. Curves in Figure 9.10 show the relative penetration depth for several projectile materials impinging on the target. From Figures 9.10-9.11, the projectile having a lower density such as aluminum have lower depth of penetration and the projectile with a high density such as gold have a higher depth of penetration. The penetration duration also show similar trends, for example, the lower density rod, such as an aluminum projectile has a smaller penetration time compared to the high-density rod. These facts are closely related to the dynamic yield strength ϕ based on the strain-rate function.

To evaluate the validity of cohesive element for high velocity impact, a simple model, shown in Figure 9.13, is considered. In this section, we use a symmetric modeling for the high velocity impact. Three different projectiles are impinging on the steel target with a high velocity V_P =5000m/sec are considered. The projectile and target for the hydrodynamic impact are illustrated in Figures 9.14-9.15. Figure 9.14 shows penetration depths for three different projectiles (tungsten, copper and aluminum rods) and an infinite steel target. From Figure 9.14, the results of cohesive element show a good agreement with the results of hydrodynamic theory. Another case is a penetration case based on the same material projectile (aluminum rod) and the steel target with different impact velocities, V_P =2000-5000m/sec. These results in Figure 9.15 also are conformed to the hydrodynamic case. From Figure 9.15 the same material and different impact velocities have only different penetration times and approximately same penetration depths. Figure 9.16 shows penetration shapes of two different material projectiles (copper and tungsten rods) induced from the high impact velocity V_P =5000m/sec. In Figure 9.16, we can see that the lower density projectile (copper) has lower penetration depths and the higher density projectile (tungsten) has higher penetration depths. As a contact between the rod and the target develops, we can see that the higher density projectile will lead to the steel target fragmentation and a severe deformation of the rod occurs as compared to the case with the lower density projectile. Figure 9.17 suggests the penetration deformed shapes of the aluminum rod induced from the high impact velocities V_P =2000 m/sec and V_P =4000m/sec, respectively. From Figures 9.16-9.17, we can estimate that the high velocity impact is dependent on the density of the projectile but not as much upon the projectile velocity itself. And the fast eroding projectile has a shorter impacting/contact time, but the penetration depths remain the same. From Eqs.(9.14)-(9.17), we can infer these facts.

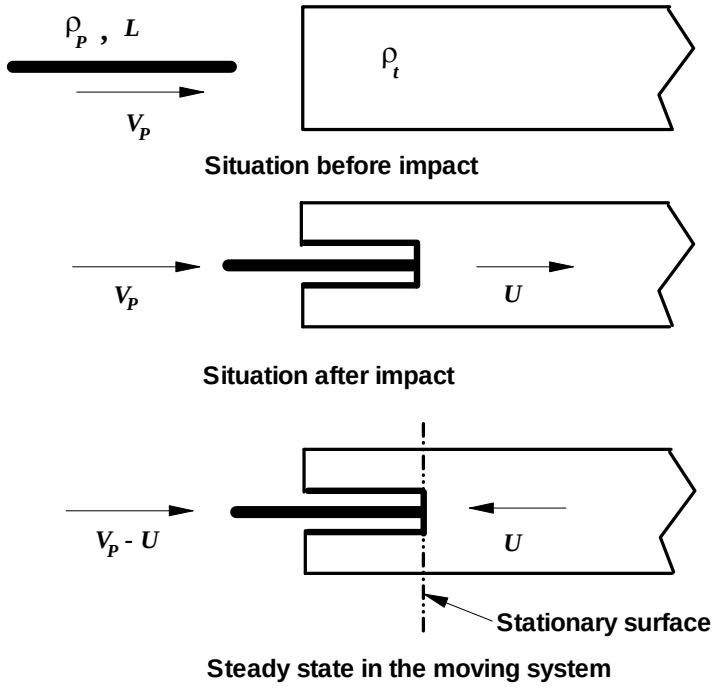

Figure 9.8: Penetration process of the high velocity projectile.

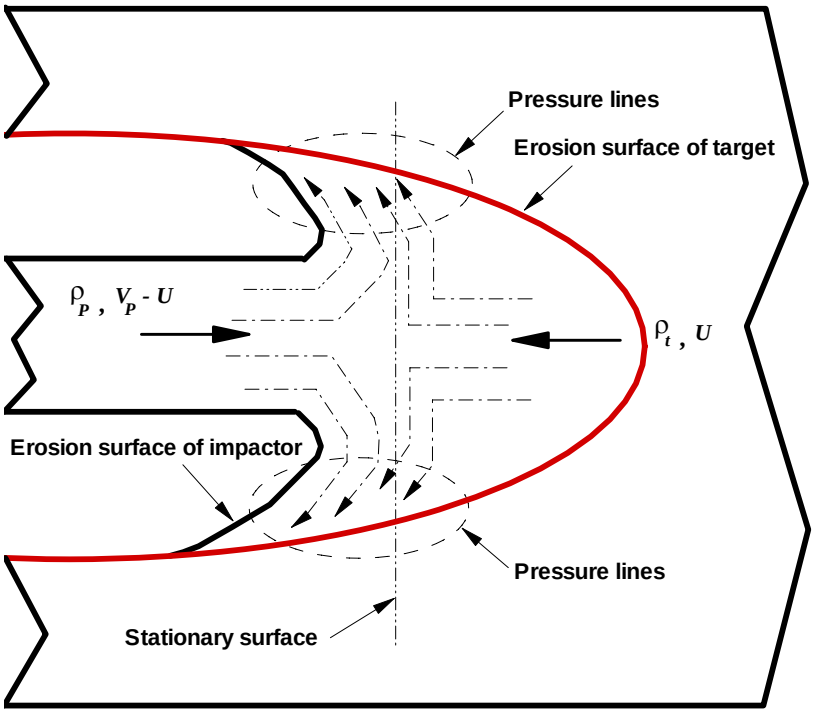

Figure 9.9: Erosion region between the high velocity projectile and the target.

Table9.3 Physical and experimental properties of impact rod from Ref. [9.9].

Metal types	Length L ,cm	Diam. d ,cm	Density ρ , g/cc	Critical Vel. V_0 ,cm/ μ sec	Adjustable Parameter a
Gold	0.467	0.0635	19.30	0.0479	0.90052
Lead	0.465	0.0737	11.09	0.0583	0.81329
Copper	0.432	0.0635	8.96	0.0672	0.81705
Tin	0.540	0.0711	7.30	0.0675	0.76894
Aluminum	0.801	0.0787	2.70	0.1170	0.68072

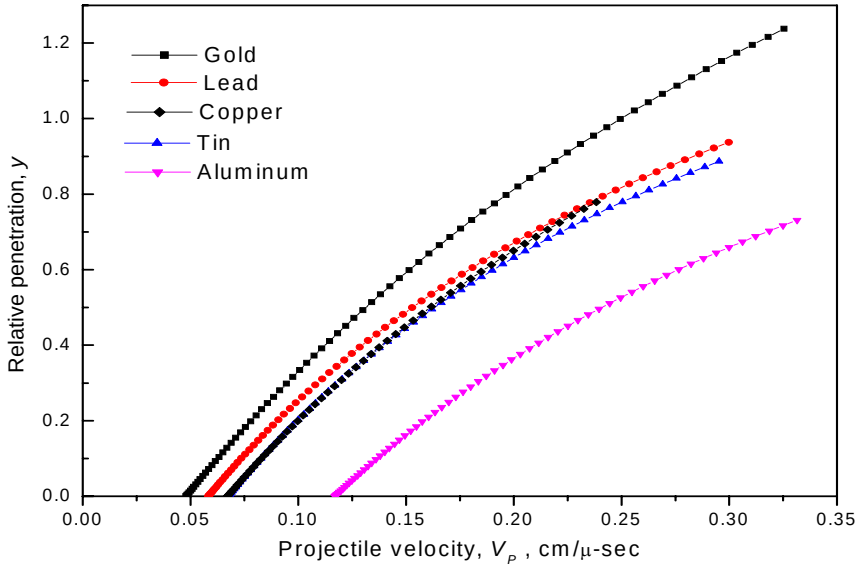

Figure 9.10: Penetration as function of projectile velocity for high velocity impacts.

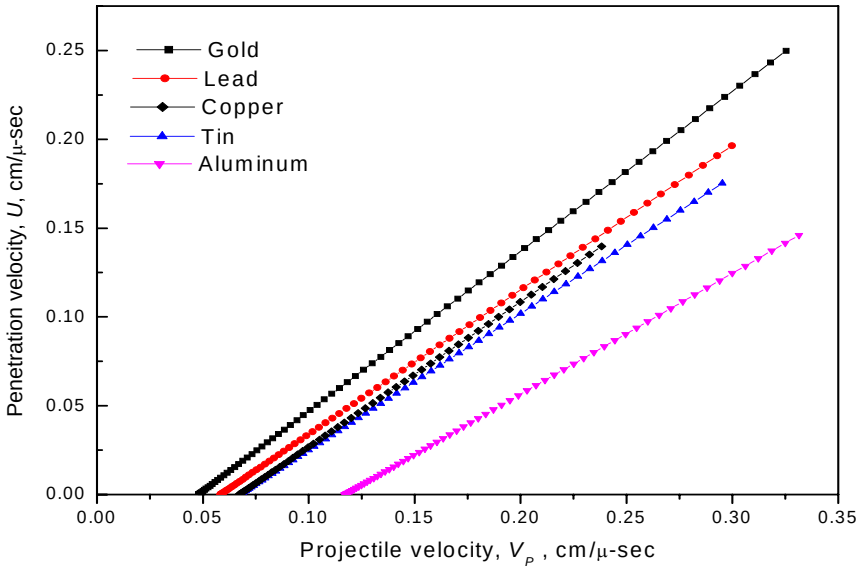

Figure 9.11: Penetration velocity as function of projectile velocity for high velocity impacts.

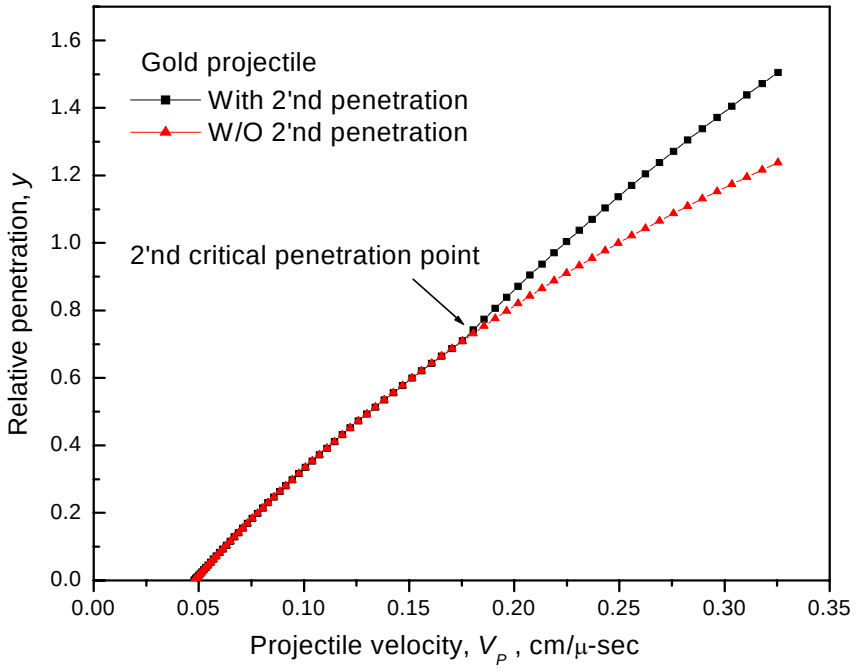

Figure 9.12: Penetration of a gold projectile into an aluminum plate.

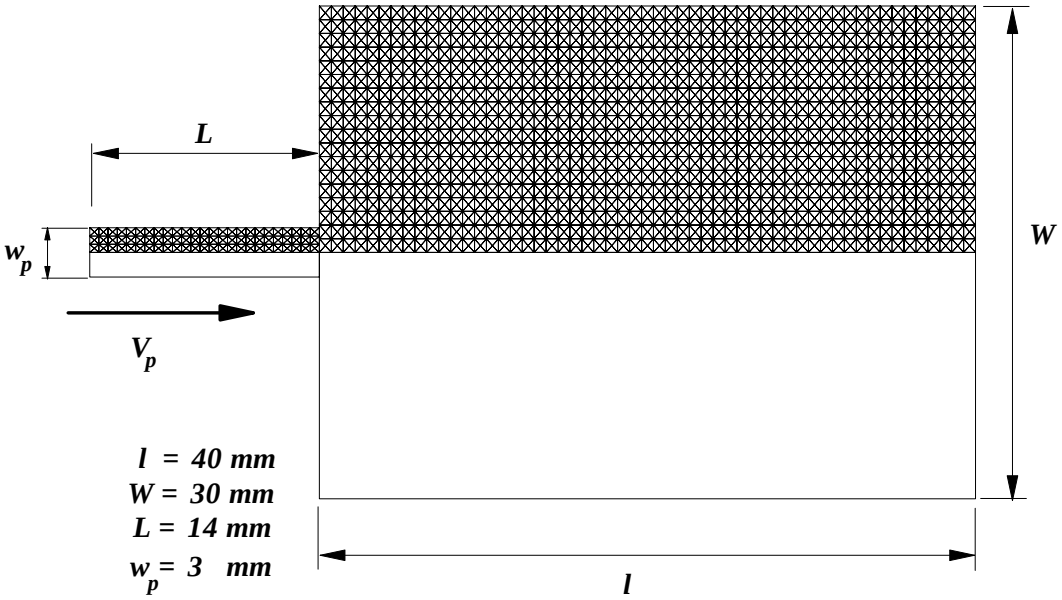

Figure 9.13: Schematic geometry for an impacting rod and an infinite block.

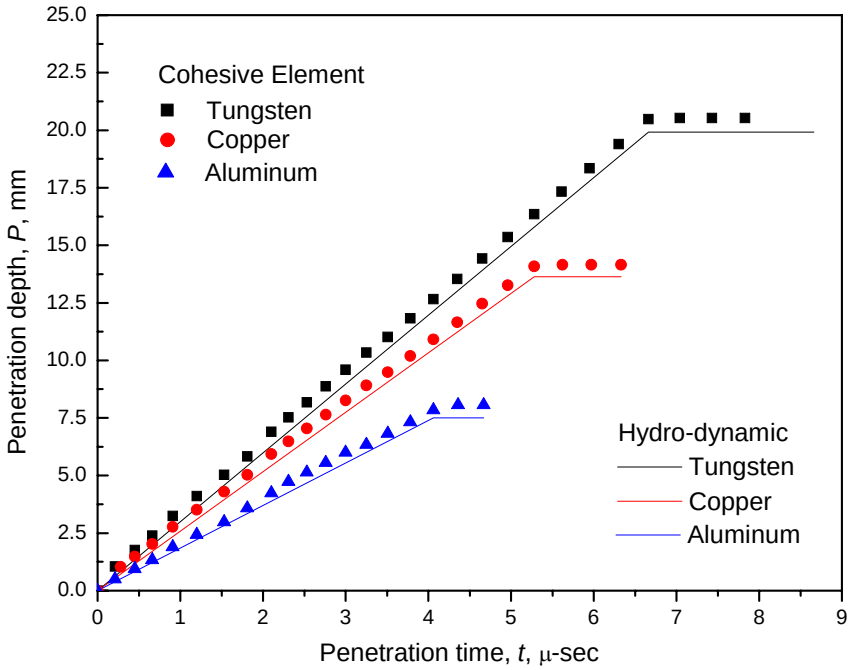

Figure 9.14: Comparison of penetrations for different projectile impacts.

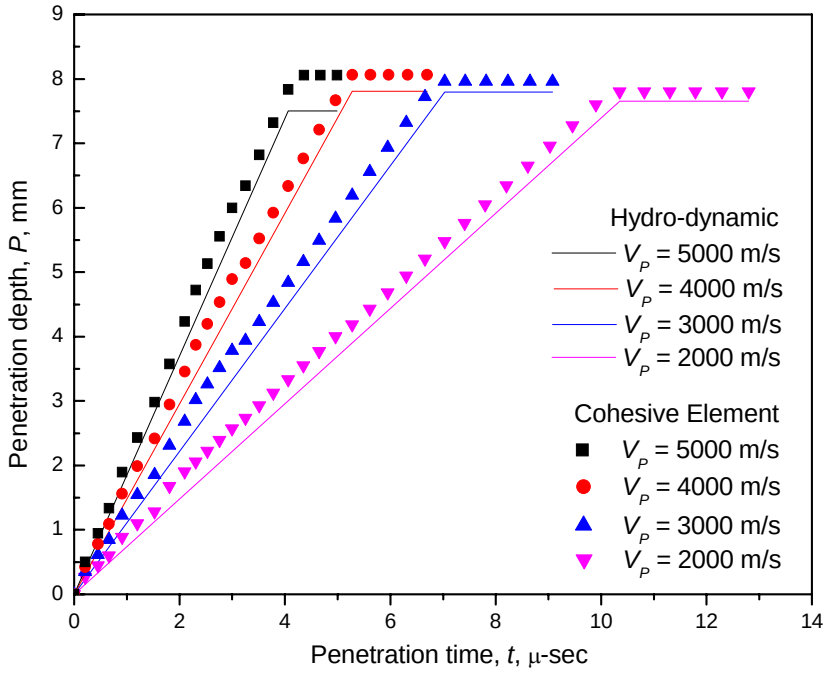

Figure 9.15: Comparison of penetrations for different projectile velocities.

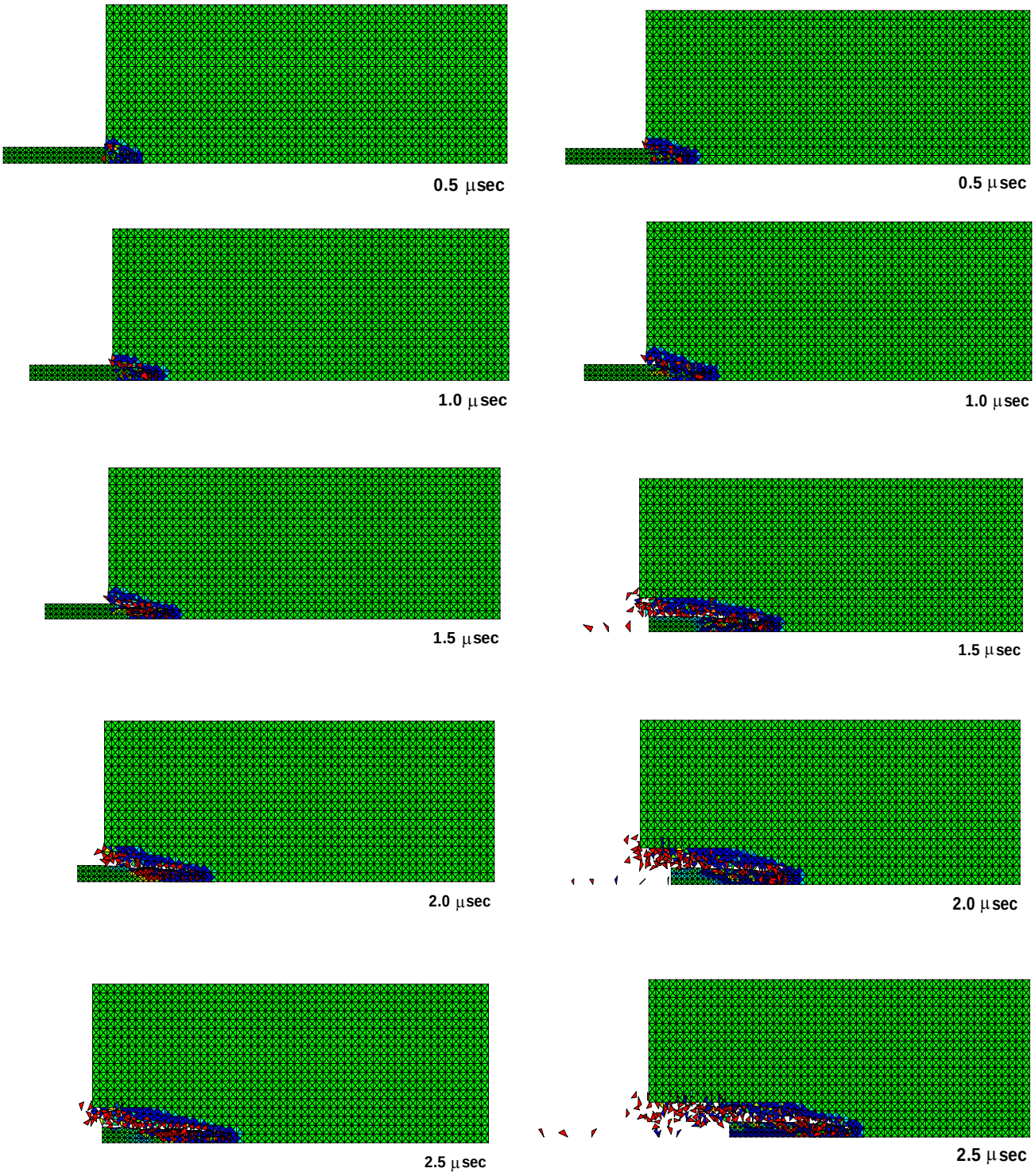

Figure 9.16: Penetration shapes for two different material projectiles with a velocity V_P =5000m/sec.

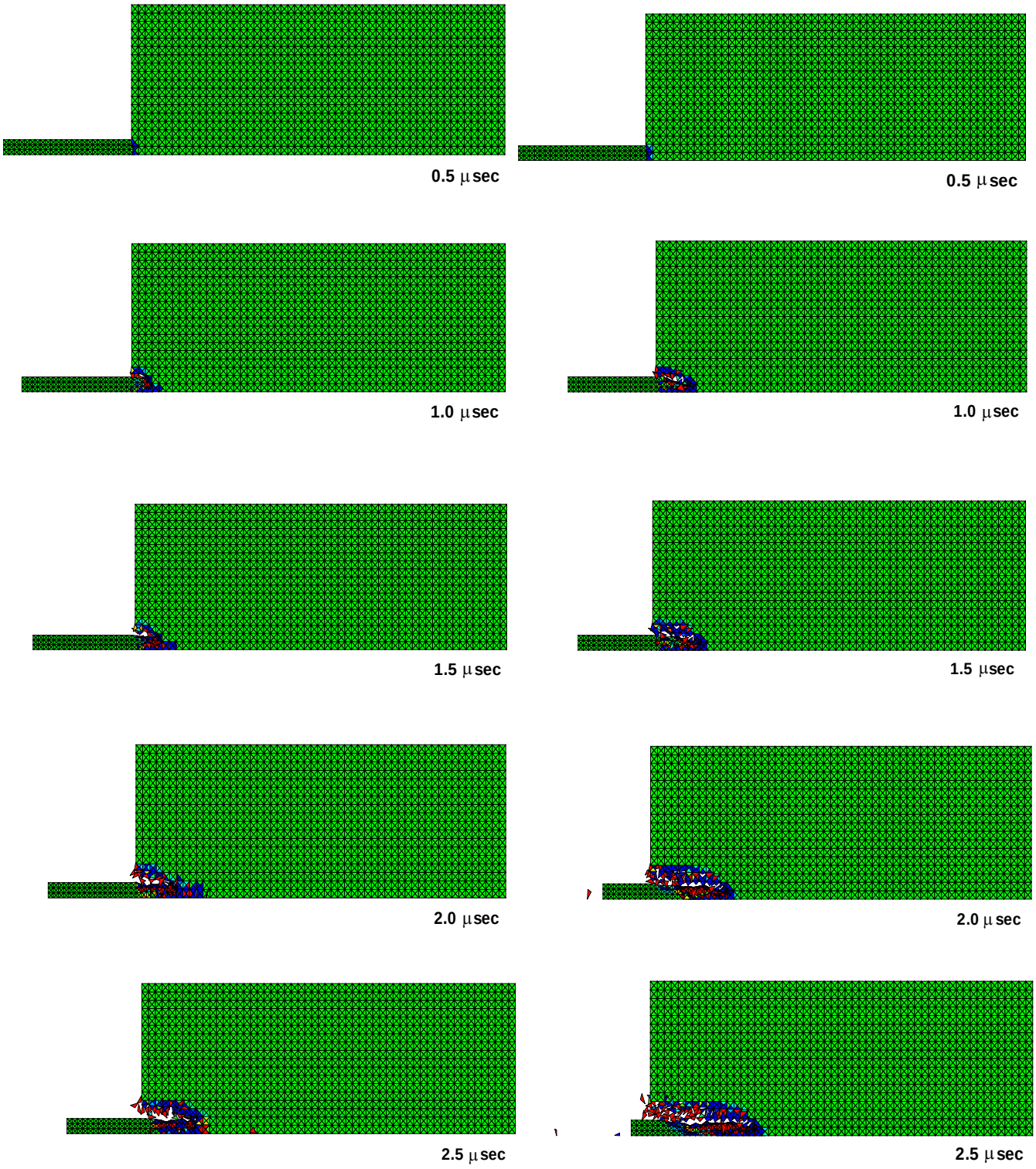

Figure 9.17: Penetration shapes of an aluminum rod with two different velocities V_P =2000 & 4000m/sec.

9.6 Penetration of Multi-layered Structures

Before checking the impact of multi-layered structures, the penetration problems for a ceramic layer subjected to impacts with several different velocities is considered here. The ceramic material is used for armor applications, because it has mechanical characteristics of stiff, brittle, and stronger in compression than in tension. Much research[9.10-9.22] on impact of ceramic armor has been done in the past. The material properties of the ceramic and ETG-100 steel are listed in Table 9.4. Figure 9.18 shows the dimension of the ceramic target (80mm$\times$10mm) and a circular-nosed steel bullet (20mm$\times$40mm) and also the contact-forces history for different impact velocities is shown. As shown in Figure 9.18, the contact forces and the contact durations depend on the impact velocity. For example, a lower impact velocity has longer contact durations and low contact forces while a high impact velocity has short contact times but higher contact forces. These facts have already been pointed in previous sections (9.2 and 9.3) while describing analytical impact modeling. If different target materials, brittle or ductile, are considered, same contact forces and duration trends will be observed. A ductile material target has longer contact duration and low contact force values while a brittle material target has the short contact time and higher contact forces for the same impact velocity.

Figures 9.19-9.20 show the deformed shapes of the target and projectile with different impact velocities. From Figures 9.19-9.20, we can see that the case of the lower impact velocity shows longer contact duration, small penetration rates and lower magnitude stress waves while the case of high impact velocity has a shorter contact time, large penetration rates and high stress waves, respectively. In the case of the high impact velocity, the penetration point reaches early. Compared to the case for the lower impact velocity, the crack propagation for the higher impact velocity takes place along the sections of the ceramic plate.

Other penetration problems in Figures 9.21-22 are ceramic-faced armors consisting of an AD-85 alumina, 8.0 mm thick, supported by 6061-T6 aluminum, 8.0 mm thick, respectively. The projectile impacts an armor plate at a transverse or oblique velocity of 850 m/sec. The dimension of projectile is based on a 7.62 mm ball projectile and consists of a steel core surrounded by a thin copper jacket. It has a maximum diameter of 7.62 mm, is 26.5 mm long, and weighs 9.5 grams. For better understanding of armor impacts, calculated kinetic and internal energies of the projectile as shown in Figure 9.23 are considered. Figure 9.24 also shows impact velocities of the projectile as the contact durations are increased, respectively. From Figures 9.23-9.24, the oblique impact case has a larger impact duration and a smaller reduction of the impact velocity than those for the normal impact case. In the previous section (9.4), these facts are inferred from Eqs. 9.15-9.18. Figure 9.25 shows several deformed projectile and target configurations at various time steps. Although the 7.62 mm ball projectile penetrates the alumina armor layer with a large number of fragmentations, the aluminum layer finally overcomes the speed of the ball projectile and stops any further penetration. This means that the alumina face can considerably reduce the impact loading of projectiles by developing a large number of cracks and the kinetic energy of the projectiles can be localized in the aluminum layer that acts as a back-up layers to prevent the bullet's futher penetration.

Another penetration problem is a projectile impacting on an armor plate consisting of an AD-85 alumina, 16.0 mm thick, see Figure 9.29. The model dimension is same as in Figure 9.22 except the layer that is consisting of the all alumina. Several different impact velocities are considered to determine corresponding penetration points and impact durations. Figure 9.30 shows that the normalized kinetic and internal energies of the projectile and penetration points with different impact velocities. The normal and oblique impact configurations of the plate and projectile are presented in Figures 9.25, 9.27 and 9.31, respectively. The cohesive element depicts more detailed crack propagations and the evolution of fracture patterns along the penetration path of projectile, see Figures 9.26, 9.28 and 9.32. In Figures 9.28 and 9.32, the evolutions of crack propagation are considerably dependent on the different impact directions and magnitudes of impact velocities. Also they all have different impact durations. For example, a high impact velocity induces more crack propagations than a low impact velocity, when the same material and dimensions of the target and projectile are used. These facts have been explained in section 9.4.

Table 9.4 Mechanical properties for the plate target and the circular-nosed projectile.

Materials	E	ν	σ_y	σ_u	ρ	δ
Ceramic plate	370.0 GPa	0.22	3700 MPa	1500 MPa	3920 Kg/m^3	3.81×10^{-4} mm
Steel projectile	206.8 GPa	0.29	1030 MPa	590 MPa	7800 Kg/m^3	

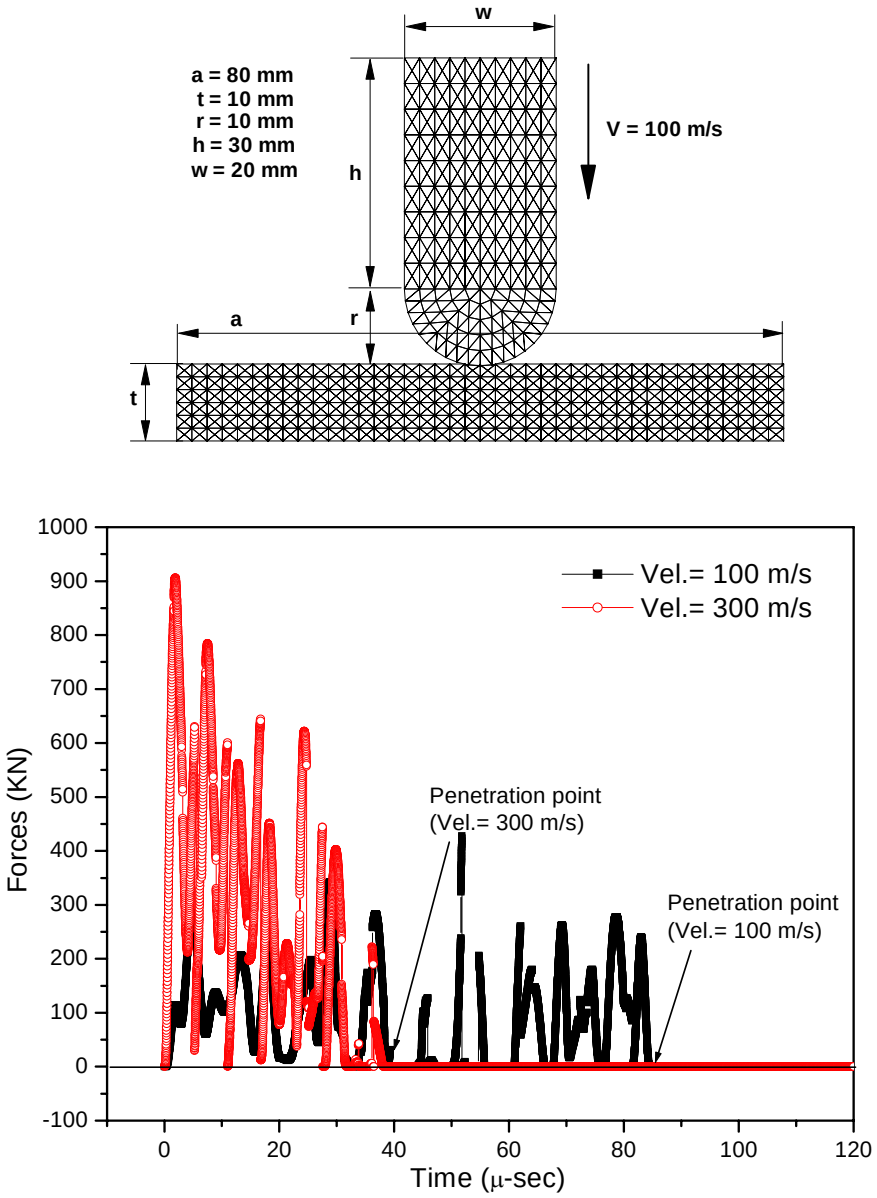

Figure 9.18: Contact forces' history and model of a ceramic plate target and a circular-nosed projectile.

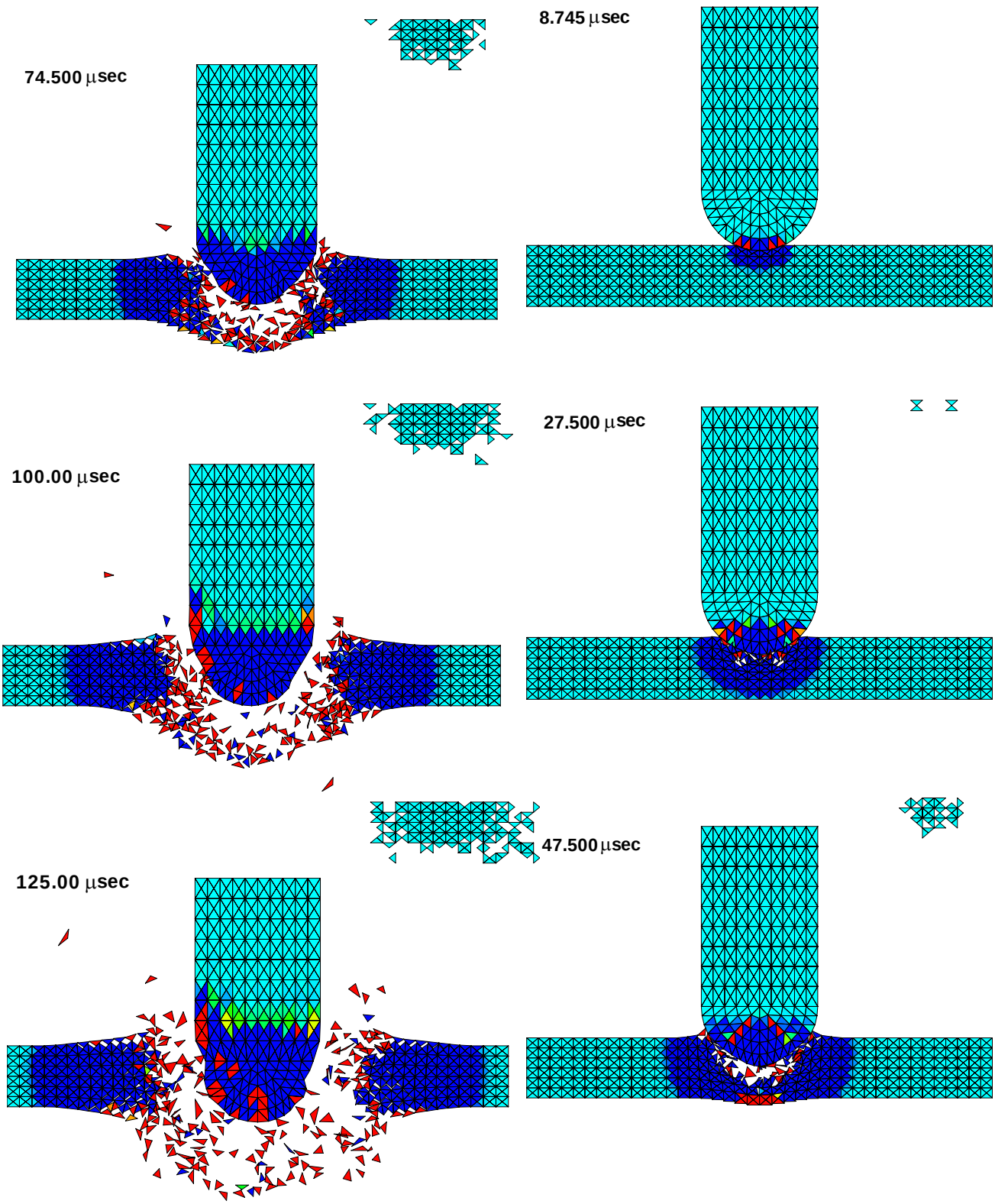

Figure 9.19: Deformed shapes of a ceramic plate target and a circular-nosed projectile (V =100m/sec).

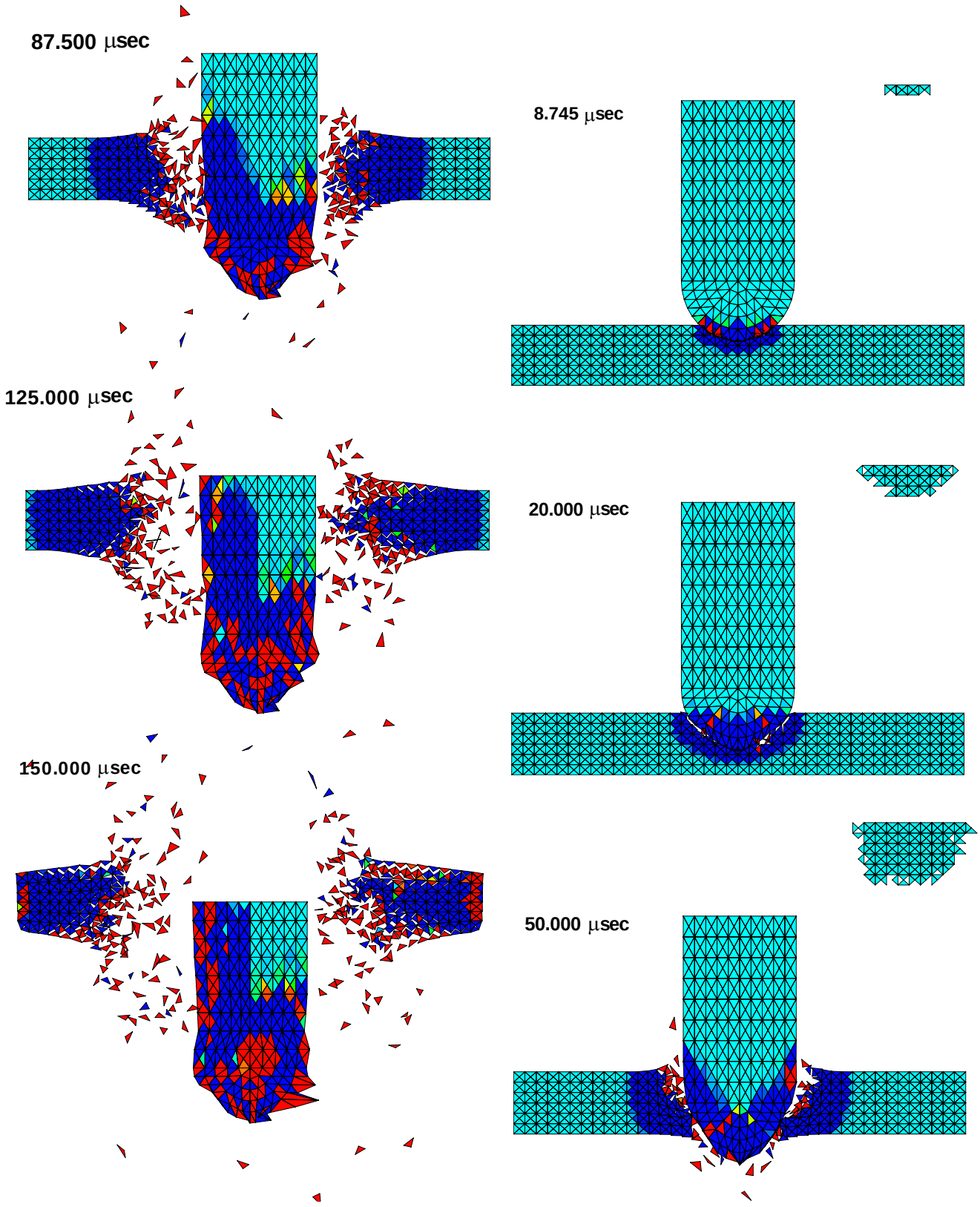

Figure 9.20: Deformed shapes of a ceramic plate target and a circular-nosed projectile (V =300m/sec).

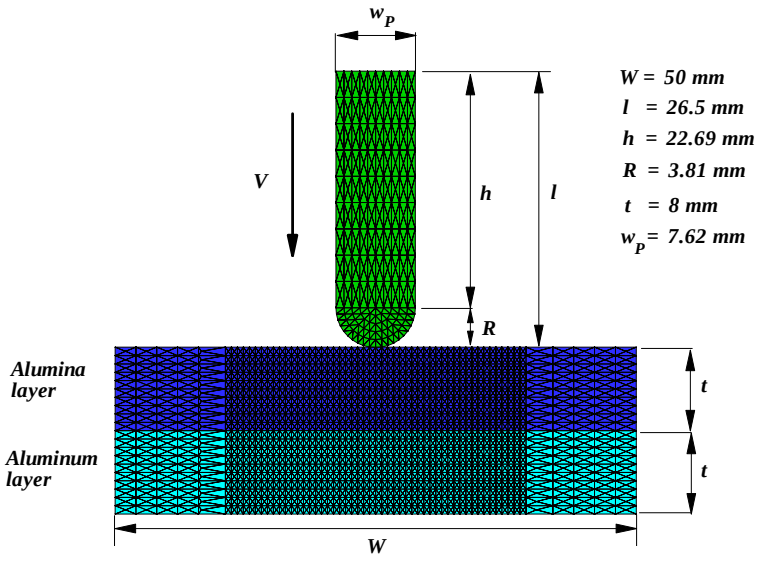

Figure 9.21: A 7.62 mm projectile and an armor plate consisting of AD-85 alumina bonded to 6061-T6 aluminum.

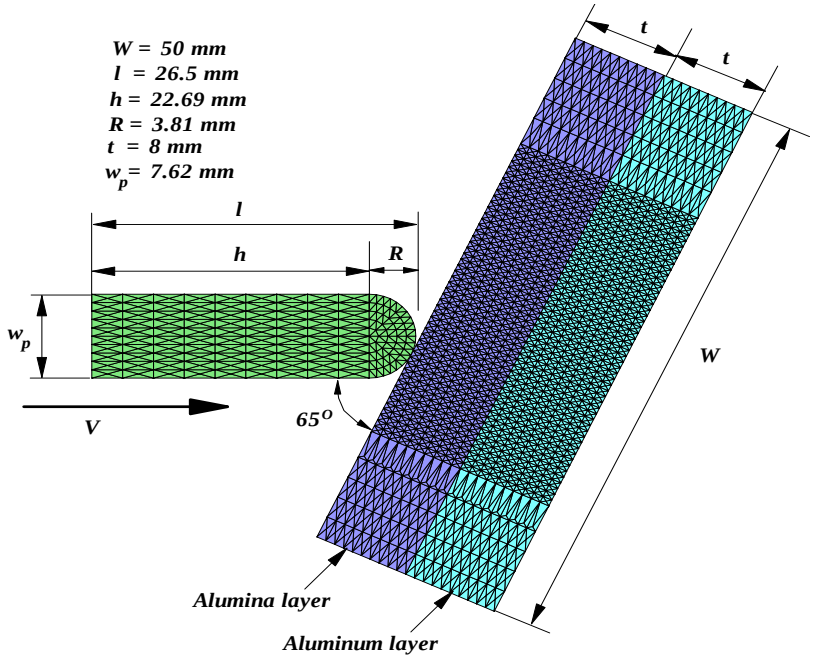

Figure 9.22: Oblique impact of a 7.62 mm projectile and an armor plate.

Table 9.5 Mechanical properties for AD-85 alumina and 6061-T6 aluminum.

Materials	E	ν	σ_y	σ_u	ρ	δ
AD-85 alumina	378.0 GPa	0.24	3790 MPa	1515 MPa	3810 Kg/m^3	3.81×10^{-4} mm
6061-T6 aluminum	68.9 GPa	0.33	310.0 MPa	200.0 MPa	2705 Kg/m^3	1.54×10^{-3} mm

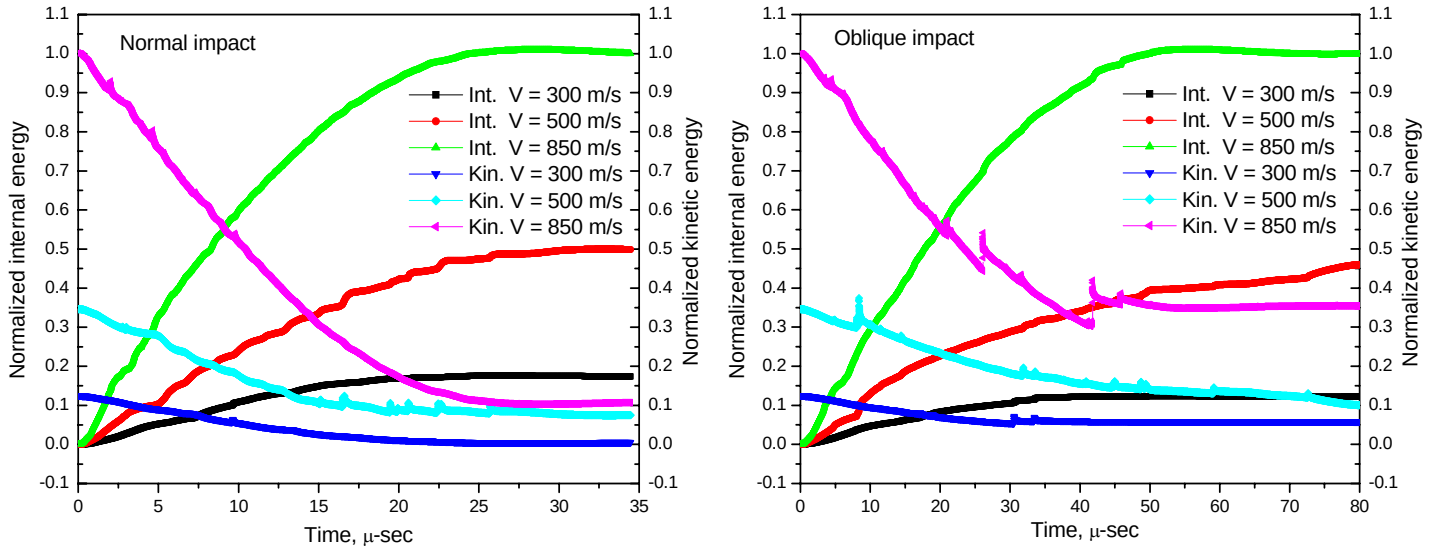

Figure 9.23: Normalized kinetic and internal energies of normal and oblique projectiles.

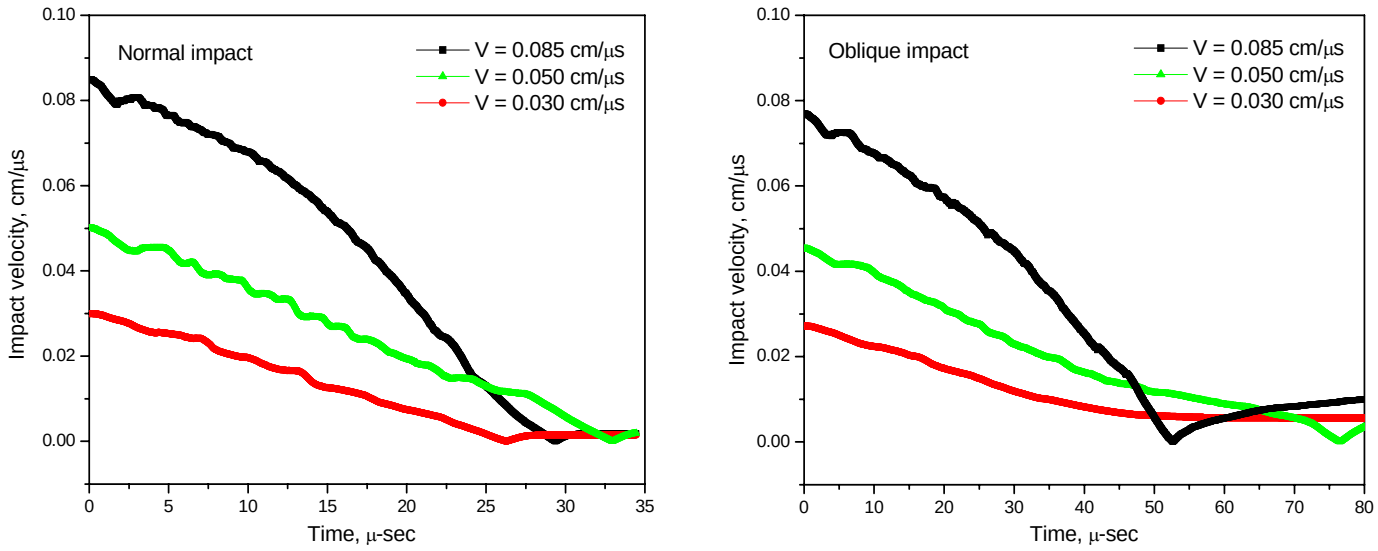

Figure 9.24: Impact velocities of normal and oblique projectiles.

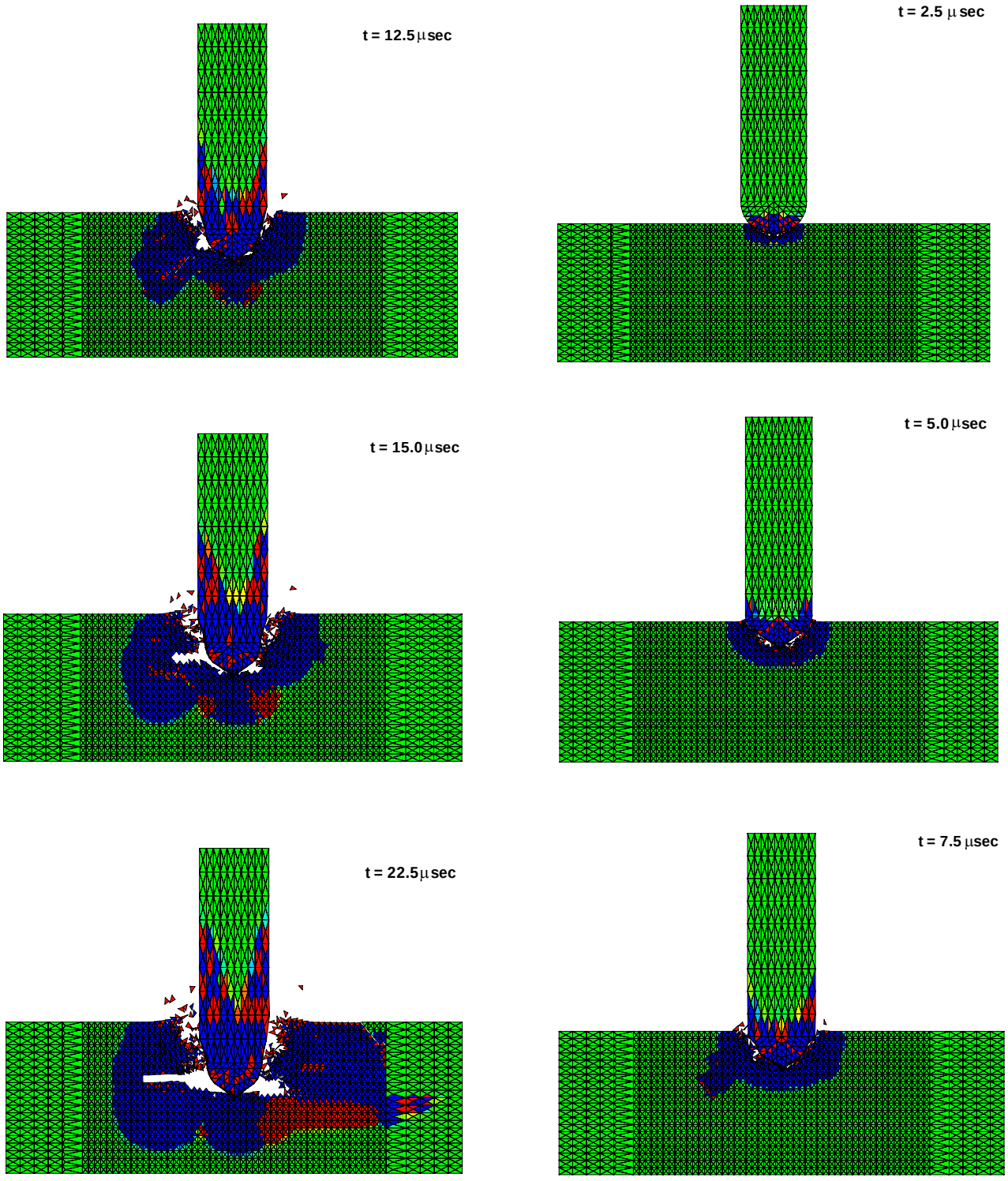

Figure 9.25: Calculated configurations of an armor plate and a 7.62 mm ball projectile (V =850 m/sec).

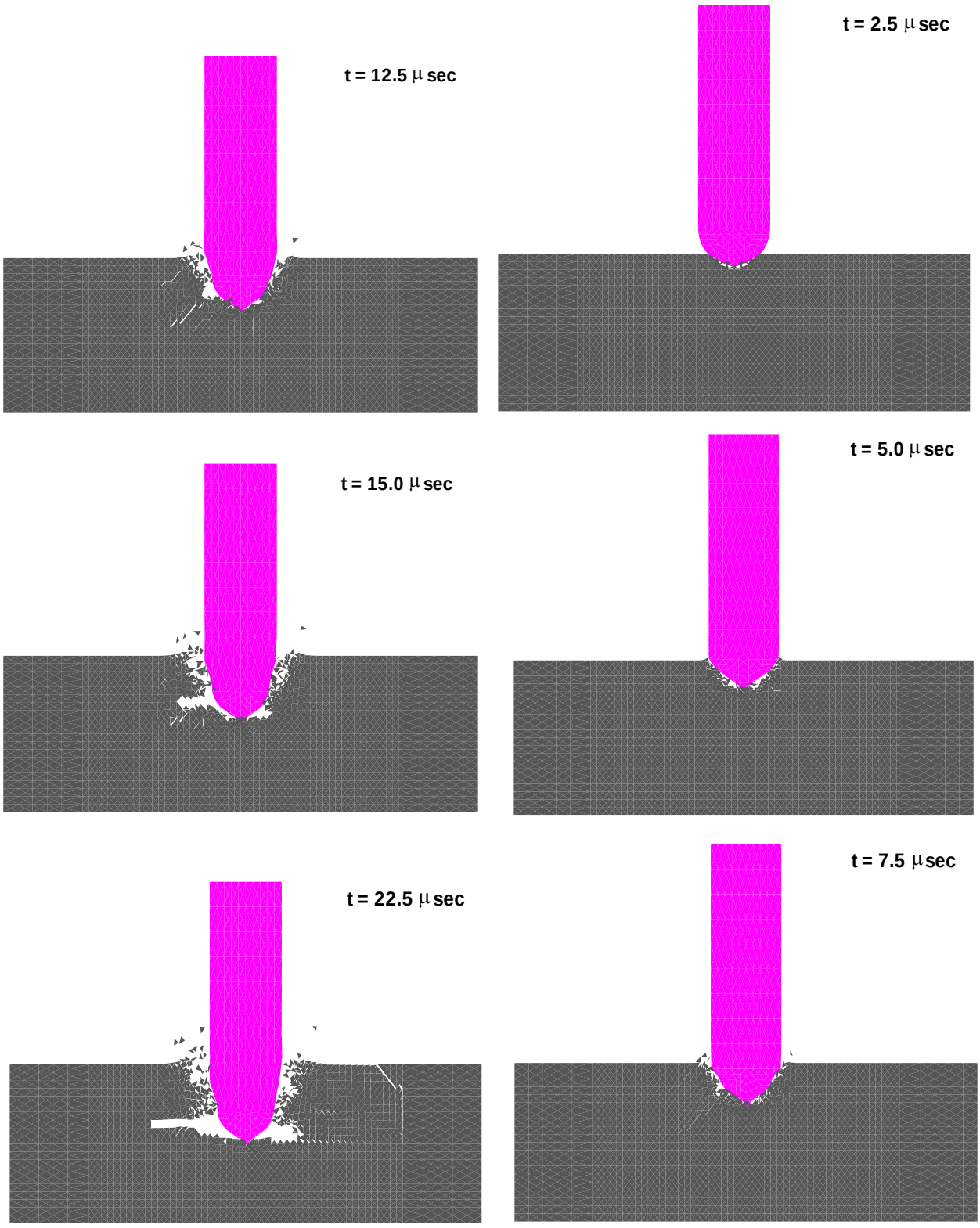

Figure 9.26: Fracture patterns of an armor plate and a 7.62 mm ball projectile (V =850 m/sec).

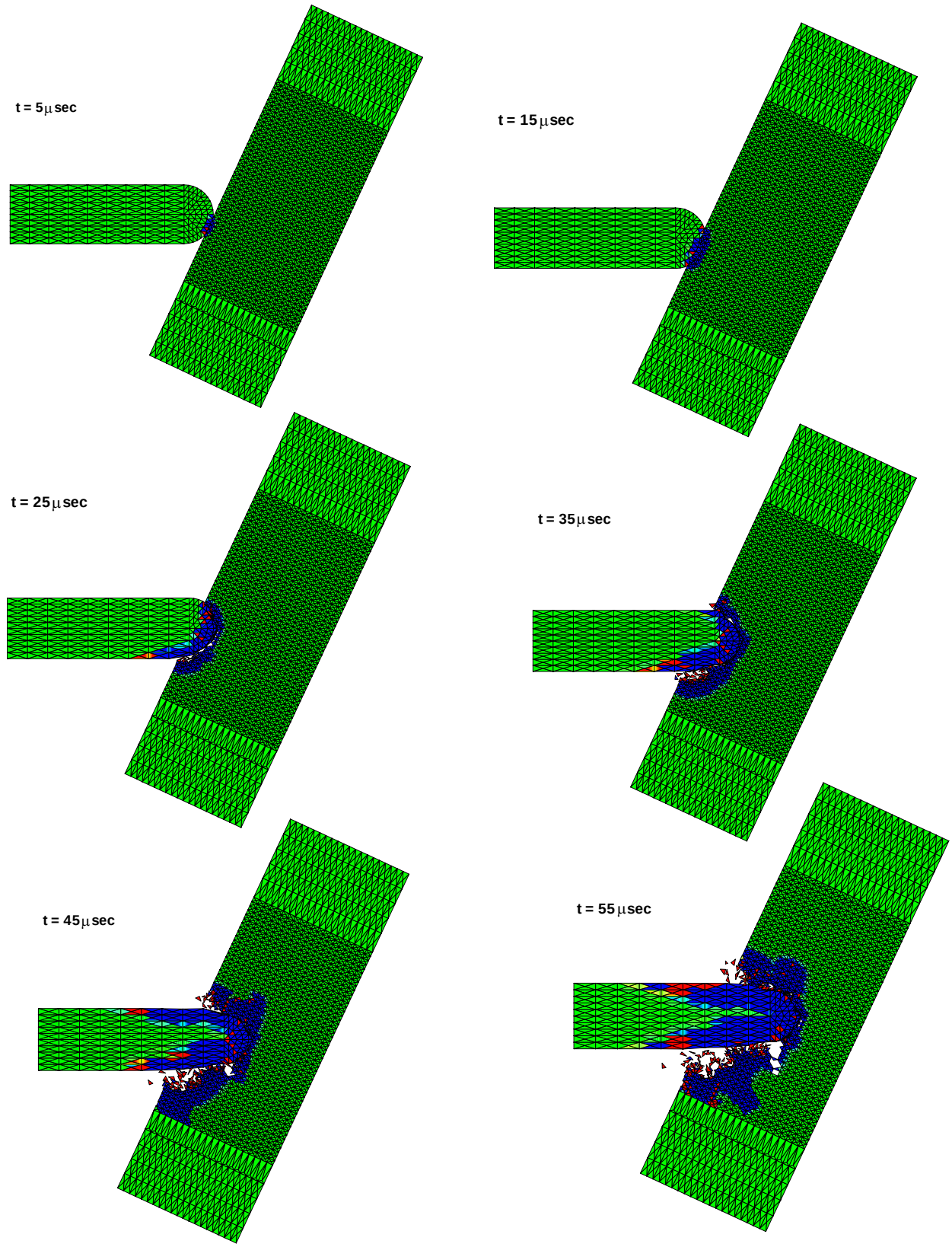

Figure 9.27: Calculated configurations of an armor plate and a 7.62 mm ball projectile (V =850 m/sec).

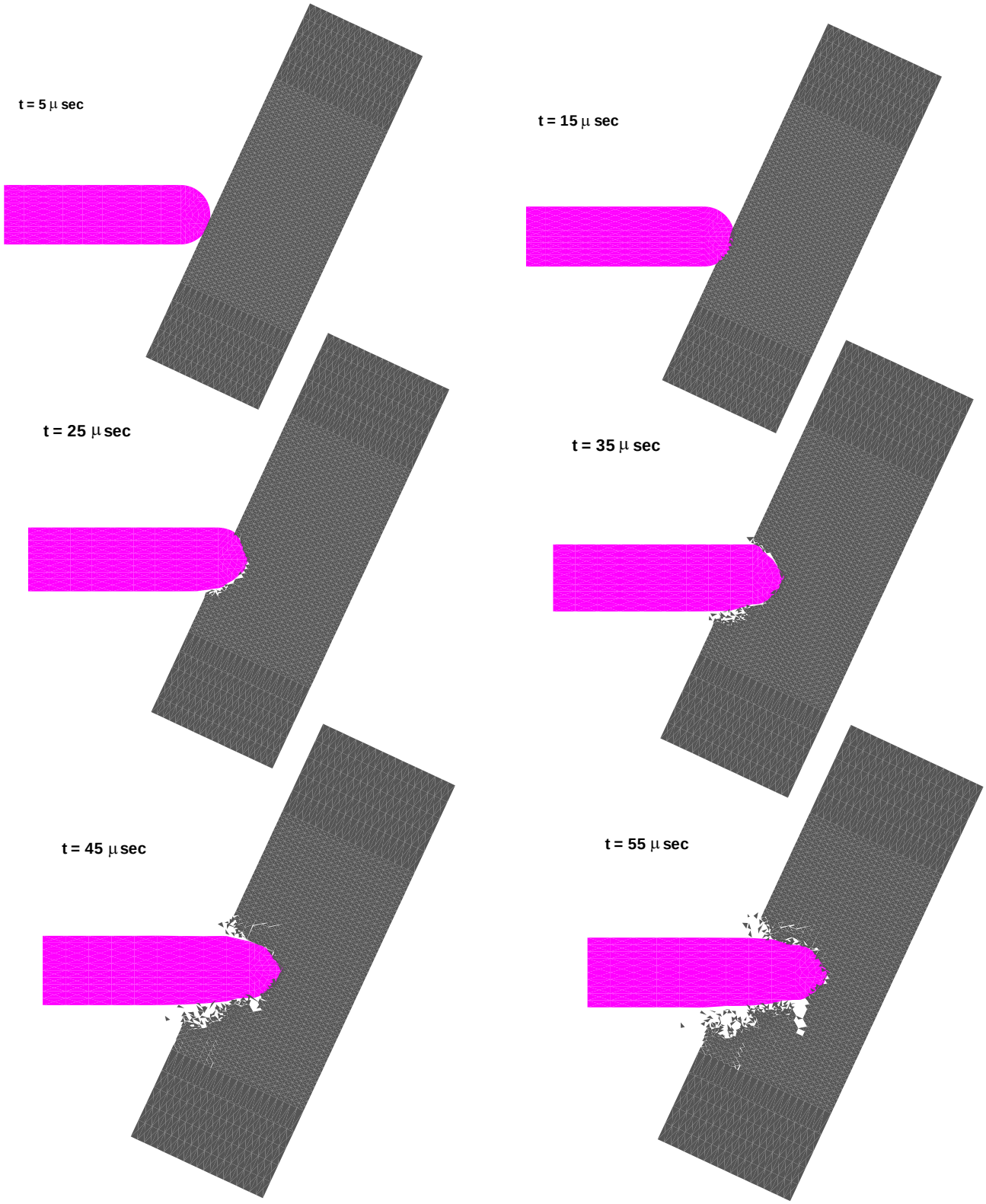

Figure 9.28: Fracture patterns of an armor plate and a 7.62 mm ball projectile (V =850 m/sec).

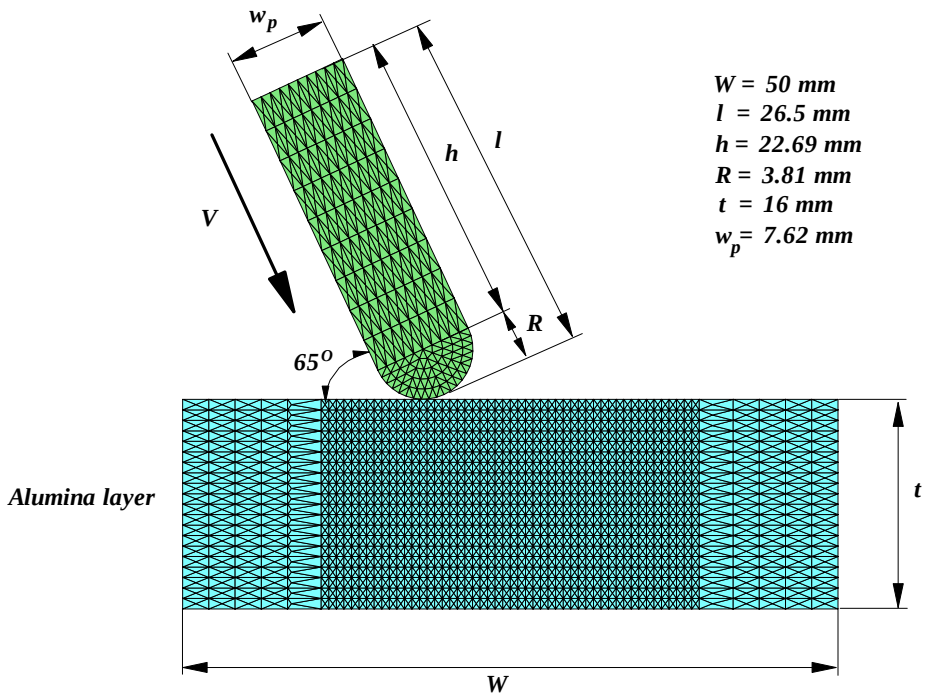

Figure 9.29: Oblique high-velocity impact of a 7.62 mm projectile and an alumina plate.

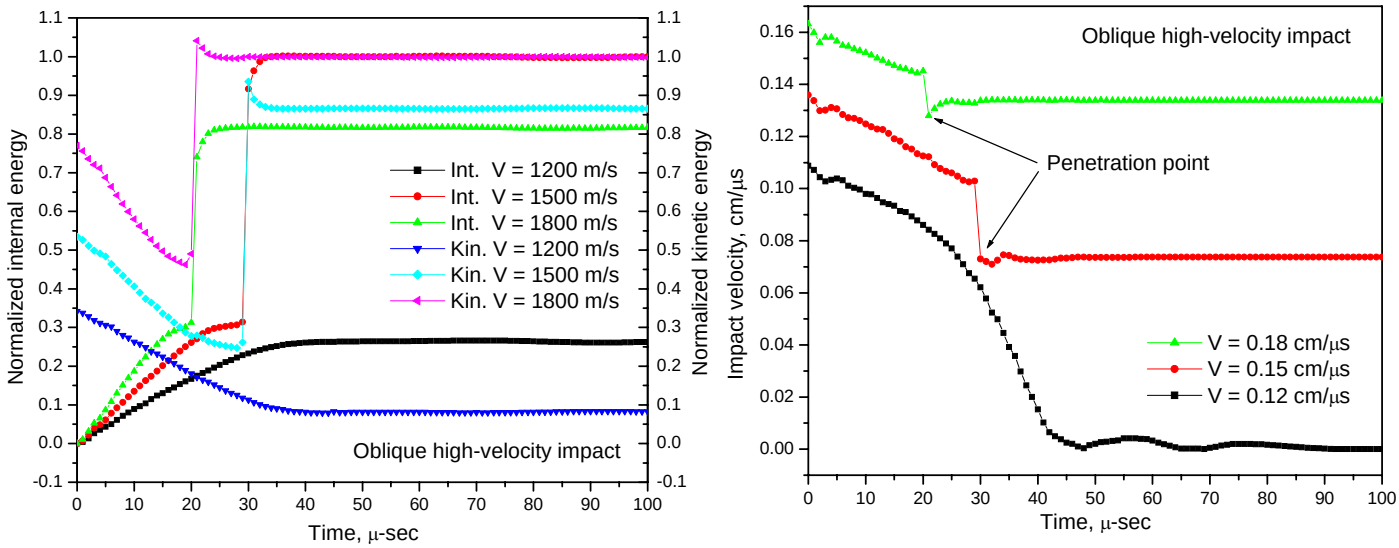

Figure 9.30: Normalized kinetic and internal energies and impact velocities of high speed-oblique projectiles.

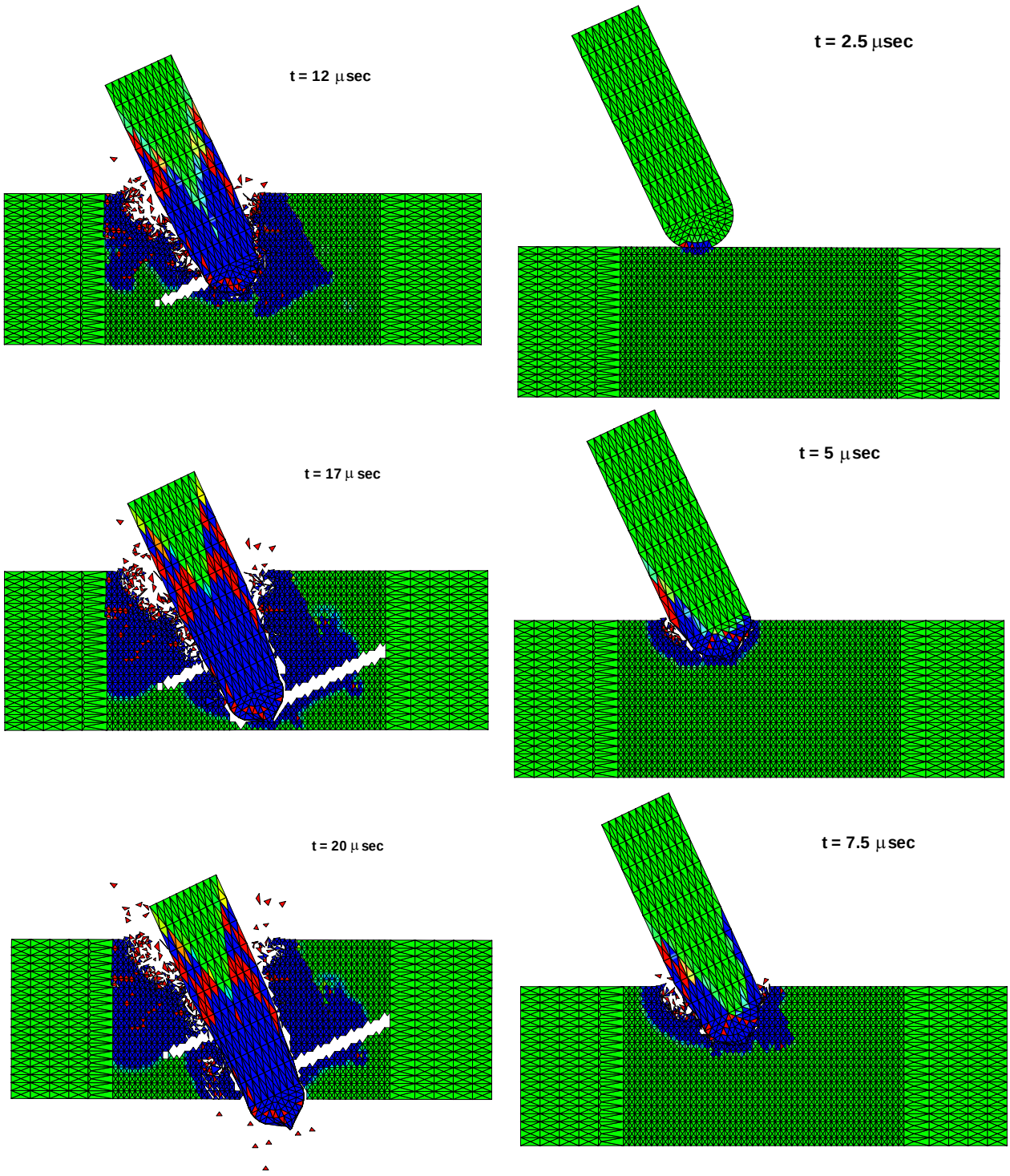

Figure 9.31: Calculated configurations of an alumina plate and a 7.62 mm ball projectile (V =1800 m/sec).

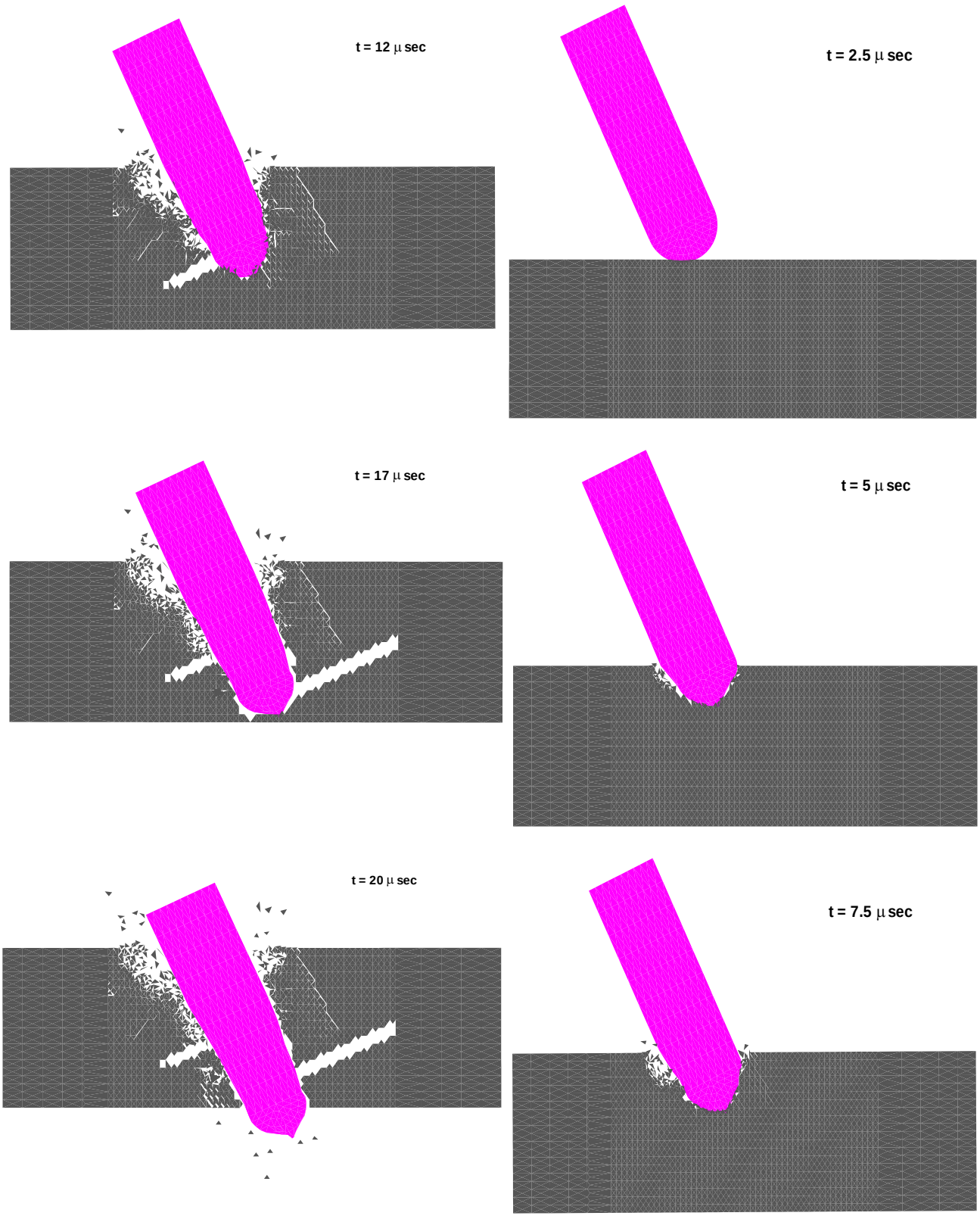

Figure 9.32: Fracture patterns of an alumina plate and a 7.62 mm ball projectile (V =1800 m/sec).

REFERENCES

9.1 Goldsmith, W., *Impact*, Edward Arnold, London, 1960.

9.2 Calder, C.A. and Goldsmith, W., "Plastic Deformation and Perforation of Thin Plates Resulting from Projectile Impact," *International Journal of Solids and Structures*, Vol. 7, No. 7, 1971, pp. 863-881.

9.3 Calder, C.A., *Plastic Deformation and Perforation of Thin Plates Resulting from Projectile Impact*, Ph.D. Thesis, University of California, U.S.A., 1969.

9.4 Goldsmith, W. and Finnegan, S.A., "Penetration and Perforation Processes in Metal Targets at and above Ballistic Velocities," *International Journal of Mechanical Sciences*, Vol. 13, No. 10, 1971, pp. 843-866.

9.5 Mayseless, M., Goldsmith, W., Virostek, S.P. and Finnegan, S.A., "Impact on Ceramic Targets," *Journal of Applied Mechanics,* Vol. 54, June, 1987, pp. 373-378.

9.6 Birkhoff, G., MacDougnall, D.P., Pugh, E.M. and Taylor, G., "Explosives with Lined Cavities," *Journal of Applied Physics,* Vol. 19, No. 6, 1948, pp. 563-582.

9.7 Pack, D.C. and Evans, W.M., "Penetration by High-Velocity ('Munroe') Jets: I," *Proceedings of Physics and Society,* Vol. B-64, 1951, pp. 298-302.

9.8 Evans, W.M. and Pack, D.C., "Penetration by High-Velocity ('Munroe') Jets: II," *Proceedings of Physics and Society,* Vol. B-64, 1951, pp. 303-310.

9.9 Allen, W.A., Meloy, G.E. and Rogers, J.W., "Hyper-velocity Precision Impact Instrument," *The Review of Scientific Instruments,* Vol. 31, No. 7, 1960, pp. 726-730.

9.10 Bless, S.J., Rosenberg, Z. and Yoon, B., "Hypervelocity Penetration of Ceramics," *International Journal of Impact Engineering*, Vol. 5, No. 1-4, 1987, pp. 165-171.

9.11 Bless, S.J., *Impact Behavior of Ceramics*, University of Dayton Research Institute, Dayton, Ohio, U.S.A., 1987.

9.12 O'Donnell, R.G., Woodward, R.L., Gooch Jr, W.A. and Perciballi, W.J., "Fragmentation of Alumina in Ballistic Impact as a Function of Grade and Confinement," *Proceedings 12'th International Symposium on Ballistics*, San Antonio, TX, U.S.A., 1990.

9.13 Ravid, M., Bodner, S.R. and Holcman, I., "Application of Two-Dimensional Analytical Models of Ballistic Penetration to Ceramic Armor," *Proceedings 11'th International Symposium on Ballistics*, Brussels, Belgium, 1989.

9.14 Reijer, P.C. den, "Penetration of 7.62mm Projectiles into Ceramic Faced Armor, *Proceedings 11'th International Symposium on Ballistics*, Brussels, Belgium, 1989.

9.15 Shockey, D.A., Marchand, A.H., Skaggs, S.R., Cort, G.E., Burkett, M.W. and Parker, R., "Failure Phenomenology of Confined Ceramic Targets and Impacting Rods," *International Journal of Impact Engineering*, Vol. 9, No. 3, 1990, pp. 263-275.

9.16 Prior, A.M. and Hetherington, J.G., "The Penetration of Composite Armor by Small Arms Ammunition," *Proceedings 9'th International Symposium on Ballistics*, Shrivenham, England, 1986.

9.17 Prior, A.M. and Hetherington, J.G., "The Penetration of Lightweight Armors by Small Arms Ammunition," *Proceedings 10'th International Symposium on Ballistics*, San Diego, CA, U.S.A. 1987.

9.18 Rosenberg, Z. and Tsaliah, J., "Applying Tate's Model for the Interaction of Long Rod Projectiles with Ceramic Targets," *International Journal of Impact Engineering*, Vol. 9, No. 2, 1990, pp. 247-251.

9.19 Raymond, L.W., "A Simple One-Dimensional Approach to Modeling Ceramic Composite Armor Defeat," *International Journal of Impact Engineering*, Vol. 9, No. 4, 1990, pp. 455-474.

9.20 Wimmer, J.M. Bransky, I. and Tallan, N.M., "Impact Resistance of Structural Ceramics," *Air Force Materials Laboratory*, WPAFB, Ohio, U.S.A., 1976, AD-A037165.

9.21 Camacho, G.T. and Ortiz, M., "Computational Modeling of Impact Damage in Brittle Materials," *International Journal of Solids and Structures*, Vol. 33, No. 20-22, 1996, pp. 2899-2938.

9.22 Camacho, G.T., *Computational Modeling of Impact Damage and Penetration of Brittle and Ductile Solids*, Ph.D. Thesis, Brown University, U.S.A., 1996.

Chapter 10 Impact Analysis of Micro-Cracked Textile Composites

10.1 Introduction

In Chapter 9, an analytical impact modeling considering the results of using cohesive elements was studied and then applied to solve impact problems of multi-layered structures. This chapter is focused on an integrated numerical modeling enabling one to investigate the dynamic behavior and failure of 2-D textile composite and 3-D orthogonal woven composite structures weakened by micro-cracks and subjected to ballistic-impact type loads. The integrated numerical modeling is based on: I) determination of governing equations via a three-level hierarchy: micro-mechanical unit cell analysis, layer-wise analysis accounting for transverse strains and stresses, and structural analysis based on anisotropic plate layers, II) development of an efficient computational approach enabling one to perform transient response analyses of 2-D plain woven and 3-D orthogonal woven composite structures featuring the matrix cracking and exposed to time-dependent loads of the ballistic type, III) determination of the structural characteristics of the textile-layered composites and their degraded features under smeared and discrete cracks, and assessment of the implications of stiffness degradation on dynamic response to impact loads, and finally, IV) the study of the micro-crack propagations in textile layered composites.

10.2 Technical Approach of Micro-Cracked Textile Composites' Impact Modeling

To solve the problem of dynamic response of the 2-D textile and 3-D woven textile composites, shown in Figure 10.1, a thorough study of their mechanical properties and structural behavior is needed. For example, the main difficulty in the textile composite structures is the computational complexity in terms of geometry and material modeling. A review of publications on the mechanical property predictions and static response analysis of 3-D woven composites can be found in several studies. These structures were also investigated in previous chapters of this study. In Ref. [10.1], an example of multi-scale predictive analysis of 3-D woven composites exposed to static loads was presented. Some aspects of the aforementioned publication are implemented in this work for developing a dynamic analysis approach.

Studying damage and failure of the 2-D textile and the 3-D orthogonal woven textile composite structures under severe dynamic loads involves a number of issues of high complexity that should be addressed such as: complex damage modes in the textile composite materials; the material behavior under different strain rates, and determination of the constitutive behavior of composites in the presence of matrix cracking, matrix and/or fiber yielding. It is essential to develop a computational methodology that may lead to an improved understanding of the impact mechanisms about the textile layered structures.

To solve the dynamic response of 2-D and 3-D woven textile composite structures featuring matrix cracking, see Figure 10.2, this study uses the following three hierarchal steps: (i) unit cell micro-level (similar to the static analysis Ref. [10.1]), (ii) homogenized warp and fill fiber ply level (thus modeling 2-D and 3-D woven composite in a layer-wise fashion, similar to the "discrete layer" approach in Ref.[10.1]), and (iii) by adopting a thick anisotropic layer, the structural model is implemented. In order to validate some results obtained within this structural model, the degradation of structural characteristics are compared with results as shown in previous chapters.

Moreover, additional numerical schemes; micro-mechanical equations, the self-consistent method and cohesive element scheme, are applied into the three hierarchical levels at each time-step. The implementation of the three hierarchical levels is essential in order to get solutions of the behavior of 2-D and 3-D degraded textile composite structures exposed to impact loads. To fulfill the three hierarchical levels, in the context of this research, a numerical program on the dynamic modeling of textile composite structures, of layer type and describe the crack propagation problems, the cohesive element scheme is developed.

10.2.1 Micro-mechanical Analysis

As a first step, the 2-D and 3-D micro-model is applied to determine the effective elastic characteristics via the laminate model/Repeating Unit Cell (RUC) concept shown in Figure.10.3. The laminate model consists of four lamina layers: the warp, the fill, and the top and the bottom laminae, these are all represented in Figure 10.4. To calculate the effective elastic properties, micro-mechanical equations of composites are used, and in this context, the iso-stress method is applied for the fiber and matrix components in each lamina. Within this step, the crack density scheme for the matrix cracking is used to calculate the degraded effective elastic properties in the yarns that depend on geometrical parameters, such as yarn-thickness, tow-packing factors and fiber packing types, etc. The matrix cracking is expressed as a function of the crack density defined as the average number of cracks within a control domain. For the cracked structures, the self-consistent scheme and the relationship between stress and strains are applied

$\sigma = C\varepsilon$, $\varepsilon = S\sigma$, $CS = SC = I$,

$$Q = C - CPC \tag{10.1}$$

Here, C and S are the stiffness and compliance matrices, and I is the unit diagonal matrix. Also σ and ε are stress and strain matrices, respectively. The matrices P and Q are the relative stiffness and compliance matrices about the matrix C and S , respectively. All components in the stiffness and compliance matrices include the crack density values. To find the overall stiffness and compliance matrices for the yarns, the relations between the average values for the stress and strain are used

$$\sum v_r = 1,\ \overline{\sigma}_{avg} = \sum v_r \overline{\sigma}_r ,\ \overline{\varepsilon}_{avg} = \sum v_r \overline{\varepsilon}_r \tag{10.2}$$

Here, r means the fiber and matrix phases in the yarns. To get the relative dimensions of the fiber and the matrix in the yarns, this study introduces volume weight factors, such as volume fractions (v_r); these terms will intervene in the constitutive relations for fiber and matrix phases that have to satisfy the equilibrium and compatibility equations within micro-yarn slices. The volume fractions for the fiber and matrix phase are used to define the overall stiffness and compliance of the yarns. By considering the average values for the stress and strain in the yarn slices, transformation stiffness matrices of the fill and warp yarns are derived, and the respective relations are supplied in Appendix A.

By determining the stiffness and compliance quantities related to the yarns in each layer, and extending this micro-mechanical analysis into the direction of the z-axis, the effective properties of sub-laminate layers will be evaluated in the next step for determining the constitutive relation, for performing an analysis using a layer-wise approach.

10.2.2 Layer-wise Analysis

This study considers each warp and fill layer of fibers with their associated resin as a homogenized anisotropic lamina having effective properties determined in Step 1 (Micro-mechanical analysis). For example, a 3-D woven composite with 2 “warp”, 3 “fill” and 2 “surface” effective composite laminae will be treated as a 7-layer laminate. As a result, a layer-wise approach shown in Figure 10.6 will be applied to the components of lamina layers (upper surface, fill, warp and lower surface laminae). A laminate with assumed boundary conditions subjected to impact/ballistic loads is studied. When the resulting damage is taken into account, the respective degraded/effective elastic properties of each lamina need to be used. For the 2-D plain woven composite, the sub-domain zone shown in Appendix B is considered using a layer-wise analysis.

By combining several sub-laminate layers, a thick laminate is formed within an RUC. A typical repeating cell contains N composite laminas including the fill, warp and z-yarns in an arbitrary orientation. The coordinate system is set up such that warp (x) and fill (y) axes lie in the plane of the yarns and z-axis (z) is perpendicular to this plane. Within the RUC, the following effective properties of stresses and strains are defined as

$$\overline{\sigma}_{ij} = \frac{1}{V}\int_V \sigma_{ij} dV \ , \ \overline{\varepsilon}_{ij} = \frac{1}{V}\int_V \varepsilon_{ij} dV \tag{10.3}$$

In the above equations, V is a representative volume that contains the total thickness of the RUC, and its in-plane dimensions are considered to be infinitesimal so that the stresses and strains ($\sigma_{ij} = \overline{\sigma}_{avg}, \varepsilon_{ij} = \overline{\varepsilon}_{avg}$) in each lamina are uniform in the planar directions. Since the stresses and strains in each lamina are constant, Eq. 10.3 can be integrated to yield

$$\overline{\sigma}_{ij} = \sum_{k=1}^{N} \nu_k \sigma_{ij}^{(k)} \ , \ \overline{\varepsilon}_{ij} = \sum_{k=1}^{N} \nu_k \varepsilon_{ij}^{(k)} \ , \ \nu_k = \frac{t_k}{h} \tag{10.4}$$

Here $\sigma_{ij}^{(k)}$ and $\varepsilon_{ij}^{(k)}$ are the stresses and strains in the k th sub-laminate layer, and ν_k and t_k are the volume fraction and thickness of the k the sub-laminate layer, respectively, and h is the total thickness of the RUC. Within the 3-D orthogonal woven composites, the fill and warp planes are symmetric for every constituent lamina in the sub-laminates. As a result of this symmetry, the effective elastic constant matrix is in the form of a 6 by 6 matrix. From the matrix of effective elastic constants, effective engineering properties of the RUC can be obtained. Also, the effective elastic constants includes the degraded elastic properties dependent on the transversely matrix cracking of the yarns. The predictions based on this methodology have been already evaluated against the results of the effective elastic properties in the 3-D woven textile composites obtained using other models. The results of these comparisons are presented in previous chapters. For the 2-D textile composites, the degraded fill and warp yarns have already been studied using the RUC concept. Also, the predictions based on Sine Function Models (SFM I & II) in Chapters 2 and 3 have been compared with other model results (see Naik[10.2] and Scida *et al.*[10.3]). Our results, obtained using two relatively simple models, show a good agreement with the results provided by other complex models.

10.2.3 Structural Analysis

The structural analysis of damaged textile composite structures under impact loads, consists of two main types; continuous cracking and discontinuous cracks. The former part is dependent on crack densities, and this will lead to the degraded elastic modulus. The latter is related to cohesive element modeling[10.4]. However, the latter part is a more complicated problem, because contact between striker and target structures must be included. Furthermore, the target and striker will experience severe ballistic loads and a large number of cracks develop in sections of textile layered structures. We have already mentioned this phenomenon in previous chapters.

Further, using the undamaged effective elastic properties in each lamina, the equivalent elastic properties of the textile composite, assumed to be a single-layer anisotropic material, are determined using the iso-strain method. This method assumes the same strains in each lamina along the z-axis. In the second step, the "degraded" effective elastic properties of the textile layered composite are predicted. The micro-cracks illustrated in Figure 10. 3 are produced at the limit load level, particularly on the tension side of the textile layers subjected to bending moments. To solve the case without cracks, the study assumes that some friction forces exist in the crack surfaces. As a result, the no crack case of the yarns is modeled by assigning the values for the crack density to be zero. In this research, the conditions for crack opening and crack closing will be properly modeled. Although, the curved deformation is a symmetric shape, due to presence of cracks, the coupling stiffness is not zero in general, and then the textile layer is considered to be an un-symmetric laminate. In this work, the conditions for the crack opening and the crack closure are based on the sign of the total strains that are perpendicular to the plane containing fill and warp yarn sections. These concepts based on the warp yarns are expressed as

If $\varepsilon_{22} = \varepsilon_{22}^{o} + z\kappa_{22} > 0$, the crack opens

If $\varepsilon_{22} = \varepsilon_{22}^{o} + z\kappa_{22} < 0$, the crack closes (10.5)

In Eq. 10.5, ε^o and κ are the membrane and bending curvature, respectively. The constitutive information will be addressed at the material points (Gauss points) within each element or in the Repeating Unit Cell (RUC) in the cohesive/finite element structural modeling.

To obtain tangent stiffness matrix and the updated state of stress, our model has to first find whether the crack is opened or closed after each time-step by considering the sign of the transverse stresses or strains at the material points within the element or the RUC. Depending on the opening and closing of a crack, the stiffness terms in the constitutive relation corresponding to the transverse direction, are assumed to be changed/unchanged. The finite element analysis will be performed until the state of crack opening and closing in the textile composite becomes unchanged. The scheme to update the degraded tangent stiffness is implemented using an iterative method.

The computation of the tangent stiffness matrix for each textile lamina is one of the two major tasks performed by the micro-mechanical analysis; the other is to update total stresses and strains taking into account the degraded constitutive behavior. The tangent stiffness for the RUC/element is built up from tangent stiffness relations for the two constitutive phases, fiber and matrix of the yarns, and these are based on the crack density. After a load step is applied at the structural analysis level, the decomposition process is performed using the tangent material law used at the material points in the RUC/element. Finally, the stress and strain increments in each of the fill, warp and z-yarns in the unit cell micro-level are extracted for each sub-laminate layer within the RUC/element.

During the analysis under impact loads, various micro-mechanical responses are examined in order to identify potential crack modes, the load magnitudes at which initial failure occurs, and the way in which the subsequent failure modes develop as a result of increased load. At the end of each stress update, the conditions for the crack opening and the crack closing are applied to examine the presence of micro-cracks in the RUC/element. If the cracks in the RUC/element are examined, a stiffness degradation scheme is activated. Depending upon the cracks or no cracks in the lamina, the axial or transverse stresses are immediately relieved or un-relieved, and the lamina tangent stiffness matrix is degraded or updated. After the accomplishment of this step, the stress integration is performed again to redistribute the loads that the lamina of cracked RUC/element could not sustain and check if additional cracks of RUC/element are triggered.

10.3 Review of General Shell Structures' Dynamic Behaviors

Before the problem of dynamic response of the textile composite shells are solved, this section considers the dynamic behaviors of shell structures based on a degenerated shell element. This section does not consider static behaviors of the shell structures that are described in Appendix F.

The first case, a simply supported rectangular plate under a suddenly applied Heaviside load ($q = 1/100$ lb/in^2) over the blue-lined area depicted in Figure 10.6 is considered and modeled by a quarter plate modeling consisting of 35 elements. Two variants of this problem are presented for ratios of length/thickness ratios (α) of 5:1and 10:1. The simply supported rectangular plate was suggested in Hinton[10.5] *et al.* and Reismann and Lee[10.6]. In this model, the central deflection and central bending moment for a centrally loaded rectangular plate of $\beta = 1.4142$ are considered and the results are compared with the thin plate solution of Reismann and Lee[10.6]. Figures 10.7-10.8 show dimensionless results of the different length/thickness ratios, respectively and are compared to those of Refs. [10.5-10.6].

The second problem investigates the effects of initial stress on the simply supported rectangular plate. The same geometry, loading and material properties of Ref. [10.7] are used to describe transient dynamic behavior. Prior to and during the application of the transverse load, the plate is subjected to a constant and uniformly distributed membrane pre-stress $\sigma_x = EF_x$ in the direction of the plate edge of length a as shown in Figure 10.9. For different initial stress conditions, Figure 10.10 shows the time history of the plate center deflection and bending moments with the thickness ratio, α=0.1, respectively. The present dimensionless results are compared with those of Reismann and Tendorf[10.7].

The second type is a clamped circular plate subjected to a suddenly applied uniformly distributed load. This study uses a quarter modeling of the plate as shown in Figure 10.11 consisting of 41 elements. The plate is rigidly clamped at its edge and the step load $q = 0.1\,\text{lb/in}^2$ applied on its upper surface and the time step $\Delta t = 0.6\mu\,\text{sec}$. As shown in Figure 10.12, the time history of the plate central deflections and bending moments are presented respectively. The linear response is compared with the results presented in Ref. [10.5] and [10.8].

The third example is a deep spherical cap with clamped boundary conditions. The shell shown in Figure 10.13 consisting of 41 elements is subjected to a distributed step pressure of $P = 600\,\text{lb/in}^2$ and the time step $\Delta t = 1\times10^{-5}$ sec. A thin spherical cap with a central angle of $2\alpha = 120^\circ$, radius of $R = 20$in and thickness of h =0.3in is considered. The mass density of the cap is $\rho = 7.33\times10^{-4}$ lb-sec^2/in^4. Cap properties are: $E = 30\times10^6$ p.s.i., $\nu = 0.3$ and $G = 1.54\times10^7$ p.s.i. Also the center deflection and the residual force in Figure 10.14 are presented at various time steps.

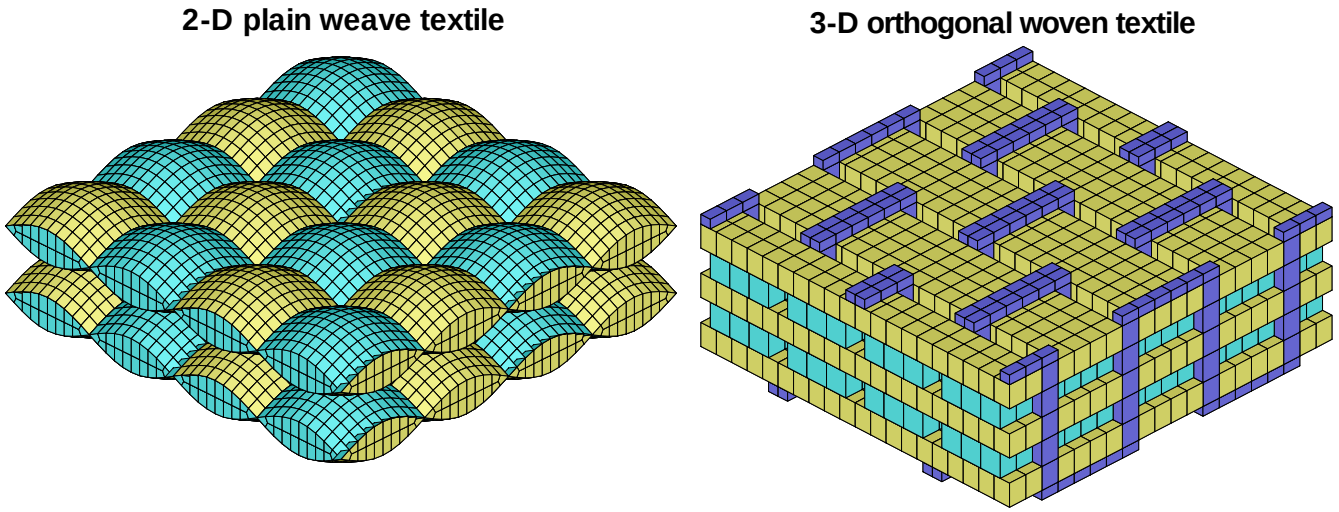

Figure 10.1: The 2-D plain weave and 3-D orthogonal woven fabric without resin.

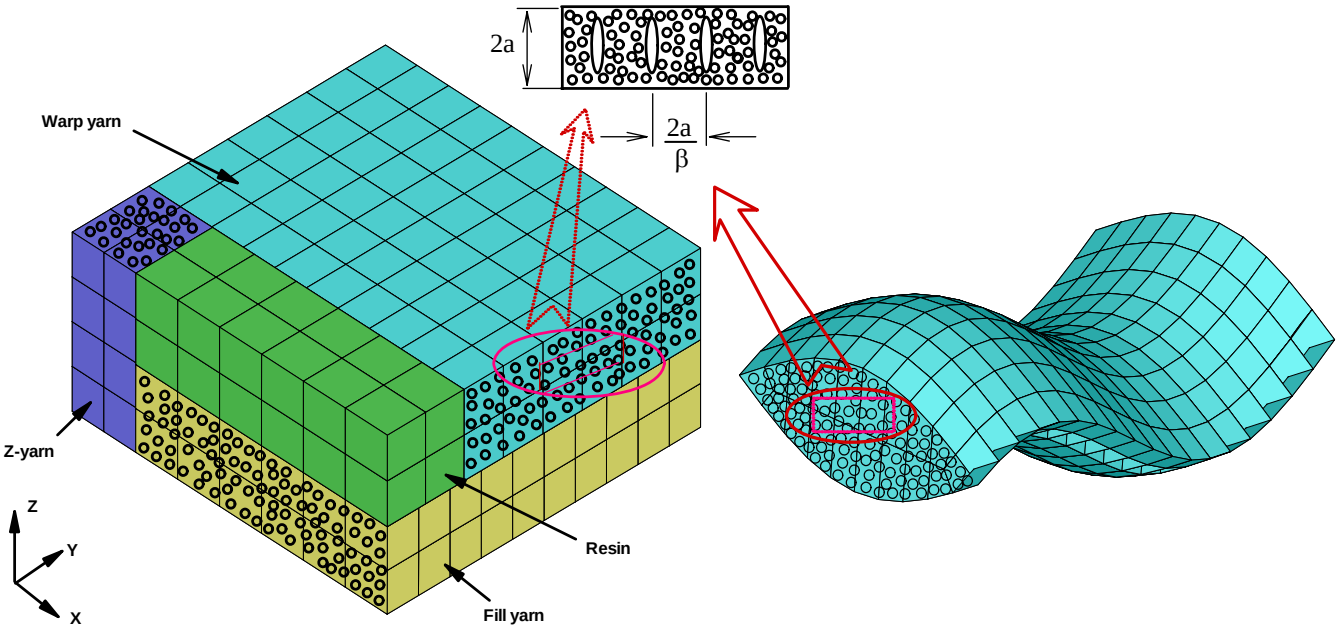

Figure 10.2: The unit cell model of 3-D woven and 2-D plain woven yarn with small slit cracks.

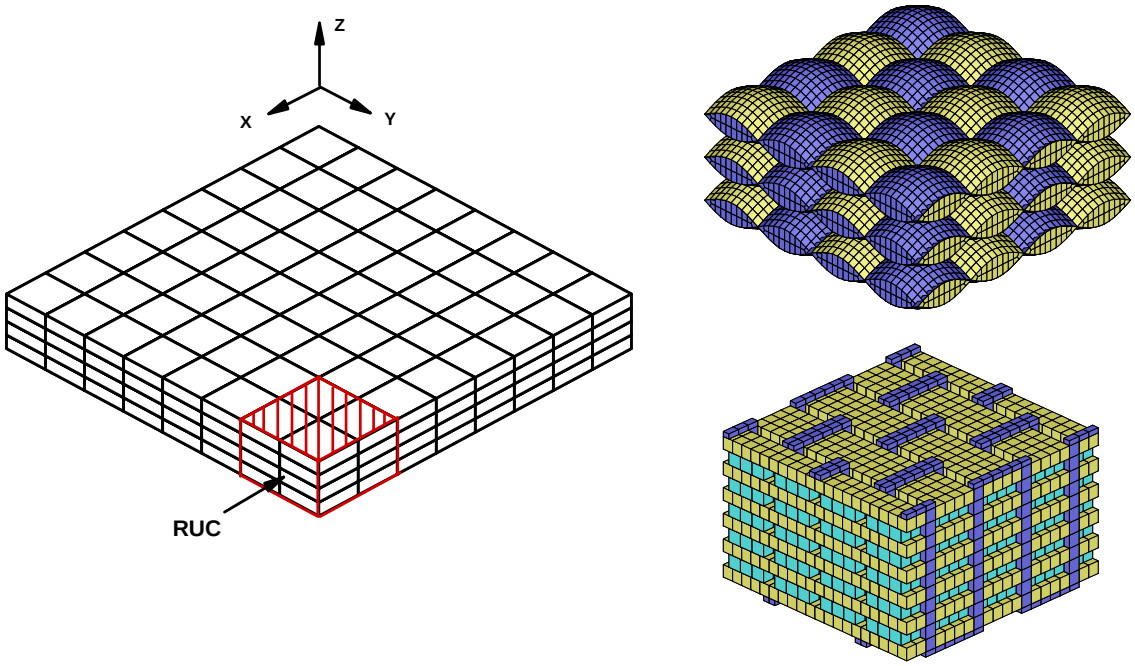

Figure 10.3: A textile panel with 4 by 4 RUC and 2-D & 3-D textile shapes of 2 by 2 RUC.

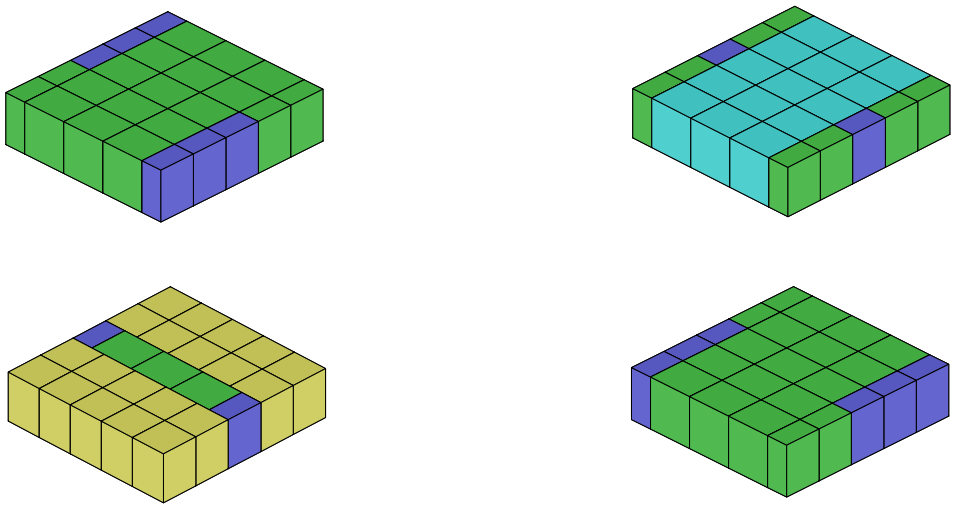

Figure 10.4: Four lamina layers of 3-D orthogonal woven fabric (top, fill, warp and bottom lamina).

Level 1: Micro-mechanical analysis

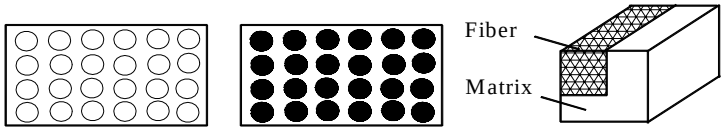

Level 2: Layer-wise analysis

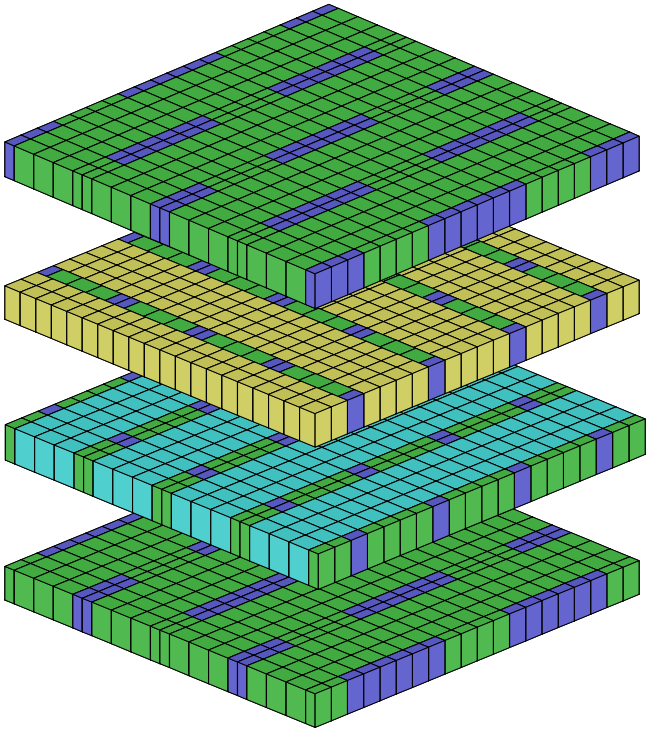

Level 3: Structural analysis

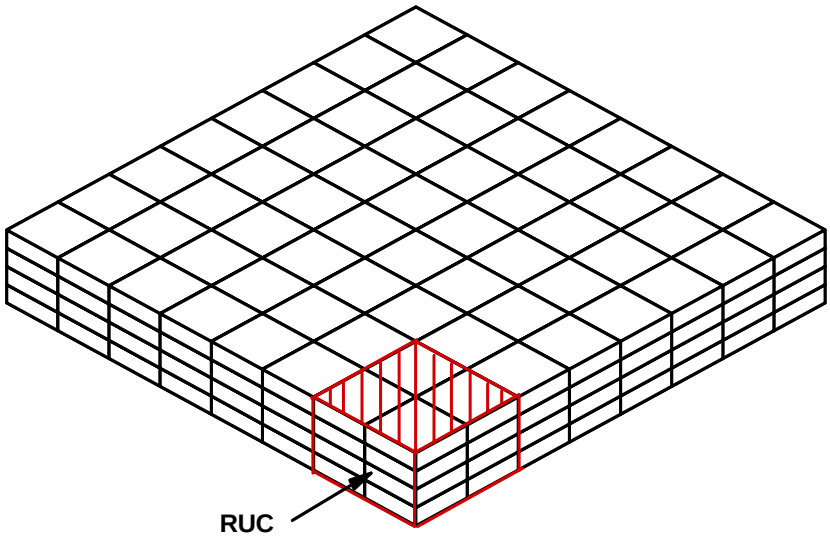

Figure 10.5: Three-level hierarchy modeling (micro, layer-wise and structural analyses).

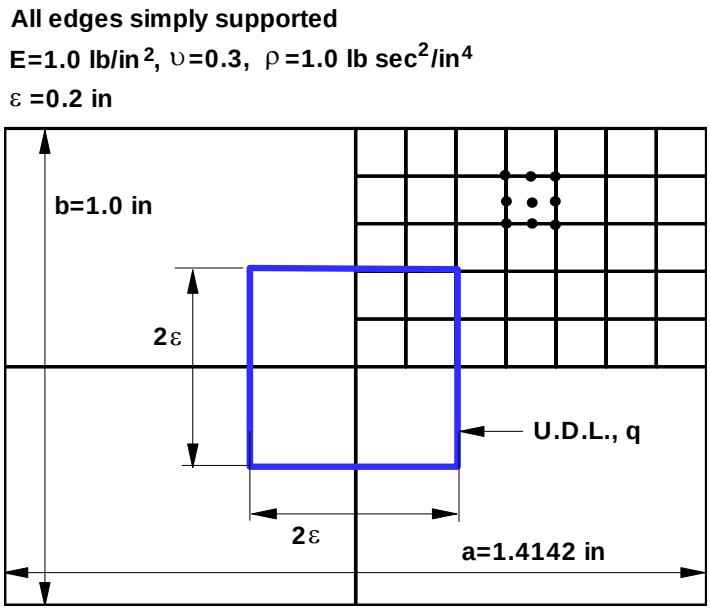

Figure 10.6: Finite element mesh for simply supported rectangular plate problem.

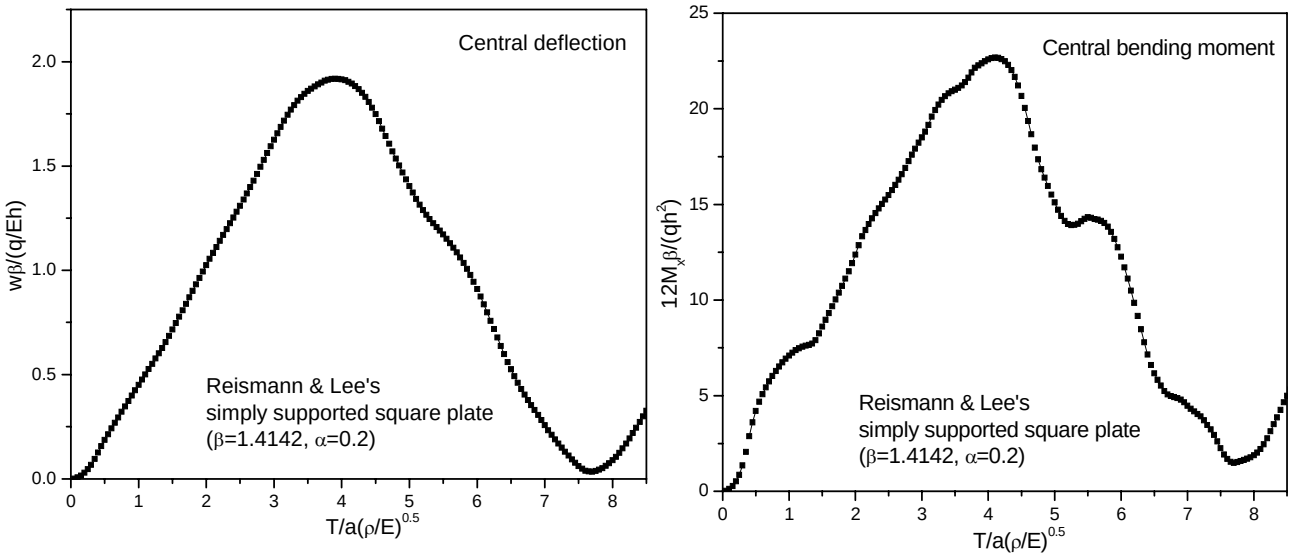

Figure 10.7: Central deflection and bending moment history for $\alpha = 0.2$.

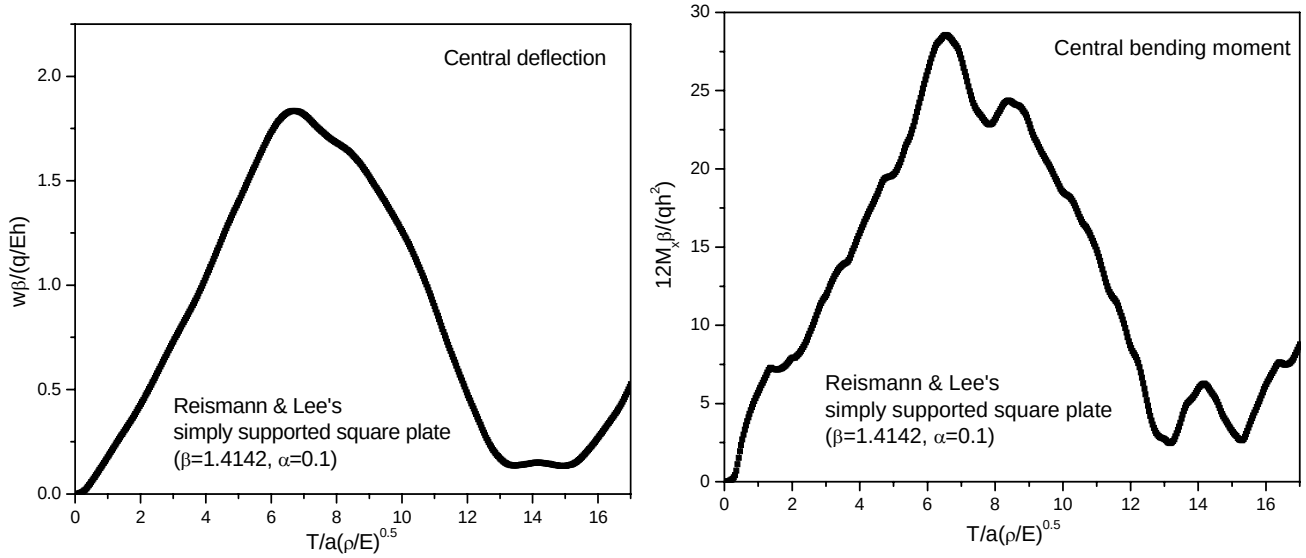

Figure 10.8: Central deflection and bending moment history for $\alpha = 0.1$.

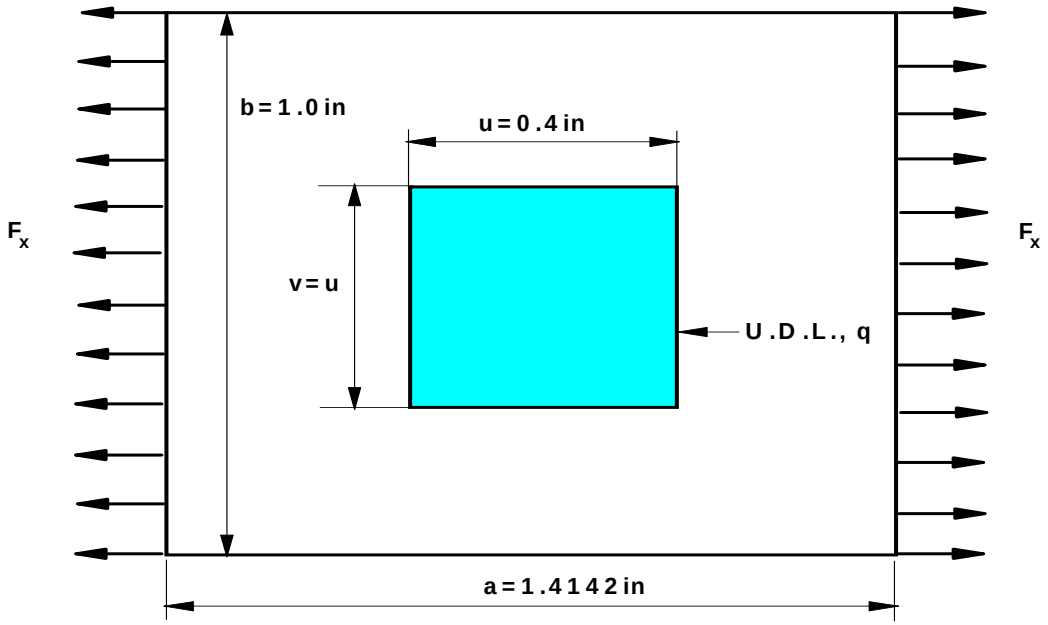

Figure 10.9: Problem plate geometry and loading.

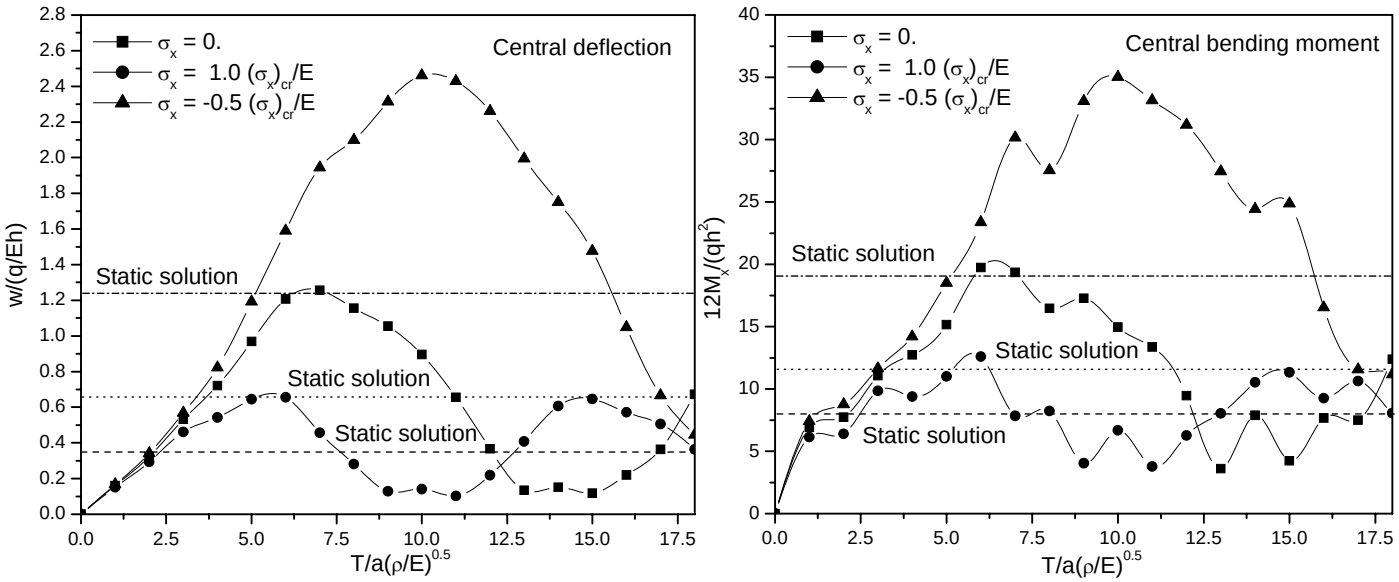

Figure 10.10: Central deflection and bending moment history for an initially stressed plate.

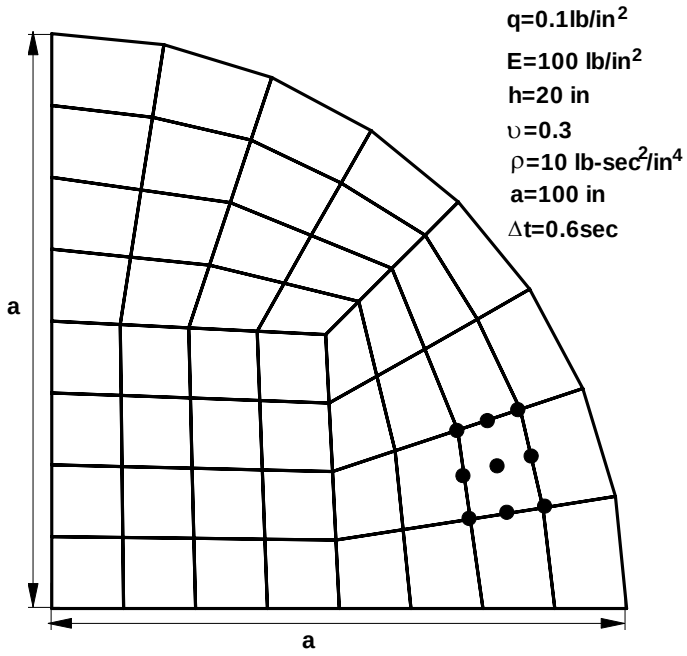

Figure 10.11: Symmetric quadrant of clamped circular plate.

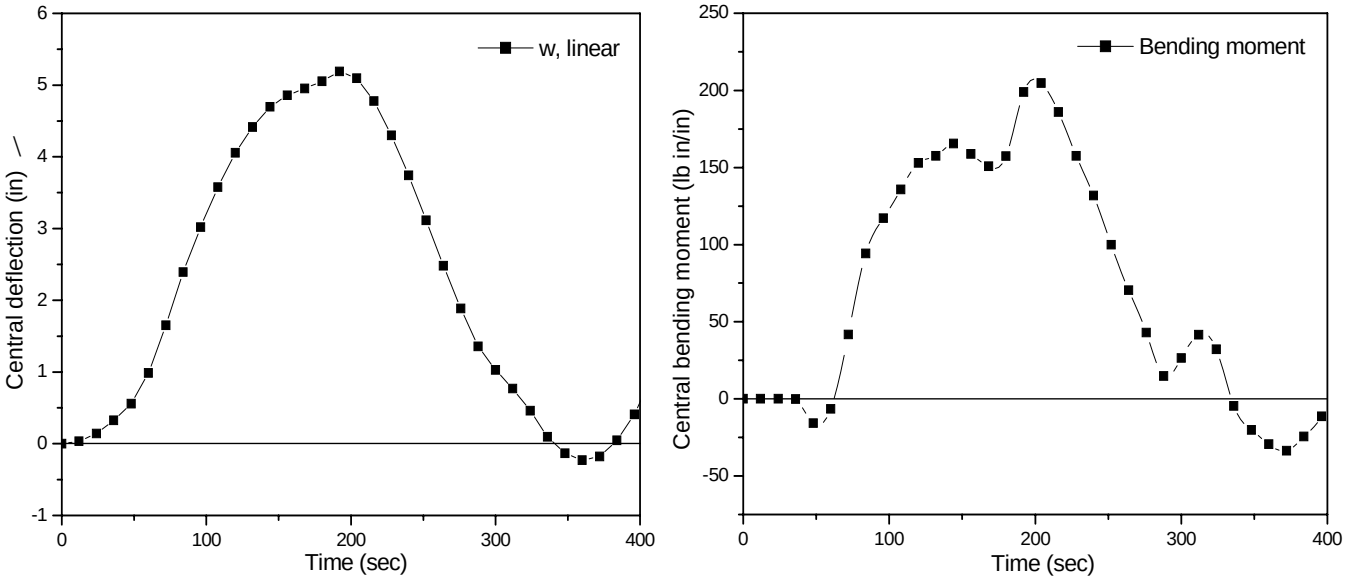

Figure 10.12: Central deflection and bending moment versus time.

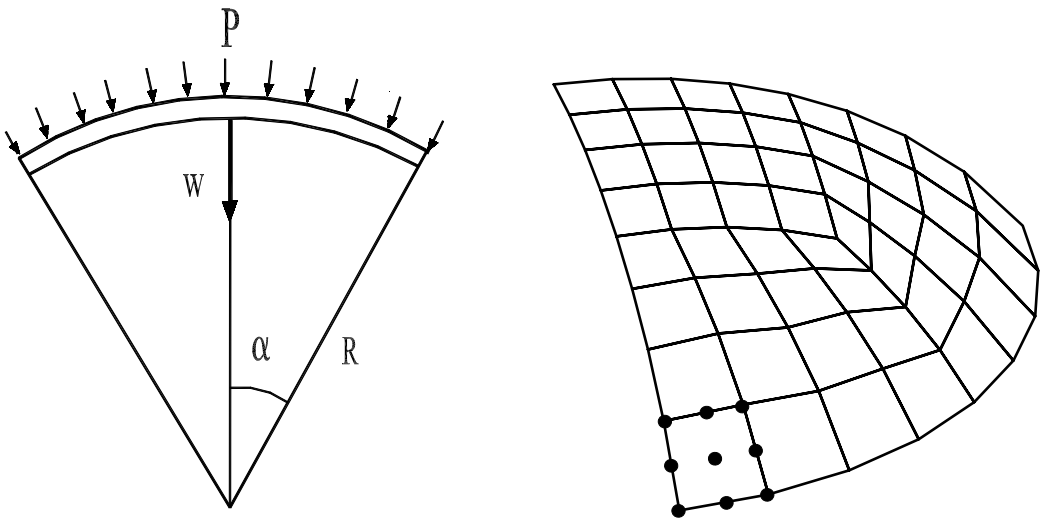

Figure 10.13: Symmetric quadrant of the spherical cap with uniform pressure.

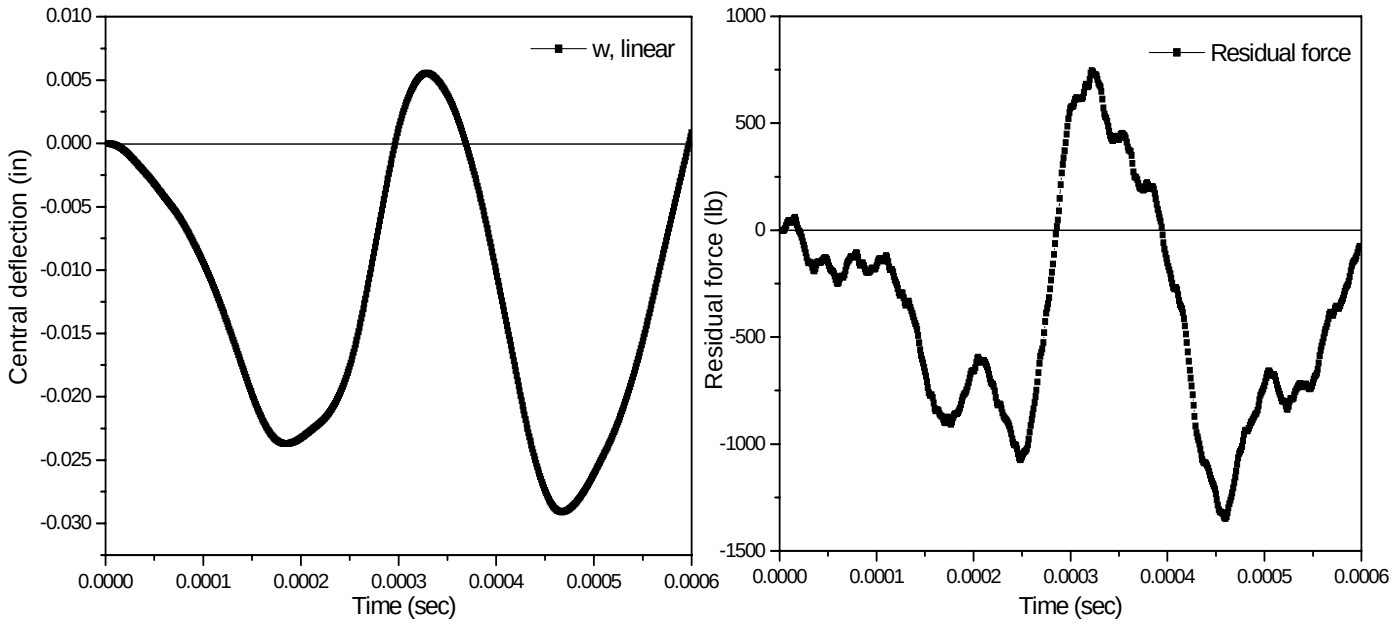

Figure 10.14: Central deflection and residual force versus time.

10.4 Dynamic Behaviors of Textile Shell Structures

This study considers a clamped circular textile-layered plate subjected to a suddenly applied uniformly distributed load shown in Figure 10.15. Material properties of Hercules AS4 Graphite & 3501-6 Epoxy as suggested in Ref. [10.2] are used. The plate shown in Figure 10.15 modeled using 41 elements is subjected to a distributed step pressure of $P = 0.55$ MPa using the time step $\Delta t = 25 \times 10^{-4}$ sec and boundary conditions of clamped edges are used. The radius and thickness are $a = 440$mm and h =3mm are considered. Layers of plate that consist of 2 plain–woven textiles modeled by Sine Function Model I and yarn sizes of 2K, 10K and 18K are used here. Figure 10.16 shows that the large yarn size has larger deflections to the uniform loading.

In Figure 10.17, a textile-layered spherical cap subjected to a suddenly applied uniform load is described. Material properties of E-glass/Vinylester as suggested in Ref. [10.3] are used. The 41 degenerated shell elements, the uniform pressure $P = 6 psi$, the time step $\Delta t = 10^{-5}$ sec, the radius $R = 13$in, the thickness t =0.03in and the central angle of $2\alpha = 46^{\circ}$ are used. The shell stacking sequence is $[\text{plain-woven}]_3$ modeled by Sine Function Model I and the yarn geometry is given in Ref. [10.3]. Figure 10.18 shows that the crack densities and gap lengths affect the central deflections. From Figure 10.18 large values of crack density show large changes in the deflection of the plate with an increase in the gap length.

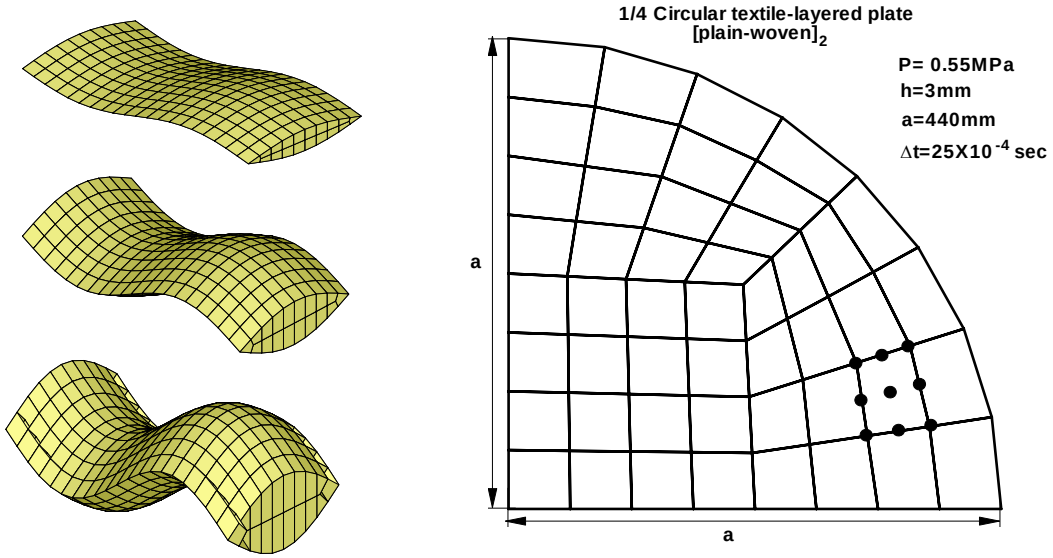

Figure 10.15: Three yarn sizes and symmetric quadrant of clamped circular textile-layered plate.

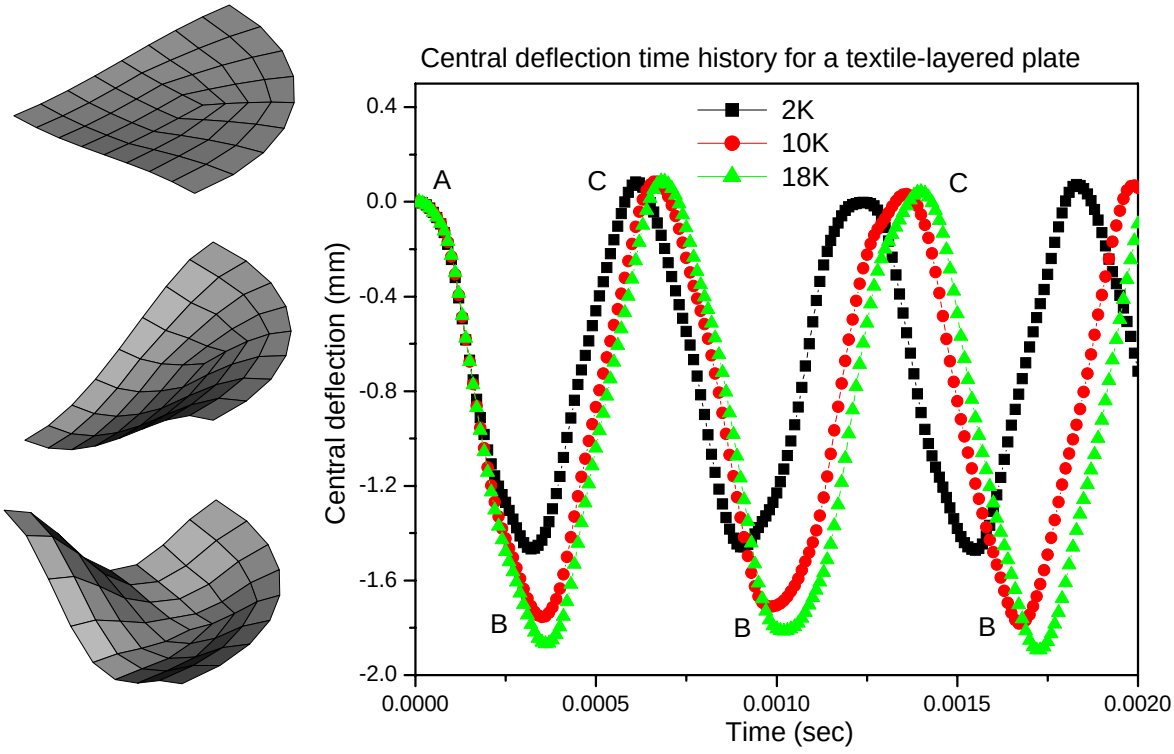

Figure 10.16: Plate deformations at three different points and central deflection time history.

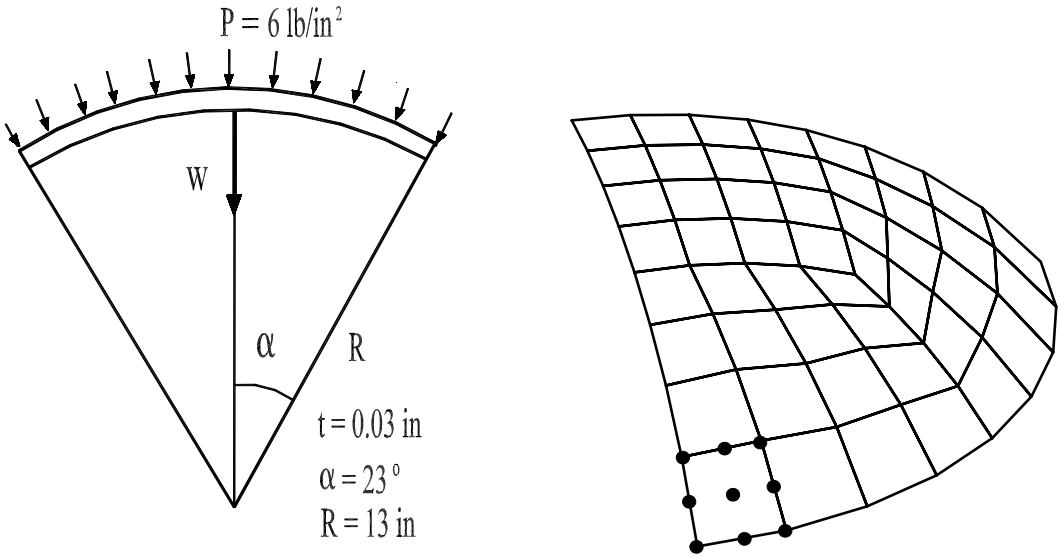

Figure 10.17: Symmetric quadrant of the spherical textile layered cap with uniform pressure.

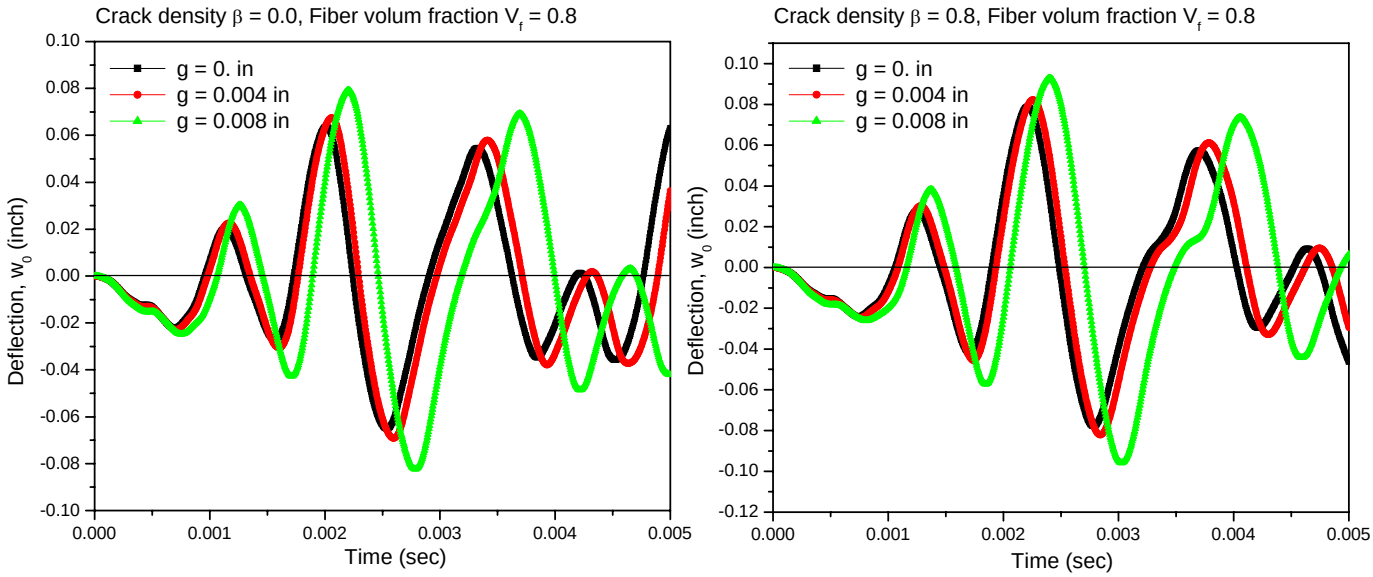

Figure 10.18: Central deflection time histories with various crack densities and gap-lengths.

10.5 Main Categories of Ballistic Impact Behaviors in Textile Layered Structures

In previous chapters, we have presented a cohesive element scheme and contact algorithms for studying the impact problems of layered structures using the cracked/un-cracked elements. In Section 10.2, we mention same basic approaches for studying the impact problems related to the textile shell structures. Here we present same reference textile composite example structures under impact loads. We use the concept of damage tolerance to define loss of mechanical stiffness under ballistic impact. The concept of damage tolerance is increasingly being used to develop safe armor structures. To obtain highly accurate numerical dynamic results for the textile shell structures, our research considers three design parameters: (i) bulk modulus, (ii) layered types and (iii) geometrical yarn shapes.

The first design parameter, the bulk modulus, represents the presence of the micro cracked/un-cracked textile yarns. These moduli are calculated from the micro-mechanical equations described earlier in Chapters 2-3 and were used to calculate the Repeating Unit Cell's effective moduli. To specify the elastic properties of the cracked yarns, the crack density is specified. Furthermore, various crack density values are considered to monitor the structural behaviors during a ballistic impact, and the effect of the crack density on the damage tolerance is studied.

The second design parameter, the layered types are defined by the textile composite types, such as 2-D plain weaves, 2-D braids and 3-D orthogonal woven textile composites. The damage tolerance is one of the characteristics that we investigate to determine when an armor structure reaches the critical status, a catastrophic point. The stiffness is often used to represent the damage status. Here, we study energy transfer between the kinetic energy of the ballistic projectiles and the strain energy of textile composite targets during an impact. A relatively simple form of stiffness can show the energy transfer from the kinetic energy to the strain energy. We define a simple equation to describe the damage tolerance D_t of the textile composite shell structures.

$$D_t = \frac{\|K_0 - \Delta K\|}{\|K_0\|} \tag{10.6}$$

Here ΔK is the loss of stiffness and K_0 is the original stiffness of the textile target structure. During the impact, the cracking and fragmentations are modeled by the cohesive elements to show fracture formations in the textile composite shell structures.

The third design parameter describing the geometrical yarn shapes in the textile composite is studied for investigating the damage tolerance behavior. In previous Chapters, we have shown that the mechanical behavior of the textile composite depends considerably on geometrical shapes of the yarns, for example, the flat-balanced weave (Naik[10.2] model) and the oval or lenticular shaped weave (Sine Function Model I&II). These are associated with the first category to obtain the Repeating Unit Cell's moduli. The other parameters are related to the projectile, such as length, diameter and nose type. Although these are important parameters to investigate the damage tolerance of target structure, this study focuses on the stiffness changes in the target, because the stiffness changes in a target represents the energy transfer between the projectile's kinetic energy and the target's strain energy. Also the stiffness changes can be used as an independent parameter to check the dynamic response of a textile shell structure. Figure 10.19 shows several steps for studying textile composite structures' dynamic behavior with a sub-step to check damaged elements and update the stiffness matrix at each time step. Analysis of un-damaged structures does not require this additional sub-step.

Step 1: Specify initial parameters such as the number of time steps, initial velocities, accelerations and displacements.

Step 2: Set up the geometry and material data, boundary conditions.

Step 3: Initialize the stiffness matrix $\mathbf{K}$.

Step 4: Assemble the effective inertia matrix.

$$\mathbf{M}_{eff} = \left[\frac{1}{2\Delta t}\mathbf{C} + \frac{1}{\Delta t^2}\mathbf{M} \right]$$

Step 5: Decompose the effective inertia matrix.

$$\mathbf{M}_{eff} = \mathbf{U}^T \mathbf{D}\ \mathbf{U}$$

Step 6: Find the accelerations $\ddot{\mathbf{u}}$ from the equation of motion, by using initial conditions $\mathbf{u}_0 \,\&\, \dot{\mathbf{u}}_0$.

Step 7: Read the applied loads and form the applied load vectors $\mathbf{P}$, the cohesive load vectors $\mathbf{F}_C$ and the body force vector $\mathbf{F}_B$.

Step 8: Begin the loop over time increments.

Step 8.1: Assemble the nodal load vectors $\mathbf{F} = \mathbf{F}_B + \mathbf{F}_C$.

Step 8.2: Form the effective load vectors $\mathbf{P}_{eff}$.

$$\mathbf{P}_{eff_t} = \mathbf{P}_t - \mathbf{F}_t - \left[-\frac{2}{\Delta t^2}\mathbf{M} \right] \mathbf{u}_t - \left[\frac{1}{\Delta t^2}\mathbf{M} - \frac{1}{2\Delta t}\mathbf{C} \right] \mathbf{u}_{t-\Delta t}$$

Step 8.3: Solve for the new displacement increments.

$$\mathbf{U}^T \mathbf{D}\ \mathbf{U}\ \mathbf{u}_{t+\Delta t} = \mathbf{P}_{eff_t}$$

Step 8.4: Update the geometry, velocity, stresses and strains.

Step 8.5: Check degraded elements and update the stiffness matrix $\mathbf{K}$.

Step 8.6: Store results from this time step.

Step 9: End the loop over the time increments.

Step 10: End.

Figure 10.19: Main steps for textile composite structures' dynamic behaviors with the cohesive element.

10.6 Ballistic Impact Examples of 2-D Plain Woven, 2-D Braided and 3-D Woven Textile Structures

In general, the ballistic resistance of an armor plate, such as that made from a ceramic material, is strongly enhanced by adding some of ductile backing plates, made of aluminum, or several textile composites. Such a structure is usually called a multi-layered plate. To study the role of textile composite structures in the armor impact performance, our numerical simulations of impact focuses on two different textile type structures: 2-D plain woven and 2-D braided, Naik[10.2] model and Sine Function Model I (SFM I) are used to calculate the effective moduli and the effect of different values of crack density parameter is included. To simulate the ballistic impact, a multi-layered composite plate where a ceramic facing is backed by the 2-D plain woven and 2-D braided textile (12K yarn size) is used respectively. To obtain the 2-D plain woven and braided textile modeling, this study considers the same material and dimensions for the 2-D flat-balanced braids as those suggested in Ref. [10.2] and with same materials, the Sine Function Model I is used to model a different geometrical shape; i. e., lenticular strand sections and sinusoidal curved yarns. In addition, the simulation considers different impact directions of projectiles, normal or oblique. Impact direction of a projectile is an important factor in modeling armor ballistic resistance to find the optimal backing and facing layer thickness. Another important factor in the armor modeling is the

projectile energy: kinetic and strain energy. All these factors are considered for a case of multi-layered plate backed by the 3-D orthogonal woven textile, and like the 2-D plain woven and 2-D braided textile, the same impact simulation of the 3-D orthogonal woven textile is conducted. In the 3-D orthogonal woven textile layer, the same material properties as suggested in Ref. [10.9], and the geometrical dimensions given in Table 5.6 of Chapter 5 are used. The material properties of alumina layer (AD-85 alumina) are given in Table 9.5 of Chapter 9.

First case, a 2-D plain woven textile and ceramic layered plate, is explored. Figure 10.20 shows the multi-layered armor plate and a 7.62 mm bullet impacts at a velocity of 850 m/sec, both along the normal and an oblique direction respectively. Figure 10.21 shows a normal velocity time-history of projectile with different yarn types. In Naik's model, the small crack density shows a larger reduction in the projectile of velocity than that for a structure with a large crack density. For Sine Function Model I, the velocity time-history is almost the same as the velocity time history with different crack densities. This problem is basically induced from the stiffness rigidity of the yarns' shapes in the multi-layered armor plate, for example, the flat-plain weave and elliptical plain weave. From the previous chapter, we know that the different crack densities are highly dependent on the geometrical yarn shapes and considerably affect the equivalent moduli of the 2-D plain woven textiles. In the kinetic and internal energies of the normal impact the Naik model shows little very impact of different crack densities on energy values, The Sine Function Model I, however, shows a more larger influence on the normalize energy as shown in Figure 10.22. In the oblique impact case, the impact velocity time history plot show almost the same behavior using both Naik as well as Sine Function Model I, see Figure 10. 23. In the kinetic and internal energies for the oblique impact case presented in Figure 10.24, these two models show different trends as a function of crack density as compared to the normal impact case. We know that the flat-plain weave has more sensitive transverse components of stiffness under the oblique impact and the Sine Function Model I has more sensitive in-plane components of stiffness under the normal impact, for the same crack density values. Consequently these results show that the geometrical yarn shapes have significant influence on the stiffness rigidity of the textile composite structures. The contact force time histories of Naik and Sine Function Model I cases are shown in Figures 10.25-10.26.

The second case is the 2-D braided textile and ceramic layered plate. The Naik model considers two different yarn sizes (2K & 18K) and the same braid angle (45 degree) to simulate the normal and oblique impacts. As the previous case of 2-D plain weave and ceramic layered plate, this case also shows the influence on projectile velocity, for normal and oblique impact velocities for both the yarn sizes, see Figure 10.27. In the oblique impact case, the 2K yarn case has smaller fiber components, and fiber volume fractions, than those for the 12K yarn case within the repeating unit cell. Moreover, these different fiber volume fractions lead to different values of kinetic and internal energies of the projectile during the impact. From Figure 10.28, the 18K yarn for the oblique impact has a bigger decline in the kinetic energy values than for the normal impact case. The different reduction in impact velocity is induced from the yarn stiffness, such as a 2-D plain weave and ceramic layered plate. The Sine Function Model I case for the 2-D braided and ceramic layered plate has same trend for the projectile velocity as compared to the impact of 2-D plain weave and ceramic layered plate. This is shown in Figure 10.29.

For the kinetic and internal energies of the normal impact, the Sine Function Model I for 2-D braided and ceramic layered plate has the same trends as that for the oblique impact using the Naik model for 2-D plain weave and ceramic layered plate. This is shown in Figure 10.30. However, under an oblique impact case, for both the 2-D braids using the Sine Function Model I and ceramic layered plate, we see similar trends of kinetic and internal energies that are shown by the Sine Function Model I for the 2-D plain weave and ceramic layered plate in the normal impact. These results also show that the yarn stiffness is considerably related to the crack density and the geometrical shapes of the 2-D braid yarns. The contact force time histories of Naik and Sine Function Model I cases are shown in Figures 10.31-10.32.

The third case is the 3-D orthogonal woven textile and ceramic layered plate. The 3-D orthogonal woven textile composite is based on Tan's model[10.9] of 3-D orthogonal weaves and the ceramic layer is bonded with this 3-D woven textile layer. This 3-D orthogonal woven textile and ceramic layered plate is analyzed by two impact velocity types, normal and oblique impacts. Figure 10.33 shows a similar

reduction in the projectile velocities as compared to the normal impact of 2-D braids using the Sine Function Model I and the oblique impact of 2-D plain weaves described by the Naik model. The kinetic and internal energies for the 3-D orthogonal woven textile and ceramic layered plate show the same characteristics as that for 2-D plain woven and ceramic layered plate subjected to oblique impact and the 2-D braided and ceramic layered plate subjected to normal impacts, see Figure 10.34. In both the oblique and normal impact cases, the 3-D orthogonal woven textile and ceramic layered plate shows two characteristics: 2-D plain woven and 2-D braided and ceramic layered plate. So we can see that the stiffness of 3-D orthogonal woven textile and ceramic layered plate is significantly related to the geometrical forms in the repeating unit cell and affected by various crack densities. Figure 10.35 shows contact force time histories for the 3-D orthogonal woven textile and ceramic layered plate subjected to both the normal and oblique impact.

From the impact results of three different armor plates, we see that their stiffness reductions under impact loads are considerably dependent on the geometrical shapes and micro-cracking of yarns in the Repeating Unit Cell (RUC). However there still remains one problem to model the damage during the impact process of textile layered composites. This study uses Eq. (10.6) to find the comparative damage behavior for three different textile layers' results.

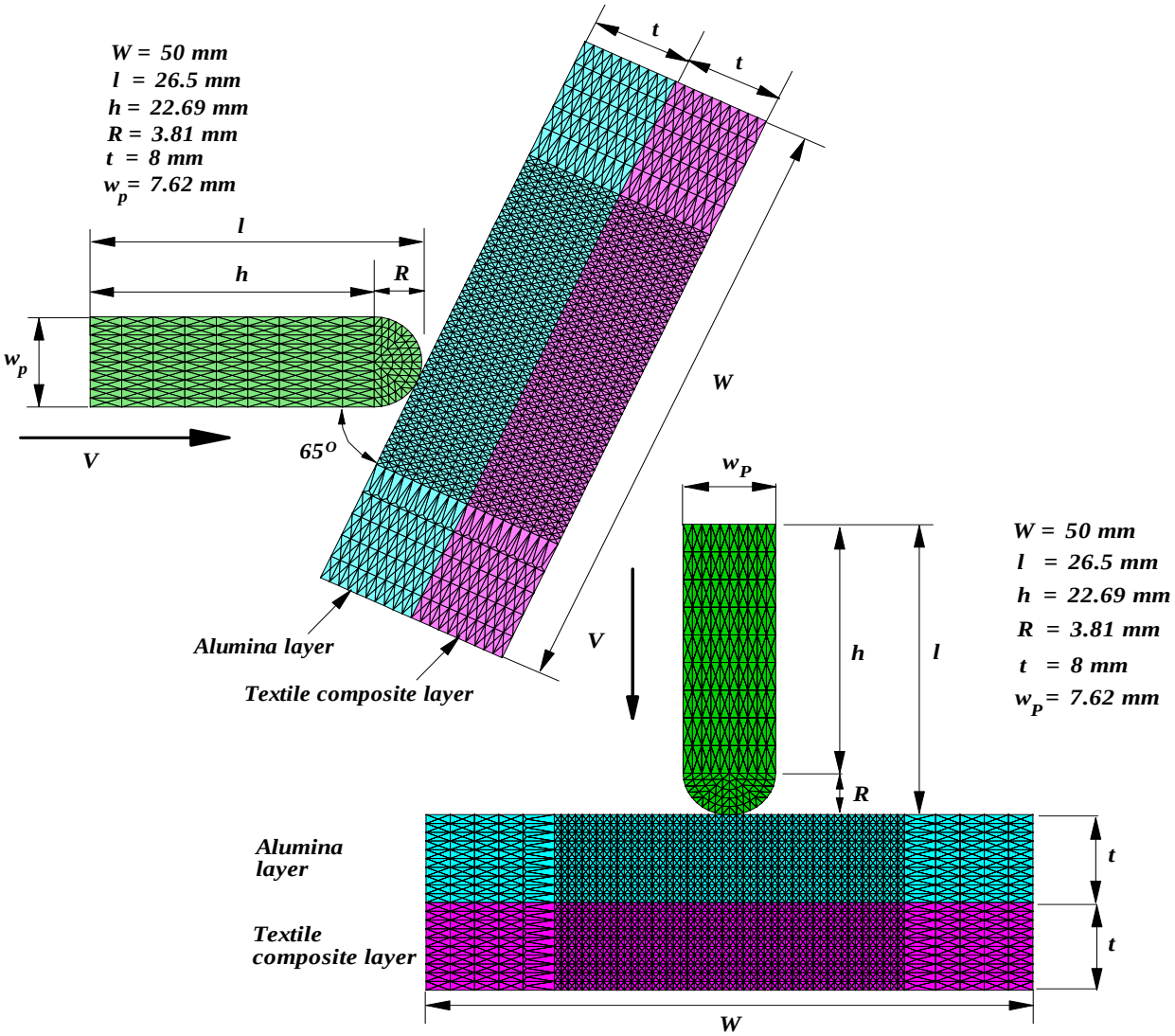

Figure 10.20: Normal/oblique impact modeling of a 7.62 mm projectile and an alumina and textile layered plate.

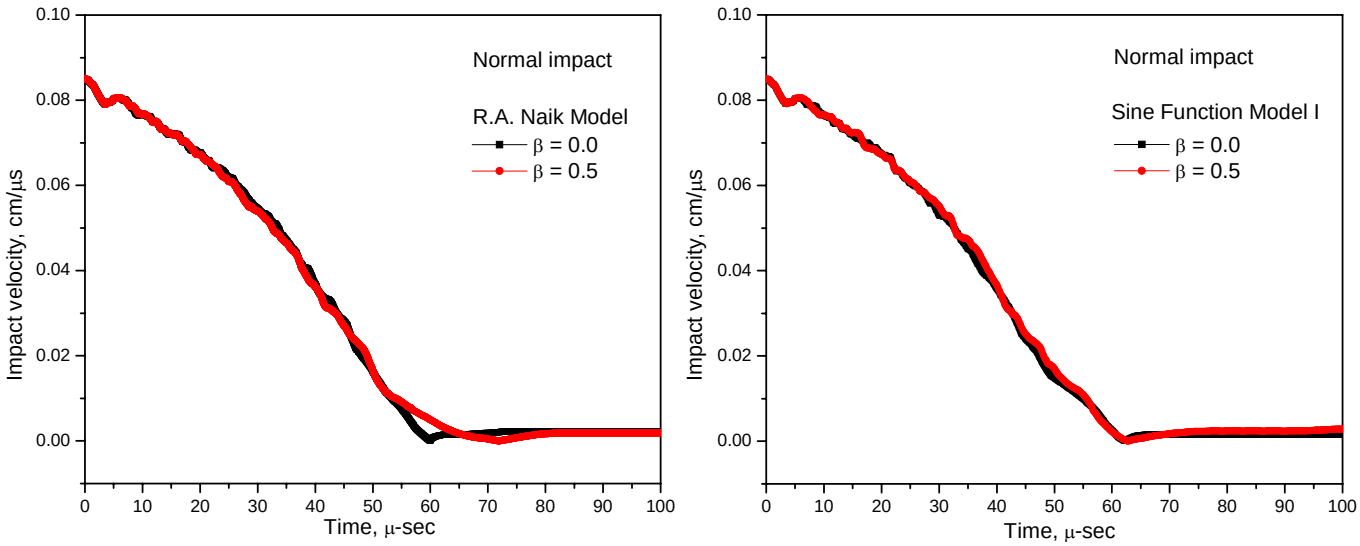

Figure 10.21: Normal impact velocities of the projectile in two different 2-D plain weave and ceramic layered plates.

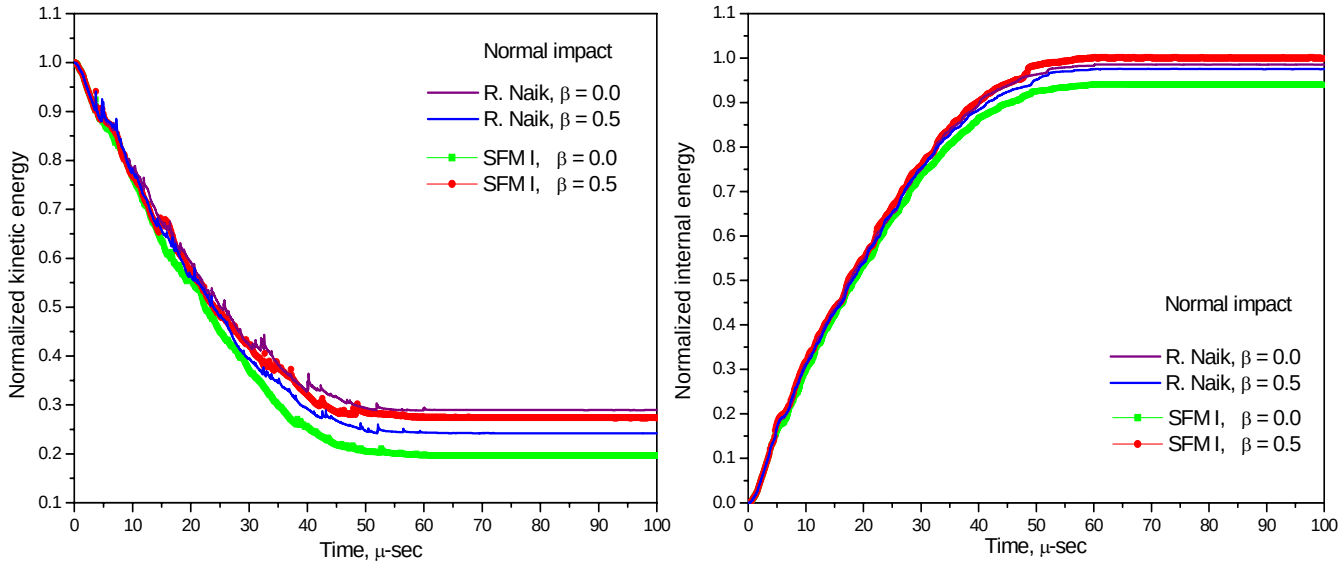

Figure 10.22: Normalized internal and kinetic energies of the projectile during normal impact.

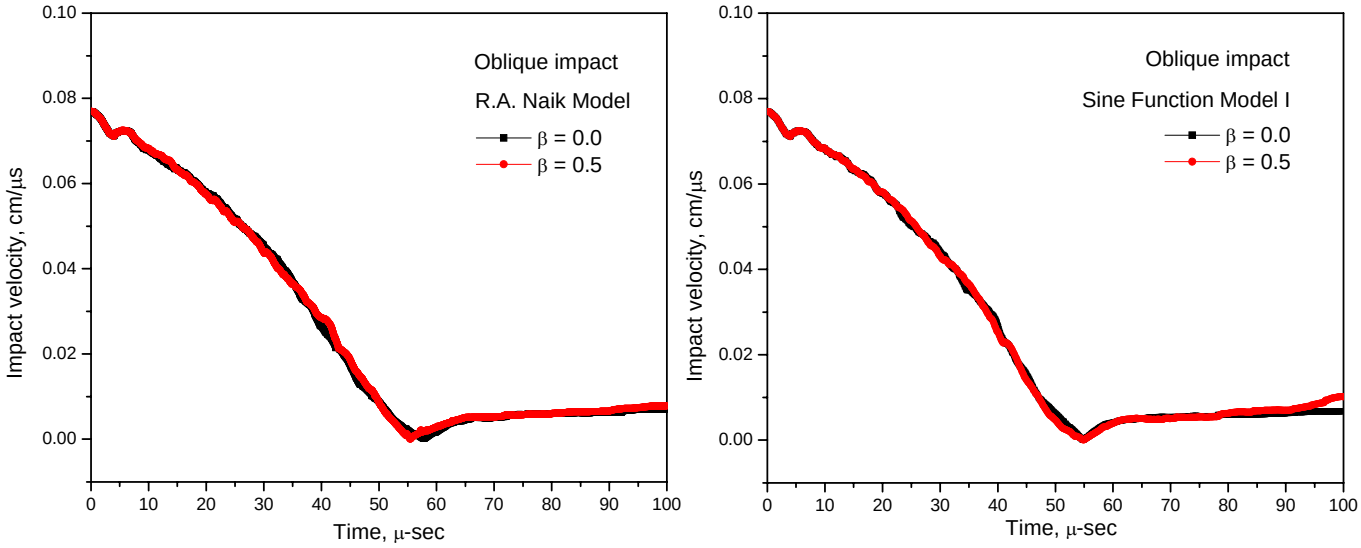

Figure 10.23: Oblique impact velocities of the projectile in two different 2-D plain weave and ceramic layered plates.

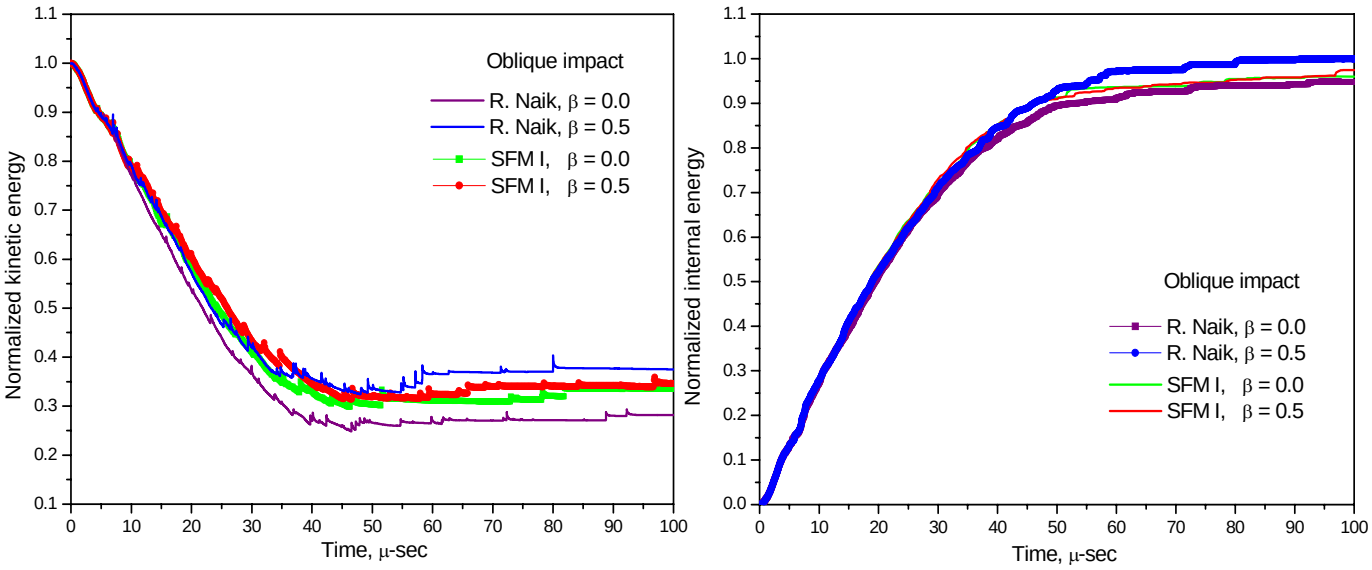

Figure 10.24: Normalized internal and kinetic energies of the projectile in the oblique impact.

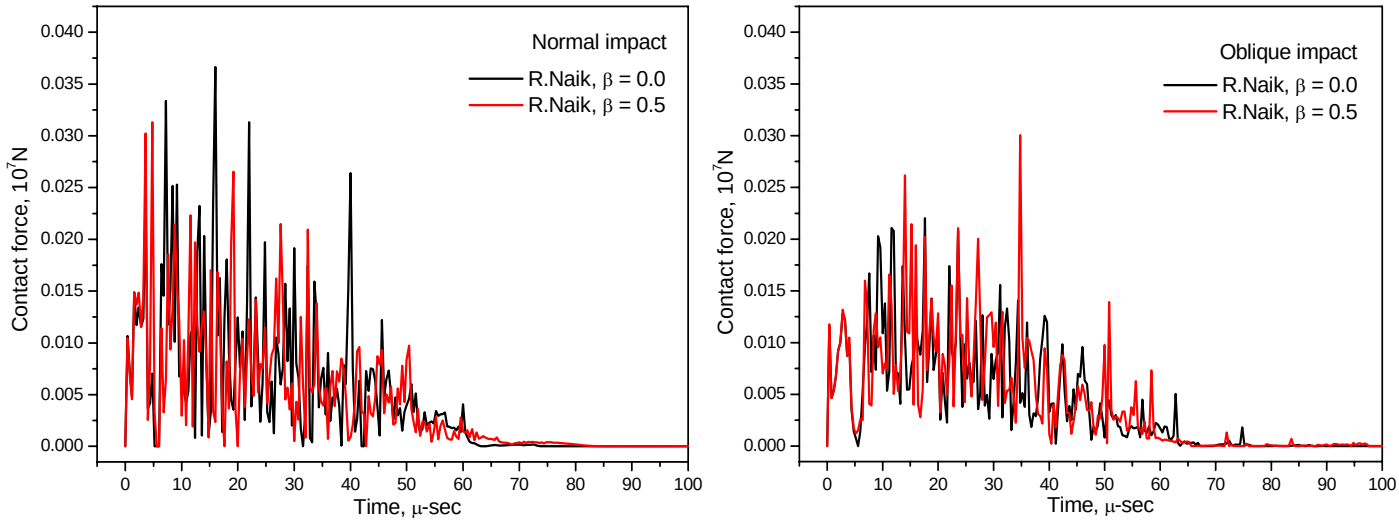

Figure 10.25: Contact forces of the normal/oblique impact projectile into a 2-D plain weave and ceramic layered plate.

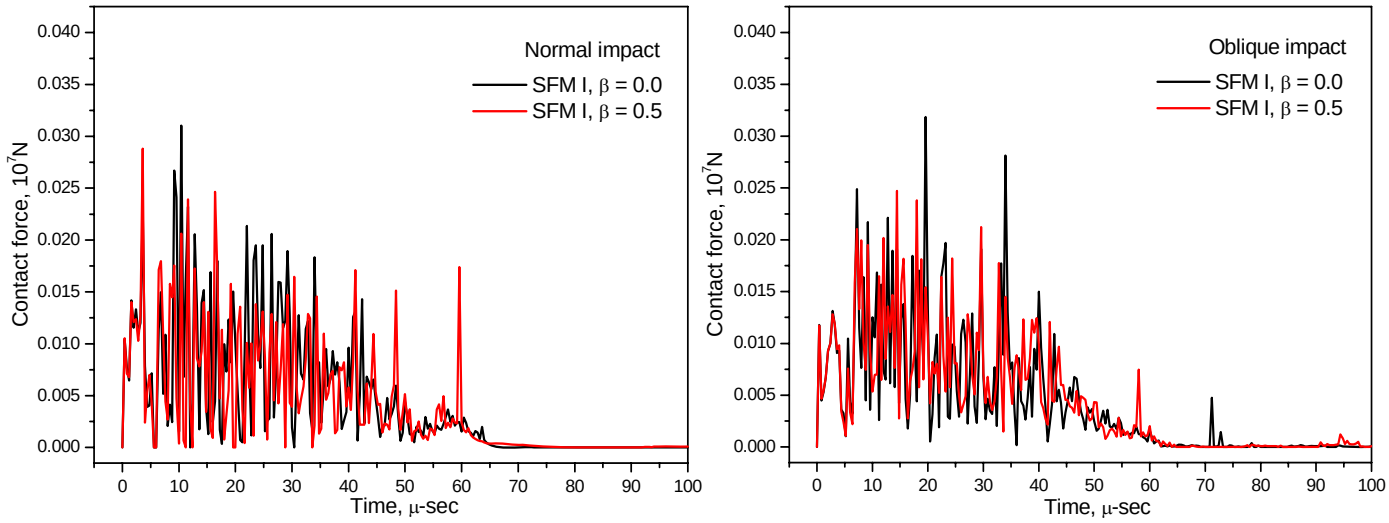

Figure 10.26: Contact forces of the normal/oblique impact projectile into a 2-D plain weave and ceramic layered plate.

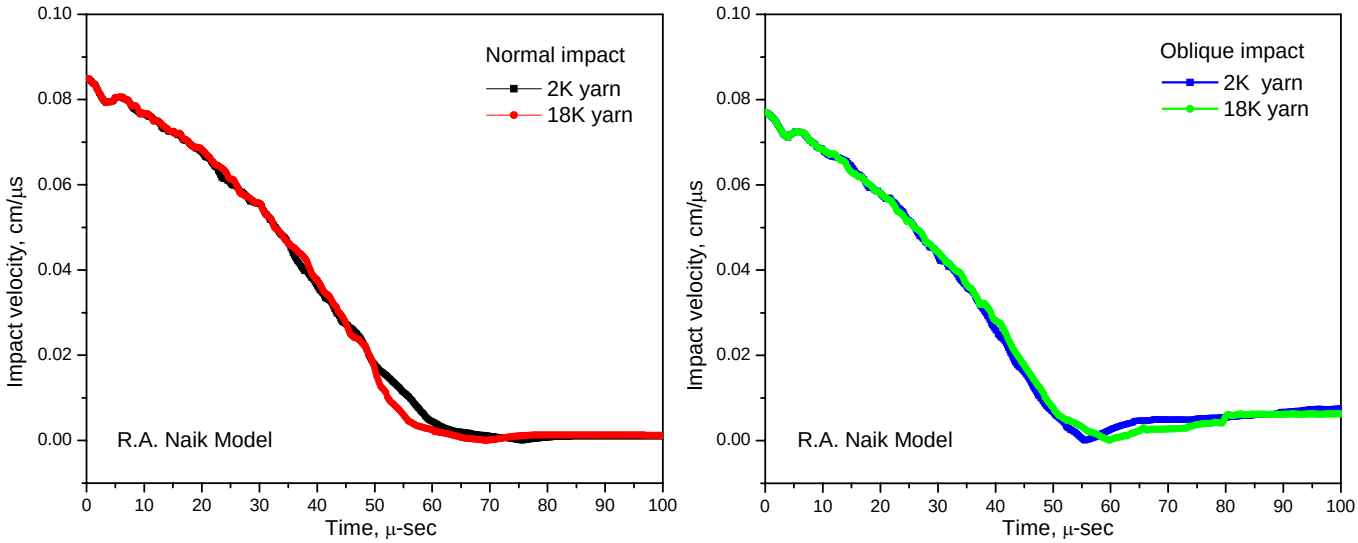

Figure 10.27: Normal and oblique impact velocities of the projectile in a different 2-D braid and ceramic layered plate.

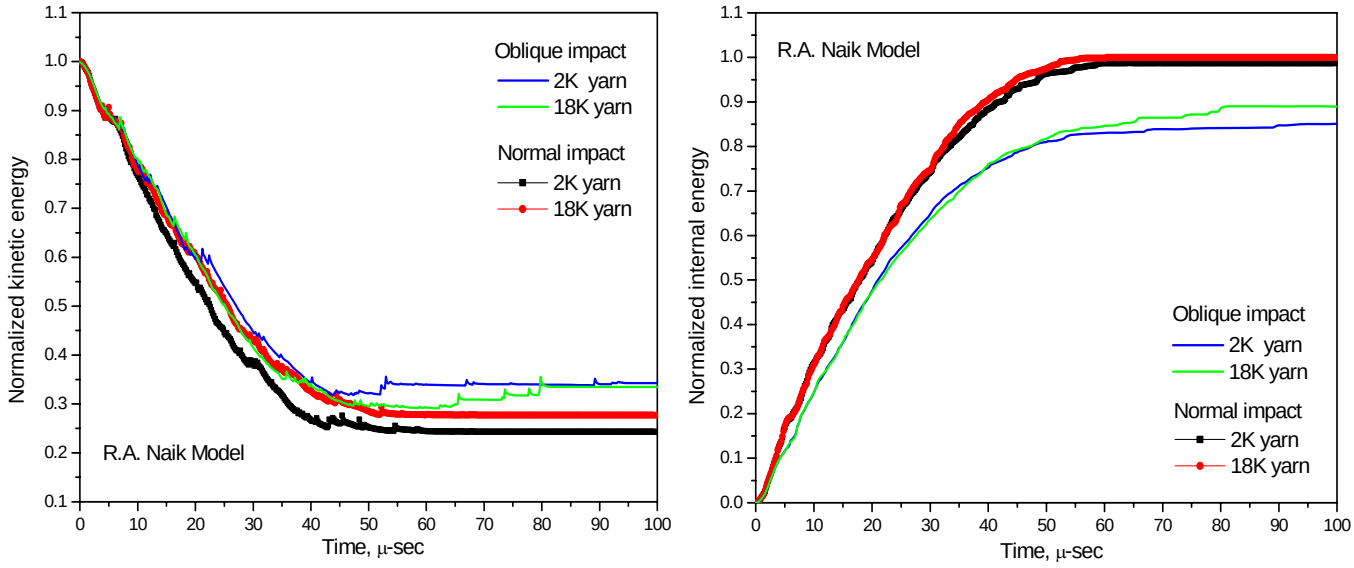

Figure 10.28: Normalized internal and kinetic energies of the projectile in the normal and the oblique impact.

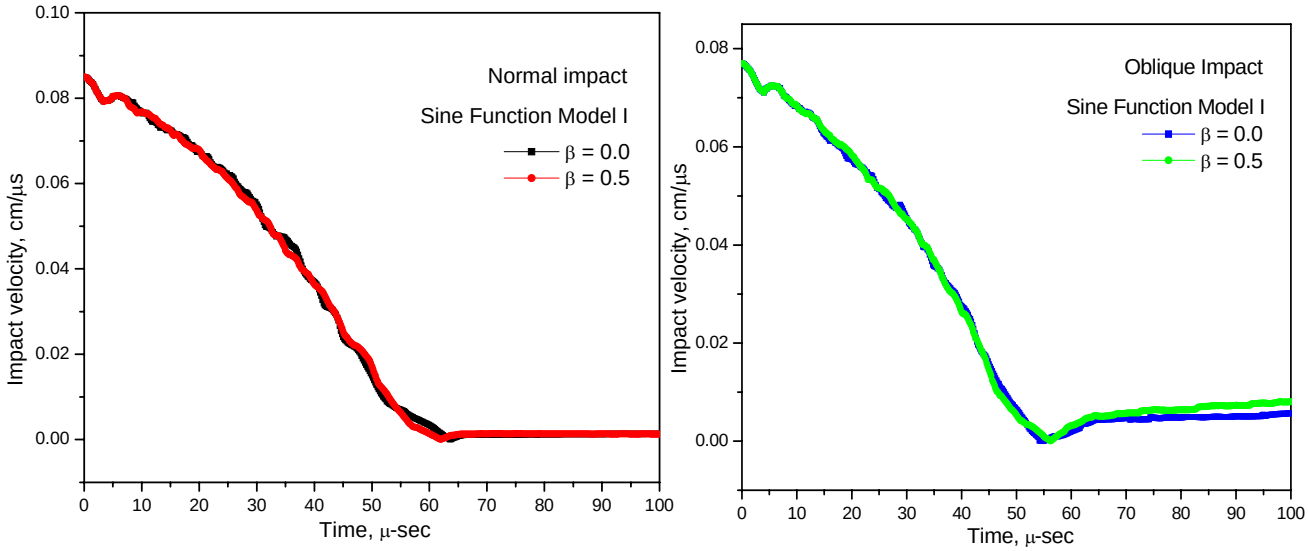

Figure 10.29: Normal and oblique impact velocities of the projectile in a different 2-D braid and ceramic layered plate.

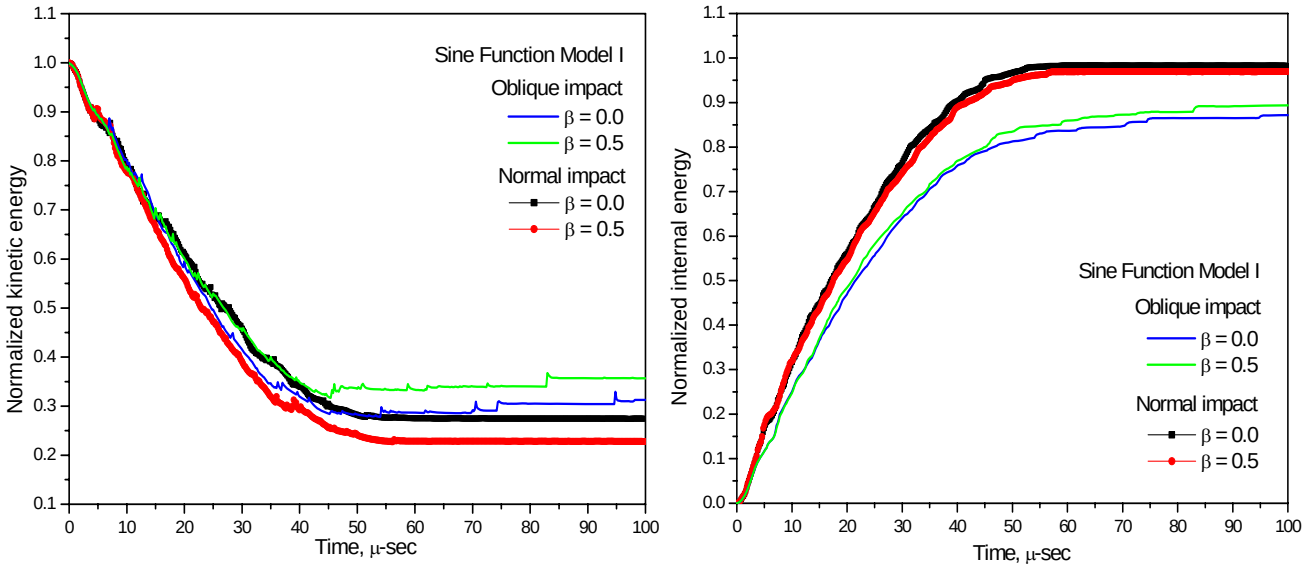

Figure 10.30: Normalized internal and kinetic energies of the projectile in the normal and the oblique impact.

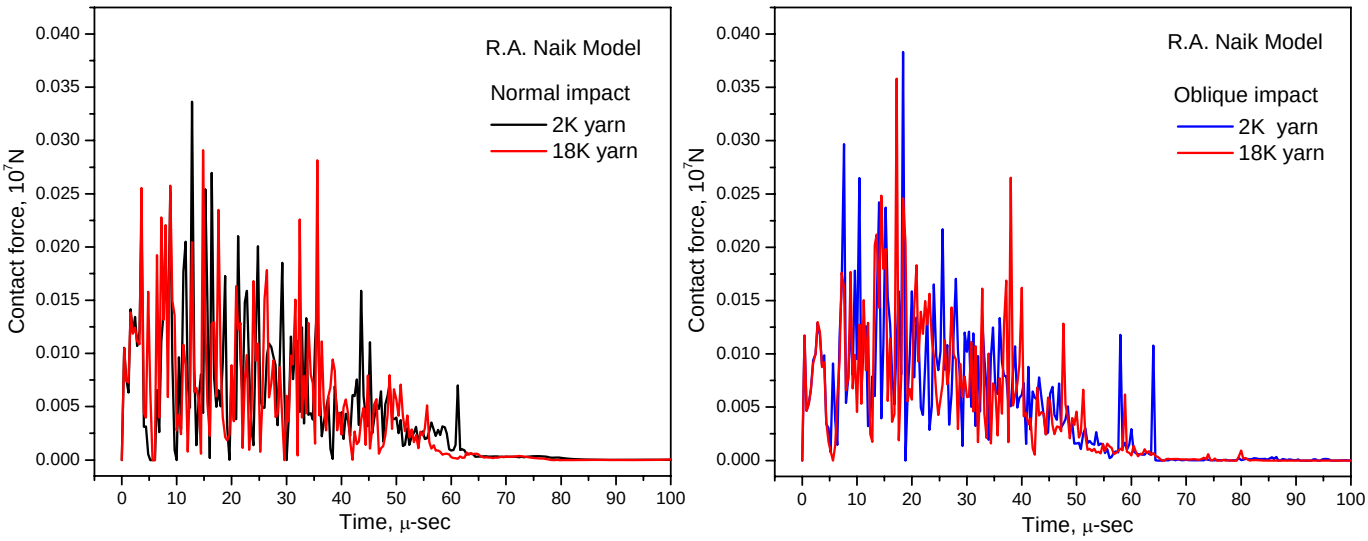

Figure 10.31: Contact forces of the normal/oblique impact projectile into a 2-D braid and ceramic layered plate.

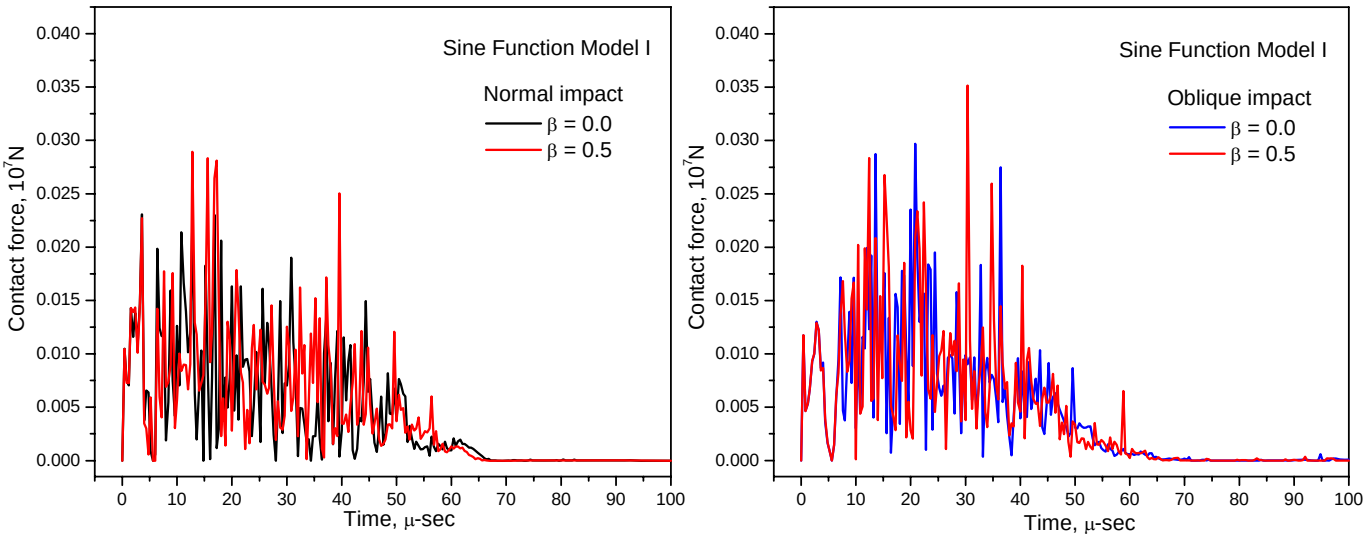

Figure 10.32: Contact forces of the normal/oblique impact projectile into a 2-D braid and ceramic layered plate.

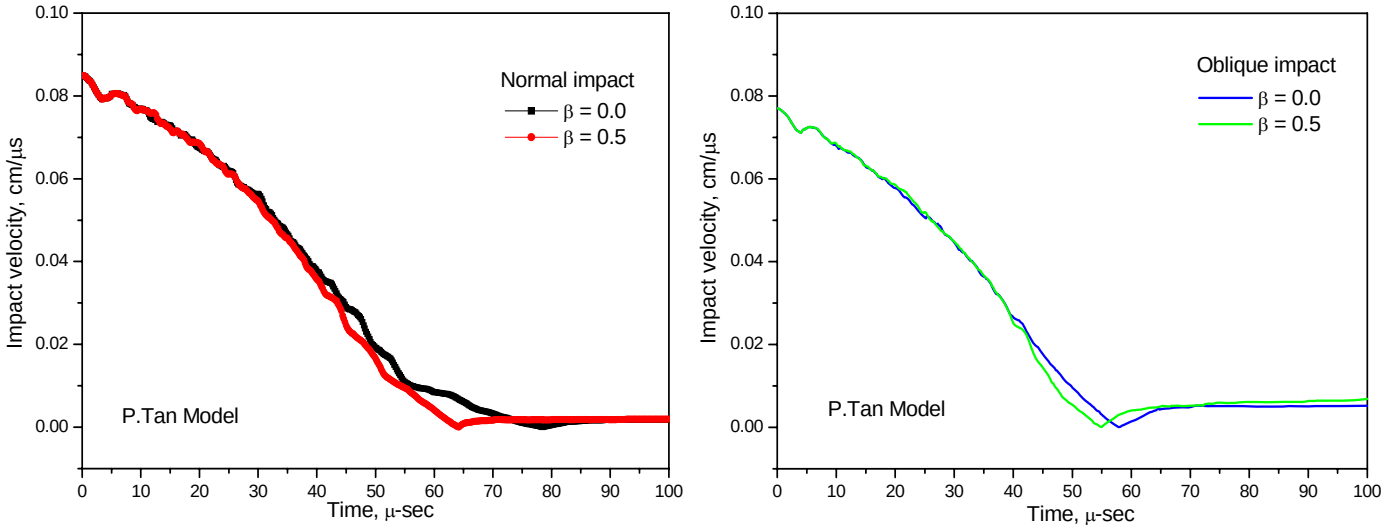

Figure 10.33: Normal impact velocities of the projectile in a different 3-D orthogonal weave and ceramic layered plate.

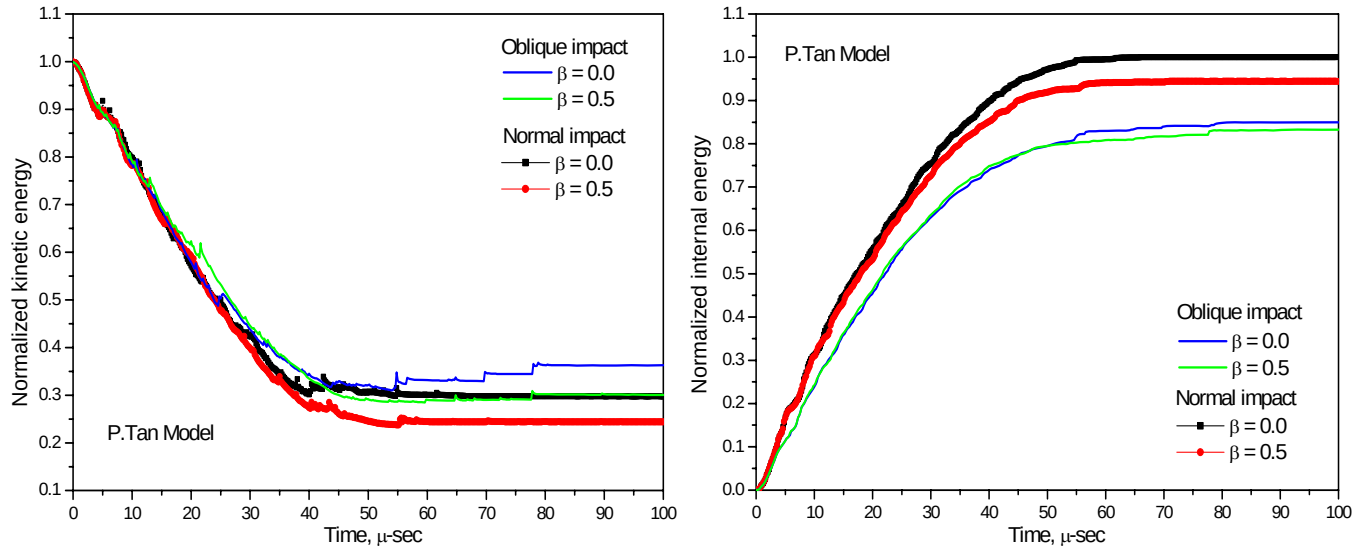

Figure 10.34: Normalized internal and kinetic energies of the projectile in the normal impact.

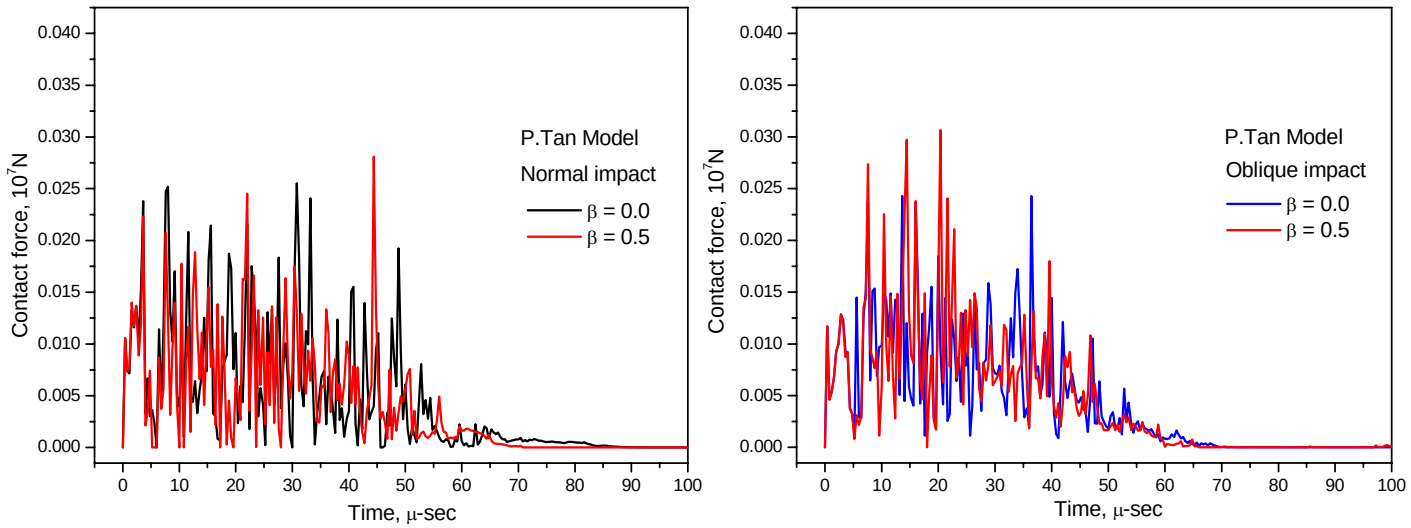

Figure 10.35: The normal/oblique impact projectile contact forces of 3-D orthogonal weave and ceramic layered plate.

10.7 Damage Behavior of 2-D Plain Woven, 2-D Braided and 3-D Woven Textile Structures

The effect of stiffness loss during an impact is investigated, and Eq.(10.6) is used to obtain the time history for three damaged different armor plates. Figures 10.36-37 show the damage behavior of normal and oblique impact cases for 2-D plain woven, 2-D braided (Naik model) and 3-D orthogonal woven textile and ceramic layered plates. As expected under normal impact, the 3-D woven textile and ceramic-layered plate shows a good damage resistance as compared to the 2-D plain woven or the 2-D braided textile and ceramic layered plates, because the different yarn geometry (z-yarns) has a greater damage resistance along the normal impact direction and also the z-yarn has a role in preventing the transverse micro-cracking of the matrix in the in-plane direction.

In the yarn section shapes, the plate modeled using Sine Function Model I has a better damage characteristics than modeled by Naik model. This can be explained by the fact that some regions of the yarn are geometrically placed along the normal direction, the z-axis while the flat-balanced yarns are mostly placed in the in-plane direction, the x and the y-axes. The yarn geometry shapes of fills and warps in the Sine Function Model I play a role in providing a better damage resistance against the impact loading, while the flat-balanced yarns represented by Naik model have a reduced stiffness in the impact direction. They do have a high value of in-plane stiffness, however, that makes them somewhat less susceptible to oblique impact.

In the oblique impact case, two models show similar damage parameter time histories. The 2-D plain braided (Naik model) and ceramic layered plate show a little better damage resistance than that of composite modeled using Sine Function Model I. An interesting fact that was found again is that both the stiffness changes and damage tolerances of textile layered armor plates are affected by both the yarn geometry and the angle of incidence of the impact. These factors, yarn geometry and angle of incidence of impact, partially affect the overall damage behavior of the textile layered armor plates.

The cohesive element is used to study the crack propagations and fragmentations when the target is subjected to an oblique or normal impact velocity (V=850m/sec), respectively, see Figures 10.38, 10.39, 10.40 and 10.41. Figures 10.30 and 10.38 show the impact configurations of the projectile and the armor plate consisting of the 2-D plain woven textile layer modeled by the SFM I and a ceramic layer made of alumina. Figures 10.39 and 10.41 present the evolution of fracture patterns at different time steps. From

Figures 10.39 and 10.41, we can see that the 2-D plain woven textile layer prevents the projectile penetration by developing a number of cracks and fragmentations that absorb a considerable amount of energy. These fracture evolutions are explained by the energy loss from the ballistic projectile while breaking the armor plate. The energy transformation induces a number of micro-cracks and fragmentations during very short impact duration.

10.8 Dependency of Mesh Unit Cell Sizes

The impact behavior of textile and ceramic layered plates is studied by three different unit cell mesh sizes while keeping the same modeling for the projectiles, see Fig. 10.42. As depicted in Fig. 10.42, the impact simulations use only the different layout of the mesh in the target layers. The first model is based on a local fine-meshed region consisting of a smaller sized mesh for the unit cell and impacted with a projectile. The second model uses a larger mesh unit cell modeled by a large-span length compared to the height of the mesh unit cell. The other model consists of a small span length and a large height of the mesh unit cell, and more thick layers consist of the target layers compared to the second model.

On the modeling side, the same material properties, model dimensions, impact directions of projectile and impact velocity used in the section 10.6 are applied to these cases. The 2-D braided textile layer is modeled by the Sine Function Model I and the 12 K yarn bundle is used. The 3-D orthogonal woven textile layer is defined by Tan model and the 12 K yarn sizes also are used. The stiffness values of the textile layers are used to check the damage tolerance, such as Eq.(10.6), and the relative damage tolerance is compared together with three different mesh unit cell sizes.

To find the different damage tolerances, the impact simulations consider the two different impact directions, normal and oblique. From the impact velocity and damage tolerance histories of Figs.10.43-10.46, the results, most significantly, indicate that the impact behaviors of the textile and ceramic layered plate are highly sensitive to the different unit cell mesh sizes of targets. These different results are induced from the mesh alignments or mesh textures. In particular, the impact between the same projectile (slave elements) and the different targets (master elements) induces different contact interactions or erosion procedures along the contact surfaces. These phenomena are main factors to make different impact velocity and damage tolerance histories. For example, the impact velocity and damage tolerance results obtained using the second and the third models show similar results even though different mesh unit cells are used, the mesh designs of these two models are relatively similar, however, as compared to the local fine-meshed design employed in the first model. However the local fine-meshed modeling has more accurate results compared to the general /regular mesh texture modeling. The similar dependency of mesh unit cells in the dynamic fracture was studied in Refs. [10.10-10.14].

Although the local fine-meshed modeling has been used in the impact simulation, the dynamic behaviors of textile and ceramic layered plates are not completely analyzed. For example, the damage regions in the layers are not clearly defined during the impact/contact phenomena. To solve these problems, one modeling, meso-scale modeling, was suggested in previous studying of Refs.[10.15-10.20]. The meso-scale modeling in the textile composite structure is briefly explained in the next section.

10.9 Meso-scale Modeling of Textile Composite Structures

Meso-scale modeling of textile composites in the impact simulations mainly aims to predict more detailed dynamic behaviors during the impact that can not be studied using the macro-scale modeling only. In order to make such predictions, there is a need for a numerical model that is based on more specified internal geometry of the textile composite. In this case, the geometry of a Repeating Unit Cell (RUC) is used. To construct meso-scale modeling for the textile composites, there is always involved some kind of mesh generation. To describe the textile composite geometry and analyze the impact using meso-scale impact modeling, this study developed a mesh generation program, an in-house code, based on Fortran 77/90, Visual C^{++} and Assembler languages. However, the meso-scale modeling needs a extremely large number of elements, nodes and CPU time as compared to macro-scale modeling. The benefit is that a considerably more accurate solution is obtained. The analyses for meso-scale impact modeling on the textile layered structures are not mentioned here to save space. We only want to show a simple procedure

applicable at the meso-scale modeling. This section briefly introduces the procedures of meso-scale modeling on the textile composite structures. The meso-scale modeling consists of three main steps, such a geometry modeling of Repeating Unit Cell, a layer modeling and a structural modeling.

10.9.1 Geometry Modeling of Repeating Unit Cell

This step constructs the three-dimensional shape of orthogonally interfaced textile yarns based on the Repeating Unit Cell. To describe the interlaced yarn geometry, the geometrical surface equations, such as Sine Function Model I, are derived in Chapter 2. This step makes the three component geometry: fill/warp yarns and resin layers in the Repeating Unit Cell. These components' geometries are described in Chapter 2. So, for brevity, this section is not repeated in. Also the material properties for the yarns and resin are specified by the respective micro-mechanical equations suggested in previous Chapters 2-3. After constructing the shape of Repeating Unit Cell (RUC), all geometry data of RUC is applied to the 2'nd step, the layer modeling.

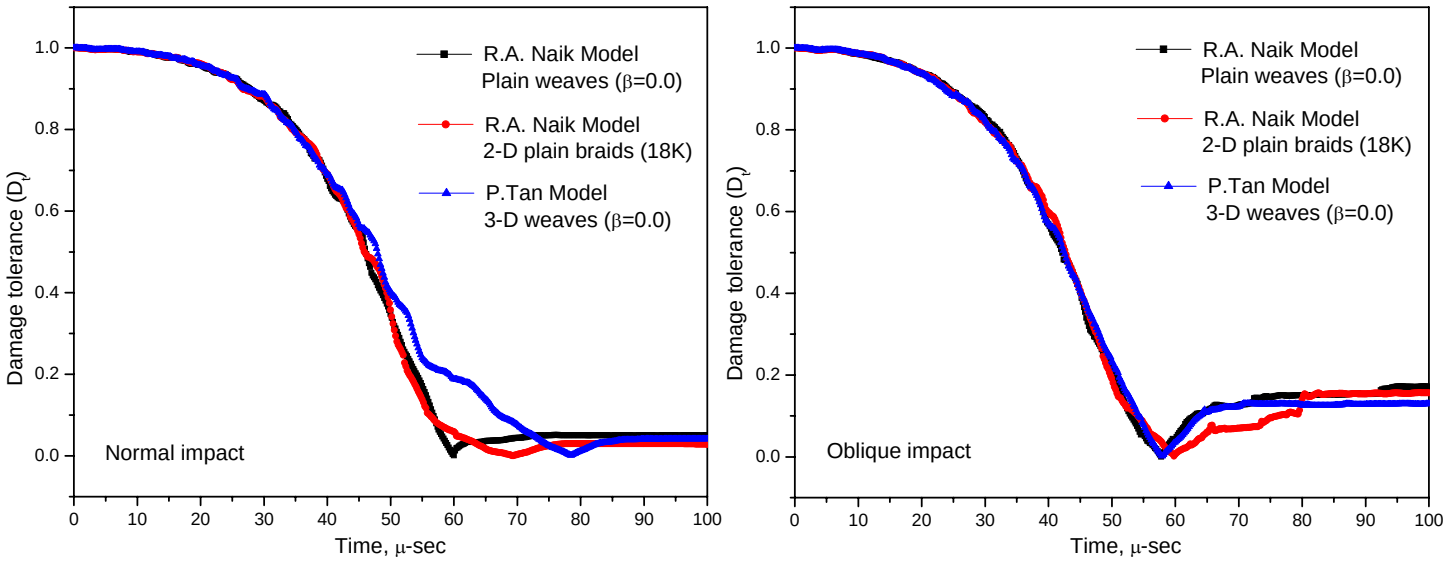

Figure 10.36: The damage tolerances of normal/oblique impact cases in R.A. Naik model and P. Tan model.

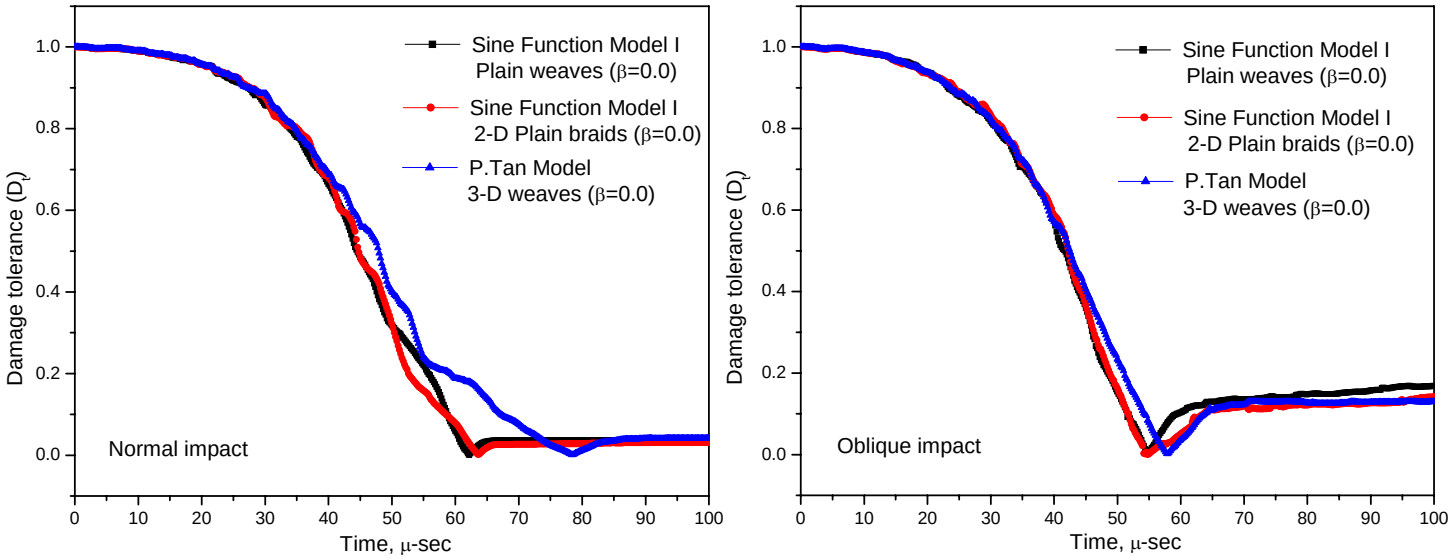

Figure 10.37: The damage tolerances of normal/oblique impact cases in Sine Function Model I and P. Tan model.

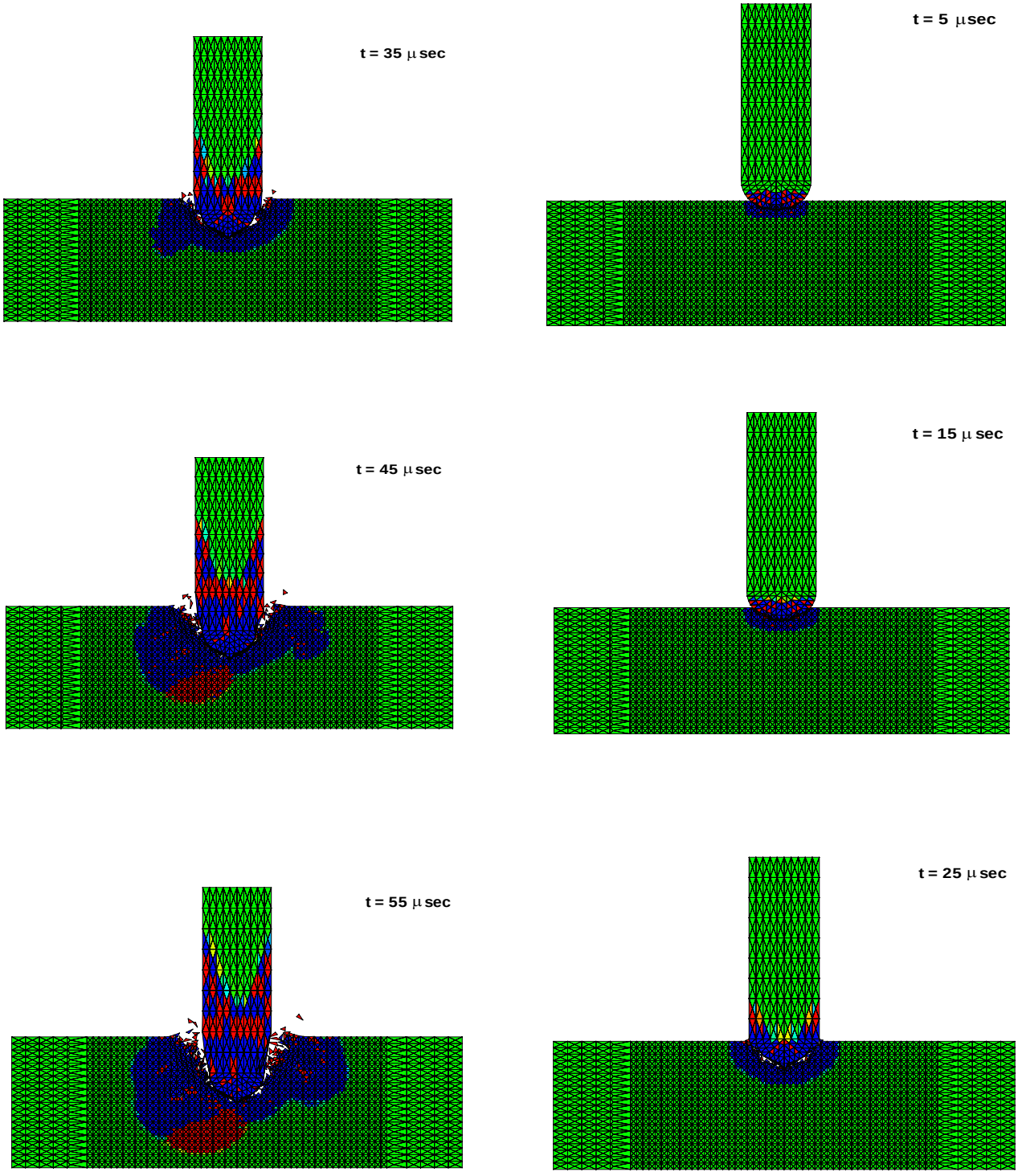

Figure 10.38: Normal impact configurations of a 2-D plain woven textile layered armor plate and a bullet.

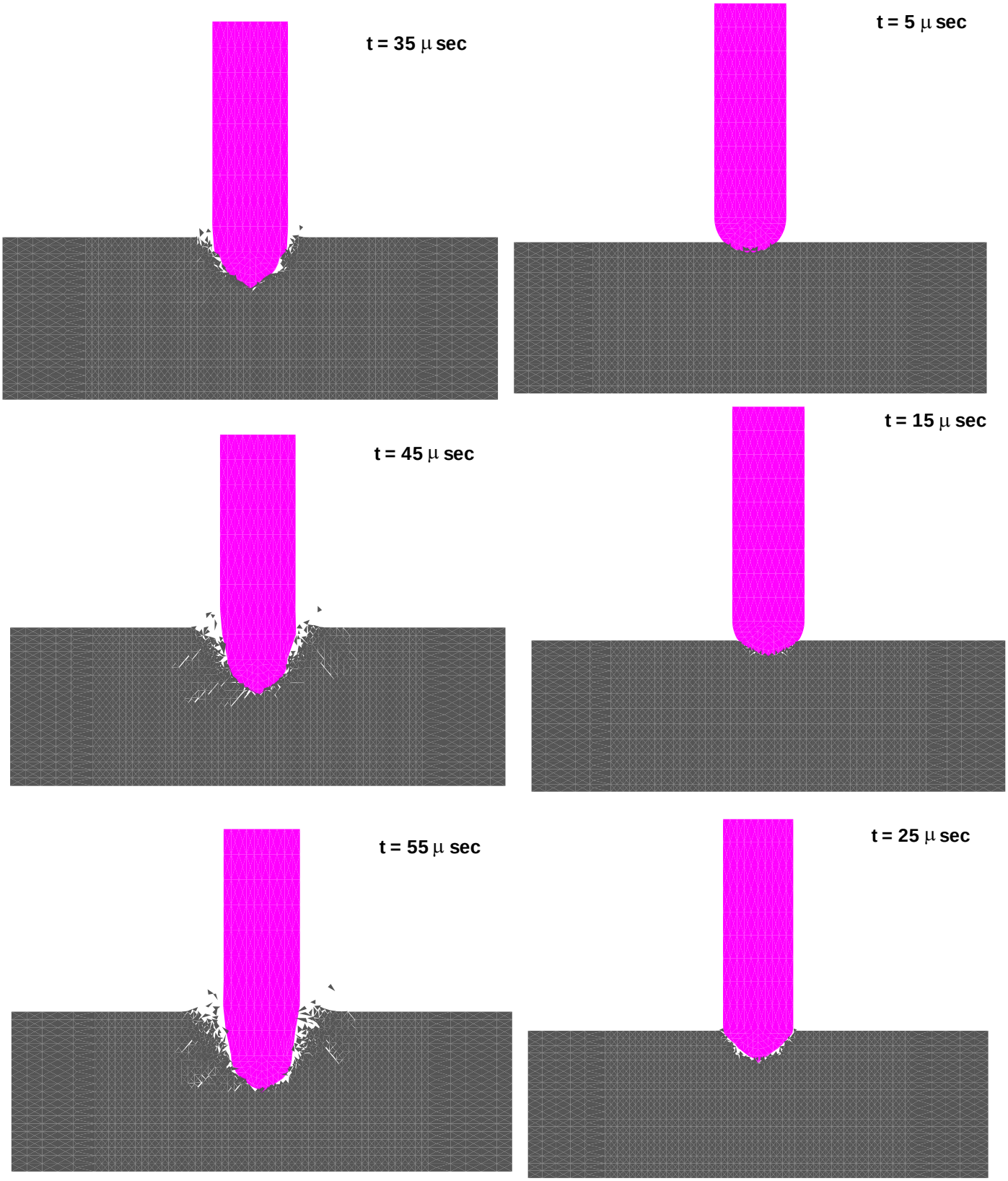

Figure 10.39: Fracture patterns of a 2-D plain woven layered armor plate and a bullet (V = 850 m/sec).

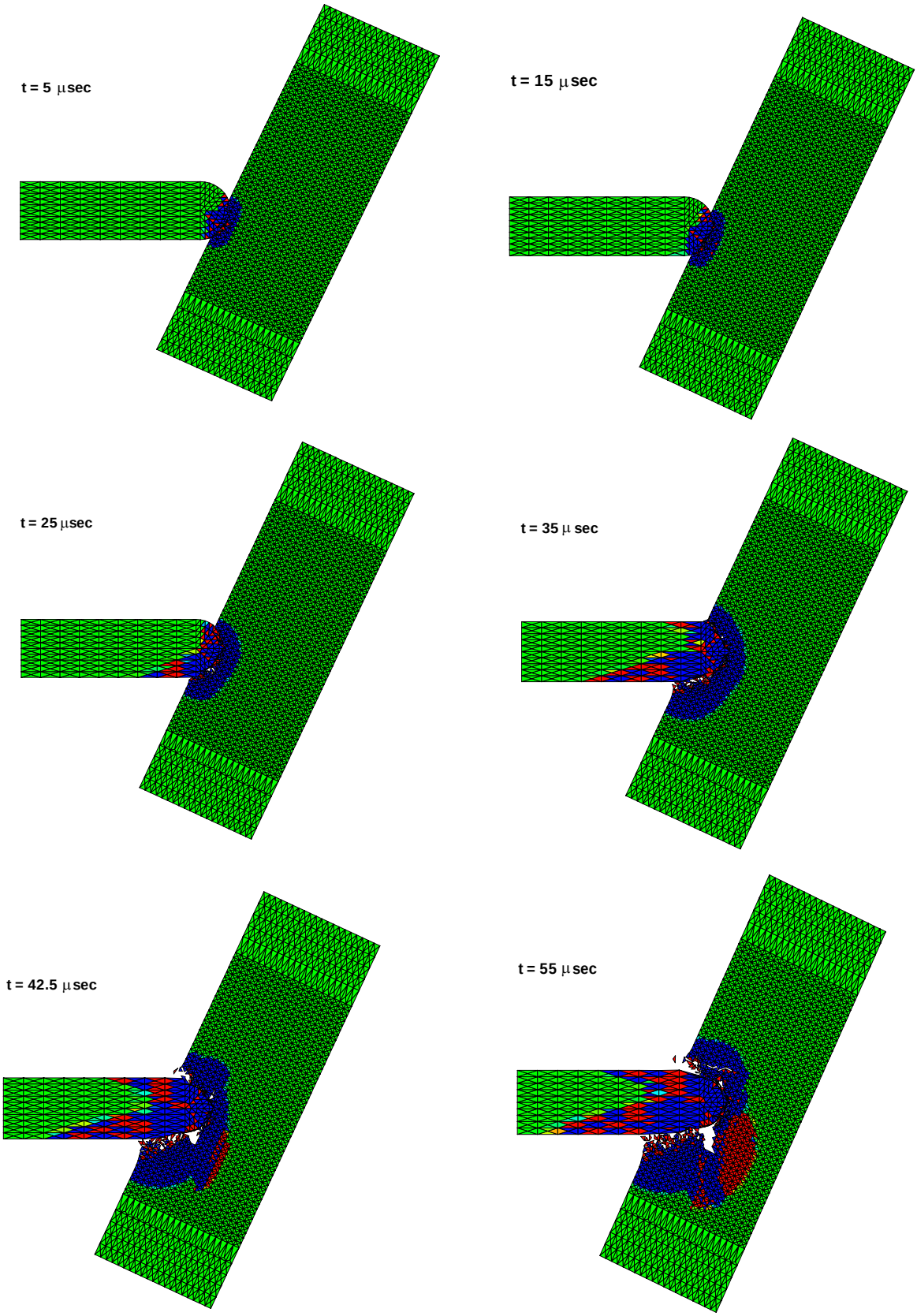

Figure 10.40: Oblique impact configurations of a 2-D plain woven textile layered armor plate and a bullet.

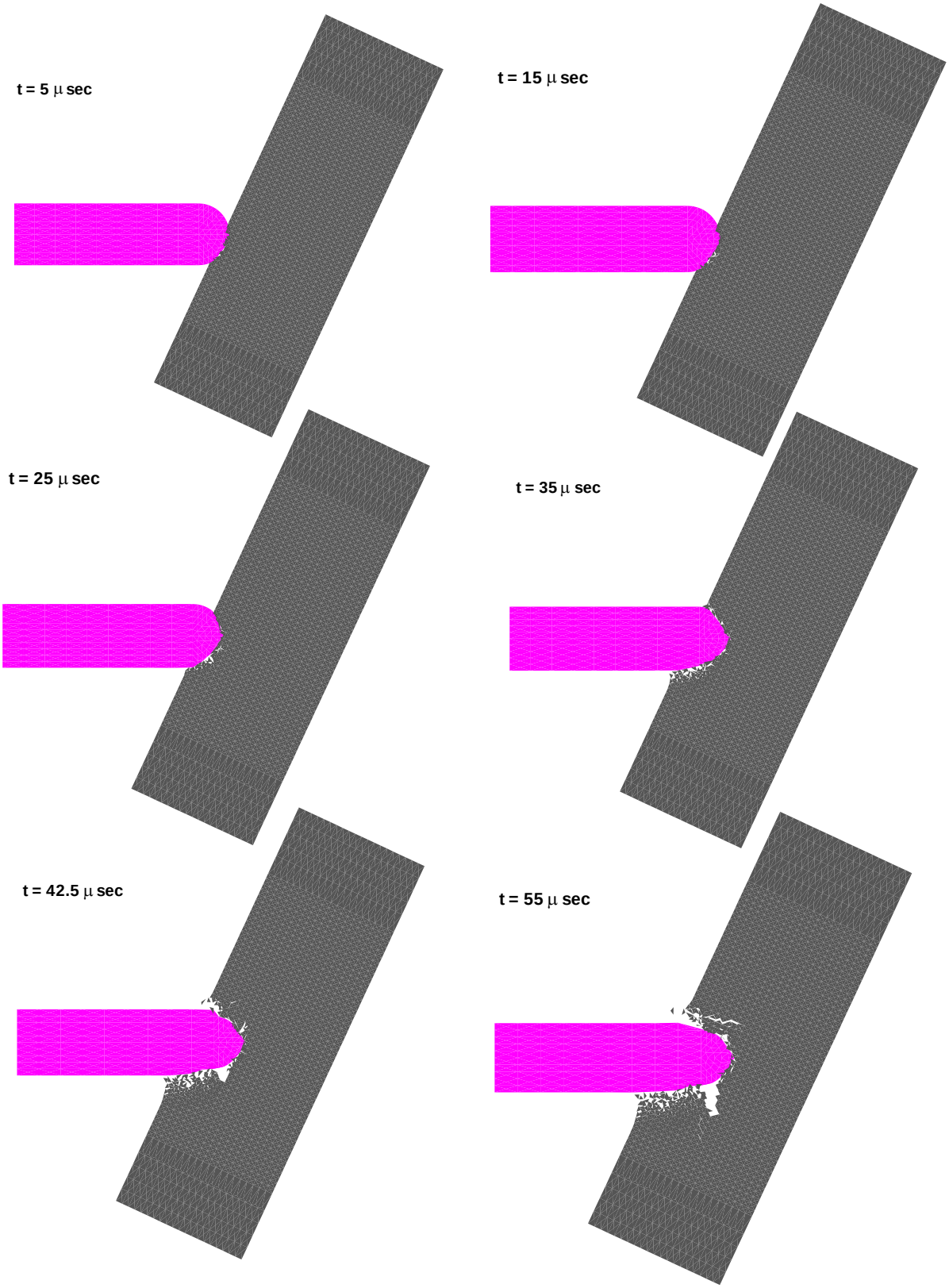

Figure 10.41: Fracture patterns of a 2-D plain woven layered armor plate and a bullet (V = 850 m/sec).

10.9.2 Layer Modeling

In general, a multi-layered plate consists of several textile composite layers. The three-dimensional shape of a textile layer is assembled from a number of Repeating Unit Cells. In order to model a layer with a number of RUCs, a mesh generation scheme is needed. For example, the element or node connections between the Repeating Unit Cells are correctly specified. The other problem is the interfaced layers between the fill/warp yarns and between the resin and yarns. The interface layers have a role to connect the different components and also transform the loading to other components during the impact simulations. After determining the layer geometry, a structural modeling is applied to assemble several layer modeling.

10.9.3 Structural Modeling

This structural modeling combines several layer modeling that are determined by the 2'nd step, and constructs a multi-layered structure. In the structural modeling, the common nodes are used to connect between the different layers and the common nodes have a role to transform the loading and keep the same degree of freedom, but the element numbers are the different numbers. The boundary conditions, impact directions and impact velocity of projectiles also are specified in this step. Another problem is the damage modeling in this step. As the damage criterion for the micro-cracked textile composite was used in Chapter 6, the modeling of damage consists of a damage criterion and a scheme to reduce the stiffness of the material properties based on the stresses at the Gauss integration points within the elements.

For an easy understanding of meso-scale modeling, some of geometrical shapes of two main steps (layer modeling and structural modeling) are introduced in Figs. 10.47-10.49, respectively.

10.10 Concluding Remarks

We have developed a computational model that enables predictions of damage progressions of dynamic fracture and fragmentation in the textile layered armor structures subjected to ballistic impact velocity loading. The impact of textile layered armor structures has been investigated to show the ability of the armor materials by modeling these using the cohesive element approach. From the comparisons of results for different textile layered armor plates, the textile layered armor structure having a good damage resistance is suggested, although this structure develops a number of cracks, fragmentations and erosion during the projectile penetration.

However, our computational modeling, an integrated numerical modeling, has still some limitation to fully perform the 3-D modeling using a 2-D cohesive element formulation. In practice, the armor structures when subjected to ballistic impact loading show complex phenomena of cracking, fragmentation and erosion. For example, the complex paths of micro-cracking are not limited only to be present in much more in-plane directions. Complex crack paths have been observed in a number of experimental studies. To overcome this shortcoming, computational model for investigating 3-D fracture problems are needed.

An additional limitation of the computational model that is based on the cohesive element modeling is related to the meso- scale or macro-scale modeling to understand impact mechanics of textile layered structures. At the meso-scale modeling of the textile layered structures, a number of elements form the 3-D yarn geometry and large computational time is needed to analyze the meso-scale modeling, while at the macro-scale, the number of elements is rather small and computational time is also small compared to the meso-scale modeling. These two modeling have both good-points and shortcomings in the finite element analyses. In this chapter, one simple integrated numerical modeling with the macro-scale modeling is used to check damage tolerances of these structures. The potential multi-scale computational models to solve problems related to the impact of textile layered composite structures are future challengeable studies.

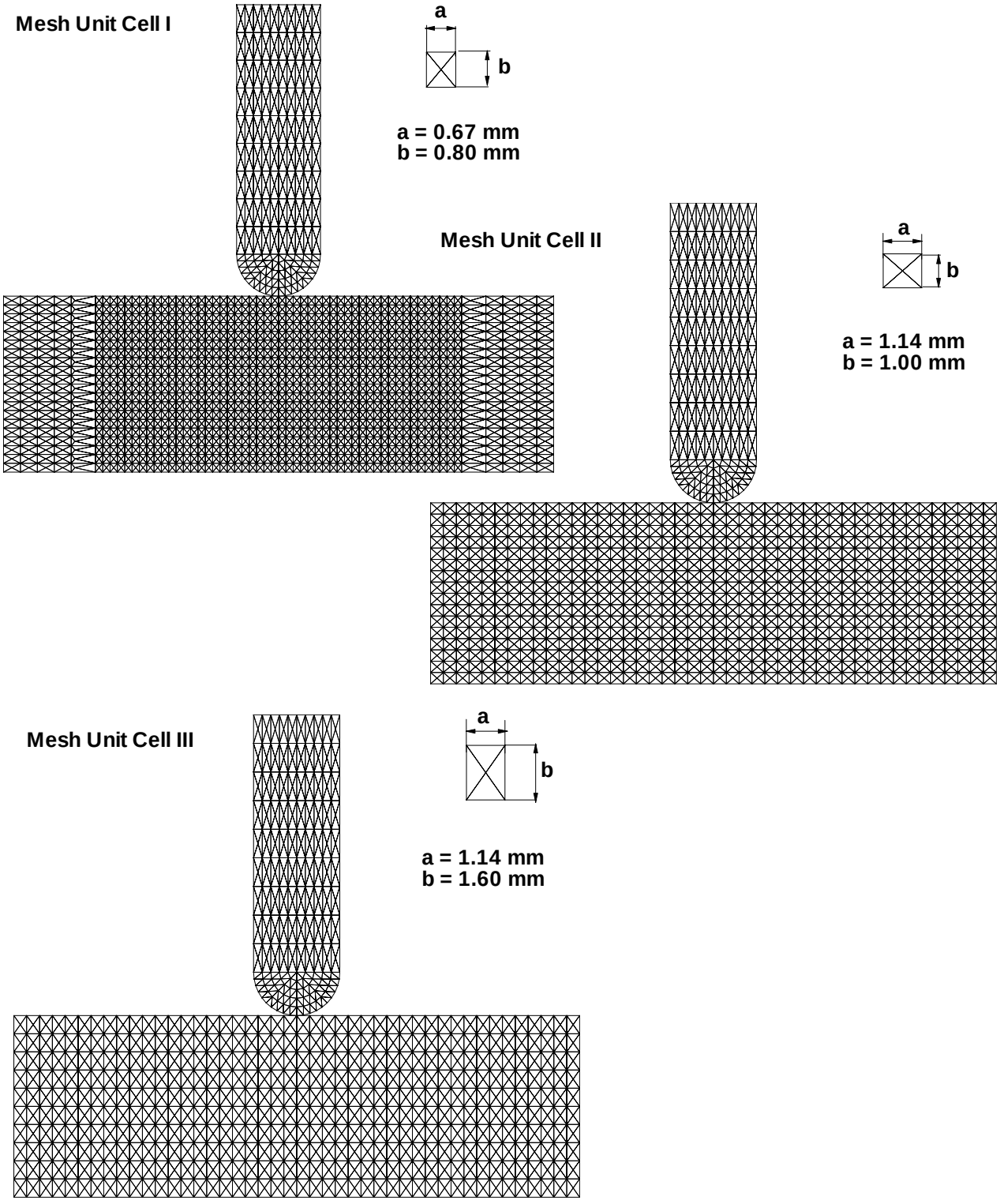

Figure 10.42: Three different mesh unit cells for the textile and ceramic layered plates.

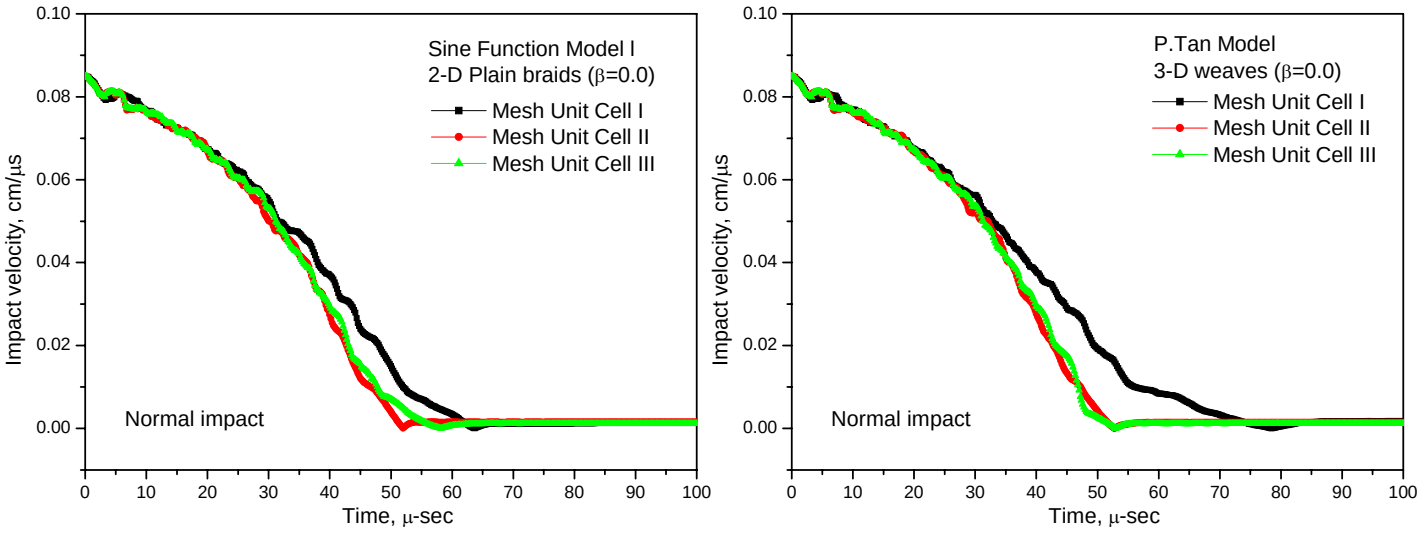

Figure 10.43: Normal impact velocities of the projectile in different mesh unit cells.

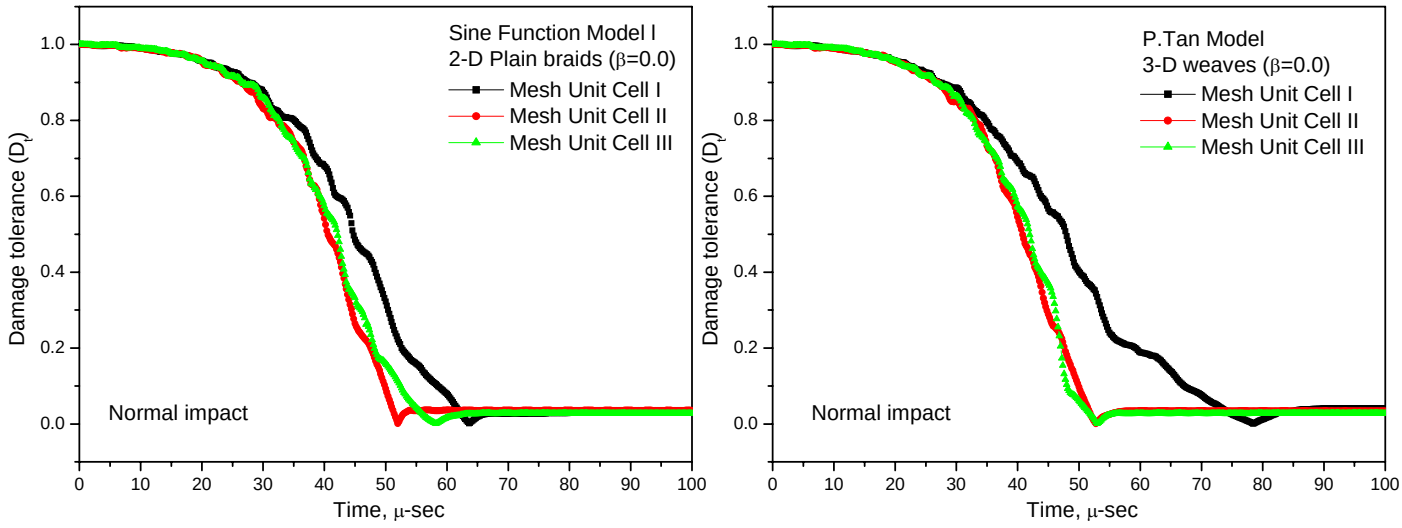

Figure 10.44: The damage tolerances of normal impact cases in Sine Function Model I and P. Tan model.

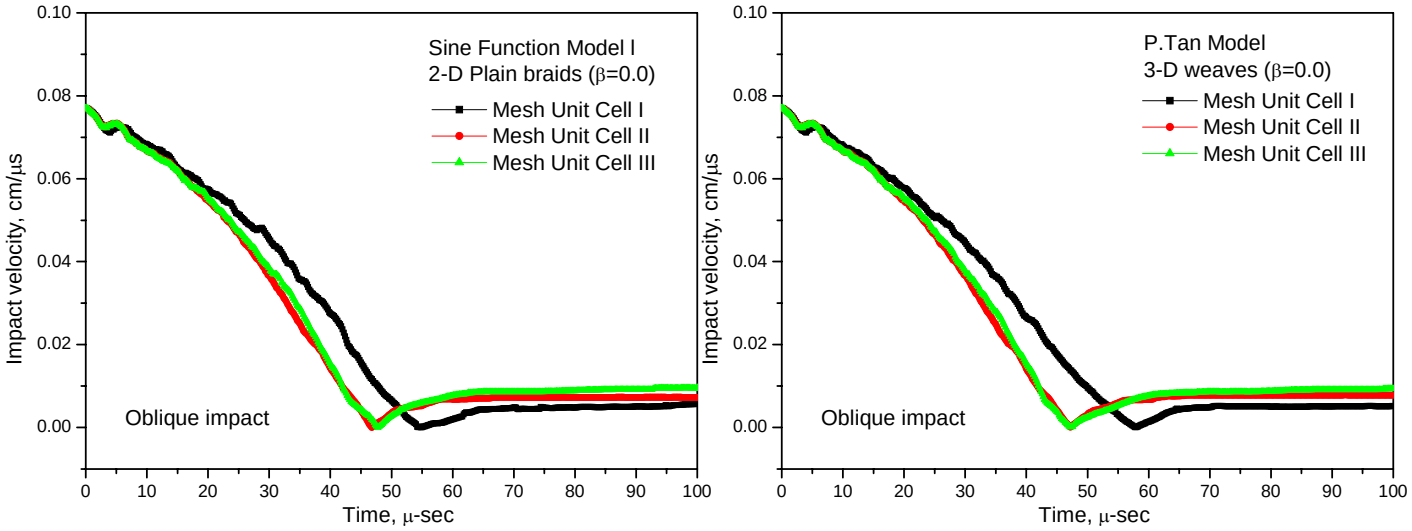

Figure 10.45: Oblique impact velocities of the projectile in different mesh unit cells.

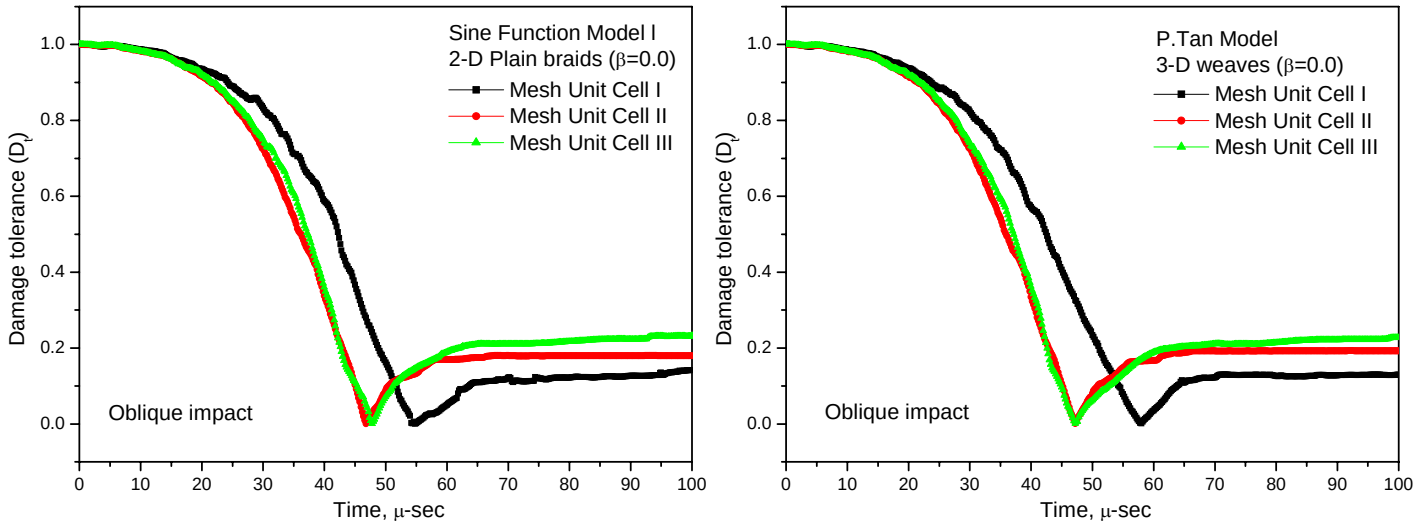

Figure 10.46: The damage tolerances of oblique impact cases in Sine Function Model I and P. Tan model.

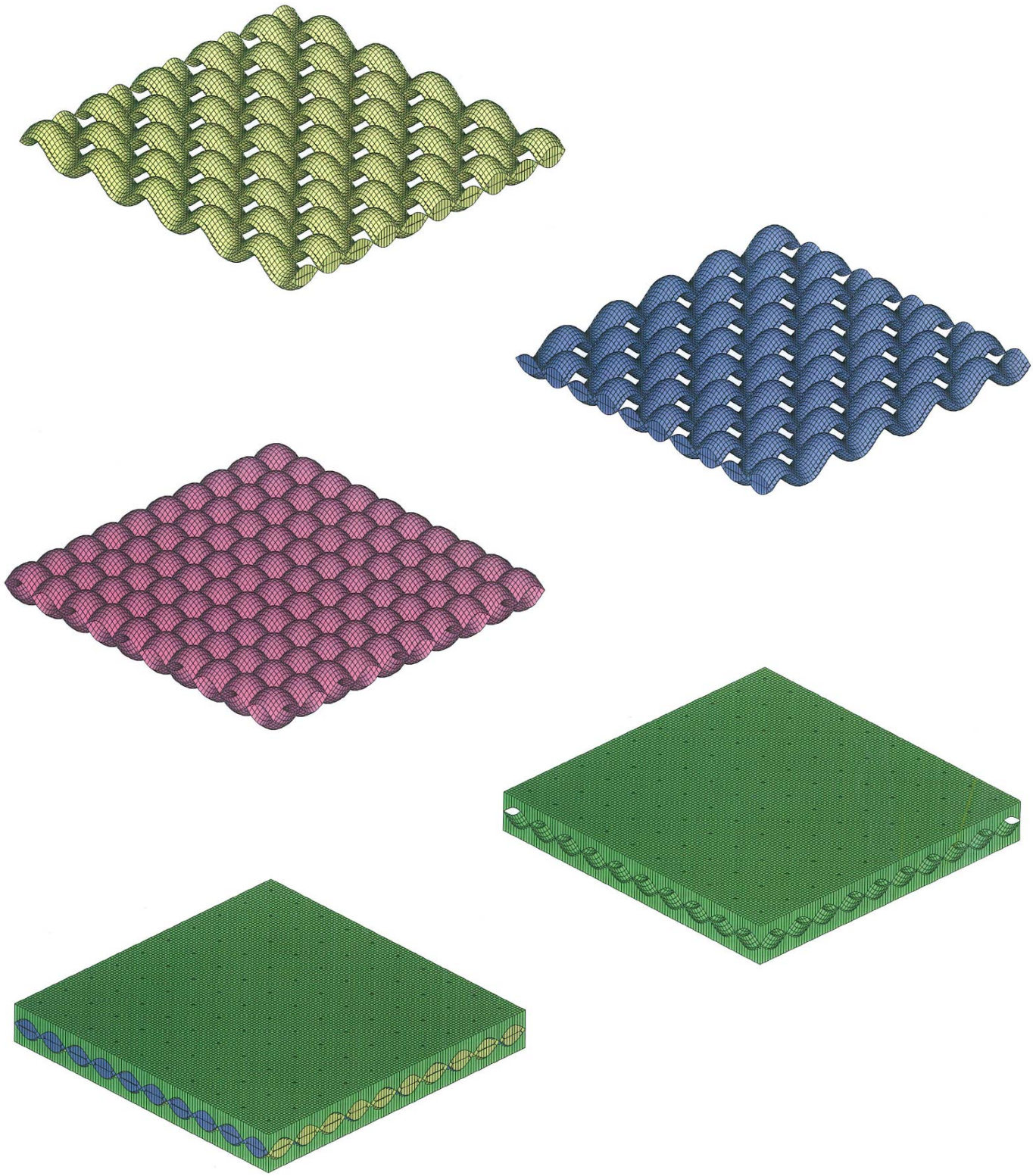

Figure 10.47: Components and one layer for the 2-D plain woven textile composites.

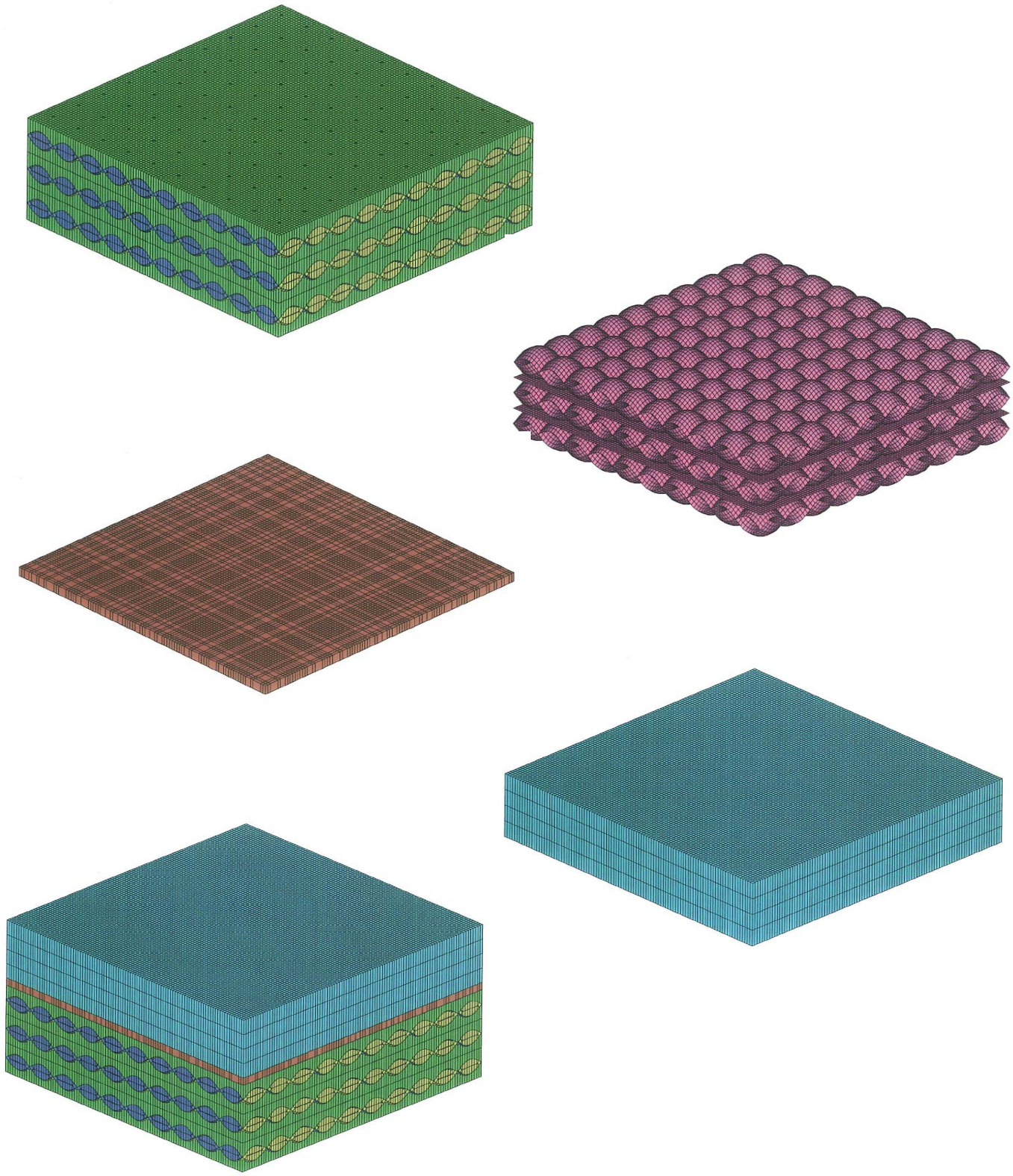

Figure 10.48: Components and one multi-layer with a ceramic and 2-D plain woven textile composite.

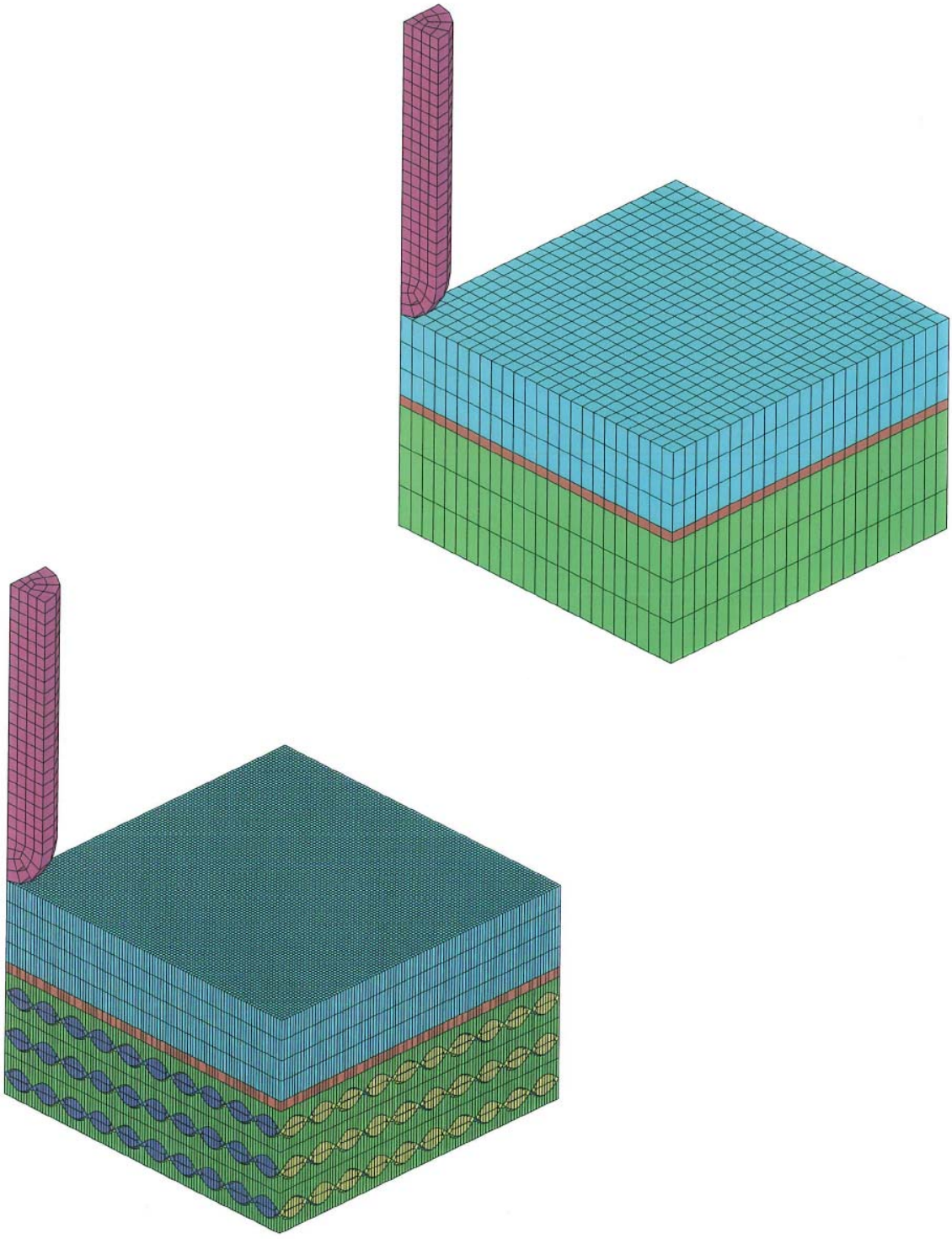

Figure 10.49: Macro- and meso-impact modeling for a 2-D plain woven textile and ceramic layered plate.

REFERENCES

10.1 Bogdanovich, A.E., "Multi-scale Predictive Analysis of 3-D Woven Composites," *Proc. of 35th Int. SAMPE Technical Conference,* Vol. 35, Dayton, OH, September 28-October 2, 2003.

10.2 Naik, R.A., "Analysis of Woven and Braided Fabric Reinforced Composites," NASA Contract Report CR-194930, 1994.

10.3 Scida, D., Aboura, Z., Benzeggagh, M.L. and Bocherens, E., "A Micro-mechanics Model for 3D Elasticity and Failure of Woven-Fiber Composite Materials," *Composites Science and Technology*, Vol. 59, No. 4, 1999, pp. 505-517.

10.4 Xu, X.-P. and Needleman, A., "Numerical Simulations of Fast Crack Growth in Brittle Solids," *Journal of the Mechanics and Physics of Solids*, Vol. 42, No. 9, 1994, pp. 1397-1434.

10.5 Hinton, E., Owen, D.R.J. and Shantaram, D., "Dynamic Transient Linera and Nonlinear behavior of Thick and Thin Plates, "The Mathematics of Finite Element and Applications II (MAFELAP 1975), Academic Press, New York and London, 1976, pp. 423-438.

10.6 Reismann H. and Lee, Y.C., "Forced motion of Rectangular Plates," Proceedings of the 4'th Biennial South-Eastern Conference, Tulane University, New Orleans, Pergamon Press, New York, 1968.

10.7 Reismann H. and Tendorf, Z.A., "Dynamics of Initially Stressed Plates," *Journal of Applied Mechanics*, Vol. 43, June, 1976, pp. 304-308.

10.8 Hinton, E., "The Dynamic Transient Analysis of Axisymmetric Circular Plates by the Finite Element Method," *Journal of Sound and Vibration*, Vol. 46, No. 4, 1976, pp. 465-472.

10.9 Tan, P., Tong, L. and Steven, G..P., "Modeling Approaches for 3-D Orthogonal Woven Composites," *Journal of Reinforced Plastic and Composites*, 1998, Vol. 17, No. 6, pp. 545-577.

10.10 Kalthoff, J.F. and Winkler, S., "Failure Mode Transient at High Rates of Shear Loading," *International Conference on Impact Loading and Dynamic Behavior of Materials*, Chiem, C.Y., Kunze, H.D. and Meyer, L.W. eds., 1987, pp. 185-195.

10.11 Belytschko, T. and Tabbara, M.R., "Dynamic Fracture using Element-free Galerkin Methods," *International Journal of Numerical Methods in Engineering*, Vol. 39, No. 6, 1996, pp. 923-938.

10.12 Frund, B., *Dynamic Fracture Mechanics*, Cambrige University Press, New York, 1990.

10.13 Rahul-Chandra, K., "Dynamic Fracture of Nominally Brittle Materials," *International Journal of Fracture*, Vol. 90, No. 1, pp. 83-102.

10.14 Klein, P.A., Foulk, E. P., Chen, E.P., Wimmer, S.A. and Gao, H., "Physical-based Modeling of Brittle Fracture: Cohesive Formulations and the Application of Meshfree Methods," SAND2001-8099, Sandia National Laboratories, Albuquerque, NM87185, 2000.

10.15 Duan, Y., Kneefe, M., Bogetti, T.A. and Cheeseman, B.A., "Modeling Friction Effects on the Ballistic Impact Behavior of A Single-Ply High-Strength Fabric," *International Journal of Impact Engineering*, Vol. 31, No. 8, 2005, pp.996-1012.

10.16 Duan, Y., Kneefe, M., Bogetti, T.A. and Cheeseman, B.A., "Modeling the Role of Friction during Ballistic Impact of A High-Strength Plain-Weave Fabric," *Composite Structures*, Vol. 68, No. 3, 2005, pp. 331-337.

10.17 Gu, B., "Ballistic Penetration of Conically Cylindrical Steel Projectile into Plain-Woven Fabric Target-A Finite Element Simulation," *Journal of Composite Materials*, Vol. 38, No. 22, 2004, pp. 2049-2074.

10.18 Gu, B. and Xu, J., "Finite Element Calculation of 4-Step 3-Dimensional Braided Composite under Ballistic Perforation," *Composites: Part B*, Vol. 35, No. 4. 2004, pp. 291-297.

10.19 Gu, B. and Yuling, L., "Ballistic Perforation of Conically Cylindrical Steel Projectile into Three-Dimensional Braided Composites," *AIAA Journal*, Vol. 43, No. 2, 2005, pp. 426-434

10.20 Hur, H.-K., Johnson, E.R. and Kapania, R.K., "Degraded Strength Prediction of Micro-Cracked Plain Woven Textile Composites," *The 47th AIAA Structural Dynamics and Materials Conference*, May 1-May 4, 2006, Rhode Island, Newport, AIAA-2006-2173.

Chapter 11 Summary and Conclusion

In this thesis, several numerical models to predict the effective modulus and mechanical properties of the Repeating Unit Cell (RUC) in textile composites are presented. A transient dynamic analysis combined with a simple discontinuous crack element, cohesive element modeling, has been introduced to study penetration phenomena and crack growth under impact in armor structures made of textile composites.

11.1 Summary

In summary, the main achievements of the work presented in this dissertation are:

1) Three analytical homogenization modeling, Sine Function Model I & II and sub-cell block model, have been developed which can be used to study effective moduli of textile composites using Repeating Unit Cell. The composites considered are the 2-D plain woven, 2-D braided, 2-D tri-axial braided and 3-D orthogonal woven textile composite. As such, the computational models suggested here can be used to predict mechanical characteristics and coefficients of thermal expansion (CTE) of the RUC, for various geometrical variables with the degraded micro-crack scheme are considered. In addition, this modeling presents a user of these composites with details on the equations that represent geometrical surface of composites which are very helpful for understanding the 3-dimensional geometry of a textile composite structure for RUC modeling.

2) A new progressive failure technique using user defined material (UMAT) in ABAQUS was developed to predict failure strengths of the 2-D degraded plain woven textile using the RUC modeling. The unique feature of this technique is that it can analyze the failure problem of micro-cracked textile composites using a simple scheme to obtain degraded material properties under damage.

3) A discontinuous crack element, cohesive element scheme, was developed to conduct crack propagation analysis induced from an impact loading. Two contact algorithms for un-cracked or cracked elements were developed to obtain the contact-boundary between the target and the projectile or between two cracked elements during the dynamic penetration process.

4) Several numerical examples of high ballistic impact were conducted with steel projectiles and 7.62 mm bullets impacting ceramic armor plates and a ceramic faced armor with some different layers of backed-up plates, i.e. 2-D plain woven, 2-D braided and 3-D orthogonal woven textile composites. The resulting series of penetrations show details of the projectile/armor plate interaction and the process governing the cracking in textile composites during the impact/contact.

5) The numerical results for ceramic faced and textile layered armor plates have resulted in a better understanding of:
   - the cracking behavior of a ceramic layer
   - the textile layers dynamic behaviors
   - the influence of different yarn shapes: flat-balanced or oval type
   - the effects of textile layer forms: 2-D plain woven, 2-D braided and 3-D orthogonal woven textile composites on the armor performance, and
   - the dynamic behaviors of different textile layers in the armor plate subjected to the normal or oblique high velocity impact of 7.62 mm ball bullet.

6) An improved understanding of the modeling associated with studying dynamic fracture of textile composites under impact has resulted in identifying damage tolerance behavior of textile composite layers using degraded stiffness when micro-cracking in the armor occurs. On the basis of this information, an integrated computational modeling for ballistic impact penetration is proposed.

11.2 The Sine Function Model I & II (SFM I &II) and Sub-cell Block Model

The theoretical work has resulted in the development of the RUC geometrical modeling of the 2-D plain woven, 2-D braided, 2x2 2-D tri-axial braided and the 3-D orthogonal woven textile composite. With micro-mechanical equations of composites, the effective properties of these different textile composites have been predicted and were compared with existing models.

The Sine Function Model I & II (SFM I & II) use the equations to represent geometrical surface to form the 3-dimensional RUC shapes of textile composites. To obtain the 3-dimensional shapes, several geometrical input parameters are introduced, and after using a numerical integration scheme and calculating the equivalent stiffness and compliance of RUC, the RUC effective moduli are predicted. This study has shown that these modeling are very simple schemes compared to a detailed 3-D finite element analysis requiring complex geometrical modeling, i.e. mesh-generation, and theoretical formulations.

The comparison of the results calculated from the SFM I and II and other several models have indicated that the SFM I and II have a good capability of predicting the equivalent modulus of the textile composite RUC. The model's ability to be used for numerical homogenizations for the textile composites was illustrated by a series of numerical examples. The SFM I & II and sub-cell block model also are capable of predicting the mechanical characteristics and coefficients of thermal expansion (CTE) of the RUC based on the iso-strain assumption and the strain energy. Although the SFM I & II show good geometrical modeling capabilities, there are some limitations of representing complex geometry of textile composite structures, i.e., the 2x2 2-D tri-axial braids. In case of the 2x2 2-D tri-axial braids, more intricate numerical schemes and geometry assumptions are required to get the equivalent stiffness and compliance of RUC. This limitation can be removed in future.

11.3 The Failure Analysis of Micro-Cracked Textile Composite

The failure analyses of the micro-cracked textile composites were started with the assumptions of degraded textile yarns using the micro-mechanical equations and a crack-density scheme. The unique feature of this approach is that the micro-cracked textile composite can be analyzed by a damage modeling scheme that degrades the stiffness and implements it in a commercial finite element program (ABAQUS) by using the concept of user define material subroutine (UMAT). From several numerical examples, the failure analysis of the micro-cracked textile composites indicates good agreements with other results available in the existing literature.

However, our model still needs many improvements to predict failure strengths of the degraded textile composites. To represent the matrix properties, a more accurate stress-strain relationship is needed to incorporate non-linear constitutive behavior of the complex textile composites. This is because the textile yarns are considerably dependent on the complex geometry, such as the crimp angles. This study uses the general power law used in the unidirectional composites. The power law effectively worked in the unidirectional composite behaviors, while this power law is only partially useful in representing the textile composite behaviors. Another problem is the predicted degradation factors to be well coincident with the experiment data. In future study, a more exact degradation factors based on the stress and strain components have to be found.

11.4 The Contact and Impact Mechanics of Cohesive Element Modeling

The discontinuous crack element, cohesive element, has been introduced to describe crack shapes and propagations in the damaged solid structures. This study has extended the fundamental continuum equations of cohesive zone model to dynamic fracture problems including the contact and impact phenomena. In several examples, the cohesive element modeling has proved to be a good computational model for studying dynamic fracture when the structures are subjected to impact loading and where contact forces during impact act on the target and the projectile structures.

From a deeper understanding of the cohesive element modeling, this study has tried to investigate the dynamic fracture of textile layered and multi-layered structures. In this study, some contact algorithms for

continuous cracking and discontinuous cracking elements, such as empirical contact, surface contact and erosion scheme are presented. A good separation algorithm in contact simulations has shown an ability to analyze the complex dynamic fractures such as cracking elements and post-ruptured elements.
Although these contact algorithms have efficiently analyzed the complex dynamic cracking, some improvements are needed to apply more elaborate modeling, i.e. 3-dimensional contact model, because the 2-dimensional contact algorithms can not be applied to the 3-dimensional contact conditions. The 3-dimensional contact modeling has a more comprehensive contact modeling approach, the so called master and slave structures, and complex crack phases during the contact process also are involved. Another problem is the friction contact modeling. The friction contact problem is one of challenges to be met in a future study.
To implement penetrations of homogeneous structures, a simple combined impact modeling based on the empirical impact approach and cohesive element modeling was introduced. The combined impact modeling was verified by the comparisons between this study and previous literature. The combined impact modeling has been considerably useful at the low impact velocity, while over-predicted values were calculated at the high impact velocity. The over-predicted values of penetration displacement, velocity and force were induced from unknown empirical parameters that are estimated from the experiments of high velocity penetrations. To avoid the over-predicted values, the cohesive elements with a hydrodynamic theory and an erosion contact algorithm were applied into the high velocity penetrations of multi-layered structures. In addition dynamic behaviors of the multi-layered structures using the cohesive element modeling were studied by different impact directions and impact velocities, normalized kinetic and internal energies.
Although the cohesive element analysis shows good numerical results for the high impact penetration, some shortcomings are there in our numerical models. As the finite element analyses induce errors when different element mesh sizes and target material types (brittle/ductile) are applied into the high velocity penetration studies, the cohesive element modeling induces similar errors. In future research, a better understanding of the penetration mechanisms as modeled in the cohesive element analysis is needed to overcome this limitation.

11.5 The Impact Analysis of Micro-Cracked Textile Composites

An integrated numerical modeling has been developed which can be used to analyze the armor plates, such as micro-cracked textile layered plates on the ballistic performance. This 2-dimensional penetration model simulates the dynamic response of both the projectile and armor plate under an impact. This modeling has been started from a micro-mechanical level in which the fill and warp yarns have transverse micro-cracking of matrix and used degraded properties calculated by micro-mechanical equations. This model was extended to a layer-wise level and ultimately to a structural level analysis, i.e. macro-modeling consisting of a number of Repeating Unit Cells. Using these three level hierarchies, the textile layered and armor plates have been analyzed. Although changes in geometrical yarn shapes and degraded yarn stiffness have been used, the results of three different textile layered armor structures have shown some similar dynamic behaviors against normal or oblique impact projectiles at high impact speeds.
In future study, a more accurate computational modeling, micro-scale modeling, for the textile layered structures is needed to simulate the exact dynamic fracture behaviors during penetration by a projectile, because the three hierarchical analyses is based on maso-scale dimensions and has a limitation to obtain a detailed fracture formations. However the micro-scale modeling has some limitations in simulating the textile layered armor plates; requirement for a large number of elements and thus large computational time is required. Similarly, more efficient computational algorithms for the ballistic penetration must be developed in a future study.

Appendix A: Transformation Matrix of Yarns

The transformation matrix (T) for the strain equation is specified by the rotation angle (θ_r) and the crimp angle (θ_{c1}, θ_{c2} or θ_c) shown in Figure A-1. The rotation angle rotates about the z-axis and the crimp angle rotates about the x-axis, simultaneously. A small yarn region can be defined as a function of the rotation and crimp angles along the undulation geometry. The components for the transformation matrix are

$$[T] = \begin{bmatrix} a_{11}^2 & a_{12}^2 & a_{13}^2 & a_{12}a_{13} & a_{11}a_{13} & a_{11}a_{12} \\ a_{21}^2 & a_{22}^2 & a_{23}^2 & a_{22}a_{23} & a_{23}a_{21} & a_{21}a_{22} \\ a_{31}^2 & a_{32}^2 & a_{33}^2 & a_{32}a_{33} & a_{31}a_{33} & a_{31}a_{32} \\ 2a_{21}a_{31} & 2a_{32}a_{22} & 2a_{23}a_{33} & (a_{22}a_{33}+a_{23}a_{32}) & (a_{23}a_{31}+a_{21}a_{33}) & (a_{21}a_{32}+a_{22}a_{31}) \\ 2a_{11}a_{31} & 2a_{12}a_{32} & 2a_{13}a_{33} & (a_{32}a_{13}+a_{33}a_{12}) & (a_{11}a_{33}+a_{13}a_{31}) & (a_{31}a_{12}+a_{32}a_{11}) \\ 2a_{11}a_{21} & 2a_{12}a_{22} & 2a_{13}a_{33} & (a_{12}a_{23}+a_{13}a_{22}) & (a_{13}a_{21}+a_{11}a_{23}) & (a_{11}a_{22}+a_{12}a_{21}) \end{bmatrix}$$

Here, the components of a_{ij} (i and j =1~3) are expressed by

$$[a] = \begin{bmatrix} \cos(\theta_c)\cos(\theta_r) & \sin(\theta_r)\cos(\theta_c) & \sin(\theta_c) \\ -\sin(\theta_r) & \cos(\theta_r) & 0 \\ -\cos(\theta_r)\sin(\theta_c) & -\sin(\theta_r)\sin(\theta_c) & \cos(\theta_c) \end{bmatrix} \quad \text{(A.1)}$$

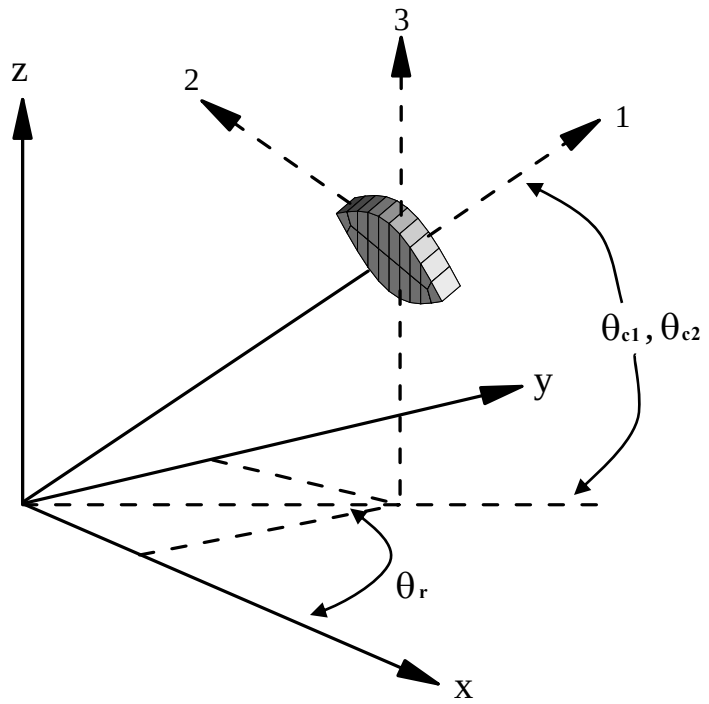

Figure A-1: Yarn directions in the x - y - z and 1-2-3 coordinates.

Appendix B: Transformation Stiffness Matrix of Yarns

To calculate the transformation stiffness matrices of the fill and warp yarns, the average phase values for the stress and strain are considered. By using the average phase value of stress, $\overline{\sigma} = \sum v_r \overline{\sigma}_r$, $\sum v_r = 1$, we assume that each yarn consists of the total N number of yarn slices and that each yarn slice involves transversely isotropic materials. The relationships between the 1-2-3 local and $x-y-z$ global coordinates will be described as the transformation matrix, suggested in Appendix A. So, the average phase value of stress is rewritten in matrix forms:

$$\begin{aligned}\{\overline{\sigma}\} &= V_{f1}\ \{\overline{\sigma}\}_{fill} + V_{f2}\ \{\overline{\sigma}\}_{warp} + V_f^r\ \{\overline{\sigma}\}_{resin} \\ &= V_{f1}\ \left[\overline{C}_{eqf}\right]\ \{\overline{\varepsilon}\}_{fill} + V_{f2}\ \left[\overline{C}_{eqw}\right]\ \{\overline{\varepsilon}\}_{warp} + V_f^r\ \left[\overline{C}_{eqr}\right]\ \{\overline{\varepsilon}\}_{resin}\end{aligned} \quad \text{(B.1)}$$

Let us consider the iso-strain assumption, $\{\overline{\varepsilon}\} = \{\overline{\varepsilon}\}_{fill} = \{\overline{\varepsilon}\}_{warp} = \{\overline{\varepsilon}\}_{resin}$, in Eq. (B.1). The Eq. (B.1) is rewritten as:

$$\{\overline{\sigma}\} = \frac{1}{V}\left[\ \sum_{m=1}^{N} v_m^f\ \left[\overline{C}_{eqf}\right] + \sum_{m=1}^{N} v_m^w\ \left[\overline{C}_{eqw}\right] + \sum_{m=1}^{N} v_m^r\ \left[\overline{C}_{eqr}\right]\ \right]\ \{\overline{\varepsilon}\} \quad \text{(B.2)}$$

Here, v_m^f , v_m^w and v_m^r mean the volumes of fill, warp and resin for the m^{th} yarn slice, respectively. From Eqs. (B.1) and (B.2), the transformation stiffness matrices will be derived:

$$\left[\overline{C}_{eqf}\right] = \left[T_m\right]_{fill}^T\ \left[C^f\right]_m\ \left[T_m\right]_{fill},\ \left[\overline{C}_{eqw}\right] = \left[T_m\right]_{warp}^T\ \left[C^w\right]_m\ \left[T_m\right]_{warp} \quad \text{(B.3)}$$

Here, superscript T means transposed matrix and C_{ij}^f and C_{ij}^w (6×6) are stiffness matrices of the fill and warp for the m^{th} yarn slice. By applying the transformation matrix and the rotation angles of fill and warp yarns, the transformation stiffness matrices can be found. For the fill and warp yarns, the rotation angles $\theta_r = \pi/2$ and $\theta_r = 0$ are applied to Eq. (A.1), and then the transformation matrices in the m^{th} yarn slice $\left[T_m\right]_{fill}$ and $\left[T_m\right]_{warp}$ are derived. The crimp angles (θ_{c1} , θ_{c2} or θ_c) of fill and warp yarns, are defined as $s = \sin(\theta_c)$ and $c = \cos(\theta_c)$. So the transformation matrices for the m^{th} yarn slice in the fill and warp are:

$$\left[T_m\right]_{fill} = \begin{bmatrix} 0 & c^2 & s^2 & cs & 0 & 0 \\ 1 & 0 & 0 & 0 & 0 & 0 \\ 0 & s^2 & c^2 & -cs & 0 & 0 \\ 0 & 0 & 0 & 0 & c & s \\ 0 & -cs & cs & c^2-s^2 & 0 & 0 \\ 0 & 0 & 0 & 0 & s & c \end{bmatrix} \quad \text{(B.4)}$$

$$\left[T_m\right]_{warp} = \begin{bmatrix} c^2 & 0 & s^2 & 0 & cs & 0 \\ 0 & 1 & 0 & 0 & 0 & 0 \\ s^2 & 0 & c^2 & 0 & -cs & 0 \\ 0 & 0 & 0 & c & 0 & -s \\ -cs & 0 & cs & 0 & c^2-s^2 & 0 \\ 0 & 0 & 0 & s & 0 & c \end{bmatrix} \quad \text{(B.5)}$$

From equations (B.3), (B.4) and (B.5), the components of the transformation stiffness matrix, $\overline{C}_{eqf}^{ij}$ and $\overline{C}_{eqw}^{ij}$, (i & j =1~6) are obtained.

$$\left[\overline{C}_{eqw}\right] = \begin{bmatrix} \overline{C}_{eqw}^{11} & \overline{C}_{eqw}^{12} & \overline{C}_{eqw}^{13} & 0 & \overline{C}_{eqw}^{15} & 0 \\ \overline{C}_{eqw}^{21} & \overline{C}_{eqw}^{22} & \overline{C}_{eqf}^{23} & 0 & \overline{C}_{eqw}^{25} & 0 \\ \overline{C}_{eqw}^{13} & \overline{C}_{eqw}^{23} & \overline{C}_{eqw}^{33} & 0 & \overline{C}_{eqw}^{35} & 0 \\ 0 & 0 & 0 & \overline{C}_{eqw}^{44} & 0 & \overline{C}_{eqw}^{46} \\ \overline{C}_{eqw}^{15} & \overline{C}_{eqw}^{25} & \overline{C}_{eqw}^{35} & 0 & \overline{C}_{eqw}^{55} & 0 \\ 0 & 0 & 0 & \overline{C}_{eqw}^{46} & 0 & \overline{C}_{eqw}^{66} \end{bmatrix} \tag{B.6}$$

$$\left[\overline{C}_{eqf}\right] = \begin{bmatrix} \overline{C}_{eqf}^{11} & \overline{C}_{eqf}^{12} & \overline{C}_{eqf}^{13} & \overline{C}_{eqf}^{14} & 0 & 0 \\ \overline{C}_{eqf}^{21} & \overline{C}_{eqf}^{22} & \overline{C}_{eqf}^{23} & \overline{C}_{eqf}^{24} & 0 & 0 \\ \overline{C}_{eqf}^{13} & \overline{C}_{eqf}^{23} & \overline{C}_{eqf}^{33} & \overline{C}_{eqf}^{34} & 0 & 0 \\ \overline{C}_{eqf}^{14} & \overline{C}_{eqf}^{24} & \overline{C}_{eqf}^{34} & \overline{C}_{eqf}^{44} & 0 & 0 \\ 0 & 0 & 0 & 0 & \overline{C}_{eqf}^{55} & \overline{C}_{eqf}^{56} \\ 0 & 0 & 0 & 0 & \overline{C}_{eqf}^{56} & \overline{C}_{eqf}^{66} \end{bmatrix} \tag{B.7}$$

In equations (B.6) and (B.7), the components of the transformation stiffness matrix in the warp yarn are

$$\begin{aligned}
&\overline{C}_{eqw}^{11} = C_{11}^{w}\ c^4 + (2C_{55}^{w} + C_{13}^{w})\ c^2 s^2 + C_{33}^{w}\ s^4,\ \overline{C}_{eqw}^{12} = C_{12}^{w}\ c^2 + C_{23}^{w}\ s^2 \\
&\overline{C}_{eqw}^{13} = C_{13}^{w}\ (c^4 + s^4) + (C_{11}^{w} + C_{33}^{w} - 2C_{22}^{w})\ c^2 s^2, \\
&\overline{C}_{eqw}^{15} = C_{11}^{w}\ sc^3 - C_{33}^{w}\ cs^3 - (C_{13}^{w} + C_{55}^{w})\ (c^2 - s^2)\ cs, \\
&\overline{C}_{eqw}^{22} = C_{22}^{w}\ ,\ \overline{C}_{eqw}^{23} = C_{12}^{w}\ s^2 + C_{23}^{w}\ c^2,\ \overline{C}_{eqw}^{25} = (C_{12}^{w} - C_{23}^{w})\ cs\ , \\
&\overline{C}_{eqw}^{33} = C_{11}^{w}\ s^4 + (2C_{55}^{w} + C_{13}^{w})\ c^2 s^2 + C_{33}^{w}\ c^4, \\
&\overline{C}_{eqw}^{35} = C_{11}^{w}\ cs^3 - C_{33}^{w}\ sc^3 + (C_{13}^{w} + C_{55}^{w})\ (c^2 - s^2)\ cs, \\
&\overline{C}_{eqw}^{44} = C_{44}^{w}\ c^2 + C_{55}^{w}\ s^2,\ \overline{C}_{eqw}^{46} = (C_{55}^{w} - C_{44}^{w})\ cs\ , \\
&\overline{C}_{eqw}^{55} = C_{55}^{w}\ (c^4 + s^4) + (C_{11}^{w} + C_{33}^{w} - C_{13}^{w} - C_{55}^{w})\ c^2 s^2, \overline{C}_{eqw}^{66} = C_{44}^{w}\ s^2 + C_{55}^{w}\ c^2
\end{aligned} \tag{B.8}$$

While the components of the transformation stiffness matrix in the fill yarn are

$$\begin{aligned}
&\overline{C}_{eqf}^{11} = C_{22}^{f}\ , \overline{C}_{eqf}^{12} = C_{12}^{f}\ c^2 + C_{23}^{f}\ s^2, \\
&\overline{C}_{eqf}^{13} = C_{12}^{f}\ s^2 + C_{23}^{f}\ c^2, \overline{C}_{eqf}^{14} = (C_{12}^{f} - C_{23}^{f})\ cs\ , \\
&\overline{C}_{eqf}^{22} = C_{11}^{f}\ c^4 + (2C_{55}^{f} + C_{13}^{f})\ c^2 s^2 + C_{33}^{f}\ s^4, \\
&\overline{C}_{eqf}^{23} = C_{13}^{f}\ (c^4 + s^4) + (C_{11}^{f} + C_{33}^{f} - 2C_{55}^{f})\ c^2 s^2, \\
&\overline{C}_{eqf}^{24} = C_{11}^{f}\ sc^3 - C_{33}^{f}\ cs^3 - (C_{13}^{f} + C_{55}^{f})\ (c^2 - s^2)\ cs, \\
&\overline{C}_{eqf}^{33} = C_{11}^{f}\ s^4 + (2C_{55}^{f} + C_{13}^{f})\ c^2 s^2 + C_{33}^{f}\ c^4, \\
&\overline{C}_{eqf}^{34} = C_{11}^{f}\ sc^3 - C_{33}^{f}\ sc^3 + (C_{13}^{f} + C_{55}^{f})\ (c^2 - s^2)\ cs, \\
&\overline{C}_{eqf}^{44} = C_{55}^{f}\ (c^4 + s^4) + (C_{11}^{f} + C_{33}^{f} - C_{13}^{f} - C_{55}^{f})\ c^2 s^2, \\
&\overline{C}_{eqf}^{55} = C_{44}^{f}\ c^2 + C_{55}^{f}\ s^2,\ \overline{C}_{eqf}^{56} = (C_{55}^{f} - C_{44}^{f})\ cs\ , \overline{C}_{eqf}^{66} = C_{44}^{f}\ s^2 + C_{55}^{f}\ c^2
\end{aligned} \tag{B.9}$$

Appendix C: Assumptions of Micro-cracking in Composites

This study uses the following basic assumptions for the micro-crack in composites:

i) Micro-cracks of a small scale are present in the matrix material.
ii) Slit cracks grow perpendicular to the ply's plane and parallel to its longitudinal fiber direction.
iii) They have small effects on the strength, but change the elastic modulus of multi-directionally-fiber composite.
iv) Matrix cracking is present at low load levels.

The schematic shapes of the micro-cracks are described in Figures C-1 and C-2. When the micro-cracked composites are subjected to compression and tension loads along the transverse direction of fibers, then can be feature two behaviors: crack opening and closing, see Figure C-3, respectively. To model the micro-cracking in composites, this research considers the Self-Consistent model of Laws *et al.* The fundamental assumptions of Self-Consistent model are:

i) Longitudinal slit cracks are considered.
ii) Materials and fibers are transversely isotropic with respect to fiber axis.
iii) Overall behavior of the cracked composite are orthotropic.
iv) Three-phase or two-phase model depending on the fiber diameter relative to an effective medium.

For a better understanding of the concept of micro-crack phases, see Figs. C-4 and C-5.

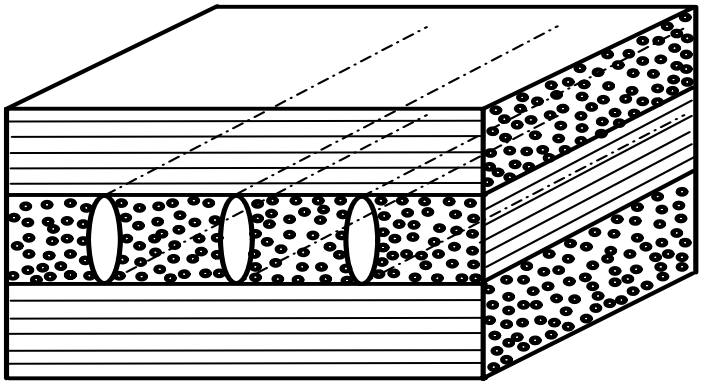

Figure C-1: Transverse micro-cracks in unidirectional plies.

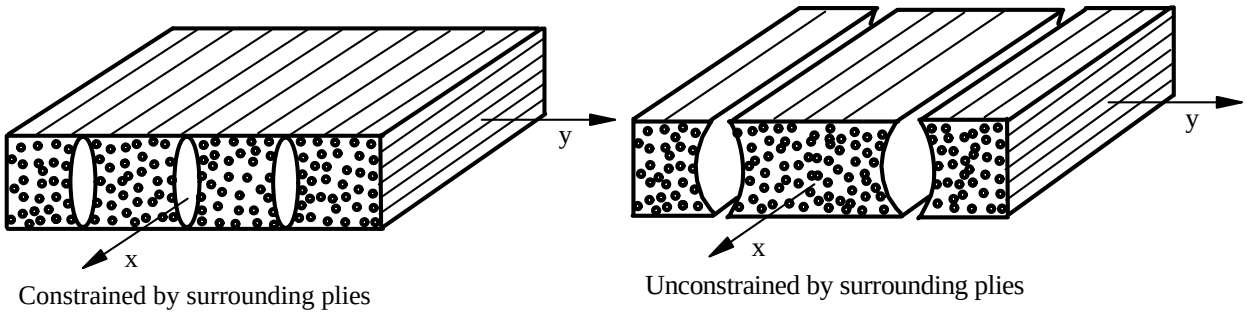

Figure C-2: Constraining behavior of adjoining plies on cracked plies.

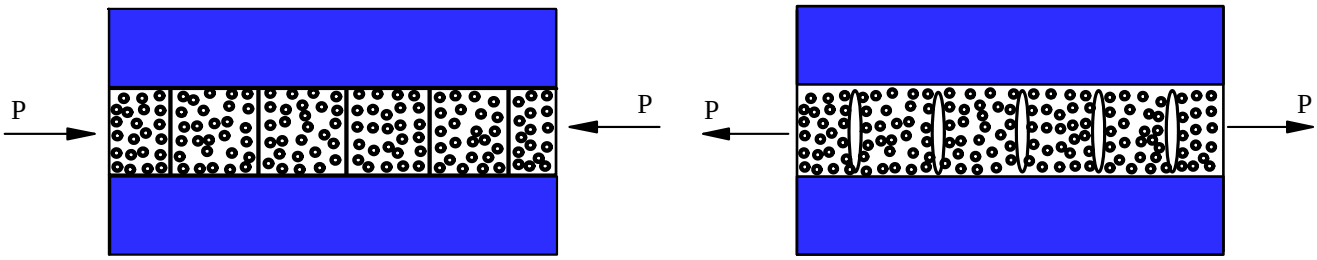

Figure C-3: A cracked ply's crack opening and closing.

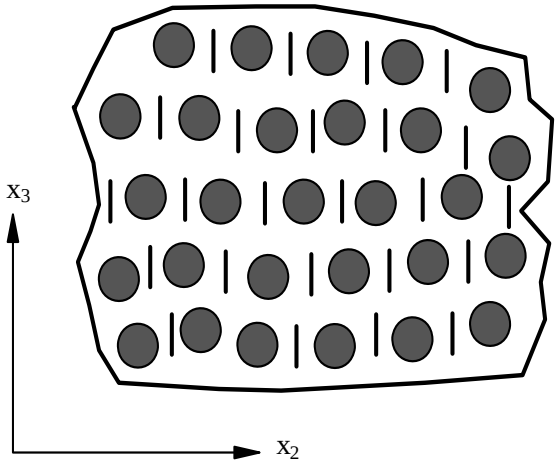

Figure C-4: A three-phase medium with longitudinal slit cracks.

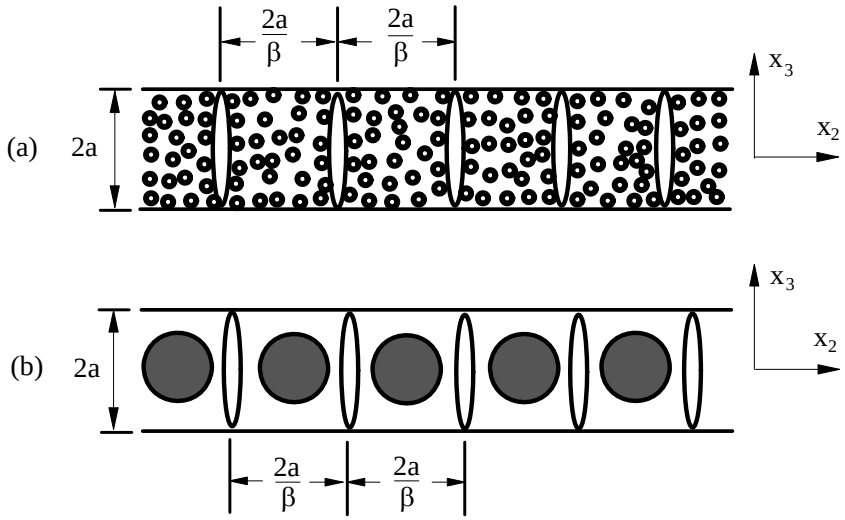

Figure C-5: (a) A two-phase filament mono-layer, (b) a three-phase filament mono-layer.

Appendix D: Micro-mechanical Model of Fiber Composites

To predict the effective engineering moduli for the micro-mechanical model of fibers in the textile yarns, the fiber is assumed in the form of a square shaped fiber in contact with two matrix regions, see Figure D-1. There are three regions, i.e., the fiber, the matrix region m_A and m_B, such as the three sub-cells. The relative dimensions of fiber and matrix regions can be given in terms of volume fractions (c_f).

$$W_f = \sqrt{c_f}\,,\; W_m = 1-\sqrt{c_f} \tag{D.1}$$

To obtain the effective stress and strain in the sub-cells, the constitutive relations for the matrix and fiber are considered. First, we assume that the axial fiber direction strains (ε_L) are the same in the fiber and the matrix and that the transverse stress (σ_T) are the same in the fiber and the matrix. The complementary stress (σ_L) and strain (ε_T) are written as

$$\left\{\begin{matrix}\varepsilon_L\\ \sigma_T\end{matrix}\right\}_A = \left\{\begin{matrix}\varepsilon_L\\ \sigma_T\end{matrix}\right\}_f = \left\{\begin{matrix}\varepsilon_L\\ \sigma_T\end{matrix}\right\}_m,\; \left\{\begin{matrix}\varepsilon_L\\ \sigma_T\end{matrix}\right\}_A = \left\{\begin{matrix}\varepsilon_L\\ \sigma_T\end{matrix}\right\}_f = \left\{\begin{matrix}\varepsilon_L\\ \sigma_T\end{matrix}\right\}_m \tag{D.2}$$

Second, in the matrix regions A and B there are assumed to be the same strains, and the effective stresses are expressed as the average stresses on the matrix regions A and B.

$$\{\varepsilon\}_C = \{\varepsilon\}_A = \{\varepsilon\}_B,\; \{\sigma\}_C = W_f\{\sigma\}_A + W_m\{\sigma\}_B \tag{D.3}$$

Here the subscript C means the effective values. Using these assumptions, the effective elastic constants for the composites are obtained as

$$Q_{ij}^C = \sqrt{c_f}\,Q_{ij}^A + (1-\sqrt{c_f})Q_{ij}^B \tag{D.4}$$

Here Q is the reduced plane stiffness for the matrix in regions A and B, respectively.

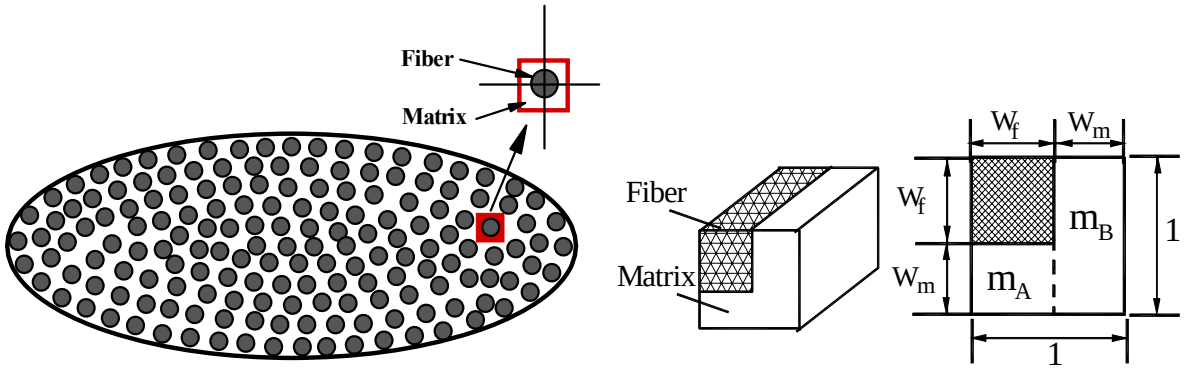

Figure D-1: Square fiber model and volume fractions in the square fiber system.

Appendix E: Elastic-Plastic Implementation

To address the elastic-plastic problem, it is necessary to consider a modeling of plastic flow in materials. Hill suggested a plastic flow theory[E-1] for the anisotropic material. From Hill's theory, the yield or the loading function, f , is defined as:

$$f = \frac{1}{2(F+G+H)}[F(\sigma_y - \sigma_z)^2 + G(\sigma_z - \sigma_x)^2 + H(\sigma_x - \sigma_y)^2 + 2L\tau_{yz}^2 + 2M\tau_{zx}^2 + 2N\tau_{xy}^2] = k \quad \text{(E.1)}$$

in which F , G , H , L , M and N are material parameters. In this equation, the hardening parameter, k , represents the size of the yield surface. Let's introduce the following function, Q ;

$$Q = f - k = 0 \quad \text{(E.2)}$$

To get the plastic strain increments, let us consider a potential function $g = f$. Then, the plastic strain increments are given as:

$$d\varepsilon_{ij}^p = d\lambda \frac{\partial g}{\partial \sigma_{ij}} = d\lambda \frac{\partial f}{\partial \sigma_{ij}}, \quad \{d\varepsilon^p\} = d\lambda \left\{\frac{\partial f}{\partial \sigma}\right\} \quad \text{(E.3)}$$

Here,

$$\{d\varepsilon^p\}^T = \{d\varepsilon_x^p \quad d\varepsilon_y^p \quad d\varepsilon_z^p \quad d\gamma_{yz}^p \quad d\gamma_{zx}^p \quad d\gamma_{xy}^p\},$$
$$\left\{\frac{\partial f}{\partial \sigma}\right\}^T = \left\{\frac{\partial f}{\partial \sigma_x} \quad \frac{\partial f}{\partial \sigma_y} \quad \frac{\partial f}{\partial \sigma_z} \quad \frac{\partial f}{\partial \tau_{yz}} \quad \frac{\partial f}{\partial \tau_{zx}} \quad \frac{\partial f}{\partial \tau_{xy}}\right\} \quad \text{(E.4)}$$

While, $d\lambda$ is a positive scalar of proportionality. The shear components used here are, the engineering plastic increments, i.e., $d\gamma_{yz}^p = 2d\varepsilon_{yz}^p$ and so on. Using the yield function, Eq. (E.1), the plastic strain increments are as follows:

$$d\varepsilon_x^p = d\lambda \frac{\partial f}{\partial \sigma_x} = \frac{d\lambda}{F+G+H}[H(\sigma_x - \sigma_y) + G(\sigma_x - \sigma_z)] = \sigma_x' d\lambda$$
$$d\varepsilon_y^p = d\lambda \frac{\partial f}{\partial \sigma_y} = \frac{d\lambda}{F+G+H}[F(\sigma_y - \sigma_z) + H(\sigma_y - \sigma_x)] = \sigma_y' d\lambda$$
$$d\varepsilon_z^p = d\lambda \frac{\partial f}{\partial \sigma_z} = \frac{d\lambda}{F+G+H}[G(\sigma_z - \sigma_x) + F(\sigma_z - \sigma_y)] = \sigma_z' d\lambda$$
$$d\gamma_{yz}^p = d\lambda \frac{\partial f}{\partial \tau_{yz}} = \frac{d\lambda}{F+G+H}[2L\tau_{yz}] = 2\tau_{yz}' d\lambda$$
$$d\gamma_{zx}^p = d\lambda \frac{\partial f}{\partial \tau_{zx}} = \frac{d\lambda}{F+G+H}[2M\tau_{zx}] = 2\tau_{zx}' d\lambda$$
$$d\gamma_{xy}^p = d\lambda \frac{\partial f}{\partial \tau_{xy}} = \frac{d\lambda}{F+G+H}[2N\tau_{xy}] = 2\tau_{xy}' d\lambda \quad \text{(E.5)}$$

In which, the stress are

$$\sigma_x' = \frac{\partial f}{\partial \sigma_x} = \frac{H(\sigma_x - \sigma_y) + G(\sigma_x - \sigma_z)}{F+G+H}$$
$$\sigma_y' = \frac{\partial f}{\partial \sigma_y} = \frac{F(\sigma_y - \sigma_z) + H(\sigma_y - \sigma_x)}{F+G+H}$$
$$\sigma_z' = \frac{\partial f}{\partial \sigma_z} = \frac{G(\sigma_z - \sigma_x) + F(\sigma_z - \sigma_y)}{F+G+H}$$
$$\tau_{yz}' = \frac{1}{2}\frac{\partial f}{\partial \tau_{yz}} = \frac{L\tau_{yz}}{F+G+H}$$

$$\tau'_{zx} = \frac{1}{2}\frac{\partial f}{\partial \tau_{zx}} = \frac{M\tau_{zx}}{F+G+H}$$

$$\tau'_{xy} = \frac{1}{2}\frac{\partial f}{\partial \tau_{xy}} = \frac{N\tau_{xy}}{F+G+H} \tag{E.6}$$

In matrix form, these plastic increments and the generalized stress components are

$$\{d\varepsilon^p\} = \{\sigma'\}d\lambda\,,\ \{\sigma'\} = \left\{\frac{\partial f}{\partial \sigma}\right\},\ \{\sigma'\}^T = \{\sigma'_x \quad \sigma'_y \quad \sigma'_z \quad 2\tau'_{yz} \quad 2\tau'_{zx} \quad 2\tau'_{xy}\} \tag{E.7}$$

In the isotropic case, the material parameters, F, G, H, L, M and N are

$$3F = 3G = 3H = L = M = N \tag{E.8}$$

It is necessary to get the matrices of the effective plastic stress and strain Effective Plastic Stress and Strain. Let's define the effective or equivalent stress within the von Mises theory for the isotropic material case. The effective or equivalent stress $\bar{\sigma}_e$ as follows:

$$\bar{\sigma}_e^2 = \frac{3}{2}\frac{1}{(F+G+H)}[F(\sigma_y-\sigma_z)^2 + G(\sigma_z-\sigma_x)^2 + H(\sigma_x-\sigma_y)^2 + 2L\tau_{yz}^2 + 2M\tau_{zx}^2 + 2N\tau_{xy}^2] \tag{E.9}$$

The plastic work increment dW_p is represented by:

$$dW_p = \sigma_x d\varepsilon_x^p + \cdots + \tau_{yz} d\gamma_{yz}^p + \cdots \tag{E.10}$$

Using Eqs. (E.5) and (E.10), the plastic work increment is:

$$dW_p = \frac{2}{3}\bar{\sigma}_e^2 d\lambda \tag{E.11}$$

This equation is obtained by comparing Eqs.(E.5) and Eq.(E.7), $f = \bar{\sigma}_e^2/3$, and then the plastic work increment dW_p is

$$dW_p = \sigma_{ij} d\varepsilon_{ij}^p = \sigma_{ij}\frac{\partial f}{\partial \sigma_{ij}}d\lambda = 2f d\lambda = \frac{2}{3}\bar{\sigma}_e^2 d\lambda \tag{E.12}$$

Eqs. (E.11) and (E.12) are redefined as:

$$dW_p = \bar{\sigma}_e d\varepsilon_p = \bar{\sigma}_e \frac{2}{3}\bar{\sigma}_e d\lambda\,,\ d\varepsilon_p = \frac{2}{3}\bar{\sigma}_e d\lambda \tag{E.13}$$

To get the effective plastic strain increment in terms of plastic strain increments, $d\varepsilon_x^p$,… $d\gamma_{xy}^p$, the following manipulations of Eq. (E.13) are needed:

$$Gd\varepsilon_y^p - Hd\varepsilon_z^p = \frac{d\lambda}{F+G+H}(FG+GH+HF)(\sigma_y-\sigma_z) \tag{E.14}$$

$$(\sigma_y-\sigma_z) = \frac{Gd\varepsilon_y^p - Hd\varepsilon_z^p}{FG+GH+HF}\frac{F+G+H}{d\lambda}$$

$$(\sigma_z-\sigma_x) = \frac{Hd\varepsilon_z^p - Fd\varepsilon_x^p}{FG+GH+HF}\frac{F+G+H}{d\lambda}$$

$$(\sigma_x-\sigma_y) = \frac{Fd\varepsilon_x^p - Gd\varepsilon_y^p}{FG+GH+HF}\frac{F+G+H}{d\lambda} \tag{E.15}$$

The shear components are

$$\tau_{yz} = \frac{d\gamma_{yz}^p}{2L}\frac{F+G+H}{d\lambda},\ \tau_{zx} = \frac{d\gamma_{zx}^p}{2M}\frac{F+G+H}{d\lambda},\ \tau_{xy} = \frac{d\gamma_{xy}^p}{2N}\frac{F+G+H}{d\lambda} \tag{E.16}$$

Substituting Eqs. (E.15) and (E.16) into Eq. (E.7),

$$\bar{\sigma}_e^2 = \frac{3}{2}\frac{F+G+H}{(d\lambda)^2}$$

$$[\frac{F(Gd\varepsilon_y^p - Hd\varepsilon_z^p)^2 + G(Hd\varepsilon_z^p - Fd\varepsilon_x^p)^2 + H(Fd\varepsilon_x^p - Gd\varepsilon_y^p)^2}{(FG+GH+HF)^2} + \frac{(d\gamma_{yz}^p)^2}{2L} + \frac{(d\gamma_{zx}^p)^2}{2M} + \frac{(d\gamma_{xy}^p)^2}{2N}] \tag{E.17}$$

from Eq. (E.1), the hardening parameter, k becomes

$$k = \frac{1}{3}\bar{\sigma}_e^2 \tag{E.18}$$

In order to derive the incremental elastic-plastic stress-strain relationships, the consistency equation is needed. Using Eq. (E.18), Eq. (E.2) is re-written as

$$Q = f - \frac{1}{3}\bar{\sigma}_e^2 = 0 \tag{E.19}$$

The consistency condition requires the state of stress to remain on the yield or on the loading surface during the plastic flow, that is $dQ = 0$.

$$dQ = df - \frac{2}{3}\bar{\sigma}_e d\bar{\sigma}_e = 0, \quad dQ = df - \frac{2}{3}\bar{\sigma}_e \frac{d\bar{\sigma}_e}{d\varepsilon_p} d\varepsilon_p = df - \frac{2}{3}\bar{\sigma}_e d\varepsilon_p H_p = 0 \tag{E.20}$$

Here $H_p = d\bar{\sigma}_e / d\varepsilon_p$, corresponding to the slope of the equilibrium stress, $\bar{\sigma}_e$, versus plastic strain curve ($\int d\varepsilon_p$). From Eq. (E.13), the consistency condition is

$$df - \frac{4}{9}\bar{\sigma}_e^2 H_p d\lambda = 0 \tag{E.21}$$

From Eq. (E.7), Eq.(E.21) is rewritten in matrix form as:

$$\{\sigma'\}^T \{d\sigma\} - \frac{4}{9}\bar{\sigma}_e^2 H_p d\lambda = 0 \tag{E.22}$$

In order to derive the incremental elastic-plastic stress-strain relationship, the positive scalar of proportionality, $d\lambda$ will also have to be determined. The stress increment is

$$[D^e]\{d\sigma\} = \{d\varepsilon\} - \{\sigma'\} d\lambda$$

$$\{d\sigma\} = [D^e]^{-1}(\{d\varepsilon\} - \{\sigma'\} d\lambda) = [C^e]\{d\varepsilon\} - [C^e]\{\sigma'\} d\lambda = [C^e]\{d\varepsilon\} - [S] d\lambda \tag{E.23}$$

Here the total strain increments are

$$\{d\varepsilon\} = \{d\varepsilon^p\} + \{d\varepsilon^e\} = \{\sigma'\} d\lambda + [D^e]\{d\sigma\}$$

$$\{d\varepsilon^e\} = [D^e]\{d\sigma\}, \ \{d\sigma\}^T = \{d\sigma_x \quad d\sigma_y \quad d\sigma_z \quad d\tau_{yz} \quad d\tau_{zx} \quad d\tau_{xy}\} \tag{E.24}$$

The increment of stress is written using the inverse matrix of [D^e].

$$\{d\sigma\} = [C^e]\{d\varepsilon^e\}$$

$$[C^e] = [D^e]^{-1} = \begin{bmatrix} c_{11} & c_{12} & c_{13} & 0 & 0 & 0 \\ c_{12} & c_{22} & c_{23} & 0 & 0 & 0 \\ c_{13} & c_{23} & c_{33} & 0 & 0 & 0 \\ 0 & 0 & 0 & c_{44} & 0 & 0 \\ 0 & 0 & 0 & 0 & c_{55} & 0 \\ 0 & 0 & 0 & 0 & 0 & c_{66} \end{bmatrix} \tag{E.25}$$

Also the matrix $[S]$ is $[C^e]\{\sigma'\}$. The components of $[S]$ are

$$[S] = [C^e]\{\sigma'\} = [s_1 \quad s_2 \quad s_3 \quad s_4 \quad s_5 \quad s_6]^T \tag{E.26}$$

The components of $[S]$ are

$$s_1 = c_{11}\sigma'_x + c_{12}\sigma'_y + c_{13}\sigma'_z, \ s_2 = c_{12}\sigma'_x + c_{22}\sigma'_y + c_{23}\sigma'_z, \ s_3 = c_{13}\sigma'_x + c_{23}\sigma'_y + c_{33}\sigma'_z,$$

$$s_4 = 2c_{44}\tau'_{yz}, \ s_5 = 2c_{55}\tau'_{zx}, \ s_6 = 2c_{66}\tau'_{xy} \tag{E.27}$$

Substitution Eq. (E.23) into Eq. (E.22), and yield

$$[\sigma']^T [C^e]\{d\varepsilon\} - [\sigma']^T [S] d\lambda - \frac{4}{9}\bar{\sigma}_e^2 H_p d\lambda = 0, \ [S]^T \{d\varepsilon\} - [\sigma']^T [S] d\lambda - \frac{4}{9}\bar{\sigma}_e^2 H_p d\lambda = 0 \tag{E.28}$$

The positive scalar of proportionality, $d\lambda$ is

$$d\lambda = \frac{[S]^T \{d\varepsilon\}}{\{\sigma'\}^T [S] + \frac{4}{9}\bar{\sigma}_e^2 H_P} \tag{E.29}$$

The denominator is

$$\{\sigma'\}^T [S] + \frac{4}{9}\bar{\sigma}_e^2 H_P = s_1\sigma'_x + s_2\sigma'_y + s_3\sigma'_z + 2s_4\tau'_{yz} + 2s_5\tau'_{zx} + 2s_6\tau'_{xy} + \frac{4}{9}\bar{\sigma}_e^2 H_P \tag{E.30}$$

By comparing Eqs.(E.23) and (E.29), the plastic stress increment is

$$\{d\sigma\} = [C^{ep}]\ \{d\varepsilon\} = \left\{ [C^e] - \frac{[S]\ [S]^T}{\{\sigma'\}^T [S] + \frac{4}{9}\bar{\sigma}_e^2 H_P} \right\} \{d\varepsilon\} \tag{E.31}$$

The elastic-plastic stress-strain matrix, $[C^{ep}]$ is

$$[C^{ep}] = [C^e] - \frac{[S]\ [S]^T}{\{\sigma'\}^T [S] + \frac{4}{9}\bar{\sigma}_e^2 H_P},\ [C^{ep}] = [C^e] - \frac{[S]\ [S]^T}{s},\ s = \{\sigma'\}^T [S] + \frac{4}{9}\bar{\sigma}_e^2 H_P \tag{E.32}$$

$$[C^{ep}] = \begin{bmatrix}
c_{11} - \frac{s_1^2}{s} & & & & & \\
c_{12} - \frac{s_1 s_2}{s} & c_{22} - \frac{s_2^2}{s} & & & \textit{sym.} & \\
c_{13} - \frac{s_1 s_3}{s} & c_{23} - \frac{s_2 s_3}{s} & c_{33} - \frac{s_3^2}{s} & & & \\
-\frac{s_1 s_4}{s} & -\frac{s_2 s_4}{s} & -\frac{s_3 s_4}{s} & c_{44} - \frac{s_4^2}{s} & & \\
-\frac{s_1 s_5}{s} & -\frac{s_2 s_5}{s} & -\frac{s_3 s_5}{s} & -\frac{s_4 s_5}{s} & c_{55} - \frac{s_5^2}{s} & \\
-\frac{s_1 s_6}{s} & -\frac{s_2 s_6}{s} & -\frac{s_3 s_6}{s} & \frac{s_4 s_6}{s} & -\frac{s_5 s_6}{s} & c_{66} - \frac{s_6^2}{s}
\end{bmatrix} \tag{E.33}$$

Similar elastic-plastic equations are also suggested in Ref. [E-1]. To describe tangent stiffness for the plastic stress increment, Eq. (E.31) is re-written in vector form $\Delta\boldsymbol{\sigma} = \mathbf{C}^{ep}\Delta\boldsymbol{\varepsilon}$. The element tangent stiffness for the increments is defined with the strain-displacement matrix $\mathbf{B}$.

$$\mathbf{K}_{ep} = \int_V \mathbf{B}^T \mathbf{C}^{ep}\ \mathbf{B}\ dV \tag{E.34}$$

The increment of element nodal forces are given as

$$\Delta\mathbf{F} = \mathbf{K}_{ep}\Delta\mathbf{u} \tag{E.35}$$

Appendix F: Numerical Verifications of Degenerated Shell Program

In this Appendix, the program of degenerated shell element is verified by comparing its results with the numerical results available in the literature. These examples cover static problems of the plate and shell structures. This study considers one plate and three shell structures to check the accuracy of the present program of degenerated shell element. The presented numerical examples were suggested in Hsiao[F-1] and Bathe and Ho[F-2], and our present solutions for the shell model are compared to their results. This study also considers work-increment-control method[F-3,F-4] to solve incremental-iterative step problems the shell structures.

1. Cantilever Plate with an End Moment

First, this study considers a cantilever plate with an end moment shown in Figure.F-1. It is modeled by 10 elements and is rotated 2π radians under the load of the end moment. The analytical solution to this classical elastic problem corresponds to a beam "rolled-up" into a circular arc of radius r and is given by $1/r = M/EI$ where M is applied end moment. A complete circle is obtained at $M = 2\pi EI/L$ where L is the length of the cantilever. This example was run using twenty elements with the following physical and geometrical properties: Young's modulus $E = 1.2\times10^5 KN/m^2$, Poisson's ratio $\nu = 0.0$, length $L = 10$ m, width $b = 1.0$ m and thickness $h = 0.1$ m.

The number of iterations required for each increment with the error tolerance of 0.0005 is about five. The deformed configurations are illustrated in Figure F-2. Our numerical results on the load-deflection are in very good agreement with the results by Hsiao[F-1] using 3 increments and by Bathe and Ho[F-2] using 12 load increments and 10-elements, see Figure F-3.

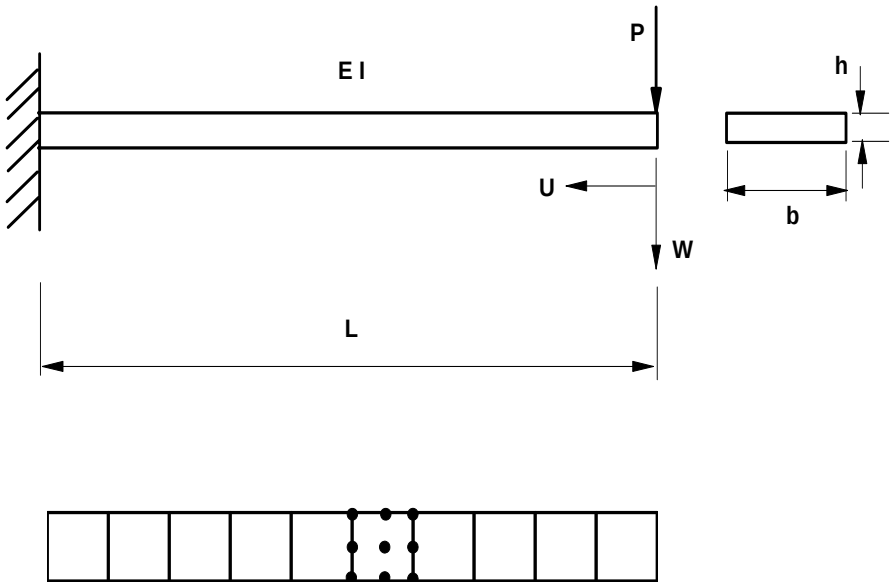

Figure F-1: Cantilever plate with an end moment.

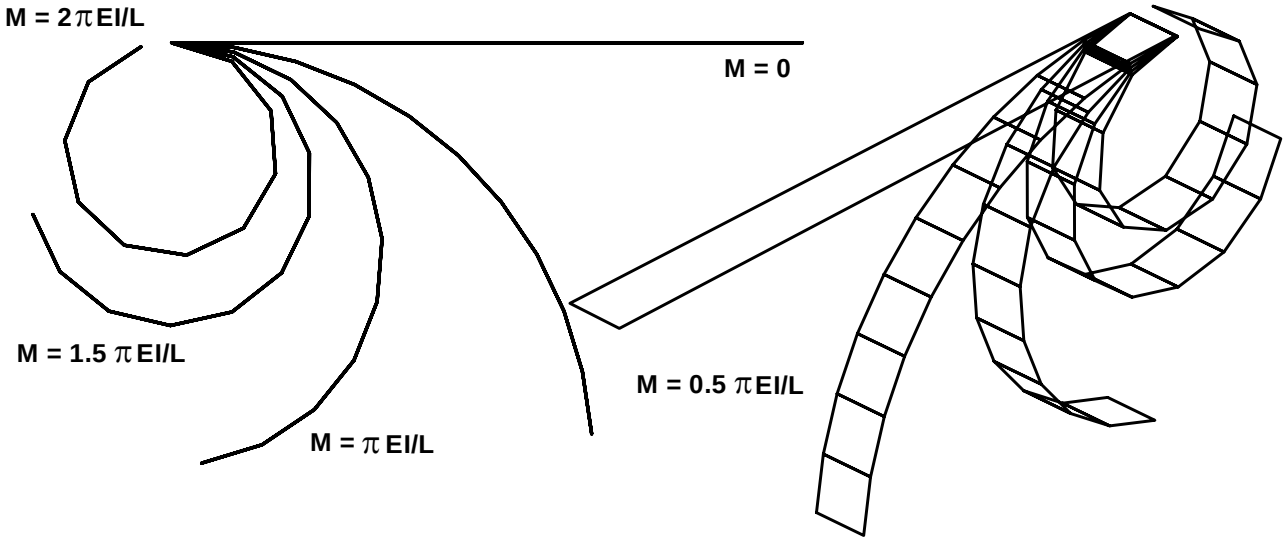

Figure F-2: Deformed cantilever plates with an end moment.

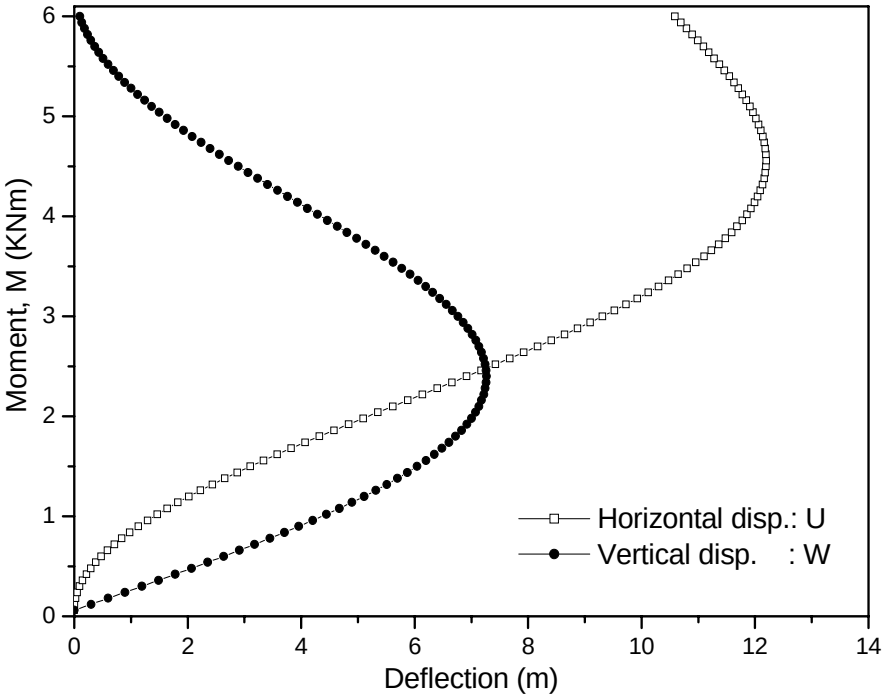

Figure F-3: Deflection curves of a cantilever plate with an end moment.

2. Hinged Cylindrical Shell Cases with a Concentrated Central Load

Figure F-4 shows circular cylindrical shells subjected to the concentrated central load. The boundary conditions in the longitudinal direction are hinged and immovable, whereas the curved edges are completely free and the center point is loaded. In this study, a symmetrical model is used, like one-quarter of the shell analyzed with a 10×10 grid. The two shell cases, different thickness, are performed to find the phenomenon of snap-back, such as $h=12.7$ mm and $h=6.35$ mm, see Figure F-4. Young's modulus is taken as $E=3.10275\text{KN/mm}^2$ and Poisson's ratio as 0.3. Figures F-5 and F-6 show the snap-back curve for the case of $h=12.7$ mm. To get load-deflection curves, six increments are considered, and at each step, iterations are performed until the error norm, $\varepsilon=0.0005$ is satisfied. The average number of iterations satisfied for one increment is four or five step. The present results compare very well with those of Ref. [F-1].

In another example, a thin shell is studied by one half reduced thickness i.e. $h=6.35$ mm. The other dimension data, element-mesh grids and boundary conditions are unchanged. The same increment-number (six-steps) is used, and at each step, the same error-tolerance, $\varepsilon=0.0005$ is considered. In this case, the five steps in the average number of iterations are used in one increment. Also the results shown in Figures F-7 and F-8 are in excellent agreement with those by Hsiao[F-1].

3. Hinged Spherical Shell Cases with a Concentrated Central Load

Figure F-9 depicts a spherical shell subjected to the concentrated load at the crown. The boundary conditions of all edges are hinged and immovable. The 10×10 grid is used for one-quarter of the shell model. The error tolerance used here is $\varepsilon=0.0005$. The results are obtained using the same increments and average number of iterations required for one step used in the hinged cylindrical shell cases. In the model dimension, a squared side (a) is 61.8034 inch part of a sphere of radius $R=100$ in. It is subjected to a concentrated load at the crown with all hinged and immovable edges. The considered Young's modulus is $E=10^3$Ksi. The used Poisson's ratio is 0.3 and the thickness is $h=3.9154$ in. Figure F-10 shows the load-deflection curve at the crown and the maximum central deflection (11.746 in) is reached using 21 increments. This result of the hinged spherical shell also shows a good agreement with the results of Ref. [F-1].

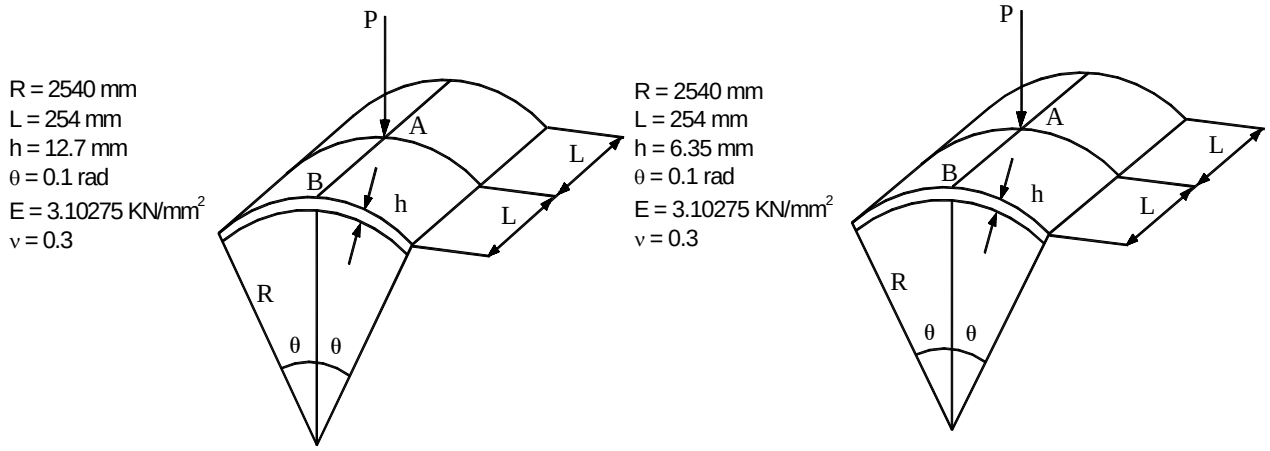

Figure F-4: Hinged cylindrical shells subjected to a concentrated load.

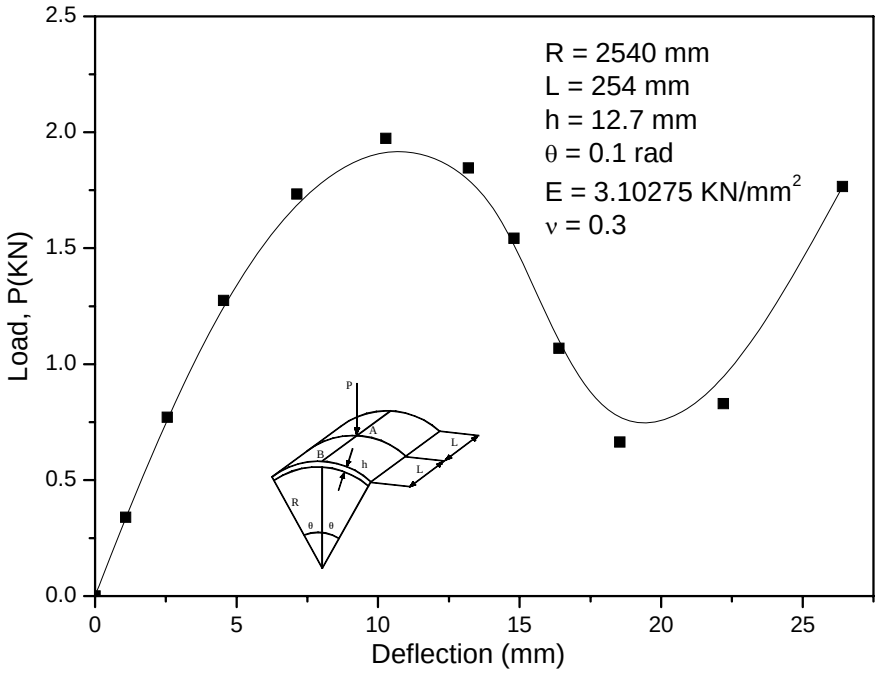

Figure F-5: Load-deflection curve at the center point of the hinged cylindrical shell.

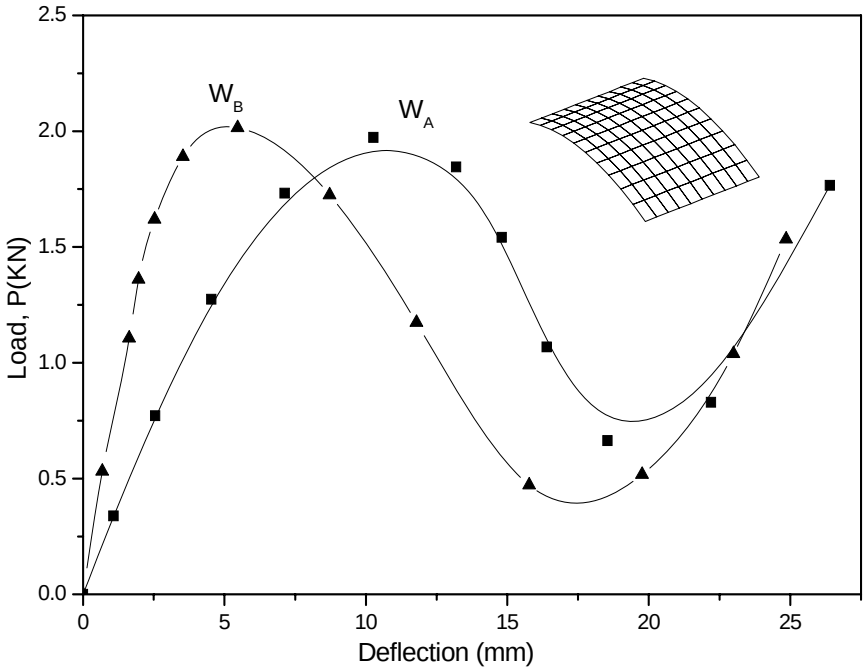

Figure F-6: Load-deflection curves at points A and B of the hinged cylindrical shell (h=12.7 mm).

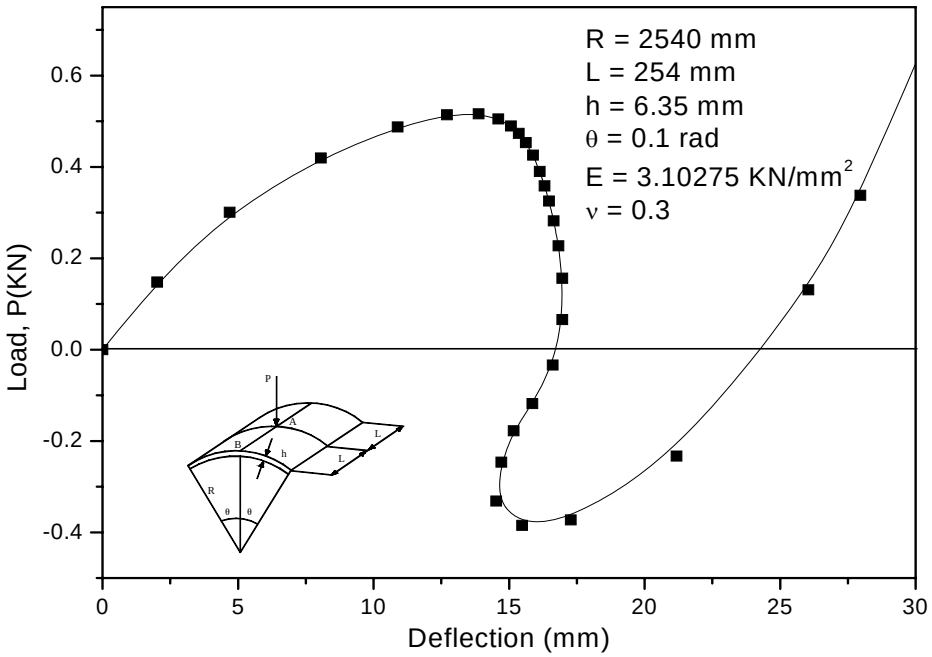

Figure F-7: Load-deflection curve at the center point of the hinged cylindrical shell.

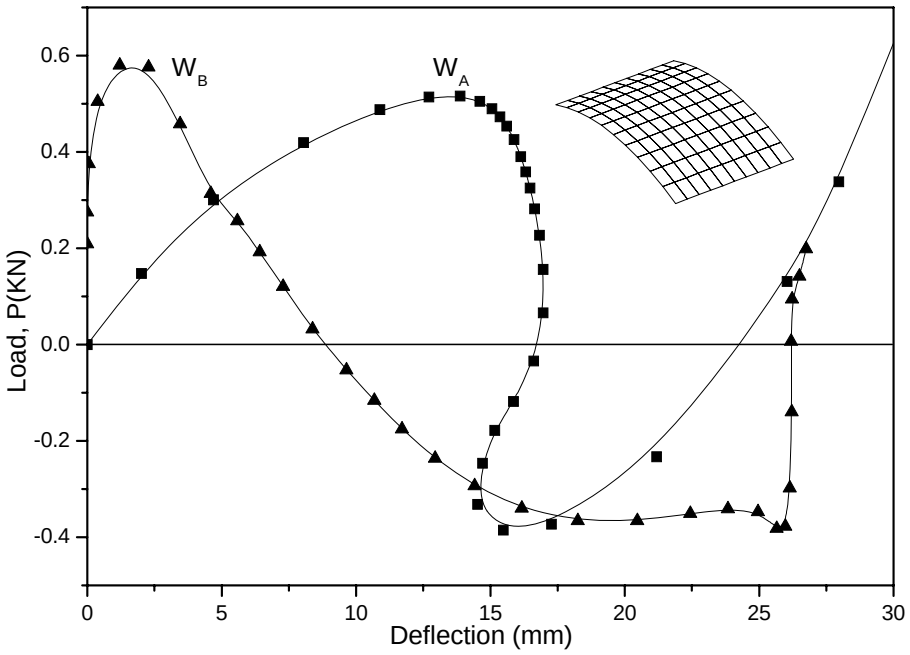

Figure F-8: Load-deflection curves at points A and B of the hinged cylindrical shell (h=6.35 mm).

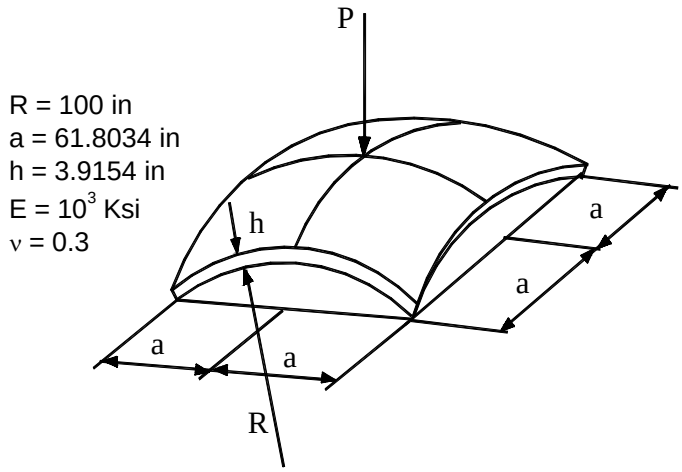

Figure F-9: The hinged spherical shell subjected to a central point load.

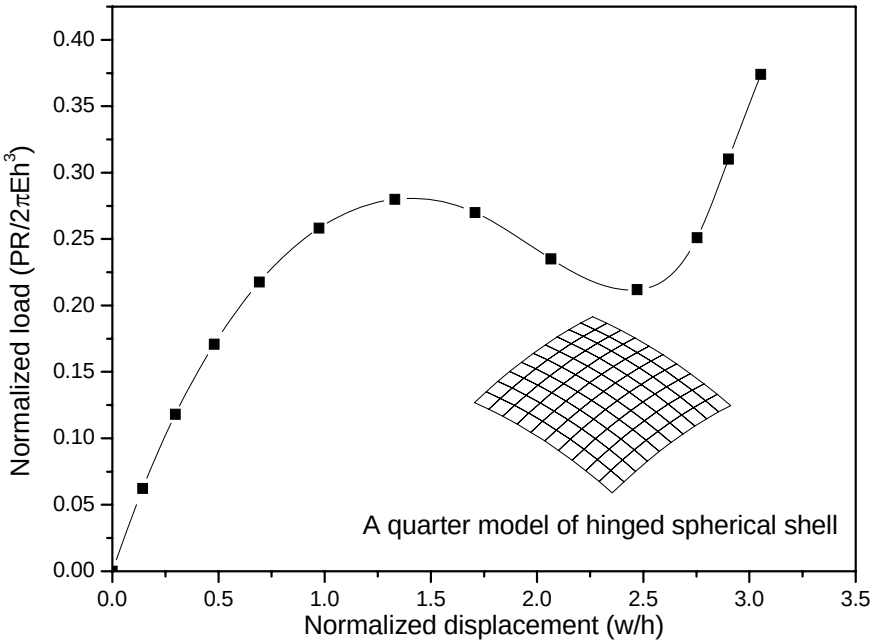

Figure F-10: Normalized load-deflection curve at the crown of the hinged spherical shell.

REFERENCES

E-1 Chen, W. F. and Han, D.J., *Plasticity for Structural Engineers*, Springer-Verlag, 1988.

F-1 Hsiao, K. M., "Nonlinear Analysis of General Shell Structures by Flat Triangular Shell Element," *Computers and Structures,* Vol. 25, No. 5, 1987, pp. 665-675.

F-2 Bathe, K. J. and Ho, L. W., "A Simple and Effective Element for Analysis of General Shell Structures," *Computers and Structures,* Vol. 13, 1981, pp. 673-681.

F-3 Yang, Y. B. and McGuire, W., "A Work Control Method for Geometrically Nonlinear Analysis," *Proceedings of International Conference on Advances in Numerical Methods in Engineering,* Swansea, U.K., 1985, pp. 913-921.

F-4 Bathe, K. J. and Dvorkin, E. N.,"On the Automatic Solution of Nonlinear Finite Element Equations," *Computers and Structures,* Vol. 17, 1983, pp. 871-879.

About the Author

Hur, Hae-Kyu was born 4 September 1966 in Kwangju-shi, Republic of Korea. In 1988, he graduated with honors from Aeronautical and Mechanical Engineering of Hankuk Aviation University, Korea. During the next four and half years, he fulfilled the military service for the Republic of Korea Special Warfare Command. In 1992, he entered Korea Electric Power Corporation as an engineer involved in the analysis and design of nuclear power plant structures. During 1995 to 1997, he studied for his Master of Science in the Aeronautical and Mechanical Engineering at Hankuk Aviation University, Korea. After finishing the M.S. studying, he worked as a research engineer at Korea Electronic Power Research Institute in Korea engaged in the development and support of the nuclear power plant structures and systems. From August 2000 to May 2001, he studied Ph.D. course in Aerospace Engineering department at Virginia Polytechnic Institute and State University. From August 2001 to December 2002, he also studied Aeronautical Engineering department at Purdue University as a Ph. D. graduate student. In January 2003, he returned to Virginia Polytechnic Institute and State University and continued the doctoral course on that time.